The contrasting geochemical behaviour of Sc and the other REE as exemplified by the Crater Lake and Ashram deposits, Québec, Canada

CAITLIN MARIE JOAN BELAND

April 2021

Department of Earth and Planetary Sciences,

McGill University, Montreal

A thesis submitted to McGill University in partial fulfillment of the requirements of the degree of Doctor of Philosophy

Contents

List of Figures

List of Tables

Abstract

Growing demand for the rare earth elements, particularly the heavy REE (HREE), has fuelled a boom in mineral exploration and scientific research on carbonatite-hosted deposits, especially those with unusual HREE enrichment. The Ashram REE deposit is such a HREE-enriched carbonatite-hosted REE deposit. This study uses textural observations of the REE minerals to establish a mineral paragenesis and reports the major and trace element compositions of these minerals. Variations in the latter are evaluated in the context of deposit-scale bulk geochemical trends and changes in lithology. Based on the results of this research, a genetic model for the Ashram deposit has been developed. Magmatic processes were important in the genesis of the deposit, but hydrothermal mobilization was the main process responsible for the concentration of the REE to potentially economic levels and the fractionation of the HREE.

The REE minerals in the Ashram deposit were precipitated from hydrothermal fluids. The composition of monazite-(Ce) varies with location in the deposit and is preferentially enriched in the light REE (LREE) with increasing distance from an irregular breccia body, underlying the zone of HREE enrichment. This body is interpreted to have been the main conduit for the mineralizing fluids, which on exiting, deposited monazite as a result of the cooling and pH buffering that accompanied their interaction with the adjacent carbonatites. Bastnäsite-(Ce) replaced monazite-(Ce) through ligand exchange, preserving the original REE distribution. Interaction of a compositionally evolving fluid with host rocks of variable bulk composition and buffering capacity resulted in deposit-scale fractionation and zonation of the REE.

A mass balance calculation was designed to quantitatively evaluate the relative importance of magmatic and hydrothermal processes in the concentration of the REE in carbonatitic systems, using the Ashram REE deposit as an example. The mass balance calculation traced each REE individually across all minerals from the primary magmatic to the secondary hydrothermal stages. The calculation showed quantitatively that at Ashram, all the REE were mobilized by hydrothermal fluids and concentrated to varying degrees in REE minerals. The extent to which the individual REE were concentrated in these minerals, however, decreased with increasing atomic number, and with decreasing fluid flow. These trends were the result of the relative thermodynamic stability of the various aqueous REE-complexes and REE minerals. Overall, magmatic and non-REE phases host a low proportion of the whole-rock REE concentration, especially of the LREE.

Scandium differs from the lanthanides and Y in that these REE behave incompatibly in most rock-forming minerals, whereas Sc behaves compatibly by partitioning strongly into ferromagnesian minerals. The study of the Crater Lake scandium deposit highlights the contrasting geochemical behaviour of Sc and the different geological processes that may lead to economic concentrations of the metal. The Crater Lake scandium deposit is the only syenite-hosted REE deposit with demonstrable production potential and in which scandium is the principal ore metal. Hedenbergite is the main scandium mineral at Crater Lake, but subordinate proportions of scandium are also hosted by hastingsite. These minerals are concentrated in cumulate layers of ferrosyenite. Fractional crystallization of hedenbergite and its concentration by gravitational settling and/or flow differentiation created ferrosyenite cumulates that potentially host a large scandium resource.

Résumé

La demande croissante pour les terres rares (ETR), en particulier les ETR lourds, a lancé une forte hausse de l'exploration minérale et de la recherche scientifique sur les gisements de carbonatites à terres rares, en particulier ceux avec un enrichissement en ETR lourds. Le gisement d'ETR d'Ashram est un gisement de type carbonatite enrichi en ETR lourds. Cette étude utilise des observations texturales des minéraux d'ETR pour établir une paragenèse minérale. L'étude rapporte aussi les compositions en éléments majeurs et traces de ces minéraux. Les variations minéralogiques, géochimiques et lithologiques sont évaluées à l'échelle du gisement. Basé sur les résultats de cette recherche, un modèle de genèse du gisement d'Ashram a été développé. Les processus magmatiques ont joué un rôle important dans la genèse du gisement, mais le mouvement des fluides hydrothermaux a été le principal processus responsable de la concentration des ETR à des niveaux potentiellement économiques ainsi que leur fractionnement concentrant les ETR lourds.

Les minéraux d'ETR dans le gisement d'Ashram ont été précipités à partir de fluides hydrothermaux. La composition de la monazite-(Ce) varie en fonction de son emplacement dans le gisement. Elle est aussi préférentiellement enrichie en ETR légèrs en s'éloignant d'un corps irrégulier de brèche sous-jacentes à la zone d'enrichissement d'ETR lourds. Ce corps est interprété comme ayant été le conduit principal des fluides minéralisants qui déposèrent de la monazite à la suite du refroidissement et de la mise en tampon qui accompagnaient l'interaction du fluide avec les carbonatites adjacentes. La bastnäsite-(Ce) a remplacé la monazite-(Ce) par échange de ligand, en préservant la distribution originale des ETR. L'interaction d'un fluide en évolution avec des roches encaissantes de composition et de capacité tampon variables a entraîné un fractionnement et une zonation des ETR à l'échelle du gisement.

Un calcul de bilan de masse, basé sur le gisement d'ETR d'Ashram, a été conçu pour évaluer de façon quantitative l'importance relative des processus magmatiques et hydrothermaux dans la concentration des ETR dans les systèmes carbonatitiques. Le calcul du bilan de masse a retracé chaque ETR individuellement à travers tous les minéraux, du stade magmatique primaire au stade hydrothermal secondaire. Le calcul a montré de façon quantitative que tous les ETR étaient mobilisées par les fluides hydrothermaux et concentrés dans les minéraux ETR à des degrés divers. La mesure dans laquelle les ETR individuels étaient concentrés dans ces minéraux

diminuait avec l'augmentation du numéro atomique et avec la diminution du débit de fluide. Ces tendances sont le résultat de la stabilité thermodynamique relative des divers complexes d’ETR aqueux et des minéraux d’ETR. Les phases magmatiques hébergent une faible proportion des ETR, en particulier des ETR légers.

Le scandium diffère des lanthanides et de l’yttrium, puisque ceux-ci se comportent de manière incompatible dans la plupart des minéraux, tandis que le scandium se comporte de manière compatible en se répartissant en minéraux ferromagnésiens. L'étude du gisement de scandium de Crater Lake met en évidence le comportement géochimique contrasté du scandium et les différents processus géologiques pouvant causer des concentrations économiques du métal. Le gisement de scandium de Crater Lake est le seul gisement d’ETR dans une syénite dans lequel le scandium est le principal minerai métallique. L'hédenbergite est le principal minéral de scandium à Crater Lake, mais des proportions moindres de scandium sont contenues dans l'hastingsite. Ces minéraux sont concentrés dans des couches cumulées de ferrosyénite. La cristallisation fractionnée de l'hédenbergite et sa concentration par sédimentation gravitationnelle et/ou différenciation de courant ont créé des cumulas de ferrosyénite qui hébergent potentiellement une importante ressource de scandium.

Acknowledgements

First and foremost, very special thanks go to my supervisor, Anthony E. Williams-Jones for his unending support, encouragement, and advice. I am grateful for Willy's expertise, patience, and sense of humour in the revising and editing of the manuscripts. I am also thankful to Willy for the opportunity to participate in international research conferences. The funding of the thesis was provided by grants from MITACS, NSERC, and Imperial Mining Group Ltd. to Dr. Anthony E. Williams-Jones and financial support to the author from the Department of Earth and Planetary Sciences, McGill University.

During fieldwork, I appreciated many spirited debates and discussions with Matthew Carter and Alex Knox (Dahrouge Geological Consulting Ltd.). I am grateful for the support, encouragement, and friendship of Brad Ulry, Ryan Woods, Dustin Hayes, and Chade Salame of Dahrouge Geological Consulting. The many weeks spent at camp were made much more enjoyable by the cooking and friendship of Trina Wellman. Thanks to Peter Cashin and Pierre Guay (Imperial Mining Group Ltd.) for the provision of logistics and data for Crater Lake, for sharing their extensive knowledge of the area, and for many fruitful discussions.

At the Department of Earth and Planetary Sciences (McGill University), Lang Shi provided invaluable help and guidance at the electron microprobe facility. Special thanks go to Olga Vasyukova for many lively discussions, sharing her in-depth scientific knowledge, and her friendship. The guidance of Vincent Van Hinsberg and John Stix were greatly appreciated throughout my Ph.D. I am grateful for my fellow graduate students, especially from Willy's research group, for help with analytical techniques and navigating the department and the city of Montreal. In particular, Rowan Wollenberg, Samantha Carruthers, and Andres Peña Castro are thanked immensely for being great friends and listeners.

My partner Nick Egan provided constant encouragement and support throughout the publication process of the manuscripts and the preparation of the thesis. I was especially heartened by the love and support of my closest friends Rimmy Dhadda and Stefan Boraks, my brothers Jon, Tim, and Nick, and my parents throughout my Ph.D.

Contributions of co-authors

Chapters 2, 3, and 4 of this thesis are original research article manuscripts that were prepared by myself and Anthony E. Williams-Jones. The contribution of the first author includes the acquisition of the geological, petrographic, and analytical data, and data treatment, analysis and interpretation. A.E. Williams-Jones was mainly involved in the planning, discussion, and interpretation of the findings and in the preparation of the manuscripts. Chapters 1 and 5 of the thesis were written by myself and were improved through editing and advice from A.E. Williams-Jones.

Preface

This research was performed in the Department of Earth and Planetary Sciences at McGill University. Access to the Eldor area, drill core, and assay data was provided by Commerce Resources Corp. and Dahrouge Geological Consulting Ltd. Fieldwork was conducted over several months during 2015 and 2016, and included regional/local mapping, and core-logging. Matthew Carter and Alex Knox assisted with the fieldwork. Access to the Crater Lake area was provided by Imperial Mining Group Ltd., and the work was accomplished over the summer of 2018 and winter of 2019, aided by Peter Cashin and Pierre Guay. Fieldwork at Crater Lake included detailed mapping and core-logging.

At McGill University, Lang Shi helped with the electron microprobe mineral analyses, Anna Jung and Longbo Yang supervised mineral analyses at the Laser Ablation ICP MS facility, and the carbon and oxygen isotope analyses were performed by Thi Hao Bui at the Stable Isotope laboratory.

The author prepared the samples (grinding), performed the analyses (SEM, EMPA, LA-ICP-MS), and carried out the data reduction and calculations. The author also interpreted the results and with the help of Dr. Anthony E. Williams-Jones, wrote the manuscripts and submitted the research for publication.

The thesis consists of three manuscripts that are the product of collaboration between the author and Dr. Anthony Williams-Jones, the supervisor of this research.

The current status of the material contained in this thesis is as follows:

Chapter 2: PUBLISHED – Beland, C.M.J., and Williams-Jones, A.E., 2021, The genesis of the Ashram REE deposit, Quebec: insights from bulk-rock geochemistry, apatite-monazite-bastnäsite replacement reactions and mineral chemistry: Chemical Geology, v. 578, 120298

Chapter 3: IN REVIEW – Beland, C.M.J., and Williams-Jones, A.E., The distribution of the REE in carbonatites: a quantitative evaluation, Chemical Geology

Chapter 4: IN REVIEW – Beland, C.M.J., and Williams-Jones, A.E., The genesis of a potential scandium ore deposit at Crater Lake, Canada, Economic Geology

Chapter 1 - Thesis Introduction

This study in economic geology focusses on two deposits in Québec: the carbonatite-hosted Ashram REE deposit and the syenite-hosted Crater Lake Sc deposit. This chapter gives a brief introduction to the economic geology of the REE, including Sc, their geochemical behaviour, the main deposit types and host rocks, and the proposed mechanisms for metal enrichment to economic concentrations. Although scandium is a rare earth element, in this chapter, the term "REE" refers only to the lanthanides and yttrium. In this thesis, the light REE (LREE) are defined as La, Ce, Pr, Nd, the term "middle REE" (MREE) refers to Sm, Eu, Gd, and the heavy REE (HREE) are defined as Tb, Dy, Y, Ho, Er, Tm, Yb, Lu.

1.1 Economic geology of the REE

The rare earth elements (REE; the lanthanides, Y, and Sc) are treated as a group because of their position in the periodic table, but each element has a specific set of end uses, most commonly in various high technology applications, including fiber optics (addition of Er, Yb improves data transfer speeds), consumer electronics (La in optical lenses of smartphones and tablets), and phosphors (Y in fluorescent and LED lighting) (Goodenough et al., 2017). Scandium is desirable as an alloy with aluminum as it decreases the density and increases the tensile strength and weldability of the alloy (Filatov Yu et al., 2000; Chhangani et al., 2020), making it highly sought after in the aerospace, automotive, and shipbuilding industries. The best-known use of the REE, however, is their use in permanent NdFeB (± Dy) magnets, which have applications in power generation, robotics, and significantly, hybrid and electric vehicles.

The global demand for the REE (excluding Sc) nearly doubled from 75,500 tonnes (t) in the year 2000 to 123,100 t in 2016 (Roskill 2016b) and is predicted to continue to increase as it is intimately tied to the hybrid and electric vehicle markets, which are forecast to increase nearly 5-fold from 2016 to 2026 (Roskill, 2016a). This surge in demand for these metals has also been influenced by political factors. China has dominated global production of the REE since the mid 1980's, (Massari and Ruberti, 2013; Wall, 2014), but export quotas introduced in 2010 highlighted the international dependency on China and resulted in a rise in prices and a boom of exploration for REE deposits elsewhere (Cordier, 2011). Since 2010, many governments have classified the REE, including Sc, as 'critical metals' (Jowitt et al., 2018), a trend that was reinforced in 2020 when the United States declared the vulnerability of their REE supply a national emergency (Executive Order 13593 (2020)).

Annually, 130,000 and 16,000 t are produced of the REE and Sc, respectively (Jowitt et al., 2018; Duyvesteyn and Putnam, 2014) from a relatively small number of mines globally. Current producers of the REE include the carbonatite-associated Bayan Obo mine (China; + Sc); the Maoniuping carbonatite (China); the Mountain Pass carbonatite (USA); Mount Weld, a laterite developed over a carbonatite (Australia); the nepheline syenite-hosted Lovozero mine (Russia); monazite sand placer operations in India (Sengupta and Van Gosen, 2016) and Australia (Jaireth et al 2014; Mudd and Jowitt, 2016); and ion-adsorption clays in China. Scandium is also produced at the carbonatite-associated Kovdor and Tomtor mines in Russia. Clearly, carbonatites are an important source of the REE and Sc. They also tend to be light rare earth (LREE; La-Nd) enriched (Pell, 1996). Indeed, these rocks are the principal source of the LREE and the deposits hosted by or associated with them are responsible for >60% of the global resources of these elements (Zhou et al., 2017). This distribution of the REE drives the prices of the metals, such that the heavy REE (HREE; Tb-Lu) are more valuable than the LREE (e.g. Dy metal: 3000 USD/kg vs Nd metal: 400 USD/kg; Hatch, 2012). There has been considerable exploration for the REE in alkaline silicate rocks (e.g., the Nechalacho, Strange Lake, and Kipawa deposits, Canada) because they are more HREE-enriched than carbonatites, though typically they feature complex REE-mineralogy (e.g., REE-rich eudialyte ($Na_{15}Ca_6Fe_3Zr_3Si(Si_{25}O_{73})(O,OH,H_2O)_3(Cl,OH)_2$) for which there are no established processing paths. The only minerals from which the REE have been extracted on a commercial scale are monazite ($LREEPO_4$), xenotime ($HREEPO_4$), bastnäsite ($LREECO_3F$), and loparite ($(Na,REE)_2Ti_2O_6$) (Jordens et al., 2013). Scandium is currently produced from baddeleyite (ZrO_2), aegirine ($NaFeSi_2O_6$), and xenotime (Liferovich et al., 1998; Kalashnikov et al., 2016; Chao et al., 1992; Fan et al., 2016; Lapin et al., 2016).

1.2 Geochemical behaviour of the REE and Sc under magmatic conditions

The geochemical behaviour of the REE and Sc is largely controlled by their ionic charge and ionic radii. With the exception of Eu^{2+} under reducing conditions and Ce^{4+} under oxidizing conditions, the REE and Sc have a 3+ charge. The lanthanides and Y are characterized by intermediate-sized ionic radii which decrease with increasing atomic number, known as the ‘lanthanide contraction’, such that the ionic radius of six-fold coordinated La^{3+} is much larger than that of Lu^{3+} (1.032 versus

0.861, respectively; Shannon, 1976). Scandium has an even smaller ionic radius of 0.745 (six-fold coordinated Sc^{3+}; Shannon, 1976), and is thus most similar to the HREE. Owing to their high ionic charge to radius ratios (>2), the lanthanides and Y behave incompatibly in most rock-forming minerals and during most magmatic processes. In marked contrast, scandium behaves compatibly in ferromagnesian minerals because its ionic radius is between that of Mg^{2+} and Fe^{2+} (0.72 and 0.78, respectively, six-fold coordination; Shannon, 1976). This difference in geochemical behaviour between Sc and the other REE has important implications for which processes may be mineralizing for the different metals.

Carbonatites and alkaline silicate rocks (e.g., syenite), the principal hosts of REE deposits globally, crystallize from magmas formed in anorogenic settings by low degrees of partial melting of the mantle (e.g. Gudfinnsson and Presnall, 2005; Bonin, 2007). These magmas are typically LREE-enriched and HREE-depleted due to melting of clinopyroxene, a significant reservoir of the REE and Sc in the mantle, and the presence of refractory garnet in the source rock, a mineral that preferentially incorporates the HREE. Carbonatite magmas may also be produced from a carbonated silicate magma by fractional crystallization or liquid immiscibility. In the former case, the REE are typically concentrated in the residual carbonatite liquid due to their incompatible behaviour, whereas the compatible behaviour of scandium leads it to fractionate into early crystallizing ferromagnesian minerals in the silicate melt. Carbonatites formed by liquid immiscibility may be further LREE-enriched and Sc-depleted, as the LREE prefer the carbonate melt and the HREE and Sc prefer the silicate melt, except for very hydrous systems (Martin et al., 2013).

1.3 Mineralizing processes for the REE in carbonatites

In carbonatite magmas, the distribution of the REE is controlled by the nature and timing of the crystallizing minerals and mineral-melt partitioning. Carbonatite complexes are commonly characterized by early apatite-rich calcite carbonatite and later Fe-Ba-Sr-REE-rich dolomite carbonatite as a result of the fractionation of apatite, phlogopite, calcite and dolomite (e.g., Le Bas and Handley, 1979; Bühn and Rankin, 1999; Xie et al., 2009). In some cases, REE-minerals such as burbankite, monazite, or bastnäsite may have crystallized directly from the carbonatite magma (e.g. Zaitsev et al., 2002; Giebel et al., 2017), though extremely rarely in sufficient proportions to constitute ore. Indeed, the only carbonatite-hosted REE deposit in which the bulk of the mineralization is interpreted to be magmatic in origin, is the Mountain Pass deposit (Olson et al., 1954; Mariano, 1989). At Mountain Pass, bastnäsite occurs in layers within carbonate minerals (Castor, 2008), a texture historically interpreted as evidence of flow-banding. Though they are not typically ore minerals for the REE, pyrochlore and fluorapatite commonly occur in carbonatites and may incorporate appreciable proportions of the REE. Moreover, apatite may strongly influence the distribution of the REE (e.g., Chakhmouradian et al., 2016, 2017) as it commonly crystallizes in significant volumetric proportions.

There are very few cases for which concentration of the REE exclusively by magmatic processes has been demonstrated. However, hydrothermal fluids of magmatic origin may play an essential role in concentrating the REE to potentially economic levels by transferring them directly from the magma to REE ore minerals (e.g., monazite) after exsolution. This has been proposed as the mineralizing mechanism for several carbonatite-hosted REE deposits, including Bayan Obo (Smith et al., 2015) and Maoniuping, China (Xie et al., 2015), Jacupiranga (Costanzo et al., 2006) and Barra do Itapirapua, Brazil (Ruberti et al, 2008), Karrat Isfjord, Greenland (Mott et al., 2013) and Wicheeda (Trofanenko et al., 2016) and Montviel, Canada (Nadeau et al., 2015). An integrated magmatic-hydrothermal model has been proposed for the carbonatite-hosted mineralization at Amba Dongar, India (Doroshkevich et al., 2009) and Phalaborwa, South Africa (Giebel et al., 2017). At these locales, carbonatite-derived hydrothermal fluids leached and remobilized the REE from primary, magmatic minerals (e.g. apatite, pyrochlore).

Unequivocal evidence for transport of the REE by carbonatite-derived hydrothermal fluids has been only rarely provided, including from the presence of REE daughter minerals (e.g., burbankite) in primary fluid inclusions from the Chilwa Island carbonatite, Malawi (Dowman et al., 2017) and by crush-leach analyses of quartz-hosted fluid inclusions from the Kalkfeld and Okurusu carbonatites (Bühn and Rankin, 1999; Bühn et al., 2002). There is, however, a large and growing body of experimental evidence that the REE can be transported in appreciable concentrations in aqueous solutions at elevated temperature (e.g., Gammons et al., 2002; Migdisov and Williams-Jones, 2008; Migdisov et al., 2009; Louvel et al., 2015; Zhou et al., 2016; Liu et al., 2017; Mair et al., 2017; Gysi et al., 2018). This transport is thought to occur through the complexation of the REE with chloride and sulfate ions. Phosphate and fluoride ions are considered depositional ligands due to the fact that monazite and fluocerite have very low solubility, which buffers the concentration of these ions to very low levels (Williams-Jones et al., 2012; Migdisov et al., 2016). Although carbonate is clearly a depositional ligand for REE-fluorocarbonate minerals like bastnäsite, it has yet to be established whether or not carbonate and/or bicarbonate ions can also act as transport ligands.

1.4 Mineralizing mechanisms for Sc

As a result of the historically low demand for scandium, there are few mineral deposits from which it has been produced and there has been very little research investigating the behavior of scandium in nature and the reasons for its concentration in these deposits. Scandium may be concentrated by a variety of processes involving magmas, hydrothermal fluids, and surface waters. The only three current Sc producers, Kovdor and Tomtor (Russia) and Bayan Obo (China) are deposits that are either magmatic in origin or formed from fluids released by magmas. A major past producer was the Zhovti Vody deposit in the Ukraine, in which the scandium is concentrated in metasomatic aegirine and riebeckite in amphibolite (Tarkhanov et al., 1992). In addition, there has been minor production from magmatic thortveitite ($(Sc,Y)_2Si_2O_7$) in NYF granitic pegmatites in Madagascar (Murdock, 1963) and Norway (e.g., Müller et al., 2015). Thus, to date, the bulk of the scandium production has been from carbonatites, from a carbonatite-related metasomatic deposit and a metasomatic deposit for which the source of the fluid is unknown. A new scandium resource was recently discovered in ferrodiorite of the Kiviniemi mafic intrusion, Finland, and the main carriers of scandium in these rocks are magmatic amphibole, clinopyroxene, and apatite (Halkoaho et al., 2020). Apart from this deposit, and those in NYF pegmatites, there are no examples of Sc deposits hosted by alkaline igneous rocks other than at Crater Lake, Québec, which is a subject of this thesis.

Clearly, fractionation of Sc-bearing minerals in carbonatite magmas is an important Sc mineralizing process, and typically occurs as early crystallizing zirconium or phosphate minerals (e.g., baddeleyite, xenotime). As outlined above, some carbonatite magmas are produced by carbonate-silicate liquid immiscibility, a process that concentrates Sc in the silicate melt (Martin et al., 2013). As was the case for the Kiviniemi deposit, fractionation of Sc-bearing minerals in silicate magmas can also be a mineralizing process. Indeed, Williams-Jones and Vasyukova (2018) reviewed the mineral-melt Sc partitioning behaviour of rock-forming minerals and showed that for common ferromagnesian minerals (e.g., clinopyroxene, amphibole), Sc prefers the mineral, and that partition coefficients increase with decreasing melt MgO content. In both carbonate and silicate magmas, however, physical segregation of the Sc-bearing mineral, either by flow differentiation or gravitational settling, can be an essential process to concentrate Sc to potentially economic levels.

Hydrothermal fluids can also play an important role in concentrating Sc, as illustrated by the metasomatic aegirine ores of the Bayan Obo and Zhovti Vody deposits. At Bayan Obo, Sc was transported and deposited by a carbonatite-derived fluid into unrelated dolomites (Smith et al., 2015). At Zhovti Vody, the replacement of magmatic amphibole by metasomatic aegirine was mediated by fluids of unknown origin (Tarkhanov et al., 1992) and it is unclear whether the fluid was the source of scandium, or concentrated Sc by leaching/remobilizing from primary minerals. Unlike the lanthanides and Y, there is little experimental data for the aqueous geochemistry of Sc at ambient temperature, and none at high temperature (reviewed in Williams-Jones and Vasyukova, 2018).

1.5 A brief history of the Eldor Carbonatite Complex and its Ashram REE deposit

This section gives an overview of the discovery of the Eldor Carbonatite Complex and its Ashram REE deposit, and the previous research conducted on them. The Eldor Carbonatite Complex is located approximately 130 km south of Kuujjuaq, in northern Québec, Canada, is exposed over an area of approximately 7 x 3 km (Sherer, 1984), and is hosted by rocks of the Labrador Trough, which is the foreland of the New Quebec Orogen, a Paleoproterozoic fold and thrust belt on the eastern margin of the Superior Province (Clark and Wares, 2006). Eldor Resources Ltd. discovered the Eldor Carbonatite Complex in 1981 from the results of a regional lake-water and sediment sampling program targeting uranium mineralization (Gagnon et al., 2012). A later airborne radiometric survey identified several anomalies, and rock samples from these targets returned high Nb-Ta-REE values. Following discovery of the carbonatite, researchers attempted to place its occurrence within a regional context. The emplacement age of the carbonatite is unknown, though it is constrained to be younger than 1870 ± 4 Ma by the U-Pb age of a rhyodacite which it crosscuts (Machado et al., 1997). Machado et al. (1997) suggested that intrusion of the Eldor carbonatite was contemporaneous with deposition of the Aulneau Formation, composed of tuffaceous dolomite and dolomitic tuffs (Dressler, 1979). Some researchers have interpreted the Aulneau formation to comprise intercalated volcanic carbonatite and sedimentary carbonate, leading to the suggestion that the Eldor carbonatite was subvolcanic with effusive equivalents in a shallow marine setting (Clark & Wares, 2006). There has been limited scientific research conducted on the carbonatites, focussed mainly on their mineral potential (Birkett and Clark, 1991) and characterization of the Nb-Ta mineralization, which occurs as pyrochlore (Wright et al., 1998).

Little mineral exploration work was conducted on and around the carbonatite until 2007, when Commerce Resources Corp. purchased the property and commenced exploration for Nb and Ta based on the historical showings. In 2009, REE mineralization was discovered in outcrop near the core of the carbonatite, and the changing global market conditions for the REE shifted the focus of exploration from Nb-Ta to the REE. The core of the Eldor Carbonatite Complex then became known as the Ashram REE deposit. Commerce Resources Corp. continues to hold the property and has evaluated the Ashram REE mineral resource through diamond drilling. The last resource estimate was completed in 2012 and used data from 16 km of drilling over 45 holes (Gagnon et al., 2012). Commerce Resources Corp. reported a measured and indicated resource of 29.3 Mt at 1.90 % total rare earth oxides (TREO, here defined as the lanthanides + Y), and another 219.8 Mt at 1.88 % TREO in the inferred category, using a cut-off grade of 1.25 % TREO. Overall, Ashram is LREE enriched, as is typical for carbonatite-hosted REE deposits. There is, however, a zone of preferential middle-heavy REE enrichment (the MHREO zone). This enrichment, which is unusual for a carbonatite, makes Ashram an especially desirable target economically. As of 2016, Commerce Resources Corp. had drilled over 25 km of drill core over 170 holes. In 2017, Saville Resources Inc. entered into an agreement with Commerce Resources Corp. to explore the Nb mineralization in the outer part of the Eldor carbonatite.

Research on the Ashram deposit has been limited to an unpublished M.Sc thesis, which provided a general description of the various lithofacies and mineralization (Schmidt, 2013). During the course of the research for the present thesis, an article describing the mineralogy and paragenesis was published (Mitchell and Smith, 2017). There is also ongoing doctoral research on the Nb mineralization in the outer part of the Eldor Carbonatite Complex by Patrik Schmidt (University of Windsor, Ontario).

1.6 A brief history of the Crater Lake Syenite Intrusion and REE-Sc deposit

This section provides a summary of the discovery of the Crater Lake intrusion and its REE-Sc deposit, and the previous research completed on them. The Crater Lake intrusion (formerly known as Misery Lake) is located approximately 200 km east-northeast of Schefferville, in northern Québec and was discovered as the result of an airborne magnetic survey that identified a prominent, 6 km wide ring-shaped anomaly (Dumont et al., 2010). After acquiring the property in 2008, Quest Uranium Corp. commissioned high resolution airborne magnetic and radiometric surveys and conducted a glacial till sampling program over the anomaly. The till sampling program returned high REE values at the edges of the circular feature, coincident with magnetic highs. Under the name Quest Rare Minerals Ltd., exploration for the REE at Crater Lake continued with bedrock mapping and diamond drilling until 2014, when the property was transferred to Imperial Mining Group Ltd (Daigle, 2017). Imperial Mining Group Ltd. geologists noted that ferrosyenite intersected in by Quest Rare Minerals drill holes targeting the magnetic highs was enriched in Sc, potentially to economic levels. The focus of their exploration therefore shifted from the REE (lanthanides + Y) to Sc (Daigle, 2017). Significant diamond drilling results include up to 262 ppm Sc (and 1.18 wt. % TREO + Y) over 167.83 m, and 351 ppm Sc (and 1.72 wt. % TREO + Y) over 27.6 m (Daigle, 2017). Additionally, a grab sample of ferrosyenite from the discovery outcrop had returned 1000 ppm Sc (Petrella et al., 2014).

Research on the Crater Lake intrusion includes age dating by government geologists (Ministère des Ressources Naturelles et de la Faune) and a M.Sc. thesis (Petrella, 2012), the results of which were later published as a scientific research article (Petrella et al., 2014). Crater Lake syenite was dated at 1409.7 ± 1.2 Ma (David et al., 2012), using U-Pb radiometric methods applied to zircon. The work of Petrella (2012) identified and characterized the different lithofacies of the intrusion, as well as the REE mineralization in the ferrosyenite. Based on field relationships, textural observations, and whole-rock geochemical trends, Petrella et al. (2014) advanced a genetic model in which the ferrosyenite represents a cumulate facies of the Crater Lake intrusion. The ferrosyenite contains abundant LREE-rich fluorapatite which was later altered hydrothermally to britholite ($(Ce,Ca)_5(SiO_4)_3OH$) (Petrella et al., 2014).

1.7 Rationale and objectives of the research

The goal of the research presented in this thesis is to contribute to the understanding of the processes which may concentrate the lanthanides and Y in carbonatites and Sc in alkaline silicate rocks, to potentially economic levels. The Ashram REE deposit provides a rare opportunity to investigate the relative importance of magmatic and hydrothermal processes in carbonatite-related REE ore formation and the processes by which the REE may be fractionated in carbonatitic environments. This is because the deposit contains several REE minerals that are spatially separated on a deposit-scale, and there is an unusual zone of middle REE (MREE; Sm, Eu, Gd) and HREE enrichment. Another striking feature of the Ashram deposit is that the mineralization is dominantly in the form of REE-phosphate (mainly monazite), whereas most carbonatite REE ores are dominated by the REE-fluorocarbonates. As previous studies of Ashram have been descriptive in nature, the objectives of the present research were to explain why the mineralization occurs dominantly as REE-phosphate, explain the spatial separation of the various REE minerals, and develop the first genetic model for the origin of mineralization at Ashram. Detailed textural observations of the REE minerals and associated phases were used to establish a mineral paragenesis for the Ashram deposit, and analyses of the major and trace element compositions of all rock-forming and REE minerals were used to evaluate the evolution of the system. A genetic model for the Ashram REE deposit was developed based on the variations in mineral compositions relative to deposit-scale bulk geochemical trends, changes in lithology, and stable C-O isotopic compositions. The mineral compositional data collected was also used in conjunction with the bulk-rock compositional data to perform mass balance calculations for the Ashram rocks to provide the first-ever quantitative evaluation of the distribution of REE in carbonatites. This study traced the contribution of each primary (magmatic) and secondary (hydrothermal) mineral to the whole-rock budget of each REE, thereby allowing a comprehensive evaluation of the changing distributions of the different REEs from the early crystallisation of the carbonatite to the development of a potentially economic REE ore deposit. Lastly, the study of the Sc mineralization at the Crater Lake REE-Sc deposit characterized the first scandium deposit discovered in Canada, and the first known syenite-hosted Sc deposit anywhere. This research used whole-rock geochemical and mineral chemical data to identify the host minerals of scandium in the ferrosyenite and developed a genetic model for the origin of the mineralization.

1.8 Thesis Organization

This thesis is manuscript-based and consists of five chapters: a general introduction (Chapter 1), three main chapters that comprise research article manuscripts (Chapters 2 to 4), and a general conclusion and summary of contributions to the scientific community (Chapter 5). Chapter 2 develops a genetic model for the REE mineralization in the Ashram deposit in the Eldor Carbonatite Complex using a combination of textural observations, mineral compositions, and deposit-scale bulk geochemical trends (published in Chemical Geology). Chapter 3 provides a quantitative evaluation of the distribution of the REE in the Ashram carbonatites that employs mineral compositions from Chapter 2 in mass balance calculations, the results of which are then interpreted in the context of the genetic model advanced in Chapter 2 (submitted to Chemical Geology and currently in review). Chapter 4 is a case study of the Sc mineralization at Crater Lake, which utilizes whole-rock geochemical and mineral chemical data to establish the distribution of Sc in the ferrosyenite and model the processes responsible for its concentration (submitted to Economic Geology and currently in review).

1.9 References

Birkett, T.C. and Clark, T., 1991, A Lower Proterozoic carbonatite at lac LeMoyne, northern Quebec: Geology and mineral potential. Geological Survey of Canada, Current Activities Forum, Program with Abstracts, p18.

Bonin, B., 2007, A-type granites and related rocks: Evolution of a concept, problems and prospects: Lithos, v. 97, p. 1-29.

Bühn, B., and Rankin, A.H., 1999, Composition of natural, volatile-rich Na-Ca-REE-Sr carbonatitic fluids trapped in fluid inclusions: Geochimica et Cosmochimica Acta, v. 63, p. 3781-3797.

Bühn, B., Rankin, A.H., Schneider, J., and Dulski, P., 2002, The nature of orthomagmatic, carbontitic fluids precipitating REE, Sr-rich fluorite: fluid inclusion evidence from the Okorusu fluorite deposit, Namibia: Chemical Geology, v. 186, p. 75-98.

Castor, S.B., 2008, The Mountain Pass Rare-Earth Carbonatite and Associated Ultrapotassic Rocks, California: The Canadian Mineralogist, v. 46, p. 779-806.

Chakhmouradian, A.R., Reguir, E.P., Couëslan, C., and Yang, P., 2016, Calcite and dolomite in intrusive carbonatites. II. Trace-element variations: Mineralogy and Petrology, v. 110, p. 361-377.

Chakhmouradian, A.R., Reguir, E.P., Zaitsev, A.N., Couëslan, C., Cheng, X., Kynicky, J., Mumin, A.H., and Yang, P., 2017, Apatite in carbonatitic rocks: Compositional variation, zoning, element partitioning and petrogenetic significance: Lithos, v. 274-275, p. 188-213.

Chao, E.C.T., Back, J.M., Minkin, J.A., and Ren, Y.C., 1992, Host-rock controlled epigenetic, hydrothermal metasomatic origin of the Bayan Obo REE-Fe-Nb ore deposit, Inner Mongolia, P.R.C.: Applied Geochemistry, v. 7, p. 443-458.

Chhangani, S., Kumar Masa, S., Mathew, R.T., Prasad, M.J.N.V., and Sujata, M., 2020, Microstructural evolution in Al-Mg-Sc alloy (AA5024): Effect of thermal treatment, compression deformation and friction stir welding: Materials Science & Engineering A, v. 772, 138790.

Clark, T. and Wares, R., 2006, Lithotectonic and Metallogenic Synthesis of the New Quebec Orogen (Labrador Trough). MM 2005-01.

Cordier, D., 2011, Rare Earths. USGS Mineral Commodity Summary.

Costanzo, A., Moore, K.R., Wall, F. and Freely, M., 2006, Fluid inclusions in apatite from Jacupiranga calcite carbonatites: Evidence for a fluid-stratified carbonatite magma chamber: Lithos, v. 91, p. 208-228.

Daigle, P.J., 2017, Crater Lake Sc-Nb-REE Project, Quebec, Canada. NI 43-101 Technical Report, prepared by P. Daigle Consulting Services for Peak Mining Corporation, NQ Exploration Inc., and Imperial Mining Group Ltd., 68 p.

David, J., Simard, M., Bandyayera, A., Goutier, J., Hammouche, H., Pilote, P., Leclerc, F., and Dion, C., 2012, Datations U-Pb effectuees dans les provinces du Superieur et de Churchill en 2010-2011 : Geologie quebec, Ministère des Ressources Naturelles et de la Faune (MRNF), RP2012-01, 30 p.

Dowman, E., Wall, F., Treloar, P.J., and Rankin, A.H., 2017, Rare-earth mobility as a result of multiple phases of fluid activity in fenite around the Chilwa Island Carbonatite, Malawi: Mineralogical Magazine, v. 81, p. 1367-1395.

Doroshkevich, A.G., Viladkar, S.G., Ripp, G.S., and Burtseva, M.V., 2009, Hydrothermal REE mineralization in the Amba Dongar Carbonatite Complex, Gujarat, India: The Canadian Mineralogist, v. 47, p. 1105-1116.

Dumont, R., Fortin, R., Hefford, S., and Dostaler, F., 2010, Serie des cartes geophysiques, parties des SNRC 13L, 13M, 23-I et 23P, leve geophysique Lac Ramusio, Region de Schefferville : Ministère des Ressources naturelles et de la Faune, DP2010-01, 6 p.

Duyvesteyn, W.P.C., and Putnam, G.F., 2014, Scandium, a review of the element, its characteristics, and current and emerging commercial applications: Sparks, Nevada, EMC Metals Corp., p. 1–12.

Dressler, B., 1979, Region de la Fosse du Labrador (56°30’-57°15’). Ministere des Richesses naturelles, Quebec; RG 195.

Fan, H.R., Yang, K.F., Hu, F.F., Liu, S., and Wang, K.Y., 2016, The giant Bayan Obo REE-Nb-Fe deposit, China: Controversy and ore genesis: Geoscience Frontiers, v. 7, p. 335-344.

Filatov Yu, A., Yelagin, V.J., and Zakharrov, V.V., 2000, New Al-Mg-Sc alloys: Materials Science & Engineering A, v. 280, p. 97-101.

Gagnon, G., Rousseau, G., Camus, Y. and Gagne, J., 2012, NI 43-101 Technical Report – Preliminary Economic Assessment, Ashram Rare Earth Deposit for Commerce Resources Corp.

Gammons, C.H., Wood, S.A., and Li, Y., 2002, Complexation of the rare earth elements with aqueous chloride at 200°C and 300°C and saturated water vapor pressure: Geochemical Society Special Publication, v. 7, p. 191-207.

Giebel, R.J., Gauert, C.D.K., Marks, M.A.W., Costin, G., and Markl, G., 2017, Multi-stage formation of REE minerals in the Palabora Carbonatite Complex, South Africa: American Mineralogist, v. 102, p. 1218-1233.

Goodenough, K.M., Wall, F., and Merriman, D., 2017, The rare earth elements: demand, global resources, and challenges for resourcing future generations: Natural Resources Research, DOI: 10.1007/s11053-017-9336-5

Gudfinnsson, G.H. and Presnall, D. C., 2005, Continuous Gradations among Primary Carbonatitic, Kimberlitic, Melilitic, Basaltic, Picritic and Komatiitic Melts in Equilibrium with Garnet Lherzolite at 3-8 GPa: Journal of Petrology, v. 46, p. 1645-1659.

Gysi, A.P., Harlov, D., and Miron, G.D., 2018, The solubility of monazite (CePO4), SmPO4, and GdPO4 in aqueous solutions from 100 to 250 degrees: Geochimica et Cosmochimica Acta, v. 242, p. 143-164.

Halkoaho, T., Ahven, M., Ramo, O.T., Hokka, J., and Huhma, H., 2020, Petrography, geochemistry, and geochronology of the Sc-enriched Kiviniemi ferrodiorite intrusion, eastern Finland: Mineralium Deposita, https://doi.org/10.007/s00126-020-00952-2

Hatch, G.P., 2012, Dynamics in the global market for rare earths: Elements, v. 8, p. 341-346.

Jaireth, S., Hoatson, D. M., and Miezitis, Y., 2014, Geological setting and resources of the major rare-earth-element deposits in Australia: Ore Geology Reviews v. 62, p. 72–128.

Jordens, A., Cheng, Y. P., and Waters, K. E., 2013, A review of the beneficiation of rare earth element bearing minerals: Minerals Engineering, v. 41, p. 97–114.

Jowitt, S.M., Mudd, G.M., Werner, T.T., Weng, Z., Barkoff, D.W., and McCaffrey, D., 2018, The Critical Metals: An overview and opportunities and concerns for the future: SEG Special Publications, no. 21, p. 25-38.

Kalashnikov, A.O, Yakovenchuk, V.N., Pakhomovsky, Y.A., Bazai, A.V., Sokharev, V.A., Konopleva, N.G., Mikhailova, J.A., Goryainov, P.M., and Ivanyuk, G.Y., 2016, Scandium of the Kovdor baddeleyite-apatite-magnetite deposit (Murmansk Region, Russia): Mineralogy, spatial distribution and potential resource: Ore Geology Reviews, v. 72, p. 532-537.

Lapin, A.V., Tolstov, A.V., and Kulikova, I.M., 2016, Distrbution of REE, Y, Sc, and Th in the unique complex rare-metal ores of the Tomtor deposit: Geochemistry International, v. 54, p. 1061-1078.

Le Bas, M.J., and Handley, C.D., 1979, Variation in apatite composition in ijolitic and carbonatitic igneous rocks: Nature, v. 279, p. 54-56.

Liferovich, R.P., Subbotin, V.V., Pakhomovsky, Y.A. and Lyalina, M.F., 1998, A new type of scandium mineralization in phoscorites and carbonatites of the Kovdor massif, Russia: Canadian Mineralogist, v. 36, p. 971-980.

Liu, W.H., Etschmann, B., Migdisov, A., Boukhalfa, H., Testemale, D., Muller, H., Hazemann, J.L., and Brugger, J., 2017, Revisiting the hydrothermal geochemistry of europium (II/III) in light of new in-situ XAS spectroscopy: Chemical Geology, v. 459, p. 61-74.

Louvel, M., Bordage, A., Testemale, D., Zhou, L., and Mavrogenes, J., 2015, Hydrothermal controls on the genesis of REE deposits: Insights from an in situ XAS study of Yb solubility and speciation in high temperature fluids (T < 400°C): Chemical Geology, v. 417, p. 228-237.

Machado, N., Clark, T., David, J. and Goulet, N., 1997, U-Pb ages for magmatism and deformation in the New Quebec Orogen: Canadian Journal of Earth Sciences, v. 34, p. 716-723.

Mair, P., Tropper, P., Harlov, D.E., and Manning, C.E., 2017, The solubility of CePO4 monazite and YPO4 xenotime in KCl-H2O fluids at 800 degrees C and 1.0 GPa: Implications for REE transport in high-grade crustal fluids: American Mineralogist, v. 102, p. 2457-2466.

Mariano, A.N., 1989, Nature of economic mineralization in carbonatites and related rocks, in Bell, K., ed., Carbonatites: Genesis and Evolution, Winchester, Massachusetts, Unwin Hyman Inc., p. 149-176.

Massari, S., and Ruberti, M., 2013, Rare earth elements as critical raw materials: Focus on international markets and future strategies: Resources Policy, v. 38, p. 36–43.

Merriman, D., 2013, A Review of the Global Supply of Rare Earths. Technical Report March, Roskill Consulting Group.

Migdisov, A.A., and Williams-Jones, A.E., 2008, A spectrophotometric study of Nd (III), Sm (III) and Er (III) complexation in sulfate-bearing solutions at elevated temperatures: Geochimica Cosmochimica Acta, v. 72, p. 5291-5303.

Migdisov, A.A., Williams-Jones, A.E., and Wagner, T., 2009, An experimental study of the solubility and speciation of the Rare Earth Elements (III) in fluoride- and chloride-bearing aqueous solutions at temperatures up to 300°C: Geochimica et Cosmochimica Acta, v. 73, p. 7087-7109.

Migdisov, A.A., Williams-Jones, A.E., Brugger, J., and Caporuscio, F.A., 2016, Hydrothermal transport, deposition and fractionation of the REE: Experimental data and thermodynamic calculations: Chemical Geology, v. 439, p. 13-42.

Mitchell, R.H., and Smith, D.L., 2017, Geology and mineralogy of the Ashram Zone carbonatite, Eldor Complex, Quebec: Ore Geology Reviews, v. 86, p. 784-806.

Mott, A.V., Bird, D.K., Grove, M., Rose, N., Bernstein, S., Mackay, H. and Krebs, J., 2013, Karrat Isfjord: A newly discovered Paleoproterozoic carbonatite-sourced REE deposit, Central West Greenland: Economic Geology, v. 108, p. 1471-1488.

Mudd, G. M., and Jowitt, S. M., 2016, Rare earth elements from heavy mineral sands: Assessing the potential of a forgotten resource: Applied Earth Science v. 125, p. 107-113.

Müller, A., Ihlen, P.M., Snook, B., Larsen, R.B., Flem, B., Bingen, B., and Williamson, B., 2015, The chemistry of quartz in granitic pegmatites of southern Norway: Petrogenetic and economic implications: Economic Geology, v. 110, p. 1737-1757.

Murdock, T.G., 1963, Mineral resources of the Malagasy Republic: United States Bureau of Mines, Information Circular 8196, p. 147.

Nadeau, O., Cayer, A., Pelletier, M., Stevenson, R., and Jébrak, M., 2015, The Paleoproterozoic Montviel carbonatite-hosted REE-Nb deposit, Abitibi, Canada: Geology, mineralogy, geochemistry and genesis: Ore Geology Reviews, v. 67, p. 314-335.

Olson, J.C., Shawe, D.R., Pray, L.C., and Sharp, W.N., 1954, Rare-earth mineral deposit of the Mountain Pass district, San Bernardino County, California, U.S. Geological Survey Professional Paper 261, p. 1-75.

Pell, J., 1996, Mineral deposits associated with carbonatites and related alkaline igneous rocks, in Mitchell, R.R., ed., Undersaturated Alkaline Rocks: Mineralogy, Petrogenesis, and Economic Potential, Mineralogical Association of Canada, Short Course Series, Winnipeg, p. 271-310.

Petrella, L., 2012, The nature and origin of REE mineralization in the Misery Syenitic intrusion, Northern Quebec, Canada: Unpublished M.Sc. thesis, Montreal, Canada, McGill University, 152 p.

Petrella, L., Williams-Jones, A.E., Goutier, J., and Walsh, J., 2014, The nature and origin of the rare earth element mineralization in the Misery Syenitic Intrusion, Northern Quebec, Canada: Economic Geology, v. 109, p. 1643-1666.

Rangott, M., Hutchin, S., Basile, D., Ricketts, N., Duckworth, G., and Rowles, T.D., 2016, Feasibility Study – Nyngan Scandium Project, Bogan Shire, NSW, Australia, NI 43 101 Technical Report prepared for Scandium International Mining Corp.

Roskill, 2016a, Lithium: Global industry, markets and outlook (13th ed.). London, UK: Roskill.

Roskill, 2016b, Rare earths: Global industry, markets and outlook (16th ed.). London, UK: Roskill.

Ruberti, E., Enrich, G.E.R., and Gomes, C.B., 2008, Hydrothermal REE fluorocarbonate mineralization at Barra Do Itapirapua, a multiple stockwork carbonatite, Southern Brazil: The Canadian Mineralogist, v. 46, p. 901-914.

Schmidt, P., 2013, High-field-strength element distribution of the Eldor carbonatite complex, Canada. Unpublished MSc thesis, Tubingen University.

Schmidt, P.T., Samson, I.M., Williams-Jones, A.E., and Smith, D.L., 2017, HFSE evolution in the Eldor Carbonatite: Mercier-Langevin, P., Dube, B., Bardoux, M., Ross, P.S., and Dion, C., Mineral Resources to Discover, *Society for Geology Applied to Mineral Deposits*, 14th Biennial Proceedings, Quebec City, Canada, p. 1371-1374

Sengupta, D., and Van Gosen, B. S., 2016, Placer-type rare earth element deposits. In P. Verplanck and M. Hitzman (Eds.), Rare earth and critical elements in ore deposits (Vol. Reviews in Economic Geology 18, pp. 81–100). Littleton, Colorado: Society of Economic Geologists.

Shannon, R.D., 1976, Revised effective ionic-radii and systematic studies of interatomic distances in halides and chalcogenides: Acta Crystallographica Section A, v. 32, p. 751-767.

Sherer, R.L., 1984, Evaluation of Selected Samples from Eldor Resources Ltd., Permit 669 Carbonatite, Quebec. *Union Molycorp Report*, 62 pages.

Smith, M.P., Campbell, L.S. and Kynicky, J., 2015, A review of the genesis of the world class Bayan Obo Fe-REE-Nb deposits, Inner Mongolia, China: Multistage processes and outstanding questions: Ore Geology Reviews, v. 64, p. 459-476.

Tarkhanov, A.V., Kulayev, A.R., Petrin, A.V., and Kozyr'kov, V.D., 1992, The Zheltorechensk vanadium-scandium deposit: International Geology Review, v. 34, p. 496-502.

Trofanenko, J., Williams-Jones, A.E., Simandl, G.J., and Migdisov, A.A., 2016, The nature and origin of the REE mineralization in the Wicheeda carbonatite, British Columbia, Canada: Economic Geology, v. 111, p 199-223.

U.S. Executive Order No. 13,593, 2020, Addressing the Threat to the Domestic Supply Chain from Reliance on Critical Minerals from Foreign Adversaries and Supporting the Domestic Mining and Processing Industries: DCPD202000746.

Wall, F., 2014, Rare earth elements. In A. G. Gunn (Ed.), Critical metals handbook (pp. 312–339). London: Wiley.

Williams-Jones, A.E., and Vasyukova, O.V., 2018, The economic geology of Scandium, the runt of the rare earth element litter: Economic Geology, v. 113, p. 973-998.

Williams-Jones, A.E., Migdisov, A.A., and Samson, I.A., 2012, Hydrothermal Mobilisation of the Rare Earth Elements – a Tale of “Ceria” and “Yttria”: Elements, v. 8, p. 355-360.

Woolley, A.R. and Kjarsgaard, B.A., 2008, Paragenetic types of carbonatites as indicated by the diversity and relative abundances of associated silicate rocks: Evidence from a global database: Canadian Mineralogist, v. 46, p. 741-752

Wright, W.R., Mariano, A.N., Hagni, R.G., 1998. Pyrochlore, mineralization, and glimmerite formation in the Eldor (Lake LeMoyne) carbonatite complex, Labrador Trough, Quebec, Canada. In: Proceedings 33rd Forum on the Geology of Industrial Minerals. Inst. Mining Metall. Petroleum, Spec., vol. 50, pp. 205–213.

Xie, Y., Hou, Z., Yin, S., Dominy, S.C., Xu, J., Tian, S., and Xu, W., 2009, Continuous carbonatitic melt-fluid exsolution of a REE-mineralisation system: Evidence from Inclusion in the Maoniuping REE Deposit, Western Sichuan, China: Ore Geology Reviews, v. 36, p. 90-105.

Xie, Y., Li, Y., Hou, Z., Cooke, D.R., Danyushevsky, L., Dominy, S.C., and Yin, S., 2015, A model for carbonatite hosted REE mineralisation – the Mianning-Dechang REE belt, Western Sichuan Province, China: Ore Geology Reviews, v. 70, p. 595-612.

Zaitsev, A.N., Demény, A., Sindern, S., Wall, F., 2002. Burbankite-group minerals and their alteration in rare earth carbonatites—source of elements and fluids (evidence from C–O and Sr–Nd isotopic data): Lithos, v. 62, p. 15–33.

Zhou, B., Li, Z., and Chen, C., 2017, Global potential of rare earth resources and rare earth demand from clean technologies: Minerals, v. 7, p. 203-217.

Zhou, L., Mavrogenes, J., Spandler, C., and Li, H.P., 2016, A synthetic fluid inclusion study of the solubility of monazite-(La) and xenotime-(Y) in H2O-Na-K-Cl-F-CO2 fluids at 800 degrees C and 0.5 GPa: Chemical Geology, v. 442, p. 121-129.

Chapter 2 - The genesis of the Ashram REE deposit, Quebec: Insights from bulk-rock geochemistry, apatite-monazite-bastnäsite replacement reactions and mineral chemistry

Preface

In this chapter, we use textural observations, mineral compositional data, bulk rock geochemistry, and stable isotope data, and variations of these data in three dimensions, to develop a genetic model for the Ashram REE deposit. The REE mineralization at Ashram is hydrothermal in origin and was produced through a series of fluid-mediated replacement reactions. Nonetheless, magmatic processes were also important in determining the initial distribution of the REE. There were two stages of carbonatite emplacement, each geochemically distinct. Rare earth element-mobilizing H_2O-CO_2 fluids were exsolved from the second carbonatite magma. These fluids were acidic, REE-bearing and utilized a central breccia as a conduit of egress, with successive pulses armouring the pathway (i.e., reducing its pH buffering capacity), preventing neutralization and allowing for the transport of the REE. Monazite compositions are spatially zoned in the deposit, with their LREE content increasing with increasing distance from the breccia. Cooling and differential pH buffering of the fluid beyond the conduit resulted in fractionation of the REE and the observed spatial zonation of the REE at Ashram, including the MHREE-enriched zone.

Abstract

Growing demand for the rare earth elements, particularly the heavy REE (HREE), has fuelled a boom in mineral exploration and scientific research on carbonatite-hosted deposits, especially those with unusual HREE enrichment. The Ashram REE deposit is such a HREE-enriched carbonatite-hosted REE deposit. Magmatic processes were important in the genesis of the deposit, but hydrothermal mobilization was the main process responsible for the concentration of the REE to potentially economic levels and the fractionation of the HREE.

The REE minerals in the Ashram deposit were precipitated from hydrothermal fluids. They comprise monazite-(Ce) and bastnäsite-(Ce), with lesser monazite-(Nd) and trace xenotime-(Y) and aeschynite-(Nd). This mineralization occurs as disseminations in breccia matrices, in veins, and as vug fillings. Monazite-(Ce) was the earliest mineral to form, followed by xenotime-(Y) and bastnäsite-(Ce). The composition of monazite-(Ce) varies with location in the deposit and is preferentially enriched in the light REE (LREE) with increasing distance from a large, irregular breccia body, underlying the zone of HREE enrichment. This body is interpreted to have been the main conduit for the mineralizing fluids which, on exiting, deposited monazite as a result of the cooling and pH buffering that accompanied their interaction with the adjacent carbonatites. Bastnäsite-(Ce) replaced monazite-(Ce) through ligand exchange (F^-, CO_3^{2-} for PO_4^{3-}), preserving the original REE distribution. Interaction of a compositionally evolving fluid with host rocks of variable bulk composition and buffering capacity resulted in a deposit-scale fractionation and zonation of the REE.

2.1 Introduction

Carbonatites are an important source of rare earth elements (REE), particularly the light REE (LREE). Indeed, the Mountain Pass carbonatite (USA) was responsible for virtually all global REE production from 1965 until 1986, when the Bayan Obo deposit (China) came on stream, making it unprofitable to continue mining at Mountain Pass (Castor and Hedrick, 2006). Based partly on studies of the Mountain Pass deposit, carbonatite-hosted REE ores have long been considered as magmatic (Olson et al., 1954; Mariano, 1989; Castor, 2008). Recent studies, however, have proposed an integrated magmatic-hydrothermal model for a number of carbonatite-hosted REE deposits, including Jacupiranga (Costanzo et al., 2006) and Barra do Itapirapua, Brazil (Ruberti et al, 2008); Amba Dongar, India (Doroshkevich et al., 2009); Maoniuping, China (Xie et al., 2015); Bear's Lodge, USA (Moore et al., 2015); Montviel (Nadeau et al., 2015) and Wicheeda, Canada (Trofanenko et al., 2016); and the REE-mineralization at Phalaborwa, South Africa (Giebel et al., 2017). According to these studies, hydrothermal fluids of magmatic origin play an essential role in concentrating the REE to potentially economic levels, either by transferring them directly from the magma and/or by leaching and remobilizing them from primary minerals. For some deposits, e.g., Bayan Obo, China (Smith et al., 2015) and Karrat Isfjord, Greenland (Mott et al., 2013), it has been proposed that carbonatite-derived fluids transported the REE and deposited them in unrelated country rock. In the case of Bayan Obo, it was also recently proposed that the hosts are carbonatites rather than marble (Chen et al., 2020). Despite the considerable body of evidence that has been collected in support of a role for hydrothermal fluids in the formation of carbonatite REE deposits, debate continues over the relative importance of hydrothermal and magmatic processes in the concentration of the REE.

Although transport of the REE by carbonatite-derived hydrothermal fluids has commonly been inferred, there are few cases where this has been demonstrated unambiguously. Such unequivocal evidence has been provided by REE daughter minerals (e.g., burbankite) in primary fluid inclusions from the Chilwa Island carbonatite, Malawi (Dowman et al., 2017) and by crush-leach analyses of quartz-hosted fluid inclusions from the Kalkfeld and Okorusu carbonatites (Bühn and Rankin, 1999; Bühn et al., 2002). In contrast, there is a large and growing body of experimental evidence that the REE can be transported in appreciable concentrations in aqueous solutions at elevated temperature (e.g., Gammons et al., 2002; Migdisov and Williams-Jones, 2008; Migdisov et al., 2009; Louvel et al., 2015; Zhou et al., 2016; Liu et al., 2017; Mair et al., 2017; Gysi et al., 2018). This transport is thought to occur through the complexation of the REE with chloride and sulfate ions. Phosphate and fluoride ions are considered depositional ligands due to the fact that monazite and fluocerite have very low solubility, which buffers the concentration of these ions to very low levels (Williams-Jones et al., 2012; Migdisov et al., 2016). Although carbonate is clearly a depositional ligand for REE-fluorocarbonate minerals like bastnäsite, it has yet to be established whether or not carbonate and/or bicarbonate ions can also act as transport ligands.

In most carbonatite-hosted REE deposits, bastnäsite-(Ce) is the principal ore mineral and, where monazite-(Ce) is present, it is almost invariably subordinate to bastnäsite. A notable exception is the Phalaborwa carbonatite, South Africa, where monazite is the dominant REE mineral (Giebel et al., 2017). In deposits containing significant proportions of both minerals, there is an ‘antipathic’ relationship, or strong spatial separation between the bastnäsite-(Ce) and monazite-(Ce), first recognized by Kapustin (1971). Although parageneses involving these two REE minerals have been documented, the factors responsible for the antipathic relationship between them have rarely been investigated (Giebel et al., 2017).

Among the many questions that remain regarding the genesis of REE mineralization in carbonatites, the most puzzling may be the origin of rare occurrences of heavy REE (HREE) mineralization in these rocks. Owing to their generation from mantle melts, carbonatites are intrinsically LREE-rich (Pell, 1996) and some studies have shown that carbonatite-derived hydrothermal fluids are dominated by the LREE (e.g., Bühn and Rankin, 1999; Bühn et al., 2002). There are, however, rare occurrences of carbonatite-related hydrothermal deposits or parts of such deposits that are highly enriched in the HREE, e.g., Lofdal, Namibia (76.3 % heavy rare earth oxide (HREO) / total rare earth oxide (TREO), Bodeving et al., 2017) and Chilwa Island (Dowman, 2014), respectively. In the case of Lofdal, this enrichment has been attributed to the preferential immobilization of the HREE due to the weak pH buffering capacity of the host rocks (Williams-Jones et al., 2015), whereas for Chilwa Island, the enrichment was proposed by Dowman et al. (2017) to be due to concentration of the HREE in the late-stage Fe-rich residual magma.

The Eldor Carbonatite Complex and its Ashram REE deposit provide a rare opportunity to explore the relative importance of magmatic and hydrothermal processes in carbonatite-related REE ore formation, the controls on REE-phosphate mineral deposition and the processes by which the REE may be fractionated in carbonatitic environments. This is because, although the dominant REE mineral in the Ashram deposit is monazite-(Ce), the deposit contains several REE minerals that are spatially separated on a deposit-scale, and there is an unusual zone of middle REE (MREE) and HREE enrichment.

In this contribution, we use textural observations of the REE minerals and associated phases to establish a mineral paragenesis for the Ashram deposit and report the major and trace element compositions of these minerals. Variations in the latter are evaluated in the context of deposit-scale bulk geochemical trends and changes in lithology. Based on the results of this research, we have developed a model in which carbonatite magma evolution involved late-stage exsolution of REE-bearing fluids that reworked primary mineral assemblages, and deposited REE minerals in response to the cooling and differential buffering of the fluid that occurred during its interaction with the host rock.

2.1.1 Geology of the Eldor Carbonatite Complex

The Eldor Carbonatite Complex is hosted by rocks of the Labrador Trough, which is the foreland of the New Quebec Orogen, a Paleoproterozoic fold and thrust belt on the eastern margin of the Superior Province (Fig. 2.1). This early Proterozoic basin (the Labrador Trough) experienced three cycles of rifting and sedimentation, separated by erosional unconformities (Clark and Wares, 2006). The carbonatite complex was emplaced at the end of the second of these cycles, within the volcanosedimentary Murdoch Formation and, although the emplacement age of the carbonatite is unknown, it is constrained to be younger than 1870 ± 4 Ma by the U-Pb age of a rhyodacite which it crosscuts (Machado et al., 1997). The complex was subsequently metamorphosed and deformed during the Hudsonian Orogeny (1.85 - 1.77 Ga) (Clark and Wares, 2006).

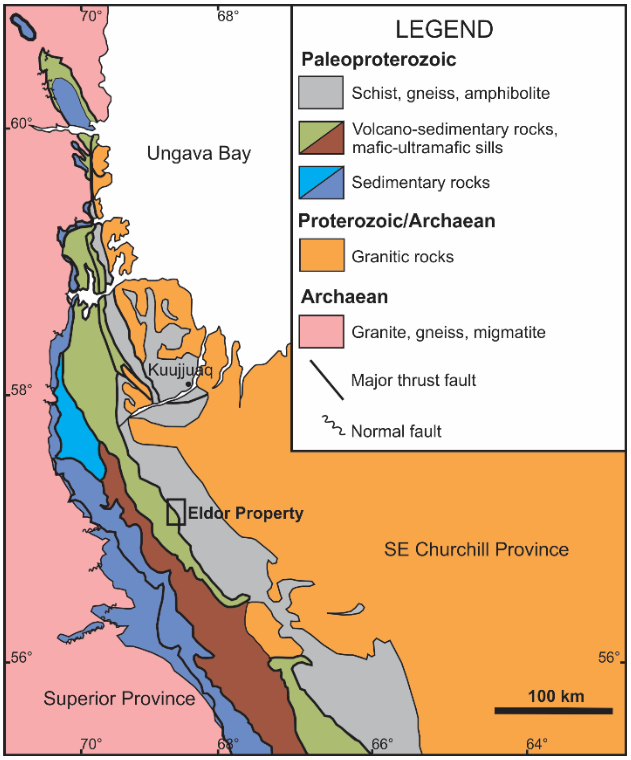

Figure 2.1: Regional geological map of the New Quebec Orogen

A map showing the location of the Eldor Carbonatite Complex (after Clark and Wares, 2006).

Commerce Resources Corp. is currently exploring the Eldor Carbonatite Complex and has reported measured and indicated resource estimates of 29.3 Mt grading 1.90 wt. % TREO, using a cut-off grade of 1.25 wt. % TREO (Gagnon et al., 2012). The carbonatite is exposed in a 7 x 3.5 km elliptical area and comprises a suite of intrusions ranging in composition from calcite- through dolomite- to ferro-carbonatite. Based on the distribution of the REE, the pluton has been subdivided into a Rim composed of REE-poor calcite- and dolomite-carbonatite (the Rim carbonatites) and a core of dolomite carbonatite and ferrocarbonatite that hosts the Ashram REE deposit (Fig. 2.2A). Exposure in the area is poor, and the bulk of the Ashram deposit lies beneath a pond. As drilling has focussed on the REE-mineralized zones, the relationships among the various units are not well known, especially the contact between the Ashram deposit and the outer part of the carbonatite. For example, the outermost unit of the Ashram deposit is typically in contact with calcite carbonatite, but its contact with the Rim dolomite carbonatite has not been observed and is inferred. The Ashram deposit is separated from greenstones on its west side by fenites (phlogopitite and arfvedsonite-albitite), the outer limit of which has not been intersected in drilling. To date, drilling has been insufficient to elucidate the subsurface orientation of both the deposit and the complex. Research on the Eldor carbonatites has been limited to a study focussed on pyrochlore in the Rim carbonatites (Wright et al., 1998), an unpublished M.Sc thesis, which provided a general description of the Ashram deposit and surrounding Rim carbonatites (Schmidt, 2013), an unpublished government report on the Eldor carbonatites (Tyson, 2014), and a paper describing the mineral paragenesis (Mitchell and Smith, 2017).

The Rim is composed of two calcite carbonatites and a dolomite carbonatite. Calcite carbonatite 1 is fine-grained and finely laminated with layers rich in apatite, magnetite, phlogopite and pyrochlore, alternating with calcite-rich layers. This assemblage (apatite-magnetite-phlogopite-pyrochlore-calcite), although not the layering, persists into the coarser-grained calcite carbonatite 2. Dolomite carbonatite cuts the calcite carbonatites and is the youngest Rim unit. It is fine-grained and contains abundant apatite and significant phlogopite and pyrochlore. Fluorite occurs locally as a cement to fragments in a breccia developed close to the contact with the Ashram deposit. Fersmite ($(Ca,Ce,Na)(Nb,Ta,Ti)_2(O,OH,F)_6$) has been observed in calcite carbonatite 1 and the dolomite carbonatite (Schmidt et al., 2017).

The Ashram deposit comprises three main zones of mineralization, namely the BD, B, and A zones (Fig. 2.2). In addition, there is a largely unmineralized breccia (Fig. 2.2B). The outermost BD zone is a fluorapatite-rich dolomite carbonatite with REE fluorocarbonate mineralization (bastnäsite-(Ce) ($LREECO_3F$), parisite-(Ce) ($Ca(LREE)_2(CO_3)_3F_2$), synchysite-(Ce) ($CaLREE(CO_3)_2F$)) grading 0.6 - 1.0 wt. % TREO (Fig. 2.3A, B). This unit is highly enriched in phosphate, with an average of 7 vol. % apatite and up to 14 wt. % P_2O_5 (Fig. 2.3B). The B zone is also a dolomite carbonatite, but with a dominant assemblage of fluorite (4 vol. %) + monazite ($REEPO_4$) and a grade of 1 - 2 wt. % TREO (Fig. 2.3C). This assemblage continues into the ferroan dolomite carbonatite of the innermost A zone, which is even more enriched in F and REE, with an average fluorite content of 8 vol. % and a grade of 1 - 3+ wt. % TREO (Fig. 2.3D). Rocks intersected in some drill holes appear to have characteristics transitional between those of the A and B zones, and accordingly have been termed A/B. Intervals of these rocks are included as a

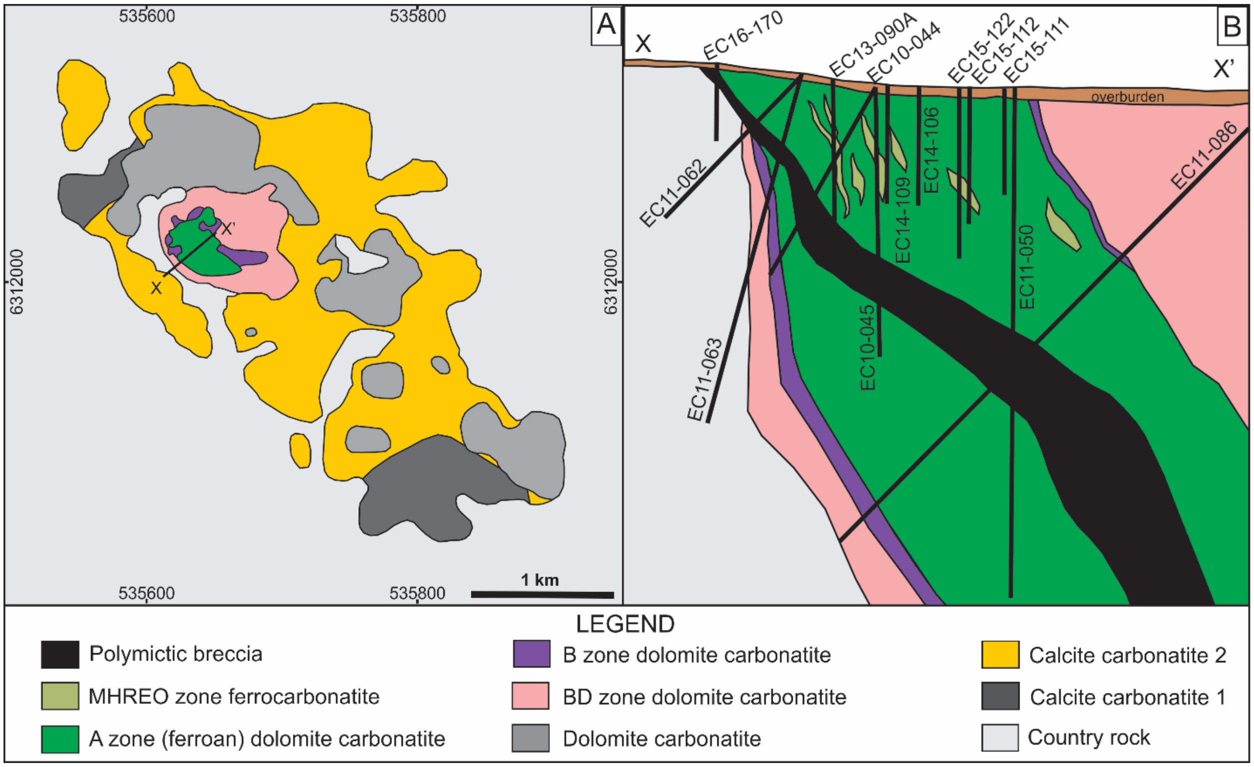

Figure 2.2: Geological map and cross-section of the Eldor Carbonatite Complex

A) A simplified geological map of the Eldor Carbonatite Complex at the 100 m level, based on information from drill core. B) A simplified cross-section of the X-X’ transect in A) including traces of the drill holes used to construct the section.

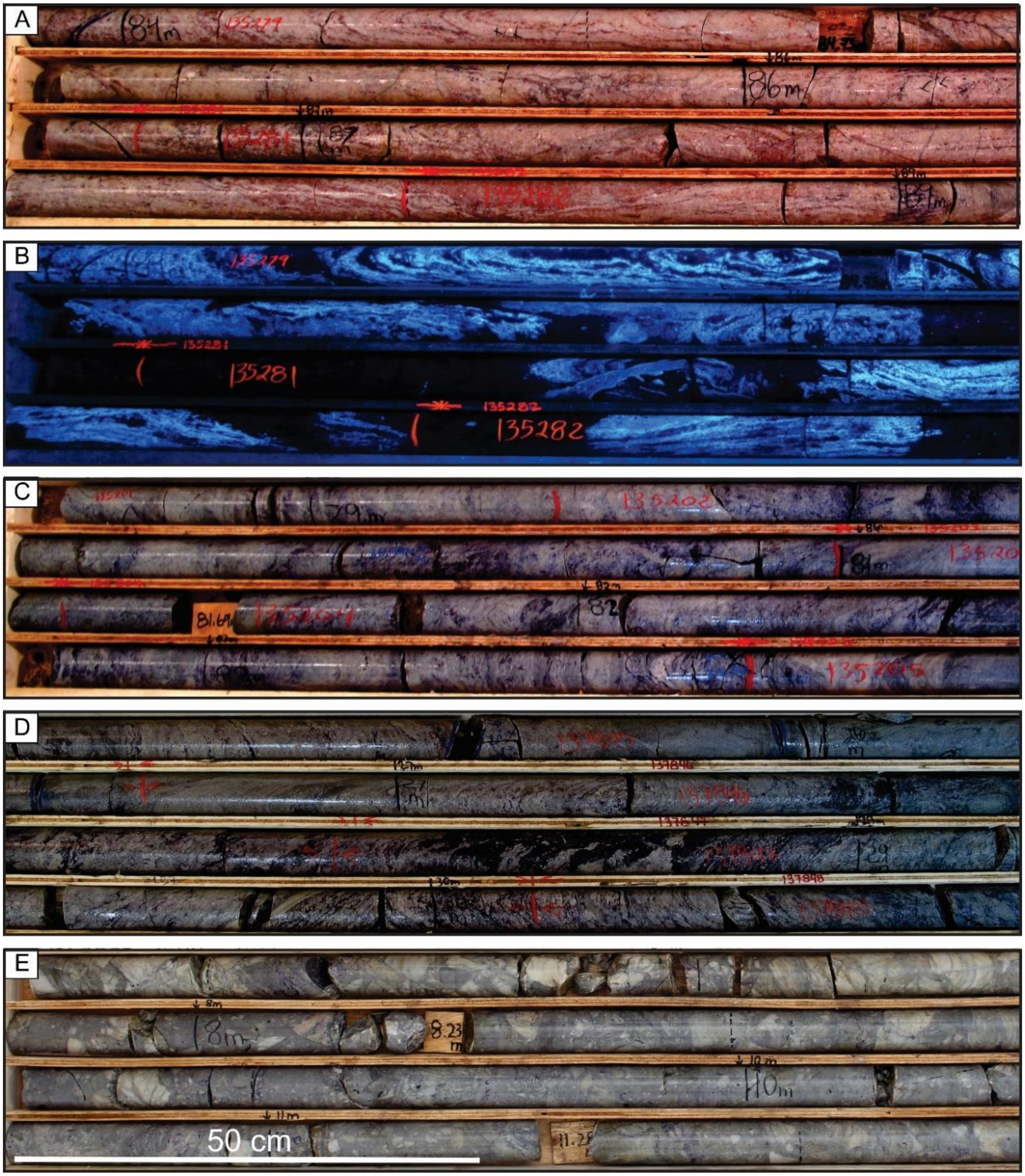

Figure 2.3: Photographs of Ashram rock types in drill core

Representative photographs of the various lithologies of the Ashram deposit. All drill core is 4.76 cm in diameter. A) BD zone dolomite carbonatite with pink REE-fluorocarbonate mineralization. B) The same intersection as in A) but photographed under UV light. The bright blue material is apatite. C) Weakly deformed B zone dolomite carbonatite with purple fluorite. Note the yellow tint from the monazite mineralization. D) Strongly deformed A zone ferroan dolomite carbonatite with purple fluorite veinlets and patches. E) Matrix-supported polymictic breccia with fluorite ± REE-fluorocarbonates in the matrix.

subdivision of the A zone in resource models. The A zone also contains the MHREO zone, which is a ferrocarbonatite containing monazite-(Nd), subordinate monazite-(Ce) and traces of xenotime-(Y) (YPO_4) and aeschynite-(Nd) ($(Nd,Ca,Fe)(Ti,Nb)_2(O,OH)_6$). This latter zone is relatively poor in fluorine, containing only minor fluorite, and has a lower REE content (1.6 wt. % TREO) than the A zone, but is enriched in the MREE (Sm, Eu, Gd) and HREE (Tb, Dy, Y, Ho, Er, Tm, Yb, Lu), with up to 20% MHREE/TREE. For the most part, the MHREO zone occurs near the top of the A zone (<100 m depth) as discontinuous pods and lenses up to a few metres in thickness.

Chemically, the Eldor Carbonatite Complex is concentrically zoned from a Rim that is enriched in P but depleted in Mg, Fe and the REE, to a core represented by the Ashram deposit that is enriched in Mg, Fe and particularly the REE, and relatively depleted in P (Table 2.1). As discussed above, the TREO grade (dominantly LREE; La, Ce, Pr, Nd) within the Ashram deposit increases progressively towards the center, then drops sharply in the MHREO zone with an accompanying enrichment in the MREE and HREE. All of the Ashram zones have elevated concentrations of F and P, but there is an antithetic relationship between the two elements, with F concentrations increasing from the BD zone to the A zone, and P concentrations decreasing in the same direction. There is also an important mineralogical change in the host of these elements, which distinguishes the BD zone from the rest of the deposit. Thus, F occurs in the BD zone dominantly in apatite and the REE-fluorocarbonate minerals, and in the B and A zones as fluorite. Likewise, apatite is the dominant phosphate mineral in the BD zone, whereas monazite-(Ce) is the dominant phosphate mineral in the B and A zones; monazite-(Nd) is the dominant phosphate mineral in the MHREO zone.

The youngest lithotype in the Eldor Carbonatite Complex is a polymictic breccia developed largely in the A zone that extends outwards into the BD zone. It is composed of a fine-grained dolomitic matrix containing clasts of local provenance, including greenstone, albitite, phlogopitite, and unmineralized BD zone material (Fig. 2.3E). Rarely, the matrix contains REE-fluorocarbonates. The breccia may be matrix- or clast-supported. Locally, it has the appearance of a crackle breccia, with little to no matrix carbonate and abundant phlogopite veinlets. Elsewhere, however, it comprises up to 80 % matrix.

In three dimensions, the breccia is an irregular, discontinuous, northward-dipping body located mainly within the P_2O_5-poor inner Ashram deposit (Fig. 2.4A), which is spatially

Table 2.1: Chemical and mineralogical compositions of the Eldor Carbonatite Complex units

Unit	***TREO (wt %)**	**MHREE / TREE (%)**	**Principal REE Minerals**	**Fe_2O_3 (wt %)**	**Principal Carbonate**	**P_2O_5 (wt %)**	**Phosphate Phase**	**F (wt %)**	**Fluorine Phase**
MHREO	1.6	≤ 20	monazite-(Nd), monazite-(Ce), xenotime-(Y)	27.42	siderite	0.58	monazite-(Nd), monazite-(Ce), xenotime-(Y)	0.55	fluorite
A	1 – 3+	~ 6	monazite-(Ce)	12.63	Fe-dolomite	0.92	monazite-(Ce)	3.74	fluorite
B	1 – 2	~ 4	monazite-(Ce)	5.97	dolomite	1.21	monazite-(Ce)	1.07	fluorite
BD	0.6 – 1.0	~ 7	REE-fluorocarbonate	4.18	dolomite	2.76	apatite	0.58	apatite, REE-fluorocarbonate
Dol Carb	-	-	-	6.17	dolomite	3.5	apatite	NA	phlogopite, apatite
Cal Carb 2	-	-	-	5.13	calcite	3.91	apatite	NA	phlogopite, apatite
Cal Carb 1	-	-	-	3.11	calcite	3.78	apatite	NA	phlogopite, apatite

'NA' – not analyzed

**TREO (wt. %) from Gagnon et al. (2012)*

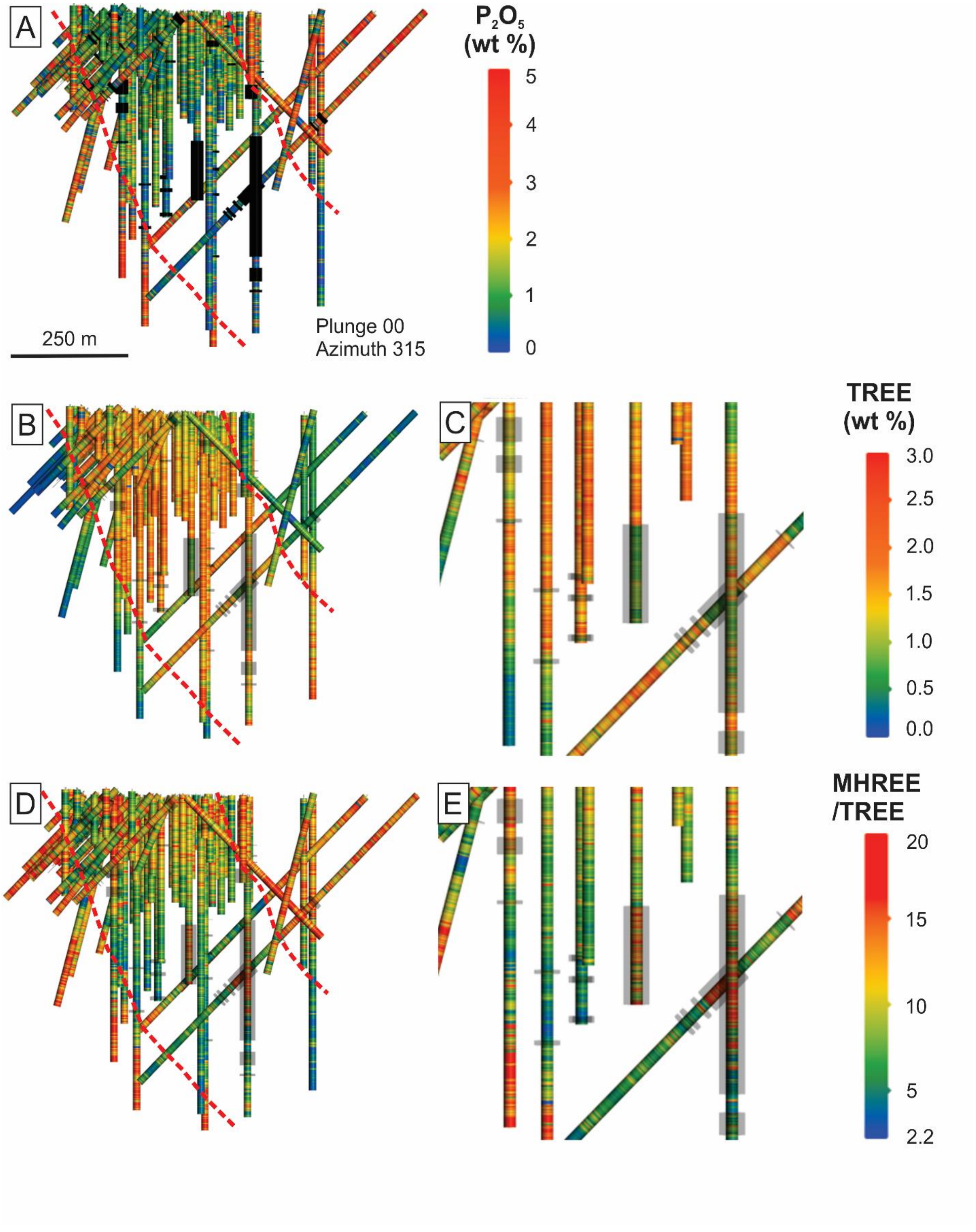

Figure 2.4: Perspective drill-hole images of the breccia

Perspective drill-hole images showing the deposit-scale distribution of selected compositional parameters centered on the breccia unit. All the images were prepared using Leapfrog Geo software from Seequent. A) Drill-hole colors coded by P_2O_5 (wt. %) content. All breccia intervals are shown in black, and there are strong alignments of these intervals. The breccia is commonly intersected within the P-poor, A zone Ashram rocks. The interpreted inner margin of the BD zone (by P_2O_5 content; wt. %) is shown by the red dashed lines. B) Drill-hole colors coded by TREE content (wt. %). Breccia intervals are shown in transparent grey. C) An enlarged view through a selected plane showing the low TREE content (wt. %) of the breccia relative to the surrounding carbonatite. D) Drill-hole colors coded by MHREE/TREE ratios. The MHREE/TREE ratios are highest in the shallowest part of the deposit, within the inner margins of the BD zone. E) An enlarged view through a selected plane showing high MHREE/TREE ratios in the breccia relative to the surrounding carbonatite.

associated with REE mineralization (Fig. 2.4B, C). Significantly, rocks with a high (> 10 %) proportion of MREE and HREE are intersected proximal to breccia intervals, and LREE concentrations increase with increasing distance from them (Fig. 2.4D, E). It is noteworthy that the peripheral intersections (beyond the dashed red lines in Fig. 2.4D), with a high proportion of MREE and HREE, have low TREE contents (Fig. 2.4B). This relative enrichment in the MREE and HREE is likely the signature of silicate minerals (e.g., amphibole; Siegel et al., 2017) in the wall-rock (in contact with the BD zone), which preferentially accommodate the MREE and HREE, albeit at low concentrations. The breccia is characterized by low bulk rock TREE contents (Fig. 2.4B, C), but high bulk rock MHREE/TREE ratios (Fig. 2.4D, E).

As discussed above, the Eldor Carbonatite Complex underwent greenschist facies metamorphism and accompanying deformation during the Hudsonian orogeny. The main effect of the metamorphism was recrystallization, which produced a granoblastic texture, largely in a low strain environment, as shown by the widespread occurrence of 120° triple junctions. Mineralogically, the evidence of metamorphism is limited to trace amounts of chlorite, most of which is observed along hairline fractures.

The deformation associated with regional metamorphism is manifested almost exclusively by zones of shearing characterized by fine-grained carbonate minerals that do not show a granoblastic texture and are locally foliated. In the Ashram deposit, these sheared zones vary in thickness from millimeters to several meters and are observed in all units, including the polymictic breccia and the breccias of the BD zone, which they overprint. The foliation is defined by thin, undulating layers of either apatite (BD zone; Fig. 2.3B) or fluorite (B, A zones; Fig. 2.3C, D) in the fine-grained dolomite. In rare cases, thin fluorite-monazite layers are observed and are interpreted to be veins that have been translated into the plane of the foliation.

2.2 Methods

Major and trace element (including the REE) bulk rock data were supplied by Commerce Resources Corp. from the results of analyses of drill core performed by Activation Laboratories, Ancaster, Ontario. All the samples were ground to 95% -200 mesh and aliquots of each powder fused with lithium metaborate/tetraborate, followed by analysis using inductively coupled plasma optical emission spectrometry (ICP-OES) for the major elements and mass spectrometry (ICP-MS) for the trace elements. The loss on ignition (LOI) was determined after fusion. Samples (1 g) were heated in an oven at 1000°C for 1 h, cooled, then weighed, with the percent loss calculated from the difference in weight before and after heating. The fluorine content was determined from 0.2 g samples fused with lithium metaborate/tetraborate in a furnace followed by leaching in deionized water to release F^- ions from the sample into a solution, which was then analysed using an ion sensitive electrode.

A total of 52 thin sections was examined petrographically using a combination of optical and scanning electron microscopy (SEM) and cold-cathodoluminescence (CL). A Hitachi SU5000 SEM, equipped with an Oxford Instruments X-Max^N 80 silicon drift detector was used for back-scattered electron (BSE) imaging, mineral identification and energy-dispersive X-ray mapping. Cathodoluminescence was required to identify different generations of fluorite, apatite and dolomite, and was carried out using a Reliotron III electron source, operated at 9 kV and 350 nA, and a 3 s exposure time.

Mineral compositions were determined in the Department of Earth and Planetary Sciences at McGill University using a JEOL JXA-8900L electron microprobe equipped with five wavelength-dispersive spectrometers and an Si(Li) energy-dispersive spectrometer. For calcite, dolomite and siderite, spot analyses were conducted at 15 kV with a 20 nA beam current using wavelength-dispersive spectrometry. Spot analyses of apatite, monazite, bastnäsite and xenotime were conducted at 20 kV and a 30 nA beam current. All analyses were performed with a 10 µm beam diameter. Data reduction was carried out using a ZAF correction procedure. The standards used, the counting times and the detection limits for each element in each mineral are reported in Appendix 2.1.

Trace element concentrations in apatite, fluorite and carbonate minerals were analysed with a laser ablation inductively-coupled plasma mass spectrometer (LA-ICP-MS). Analyses were performed at McGill University using a NewWave 213 nm Nd-YAG laser, operated at a fluence of 12 J/cm^2 for apatite, and 7 J/cm^2 for fluorite and carbonate minerals. Spots were analysed with a 30s laser warm-up, 45s ablation and 30s washout. In the case of apatite, the spots were 30 µm in diameter, and for fluorite and carbonate minerals were 80 µm in diameter. The aerosols were transported into a FINNIGAN iCapQ ICP-MS. The dwell time was 20 ms for the REE. Blocks of ≤ 15 analyses were bracketed by two analyses of the external standard SRM NIST 610, to apply a linear instrument drift correction. Element concentrations were determined using the software Iolite (Paton et al., 2011). The internal standards were the Ca content obtained by electron microprobe analysis of apatite, calcite and dolomite, and the stoichiometric Ca content for fluorite. Siderite analyses were standardized using the Fe content obtained by electron microprobe analysis.

Carbonate minerals from each lithofacies were analyzed for their stable carbon (^{12}C, ^{13}C) and oxygen (^{16}O, ^{18}O) isotope ratios at the McGill University/Geotop Stable Isotope Laboratory, using a Nu Instruments Perspective isotope ratio mass spectrometer. A total of 94 powdered carbonate samples (50-100 µg) were collected using a handheld micro-drill. An effort was made to sample coarse- and fine-grained minerals separately in rocks with variable grain size. The carbonate powders were dissolved in orthophosphoric acid at 70°C and the resulting CO_2 gas was analyzed via dual inlet following double distillation. Carbon isotope ratios were standardized to Vienna-Pee Dee Belemnite (V-PDB) and are reported as δ^{13}C values. Oxygen isotope ratios were standardized to Vienna-Standard Mean Ocean Water (V-SMOW) and are reported as δ^{18}O values. On the basis of regular analyses of an in-house standard (UQ6), the reproducibility is considered to be better than 0.05‰ for both the C and O isotope ratios.

2.3 Results

2.3.1 Bulk Lithogeochemistry

The compositions of the Eldor carbonatites in the system CaO-MgO-FeO+MnO are illustrated in Figure 2.5. These data show that the Rim carbonatites vary in composition from calciocarbonatite to magnesiocarbonatite, with an FeO+MnO proportion corresponding to that of the magnesiocarbonatite-ferrocarbonatite boundary (Fig. 2.5A). In contrast, the compositions of the

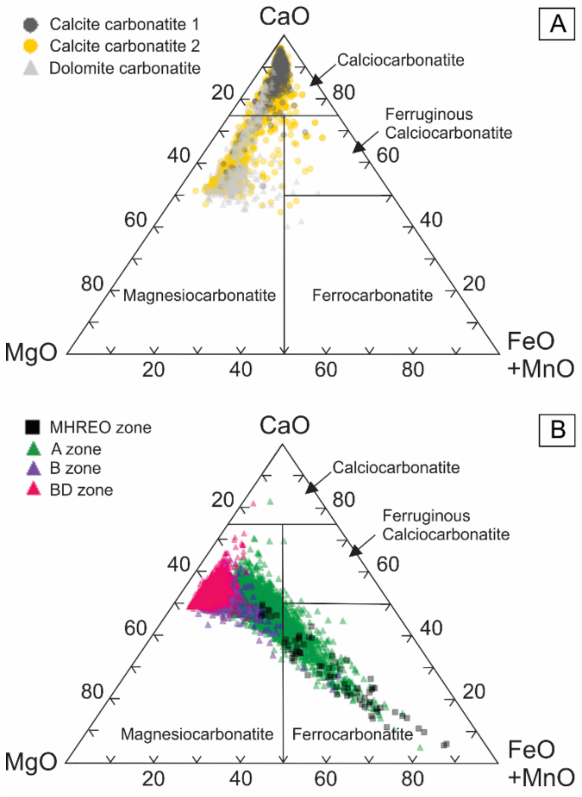

Figure 2.5: Ternary carbonatite classification diagrams

The ternary carbonatite classification diagram of Gittins and Harmer (1997), showing bulk rock compositions (in mol. %) of A) the Rim carbonatites and B) the Ashram carbonatites. The data are from drill core assays provided by Commerce Resources Corp.

Ashram carbonatites vary from Mg-rich magnesiocarbonatite to ferrocarbonatite containing over 80 % FeO+MnO (Fig. 2.5B).

Weighted median bulk compositions for each of the units in the Eldor Carbonatite Complex are reported in Table 2.2, and a selection of components (Ba, Zr, TREE, Zn) are illustrated as a function of P_2O_5 in a series of binary plots shown in Figure 2.6, to illustrate the relationships among the different lithological units. The component P_2O_5 was selected as an index of evolution because apatite was an early fractionating phase, and the only reservoir for phosphorus in the Rim carbonatites. For the above components, the various lithologies identify two groups/trends, one of which comprises the Rim carbonatites and the BD zone, and the other the B, A/B, A, and MHREO zones (Fig. 2.6).

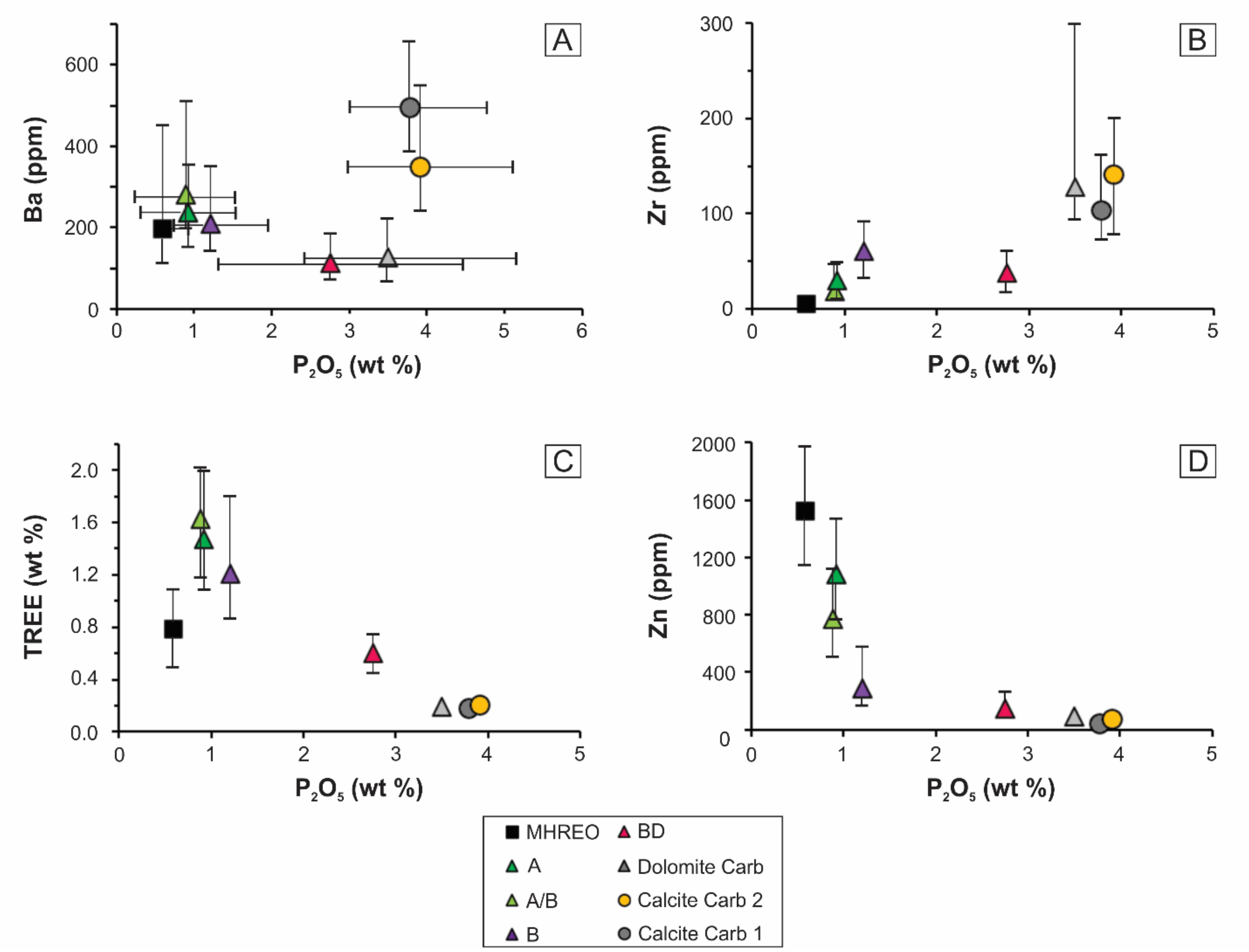

Figure 2.6: Binary plots of the selected chemical components for the Eldor Carbonatites

Binary plots of the weighted median values of selected chemical components versus the P_2O_5 content of each unit of the Eldor Carbonatite Complex, with 1st and 3rd quartile bars shown. Median values were calculated from the results of analyses of samples, varying in number from ~100 in the MHREO zone to >5000 in the A/B zone, of 1 to 2 m of drill core of variable homogeneity. In some cases, the y-axis quartile bars are smaller than the symbols and therefore are not shown. For clarity, quartile bars for the x-axis are shown only in A).

Table 2.2: Bulk rock compositions of the Eldor carbonatites

Weighted median bulk major and trace element compositions of the different units of the Eldor Carbonatite Complex

	Stage 2					**Stage 1**			
	Ashram						**Rim**		
Unit	**MHREO**	**A**	**A/B**	**B**	**Breccia**	**BD**	**Dol Carb**	**Calcite Carb 2**	**Calcite Carb 1**
*Length *(m)*	97	4188	5084	669	193	1783	1777	1396	771
SiO_2 *(wt. %)*	1.53	1.72	1.58	1.83	2.61	0.83	1.65	1.28	1.14
Al_2O_3	0.06	0.09	0.07	0.05	0.41	0.06	0.34	0.19	0.14
Fe_2O_3 (T)	27.42	12.63	9.59	5.97	10.35	4.18	6.17	5.13	3.11
MnO	2.41	1.66	1.43	1.18	0.88	0.74	0.46	0.35	0.24
MgO	7.27	11.43	13.42	15.03	13.41	15.67	13.61	5.13	2.6
CaO	11.78	25.73	27.53	27.8	26.91	29.5	31.14	39.73	46.28
Na_2O	0.02	0.03	0.02	0.03	0.05	0.03	0.06	0.06	0.06
K_2O	0.03	0.05	0.05	0.04	0.27	0.03	0.22	0.14	0.11
TiO_2	0.25	0.17	0.1	0.04	0.54	0.03	0.11	0.08	0.04
P_2O_5	0.58	0.92	0.89	1.21	2.75	2.76	3.5	3.91	3.78
F	0.55	3.74	1.99	1.07	0.44	0.58	NA	NA	NA
Sc *(ppm)*	28	52	40	45	32	21	10	10	7
V	100	69	69	55	108	35	114	77	47
Co	13	6	6	4	15	2	9	8	6
Zn	1527	1080	773	286	507	149	90	74	40
Sr	897	2106	2399	2476	2855	3367	1628	3359	4866
Zr	5	30	18	60	61	38	128	141	104
Nb	283	454	351	248	757	202	1291	1378	1431
Mo	0	6	5	8	3	4	4	3	3
Sn	22	19	10	5	10	2	3	3	3
Ba	198	236	281	208	180	114	127	349	497
La	996	3470	4140	2850	1609	1087	361	380	335
Ce	3171	6670	7649	5632	3173	2600	830	873	790
Pr	501	718	794	631	381	329	102	111	102
Nd	2254	2586	2728	2264	1431	1348	385	426	389
Sm	364	377	335	276	208	201	55	61	54
Eu	84	93	76	60	50	49	15	16	15
Gd	184	215	183	133	120	111	41	46	41
Tb	18	24	17	11	14	12	5	5	5
Dy	65	100	67	42	60	46	23	23	21
Y	219	388	242	154	227	157	92	92	85
Ho	8	14	9	6	9	6	4	4	3
Er	18	30	20	12	21	13	8	8	7
Tm	2	3	2	1	2	2	1	1	1
Yb	11	18	12	9	14	9	6	6	5
Lu	1	2	2	1	2	1	1	1	1
Hf	1	1	1	1	1	1	1	1	1
Ta	0	0	0	0	1	0	29	39	32
W	1	4	2	1	4	0	2	1	1
Pb	699	199	111	23	152	27	14	24	22

**Length refers to the total length of drill core assayed*

2.3.2 Petrographic Observations

Although evidence of shearing is common in the Eldor Carbonatite Complex, magmatic textures are locally evident and there is widespread evidence of low strain recrystallization and hydrothermal overprinting. The only potential evidence of a magmatic texture is the occurrence layers of apatite that may reflect magmatic crystal segregation. This texture, however, is restricted to the Rim carbonatites. Breccias are common in the Ashram carbonatites, especially in the BD and MHREO zones, where they are the dominant texture. In the BD zone, coarse angular clasts of early dolomite (bright red in CL) occur in a matrix of fine-grained ferroan dolomite (no CL response) (Fig. 2.7A), that in BSE images, is shown to comprise an earlier, heterogeneous, locally sheared dolomite and a later, homogeneous dolomite (Fig. 2.7B). The same relationship is evident in the Rim dolomite carbonatite, but the clasts are only rarely preserved (Fig. 2.7C). Siderite of the MHREO zone is brecciated and its fragments show evidence of multiple episodes of overprinting (Fig. 2.7D-F). In the A and B zones, the carbonatite is either a massive, fine- to medium-grained equigranular rock exhibiting an obvious granoblastic texture (Fig. 2.8A), or a weakly to strongly foliated (sheared) rock, that commonly contains millimetric to centimetric lamellae enriched in monazite and fluorite. Locally, the latter may be crosscutting (Fig. 2.8B). These two textural end-members may be separated from each other on a scale of millimeters (Fig. 2.8C) to meters. Within a given textural domain, the primary carbonate minerals (dolomite, ferroan dolomite) may be homogeneous (Fig 2.9A, B) but more commonly have undergone multiple episodes of replacement (Fig. 2.9C, D, F). The secondary carbonates may be homogeneous or display complex internal textures and also occur in vugs or veins ± fluorite ± quartz (Fig. 2.9C, E, F); in addition to dolomite and ferroan dolomite, the vugs and veins may also contain calcite, siderite, and rarely, ankerite. Vugs occur in all Ashram zones, though most commonly in the A and MHREO zones.

Fluorite and apatite are major minerals in the Eldor carbonatites. Apatite is an important phase in all the Rim lithologies and the BD zone, but occurs only in trace proportions in the B, A and MHREO zones. The characteristics of the different apatite types vary by zone. In the Rim carbonatites, most of the apatite is primary, relatively coarse-grained with an ovoid crystal shape (Fig. 2.7C), and blue-violet color in CL (Fig. 2.10A). Locally, it is mantled by fine-grained, pale violet to pale pink (in CL) secondary apatite (Fig. 2.10A). The BD zone apatite is mostly secondary, fine-grained and sucrosic, commonly with irregular grain boundaries, and is pale pink

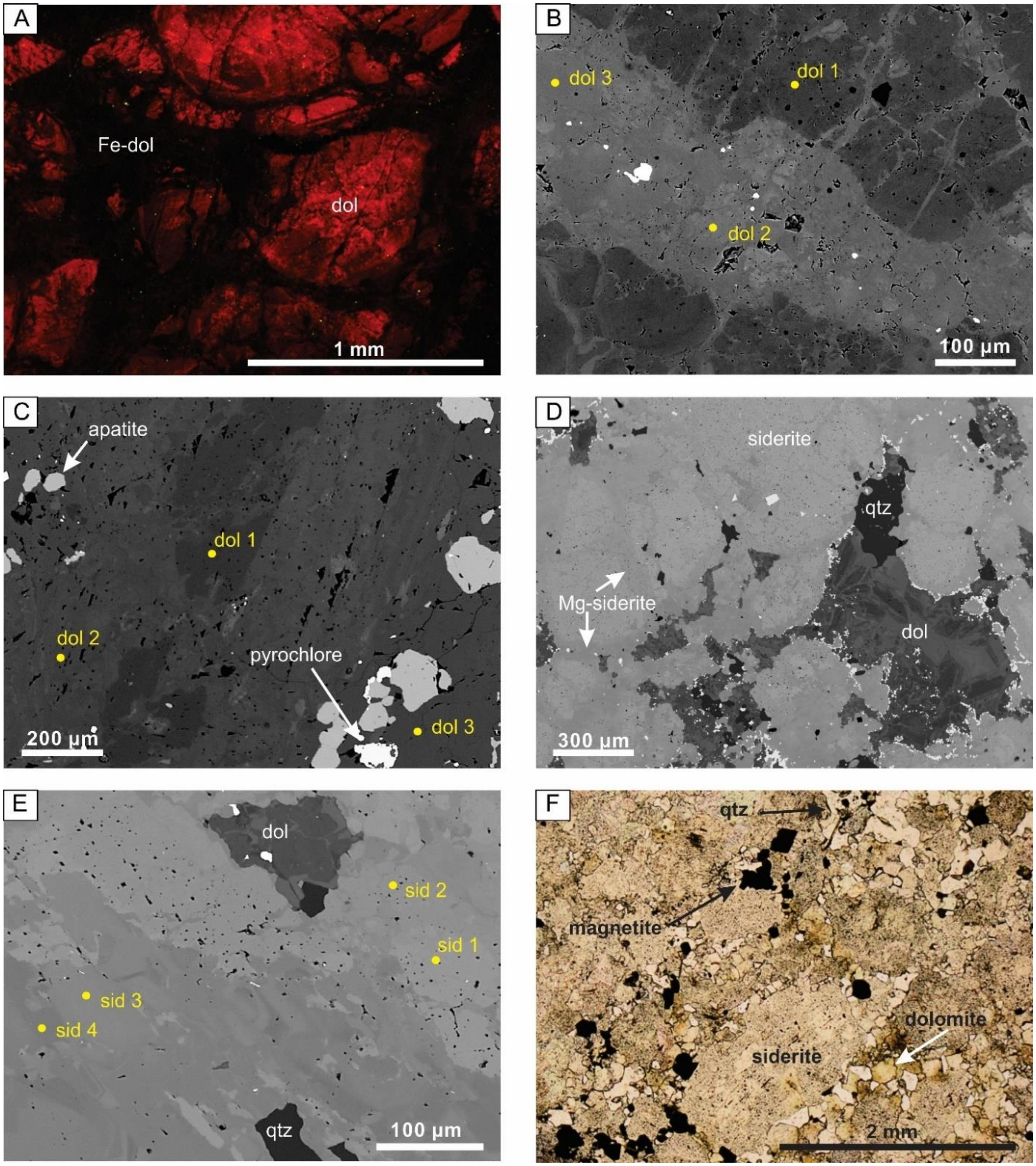

Figure 2.7: Representative images of brittle carbonate textures

The points and text in yellow correspond to carbonate compositions reported in Table 2.3. A) A CL-image of coarse-grained BD zone dolomite, displaying bright red luminescence, mantled by ferroan dolomite (dark, no CL response). B) A BSE image of brecciated BD zone dolomite crystals (dol 1) separated by a domain containing two generations of dolomite (dol 2 and 3) that are enriched in Fe. C) A BSE image of Rim dolomite carbonatite showing early, brecciated dolomite crystals (dol 1) mantled by Fe-enriched dolomite (dol 2), and finally a limpid dolomite (dol 3) generation associated with apatite and pyrochlore. D) A BSE image of brecciated siderite crystals of the MHREO zone carbonatite, mantled by magnesian siderite. There are also vugs filled with quartz and dolomite displaying complex internal textures. The white grains represent monazite-(Nd) that is clearly associated with siderite and magnesian siderite. E) A BSE image showing the compositional heterogeneity of siderite in the MHREO zone. F) A transmitted light photomicrograph of coarse-grained siderite crystals in a matrix of finer-grained dolomite, quartz, and magnetite. The brown discoloration of the dolomite commonly indicates an association with monazite-(Nd) mineralization.

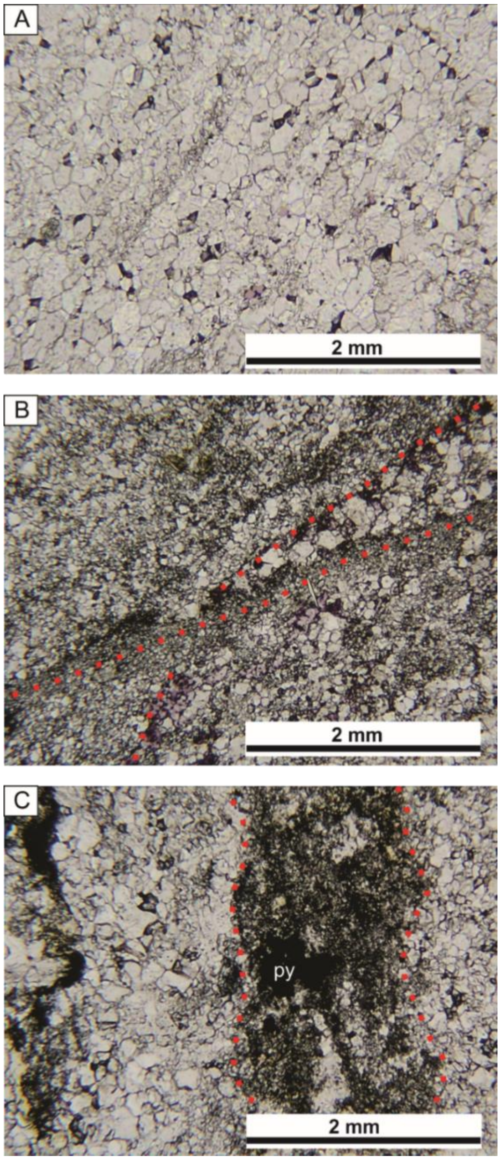

Figure 2.8: Representative images of carbonate textures from the B and A zone carbonatites

A) A transmitted light photomicrograph of mosaic-textured medium-grained dolomite. The sample was taken from the B zone. B) A transmitted light photomicrograph of deformed (sheared) dolomite carbonatite. Two distinct directions of deformation (traced in red dashed lines) are displayed in this sample taken from the A zone. C) A transmitted light photomicrograph of fine-scale textural variations. Granoblastic carbonates (center) are juxtaposed against a narrow band of sheared carbonate containing pyrite, fluorite, and monazite (right, outlined in red dashed lines), and are crosscut by a ptygmatic vein of phlogopite, fluorite, and monazite (left). The sample was taken from the A zone.

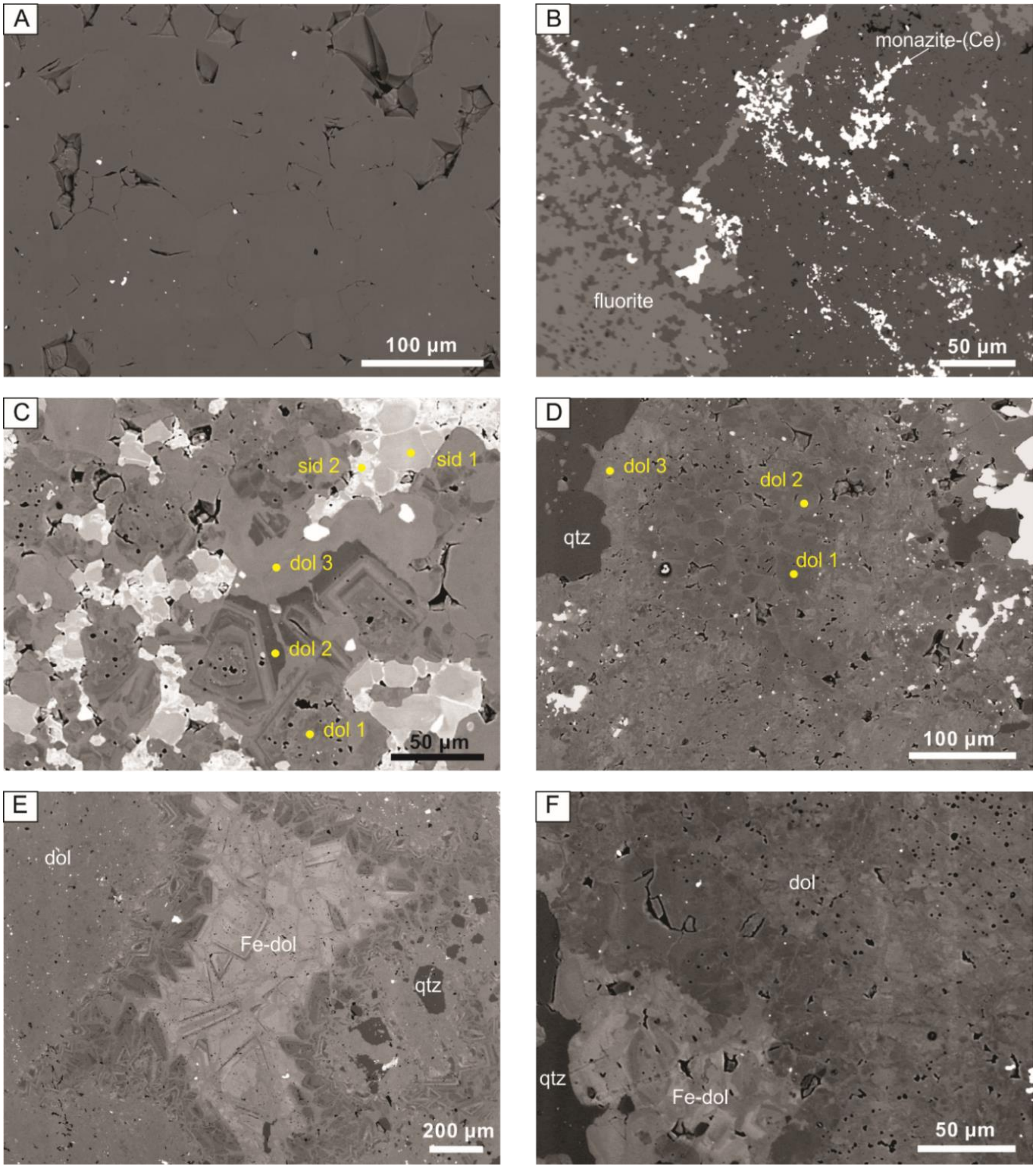

Figure 2.9: Representative BSE images of carbonate textures from the B and the A zone carbonatites

A) Homogeneous massive ferroan dolomite in the A zone. B) Homogeneous massive dolomite crosscut by veins of fluorite and monazite-(Ce) in the B zone. C) Hydrothermal alteration of A zone dolomite showing three generations of dolomite with interstitial siderite. D) Hydrothermal alteration of B zone dolomite showing three generations of dolomite. E) A vug in A zone carbonatite. Early vug dolomite prisms project into a cavity which was later infilled with ferroan dolomite. F) Vug dolomite in B zone carbonatite with late quartz.

in CL (BD-s apatite). Pale violet ovoid crystals of primary apatite (BD-p) occur locally within masses of secondary apatite (Fig. 2.10A). Apatite in this zone is commonly associated spatially with REE-fluorocarbonates. In the B zone, the apatite is fine- to medium-grained, sucrosic and white to pale grey-violet in CL (Fig. 2.10B). Rarely, the apatite crystals are surrounded by fine-grained monazite and dolomite (Fig. 2.10C). There are two types of apatite in the A zone. The first is an early, medium-grained, ovoid variety with a pale blue CL color that is extremely rare and is interpreted to be primary (A-p type). This apatite is mantled by a very fine-grained, sucrosic, secondary apatite (A-s type) with a yellow-white color in CL (Fig. 2.10D). The latter apatite also commonly occurs in veinlets and irregular millimetric-scale domains. Both the B and A-s apatite varieties are commonly intergrown on a very fine scale with royal blue (in CL) fluorite (Fig. 2.10B, D, E). Fluorite is most abundant in the A and B zones, but also occurs in the BD zone and as a cement to fragments in Rim dolomite carbonatite adjacent to the BD zone. There are three varieties of fluorite, distinguished by their CL color, namely bright green, blue-green, and royal blue fluorite (Fig. 2.10F). As mentioned earlier, fluorite in the Rim carbonatites is restricted to the dolomite carbonatite, in which it occurs in veins (< 1 cm wide) or as a cement in rare breccias. The CL color of this fluorite varies from blue-green to royal blue. In the Ashram deposit, all three varieties of fluorite are observed and all are closely associated spatially with monazite-(Ce) (or bastnäsite-(Ce) in the BD zone). Where this mineralization is disseminated, the fluorite is also disseminated. Fluorite also occurs in veins and, where this is the case, monazite-(Ce) or bastnäsite-(Ce) are commonly present. However, fluorite veins are also observed crosscutting REE mineralization. Bright green and blue-green (in CL) fluorite occur in the B, A, and MHREO zones, whereas fluorite in the BD zone is exclusively royal blue (in CL). Indeed, across the deposit, all fluorite in contact with apatite displays a royal blue color in CL (e.g. Fig. 2.10B). The relative timing of the different fluorite varieties is unclear. In some cases, bright green fluorite appears to have been earlier than blue-green fluorite, and vice versa, or rarely the fluorite displays oscillatory zoning of the two CL colors.

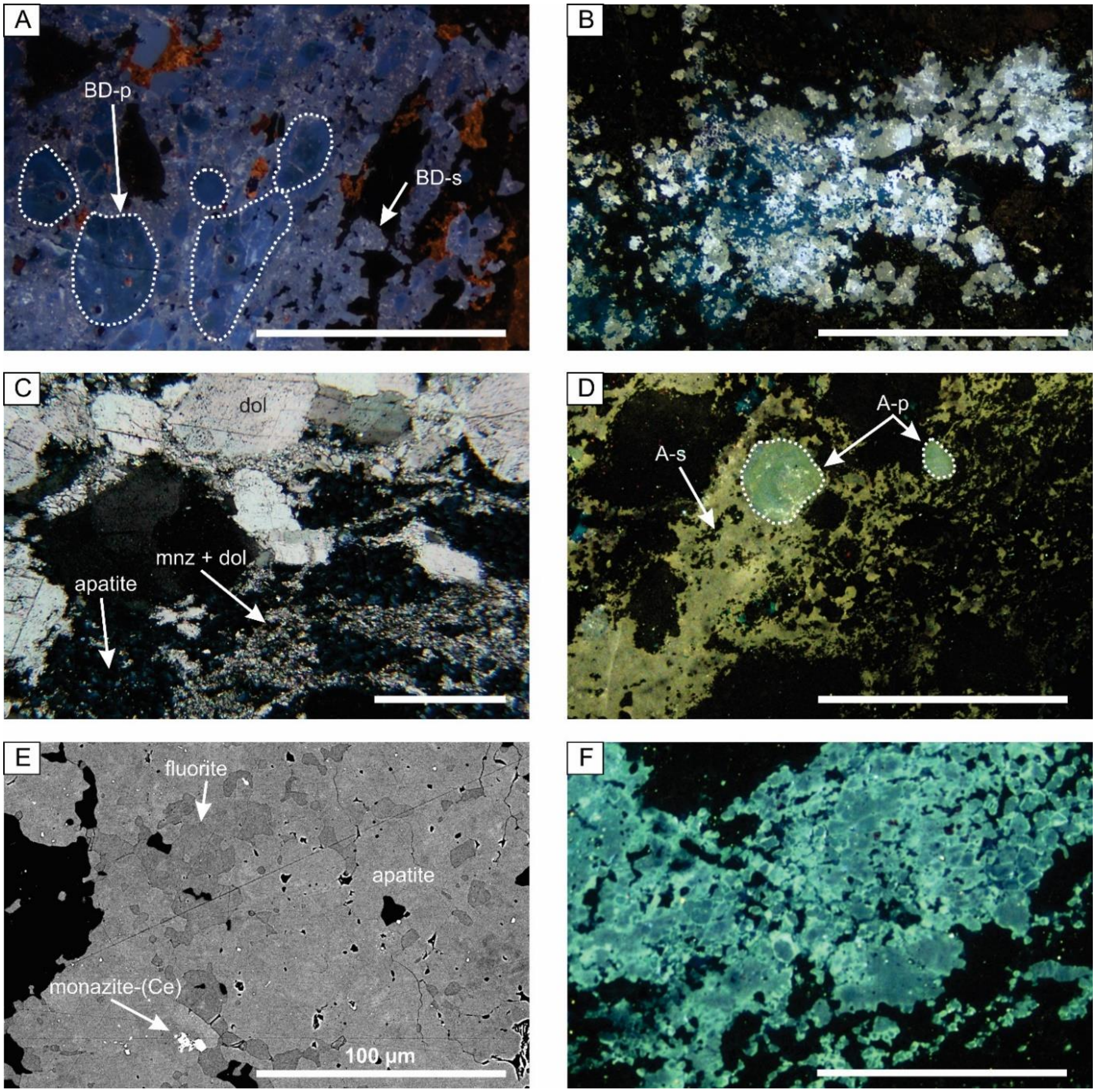

Figure 2.10: Representative images of apatite and fluorite in the Eldor carbonatites.

All scale bars are 1 mm, unless otherwise noted. A) A CL image of two types of apatite in the BD zone. Primary apatite (dashed white outline) is ovoid and violet-luminescent. Secondary apatite is fine-grained, sucrosic and pale pink to violet luminescent. Note that the same primary apatite is ubiquitous in the Rim zone and has rare secondary overgrowths. B) A CL image of apatite from the B zone. White to pale violet luminescent B type apatite is intimately intergrown with fine-grained, royal blue-luminescent fluorite. C) A cross-polarized transmitted light photomicrograph of coarse-grained dolomite in a matrix of fine-grained, sucrosic, recrystallized apatite with bands of fine-grained, intergrown monazite-(Ce) and dolomite. The sample was taken from the B zone. D) A CL image of two types of apatite in the A zone. Primary apatite (dashed white outline) is ovoid and has a pale greenish-blue luminescence. The secondary apatite is fine-grained, sucrosic and pale yellow luminescent. E) A BSE image of apatite with very fine-grained monazite-(Ce) inclusions (white) and patchy intergrown fluorite. The sample was taken from the B zone. F) A CL image of darker, blue-green-luminescent fluorite mantled by a later, bright green-luminescent generation. The sample was taken from the A zone.

The REE minerals, monazite-(Ce), bastnäsite-(Ce), parisite-(Ce), synchysite-(Ce), xenotime-(Y) and aeschynite-(Nd) occur in veins, as vug fillings, and as disseminations in breccia matrices in all the Ashram units (Fig. 2.11). Monazite-(Nd) has been observed exclusively in the MHREO zone, where it occurs at the margins of siderite crystals (Fig. 2.11A). Spatially, monazite-(Ce) is associated closely with fluorite (Fig. 2.11B). The REE-phosphates and REE-fluorocarbonates are rarely observed in contact with one another, owing to the contrast in the mineralogy of the BD zone from that of the rest of the Ashram deposit (see section 2.1.1). Where they are in contact, the REE-fluorocarbonates invariably mantle monazite-(Ce) (Fig. 2.11C, D) or replaced it (Fig. 20 of Mitchell and Smith, 2017). Xenotime-(Y) is generally associated with monazite-(Ce), which it mantles (Fig 2.11E, F). In some MHREO zone samples, xenotime-(Y) is associated with fractured, patchily altered crystals of a mineral tentatively identified as huttonite ($ThSiO_4$, Fig. 2.11F). Where apatite and monazite-(Ce) are observed in contact, monazite-(Ce) mantles apatite, and occurs in fractures within or at grain boundaries of the latter (Fig. 2.11C, D). Rarely, it occurs in domains with fine-grained dolomite in apatite (Fig. 2.10C). Aeschynite-(Nd) is commonly associated with, and later than, monazite-(Ce), xenotime-(Y), and Fe-oxides (e.g., ferrocolumbite, ilmenite, ilmenorutile). Bastnäsite-(Ce), monazite-(Ce) and -(Nd), and aeschynite-(Nd) are typically homogenous, whereas xenotime-(Y) crystals locally show oscillatory zoning. Very rarely, monazite-(Ce) crystals display a core to rim zonation, characterized by Th-enriched, La-depleted cores and Th-depleted, La-enriched rims (Fig. 2.12A-D).

Other minerals present in significant proportions in the Ashram deposit are pyrite, sphalerite, quartz, phlogopite and barite. Magnetite and bafertisite ($Ba_2Fe_4^{2+}Ti_2(Si_2O_7)_2O_2(OH)_2F_2$) are observed in the MHREO zone. Pyrite is a ubiquitous accessory mineral but is most abundant in the MHREO zone, where it occurs with sphalerite and magnetite that accompanied the replacement of siderite and magnesian siderite by dolomite (Fig. 2.7F). Its deposition predated that of the REE minerals (Fig. 2.9C). Quartz occurs in vugs in all zones, especially the MHREO zone, and is commonly associated with fluorite and/or calcite or dolomite (Fig. 2.7D, F). Phlogopite occurs in veins (mostly undeformed) in all of the Ashram units (Fig. 2.8C) and is variably associated with monazite-(Ce) and xenotime-(Y), or bastnäsite-(Ce). The REE minerals are interstitial to phlogopite, and in some cases, veins of monazite-(Ce) + fluorite + dolomite crosscut phlogopite (Fig. 2.12E). Bafertisite occurs in veins that post-dated the monazite mineralization. It is commonly in close association with magnetite, and was altered to

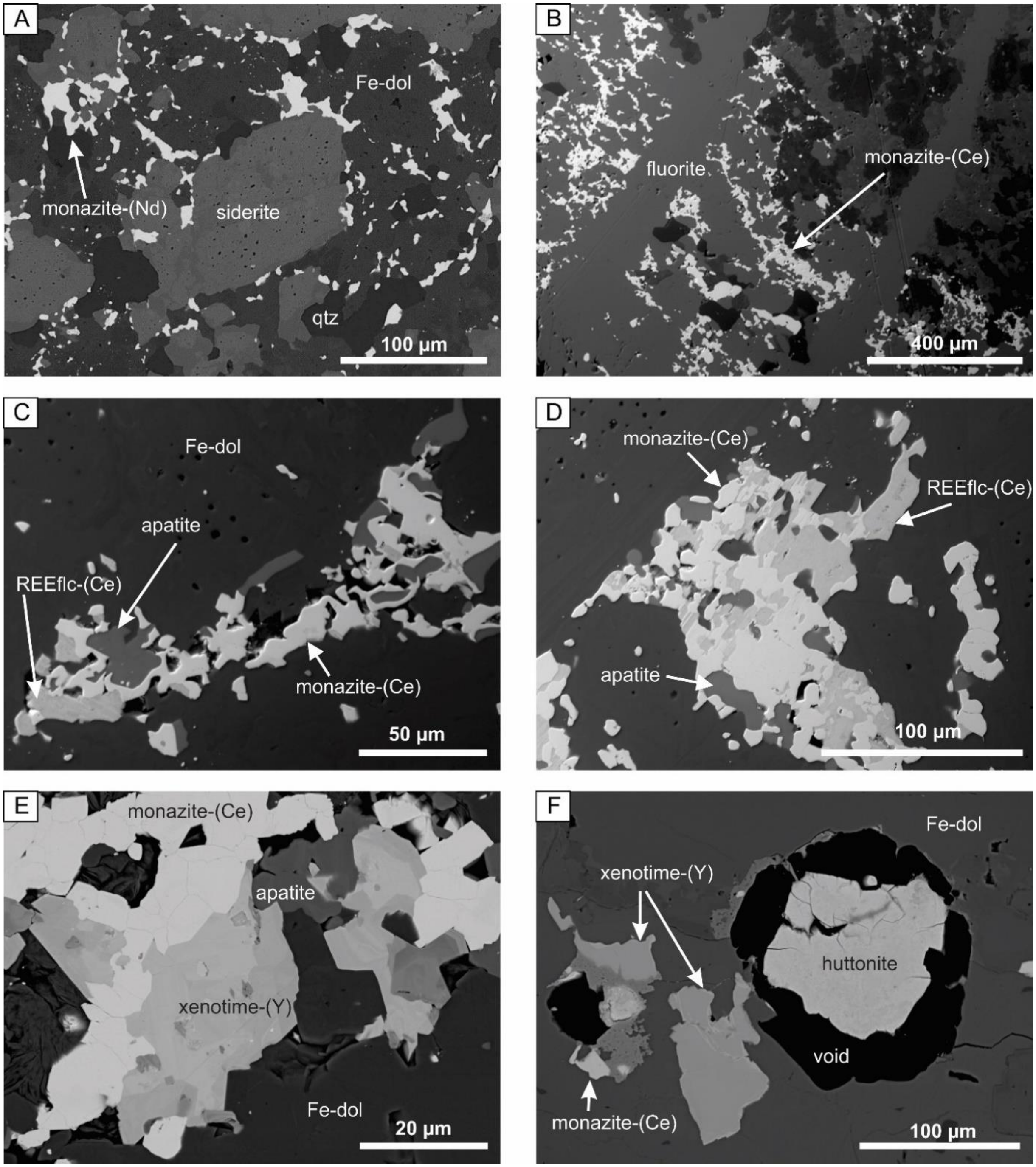

Figure 2.11: Back-scattered electron images of REE minerals, their textures and paragenetic relationships

A) Monazite-(Nd) of the MHREO zone at the margins of siderite crystals. B) Veins of fluorite and monazite-(Ce) crosscut by a later generation of fluorite veins. The sample was taken from the B zone. C) and D) Rare samples showing the relationships between apatite, monazite-(Ce) and the REE-fluorocarbonate minerals (REEflc-(Ce)). Apatite is mantled by monazite-(Ce) which, in turn, is mantled by REE-fluorocarbonates. The samples were taken from the BD zone. E) A rare sample showing the relationship between the different phosphate minerals. Apatite was earliest, followed by monazite-(Ce), which is mantled by xenotime-(Y). The sample was taken from the A zone. F) Altered "huttonite" of the MHREO zone that is spatially associated with xenotime-(Y) and monazite-(Ce).

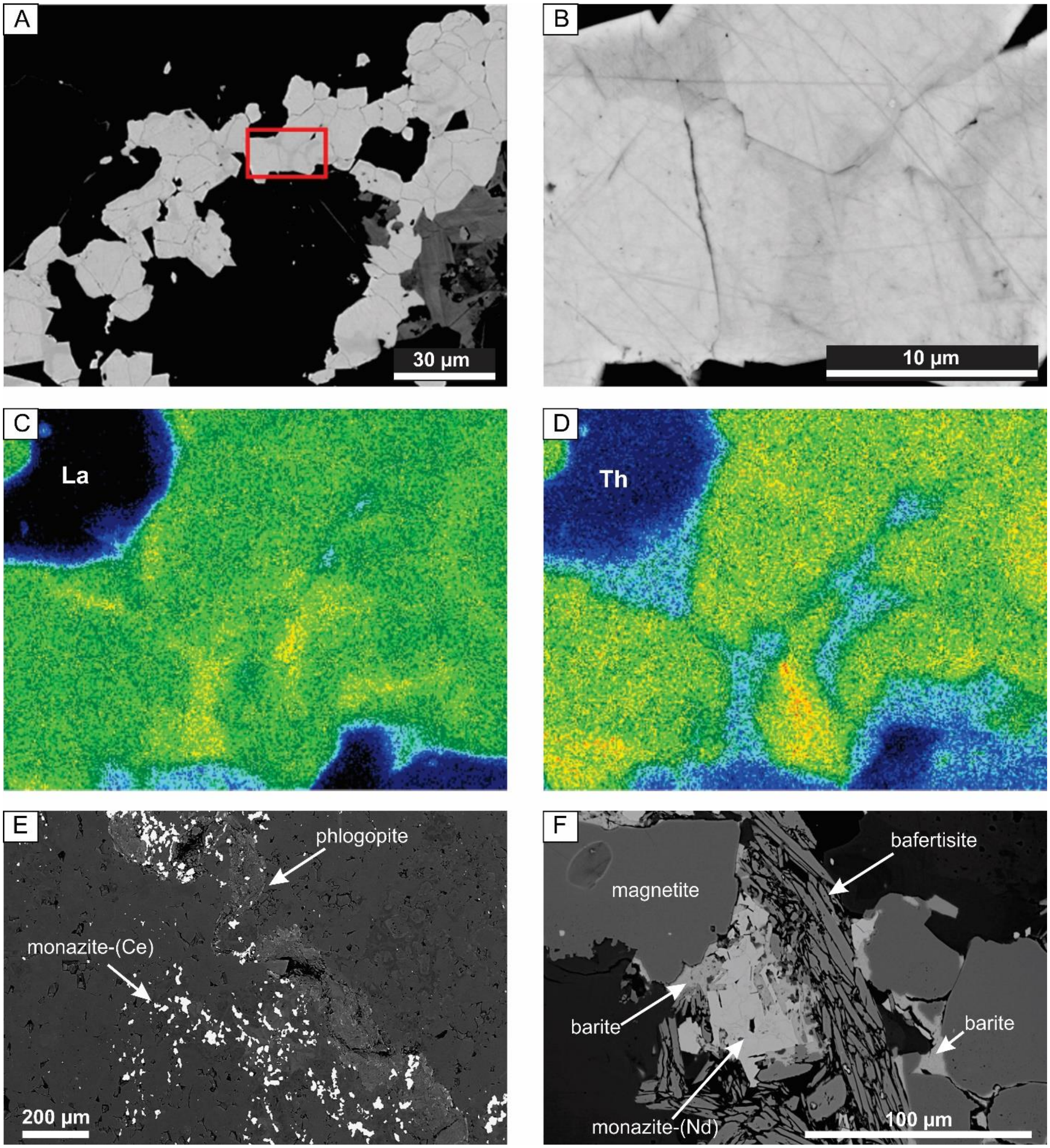

Figure 2.12: Representative images of the monazite mineralization and its paragenetic relationships

A) A BSE image showing a rare occurrence of zoned monazite crystals. The sample was taken from the A zone. The area outlined in red represents the area shown in Figs B-D. B) A BSE image of the area of interest at higher magnification. C) An EDS map of the La distribution in the area of interest. D) An EDS map of the Th distribution in the area of interest. In C) and D), the warmer colours, yellow and green, indicate higher concentrations. E) A BSE image from A zone carbonatite with patches of monazite-(Ce) and fluorite cut by a folded phlogopite veinlet. F) Late barite associated with magnetite, bafertisite, and monazite-(Nd) in the MHREO zone.

barite (Fig. 2.12F). Barite has also been rarely observed as prismatic crystals with phlogopite in vugs in the BD zone. Magbasite ($KBaFe^{3+}Mg_7Si_8O_{22}(OH)_2F_6$) was reported by Mitchell and Smith (2017) to occur in the MHREO zone but was not present in our samples.

2.3.3 Mineral Chemistry

2.3.3.1 Carbonates

Electron microprobe analyses were performed on carbonate minerals in samples collected from each lithofacies of the carbonatite complex (Table 2.3; Appendix 2.2). Calcite from the earliest Rim carbonatite, calcite carbonatite 1, has a near end-member composition with minor concentrations (< 1 wt. %) of Fe, Mg, Mn, and Sr. In calcite carbonatite 2, the calcite is enriched in Mg, and Fe relative to calcite in calcite carbonatite 1. As noted above, the Rim dolomite comprises three generations of dolomite, early clasts and later groundmass (two varieties; Fig. 2.7C). These three generations define trends of progressive depletion in Sr and enrichment in Fe. Dolomite 1 is strongly enriched in Mg relative to the other two types, and dolomite 2 is enriched in Mn. Like the dolomite clasts in the Rim dolomite carbonatite, the dolomite clasts in the BD zone are enriched in Mg and Sr relative to the later dolomite generations (Fig. 2.7B). Similarly, dolomite 2 is the dolomite most enriched in Mn. However, whereas the Fe concentration increases from dolomite 1 to 3 in the Rim carbonatite, Fe reaches its highest concentration in dolomite 2 of the BD zone. Dolomite 2 has the lowest Mg and Sr concentrations of the three generations of dolomite in the BD zone.

Three types of dolomite have been distinguished in the massive carbonate of the B zone. The first type, dolomite 1, is interpreted to be primary, and has been replaced by dolomite 2 (Fig. 2.9D). These two varieties commonly form islands within a sea of dolomite 3 (Fig. 2.9D). Concentrations of Mg decrease progressively from dolomite 1 to dolomite 3, and are matched by progressive increases in the concentrations of Fe and Mn. The Sr concentration is similar in dolomite 1 and 2, and sharply lower in dolomite 3. In the massive carbonate of the A zone, relict, early dolomite 1 is overgrown by zoned dolomite 2 (Fig. 2.9C). However, in contrast to the B zone, there is a marked increase in Mg content in dolomite 2 relative to dolomite 1 and corresponding decreases in Fe and Mn contents; the Sr content is low but increases from dolomite 1 to dolomite 2. The massive carbonate in the MHREO zone is siderite, which displays multiple stages of replacement (four stages of siderite have been distinguished). There is a progressive enrichment

Table 2.3: Representative major element oxide compositions and cation proportions of carbonate minerals

	Rim					**Ashram**							
Unit	**Cal Carb 1**	**Cal Carb 2**	**Dol Carb**			**BD**			**B**			**A**	
Sample	15029	15050	15109			15115			15141			15005	
Mineral	cc mass	cc mass	*dol1* clast	*dol2* mass	*dol3* mass	*dol1* clast	*dol2* mass	*dol3* mass	*dol1* mass	*dol2* mass	*dol3* mass	*dol1* mass	*dol2* mass
CaO (*wt. %*)	54.50	53.31	29.66	28.40	29.36	28.78	28.78	28.79	28.60	28.69	28.63	28.09	29.51
MgO	0.10	1.22	20.22	17.40	16.64	20.77	14.53	17.30	20.34	18.96	17.10	14.11	20.68
FeO	0.56	0.94	1.15	4.07	6.62	1.03	9.65	6.01	2.18	3.61	5.57	10.48	1.69
MnO	0.64	0.26	0.76	3.06	0.49	0.48	1.35	0.75	0.57	0.68	1.76	1.55	0.15
SrO	0.29	0.50	0.48	0.39	0.09	1.25	0.08	0.57	0.69	0.77	0.20	0.29	0.42
CO_2	43.91	43.77	47.73	46.68	46.80	47.69	45.61	46.58	47.62	47.29	46.74	45.49	47.55
Total	100	100	100	100	100	100	100	100	100	100	100	100	100
	O = 3							**O = 6**					
Ca (*apfu*)	0.975	0.953	0.982	0.961	0.993	0.954	0.993	0.975	0.949	0.960	0.968	0.973	0.978
Mg	0.002	0.030	0.932	0.819	0.783	0.958	0.698	0.815	0.939	0.882	0.805	0.680	0.953
Fe	0.008	0.013	0.030	0.107	0.175	0.027	0.260	0.159	0.056	0.094	0.147	0.283	0.044
Mn	0.009	0.004	0.020	0.082	0.013	0.013	0.037	0.020	0.015	0.018	0.047	0.042	0.004
Sr	0.003	0.005	0.009	0.007	0.002	0.022	0.001	0.010	0.012	0.014	0.004	0.005	0.008
C	1.001	0.997	2.014	2.012	2.017	2.014	2.005	2.010	2.014	2.016	2.015	2.008	2.007
Total	1.999	2.003	3.986	3.988	3.983	3.986	3.995	3.990	3.986	3.984	3.985	3.992	3.993

** Compositions of italicized mineral names correspond to points shown in Figures 7 and 9*

'bdl' – below the limit of detection

CO_2 contents were calculated from the difference between the analytical total and 100 wt. %

Table 2.3: Continued

	Ashram								
Unit	**A**			**MHREO**					
Sample	15005			15339				15337	
Mineral	*dol3* vug	*sid1* vug	*sid2* vug	*sid1* mass	*sid2* mass	*sid3* mass	*sid4* mass	dol vug	ank vug
CaO (*wt. %*)	27.92	0.74	0.26	0.43	0.49	0.06	0.07	29.21	27.04
MgO	13.63	18.03	13.54	2.75	4.70	7.84	11.79	17.18	8.15
FeO	11.20	35.07	39.14	53.61	50.01	48.24	42.92	6.37	19.01
MnO	1.76	4.02	4.21	4.17	4.59	4.19	4.42	0.80	2.02
SrO	0.22	bdl	bdl	bdl	bdl	bdl	bdl	bdl	0.32
CO_2	45.27	42.14	42.85	39.04	40.21	39.67	40.80	46.44	43.46
Total	100	100	100	100	100	100	100	100	100
	O = 6			**O = 3**				**O = 6**	
Ca (*apfu*)	0.971	0.014	0.005	0.009	0.010	0.001	0.001	0.990	0.979
Mg	0.660	0.460	0.348	0.077	0.129	0.214	0.313	0.810	0.410
Fe	0.304	0.501	0.565	0.843	0.770	0.738	0.638	0.168	0.537
Mn	0.048	0.058	0.062	0.066	0.072	0.065	0.067	0.021	0.058
Sr	0.004	0.000	0.000	0.000	0.000	0.000	0.000	0.000	0.006
C	2.006	0.984	1.010	1.002	1.010	0.991	0.991	2.005	2.005
Total	3.994	2.016	1.990	1.998	1.990	2.009	2.009	3.995	3.995

** Compositions of italicized mineral names correspond to points shown in Figures 7 and 9*

'bdl' – below the limit of detection

CO_2 contents were calculated from the difference between the analytical total and 100 wt. %

in Mg and a depletion in Fe from siderite 1 to siderite 4 but the Mn content is relatively unchanged (Fig. 2.7E). The dominant carbonate filling vugs in the B zone is dolomite and has the highest concentration of Fe and Mn of any of the dolomite in this zone (Fig. 2.9F). Both dolomite and siderite are important vug minerals in the A zone (Fig. 2.9C). Like the vug dolomite in the B zone, this dolomite in the A zone has the highest concentration of Fe and Mn of any dolomite in the zone. The vug dolomite in the A zone was post-dated by two generations of siderite (Fig. 2.9C) which record a progressive enrichment in Fe. In contrast to the A zone vugs, there is no siderite in the MHREO vugs, although they rarely contain ankerite, which by comparison with the dolomite in these vugs, is enriched in Mn and Sr.

The carbonate minerals of each unit were also analysed by LA-ICP-MS to establish their trace element compositions (Table 2.4; Appendix 2.3). Because of the necessarily large spot size, some of the data represents composites of two dolomite types. The Ba content of the carbonate mineral decreases progressively from calcite carbonatite 1 through calcite carbonatite 2 to the Rim dolomite carbonatite (dolomite 1; Fig. 2.13). The Ba contents of the BD zone dolomite 1 and composite (secondary dolomite) are remarkably similar to those of the primary and secondary Rim dolomite, with a Ba content < 60 ppm (Fig. 2.13). In contrast, the Ba content of the B and A zone dolomite (composites of dolomite 1 - 3) ranges up to 159 ppm, with the low end of the range being 33 ppm for the B zone, and 50 ppm for the A zone. Siderite in the A zone was too fine-grained to analyze reliably, and in the MHREO zone, has an average Ba content of 12 ppm, the lowest of any of the carbonates analyzed.

The only other elements that are present in significant concentrations in the carbonates are Zn, V, the REE including Sc, and Pb (Table 2.4). Calcite in calcite carbonatite 1 and 2 contains < 10 ppm Zn, whereas in the primary dolomite of the Rim dolomite carbonatite, the concentration ranges up to 35 ppm, and in the composite dolomite (dolomite 2 and 3), it ranges up to 23 ppm (Fig. 2.13A). The Zn contents of the primary and secondary dolomites of the BD zone carbonatite are virtually the same as those of the Rim dolomite carbonatite. In contrast, the Zn content of the B zone dolomite is generally much higher, ranging from 11 to 197 ppm, and that of the A zone dolomite is even higher (73 to 274 ppm, Fig. 2.13B). The distribution of V among the different carbonate types is remarkably similar to that of Zn, i.e., the V contents of the calcite and dolomite in the Rim and the primary dolomite of the BD zone are all very low, < 10 ppm (Fig. 2.13C.), the

Table 2.4: Trace element compositions of carbonate minerals

Mean trace element compositions of carbonate minerals in the different units of the Eldor Carbonatite Complex

Unit	**Cal Carb 1**		**Cal Carb 2**		**Dol Carb**				**BD**				**B**			
Mineral	cal		cal		dol		dol comp		dol		dol comp		dol comp		dol comp	
Sample (n)	15029 (7)		15059 (14)		15109 (7)		15109 (7)		15114 (5)		16027 (6)		16019 (16)		15127 (9)	
		1σ		1σ		1σ		1σ		1σ		1σ		1σ		1σ
Sc (*ppm*)	4	2	9	5	5	1	13	2	6	2	40	7	20	9	31	2
V	0.7	0.1	0.1	0.1	5	1	4.6	0.4	3	2	20	10	19	9	23	3
Zn	7	2	7	2	28	4	20	1	21	4	35	15	69	57	58	17
Sr	3366	365	6502	1248	4436	385	3372	147	7432	953	2703	686	2711	1503	2043	101
Ba	981	93	457	61	30	5	24	7	49	6	42	9	56	14	92	29
Pb	14	2	18	6	11	7	1.5	0.4	4	2	2	1	10	6	14	1
La	23	5	25	23	12	4	3	1	19	8	2	1	17	13	16	11
Ce	86	14	57	48	30	8	10	3	50	22	8	3	60	32	60	35
Pr	16	3	8	6	3	1	1.6	0.5	6	3	1.4	0.5	11	6	12	6
Nd	62	10	32	21	10	3	5	2	20	9	6	2	56	32	54	25
Sm	17	1	8	3	1.5	0.4	1.1	0.3	3	2	2	1	22	16	16	3
Eu	6.2	0.4	3	1	0.4	0.1	0.4	0.1	0.9	0.4	1.0	0.6	9	6	6	1
Gd	23	2	13	2	1.2	0.3	1.1	0.3	3	1	3	2	26	17	18	3
Tb	3	1	1.5	0.3	0.14	0.03	0.15	0.03	0.3	0.1	0.5	0.4	5	3	3	1
Dy	23	5	9	2	0.7	0.1	0.8	0.1	1.3	0.4	3	2	27	15	20	3
Y	136	43	53	13	3	1	4	1	6	2	12	11	103	43	94	15
Ho	5	2	2	1	0.13	0.03	0.16	0.03	0.3	0.1	0.6	0.5	5	2	4	1
Er	15	6	5	1	0.3	0.1	0.43	0.05	0.7	0.2	1.4	1.1	10	4	10	2
Tm	2	1	0.8	0.2	bdl		bdl		bdl		0.21	0.15	1.2	0.3	1.2	0.2
Yb	13	6	5	1	0.3	0.1	0.46	0.04	0.6	0.2	1.2	0.8	6	1	6	1
Lu	2	1	0.7	0.2	bdl		bdl		0.10	0.05	0.2	0.1	0.7	0.1	0.7	0.1

‘dol comp’ – composite analysis of dolomite types 2 and 3 due to the large LA-ICP-MS spot size

Table 2.4: Continued

Unit	**A**						**MHREO**		**Breccia**	
Mineral	dol comp		dol comp		vug dol		sid		dol	
Sample (n)	15020 (22)		15026 (16)		15026 (10)		15014 (12)		16038 (16)	
		1σ		1σ		1σ		1σ		1σ
Sc (*ppm*)	38	3	63	6	25	15	15	7	22	3
V	36	7	36	10	36	13	45	33	13	15
Zn	113	45	142	22	62	14	282	109	51	17
Sr	1824	147	2305	214	2667	712	7	4	3132	1125
Ba	82	32	73	17	62	48	12	5	32	10
Pb	12	2	16	4	5	3	4	2	5	3
La	11	4	9	3	1	0.7	0.2	0.1	1.3	0.6
Ce	41	12	25	5	3	2	0.8	0.3	6	1
Pr	8	2	4	1	0.5	0.3	0.2	0.1	1.2	0.2
Nd	39	12	20	4	2	1	1.5	0.5	6	1
Sm	14	4	9	1	0.9	0.4	0.8	0.4	1.9	0.4
Eu	6	1	4	1	0.6	0.2	0.3	0.1	0.8	0.2
Gd	20	4	13	2	2	1	1.2	0.6	2.1	0.4
Tb	4	1	2.6	0.4	0.4	0.1	0.2	0.1	0.3	0.1
Dy	21	4	17	3	3.1	0.4	2	1	2	1
Y	88	16	85	13	18	3	13	8	11	13
Ho	3	1	3	1	0.7	0.2	0.4	0.3	0.3	0.2
Er	8	2	8	1	2	1	1.4	0.9	1	0.8
Tm	0.9	0.2	0.9	0.2	0.3	0.1	0.2	0.1	0.1	0.1
Yb	5	1	5	1	2	1	1.4	0.8	0.8	0.7
Lu	0.7	0.2	0.7	0.1	0.3	0.1	0.2	0.1	0.1	0.1

‘dol comp’ – composite analysis of dolomite types 2 and 3 due to the large LA-ICP-MS spot size

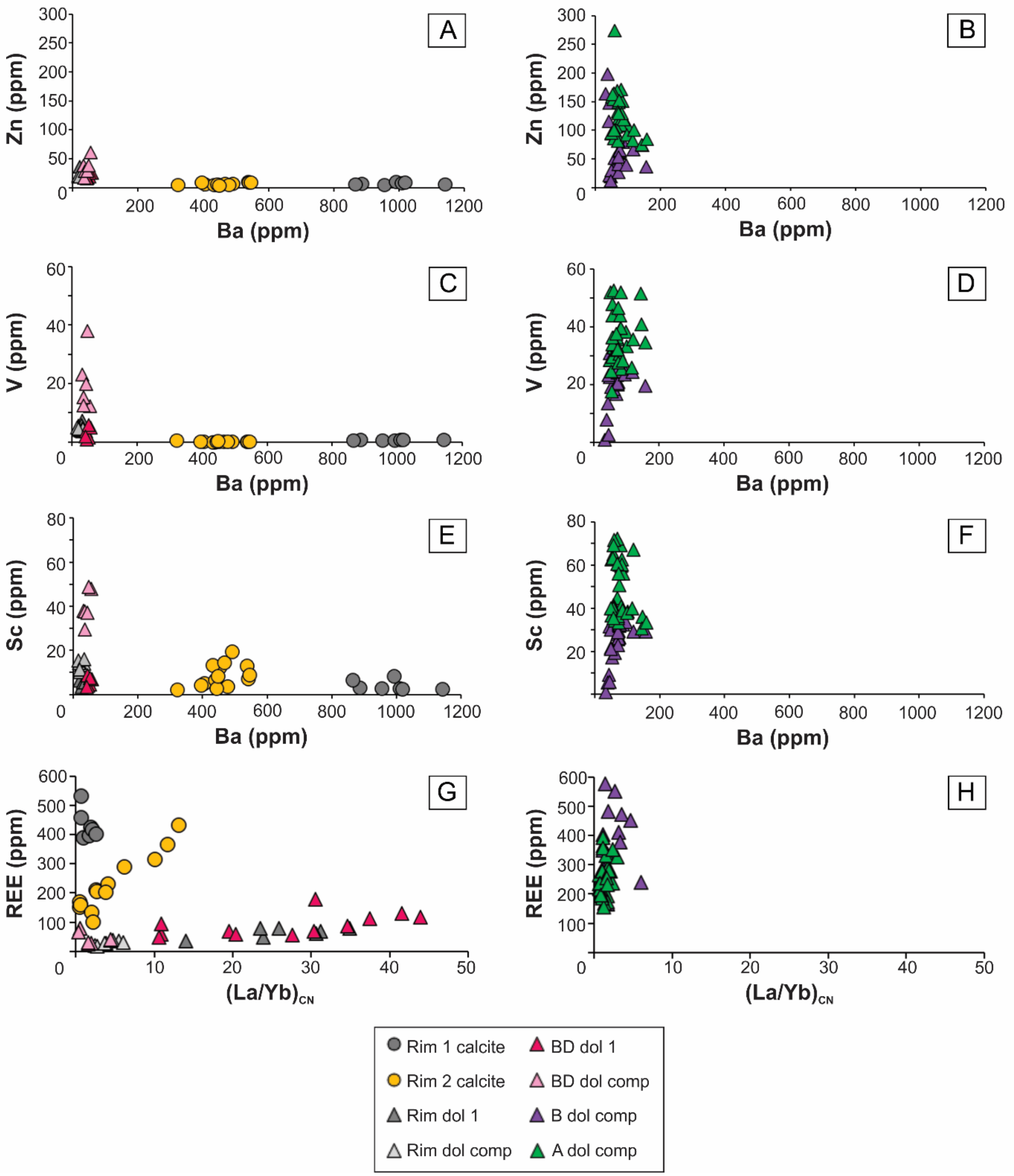

Figure 2.13: Trace element compositions of calcite and dolomite

Trace element compositions of calcite and dolomite across the Eldor Carbonatite Complex. The La and Yb values in G) and H) were normalized to CI chondrite (McDonough and Sun, 1995).

V content of the B zone dolomite ranges from a very low value, 1 ppm, to a relatively high value of 27 ppm, and the range of V contents for the A zone dolomite is significantly higher, 17 to 52 ppm (Fig. 2.13D). The only difference between the distributions of Zn and V is that the V content of the secondary BD dolomite ranges up to a relatively high value of 38 ppm (Fig. 2.13C). The absolute Sc concentrations and their distributions among the different carbonate types are very similar to those of V (Fig. 2.13E, F). Indeed, the only significant difference is that two analyses from calcite carbonatite 2 reported elevated Sc concentrations (26 and 27 ppm). Lead concentrations are lower than those of Zn, V, and Sc, and in the Rim carbonates, form two populations, one of which is < 5 ppm, and the other of which is largely between 10 and 20 ppm (Table 2.4). In the A and B zone carbonates, the Pb concentration forms a single population from < 5 ppm to ~ 30 ppm, although the lowest values are dominantly for B zone dolomite.

Chakhmouradian et al. (2016) showed that on plots of total REE concentration versus $(La/Yb)_{CN}$ (where CN refers to chondrite-normalized), the compositions of the primary carbonates in carbonatites commonly have linear distributions, which they attributed to fractional crystallization of particular REE-rich minerals such as apatite and monazite. We therefore decided to illustrate our REE data using the same parameters. As is evident from Figure 2.13G, the primary carbonates in the Rim carbonatites define three linear trends. The slopes of these trends decrease from vertical for calcite carbonatite 1 to intermediate for calcite carbonatite 2 and shallow for the dolomite carbonatite. Significantly, the distribution of the compositions of the primary BD zone dolomite is indistinguishable from that of the primary Rim dolomite; the compositions of the secondary Rim and BD zone dolomite, although very similar, are characterized by low $(La/Yb)_{CN}$ ratios. The composition of the dolomite in the A and B zones defines a single subvertical trend.

2.3.3.2 Apatite

Despite striking differences in morphology and CL color, the various types of apatite all classify as fluorapatite based on their fluorine content, and contain similar proportions of most major and minor elements (Appendix 2.4). The different apatite types can only be reliably distinguished compositionally by their trace element contents, average values for which are reported in Table 2.5 (the full data set is reported in Appendix 2.5). All ovoid apatite (primary and mainly in the Rim but also in the A and BD zones) contains much less Sr and Ba than the fine-grained secondary

Table 2.5: Mean trace element compositions of apatite

Unit	**Cal Carb 1**				**Cal Carb 2**		**Dol Carb**		**BD**				**B**		**A**			
Sample (n)	15029 (12)		15029 (4)		15049 (11)		15109 (11)		15114 (9)		15114 (5)		16010 (13)		15194 (17)		15193 (11)	
Type	Rim1-p		Rim1-s		Rim2-p		Rim3-p		BD-p		BD-s		B		A-p		A-s	
		1σ		1σ		1σ		1σ		1σ		1σ		1σ		1σ		1σ
Na (*ppm*)	945	155	1509	216	486	92	745	173	538	76	1170	58	2202	1346	1862	289	1963	540
Sr	4459	832	6163	673	4736	483	5020	584	4586	458	5859	227	16085	1306	6143	797	11997	1252
Ba	17	3	37	8	21	7	21	8	18	3	56	13	49	11	38	7	77	16
La	843	283	766	140	991	76	860	77	1025	79	349	25	556	76	678	59	395	44
Ce	2616	597	2609	329	3498	269	3016	422	3586	308	2241	180	2154	315	2227	168	2246	278
Pr	285	69	381	33	369	38	330	35	379	38	405	20	304	54	354	25	356	33
Nd	996	252	1620	131	1345	135	1167	129	1403	137	2179	56	1291	260	1629	158	1774	163
Sm	149	40	388	30	194	22	169	23	206	21	620	44	276	65	463	103	682	59
Eu	41	11	131	13	51	5	46	7	53	5	200	13	90	20	163	42	259	26
Gd	110	32	383	35	144	15	118	17	148	15	508	40	230	51	493	138	733	92
Tb	12	4	59	5	14	1	12	2	14	1	58	7	31	6	80	24	138	15
Dy	55	23	366	29	62	6	53	10	64	6	260	30	181	35	469	143	816	90
Y	198	93	1682	140	212	15	176	33	216	16	1110	142	998	229	1809	467	3811	645
Ho	9	4	67	5	9	1	8	1	10	1	38	5	32	6	72	21	127	14
Er	19	9	167	16	20	2	17	3	21	2	82	10	80	16	141	39	255	35
Tm	2	1	18	2	2.0	0.2	1.8	0.4	2.1	0.2	8	1	9	2	13	3	24	4
Yb	9	4	85	9	10	1	9	2	10	1	42	5	45	10	59	14	109	17
Lu	1.0	0.4	9	1	1.2	0.1	1.1	0.3	1.2	0.1	5.2	0.4	5	1	6	1	12	1

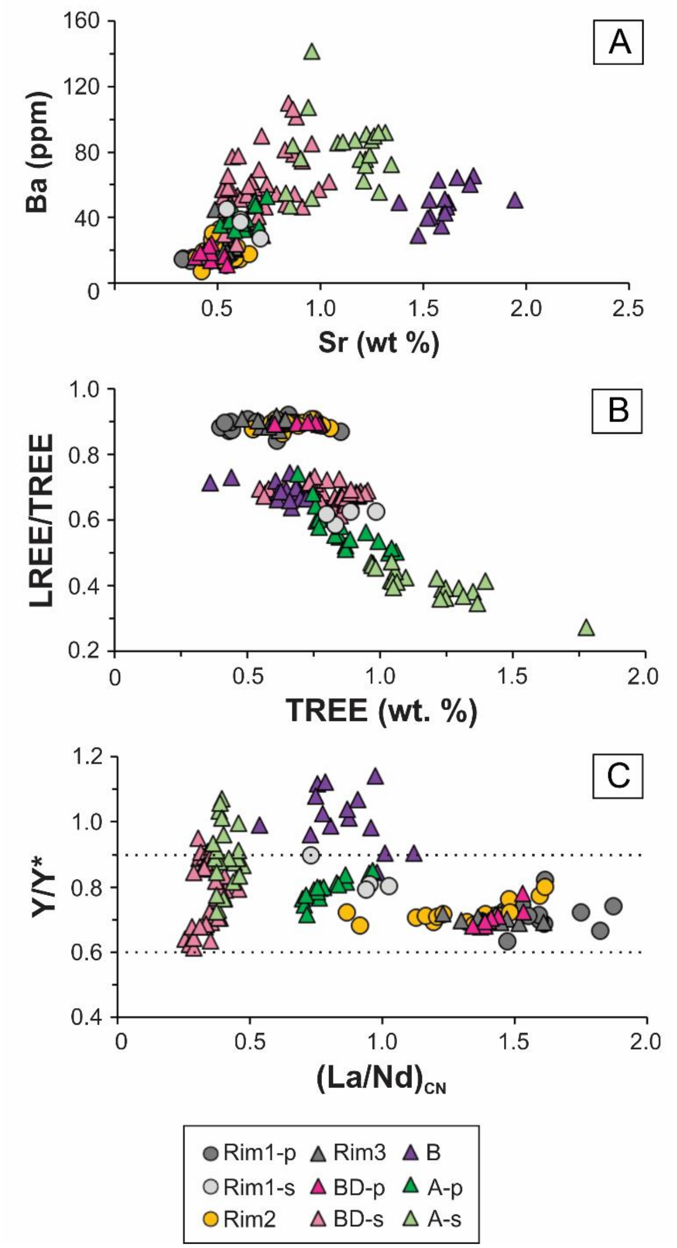

Figure 2.14: Trace element composition of apatite

The dashed lines in C) define the typical ranges in Y/Y* of igneous apatite defined by Chakhmouradian et al. (2017). The values of the REE in this diagram were normalized to CI chondrite (McDonough and Sun, 1995).

varieties (Fig. 2.14A). With the exception of the B zone apatite, the secondary apatite defines a trend of increasing Ba and Sr that extends from the composition of the primary apatite. The B zone apatite, however, forms a separate population characterized by high Sr and intermediate Ba concentrations. Primary Rim and BD apatite also contains less Na than the primary and secondary Ashram apatite (Table 2.5). The secondary Rim and BD apatite contains substantially more Na than its primary precursor, but the B and A zone secondary apatite has the highest Na content of all the apatite types analyzed (Table 2.5). The only other elements present in appreciable concentrations in the apatite are the REE.

Primary apatite from the Rim calcite and dolomite carbonatites, as well as from the BD zone, forms a single population characterized by a high LREE/TREE ratio and a relatively wide range of TREE concentrations (Fig. 2.14B). In contrast, the B zone and secondary A zone apatites define high and low LREE/TREE ends, respectively, of a linearly distributed population in which the LREE/TREE ratio decreases with increasing TREE content; the primary A zone apatite population occupies the central part of this trend. The secondary BD zone apatite forms a population parallel to that of the primary Rim and BD zone apatite but displaced to lower LREE/TREE ratios. Chakhmouradian et al. (2017) showed that the Y/Y* ratio ($Y_{CN}/(0.25*Dy_{CN} + 0.75*Ho_{CN})$) is an effective discriminant of primary and secondary apatite in carbonatites, with primary apatite being characterized by Y/Y* values between 0.6 and 0.9, and secondary apatite by values above or below this range. In Figure 2.14C, we plot this ratio as a function of $(La/Nd)_{CN}$ and, as is evident from this figure, all the primary apatite (Rim, BD, A) has igneous Y/Y* ratios. The $(La/Nd)_{CN}$ ratio varies widely and, although there is a high degree of overlap, apatite from the Rim calcite carbonatite 1 generally has the highest $(La/Nd)_{CN}$ ratio and that from calcite carbonatite 2 the lowest ratio; apatite from the Rim dolomite carbonatite and the BD zone form the central part of the distribution with $(La/Nd)_{CN}$ ratios that largely overlap. The primary A zone apatite forms a population at the lower end of the trend. As noted earlier, secondary apatite is rare in the Rim carbonatites and only that from calcite carbonatite 1 was suitable for analysis. This apatite has Y/Y* values within the primary apatite range, but is displaced to much lower $(La/Nd)_{CN}$ values than the corresponding primary apatite in calcite carbonatite 1. With the exception of the B zone apatite, all the secondary apatite in the Ashram deposit defines a trend with a $(La/Nd)_{CN}$ ratio that extends from the lower boundary of the igneous range of Y/Y* to values > 1. The B zone apatite, by contrast, has a significantly higher $(La/Nd)_{CN}$ ratio and with the exception of two analyses, all the Y/Y* values are ≥ 0.9.

2.3.3.3 Fluorite

Fluorite from the Rim dolomite carbonatite, BD zone, MHREO zone, polymictic breccia and late veins (crosscutting mineralization) was analyzed by LA-ICP-MS (Table 2.6; Appendix 2.6). Owing to the fact that fluorite is finely intergrown with monazite-(Ce) in the B and A zones, it was not possible to determine the composition of fluorite reliably for these zones, except where it occurs in veins that crosscut the mineralization. Mitchell and Smith (2017), however, reported compositions of fluorite coexisting with monazite in the A zone, based on SIMS analyses. The only elements present in significant proportions in the fluorite are Sr, Ba, and the REE. The fluorite from all the zones is enriched in Y and depleted in the other REE (Table 2.6). As is the case for the carbonate data, the Ba contents of the fluorite in the Rim dolomite carbonatite and the BD zone carbonatite are indistinguishable, and the fluorite in these units is only distinguished by the much higher HREE/TREE ratio in the BD zone (Fig. 2.15A). In contrast to the fluorite in these two units, there is a progressive decrease in the Ba content of the fluorite from the BD zone through the breccia to the MHREO zone; the late vein fluorite has a similar Ba content to the MHREO zone fluorite. This trend is matched by a corresponding increase in the HREE/TREE ratio. The compositions of the different fluorite types referred to above are all characterized by relatively low TREE contents (< 400 ppm), except for the A and MHREO zone fluorite which contains up to 600 ppm and 900 ppm TREE, respectively (Fig. 2.15B). As with the Ba content, the Sr concentration of the fluorite of the Rim dolomite carbonatite and that of the BD zone is almost indistinguishable (Fig. 2.15B). The Sr content of the breccia fluorite is somewhat higher than that of the Rim and BD zone fluorite, whereas the Sr content of the vein fluorite extends from very low values (< 400 ppm) to > 3500 ppm. The Sr and TREE contents of the MHREO zone fluorite are strongly correlated and form a linear distribution that is co-linear with, and extends from, the breccia fluorite. Although the Sr contents of the A zone fluorite are slightly higher than those of the MHREO zone fluorite, the Sr and TREE contents are linearly distributed and roughly coincident with the trend for the MHREO zone.

Table 2.6: Mean trace element composition of fluorite

Unit	**Dol Carb**		**BD**		**MHREO**				**Late Veins**				**Breccia**	
Sample (n)	15109 (15)		15116 (7)		15348 (14)		15013 (17)		15396 (15)		15222 (17)		16038 (13)	
		1σ		1σ		1σ		1σ		1σ		1σ		1σ
Sr (*ppm*)	682	148	566	104	2273	158	1601	85	1724	44	1433	961	1145	66
Ba	8	2	8	2	2	1	2	2	0.3	0.1	1.6	1.8	7	3
La	3.3	0.4	3	1	0.3	0.1	0.3	0.1	0.18	0.03	0.4	0.2	1.4	0.3
Ce	14	4	8	2	1.5	0.5	0.8	0.4	0.55	0.04	1.2	0.3	3	1
Pr	4	1	1.6	0.2	0.8	0.2	0.3	0.1	0.18	0.01	0.4	0.1	0.6	0.2
Nd	26	11	10	2	10	2	4	1	1.8	0.1	3	1	3	1
Sm	10	4	5	1	8	1	3	1	1.8	0.1	2.5	0.4	2	1
Eu	3	1	1.8	0.4	3.8	0.5	1.5	0.3	1.1	0.1	1.3	0.1	0.8	0.3
Gd	11	4	7	1	17	2	7	1	4.9	0.2	5	1	4	1
Tb	2	1	0.8	0.1	3.1	0.3	1.1	0.2	0.89	0.04	0.9	0.1	0.4	0.1
Dy	11	3	6	1	21	2	8	1	5.6	0.2	6	1	2	1
Y	126	15	155	25	654	81	352	55	183	6	186	28	123	15
Ho	3	1	1.2	0.1	3.8	0.4	1.6	0.3	1.03	0.04	1.2	0.2	0.5	0.1
Er	9	3	4	1	9	1	4	1	2.5	0.1	3	1	1.2	0.3
Tm	1.4	0.5	0.6	0.1	0.8	0.1	0.5	0.1	0.26	0.02	0.4	0.2	0.14	0.03
Yb	10	4	5	1	4	1	3	1	1.5	0.1	3	2	0.8	0.2
Lu	1.3	0.5	0.7	0.1	0.5	0.1	0.3	0.1	0.20	0.01	0.5	0.3	0.12	0.02

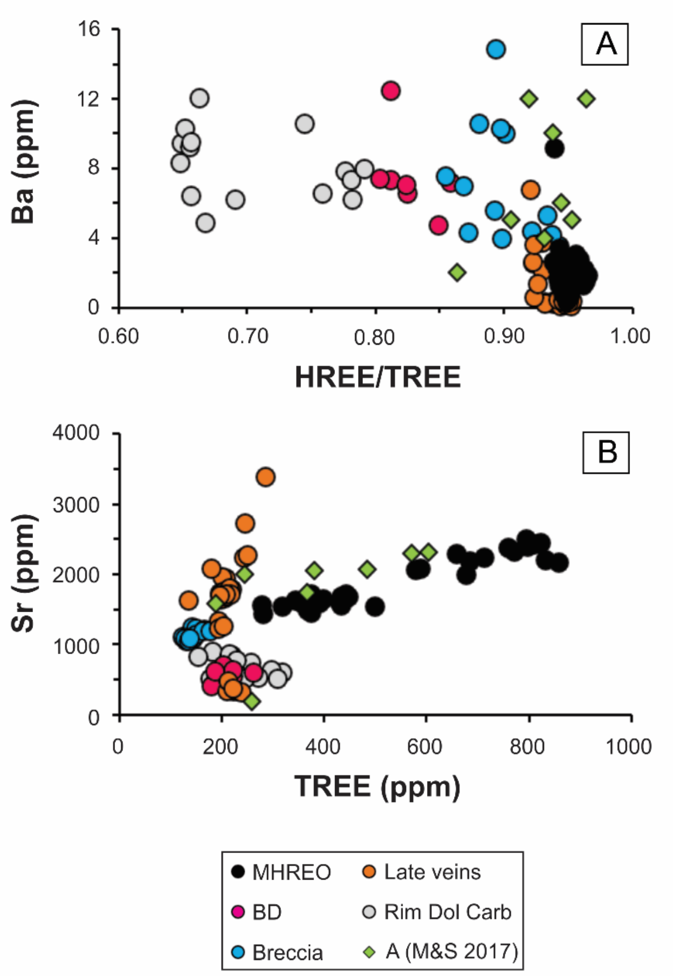

Figure 2.15: Trace element composition of fluorite

Trace element composition of fluorite in the Eldor Carbonatite Complex analyzed in this study. Also shown is the trace element composition for A zone fluorite reported by Mitchell and Smith (2017).

2.3.3.4 *REE-Minerals*

As has been already discussed, the REE mineralization in the Eldor Carbonatite Complex is concentrated in the Ashram deposit. As has also been discussed, the bulk of this mineralization occurs as monazite-(Ce) and bastnäsite-(Ce). Representative analyses of these minerals are given in Tables 2.7 and 2.8, respectively (full datasets in Appendices 2.7 and 2.8, respectively). In samples from the MHREO, A, and B zones, the compositions of monazite-(Ce) and bastnäsite-(Ce) vary systematically with location in the deposit, particularly in respect to their La and Th contents (Fig. 2.16). Both minerals display an overall enrichment in La and a depletion in Th from

Table 2.7: Representative major element oxide compositions and cation proportions of monazite-(Ce) and monazite-(Nd)

Unit	**BD**	**B**		**A**				**MHREO**	
Sample	15158	15127	15125	15020	15024	15026	16007	15002	15337
La_2O_3 (*wt. %*)	11.03	23.81	12.46	21.96	15.56	18.07	13.57	12.17	2.98
Ce_2O_3	32.82	33.17	35.12	32.94	32.21	31.86	31.68	31.29	24.33
Pr_2O_3	4.39	3.09	4.46	3.24	3.94	3.35	3.81	3.99	5.91
Nd_2O_3	16.61	8.99	13.12	9.29	13.35	11.74	13.86	12.97	26.84
Sm_2O_3	1.99	0.53	1.28	0.81	1.42	1.42	1.76	1.75	3.75
Eu_2O_3	0.45	bdl	bdl	bdl	0.19	bdl	0.40	0.36	0.73
Gd_2O_3	0.69	0.32	0.87	0.64	0.85	0.97	1.13	0.95	1.02
Dy_2O_3	bdl	bdl	bdl	0.21	bdl	bdl	bdl	bdl	bdl
Y_2O_3	0.24	0.24	0.46	0.38	0.41	0.32	0.75	0.48	0.51
ThO_2	0.79	0.17	0.52	0.40	1.12	2.15	3.21	3.29	3.90
UO_2	bdl	bdl	bdl	bdl	bdl	bdl	bdl	bdl	bdl
CaO	0.84	0.30	0.99	0.2	0.14	0.46	0.63	0.99	0.52
P_2O_5	29.32	29.32	28.91	29.74	29.76	28.89	28.02	28.9	27.66
F	0.52	0.52	0.60	0.50	0.53	0.60	0.59	0.60	0.54
Cl	bdl	bdl	bdl	bdl	bdl	bdl	bdl	bdl	bdl
SiO_2	0.22	bdl	0.33	bdl	0.31	0.45	0.64	0.24	0.77
PbO	bdl	0.09	bdl	0.10	0.12	0.23	0.26	0.29	0.39
FeO	bdl	bdl	0.27	bdl	bdl	bdl	bdl	0.27	0.52
Na_2O	bdl	NA	bdl	NA	NA	bdl	bdl	NA	bdl
SrO	0.25	NA	0.17	NA	NA	0.16	0.27	NA	0.44
O=F	-0.22	-0.22	-0.25	-0.21	-0.22	-0.25	-0.25	-0.25	-0.23
Total	99.94	100.33	99.31	100.2	99.69	100.42	100.33	98.29	100.58
					O = 4				
La (*apfu*)	0.159	0.345	0.181	0.316	0.224	0.262	0.199	0.178	0.044
Ce	0.471	0.476	0.506	0.471	0.460	0.458	0.461	0.455	0.356
Pr	0.063	0.044	0.064	0.046	0.056	0.048	0.055	0.058	0.086
Nd	0.232	0.126	0.184	0.130	0.186	0.165	0.197	0.184	0.383
Sm	0.027	0.007	0.017	0.011	0.019	0.019	0.024	0.024	0.052
Eu	0.006				0.003		0.005	0.005	0.010
Gd	0.009	0.004	0.011	0.008	0.011	0.013	0.015	0.013	0.014
Dy				0.003					
Y	0.005	0.005	0.010	0.008	0.009	0.007	0.016	0.010	0.011
Th	0.007	0.002	0.005	0.004	0.010	0.019	0.029	0.030	0.035
U									
Ca	0.035	0.013	0.042	0.008	0.006	0.019	0.027	0.042	0.022
P	0.973	0.974	0.963	0.983	0.984	0.961	0.942	0.973	0.936
F	0.064	0.065	0.075	0.062	0.065	0.075	0.074	0.075	0.068
Cl									
Si	0.009		0.013		0.012	0.018	0.025	0.010	0.031
Pb		0.001	0.000	0.001	0.001	0.002	0.003	0.003	0.004
Fe			0.009					0.009	0.017
Na									
Sr	0.006		0.004			0.004	0.006		0.010
Total	2.002	1.996	2.008	1.989	1.981	1.994	2.004	1.994	2.012

'bdl' – below the limit of detection

'NA' – Not Analyzed

Table 2.8: Representative major element oxide compositions and cation proportions of bastnäsite-(Ce)

Unit	**BD**		**B**	**A**	**MHREO**
Sample	15114	15115	15141	15004	15002
La_2O_3 (*wt. %*)	14.76	15.42	25.01	23.77	18.05
Ce_2O_3	36.77	38.07	36.15	34.90	34.80
Pr_2O_3	4.55	4.39	3.38	3.30	3.93
Nd_2O_3	13.99	13.28	8.32	9.04	11.55
Sm_2O_3	1.36	0.95	0.58	0.96	1.19
Eu_2O_3	0.14	0.14	0.14	bdl	bdl
Gd_2O_3	0.65	0.35	0.27	0.46	0.68
Dy_2O_3	bdl	bdl	bdl	bdl	bdl
Y_2O_3	0.27	0.34	0.21	0.37	0.49
ThO_2	1.05	0.65	0.16	0.68	2.03
CaO	0.59	0.89	0.06	0.89	1.13
F	8.00	8.15	8.50	8.86	7.97
Cl	bdl	bdl	bdl	bdl	bdl
SiO_2	0.39	0.34	0.20	bdl	bdl
PbO	0.12	bdl	bdl	bdl	bdl
FeO	0.38	0.32	0.29	bdl	0.29
SrO	0.12	bdl	0.07	0.16	0.23
O=F	-3.37	-3.43	-3.58	-3.73	-3.36
CO_2	20.24	20.15	20.24	20.34	21.02
Total	100.00	100.00	100.00	100.00	100.00
			O = 4		
La (*apfu*)	0.195	0.203	0.333	0.316	0.239
Ce	0.481	0.497	0.477	0.461	0.458
Pr	0.059	0.057	0.044	0.043	0.051
Nd	0.179	0.169	0.107	0.116	0.148
Sm	0.017	0.012	0.007	0.012	0.015
Eu	0.002	0.002	0.002		
Gd	0.008	0.004	0.003	0.006	0.008
Dy			0.000		
Y	0.005	0.006	0.004	0.007	0.009
Th	0.009	0.005	0.001	0.006	0.017
Ca	0.023	0.034	0.002	0.034	0.044
F	0.905	0.919	0.969	1.011	0.906
Cl					
Si	0.014	0.012	0.007		
Pb	0.001				
Fe	0.011	0.010	0.009		0.009
Sr	0.003		0.002	0.003	0.005
C	0.988	0.982	1.010	1.002	1.032

‘bdl’ – below the limit of detection

CO_2 calculated from the difference between the analytical total and 100 wt. %

the center of the deposit outwards (Fig. 2.16). The monazite-(Ce) and bastnäsite-(Ce) compositions of the BD zone deviate from this by having the lowest La concentration of any zone, despite the location of the BD zone at the edge of the Ashram deposit. They also have a higher Th content than would be expected from this location. The monazite composition within a given sample is independent of the minerals with which it is associated, e.g., fluorite, phlogopite, and xenotime. Instead, monazite compositions within a sample are tightly clustered (Fig. 2.16A). The same is also true for bastnäsite-(Ce) (Fig 2.16B).

Xenotime was identified in samples from the MHREO, A and B zones. Average compositions are given in Table 2.9 (full dataset in Appendix 2.9). All the crystals analyzed classify as xenotime-(Y), and the concentrations of their major elements do not vary systematically across the deposit (Table 2.9).

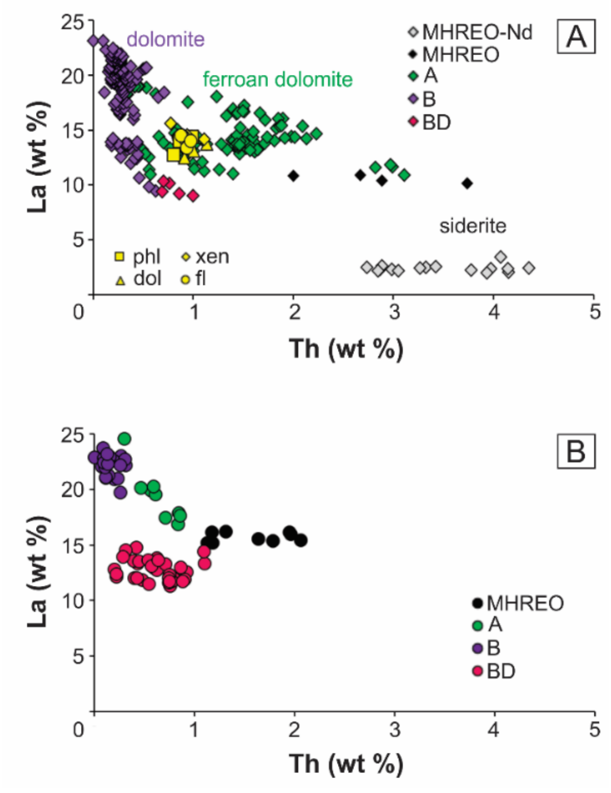

Figure 2.16: La content (wt. %) of monazite and bastnäsite as a function of Th content (wt. %) A) monazite-(Ce) and monazite-(Nd) and B) bastnäsite-(Ce). The principal carbonate mineral in each zone is indicated in A). The yellow symbols in A) represent monazite-(Ce) compositions for an A zone sample containing phlogopite (phl), dolomite (dol), xenotime-(Y) (xen) and fluorite (fl) (see text for further detail).

Table 2.9: Mean major element oxide compositions and cation proportions of xenotime-(Y)

Unit	**B**		**A**					
Sample (n)	CV15018 (12)		CV15020 (6)		CV15024 (15)		CV15026 (3)	
		1σ		1σ		1σ		1σ
Nd_2O_3 (*wt. %*)	0.09	0.15	0.28	0.15	0.32	0.20	0.10	0.18
Sm_2O_3	0.40	0.33	0.78	0.38	0.99	0.31	0.68	0.06
Eu_2O_3	0.15	0.33	0.37	0.57	0.38	0.51	0.48	0.83
Gd_2O_3	3.18	0.85	4.69	0.90	4.39	0.52	5.43	0.94
Tb_2O_3	1.03	0.22	1.42	0.17	1.17	0.20	1.38	0.22
Dy_2O_3	8.38	1.37	10.58	0.89	8.14	1.27	10.69	1.23
Y_2O_3	40.69	3.18	36.93	1.39	38.99	2.53	36.81	0.43
Ho_2O_3	1.53	0.18	1.75	0.18	1.41	0.18	1.57	0.14
Er_2O_3	3.76	0.49	3.79	0.45	3.43	0.48	3.45	0.40
Tm_2O_3	0.47	0.08	0.42	0.04	0.41	0.13	0.41	0.01
Yb_2O_3	2.51	0.34	2.17	0.32	2.33	0.42	2.15	0.16
Lu_2O_3	0.27	0.07	0.24	0.04	0.34	0.09	0.18	0.00
ThO_2	0.08	0.18	0.27	0.30	0.57	0.53	0.74	0.40
UO_2	bdl	bdl	bdl	bdl	bdl	bdl	bdl	bdl
CaO	0.55	0.42	0.33	0.15	0.18	0.12	0.82	0.98
P_2O_5	35.47	0.91	35.33	0.62	35.30	1.11	33.90	0.39
F	0.63	0.04	0.34	0.37	0.60	0.19	0.63	0.05
SiO_2	bdl		bdl		bdl		bdl	
PbO	bdl		bdl		bdl		bdl	
FeO	0.55	0.53	0.24	0.11	0.46	0.33	0.53	0.18
O=F	-0.27		-0.14		-0.25		-0.27	
Total	99.48		99.78		99.17		99.67	
				O = 4				
Nd (*apfu*)	0.001		0.003		0.004		0.001	
Sm	0.005		0.009		0.011		0.008	
Eu	0.002		0.004		0.004		0.006	
Gd	0.035		0.053		0.049		0.062	
Tb	0.011		0.016		0.013		0.016	
Dy	0.090		0.115		0.088		0.118	
Y	0.720		0.664		0.697		0.671	
Ho	0.016		0.019		0.015		0.017	
Er	0.039		0.040		0.036		0.037	
Tm	0.005		0.004		0.004		0.004	
Yb	0.025		0.022		0.024		0.022	
Lu	0.003		0.002		0.003		0.002	
Th	0.001		0.002		0.004		0.006	
U								
Ca	0.020		0.012		0.007		0.030	
P	0.999		1.011		1.004		0.983	
F	0.066		0.036		0.064		0.069	
Si								
Pb								
Fe	0.015		0.007		0.013		0.015	
Total	2.053		2.020		2.041		2.067	

'bdl' – below the limit of detection

Table 2.9: Continued

Unit	**A**		**MHREO**			
Sample (n)	CV16007 (16)		CV15013 (12)		CV15014 (3)	
		1σ		1σ		1σ
Nd_2O_3 (*wt. %*)	0.19	0.21	0.33	0.41	0.31	0.05
Sm_2O_3	1.15	0.49	1.29	0.25	1.05	0.39
Eu_2O_3	0.76	0.35	0.76	0.38	0.84	0.29
Gd_2O_3	4.53	0.93	5.64	0.80	4.94	1.76
Tb_2O_3	1.20	0.15	1.40	0.20	1.11	0.34
Dy_2O_3	8.61	0.46	9.48	1.60	7.57	2.08
Y_2O_3	37.09	1.63	36.17	2.36	39.61	4.00
Ho_2O_3	1.56	0.17	1.59	0.25	1.30	0.28
Er_2O_3	3.87	0.46	3.44	0.52	2.66	0.73
Tm_2O_3	0.54	0.11	0.45	0.07	0.32	0.10
Yb_2O_3	2.98	0.43	2.17	0.35	1.63	0.58
Lu_2O_3	0.32	0.09	0.23	0.04	0.19	0.07
ThO_2	1.01	0.72	0.55	0.48	0.59	0.57
UO_2	bdl		bdl		bdl	
CaO	0.37	0.53	0.14	0.12	0.49	0.38
P_2O_5	34.58	0.76	35.15	0.75	36.97	0.87
F	0.44	0.08	0.43	0.10	0.46	0.12
SiO_2	0.17	0.17	0.16	0.27	0.50	0.64
PbO	bdl		bdl		bdl	
FeO	0.40	0.33	0.53	0.60	0.34	0.11
O=F	-0.18		-0.18		-0.19	
Total	99.63		99.70		100.69	
			O = 4			
Nd (*apfu*)	0.002		0.004		0.004	
Sm	0.013		0.015		0.012	
Eu	0.009		0.009		0.009	
Gd	0.051		0.063		0.053	
Tb	0.013		0.016		0.012	
Dy	0.094		0.103		0.079	
Y	0.671		0.651		0.683	
Ho	0.017		0.017		0.013	
Er	0.041		0.037		0.027	
Tm	0.006		0.005		0.003	
Yb	0.031		0.022		0.016	
Lu	0.003		0.002		0.002	
Th	0.008		0.004		0.004	
U						
Ca	0.013		0.005		0.017	
P	0.996		1.007		1.014	
F	0.047		0.046		0.047	
Si	0.006		0.005		0.016	
Pb	0.000					
Fe	0.011		0.015		0.009	
Total	2.035		2.027		2.022	

‘bdl’ – below the limit of detection

2.3.4 Stable Isotope Geochemistry

Samples of calcite, dolomite and siderite were analysed for their stable carbon and oxygen isotope composition (Fig. 2.17; Appendix 2.10). Because the samples were taken using a handheld microdrill, some of the analyses refer to composites of more than one carbonate type. For example, early dolomite cores in the BD zone carbonatite (dolomite 1, red in CL) are visible in rock samples with the naked eye and were large enough to sample separately, whereas the later, fine-grained dolomite could not be separated and represents composites of dolomite 2 and 3 (Table 2.3). The latter is true for the Rim dolomite carbonatite as well as the B and A zone carbonatites, which are all fine-grained. The siderite, which is largely restricted to the MHREO zone, may represent a mixture of the two siderite types described earlier (e.g., Fig. 2.7D, Table 2.3).

Calcite from the Rim calcite carbonatites has the lowest $\delta^{13}C$ and $\delta^{18}O$ values. These data plot in the igneous carbonatite field (Fig. 2.17). The primary BD zone dolomite population straddles the upper $\delta^{13}C$-$\delta^{18}O$ limit of the igneous field. All other samples (primary and secondary) have higher $\delta^{13}C$ and $\delta^{18}O$ values than those of the igneous field, and these values are distributed along a broad trend of increasing $\delta^{13}C$ and $\delta^{18}O$ (Fig. 2.17). The $\delta^{13}C$ and $\delta^{18}O$ values of the secondary Rim dolomite extend from the upper limit of the primary BD zone dolomite and form a linearly distributed population that is co-linear with the primary carbonate population. The data for the secondary BD, B, and A zone dolomite, and the MHREO siderite form roughly parallel, linearly distributed populations with a lower $\delta^{13}C$ to $\delta^{18}O$ ratio than that of the Rim and primary BD zone populations. These populations (BD, B, A, MHREO) are displaced to progressively lower $\delta^{13}C$ from the margin to the center of the Ashram deposit.

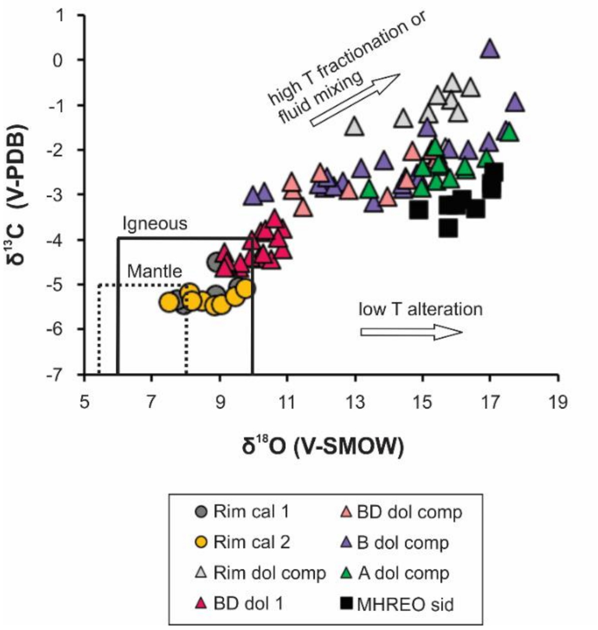

Figure 2.17: Stable C-O isotope compositions of carbonate minerals

A plot of δ^{13}C V-PDB versus δ^{18}O V-SMOW showing the distribution of carbon and oxygen isotope ratios in carbonate minerals from the different facies of the Eldor Carbonatite Complex. Also shown are the fields of mantle and primary igneous carbonatite, after Deines (1989) and Taylor et al., (1967), respectively. The arrows show the effects of low temperature alteration and high temperature fractionation/fluid mixing proposed by Deines (1989).

2.4 Discussion

2.4.1 Magmatic Evolution

Carbonatite complexes composed of multiple carbonatite facies are commonly characterized by early apatite-rich calcite carbonatite and later Fe-Ba-Sr-REE-rich dolomite carbonatite as a result of the fractionation of apatite, phlogopite, calcite and dolomite (e.g., Le Bas and Handley, 1979; Bühn and Rankin, 1999; Xie et al., 2009). This was the case for the Eldor Carbonatite Complex, which comprises early, outer apatite-rich calcite and dolomite carbonatites and later, inner REE-enriched dolomite carbonatite and ferrocarbonatite (Fig. 2.5). In contrast to many carbonatite complexes, however, the outer and inner carbonatites appear to have evolved in two separate stages.

The early carbonatites, referred to above as the Rim carbonatites, comprise calcite carbonatite 1, later calcite carbonatite 2, and even later dolomite carbonatite. This sequence records an evolution of the carbonatite compositions from high P_2O_5 and Ba values to low values of these components (Fig. 2.6A) and is interpreted to reflect the fractionation of apatite and calcite, respectively; the carbonate Ba content decreases from calcite carbonatite 1 through calcite carbonatite 2 to dolomite carbonatite (Fig. 2.13). The calcite carbonatites and dolomite carbonatite also each have their own distinctive fractionation paths, which are clearly evident on a plot of carbonate mineral REE contents versus La/Yb_{CN} (Fig. 2.13G). The calcite from calcite carbonatite 1 has the highest total REE content (533 ppm) and the lowest maximum La/Yb_{CN} ratio (2.5) of carbonate from any of the intrusions. These values provide minimum estimates of the composition of the original Rim carbonatite magma. The subsequent evolution of the REE composition of this magma was controlled by crystallization of apatite, which is the major REE phase in the calcite carbonatite 1 intrusion (~ 5500 ppm REE), making up ~8.5 % of the rock (estimated from the P_2O_5 content; 3.8 wt. %) and having a La/Yb_{CN} ratio of ~95. Crystallization of the calcite carbonatite magma terminated when the REE content of the calcite reached ~400 ppm, due to fractionation of apatite. Coincidentally, this is approximately the same as the highest REE content of calcite from calcite carbonatite 2 and likely reflects the initial REE content of the corresponding magma. With progressive crystallization of apatite (also a major phase in calcite carbonatite 2), the composition of the magma and in turn, the calcite, evolved to lower REE contents and La/Yb_{CN} ratios, as shown on Figure 2.13G. Calcite carbonatite 2 crystallization terminated when the REE content of the calcite reached ~100 ppm, which is similar to the highest REE content of dolomite in the dolomite carbonatite. The subsequent evolution of this magma, like the calcite carbonatite 1 magma, was controlled dominantly by crystallization of apatite, which drove the La/Yb_{CN} ratio to a very low value. We conclude that the differences in the fractionation trends shown in Figure 2.13G reflect crystallization of the different carbonatite types from separate batches of magma.

Although the BD zone is part of the Ashram deposit, its crystallization history was remarkably similar to that of the Rim carbonatites, and quite different from that of the other Ashram units (see below). Thus, on the plot of REE content versus La/Yb_{CN} referred to above, the composition of the BD zone dolomite has a linear distribution that is indistinguishable from the distribution of dolomite of the Rim dolomite carbonatite, except that it extends to higher La/Yb_{CN} ratios. The composition of the BD zone dolomite is also indistinguishable from that of the Rim dolomite on plots of Zn, V, and Sc versus Ba (Fig. 2.13A, C, E). The same conclusion can be reached for the composition of apatite in the BD zone and Rim dolomite carbonatite from inspection of Figure 2.14, which presents plots of Ba vs. Sr, HREE/TREE vs. TREE, and Y/Y* vs. $(La/Nd)_{CN}$, and also for the composition of fluorite (Fig. 2.15). Finally, we note that on a plot of P_2O_5 vs Ba, the bulk rock compositions of the Rim carbonatites define a linear trend of decreasing values which records their progressive evolution, and that the BD zone carbonatite terminates this trend (Fig. 2.6A). We therefore propose that the BD zone is the most evolved member of the Rim carbonatite intrusions, consistent with its location between the Rim and the Ashram zones of the Eldor Carbonatite Complex.

The composition of the Ashram A and B zone dolomite differs from that of the carbonates of the Rim carbonatites in several ways. For example, the dolomite of the A and B zones is characterized by consistently low $(La/Yb)_{CN}$ ratios, whereas these ratios range to very high values in the carbonates of the Rim carbonatites, except for calcite in calcite carbonatite 1 (Fig. 2.13G, H). The A and B zone dolomite is also characterized by very high Zn, V, and Sc concentrations, whereas the carbonates of the Rim carbonatites have very low concentrations of these elements (Fig. 2.13). These observations suggest strongly that the Ashram carbonatites, other than the BD zone, represent an intrusion separate from that of the Rim carbonatites. This conclusion is supported by the observations: 1) that the primary A zone apatite has a much lower LREE/TREE ratio than the primary apatite of the Rim carbonatites; and 2) that this ratio for the A zone apatite decreases sharply with increasing TREE content, whereas the LREE/TREE ratio of primary apatite in the Rim carbonatites is largely independent of TREE content (Fig. 2.14B). Further support for the conclusion that the Ashram carbonatites, other than the BD zone, represent a separate intrusion, is provided by the bulk rock chemistry. These data show that the Rim carbonatites have much higher P_2O_5 contents and much lower REE contents than the Ashram carbonatites (Fig. 2.6A). They also show that this intrusion crystallized from a much more evolved batch of magma. Finally, we note that the P_2O_5 and REE contents of the BD zone are intermediate between those of the Rim and the other Ashram carbonatites, consistent with our earlier conclusion that the BD zone represents the most evolved dolomite carbonatite of the Rim. The evolution of the Ashram carbonatites from the B zone through the A zone to the MHREO zone is indicated by a progressive decrease in the bulk rock P_2O_5 and Zr contents (Fig. 2.6).

For the reasons given above, we propose that there were two main stages of carbonatite magma emplacement. Stage 1, which is represented by the Rim and BD zones, had a high phosphate and low REE content, whereas Stage 2, which is represented by the B, A, and MHREO zones, had a very low phosphate and a relatively high REE content.

2.4.2 Magmatic-Hydrothermal Transition

The stable C and O isotopic compositions of the carbonate minerals provide additional support for a two-stage emplacement model. Some calcite crystals from the Rim calcite carbonatites have isotopic signatures that lie within the mantle envelope of Deines (1989), and all lie within the primary igneous carbonatite field (Taylor et al., 1967) (Fig. 2.17); primary dolomite crystals were too small to analyze without avoiding contamination by secondary dolomite. Many samples of primary BD zone dolomite also lie in the igneous carbonatite field (Fig. 2.17). In contrast, secondary BD zone dolomite, and all samples from the B, A and MHREO zones, have heavier C and O isotopic compositions. Although these compositions could reflect assimilation of marble, a rock type that is common in the area, if this were to have been the case, the Ashram carbonatites and the much more voluminous Rim carbonatites would not have preserved their primary magmatic signatures. Instead, we think it much more likely that the samples with elevated $\delta^{13}C$ and $\delta^{18}O$ values record alteration by a magmatic aqueous-carbonic fluid, which drove the C, O isotopic composition of the carbonatite to higher values. Indeed, as shown by Ray and Ramesh (2000), such a fluid would produce elevated values of the type shown in Figure 2.17, by interacting with the carbonatite through a Rayleigh fractionation process before leaving the system. They also showed that these values would define linear trends, the slopes of which would decrease with decreasing temperature of the fluid (see also Trofanenko et al., 2016). It is thus noteworthy that the data for the different carbonatite units in the Ashram deposit are linearly distributed and, moreover, that their slopes decrease inwards, i.e., from the BD and B zones to the MHREO zone. We therefore propose that the magmas forming the Eldor Carbonatite Complex were fluid-undersaturated during Stage 1 and saturated with an aqueous-carbonic fluid in Stage 2 during the emplacement of the B zone carbonatite. According to this hypothesis, these fluids altered the BD zone and Rim dolomite carbonatites, and evolved to lower temperature during the emplacement of the A and MHREO zones.

A potentially important conduit for the magmatic-hydrothermal fluids was the polymictic breccia, which, as mentioned above, developed largely within the A zone, and contains unmineralized BD zone clasts. This unit was therefore coeval with the emplacement of the Stage

2 carbonatites, but preceded REE mineralization. We interpret it to have been the product of hydro-fracturing, soon after the emplacement of the Ashram carbonatite. This unit would have had high permeability and been a low-pressure zone into which the exsolving magmatic-hydrothermal fluids would have been channelled. In view of this, and the fact that the deposit-scale zonation in REE appears to be centred on this structure (Fig. 2.4), we propose that the polymictic breccia provided the principal pathway for these fluids to alter and mineralize the various units of the Ashram deposit.

2.4.3 Hydrothermal Alteration

There is abundant textural evidence of intense and pervasive hydrothermal alteration having overprinted the Ashram carbonatites. The textural relationships among the carbonate minerals are complex and suggest that there were multiple alteration events. Indeed, all the major rock-forming minerals at Ashram exhibit hydrothermal textures, namely secondary carbonate vug infill, veins of apatite or fluorite, and multiple generations of both minerals. Chemically, however, primary and secondary (hydrothermal) carbonate minerals can only be distinguished in the BD zone. In this zone, the secondary carbonate can be distinguished from the primary, magmatic carbonate by higher V and Sc concentrations, and a lower $(La/Yb)_{CN}$ ratio (Fig. 2.13). These are also characteristics of the A and B zone carbonates.

As noted earlier, apatite in the Ashram carbonatites is largely restricted to the BD zone. There is, however, minor apatite in the A and B zones. Most of the apatite is secondary. Indeed, primary apatite is only observed in the BD and A zones, and then, only as a trace mineral. In the BD zone, the secondary apatite mantles the primary apatite and is interpreted to have formed largely by dissolution-reprecipitation of primary BD apatite (see Putnis, 2009, on textural criteria for dissolution-reprecipitation). This process, however, was accompanied by an increase in Ba and Sr, and a decrease in the LREE/TREE ratio, suggesting that the altering fluid had elevated concentrations of Ba, Sr, and the HREE. It is also noteworthy that secondary apatite at Songwe Hill mantles the primary apatite in this carbonatite, and is characterized by HREE enrichment (Broom-Fendley et al., 2016). As in the BD zone, secondary apatite in the A zone is enriched in Ba, Sr, and the HREE, relative to the primary A zone apatite, but in contrast to secondary apatite in the BD zone, the enrichment in HREE was accompanied by an enrichment in TREE (Fig. 2.14).

Although the origin of the apatite in the B zone (rare) is unknown, its intimate intergrowth with probable secondary fluorite and its textural similarity to secondary Rim, BD, and A zone apatite (fine-grained, sucrosic), suggest strongly that it is hydrothermal in origin. Moreover, all B zone apatite has Y/Y* ratios well outside the range of igneous apatite proposed by Chakhmouradian et al. (2017) (Fig. 2.14C). The B zone apatite, however, differs from secondary apatite in the BD and A zones by having a substantially higher Sr content. This may indicate that, whereas Sr in secondary apatite in the BD and A zones was partly inherited from primary apatite and came partly from the fluid (secondary BD and A zone apatite has a higher Sr content than primary apatite in these zones), the Sr of the B zone apatite was derived entirely from the fluid, consistent with the absence of primary apatite in this zone.

2.4.4 REE Mineralization

As discussed earlier, the bulk of the REE mineralization in the Ashram deposit occurs as monazite-(Ce), except for the BD zone, where bastnäsite-(Ce) is the dominant REE mineral. The textural relationships, e.g., the concentration of most of the monazite and bastnäsite in veins and vugs, show that this mineralization is hydrothermal in origin. An unusual feature of the deposit is that monazite, rather than bastnäsite, is the main REE mineral. We attribute this to the unusually high proportion of apatite in the Eldor Carbonatite Complex, and propose that much of the monazite formed at the expense of apatite, via the reaction:

$$\underset{\text{apatite}}{Ca_5(PO_4)_3F} + 3F^- + 3REE^{3+} = \underset{\text{fluorite}}{2CaF_2} + \underset{\text{monazite}}{3REEPO_4} + 3Ca^{2+} \qquad (1)$$

This hypothesis is supported by the observation that where monazite is in contact with apatite, it mantled and replaced the latter (Fig. 2.11C, D). Whether monazite nucleates during dissolution of apatite depends on the availability of the REE, which may be supplied by the fluid or the apatite (Harlov, 2015). As we show below, the REE for monazite deposition at Ashram must have been supplied by the fluid, assuming that P, a relatively immobile element (Poitrasson et al., 2004; Louvel et al., 2015), was conserved during alteration of apatite to monazite. Indeed, the amount of REE required to produce the monazite ores is considerably higher than can be explained by the concentration of the REE in apatite. For example, the median P_2O_5 content of the A zone is 0.92 wt. %. If all the P in monazite was originally in apatite, which contains, on average, 0.8 wt.

% TREE, the alteration of apatite to monazite would have produced a rock with roughly the same TREE proportion, which is half the median whole-rock TREE content of 1.47 wt. %.

An important feature of Reaction 1 is that apatite is replaced by fluorite, textural support for which is provided by the observation that fluorite is invariably interstitial to apatite and commonly embayed the latter (Fig. 2.10E). This reaction explains the near absence of apatite in the B, A, and MHREO zones, and the common occurrence of fluorite and monazite in secondary dolomite-bearing vugs and veins (Fig. 2.11B). The trace amounts of monazite in the BD zone are interpreted to have formed by the same reaction, given the high abundance of apatite in this zone. Moreover, as we discuss below, the initial proportion of monazite was almost certainly much higher.

The textural relationships between monazite-(Ce) and bastnäsite-(Ce) discussed earlier (Fig. 11C, D) show that bastnäsite-(Ce) replaced monazite-(Ce), according to the reaction:

$$\underset{\text{monazite}}{3REEPO_4} + 5Ca^{2+} + 4F^{-} + 3H_2O + 3CO_3^{2-} \rightarrow \underset{\text{bastnäsite}}{3REECO_3F} + \underset{\text{apatite}}{Ca_5(PO_4)_3F} \tag{2}$$

(a similar reaction was proposed by Giebel et al., 2020, for the Phalaborwa carbonatite). In the B, A, and MHREO zones, bastnäsite-(Ce) is a minor phase because of the precipitation of fluorite to a very late stage in the evolution of the hydrothermal system, via the reaction:

$$Ca^{2+} + 2F^{-} = CaF_2 \tag{3}$$

This buffered the activity of F^- to very low levels, largely precluding the formation of bastnäsite-(Ce) (Reaction 2); assuming conditions of 400 °C, 500 bars (see Williams-Jones et al., 2012) and $a\mathrm{Ca}^{2+}$ of 1, $a\mathrm{F}^{-}$ potentially could be as low as 10^{-7}, based on calculations using Unitherm (Shvarov and Bastrakov, 1999), although higher values are predicted for NaCl-bearing solutions (Tropper and Manning, 2007). In contrast, the failure of fluorite to precipitate in the BD zone, except as a product of Reaction 1, ensured a relatively high F^- activity, which drove Reaction 2 to the right, precipitating bastnäsite-(Ce).

As reported earlier, the bulk REE grade reaches a maximum in the A zone and decreases towards both the B and the MHREO zones, whereas the proportion of MHREE in the bulk rock decreases progressively from the MHREO zone to the B zone (Table 2.1). The latter is reflected in the proportion of LREE in both monazite and bastnäsite, which increases from the MHREO zone to the B zone. There is also a corresponding decrease in Th (Fig. 2.16). This deposit-scale compositional variation, in the case of monazite, is observed at the scale of single crystals as well. Thus, LREE-poor, Th-rich monazite was replaced by a LREE-rich, Th-poor variety of monazite (Fig. 2.12A-D). These observations show that the zonation of MHREE/TREE ratios occurred spatially at the scale of the deposit, as well as temporally.

Earlier we proposed that the polymictic breccia provided the principal pathway for these fluids to alter and mineralize the various units of the Ashram deposit. This unit is characterized by a low TREE content and a high MHREE/TREE ratio. Moreover, there is a progressive enrichment of La and a depletion of Th in the monazite with increasing distance from the breccia. As we will now show, these observations are important evidence in support of the above hypothesis. In order to understand their significance, however, we need first to understand how the REE are mobilized in F-rich hydrothermal fluids.

Although the REE form very strong complexes with F^- (Migdisov and Williams-Jones, 2007; Migdisov et al., 2009), modelling by Migdisov and Williams-Jones (2014) showed that at acidic to near-neutral pH conditions, the aF^- is very low, even in F-rich fluids, due to the weak dissociation of HF and the very low solubility of fluocerite ($REEF_3$). Consequently, the REE are transported dominantly as REE-Cl complexes in these fluids, despite their much weaker stability. Migdisov et al. (2009) also showed that the stability of REE-Cl complexes (and also REE-F complexes) in aqueous fluids decreases with increasing atomic number, and the difference in their stability increases with increasing temperature, such that at ≥ 250°C, La-Cl complexes are 1.5 orders of magnitude more stable than Lu-Cl complexes. Although the pH of the Ashram fluids is not known, it is reasonable to speculate that the fluid was CO_2-rich, based on fluid inclusion studies of other carbonatites (e.g. Bühn and Rankin, 1999; Williams-Jones and Palmer, 2002; Walter et al., 2021), and therefore acidic. Moreover, these studies have shown that the fluids contain variable but relatively high concentrations of Cl^-, i.e., salinity in the range of 5 to 25 wt. % NaCl equivalent (Williams-Jones and Palmer, 2002; Dowman et al., 2017). In summary, the REE at Ashram are interpreted to have been transported as chloride complexes and the LREE to have been considerably more mobile than the MHREE.

In principle, the observed increase in the MHREE/TREE ratio from the B to the MHREO zone (see section 2.1.1) could reflect an increase in pH due to fluid-rock interaction, or cooling of the fluid. Hydrothermal fluids derived from a carbonatite are expected to be strongly enriched in LREE (LREE >> HREE) (Bühn and Rankin, 1999; Bühn et al., 2002). Accordingly, if an acidic fluid with LREE >> HREE interacts with a rock having low pH buffering capacity, it will precipitate only the most insoluble REE, resulting in a HREE-rich rock with a low total REE concentration (Migdisov and Williams-Jones, 2014; Williams-Jones et al., 2015). Conversely, interaction of the same fluid with a strong buffer will result in precipitation of all the dissolved REE, producing a LREE-rich rock with a high total REE content. The solubility product of carbonate minerals, and thus, their relative pH buffering capacity increases in the order siderite < ankerite < dolomite < calcite (the values of log K_{sp} were calculated for 400°C, 500 bars, using the Hch software package of Shvarov and Bastrakov, 1999, are -18.1, -16.8, -15.8, and -15.2, respectively, normalized to constant CO_3^{2-}). We therefore propose that the differing buffering capacity of the carbonate minerals contributed to the deposit-scale zonation of MHREE/TREE at Ashram and support this proposal with the observation that the LREE proportions of the monazite (and bastnäsite) increase with decreasing Fe content of the host carbonate minerals (Fig. 2.16A). Further support for this hypothesis is provided by the observation that monazite-(Nd) occurs exclusively in association with siderite, and xenotime-(Y) occurs predominantly in the siderite-hosted MHREO zone. The deposit-scale distribution of different REE-phosphate mineral compositions is thus consistent with the interaction of a REE-bearing, acidic hydrothermal fluid with host rocks of variable pH buffering capacity. In the siderite host rocks, the overall grade is low, but the proportion of MHREE/TREE is relatively high, whereas the dolomite rocks are host to higher grade, LREE-rich mineralization. It is noteworthy that the breccia has TREE contents and MHREE/TREE ratios (Table 2.2) similar to those of the MHREO zone, consistent with our model in which the breccia is the conduit for the mineralizing fluids. The breccia would therefore have experienced the highest fluid:rock ratio and lost a greater proportion of its pH buffering capacity than the other units, resulting in a rock with a low REE grade, but a relatively high MHREE/TREE ratio.

As has already been mentioned, the spatial variation of monazite composition discussed above could also reflect cooling of the fluid with distance from the conduit (breccia), i.e., from the MHREO zone to the B zone. Indeed, the progressive decrease in the Th content of monazite from the MHREO zone to the B zone matches observations from experiments which show that the Th concentration of monazite decreases with decreasing temperature (Harlov et al., 2003, 2005; Migdisov et al., 2019). The spatial and temporal (Figs. 2.12A-D, 16) trend in the La content of the monazite (the proportion of La increases from the MHREO zone to the B zone) is also consistent with this cooling model, as shown by the results of theoretical modelling in which La is mobilized further down a gradient of decreasing temperature than other REE (Williams-Jones et al., 2012). In summary, we propose that the observed deposit-scale variation in monazite composition through the B, A, and MHREO zones was the cumulative product of hydrothermal fractionation of the REE by the cooling of a REE-bearing fluid as it exited the breccia and interacted with rocks of progressively higher pH buffering capacity. It is noteworthy that this deposit-scale zonation in LREE/HREE centered on a fluid conduit has also been observed at the Ranger uranium deposit, Australia (Fisher et al., 2013), and at the Lofdal REE deposit, Namibia (Williams-Jones et al., 2015), and likely had a similar origin at these deposits (Williams-Jones et al., 2015).

A question that we have not yet addressed is the relative timing of monazite and xenotime. According to our model explaining the deposit-scale variation in monazite composition (HREE-enriched closest to the breccia), xenotime should have precipitated first. The observation, however, that xenotime mantles monazite in vugs and veins (Fig. 2.11E, F), clearly indicates that deposition of xenotime post-dated the crystallization of monazite. The reason for this paragenesis is apparent from a consideration of the equilibrium constants of the following reactions:

$Ce^{3+} + PO_4^{3-} = CePO_4$ log K = 37.91 (4)

$Yb^{3+} + PO_4^{3-} = YbPO_4$ log K = 37.67 (5)

$Ce^{3+} - Yb^{3+} = CePO_4 - YbPO_4$ log K = 0.24 (6)

The equilibrium constants, K, for these reactions were calculated for 400°C and 500 bars (see above) using thermodynamic data reported in Shock and Helgeson (1988), Shock et al. (1997), Popa and Konings (2006), and Gysi et al. (2015). As there are no thermodynamic data for YPO_4, we represented the xenotime composition using $YbPO_4$. The equilibrium constant, K, for Reaction 6, which is given by the relationship $a\text{Yb}^{3+}/a\text{Ce}^{3+}$ is thus $10^{0.24}$, or 1.74. According to Le Châtelier’s Principle, the products side of Reaction 6 is favored by increasing $a\text{Ce}^{3+}$ and/or decreasing $a\text{Yb}^{3+}$. It therefore follows that any ratio of $a\text{Yb}^{3+}/a\text{Ce}^{3+}$ with a value less than 1.74

will favor the right-hand side of Reaction 6, i.e., saturation of the fluid with monazite and undersaturation in xenotime. Although we have no information on the concentrations of the REE in the mineralizing fluid, a rough insight into the probable Yb/Ce of this fluid is provided by fluid inclusion and bulk rock data reported in Bühn and Rankin (1999) for the Kalkfeld carbonatite (the only carbonatite for which the REE composition of the fluid and the host rock have been reported). The average Yb/Ce of the Kalkfeld fluid is 0.01 and the corresponding Yb/Ce for the carbonatite is 0.0037. Significantly, the Yb/Ce for the MHREO zone at Ashram is 0.0034, which is almost identical to the ratio for the Kalkfeld carbonatite; the ratios for the other Ashram zones are slightly lower. It is therefore reasonable to assume, to a first approximation, that the Ashram fluids had a Yb/Ce ratio ≤ 0.01. As the activity coefficients of Yb^{3+} and Ce^{3+} are very similar (Migdisov et al., 2009), we can further assume that the $a\text{Yb}^{3+}/a\text{Ce}^{3+}$ would have been less than 0.01. Given that the equilibrium constant, K, of Reaction 6 is very much higher (1.74), we can conclude that the fluid would have saturated relatively early in monazite and much later in xenotime, thereby explaining why xenotime invariably mantles monazite.

Traces of aeschynite-(Nd) occur in veins and are associated with, but later than, monazite-(Ce) and xenotime-(Y). We propose that aeschynite-(Nd) was deposited as a result of the reworking of earlier Nb-bearing minerals by late REE-bearing fluids. Another secondary Nb mineral, samarskite-(Y), which was described by Mitchell and Smith (2017) but not identified in our samples, is also interpreted to have been deposited by these fluids. Potential sources of Nb for aeschynite-(Nd) and samarskite-(Y) are ferrocolumbite and ilmenorutile, which occur in trace (< 1 vol. %) amounts in the Ashram carbonatites.

2.5 Genetic Model

We propose the following model for the genesis of the REE mineralization of the Ashram deposit (Fig. 2.18). The first stage of carbonatite emplacement produced the Rim and BD zones, and involved magmas with a low concentration of REE, and a high concentration of P (Fig. 2.18A). This was followed by the emplacement of a second stage of carbonate magmas, represented by the B, A and MHREO zones, and characterized by high REE and F and low P contents (Fig 2.18B). Both stages of magmas crystallized their own distinct, primary apatite, though apatite was considerably more abundant in the Stage 1 magmas. Emplacement of the second stage of carbonate magmas (Stage 2) was accompanied by brecciation. These magmas exsolved a REE- and F-bearing

H_2O-CO_2 fluid that altered the B, A, and MHREO zones, as well as the BD zone (Fig. 2.18C), using the breccia as a conduit to access the different REE-bearing units. On interaction with its host (the Stage 2 carbonatites and late Stage 1 dolomite carbonatite, BD zone), the fluid altered primary apatite to monazite and fluorite (Reaction 1; Fig. 2.18D). In the apatite-poor B, A and MHREO zones, prolonged fluid-rock interaction resulted in nearly complete consumption of apatite, whereas in the apatite-rich BD zone, this was not the case. Evolution of the hydrothermal system led to the subsequent replacement of monazite by bastnäsite in the BD zone and deposition of fluorite in the B, A, and MHREO zones. The latter buffered the fluoride activity to very low levels, thereby largely precluding the replacement of monazite by bastnäsite in these zones (Fig. 2.18E). Xenotime was a late, trace mineral that saturated in the fluid after precipitation of most of the LREE as monazite. Finally, Nb was remobilized and deposited as trace aeschynite-(Nd) by late-stage fluids.

The deposit-scale zonation of the mineralogy and the REE distribution, including the zone of unusual MHREE enrichment, is attributed to the cooling and pH buffering of the hydrothermal fluid as it travelled upward and outward from the breccia. The fluid was at its highest temperature as it exited this conduit and its pH was buffered only weakly by siderite of the MHREO zone. This ensured that monazite proximal to the conduit was strongly depleted in La and enriched in Th (monazite-(Nd)). On leaving the breccia, the fluid cooled and was gradually buffered to higher pH as it passed through dolomitic rocks with progressively lower Fe content, allowing it to deposit monazite with correspondingly higher proportions of La and lower proportions of Th. In summary, the lightest REE were able to travel the furthest from the breccia and produce the deposit scale separation of the light from the heavy REE, which is a striking feature of the Ashram carbonatite.

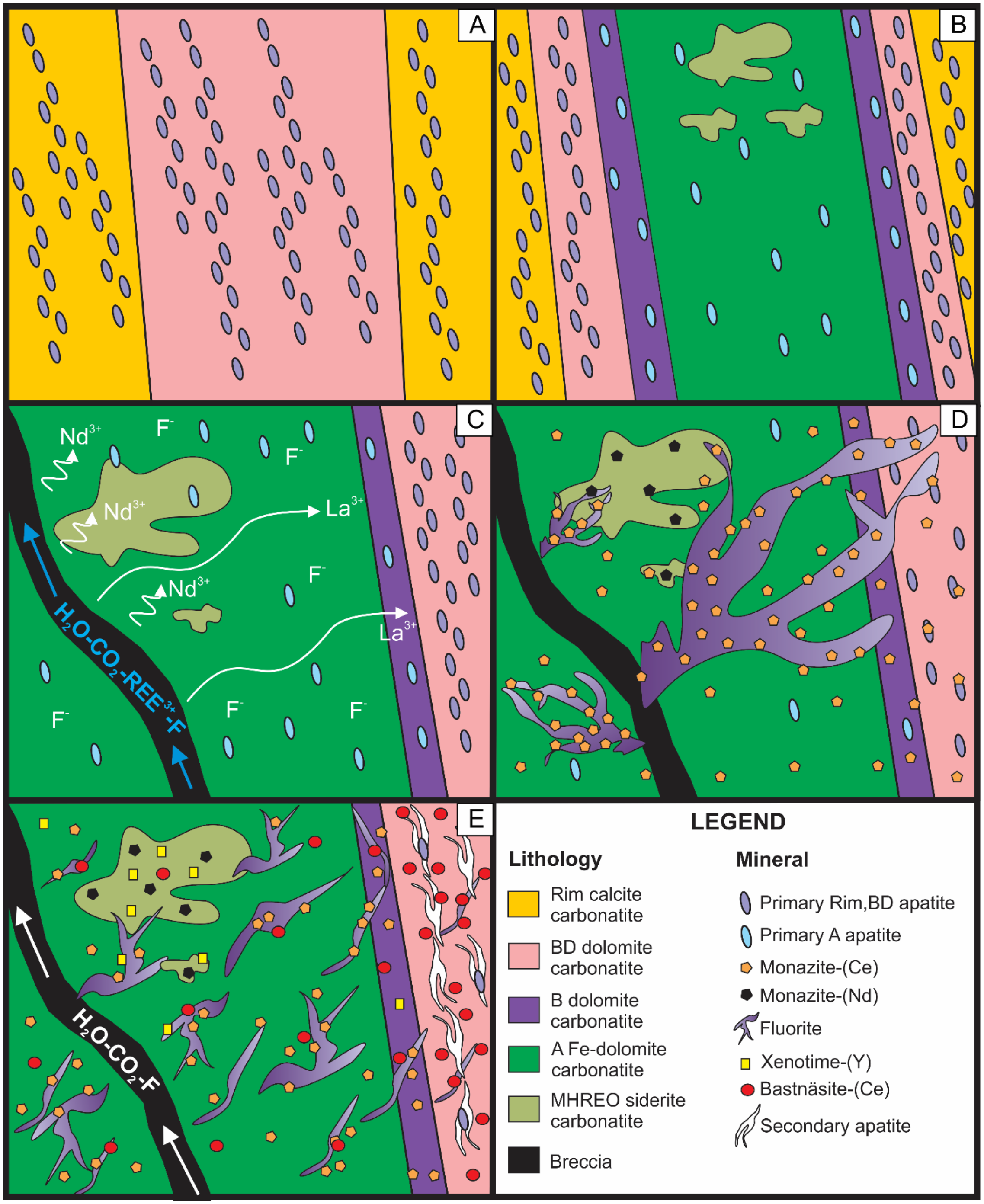

Figure 2.18: A cartoon summarizing the proposed genetic model for the Ashram deposit

A) Stage 1: Emplacement of the primary apatite-rich Rim calcite carbonatites and the Rim and BD zone dolomite carbonatites. B) Stage 2: Emplacement of the phosphate-poor Ashram carbonatite magma that formed the B, A and MHREO zone carbonatites. C) Brecciation accompanied by exsolution of a H_2O-CO_2-REE^{3+}-F-Cl fluid from the Stage 2 carbonatites, transport of this fluid in the breccia conduit, and its transfer into the surrounding carbonatite; on exiting the conduit, the REE were fractionated leading to the more distal mobilization of La^{3+} relative to Nd^{3+}. D) Deposition of fluorite and monazite at the expense of primary apatite (Reaction 1); monazite-(Nd) is only deposited in MHREO siderite, proximal to the breccia.

Replacement of apatite by monazite is nearly complete in the B, A, and MHREO zones, and partially complete in the BD zone. E) A later, REE-poor H_2O-CO_2-F-Cl fluid partially replaces monazite-(Ce) in the B and A zones, depositing bastnäsite-(Ce) (Reaction 2). In the BD zone, monazite-(Ce) is completely replaced by bastnäsite-(Ce) and primary apatite is replaced by secondary apatite.

2.6 Conclusions

The REE mineralization at Ashram is hydrothermal in origin and was produced through a series of fluid-mediated replacement reactions. Nonetheless, magmatic processes were also important in determining the initial distribution of the REE. There were two stages of carbonatite emplacement, each geochemically distinct. Rare earth element-mobilizing H_2O-CO_2 fluids were exsolved from the Stage 2 carbonatite magmas. These fluids were acidic, REE-bearing and utilized a central breccia as a conduit of egress, with successive pulses armouring the pathway (i.e., reducing its pH buffering capacity), preventing neutralization and allowing for the transport of a large mass of the REE. Cooling and differential pH buffering of the fluid beyond the conduit resulted in fractionation of the REE and the observed spatial zonation of the REE at Ashram, including the MHREE-enriched zone. The evolving composition of the fluid and its interaction with host rocks of variable bulk composition and pH buffering capacity resulted in a REE-phosphate-rich deposit with large-scale, antipathic separation of monazite + fluorite and bastnäsite + apatite. Ashram had a long-lived history in which the combination of magmatic zone-refinement and hydrothermal mobilization contributed to the formation of a potentially economic carbonatite-hosted REE deposit.

Acknowledgements

The research presented in this manuscript was supported financially by a MITACS grant to Diversification de l'exploration minerale au Quebec (DIVEX) and a NSERC Discovery Grant to AEW-J. Commerce Resources Corp. and Dahrouge Geological Consulting Ltd. provided access to the site, drill core and assay data. Matthew Carter and Alex Knox shared their valuable insights of the deposit geology with us. Lang Shi helped extensively with the electron microprobe analyses and Thi Hao Bui carried out the C-O isotope analyses. Olga Vasyukova and Rowan Wollenberg provided valuable advice on mineral chemistry and the use of thermodynamic software. The manuscript was improved significantly by the reviews of R. Johannes Giebel and Anton Chakhmouradian.

References

Bodeving, S., Williams-Jones, A.E., and Swinden, S., 2017, Carbonate-silicate immiscibility, REE mineralising fluids, and the evolution of the Lofdal Intrusive Suite, Namibia: Lithos, v. 268-271, p. 383-398.

Broom-Fendley, S., Styles, M.T., Appleton, J.D., Gunn, G., and Wall, F., 2016, Evidence for dissolution-reprecipitation of apatite and preferential LREE-mobility in carbonatite-derived late-stage hydrothermal processes: American Mineralogist, v. 101, p. 596-611.

Bühn, B., and Rankin, A.H., 1999, Composition of natural, volatile-rich Na-Ca-REE-Sr carbonatitic fluids trapped in fluid inclusions: Geochimica et Cosmochimica Acta, v. 63, p. 3781-3797.

Bühn, B., Rankin, A.H., Schneider, J., and Dulski, P., 2002, The nature of orthomagmatic, carbontitic fluids precipitating REE, Sr-rich fluorite: fluid inclusion evidence from the Okorusu fluorite deposit, Namibia: Chemical Geology, v. 186, p. 75-98.

Castor, S.B., and Hedrick, J.B., 2006, Rare earth elements, in Kogel, J.E., Trivedi, N.C., Barker, J.M., eds., Industrial Minerals and Rocks, 7th ed.: Littleton, Colorado, Society for Mining, Metallurgy and Exploration, p. 769-792

Castor, S.B., 2008, The Mountain Pass Rare-Earth Carbonatite and Associated Ultrapotassic Rocks, California: The Canadian Mineralogist, v. 46, p. 779-806.

Chakhmouradian, A.R., Reguir, E.P., Couëslan, C., and Yang, P., 2016, Calcite and dolomite in intrusive carbonatites. II. Trace-element variations: Mineralogy and Petrology, v. 110, p. 361-377.

Chakhmouradian, A.R., Reguir, E.P., Zaitsev, A.N., Couëslan, C., Cheng, X., Kynicky, J., Mumin, A.H., and Yang, P., 2017, Apatite in carbonatitic rocks: Compositional variation, zoning, element partitioning and petrogenetic significance: Lithos, v. 274-275, p. 188-213.

Chen, W., Liu, H.-Y., Lu, J., Jiang, S.-Y., Simonetti, A., Xu, C., and Zhang, W., 2020, The formation of the ore-bearing dolomite marble from the giant Bayan Obo REE-Nb-Fe deposit, Inner Mongolia: insights from micron-scale geochemical data: Mineralium Deposita, v. 55, p. 131-146.

Clark, T., and Wares, R., 2006, Lithotectonic and Metallogenic Synthesis of the New Quebec Orogen (Labrador Trough). MM 2005-01.

Costanzo, A., Moore, K.R., Wall, F. and Freely, M., 2006, Fluid inclusions in apatite from Jacupiranga calcite carbonatites: Evidence for a fluid-stratified carbonatite magma chamber: Lithos, v. 91, p. 208-228.

Deines, P., 1989, Stable isotope variations in carbonatites, in Bell, K., ed., Carbonatites, genesis and evolution: London, UK, Unwin Hyman Ltd., p. 301-359.

Doroshkevich, A.G., Viladkar, S.G., Ripp, G.S., and Burtseva, M.V., 2009, Hydrothermal REE mineralization in the Amba Dongar Carbonatite Complex, Gujarat, India: The Canadian Mineralogist, v. 47, p. 1105-1116.

Dowman, E, 2014, Mineralisation and Fluid Processes in the Alteration Zone Around the Chilwa Island and Kangankunde Carbonatite Complexes, Malawi: Unpublished Ph.D. thesis, London, UK, Kingston University.

Dowman, E., Wall, F., Treloar, P.J., and Rankin, A.H., 2017, Rare-earth mobility as a result of multiple phases of fluid activity in fenite around the Chilwa Island Carbonatite, Malawi: Mineralogical Magazine, v. 81, p. 1367-1395.

Fisher, L.A., Cleverley, J.S., Pownceby, M., and MacRae, C., 2013, 3D representation of geochemical data, the corresponding alteration and associated REE mobility at the Ranger uranium deposit, Northern Territory, Australia: Mineralium Deposita, v. 48, p. 947-966.

Gammons, C.H., Wood, S.A., and Li, Y., 2002, Complexation of the rare earth elements with aqueous chloride at 200°C and 300°C and saturated water vapor pressure: Geochemical Society Special Publication, v. 7, p. 191-207.

Gagnon, G., Rousseau, G., Camus, Y., and Gagne, J., 2012, Ashram Rare Earth Deposit, Preliminary Economic Assessment. NI 43-101 Technical Report, Prepared by SGS Geostat Canada for Commerce Resources, 202 p.

Giebel, R.J., Gauert, C.D.K., Marks, M.A.W., Costin, G., and Markl, G., 2017, Multi-stage formation of REE minerals in the Palabora Carbonatite Complex, South Africa: American Mineralogist, v. 102, p. 1218-1233.

Gittins, J., and Harmer, R.E. (1997). What is ferrocarbonatite? A revised classification: Journal of African Earth Sciences, v. 25, p. 159-168.

Gysi, A.P., Williams-Jones, A.E., and Harlov, D.E., 2015, The solubility of xenotime-(Y) and other HREE phosphates (DyPO4, ErPO4 and YbPO4) in aqueous solutions from 100 to 250 degrees C and p(sat): Chemical Geology, v. 401, p. 83-95.

Gysi, A.P., Harlov, D., and Miron, G.D., 2018, The solubility of monazite (CePO4), SmPO4, and GdPO4 in aqueous solutions from 100 to 250 degrees: Geochimica et Cosmochimica Acta, v. 242, p. 143-164.

Harlov, D.E., Forster, H.-J., and Schmidt, C., 2003, High P-T experimental metasomatism of a fluorapatite with significant britholite and fluorellestadite components: implications for LREE mobility during granulite-facies metamorphism: Mineralogical Magazine, v. 67, p. 61-72.

Harlov D.E., Wirth R., and Förster, H.J., 2005, An experimental study of dissolution-reprecipitation in fluorapatite: fluid infiltration and the formation of monazite: Contributions to Mineralogy and Petrology, v. 150, p. 268-286.

Harlov, D.E., 2015, Apatite: a fingerprint for metasomatic processes: Elements, vol 11, p. 171-176.

Kapustin, Y.L., 1971, Mineralogy of carbonatites (English translation, 1980): New Delhi, India, Amerind Publishing Co, 259 p.

Le Bas, M.J., and Handley, C.D., 1979, Variation in apatite composition in ijolitic and carbonatitic igneous rocks: Nature, v. 279, p. 54-56.

Liu, W.H., Etschmann, B., Migdisov, A., Boukhalfa, H., Testemale, D., Muller, H., Hazemann, J.L., and Brugger, J., 2017, Revisiting the hydrothermal geochemistry of europium (II/III) in light of new in-situ XAS spectroscopy: Chemical Geology, v. 459, p. 61-74.

Louvel, M., Bordage, A., Testemale, D., Zhou, L., and Mavrogenes, J., 2015, Hydrothermal controls on the genesis of REE deposits: Insights from an in situ XAS study of Yb solubility and speciation in high temperature fluids (T < 400°C): Chemical Geology, v. 417, p. 228-237.

Machado, N., Clark, T., David, J., and Goulet, N., 1997, U-Pb ages for magmatism and deformation in the New Quebec Orogen: Canadian Journal of Earth Science, v. 34, p. 716-723.

Mair, P., Tropper, P., Harlov, D.E., and Manning, C.E., 2017, The solubility of CePO4 monazite and YPO4 xenotime in KCl-H2O fluids at 800 degrees C and 1.0 GPa: Implications for REE transport in high-grade crustal fluids: American Mineralogist, v. 102, p. 2457-2466.

Mariano, A.N., 1989, Nature of economic mineralization in carbonatites and related rocks, in Bell, K., ed., Carbonatites: Genesis and Evolution, Winchester, Massachusetts, Unwin Hyman Inc., p. 149-176.

McDonough, W.F., Sun, S.-S., 1995, The composition of the Earth: Chemical Geology, v. 120, p. 223-253.

Migdisov, A.A., and Williams-Jones, A.E., 2008, A spectrophotometric study of Nd (III), Sm (III) and Er (III) complexation in sulfate-bearing solutions at elevated temperatures: Geochimica Cosmochimica Acta, v. 72, p. 5291-5303.

Migdisov, A.A. and Williams-Jones, A.E., 2014, Hydrothermal transport and deposition of the rare earth elements by fluorine-bearing aqueous liquids: Mineralium Deposita, v. 49, p. 987-997.

Migdisov, A.A., Williams-Jones, A.E., and Wagner, T., 2009, An experimental study of the solubility and speciation of the Rare Earth Elements (III) in fluoride- and chloride-bearing aqueous solutions at temperatures up to 300°C: Geochimica et Cosmochimica Acta, v. 73, p. 7087-7109.

Migdisov, A.A., Williams-Jones, A.E., Brugger, J., and Caporuscio, F.A., 2016, Hydrothermal transport, deposition and fractionation of the REE: Experimental data and thermodynamic calculations: Chemical Geology, v. 439, p. 13-42.

Migdisov, A.A., Guo, X., Nisbet, H., Xu, H., and Williams-Jones, A.E., 2019, Fractionation of REE, U and Th in natural ore-forming hydrothermal systems: Thermodynamic modeling: Journal of Chemical Thermodynamics, v. 128, p. 305-319.

Mitchell, R.H., and Smith, D.L., 2017, Geology and mineralogy of the Ashram Zone carbonatite, Eldor Complex, Quebec: Ore Geology Reviews, v. 86, p. 784-806.

Moore, M., Chakhmouradian, A.R., Mariano, A.N., and Sidhu, R., 2015, Evolution of rare-earth mineralization in the Bear Lodge carbonatite, Wyoming: Mineralogical and isotopic evidence: Ore Geology Reviews, v. 64, p. 499-521.

Mott, A.V., Bird, D.K., Grove, M., Rose, N., Bernstein, S., Mackay, H. and Krebs, J., 2013, Karrat Isfjord: A newly discovered Paleoproterozoic carbonatite-sourced REE deposit, Central West Greenland: Economic Geology, v. 108, p. 1471-1488.

Nadeau, O., Cayer, A., Pelletier, M., Stevenson, R., and Jébrak, M., 2015, The Paleoproterozoic Montviel carbonatite-hosted REE-Nb deposit, Abitibi, Canada: Geology, mineralogy, geochemistry and genesis: Ore Geology Reviews, v. 67, p. 314-335.

Olson, J.C., Shawe, D.R., Pray, L.C., and Sharp, W.N., 1954, Rare-earth mineral deposit of the Mountain Pass district, San Bernardino County, California, U.S. Geological Survey Professional Paper 261, p. 1-75.

Paton, C., Hellstrom, J., Paul, B., Woodhead, J., and Hergt, J., 2011, Iolite: Freeware for the visualisation and processing of mass spectrometric data: Journal of Analytical Atomic Spectrometry, v. 26, p. 2508.

Pell, J., 1996, Mineral deposits associated with carbonatites and related alkaline igneous rocks, in Mitchell, R.R., ed., Undersaturated Alkaline Rocks: Mineralogy, Petrogenesis, and Economic Potential, Mineralogical Association of Canada, Short Course Series, Winnipeg, p. 271-310.

Poitrasson, F., Oelkers, E., Schott, J., and Montel, J.M., 2004, Experimental determination of synthetic $NdPO_4$ monazite end-member solubility in water from 21 degrees C to 300 degrees C: implications for rare earth element mobility in crustal fluids: Geochimica et Cosmochimica Acta, v. 68, p. 2207-2221.

Popa, K., and Konings, R.J.M., 2006, High-temperature heat capacities of EuPO4 and SmPO4 synthetic monazites: Thermochimica Acta, v. 445, p. 49-52.

Putnis, A., 2009, Mineral replacement reactions: Reviews in Mineralogy and Geochemistry, v. 70, p. 87-124.

Ray, J.S., and Ramesh, R., 2000, Rayleigh fractionation of stable isotopes from a multicomponent source: Geochimica et Cosmochimica Acta, v. 64, p. 299-306.

Ruberti, E., Enrich, G.E.R., and Gomes, C.B., 2008, Hydrothermal REE fluorocarbonate mineralization at Barra Do Itapirapua, a multiple stockwork carbonatite, Southern Brazil: The Canadian Mineralogist, v. 46, p. 901-914.

Schmidt, P. T., 2013, High-field-strength element distribution of the Eldor carbonatite complex, Canada: Unpublished M.Sc. thesis, Tübingen, Germany, The University of Tübingen, 173 p.

Schmidt, P.T., Samson, I.M., Williams-Jones, A.E., and Smith, D.L., 2017, HFSE evolution in the Eldor Carbonatite: Mercier-Langevin, P., Dube, B., Bardoux, M., Ross, P.S., and Dion, C., Mineral Resources to Discover, *Society for Geology Applied to Mineral Deposits,* 14th Biennial Proceedings, Quebec City, Canada, p. 1371-1374

Shock, E.L., Sassani, D.C., Willis, M., and Sverjensky, D.A., 1997, Inorganic species in geologic fluids: Correlations among standard molal thermodynamic properties of aqueous ions and hydroxide complexes: Geochimica et Cosmochimica Acta, v. 61, p. 907-950.

Shock, E.L., and Helgeson, H.C., 1988, Calculation of the thermodynamic and transport properties of aqueous species at high pressures and temperatures: Correlation algorithms for ionic species and equation of state predictions to 5 kb and 1000°C: Geochimica et Cosmochimica Acta, v. 52, p. 2009-2036.

Shvarov, Y., and Bastrakov, E., 1999, HCh: a software package for geochemical equilibrium modelling - user's guide, Australian Geological Survey Organisation, Record 1999/25, 61 p.

Siegel, K., Williams-Jones, A.E., and van Hinsberg, V.J, 2017, The amphiboles of the REE-rich A-type peralkaline Strange Lake pluton fingerprints of magma evolution: Lithos, v. 288-289, p. 156-174

Smith, M.P., Campbell, L.S. and Kynicky, J., 2015, A review of the genesis of the world class Bayan Obo Fe-REE-Nb deposits, Inner Mongolia, China: Multistage processes and outstanding questions: Ore Geology Reviews, v. 64, p. 459-476.

Taylor, H.P., Frechen, J., and Degens, E.T., 1967, Oxygen and carbon isotope studies of carbonatites from the Laacher See District, West Germany and the Alno District, Sweden: Geochimica et Cosmochimica Acta, v 31, p. 407-430.

Trofanenko, J., Williams-Jones, A.E., Simandl, G.J., and Migdisov, A.A., 2016, The nature and origin of the REE mineralization in the Wicheeda carbonatite, British Columbia, Canada: Economic Geology, v. 111, p 199-223.

Tropper, P., and Manning, C.E., 2007, The solubility of fluorite in H2O and H2O-NaCl at high pressure and temperature: Chemical Geology, v. 242, p. 299-306.

Tyson, R., 2014, Mineralogy, lithology, paragenesis & dating of the Eldor carbonatite, Work in Progress, Ministere de Ressources Naturelles et de la Faune, GM68875

Walter, B.F., Giebel, R.J., Steele-MacInnis, M., Marks, M.A., Kolb, J., and Markl, G., 2021, Fluids associated with carbonatitic magmatism: A critical review and implications for carbonatite magma ascent: Earth-Science Reviews, v. 215, 103509.

Williams-Jones, A., and Palmer, D., 2002, The evolution of aqueous–carbonic fluids in the Amba Dongar carbonatite, India: implications for fenitisation: Chemical Geology, v. 185, p. 283–301.

Williams-Jones, A.E., Migdisov, A.A., and Samson, I.A., 2012, Hydrothermal Mobilisation of the Rare Earth Elements – a Tale of "Ceria" and "Yttria": Elements, v. 8, p. 355-360.

Williams-Jones, A.E., Wollenberg, R., and Bodeving, S., 2015, Hydrothermal fractionation of the rare earth elements and the genesis of the Lofdal REE deposit, Namibia [ext. abs.] Symposium on Strategic and Critical Materials Proceedings, November 13-14, 2015, Victoria, British Columbia, British Columbia Ministry of Energy and Mines, British Columbia Geological Survey Paper 2015-3, pp. 125-130.

Wright, W.R., Mariano, A.N., and Hagni, R.G., 1998, Pyrochlore mineralization and glimmerite formation in the Eldor (Lake LeMoyne) carbonatite complex, Labrador Trough, Quebec, Canada: Proceedings 33rd Forum on the Geology of Industrial Minerals Inst. Mining Metall. Petroleum, Spec., vol. 50, p. 205-213.

Xie, Y., Hou, Z., Yin, S., Dominy, S.C., Xu, J., Tian, S., and Xu, W., 2009, Continuous carbonatitic melt-fluid exsolution of a REE-mineralisation system: Evidence from Inclusion in the Maoniuping REE Deposit, Western Sichuan, China: Ore Geology Reviews, v. 36, p. 90-105.

Xie, Y., Li, Y., Hou, Z., Cooke, D.R., Danyushevsky, L., Dominy, S.C., and Yin, S., 2015, A model for carbonatite hosted REE mineralisation – the Mianning-Dechang REE belt, Western Sichuan Province, China: Ore Geology Reviews, v. 70, p. 595-612.

Zhou, L., Mavrogenes, J., Spandler, C., and Li, H.P., 2016, A synthetic fluid inclusion study of the solubility of monazite-(La) and xenotime-(Y) in H2O-Na-K-Cl-F-CO2 fluids at 800 degrees C and 0.5 GPa: Chemical Geology, v. 442, p. 121-129.

Chapter 3 - The distribution of the REE in carbonatites: A quantitative evaluation

Preface

The previous chapter (2) characterized the various units of the Eldor Carbonatite Complex and used several lines of evidence, including major and trace element compositions from all major minerals, to develop a genetic model for the Ashram REE deposit. Textural evidence was presented to show that the REE minerals occur in breccia matrices, in veins, and as vug fillings, and are therefore hydrothermal in origin. The genetic model emphasizes the essential role of hydrothermal fluids in the formation of the Ashram REE deposit. Chapter 3 uses the mineral compositional data collected in Chapter 2 to perform a mass balance calculation. The calculation traces each REE individually through all rock-forming and REE-bearing minerals across all zones to quantitatively evaluate the relative importance of magmatic and hydrothermal processes in the genesis of the deposit. The results of the mass balance calculation of Chapter 3 are also evaluated in the context of the genetic model advanced in Chapter 2. Chapter 3 is the first example of a quantitative evaluation of the distribution of the REE in carbonatites.

Abstract

The LREE enrichment of carbonatites is generally considered to be an intrinsic characteristic of the rocks. Although all carbonatite magmas are inherently LREE-enriched, not all carbonatites are hosts to REE minerals, and even fewer are sufficiently enriched in the REE to form economic deposits. The origin of these deposits is still debated, particularly in respect to the relative importance of magmatic and hydrothermal processes in the concentration of the REE. The evidence to support either origin has focussed on the mineralization, with little attention to the contribution of the rock-forming minerals to the overall REE budget. We evaluate the changing REE contents of all minerals (primary and secondary) in the Ashram carbonatite-hosted REE deposit, Canada, and use these data, in combination with the changing proportions of each mineral, to calculate their contributions to the overall REE budget of the carbonatites. Our mass balance calculation traced each REE individually across all minerals from the primary magmatic to the secondary hydrothermal stages. The calculation showed quantitatively that at Ashram, all the REE were mobilized by hydrothermal fluids and concentrated to varying degrees in REE minerals. The extent to which the individual REE were concentrated in these minerals, however, decreased with increasing atomic number (and/or decreasing ionic radius, e.g., Y), and with decreasing fluid flow (fluid-rock ratio), such that, in all zones, La is more strongly concentrated than Lu, and across zones, La is most strongly concentrated in areas of greatest fluid flow. These trends were the result of the relative thermodynamic stability of the various aqueous REE-complexes and REE minerals. Overall, magmatic and non-REE phases host a low proportion of the whole-rock REE concentration, especially of the LREE.

3.1 Introduction

Carbonatites are the principal source of the light rare earth elements (LREE) and the deposits hosted by or associated with them are responsible for >60% of the global resources of these elements (Zhou et al., 2017). The LREE enrichment of carbonatites is generally considered to be an intrinsic characteristic arising from the mechanism of melt generation, either by small degrees of partial melting of the mantle (with or without subsequent fractional crystallization) or by liquid immiscibility (e.g., Wyllie and Tuttle, 1960; Veksler and Lentz, 2006; Woolley and Kjarsgaard, 2008; Ghosh et al., 2009; Brooker and Kjarsgaard, 2011). The REE, with the exception of Sc, behave incompatibly in most magmatic systems because of their 3+ charge and relatively large ionic radii, especially the low atomic number LREE, and as such, small degrees of partial melting of mantle rocks preferentially enrich carbonatite liquids in these elements (Pell, 1996). In the case of melt generation by carbonate-silicate liquid immiscibility, the partition coefficients for the LREE favour their concentration in the carbonatite liquid (Martin et al., 2013).

Although all carbonatite magmas are inherently LREE-enriched, not all carbonatites are hosts to REE minerals, and even fewer are enriched in the REE to potentially economic levels. Carbonatite-hosted REE ores have been long considered magmatic, based largely on studies of the Mountain Pass deposit (Olson et al., 1954; Mariano, 1989; Castor, 2008). Recently, however, a number of studies have proposed a magmatic-hydrothermal model for these deposits, in which hydrothermal fluids of magmatic origin concentrate the REE either by direct transfer from the magma and/or by leaching and remobilization from primary minerals (e.g., Costanzo et al., 2006; Ruberti et al., 2008; Doroshkevich et al., 2009; Moore et al., 2015; Nadeau et al., 2015; Xie et al., 2015; Trofanenko et al., 2016; Giebel et al, 2017; Smith et al., 2018). Trofanenko et al. (2016), for example, presented textural and stable C-O isotopic evidence showing that REE-fluorocarbonate mineralization co-precipitated with hydrothermal dolomite in the Wicheeda carbonatite in British Columbia. Commonly, however, the evidence to support either origin is exclusively textural. Once REE minerals have been identified, it is then generally assumed that these minerals are the principal carriers of REE in the rocks (e.g., Mitchell and Smith, 2017) and that whichever process, magmatic or hydrothermal, crystallized the REE mineral, was responsible for the concentration of the REE. Almost invariably, little or no attention is paid to the contribution of the major rock-forming minerals to the overall REE budget of the carbonatite. The relative importance of magmatic and hydrothermal processes in concentrating the REE, however, cannot be fully evaluated without determining this contribution. Such an evaluation would require determining the REE content of each of the major igneous rock-forming minerals, e.g., calcite, dolomite, pyroxene, amphibole, and apatite, and in some cases, even fluorite, and summing these contents weighted to the proportions of the corresponding minerals in the bulk rock. To our knowledge this has not been done previously.

Despite a considerable number of studies reporting the REE contents of non-REE minerals in carbonatites notably, clinopyroxene and amphibole (Reguir et al., 2012; Doroshkevich et al., 2017; Zhang et al., 2019), apatite (e.g. Hogarth, 1989; Ngwenya, 1994; Wall and Mariano, 1996; Belousova et al., 2002; Broom-Fendley et al., 2016, 2017; Chakhmouradian et al., 2017; Smith et al., 2018), carbonates (Xu et al., 2007; Chakhmouradian et al., 2016; Doroshkevich et al., 2017; Cheng et al., 2018; Smith et al., 2018) and fluorite (e.g. Santos et al., 1996; Bühn et al., 2003; Huang et al., 2007; Xu et al., 2008, 2012; Mao et al., 2015; Broom-Fendley et al., 2017; Mitchell and Smith, 2017; Ozturk et al., 2019), these studies only considered some of the minerals present in the rock, thereby providing an incomplete characterisation of the distribution of the REE in the carbonatite. In these studies, the REE content of the non-REE minerals was investigated to identify potential sources for the REE presently contained in REE minerals, e.g., bastnäsite-(Ce) or monazite-(Ce), or to trace the evolution of the magma, but not to evaluate the whole-rock REE budget.

In this contribution, we evaluate the changing REE contents of all minerals (primary and secondary) in the Ashram carbonatite REE deposit, Canada, with the evolution of the system from the magmatic to the hydrothermal stage and use these data in combination with the changing proportions of each mineral to calculate their contributions to the overall REE budget of the carbonatite. The calculation traces the contribution of each primary (magmatic) and secondary (hydrothermal) mineral to the whole-rock budget of each REE, thereby allowing a comprehensive evaluation of the changing distributions of the different REEs from the early crystallisation of the carbonatite to the development of a potentially economic REE ore deposit. We use the results of this calculation to evaluate the relative importance of magmatic and hydrothermal phases in concentrating the REE and provide an explanation for the origin of LREE-enrichment in carbonatite-hosted REE deposits.

3.1.1 Geology of the Eldor Carbonatite Complex

The Eldor carbonatite complex is located approximately 130 km south of Kuujjuaq, in northern Québec, Canada, and was emplaced in the Labrador Trough, which is the foreland of the New Quebec Orogen, a Paleoproterozoic fold and thrust belt on the eastern margin of the Superior Province (Clark and Wares, 2006). The Labrador Trough is a rift basin that experienced three cycles of volcanism and sedimentation (Clark and Wares, 2006), the second of which coincided with the emplacement of the Eldor carbonatite. Although the age of the carbonatite has not been determined, it is constrained to be less than 1870 ± 4 Ma by the U-Pb age of a rhyodacite, which it crosscuts (Machado et al., 1997). The complex was subsequently deformed and metamorphosed to greenschist facies during the Hudsonian Orogeny (1.82 - 1.77 Ga) (Clark and Wares, 2006).

Commerce Resources Corp. is currently exploring the Eldor carbonatite complex and has reported measured and indicated resource estimates of 29.3 Mt at 1.90 % total rare earth oxides (TREO), using a cut-off grade of 1.25 % TREO (Gagnon et al., 2012). The carbonatite is exposed in a 7 x 3.5 km elliptical area and comprises a suite of intrusions ranging in composition from calcite- through dolomite- to ferro-carbonatite, as well as Na- and K- fenites. The pluton has been subdivided into a Rim composed of REE-poor calcite- and dolomite-carbonatite and a core of dolomite carbonatite and ferrocarbonatite that hosts the Ashram REE deposit (Fig. 3.1).

In the context of the study presented in this paper, the following is a summary of what is currently known of the Ashram REE deposit, which is based largely on the results of a study by Beland and Williams-Jones (2021). The Ashram deposit comprises three main zones of mineralization, namely the BD, B, and A zones (Fig. 3.1A, Table 3.1). The outermost BD zone is a fluorapatite-rich, dolomite carbonatite containing rare earth fluorocarbonate mineralization (bastnäsite-(Ce) ($REECO_3F$), parisite-(Ce) ($Ca(Ce,La)_2(CO_3)_3F_2$), synchisite-(Ce) ($CaCe(CO_3)_2F$)) and trace monazite-(Ce) ($REEPO_4$). This unit is extremely rich in phosphate, with an average of 7 vol. % fluorapatite and up to 14 wt. % P_2O_5. It also contains variable, but minor proportions of calcite (Beland and Williams-Jones, 2021). The B zone is a thin, discontinuous rind between the BD and A zones (Fig. 1B) and is a dolomite carbonatite containing 4 vol. % fluorite and 1 vol. % monazite-(Ce) ($REEPO_4$) on average, with minor proportions of REE fluorocarbonate minerals. This zone passes into the innermost A zone, a ferroan dolomite carbonatite, which is even richer in fluorite (average 8 vol %) and contains 2 vol. % monazite-(Ce) on average. Like the B zone, it contains minor proportions of REE fluorocarbonate minerals. The central, upper part of the A zone (< 100 m depth) is referred to as the MHREO zone, because of its higher proportion of the middle REE, which occur in monazite-(Nd). It consists of discontinuous veins, pods and lenses varying from ~5 cm to a few metres in thickness. The MHREO zone is a fluorite-poor ferrocarbonatite, with siderite as its dominant carbonate mineral. There is also subordinate monazite-(Ce). Approximately 50 vol. % of the LREE mineralization in the MHREO zone occurs in the form of REE fluorocarbonate minerals. The REE-minerals are concentrated along the

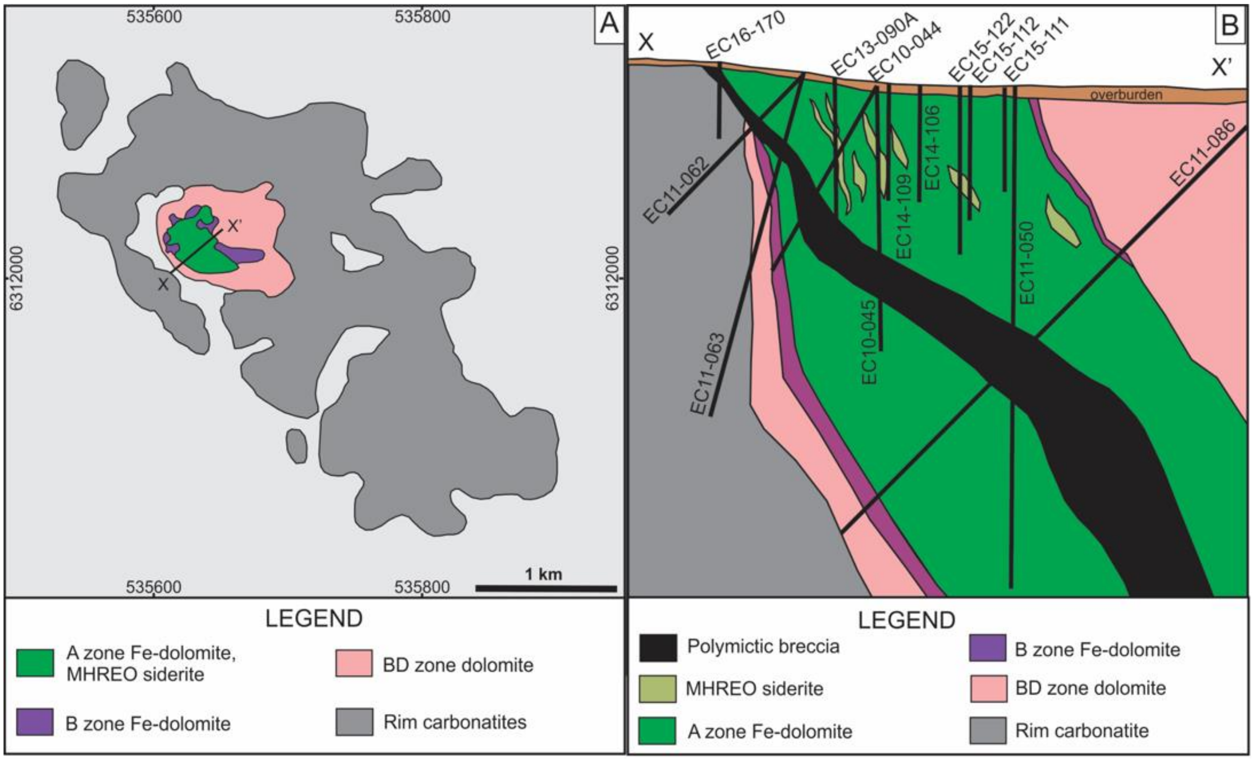

Figure 3.1: Geological map and cross section of the Eldor Carbonatite

A) A simplified geological map of the Eldor carbonatite complex at the 100 m level, based on information from drill core B) A simplified cross-section of the X-X’ transect in A), including traces of drill holes used to construct the section. Modified after Beland and Williams-Jones (2021).

Table 3.1: Chemical and mineralogical compositions of the different units of the Ashram REE deposit

Zone	**TREO (wt. %)**	**Principal REE Minerals**	**Principal Carbonate**	**P_2O_5 (wt. %)**	**Phosphate Phase**	**F (wt. %)**	**Fluorine Phase**
MHREO	1.6	monazite-(Nd), monazite-(Ce)	siderite	0.58	REE-phosphates	0.55	fluorite
A	1 – 3+	monazite-(Ce)	Fe-dolomite	0.92	REE-phosphates	3.74	fluorite
B	1 – 2	monazite-(Ce)	dolomite	1.21	REE-phosphates	1.07	fluorite
BD	0.6 – 1	REE-fluorocarbonates	dolomite	2.76	apatite	0.58	apatite, REE-fluorocarbonates

margins of siderite crystals and the edges of vugs filled with quartz and dolomite. This unit also contains trace magnetite. Xenotime-(Y) (YPO_4) and aeschynite-(Nd) ($(Nd,Ca,Fe)(Ti,Nb)_2(O,OH)_6$) occur in trace amounts in all the zones except the BD zone, where it is absent.

The youngest lithotype in the Ashram deposit is an unmineralized polymictic breccia developed largely in the A zone and extends outwards into the BD zone. The breccia contains unmineralized BD zone clasts and was interpreted by Beland and Williams-Jones (2021) to be the product of hydro-fracturing, coeval with the emplacement of the B and A zone carbonatites. In three dimensions, the breccia is an irregular, discontinuous, northward-dipping body that is spatially associated with REE mineralization. Rocks intersected proximal to breccia intervals have a high (> 10 %) proportion of MREE and HREE; LREE proportions increase with increasing distance from the breccia. The breccia is characterized by low bulk rock TREE contents but high bulk rock MHREE/TREE ratios.

The REE minerals, monazite-(Ce), bastnäsite-(Ce) (and other REE-fluorocarbonates), xenotime-(Y) and aeschynite-(Nd) occur in veins and as vug fillings in all the zones described above, and as disseminations in the breccia matrix. They are hydrothermal in origin (Beland and Williams-Jones, 2021). Because of the major mineralogical differences between the BD zone and the rest of the Ashram deposit, the different P- and F-bearing REE minerals are rarely observed in contact with each other. Where they are observed together, monazite mantles fluorapatite and the REE-fluorocarbonates mantle monazite. Xenotime-(Y) is commonly associated with monazite-(Ce) and rarely, with fluorapatite. In both cases, xenotime-(Y) was deposited later and mantles the other minerals. Monazite-(Nd) has been observed exclusively in the MHREO zone, where it occurs at the margins of siderite crystals. Aeschynite-(Nd) is commonly associated with, and crystallized later than monazite-(Ce), xenotime-(Y), and ilmenite. The presence of trace bastnäsite-(La) and -(Nd) was reported by Mitchell and Smith (2017).

There is abundant textural evidence of intense and pervasive hydrothermal alteration having overprinted the Ashram carbonatites. Only the BD zone carbonatite contains primary dolomite (as evidenced by its stable C-O isotopic composition), and it is mantled by a chemically distinct, secondary, ferroan dolomite. Dolomite and ferroan dolomite of the B and A zones share the same chemical characteristics as the secondary dolomite of the BD zone. Primary fluorapatite is only observed in the BD and A zones, and then, only as a trace mineral. All other rock-forming minerals at Ashram exhibit hydrothermal textures, namely secondary carbonate vug infill, veins of fluorapatite or fluorite, and multiple generations of both minerals. The occurrence of the REE minerals in veins and vugs, and in association with hydrothermal minerals (e.g., secondary fluorapatite and fluorite) indicates a secondary origin for the REE mineralization at Ashram.

3.1.2 Genetic Model for the Ashram Deposit

As discussed in Beland and Williams-Jones (2021), the monazite (and bastnäsite) are compositionally zoned on the deposit scale, with concentration of Th and the proportions of the LREE decreasing and increasing, respectively, from the center of the deposit towards its margins. In the centre, the monazite is dominantly Th-rich monazite-(Nd) and at the margins, Th-poor monazite-(Ce). The bulk rock MHREE/TREE at the center of the deposit, i.e., proximal to the breccia, also decreases outwards. The deposit-scale variation in monazite composition is correlated with the host carbonate composition, such that the proportion of LREE in monazite increases with decreasing Fe content of the carbonate. This was interpreted by Beland and Williams-Jones (2021) as evidence that the breccia was the principal pathway for a carbonatite-derived H_2O-CO_2, REE-bearing fluid that altered and mineralized the various units of the Ashram deposit. The REE were fractionated through the combined effects of the differential pH buffering of the rock (siderite has a much lower pH buffering capacity than calcite) and cooling along the fluid pathway. Bastnäsite is interpreted to have replaced monazite because it mantles the monazite and, within each zone, bastnäsite REE compositions are very similar to those of the corresponding monazite. Xenotime was a late, trace mineral that saturated in the fluid after precipitation of most of the LREE as monazite. Finally, Nb was remobilized and deposited as trace aeschynite-(Nd) by late-stage fluids. Overall, the deposit-scale zonation in mineralogy and REE distribution at Ashram was the result of REE fractionation along the fluid pathway due to cooling and variations in the pH buffering capacity of the different host rocks with which the fluid interacted, allowing the lightest (and therefore most mobile) REE to travel the furthest from the breccia that provided the conduit for the mineralizing fluid.

3.2 Methodology

3.2.1 Model Overview

As mentioned above, the objective of our study was to evaluate the relative importance of hydrothermal and magmatic processes in concentrating the REE by determining the contributions of primary magmatic and secondary minerals (REE and non-REE minerals) to the evolving REE budget of the Ashram carbonatite. A schematic diagram explaining the model inputs and methodology is provided in Figure 3.2. The model has two parts; a normative calculation and a REE budget calculation. The former involved determining the mass proportions of the major rock-forming minerals present in the different zones of the Ashram deposit from the bulk rock composition (major elements) and the compositions of these minerals. This was done using the relationship X = A/B, where X is a vector of the normative mineral proportions (unknown), A is a vector of the bulk concentration of each element and B is a matrix of mineral compositions (Piché and Jébrak, 2004).

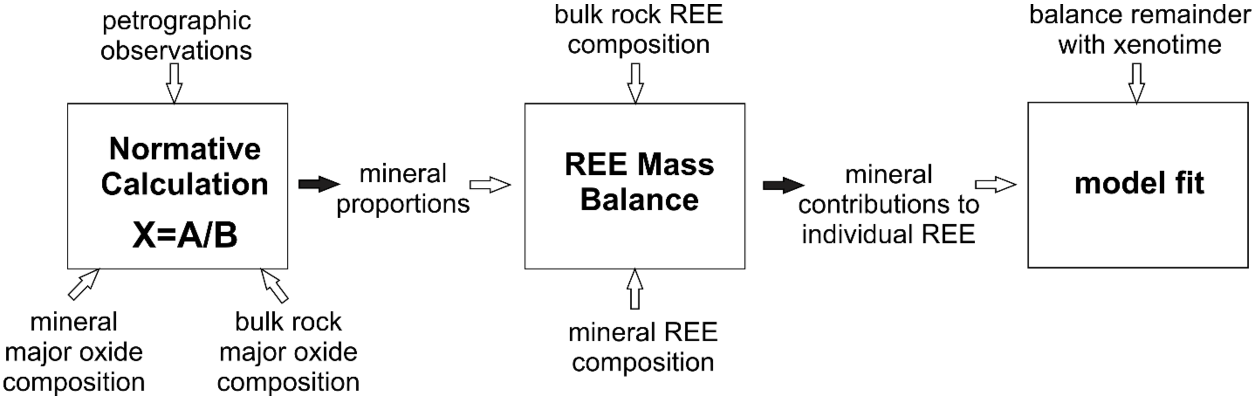

Figure 3.2: Schematic diagram of model calculations

The white arrows represent input data and the black arrows represent output data of the various stages of the model calculations.

The following minerals occur in major/minor volumetric proportions in the Ashram carbonatite: dolomite, ferroan dolomite, siderite, calcite, phlogopite, chlorite, quartz, pyrite, magnetite, ilmenite, fluorapatite, monazite, fluorite, bastnäsite, and synchysite (Beland and Williams-Jones, 2021). As pyrite and magnetite contain Fe as the only cation, monazite contains only and P and the REE, and bastnäsite and synchysite contain only F, the REE and the carbonate ion, their proportions could be calculated before the normative calculation, and the corresponding proportions of Fe, P, and F subtracted from the bulk rock concentration vector, A. Pyrite and magnetite mass proportions were estimated from their apparent volume proportions estimated petrographically and their density. As mentioned above, the Th and LREE contents of Ashram monazite are inversely correlated. We note also that all the zones have bulk rock Th/Ce ratios very similar to, but slightly higher than those of the corresponding average monazite composition (or bastnäsite for the BD zone) (Fig. 3.3). We therefore calculated the proportions of monazite, bastnäsite and synchysite in the different zones from the bulk rock Th content and the corresponding Th content in monazite, bastnäsite and synchysite. The relative proportions of bulk rock Th content apportioned to the different REE minerals was guided by petrographic observations. For example, for the bastnäsite-dominated BD zone, only a small proportion of the bulk rock Th was assigned to monazite, with the balance going to bastnäsite and synchysite. The normative mineral proportions were calculated following this correction of the Fe, P and F values for the bulk rock element composition vector A.

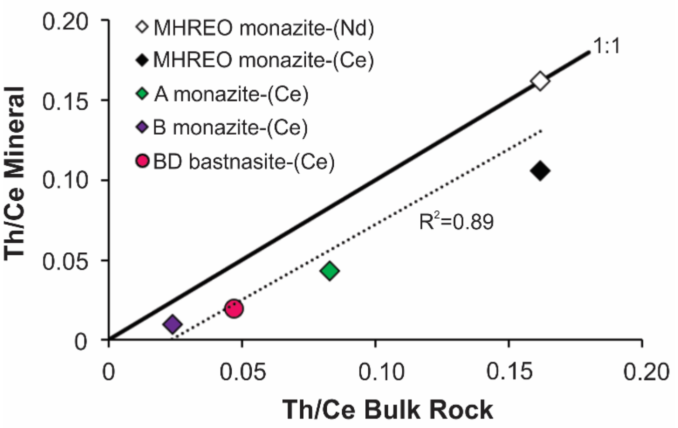

Figure 3.3: Bulk rock Th/Ce versus LREE mineral Th/Ce

The average Th/Ce ratio of the LREE minerals compared to the average bulk rock Th/Ce ratio for a given Ashram zone. A 1:1 relationship is shown by the solid black line, and the line of best fit through the data is shown by the dashed black line.

The normative mineral proportions were multiplied by the corresponding concentrations of each REE for the different minerals to determine the contribution of each mineral to the overall REE budget. In principle, the sum of these contributions should equal the measured bulk rock concentration. The fit of the model to the data was therefore evaluated for each of the rare earth elements by the percentage difference between the calculated and measured values, where negative and positive values represent over- and under-estimates by the model of the measured values, respectively, and 0% is a perfect fit. The overall fit of the model mineral assemblage was evaluated by the sum of squared residuals for each element (to remove the effect of negative numbers), where 0 is a perfect fit.

Inputs to the model comprised the major element and corresponding REE compositions for both the bulk rocks and minerals. The bulk rock chemical data were obtained from the Commerce Resources Corp. database of Ashram drill core assays, which were performed by Activation Laboratories in Ancaster, Ontario, and comprised all major elements and a large number of trace elements, including the full set of REE. All samples were ground to 95% -200 mesh and aliquots of each powder fused with lithium metaborate/tetraborate, followed by analysis using inductively coupled plasma optical emission spectrometry (ICP-OES) for the major elements and mass spectrometry (ICP-MS) for the trace elements. The loss on ignition (LOI) was determined after fusion. Samples (1 g) were heated in an oven at 1000°C for 1 h, cooled then weighed, with the percent loss calculated from the difference in weight before and after heating. The fluorine content was determined from 0.2 g samples fused with lithium metaborate/tetraborate in a furnace to release F^- ions from the sample into a solution, which was then analysed using an ion sensitive electrode.

Stoichiometric compositions were assumed for pyrite, magnetite, phlogopite, chlorite (clinochlore), fluorite, and quartz. The major element compositions of the other minerals were taken from Beland and Williams-Jones (2021). The REE compositions of the various minerals are from Beland and Williams-Jones (2021), except that for A zone fluorite, which was taken from Mitchell and Smith (2017).

3.2.2 Bulk Rock Selection

Owing to the small-scale heterogeneity (interfingering of units) of the Ashram rocks and the minimum sample length restrictions of exploration core sampling (approximately 1 to 2 m assay length), the average composition of each zone represents a mixture of rock types rather than discrete units. In order to obtain a more representative bulk composition of each rock unit (rather than economic ‘zone’), a sample population was selected for each Ashram zone. For the more voluminous BD, B, and A zones, assay intervals were selected after visual examination of core photos to produce a sample population consisting of 15-20% of the total number of meters drilled for each zone (Table 3.2). Care was taken to omit any core observed to contain multiple units or displaying visible evidence of alteration (e.g., iron oxides) or rubble zones. In contrast to the BD, B, and A zones, the ferrocarbonatite comprising the MHREO zone occurs in thin veins, dykes and pods, and consequently there were very few intersections of pure ferrocarbonatite. Intersections containing less than 50% ferrocarbonatite were omitted. For this zone, the sample population represents ~ 75% of the total (discrete) number of meters drilled (Table 3.2). For each zone, the sample population compositions were weighted by their assay length and averaged. The average bulk rock major element and REE compositions of the sample populations for each zone used in the model are reported in Table 3.3. Figure 3.4 shows the average weight % of each major element oxide of the sample population, compared to that of the total data set for each zone. In most cases, the difference between the average value for the sample population and the total data set is less than the symbol size. The chondrite-normalized REE profile of each sample population is compared to that of the total data set for each zone in Figure 3.5. From this figure, it is evident that, although the average compositions of the sample populations are very similar to those of the total populations for each zone, there are some differences, most notably for the BD zone, in which the concentrations of the heavy REE (HREE) are significantly lower in the total population than in the sample population.

Table 3.2: Sample population interval lengths

	2014 Data Set	**Sample Population**	**% Sampled**
	# of m	# of m	
MHREO	71	53	74
A	4188	723	17
B	669	133	20
BD	1783	251	14

Table 3.3: Bulk rock compositions of the Ashram deposit zones used in the model

	MHREO	**A**	**B**	**BD**
SiO_2 (*wt. %*)	4.79	3.19	4.32	2.34
Al_2O_3	0.12	0.17	0.09	0.15
Fe_2O_3(T)	49.62	21.80	11.34	7.93
MnO	4.57	2.79	2.08	1.37
MgO	14.16	19.31	24.75	27.84
CaO	23.34	43.69	50.48	53.24
K_2O	0.06	0.10	0.09	0.11
TiO_2	0.73	0.35	0.14	0.09
P_2O_5	1.07	1.56	2.27	5.92
F	1.42	6.92	4.42	1.00
ThO_2	0.12	0.11	0.03	0.03
total	100	100	100	100
La (*ppm*)	1566	3836	4235	1182
Ce	4127	7149	7394	2724
Pr	599	746	720	337
Nd	2478	2536	2445	1333
Sm	384	312	284	202
Eu	88	79	66	53
Gd	190	195	130	117
Tb	20	23	13	14
Dy	81	96	49	62
Y	278	385	196	239
Ho	10	14	7	9
Er	21	29	15	21
Tm	2	3	2	2
Yb	13	17	10	14
Lu	2	2	1	2

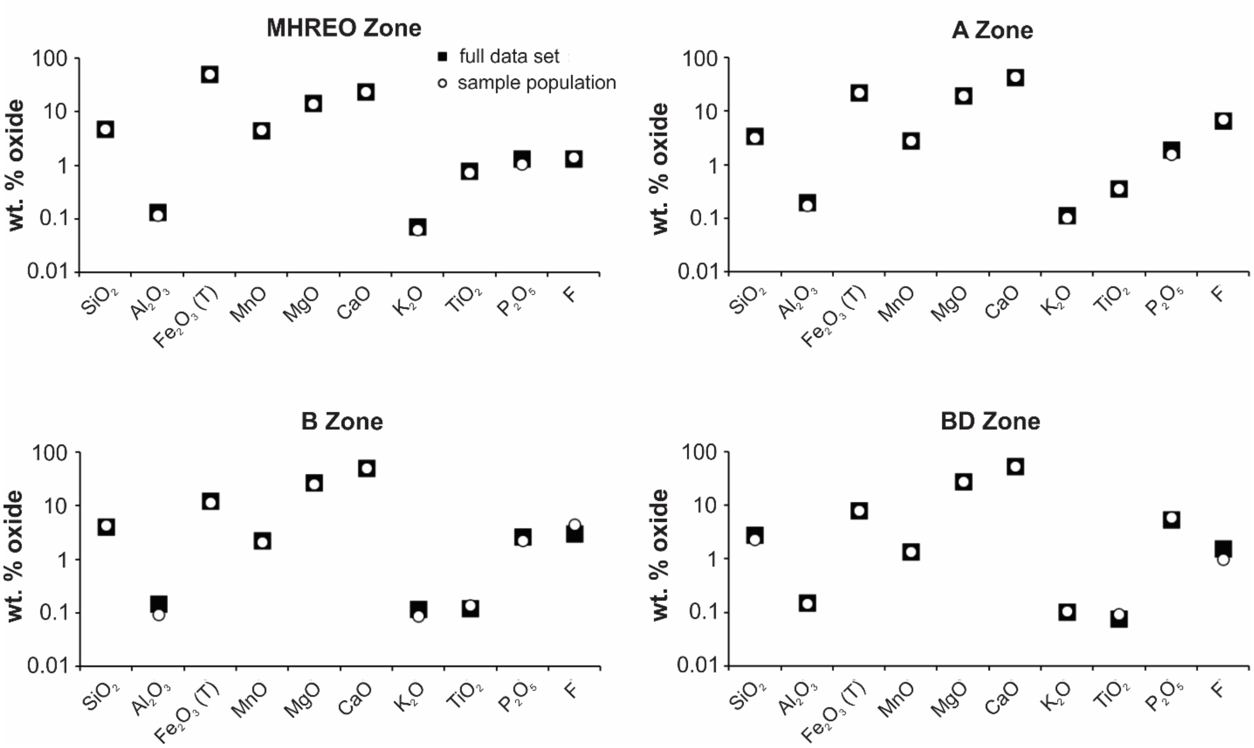

Figure 3.4: Comparison of major element compositions of the data set and sample populations

The average major element bulk rock composition of each zone (total data set) compared to that of the selected sample population. The difference is generally less than the symbol sizes.

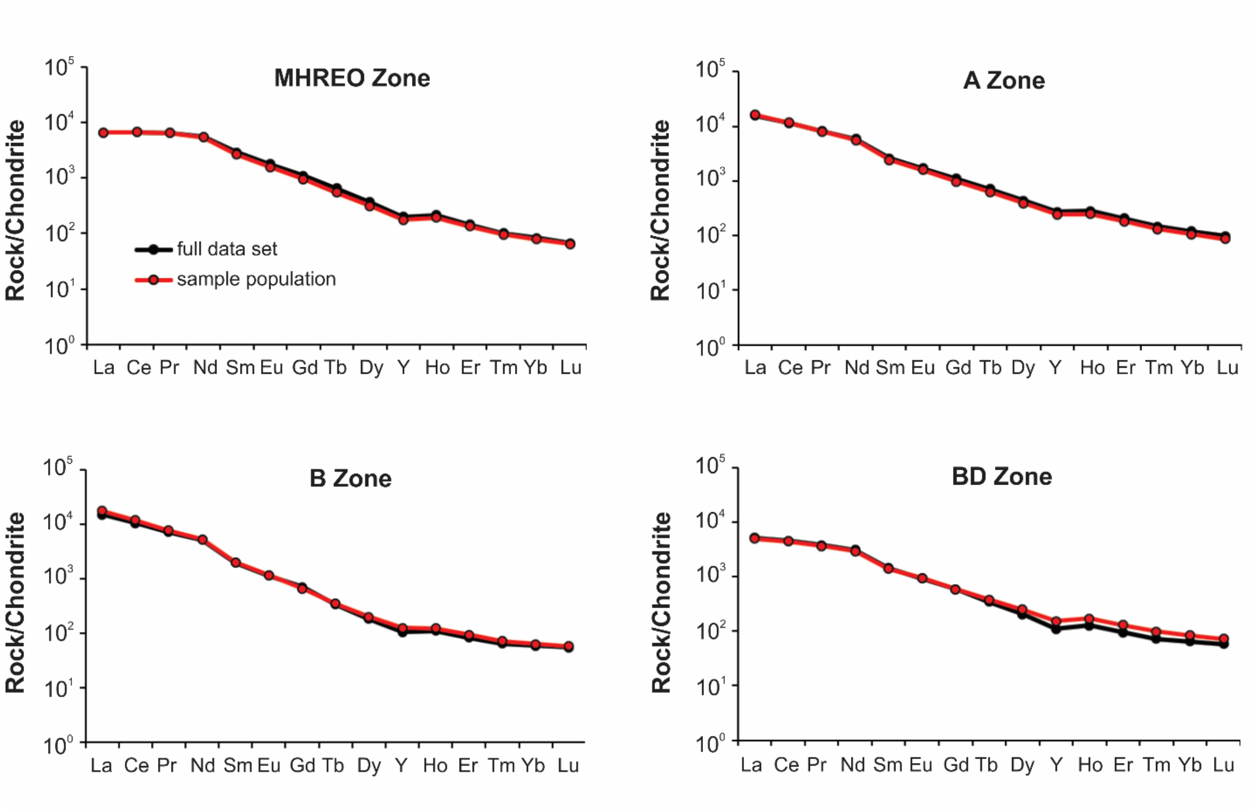

Figure 3.5: Comparison of REE compositions of the data set and sample populations

The average bulk rock REE distribution profiles of each Ashram zone (full data set) compared to that of the selected sample population. The REE values were normalized to CI chondrite (McDonough and Sun, 1995).

3.2.3 Mineral Compositions

The major element and REE compositions of the various major non-REE and REE minerals in each of the zones are reported in Tables 3.4 and 3.5, respectively. The monazite-(Ce), monazite-(Nd), and bastnäsite-(Ce) compositions are averages either for a zone, or for groups within a zone and xenotime compositions are representatives for each zone. Although, as noted above, the major element concentrations for fluorite were assumed to be stoichiometric for the normative calculation, measured REE concentrations were used in the REE calculation; the REE content of this mineral is too low to have affected the normative calculation (Table 3.5).

Within a given zone, monazite-(Ce) varies significantly in composition (Beland and Williams-Jones, 2021). In particular, monazite-(Ce) from the A zone varies considerably in its Th content, whereas the La content remains relatively constant. By contrast, monazite-(Ce) from the

Table 3.4: Mineral major element oxide compositions used in the normative calculation

Mineral		SiO_2	Al_2O_3	Fe_2O_3 (T)	MnO	MgO	CaO	K_2O	TiO_2	P_2O_5	F	ThO_2	total
*Quartz		1											1
*Pyrite				1									1
*Magnetite				1									1
*Phlogopite		0.44	0.12			0.29		0.11			0.03		1
*Ilmenite				0.53					0.47				1
*Chlorite		0.34	0.19	0.19		0.28							1
*Calcite							1						1
Fluor-apatite	BD						0.54			0.42	0.03		1
	B						0.53			0.42	0.04		1
	A						0.54			0.42	0.04		1
Fluorite	BD						0.72				0.28		1
	A						0.72				0.28		1
	MHREO						0.72				0.28		1
Dolomite	BD			0.03	0.01	0.4	0.56						1
Fe-dolomite	BD			0.13	0.02	0.31	0.54						1
	B			0.04	0.01	0.39	0.56						1
	A			0.13	0.02	0.32	0.54						1
Siderite	MHREO			0.92	0.05	0.03							1
Bastnäsite-(Ce)	BD	0.04					0.06				0.87	0.04	1
	B	0.03					0.02				0.93	0.02	1
	A	0.01					0.08				0.84	0.07	1
	MHREO	0					0.1				0.73	0.16	1
Monazite-(Ce)	BD	0.01					0.03			0.93	0.02	0.02	1
	B 1	0					0.02			0.95	0.02	0.01	1
	B 2	0					0.01			0.96	0.02	0.01	1
	A 1	0					0.01			0.95	0.02	0.02	1
	A 2	0.01					0.01			0.91	0.02	0.05	1
	A 3	0.01					0.02			0.88	0.02	0.07	1
	A 4	0.02					0.01			0.85	0.02	0.1	1
	MHREO	0.01					0.05			0.83	0.02	0.09	1
Monazite-(Nd)		0.02					0.01			0.84	0.02	0.1	1
Synchysite-(Ce)		0.01					0.68				0.24	0.07	1

*‘ * ’ denotes a mineral for which a stoichiometric major oxide composition was used. All other compositions are based on those reported in Beland and Williams-Jones (2021)*

B zone has a highly variable La content but a relatively constant Th content (Beland and Williams-Jones, 2021). In these cases, an average composition for each mineral for each zone is not representative. Thus, monazite compositions for the A zone were subdivided into four groups based on their Th content (< 1%, 1-2%, 2-3%, and > 3%). Monazite compositions for the B zone were subdivided into two groups based on their La content (< 17%, > 17%). Average compositions were then calculated for each group. A comparison of the compositions used in the model with the full data set of Beland and Williams-Jones (2021) is provided in Figure 3.6.

All the data for the REE minerals, monazite, bastnäsite, synchysite, and xenotime were obtained using an electron microprobe (see Beland and Williams-Jones 2021 for details of the analytical method). Detection limits for Eu, Dy and Ho are relatively high for these minerals, and in most analyses, concentrations of these elements were below the detection limit (Beland and Williams-Jones, 2021). Terbium is rarely, if ever, analyzed in monazite or bastnäsite due to its low abundance. Although monazite and bastnäsite contain very little Eu, Tb, Dy and Ho, these minerals are nevertheless considered to be the major carriers of these elements in the Ashram rocks due to the high abundance of monazite and bastnäsite. To fill in the gaps in measured REE contents, all, or some combination of the above four elements were interpolated by normalizing the measured REE values to chondrite (McDonough and Sun, 1995) and assuming a smooth profile, with no Eu anomaly. This is illustrated in Figure 3.7, which compares the chondrite- normalized REE profile of B zone monazite-(Ce) 2 measured by Beland and Williams-Jones (2021), to the interpolated REE profile used in the model.

Table 3.5: Mineral REE compositions used in the REE mass balance calculations

Mineral	**Fluorapatite**			**Fluorite**			**Dolomite**	**Fe-dolomite**			**Siderite**	**Xenotime-(Y)**		
Unit	BD	B	A	BD	A	MHREO	BD	BD	B	A	MHREO	B	A	MHREO
La (*ppm*)	375	546	377	3	2	0.3	22	2	16	11	0.1			
Ce	2500	2164	2209	8	4	1	58	8	60	41	1			
Pr	419	308	347	2	1	1	7	1	12	8	0.2			
Nd	2079	1327	1780	10	4	10	22	6	54	39	1			2521
Sm	565	298	705	5	4	8	4	2	16	14	1	3656	6830	14134
Eu	181	98	270	2	3	4	1	1	6	6	0.3	3941	6756	8895
Gd	441	256	809	7	13	17	3	3	18	20	1	31042	40135	51847
Tb	53	36	148	1	3	3	0.3	1	3	4	0.2	8710	8710	12459
Dy	239	208	873	6	26	21	1	3	20	21	2	79325	80815	79900
Y	907	1115	3743	155	513	654	6	12	94	88	13	320702	295881	283115
Ho	35	36	133	1	7	4	0.3	1	4	3	0.4	12215	11983	11208
Er	77	87	256	4	20	9	1	1	10	8	1	27615	30964	24935
Tm	9	10	23	1	2	1	0.1	0.2	1	1	0.2	3442	4166	3216
Yb	48	48	105	5	2	4	1	1	6	5	1	18969	23909	16824
Lu	6	6	12	1	2	0.5	0.1	0.2	1	1	0.2	1719	3178	2213
Method	LA	LA	LA	LA	SIMS*	LA	LA	LA	LA	LA	LA	WDS	WDS	WDS
Type	Avg	Avg	Avg	Avg	Single	Avg	Avg	Avg	Avg	Avg	Avg	Rep	Rep	Rep

*'LA' – analyzed by LA-ICP-MS, 'Avg' – average composition, 'G Avg' – grouped, then averaged (explained in section 2.3), 'Rep' – representative analysis, ' * ' – a single analysis of A zone fluorite (analyzed by SIMS) from Mitchell and Smith (2017). All other compositions are based on those reported in Beland and Williams-Jones (2021).*

Table 3.5: Continued

Mineral	**Monazite-(Nd)**	**Monazite-(Ce)**								**Bastnäsite-(Ce)**				**Synchysite-(Ce)**
Unit		BD	B 1	B 2	A 1	A 2	A 3	A 4	MHREO	BD	B	A	MHREO	
La (*ppm*)	23986	94086	129435	199149	165976	140671	149482	114944	105659	127815	221966	193784	157019	65216
Ce	206194	280208	289080	288638	276843	283227	272848	273207	265918	313914	312782	297140	294729	186204
Pr	49996	37494	35302	25614	29621	31758	29678	33732	33762	39190	27091	29112	33135	26178
Nd	230803	142415	111766	68126	91720	100750	88706	117856	107392	118840	70711	88886	97136	90872
Sm	32207	17161	9960	8880	9080	10572	12404	15494	14591	9955	4918	7962	10653	12550
Eu	5809	3869	2534	1468	2365	2534	2815	3209	3378	2083	1209	1971	2815	3159
Gd	10378	5995	4797	3098	6487	6095	6636	8190	7978	4085	2603	4712	6149	6469
Tb	650	361	307	253	542	542	542	722	433	361	253	433	433	542
Dy	1737	700	738	738	1773	1680	496	1473	490	984	615	1230	984	331
Y	3299	1906	2936	1970	2907	2760	3168	4331	3203	1917	1798	3385	3426	7100
Ho	44	22	49	38	38	38	44	55	38	55	27	55	55	5
Er														
Tm														
Yb														
Lu														
Method	WDS	WDS	WDS	WDS	WDS	WDS	WDS	WDS	WDS	WDS	WDS	WDS	WDS	WDS
Type	Avg	Avg	G Avg	G Avg	G Avg	G Avg	G Avg	G Avg	Avg	Avg	Avg	Avg	Avg	Avg

*‘LA’ – analyzed by LA-ICP-MS, ‘Avg’ – average composition, ‘G Avg’ – grouped, then averaged (explained in section 2.3), ‘Rep’ – representative analysis, ‘ * ‘ – a single analysis of A zone fluorite (analyzed by SIMS) from Mitchell and Smith (2017). All other compositions are based on those reported in Beland and Williams-Jones (2021).*

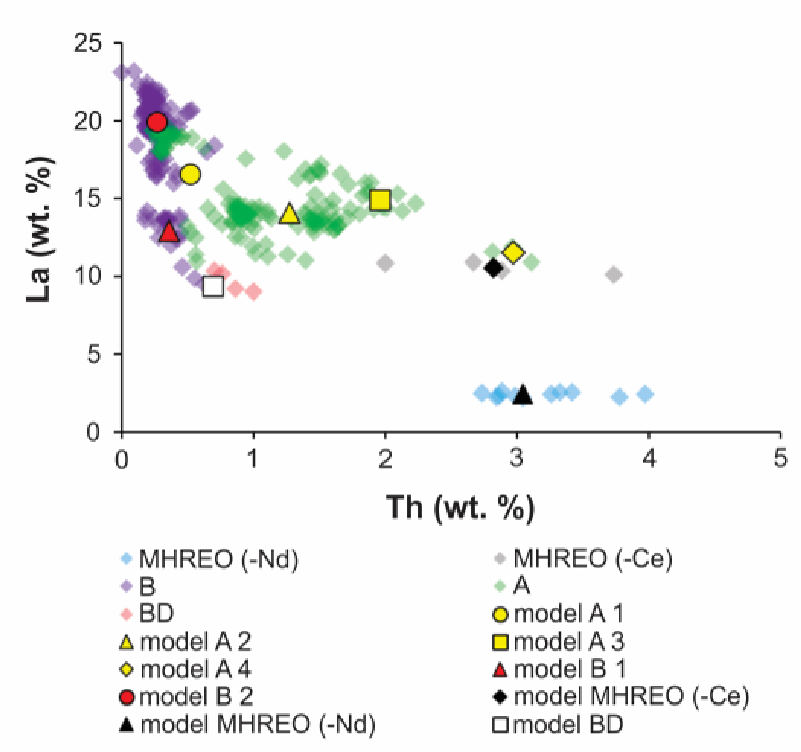

Figure 3.6: Model monazite Ce contents (wt. %) as a function of Th content (wt. %)

Monazite compositions used in the model, compared to the full data set of Beland and Williams-Jones (2021). All compositions are monazite-(Ce), unless otherwise noted.

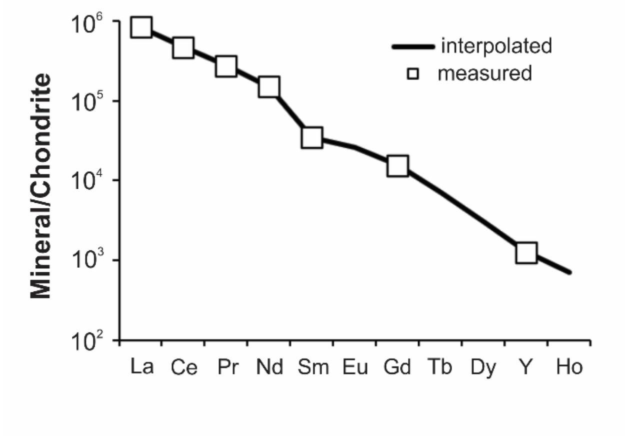

Figure 3.7: REE distribution interpolation example

An example of the interpolation method used for gaps in measured mineral compositions. The measured elements are normalized to CI chondrite (McDonough and Sun, 1995), and a smooth line is fitted through them, allowing the concentrations of the missing elements (e.g. Eu) to be reasonably estimated.

3.2.4 Assumptions/Known Errors

It was necessary to make several simplifications in the model that introduced errors. These errors, however, are considered to be negligible. For example, Mitchell and Smith (2017) identified trace phases that contain Ti, which are not considered in our model, including bafertisite ($Ba_2Fe_4Ti_2(Si_2O_7)O_2(OH)_2F_2$), aeschynite-(Nd) ($(Nd,Ca,Fe)(Ti,Nb)_2(O,OH)_6$), and niobian rutile. With the exception of aeschynite, these minerals do not readily incorporate the REE, and therefore their omission has no effect on the mass balance of the REE. The A zone contains the most bulk rock Nb of any zone, at 516 ppm Nb (Beland and Williams-Jones, 2021). If all the Nb was contained in aeschynite-(Nd), then the maximum contribution of the mineral to the bulk rock Nd budget would be 258 ppm. In the BD zone, which has the lowest bulk rock Nb content of any zone (214 ppm), the maximum contribution of aeschynite-(Nd) to the bulk rock Nd would be 107 ppm. These potential Nd contributions represent approximately 10% of the bulk rock Nd (Table 3.3). However, there are several other, more common Nb-bearing minerals, and thus the contribution of aeschynite-(Nd) to the bulk rock REE budget is insignificant and its omission from the model did not significantly affect the mass balance calculation.

Xenotime was not included in the normative calculation because it is also a trace mineral and does not readily incorporate Th^{4+} (Boatner, 2002). It is present in such small quantities (< 0.1 vol %) that its effect on both the ThO_2 and P_2O_5 budgets is negligible. It is, however, volumetrically the most significant and most HREE-rich mineral and was therefore included in the REE mass balance calculation.

Petrographic examination of B and A zone samples indicated that calcite is a common secondary mineral (occurring in veins and vugs), although its proportion is highly variable (< 1 - 10 vol % in individual samples). This late (secondary) calcite was not considered in the model for these zones, and all the excess CaO was instead assigned to dolomite. This may have resulted in an overestimation of the content of REE hosted in carbonates, as late calcite is REE-poor (<30 ppm, unpublished data), whereas massive, rock-forming dolomite contains significant REE (up to 359 ppm REE in B zone dolomite, Beland and Williams-Jones, 2021). The sensitivity of the model REE distribution to the ratio of late calcite to early dolomite was tested and is discussed below.

Lastly, estimates of the siderite proportion are the least reliable for two reasons. Firstly, iron oxides produced by alteration and/or weathering are not taken into account by the model, which could have resulted in an overestimate of the siderite proportion, despite the steps taken during the selection of the sample populations to eliminate assays compromised by this effect (see section 3.2.2 above). Siderite proportions are also strongly influenced by the assigned pyrite (+ magnetite, MHREO) proportions. The sensitivity of the REE concentration predicted by the model to the pyrite proportion was tested, as discussed below.

3.3 Results

The model fit for each Ashram zone is summarized in Table 3.6. In all zones, the model is able to match bulk REE compositions to within 20 % for all REE except Sm and Eu. The best fit model mineral assemblages are given in Table 3.7.

3.3.1 MHREO Zone

Based on estimates from optical microscopy, we assigned pyrite a proportion of 5 wt. % and magnetite a proportion of 0.1 wt. % (to reflect its trace content) for the MHREO zone. The MHREO zone does not contain a distinct generation of dolomite, but is hosted within the A zone, thus dolomite from the A zone was chosen for the REE budget calculation to reflect this mixture. Similarly, lacking fluorapatite compositional data for the MHREO zone, secondary fluorapatite (A2) from the A zone was used in the REE budget calculation. The predicted carbonate proportion of the rock is 48 wt. % siderite and 30 wt. % ferroan dolomite. The model predicts a total proportion of LREE minerals of 1.7 wt. % (0.9 wt. % REE fluorocarbonates, 0.8 wt. % monazite). Monazite-Nd is the dominant model LREE phase. To balance the HREE, 0.1 wt. % xenotime-(Y) was required.

3.3.2 A Zone

The pyrite proportion for the A zone was estimated from optical microscopy to be 2 wt. % based on visual estimates. The predicted carbonate proportions are 51 wt. % ferroan dolomite and 18 wt. % siderite. The model predicts the presence of 2.3 wt. % LREE minerals (0.6 wt. % REE fluorocarbonates, 1.7 wt. % monazite). Monazite-(Ce) A1 is the dominant model LREE phase. To balance the HREE, 0.1 wt. % xenotime-(Y) was required.

Table 3.6: Summary of the model fit to the data for each Ashram zone

		MHREO	**A**	**B**	**BD**
% difference (true-calc/true*100)	La	14	3	10	20
	Ce	4	10	5	5
	Pr	-8	8	-6	-1
	Nd	-2	15	5	12
	Sm	8	23	22	20
	Eu	9	19	16	17
	Gd	3	4	8	11
	Tb	0	-2	11	11
	Dy	-7	-1	-1	2
	Y	-21	-4	-11	9
	Ho	0	5	-2	10
	Er	0	2	4	10
	Tm	-9	-10	-4	5
	Yb	-4	8	5	4
	Lu	0	-2	10	5
	Sum of Squared Residuals	1003	1515	1410	1884
absolute difference (true-calc) (ppm)	La	219	96	406	238
	Ce	162	725	376	134
	Pr	-50	59	-46	-4
	Nd	-57	382	134	158
	Sm	29	73	64	41
	Eu	8	15	11	9
	Gd	6	8	10	13
	Tb	0	0	1	2
	Dy	-6	-1	0	1
	Y	-57	-16	-22	22
	Ho	0	1	0	1
	Er	0	1	1	2
	Tm	0	0	0	0
	Yb	-1	1	0	1
	Lu	0	0	0	0

Table 3.7: Best fit model mineral assemblages for each Ashram zone

		MHREO	**A**	**B**	**BD**
Quartz		4	3	4	2
Pyrite		5	2	0.5	0.5
Magnetite		0.1			
Phlogopite		0.6	0.9	0.8	0.9
Ilmenite		2	0.7	0.3	0.2
Chlorite		0.3	0.3	0.0	0.2
Calcite					4
Fluorapatite		1.0	0.0	1	14
Fluorite		3	23	13	0.5
Dolomite	BD				49
Fe-dolomite	BD				25
	B			74	
	A	38	51		
Siderite		45	18	4	3
Bastnäsite-(Ce)	BD				0.6
	B			0.6	
	A		0.6		
	MHREO	0.5			
Monazite-(Ce)	BD				0.1
	B 1			1	
	B 2			0.3	
	A 1		1		
	A 2		0.2		
	A 3		0.2		
	A 4		0.2		
	MHREO	0.1			
Monazite-(Nd)		0.6			
Synchysite-(Ce)		0.4			
Xenotime-(Y)		0.1	0.1	0.0	0.0
total LREE minerals		1.7	2.3	2.4	0.7
total REEflc		0.9	0.6	0.6	0.6
total monazite		0.8	1.7	1.8	0.1
REEflc/total mineralization		0.5	0.3	0.2	0.9

'REEflc' refers to the REE-fluorocarbonates

3.3.3 B Zone

A pyrite proportion of 0.5 wt. % was assigned based on optical microscopic estimates. As there are no data for B zone fluorite, it was assumed to have the composition of the BD zone fluorite. The predicted carbonate proportions are 74 wt. % B zone ferroan dolomite and 4 wt. % siderite. The model predicts a proportion of 2.4 wt.% LREE minerals (0.6 wt. % bastnäsite, 1.8 wt. % monazite), with monazite-(Ce) B1 as the dominant model LREE mineral. Less than 0.1 wt. % xenotime-(Y) was required to balance the HREE.

3.3.4 BD Zone

From petrographic observations, a pyrite proportion of 0.5 wt. % was assigned for the normative calculation, as well as a 2:1 ratio of early BD dolomite to BD ferroan dolomite. For this zone, there was excess CaO (relative to MgO, MnO, F), resulting in a calcite proportion of 4 wt. %. For the purpose of the REE budget calculation, we considered this to be secondary calcite containing no REE (see section 2.3 above). A total of 0.7 wt. % LREE minerals (0.6 wt. % REE fluorocarbonates, 0.1 wt. % monazite) was estimated, with bastnäsite-(Ce) as the dominant model LREE phase. Less than 0.1 wt. % xenotime-(Y) was required to balance the HREE.

3.3.5 Mineral Contributions to Individual REE

The percent contribution of the various minerals to the model budget of each individual REE for the different zones was calculated and is shown in Figure 3.8 (and Appendices 3.1 – 3.4). In all cases, monazite and bastnäsite account for most of the total LREE bulk rock budget. Variable but significant proportions of the bulk rock MREE and HREE in all zones, however, are hosted by the 'gangue' minerals fluorite (hydrothermal), fluorapatite and the carbonates (magmatic-hydrothermal). The proportions of MREE and HREE in gangue minerals are lowest the MHREO and A zones, i.e., between 3 – 9 wt. % and 12 – 38 wt. % (up to 41 wt. % Y), respectively. These proportions are higher in the B zone, in which 7 – 15 wt. % of the MREE and 27 – 61 wt. % of the HREE are hosted in gangue minerals. They are highest, however in the BD zone, where non-REE minerals host 50 – 61 wt. % of the bulk rock MREE and 55 – 62 wt. % of the bulk rock HREE.

Fluorite is a minor but important host of the HREE in all zones except the BD zone, which contains < 1 wt. % fluorite. Excluding Y, fluorite accounts for 0.5 – 1 wt. %, 3 – 19 wt. % and 1 – 7 wt. % of the HREE in the MHREO, A, and B zones, respectively. The upper limits increase considerably if Y is included because fluorite in all the zones is strongly enriched in Y. Owing to the high proportion of fluorite in the A zone (23 wt. %), the addition of Y increases the upper limit of the HREE range in the A zone to 29 wt. %; fluorite also accounts for 0.5 – 2 wt. % of the MREE in this zone.

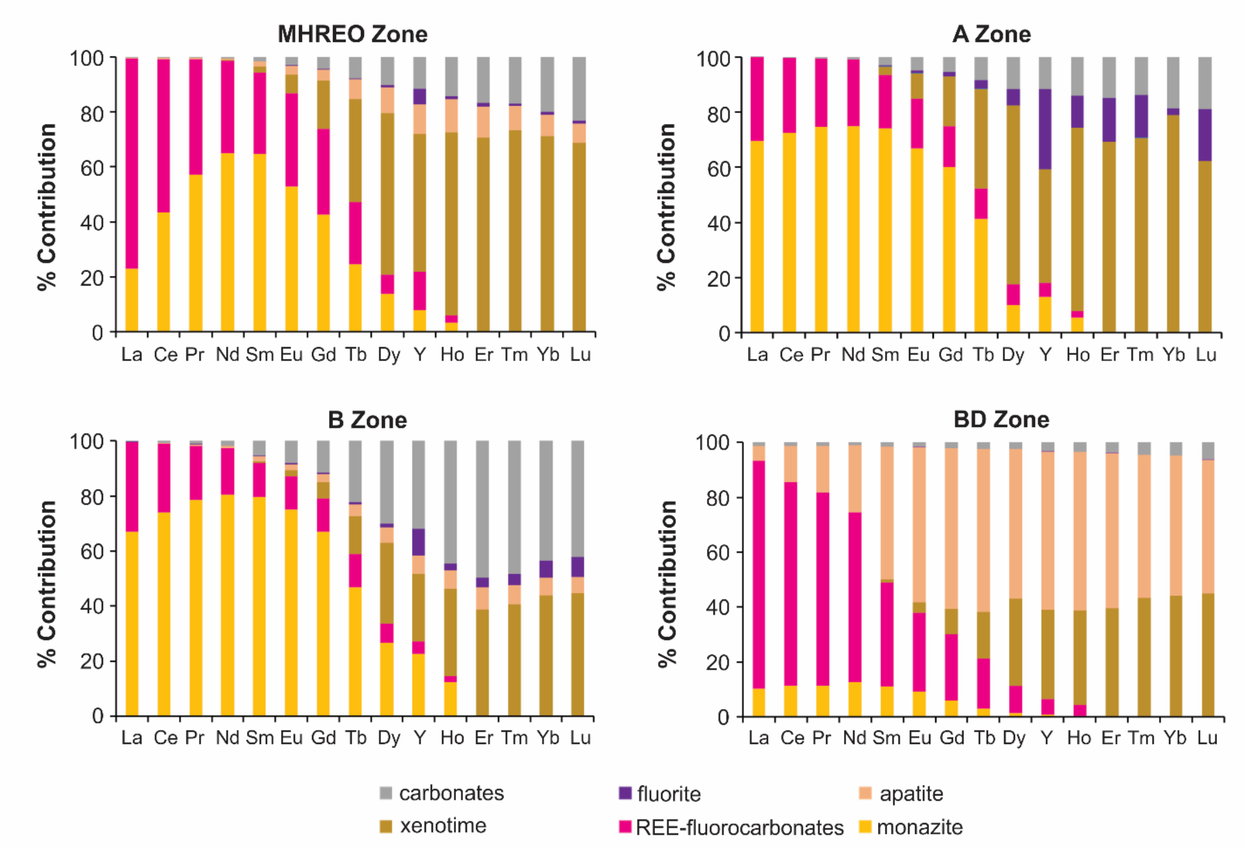

Figure 3.8: Model mineral REE contributions to the bulk REE contents

A series of bar diagrams illustrating the model mineral contributions (% of the calculated total per element) to the individual REE contents for each Ashram zone.

Carbonate minerals also host significant proportions of the MREE and HREE in all zones, particularly the B zone. Siderite is relatively REE-poor (24 ppm REE, Table 3.5) but HREE-enriched (HREE/TREE = 0.79). Thus, owing to its high proportion in the MHREO zone (45 wt. %), it hosts 1 - 6 wt. % of the bulk rock HREE. In both the MHREO and A zones, dolomite contains 2 – 5 wt. % of the MREE and 7 – 18 wt. % of the HREE. In the BD zone, it contains a lower proportion of the MREE and HREE (1 – 2 wt. % and 2 – 6 wt. %, respectively) but notably, 1 wt.

% of all the LREE. Significantly, dolomite is the most important host of the HREE (22 – 49 wt. %) in the B zone, more so than xenotime (14 – 44 wt. %). Dolomite also makes an important contribution to the B zone bulk rock MREE and LREE budgets, at 5 – 11 wt. % and up to 2 wt. %, respectively.

Fluorapatite is host to a considerable proportion of the MREE and HREE in all zones, except the A zone, where its proportion is very low (< 0.1 wt. %). In the MHREO zone, 2 – 4 wt. % and 7 – 12 wt. % of the MREE and HREE, respectively, are contained in fluorapatite. In the B zone, fluorapatite accounts for 2 – 3 wt. % and 4 – 8 wt. % of the MREE and HREE, respectively, and up to 1 wt. % of the LREE. In the BD zone, which has the highest proportion of fluorapatite (14 wt. %), fluorapatite is an important host to all the REE, containing between 5 and 59 wt. % of them. Indeed, it is the most significant host of all the REE heavier than Nd. Furthermore, it hosts a substantial proportion of the bulk rock LREE (5 – 24 wt. %).

3.4 Discussion

3.4.1 Suitability of Model Mineral Assemblages

The proportions of the different minerals predicted by our model for each zone and their contributions to the corresponding REE budgets are consistent with estimates based on visual inspection of the core/thin sections and bulk rock REE concentrations, respectively. In core, the BD zone may locally contain more fluorite than predicted but, overall, the fluorite content is very low, supporting the prediction that this zone contains < 1 wt.% fluorite. Satisfactory fits of the model to the bulk rock REE compositions were obtained while forcing the relative proportions of monazite and REE fluorocarbonates (guided by petrographic observations) during the correction to the bulk composition. In the case of the MHREO, A and B zones, the REE fluorocarbonates were assumed to account for approximately 50, 25 and 25 % of the LREE mineralization, respectively, based on petrographic observations and observations in drill core. To achieve an acceptable fit to the LREE for the BD zone, a monazite proportion equal to 10 % of the total LREE mineralization was required, which is a much higher than the trace proportion of monazite observed in thin section in this zone. This discrepancy is explained by the heterogeneity of the bulk rock samples, and likely reflects the difficulty of removing all samples containing B zone material from the sample population.

3.4.2 Evaluation of Fit and Sources of Error

Although the model predicted the distribution of each REE to within 25 % of the average bulk rock value, there are some sources of error that merit discussion. Firstly, as explained above, some of the assay intervals likely sampled carbonatite from more than one zone. The modeled carbonatite for the MHREO zone, for example, contains 30 wt. % dolomite (Table 3.7) reflecting the discontinuous and irregular shape of the ferrocarbonatite intrusion and the impossibility of obtaining a 'pure' bulk rock sample population. In all cases, a better fit can be achieved, if minor proportions of REE mineral compositions from other zones are included. For example, using a B zone monazite composition for the BD zone REE calculation (instead of BD zone monazite), results in a better fit through the LREE (Fig. 3.9) and a better overall fit to the data, with a sum of squared residuals of 1493 (versus 1884 with BD zone monazite). Similarly, better fits of the model to the data can be achieved using bastnäsite-(La) or –(Nd), as reported by Mitchell and Smith (2017), however, for the sake of simplicity, the REE mineral compositions for each zone used in the calculations were based on the data reported by Beland and Williams-Jones (2021).

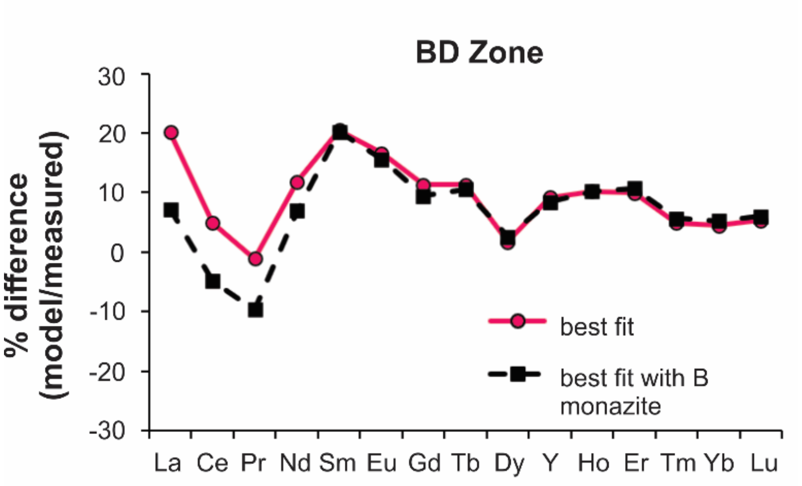

Figure 3.9: BD zone model fit adjustment

The model fit (% difference) for the BD zone (solid pink line). A better fit through the LREE can be achieved by using a B zone monazite composition (dashed line, see section 3.4.2 for detail).

The poorest fits for all the zones were for the middle REE (Sm-Gd) (Table 3.6). This is partly because detection limits for these elements in monazite and bastnäsite, which were analyzed using the electron microprobe, are relatively high, and the middle REE occur in smaller proportions in the LREE-dominant minerals. The large error for the middle REE can be attributed, in part, to the use in the model of lower resolution electron microprobe Sm-Gd data to match higher resolution ICP-MS bulk rock data. In addition, Mitchell and Smith (2017) identified trace bastnäsite-(Nd) in some samples (they did not report compositional data for this mineral). As monazite-(Nd) contains more Sm-Gd than monazite-(Ce) (Table 3.5), bastnäsite-(Nd) should also contain a higher proportion of these elements than bastnäsite-(Ce). It is possible that inclusion in the model of trace amounts of bastnäsite-(Nd) would have improved the fit for the MREE, but in the absence of compositional data for this mineral (we have not observed bastnäsite-(Nd)) this issue cannot be addressed further. The lack of REE data for fluorite in the B and A zones, because it is intergrown with monazite and could not be analyzed reliably, is also problematic. As occurrences of fluorite enriched in the middle REE have been reported for carbonatite-hosted REE deposits such as Mato Preto, Brazil (Santos et al., 1996), and Maoniuping (Huang et al., 2007; Xu et al., 2008; Xu et al., 2012) and Lizhuang (Xu et al., 2012), China, it is possible that fluorite enriched in the middle REE may be present in the B and A zones. This could explain the poor fit of our model to the Sm-Gd bulk rock compositions for these zones.

It is important to evaluate the error in the model in absolute terms, as well as in relative proportions. The absolute differences (in ppm) between the model and bulk-rock REE concentrations are reported in Table 3.6. Significantly, for all the HREE, except Y, the absolute difference is ≤ 6 ppm (compared to relative differences of up to 11 %), and for many of the HREE in the various zones, the absolute difference is less than 1 ppm. These elements are present in low concentrations (Table 3.3) such that an over- (or under-) prediction of the model by 1 ppm can result in a large proportional difference (e.g., for B zone Tb, 1 ppm = 11 %; Table 3.6). In these cases, we consider the fits of the model to the data to be excellent. We also note that the poorest fits to the model (up to 23 % misfit) are for samples for which the bulk rock MREE contents are low (maximum = 384 ppm Sm, MHREO zone, Table 3.3); the absolute difference reaches a maximum of 73 ppm (Table 3.6). Given the heterogeneity of the bulk rock data set (and large associated error), we consider the fit of the model to the data to be good both in terms of proportional and absolute differences.

3.4.3 Model Sensitivity

As discussed above, the estimates of siderite proportions are linked directly to the proportion of pyrite (and magnetite, MHREO zone) assumed in the normative calculation; the estimates for both siderite and (Fe-) dolomite were increased by omitting vug calcite from the normative calculation for the A and B zones. The sensitivity of the model to the assumptions made for pyrite + magnetite, and vug calcite are therefore tested below.

Any inaccuracy in siderite estimation would only have impacted significantly on calculations for the MHREO zone, which contains a high proportion of siderite. We evaluated the sensitivity of the model to pyrite + magnetite assignments for the MHREO zone by arbitrarily changing the assigned value by increments of +/- 5 wt. %. By doing so, the overall fit of the model for any given REE changes by a maximum of 2 % (Table 3.8). Siderite is REE-poor (24 ppm TREE), but HREE-enriched (Table 3.5), thus the model fit is most sensitive to the HREE, though not strongly affected by them. Furthermore, the calculated contribution of carbonate minerals to the overall budget for each REE changed by a maximum of 2 % for Lu (Table 3.9). We are therefore confident that any error in our petrographic estimates of pyrite and magnetite proportions did not result in substantial differences in the model output.

The proportion of calcite in vugs observed petrographically is variable but is less than 10 vol. %. Omitting vug calcite from the normative calculation is expected to have the greatest impact on the B zone model because its carbonates contain the most REE (up to 360 ppm, Table 3.5) and vug calcite is considered REE-barren (unpublished data, Beland and Williams-Jones, 2021). Incorporating vug calcite results in lower and higher estimates of dolomite and siderite proportions, respectively. We assigned a vug calcite proportion of up to 10 wt. % to the B zone to test the sensitivity of the model to this factor. This had a considerable impact on the overall fit of the model, with differences of up to 12 % for individual REE (Table 3.8), and a decrease in the calculated contribution of carbonate minerals to the overall budget of each REE by a maximum of 7 % (Table 3.9). Nonetheless, vug calcite rarely accounts for 10% of the rock, and in many cases is absent, such that we consider the omission reasonable.

Table 3.8: Sensitivity of the model fit to varying mineral proportions

		Proportion of Pyrite + Magnetite					**Proportion of Calcite**		
		20	15	10	**5**	0	**0**	5	10
% difference (true-calc/true*100)	La	14	14	14	**14**	14	**10**	10	10
	Ce	4	4	4	**4**	4	**5**	5	5
	Pr	-8	-8	-8	**-8**	-8	**-6**	-6	-6
	Nd	-2	-2	-2	**-2**	-2	**5**	6	6
	Sm	8	8	8	**8**	8	**22**	23	23
	Eu	9	9	9	**9**	9	**16**	17	18
	Gd	3	3	3	**3**	3	**8**	9	10
	Tb	0	0	0	**0**	0	**11**	13	15
	Dy	-7	-7	-7	**-7**	-7	**-1**	3	6
	Y	-20	-20	-20	**-21**	-21	**-11**	-7	-3
	Ho	0	0	0	**0**	0	**-2**	4	9
	Er	1	1	1	**0**	0	**4**	9	15
	Tm	-7	-8	-8	**-9**	-9	**-4**	1	7
	Yb	-2	-3	-4	**-4**	-5	**5**	9	14
	Lu	2	1	0	**0**	-1	**10**	14	18
	Sum of Squared Residuals	944	961	981	**1003**	1026	**1410**	1702	2330

Bolded columns denote the mineral proportions used in the final model fits

Table 3.9: Carbonate mineral contribution sensitivity

Variations in carbonate mineral contributions to the individual REE budgets as a result of changing mineral proportions

	Proportion of Pyrite + Magnetite					**Proportion of Calcite**		
	20	15	10	**5**	0	**0**	5	10
La	0.3	0.3	0.3	**0.3**	0.3	**0.3**	0.3	0.2
Ce	0.4	0.4	0.4	**0.4**	0.4	**0.6**	0.6	0.5
Pr	0.4	0.4	0.4	**0.4**	0.4	**1**	1	0.8
Nd	0.5	0.5	0.5	**0.5**	0.5	**2**	2	1
Sm	1	1	1	**1**	1	**5**	5	4
Eu	3	3	3	**3**	3	**8**	7	6
Gd	4	4	4	**4**	4	**11**	10	9
Tb	7	7	7	**7**	7	**22**	20	18
Dy	9	9	9	**9**	9	**30**	27	25
Y	10	10	11	**11**	11	**32**	29	27
Ho	13	13	13	**13**	13	**45**	42	38
Er	15	15	15	**16**	16	**50**	47	43
Tm	15	15	15	**16**	16	**48**	45	42
Yb	18	18	18	**19**	19	**43**	41	37
Lu	20	21	21	**22**	22	**42**	39	36

Bolded columns denote the mineral proportions used in the final model fits

3.4.4 Implications

The model described earlier demonstrates quantitatively the importance of hydrothermal remobilization in the formation of a potentially economic carbonatite-hosted REE deposit. This model shows that without a hydrothermal system, the Ashram REE deposit would not exist. In all the zones, the LREE are hosted dominantly in REE-minerals that are hydrothermal in origin. Indeed, 97 % or more of the LREE in the B, A and MHREO zones are hosted in the hydrothermal minerals monazite and bastnäsite (Table 3.10, Fig. 3.10A); the proportion of LREE in REE minerals (mainly bastnäsite-(Ce)) in the BD zone is ≥ 75 %. The proportion of a given REE hosted by REE minerals, however, decreases with increasing atomic number (Table 3.10, Fig. 3.10A) within each zone, reaching a plateau through the HREE. For example, more La is hosted in REE minerals than Ce, and in turn, more Ce is hosted in monazite and bastnäsite than Nd, and so on.

Table 3.10: Percentage of REE hosted by REE-minerals for each Ashram zone

	MHREO	**A**	**B**	**BD**
La	99	100	99	93
Ce	99	100	99	86
Pr	99	99	98	82
Nd	99	99	97	75
Sm	96	97	93	50
Eu	94	94	89	42
Gd	91	93	85	39
Tb	85	88	73	38
Dy	80	82	63	43
Y	76	59	52	39
Ho	73	74	46	39
Er	71	69	39	39
Tm	74	71	41	43
Yb	72	79	44	44
Lu	69	62	45	45

Qualitatively, there is also a strong positive correlation between the proportion of a given REE hosted in REE minerals and the fluid to rock ratio of the zone (Fig. 3.10B). According to the genetic model for the Ashram deposit advanced by Beland and Williams-Jones (2021), the polymictic breccia was the conduit for the mineralizing fluid, and is most proximal to the MHREO zone, and most distal to the BD zone. For most of the REE, the proportion hosted in REE minerals

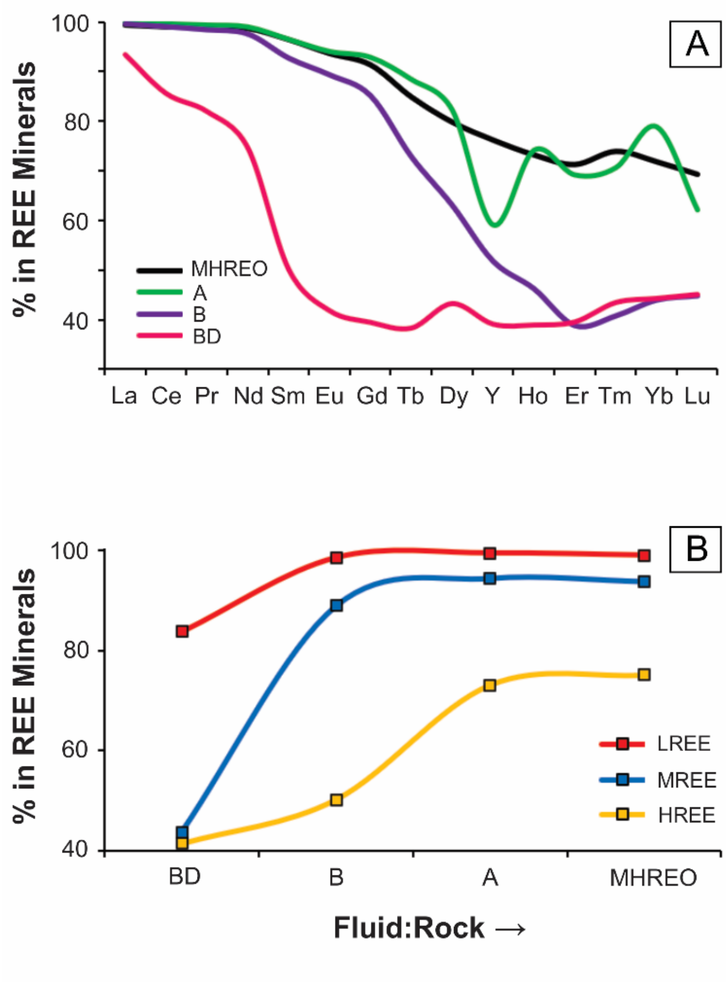

Figure 3.10: Proportion of REE hosted by REE minerals

A) The percentage of a each REE (% of model total per element) hosted by REE minerals for each Ashram zone. B) The percentage of the REE grouped by atomic weight (LREE, MREE, HREE) hosted in REE minerals for each zone. Also shown is the relative fluid:rock ratio of the different Ashram zones (see text for detail).

is highest in the MHREO zone, which would have experienced the highest fluid to rock ratio, and decreases steadily through the A and B zones to the BD zone, for which the fluid to rock ratio was lowest. For example, the proportion of Nd hosted by monazite and bastnäsite in the MHREO, A, B and BD zones, is 99, 99, 97, and 75 %, respectively (Table 3.10). The exceptions to this order are for La and Ce, 100% of which are hosted in REE minerals in the A zone, compared to 99% in the MHREO zone. Given the heterogeneity of the bulk rock compositions, this is negligible in the context of the overall distribution of the REE by zone.

Magmatic phases account for a small proportion of the overall REE budget, although significant proportions of the HREE are hosted in carbonate minerals and fluorapatite, and account for up to 50 and 60 wt. %, respectively, of the total HREE content of the zones. These proportions increase with decreasing fluid to rock ratio, such that a smaller proportion of the HREE are hosted in fluorapatite and carbonate minerals in the MHREO zone than in the BD zone. In contrast, in the BD zone, though the bulk of the LREE are contained in bastnäsite, up to 24 wt. % are hosted by fluorapatite (Fig. 3.8, Appendix 3.4). It is important to note that this fluorapatite was hydrothermally altered from a primary magmatic precursor (Beland and Williams-Jones, 2021) and, thus, its REE content and their distribution have been affected by hydrothermal processes. Consequently, the only minerals in the minerals observed at Ashram that may be considered truly magmatic are the carbonates (dolomite, siderite), and even dolomite and siderite were not entirely unaffected by fluid, as indicated by their stable C-O isotopic compositions (Beland and Williams-Jones, 2021).

Our model quantitatively illustrates that all the REE at Ashram have been mobilized by hydrothermal fluid and the degree to which they were concentrated in hydrothermal minerals was a function of their atomic number and, qualitatively, the fluid to rock ratio. Hydrothermal activity was particularly effective in concentrating the metals in REE-minerals to potentially economic levels. The trends shown in Figure 3.10 are the manifestation of two important thermodynamic drivers, namely the stability of REE complexes in aqueous fluid and the stability of the REE minerals.

It has been well-documented from experimental studies that the REE can be transported by aqueous solutions (e.g., Gammons et al., 2002; Migdisov and Williams-Jones, 2008; Migdisov et al. 2009). The bulk of REE transport in hydrothermal fluids is thought to be achieved through complexation with chloride and sulfate, whereas carbonate, fluoride and phosphate are considered depositional ligands (Migdisov et al., 2016 and references therein). In fluorine-bearing systems, transport of the REE is mainly achieved through chloride complexes but is largely limited to acidic conditions because at higher (intermediate pH), $REEF_3$ will precipitate, effectively removing all the REE from solution (Migdisov and Williams-Jones, 2014). There is, however, some evidence that the REE may be transported by hydroxy-fluoride complexes at extremely high pH (see Vasyukova and Williams-Jones, 2018). The stability of REE-Cl complexes in aqueous fluids decreases with increasing atomic number, and the difference increases with increasing temperature, so that at ≥ 250°C, La-Cl complexes are 1.5 orders of magnitude more stable than those with Lu (Migdisov et al., 2009). In marked contrast, the stability of REE-sulfate complexes appears to be independent of atomic number at all temperatures investigated (Migdisov et al., 2016). Current understanding of the character of carbonatite-derived hydrothermal fluids is limited to studies of a few complexes, namely Amba Dongar, India (Palmer and Williams-Jones, 1996; Williams-Jones and Palmer, 2002), Bayan Obo (Smith and Henderson, 2000; Smith et al., 2000) and Maoniuping, China (Xu et al., 2004; Xie et al., 2009), Kalkfeld (Bühn and Rankin, 1999) and Okurusu (Bühn et al., 2002), Namibia, and Chilwa Island, Malawi (Dowman et al., 2017). These studies have concluded that carbonatitic fluids are typically mixed H_2O-CO_2-NaCl fluids, and in all cases, that chloride was the dominant anion, except at Maoniuping, where sulfate was dominant (Xie et al., 2009). Thus, results of our model indicating that within each of the zones at Ashram, La is much more strongly concentrated in REE minerals than is Lu, can be directly tied to the thermodynamic stability of the different REE-Cl complexes. At Ashram, there was progressive concentration of the REE with decreasing atomic number because the mobility of REE in chloride-dominated aqueous systems increases progressively with decreasing atomic number. Furthermore, the predicted trend of an increase in the concentration of the REE in REE minerals with increasing fluid:rock ratio (Fig. 3.10B) is consistent with the variations in REE-Cl complex stability, such that increased fluid flow leads to increased concentration of the most mobile elements.

The stability of the minerals also plays an important role in creating a LREE-rich deposit and can be evaluated by considering the following precipitation reactions:

$Ce^{3+} + PO_4^{3-} \leftrightarrow CePO_4$ (monazite) log K = 33.21 (1)

$Eu^{3+} + PO_4^{3-} \leftrightarrow EuPO_4$ log K = 32.73 (2)

$Yb^{3+} + PO_4^{3-} \leftrightarrow YbPO_4$ (xenotime) log K = 32.99 (3)

The equilibrium constants, K, for these reactions were calculated for 250°C and P_{sat} (Shock and Helgeson, 1988; Shock et al., 1997; Popa and Konings, 2006; Gysi et al., 2015) and indicate that precipitation of monazite (Reaction 1) is favoured slightly over that of xenotime (Reaction 3), and that precipitation of both is favoured over precipitation of MREE phosphate (Reaction 2). Therefore, the preferential deposition of LREE-phosphates is due in part to their being more insoluble than MREE- or HREE-phosphates. As shown above, however, it is unlikely that the REE would have been transported in equal proportions in a chloride-dominated system. Using values of the first formation constants of REE-Cl complexes at 250°C obtained experimentally by Migdisov et al., (2009) as an estimate of the relative concentrations of the REE in a chloride-rich fluid and Reactions 1 to 3, we estimated the amount of phosphate that is expected to precipitate by assigning a $\log Ce^{3+}$ concentration of 3.8, a $\log Eu^{3+}$ concentration of 3.1, a $\log Yb^{3+}$ concentration of 2.5 and a constant $\log PO_4^{3-}$ concentration of 1. The resultant $\log CePO_4$, $\log EuPO_4$ and $\log YbPO_4$ values are 37.01, 35.83 and 35.49, respectively, demonstrating that the amount of monazite predicted to precipitate exceeds that of xenotime by 1.5 orders of magnitude, and that the amount of REE-phosphate likely to precipitate decreases with increasing atomic number of the REE.

The magmatic enrichment of the carbonatites in LREE relative to the HREE would certainly have had an influence on the occurrence of LREE mineralization in these rocks. Our model, however, demonstrates that hydrothermal processes took these magmatic REE and redistributed them so as to form a potentially economic deposit. There would be no Ashram REE deposit without a hydrothermal system and the LREE enrichment is the result of the combined effects of the greater mobility of the LREE (stability of LREE-Cl complexes) and the greater insolubility of monazite (stability of the LREE mineral phase).

3.5 Conclusions

Our mass balance calculation traced each REE individually across all minerals from primary magmatic to secondary hydrothermal stages in all zones of the Ashram deposit. The calculation showed quantitatively that at Ashram, all the REE were mobilized by hydrothermal fluids to be concentrated in REE minerals. The degree to which the individual elements were concentrated in REE minerals, however, decreased with increasing atomic number, and with decreasing fluid flow (fluid:rock ratio), such that, in all zones, La is more strongly concentrated than Lu, and across zones, La is most strongly concentrated in areas of greatest fluid flow. These trends are the result of the relative thermodynamic stability of the various REE-complexes and REE minerals in aqueous fluids. Overall, magmatic and non-REE phases host a low proportion of the whole-rock REE budget, especially the LREE.

Acknowledgements

The research presented in this manuscript was supported financially by a MITACS grant to Diversification de l'exploration minerale au Quebec (DIVEX) and a NSERC Discovery Grant to AEW-J. Commerce Resources Corp. provided access to the assay data.

References

Beland, C.M.J. and Williams-Jones, A.E., 2021, The genesis of the Ashram REE deposit, Quebec: Insights from bulk-rock geochemistry, apatite-monazite-bastnäsite replacement reactions and mineral chemistry: Chemical Geology, in review

Belousova, E., Griffin, W., O'Reilly, S.Y., and Fisher, N., 2002, Apatite as an indicator mineral for mineral exploration: trace-element compositions and their relationship to host rock type: Journal of Geochemical Exploration, v. 76, p. 45-69.

Boatner, L.A., 2002, Synthesis, structure and properties of monazite, pretulite and xenotime: Reviews in Mineralogy and Geochemistry, v. 48, p. 87-121.

Brooker, R.A. and Kjarsgaard, B.A., 2011, Silicate-Carbonate Liquid Immiscibility and Phase Relations in the System SiO2-Na2O-Al2O3-CaO-CO2 at 0.1-2.5 GPa with Applications to Carbonatite Genesis: Journal of Petrology, v. 52, p. 1281-1305.

Broom-Fendley, S., Styles, M.T., Appleton, J.D., Gunn, G., and Wall, F., 2016, Evidence for dissolution-reprecipitation of apatite and preferential LREE-mobility in carbonatite-derived late-stage hydrothermal processes: American Mineralogist, v. 101, p. 596-611.

Broom-Fendley, S., Brady, A.E., Wall, F., Gunn, G., and Dawes, W., 2017, REE minerals at the Songwe Hill carbonatite, Malawi: HREE-enrichment in late-stage apatite: Ore Geology Reviews, v. 81, p. 23-41.

Bühn, B., Rankin, A.H., Schneider, J., and Dulski, P., 2002, The nature of orthomagmatic, carbontitic fluids precipitating REE, Sr-rich fluorite: fluid inclusion evidence from the Okorusu fluorite deposit, Namibia: Chemical Geology, v. 186, p. 75-98.

Bühn, B., Schneider, J., Dulski, P., and Rankin, A., 2003, Fluid-rock interaction during progressive migration of carbonatitic fluids, derived from small-scale trace element and Sr, Pb isotope distribution in hydrothermal fluorite: Geochimica et Cosmochimica Acta, v. 67, p. 4577-4595.

Bühn, B., and Rankin, A.H., 1999, Composition of natural, volatile-rich Na-Ca-REE-Sr carbonatitic fluids trapped in fluid inclusions: Geochimica et Cosmochimica Acta, v. 63, p. 3781-3797.

Castor, S.B., 2008, The Mountain Pass Rare-Earth Carbonatite and Associated Ultrapotassic Rocks, California: The Canadian Mineralogist, v. 46, p. 779-806.

Chakhmouradian, A.R., Reguir, E.P., Coueslan, C., and Yang, P., 2016, Calcite and dolomite in intrusive carbonatites. II., Trace-element variations: Mineralogy and Petrology, v. 110, p. 361-377.

Chakhmouradian, A.R., Reguir, E.P., Zaitsev, A.N., Coueslan, C., Xu, C., Kynicky, J., Mumin, A.H. and Yang, P., 2017, Apatite in carbonatitic rocks: Compositional variation, zoning, element partitioning and petrogenetic significance: Lithos, v. 274, p. 188-213.

Cheng, Z., Zhang, Z., Aibai, A., Kong, W., and Holtz, F., 2018, The role of magmatic and post-magmatic hydrothermal processes on rare-earth element mineralization: A study of the Bachu carbonatites from the Tarim Large Igneous Province, NW China: Lithos, v. 314-315, p. 71-87.

Clark, T., and Wares, R., 2006, Lithotectonic and Metallogenic Synthesis of the New Quebec Orogen (Labrador Trough). MM 2005-01.

Costanzo, A., Moore, K.R., Wall, F. and Freely, M., 2006, Fluid inclusions in apatite from Jacupiranga calcite carbonatites: Evidence for a fluid-stratified carbonatite magma chamber: Lithos, v. 91, p. 208-228.

Doroshkevich, A.G., Viladkar, S.G., Ripp, G.S., and Burtseva, M.V., 2009, Hydrothermal REE mineralization in the Amba Dongar Carbonatite Complex, Gujarat, India: The Canadian Mineralogist, v. 47, p. 1105-1116.

Doroshkevich, A.G., Veksler, I.V., Klemd, R., Khromova, E.A. and Izbrodin, I.A., 2017, Trace-element composition of minerals and rocks in the Belaya Zima carbonatite complex (Russia): Implications for the mechanisms of magma evolution and carbonatite formation: Lithos, v. 284-285, p. 91-108.

Dowman, E., Wall, F., Treloar, P.J., and Rankin, A.H., 2017, Rare-earth mobility as a result of multiple phases of fluid activity in fenite around the Chilwa Island Carbonatite, Malawi: Mineralogical Magazine, v. 81, p. 1367-1395.

Gagnon, G., Rousseau, G., Camus, Y., and Gagne, J., 2012, Ashram Rare Earth Deposit. Preliminary Economic Assessment. NI 43-101 Technical Report, Prepared by SGS Geostat Canada for Commerce Resources, 202 pp.

Gammons, C.H., Wood, S.A., and Li, Y., 2002, Complexation of the rare earth elements with aqueous chloride at 200°C and 300°C and saturated water vapor pressure: Geochemical Society Special Publication, v. 7, p. 191-207.

Ghosh, S., Ohtani, E., Litasov, K.D., and Terasaki, H., 2009, Solidus of carbonated peridotite from 10-20 GPa and origin of magnesiocarbonatite melt in the Earth’s deep mantle: Chemical Geology, v. 262, p. 17-28.

Giebel, R.J., Gauert, C.D.K., Marks, M.A.W., Costin, G., and Markl, G., 2017, Multi-stage formation of REE minerals in the Palabora Carbonatite Complex, South Africa: American Mineralogist, v. 102, p. 1218-1233.

Gysi, A.P., Williams-Jones, A.E., and Harlov, D.E., 2015, The solubility of xenotime-(Y) and other HREE phosphates (DyPO4, ErPO4 and YbPO4) in aqueous solutions from 100 to 250 degrees C and p(sat): Chemical Geology, v. 401, p. 83-95.

Hogarth, D.D., 1989, Pyrochlore, apatite and amphibole: distinctive minerals in carbonatite, in Bell, K., ed., Carbonatites, genesis and evolution: London, UK, Unwin Hyman Ltd., p. 301-359.

Huang, Z.L., Xu, C., McCaig, A., Liu, C.Q., Wu, J., Xu, D.R., Li, W.B., Guan, T., Xiao, H.Y., 2007, REE geochemistry of fluorite from the Maoniuping REE deposit, Sichuan Province, China: implications for the source of ore-forming fluids. *Acta Geologica Sinica* **81:** 622-636.

Machado, N., Clark, T., David, J., Goulet, N., 1997, U-Pb ages for magmatism and deformation in the New Quebec Orogen. *Canadian Journal of Earth Science* **34:** 716-723.

Mao, M., Simandl, G.J., Spence, J., Marshall, D. (2015). Fluorite trace-element chemistry and its potential as an indicator mineral: Evaluation of the LA-ICP-MS method. In: Simandl, G.J. and Neetz, M., (Eds.), Symposium on Strategic and Critical Materials Proceedings, November 13-14, 2015, Victoria, British Columbia. British Columbia Ministry of Energy and Mines, British Columbia Geological Survey Paper 105-3, pp. 251-264.

Mariano, A.N., 1989, Nature of economic mineralization in carbonatites and related rocks, in Bell, K., ed., Carbonatites: Genesis and Evolution, Winchester, Massachusetts, Unwin Hyman Inc., p. 149-176.

Martin, L.H.J., Schmidt, M.W., Mattsson, H.B. and Guenther, D., 2013, Element partitioning between immiscible carbonatite and silicate melts for dry and H2O-bearing systems at 1-3 GPa: Journal of Petrology, v. 54, p. 2301-2338.

McDonough, W.F., and Sun, S.S., 1995, The composition of the Earth: Chemical Geology, v. 120, p. 223-253.

Migdisov, A.A., and Williams-Jones, A.E., 2008, A spectrophotometric study of Nd (III), Sm (III) and Er (III) complexation in sulfate-bearing solutions at elevated temperatures: Geochimica Cosmochimica Acta, v. 72, p. 5291-5303.

Migdisov, A.A., Williams-Jones, A.E., and Wagner, T., 2009, An experimental study of the solubility and speciation of the Rare Earth Elements (III) in fluoride- and chloride-bearing aqueous solutions at temperatures up to 300°C: Geochimica et Cosmochimica Acta, v. 73, p. 7087-7109.

Migdisov, A.A. and Williams-Jones, A.E., 2014, Hydrothermal transport and deposition of the rare earth elements by fluorine-bearing aqueous liquids: Mineralium Deposita, v. 49, p. 987-997.

Migdisov, A.A., Williams-Jones, A.E., Brugger, J., and Caporuscio, F.A., 2016, Hydrothermal transport, deposition and fractionation of the REE: Experimental data and thermodynamic calculations: Chemical Geology, v. 439, p. 13-42.

Mitchell, R.H., and Smith, D.L., 2017, Geology and mineralogy of the Ashram Zone carbonatite, Eldor Complex, Quebec: Ore Geology Reviews, v. 86, p. 784-806.

Moore, M., Chakhmouradian, A.R., Mariano, A.N., and Sidhu, R., 2015, Evolution of rare-earth mineralization in the Bear Lodge carbonatite, Wyoming: Mineralogical and isotopic evidence: Ore Geology Reviews, v. 64, p. 499-521.

Nadeau, O., Cayer, A., Pelletier, M., Stevenson, R., and Jébrak, M., 2015, The Paleoproterozoic Montviel carbonatite-hosted REE-Nb deposit, Abitibi, Canada: Geology, mineralogy, geochemistry and genesis: Ore Geology Reviews, v. 67, p. 314-335.

Ngwenya, B., 1994, Hydrothermal rare earth mineralisation in carbonatites of the Tundulu complex, Malawi: processes at the fluid/rock interface: Geochimica et Cosmochimica Acta, v. 58, p. 2061-2072.

Olson, J.C., Shawe, D.R., Pray, L.C., and Sharp, W.N., 1954, Rare-earth mineral deposit of the Mountain Pass district, San Bernardino County, California, U.S. Geological Survey Professional Paper 261, p. 1-75.

Ozturk, H., Altuncu, S., Hanilci, N., Kasapci, C., and Goodenough, K.M., 2019, Rare earth element-bearing fluorite deposits of Turkey: An overview: Ore Geology Reviews, v. 105, p. 423- 444.

Palmer, D., and Williams-Jones, A.E., 1996, Genesis of the carbonatite-hosted fluorite deposit at Amba Dongar, India: evidence from fluid inclusions, stable isotopes, and whole-rock mineral geochemistry: Economic Geology, v. 91, p. 934-950.

Piché, M., and Jébrak, M., 2004, Normative minerals alteration indices developed for mineral exploration: Journal of Geochemical Exploration, v. 82, p. 59-77.

Pell, J., 1996, Mineral deposits associated with carbonatites and related alkaline igneous rocks, in Mitchell, R.R., ed., Undersaturated Alkaline Rocks: Mineralogy, Petrogenesis, and Economic Potential, Mineralogical Association of Canada, Short Course Series, Winnipeg, p. 271-310.

Popa, K., and Konings, R.J.M., 2006, High-temperature heat capacities of EuPO4 and SmPO4 synthetic monazites: Thermochimica Acta, v. 445, p. 49-52.

Reguir, E.P., Chakhmouradian, A.R., Pisiak, L., Halden, N.M., Yang, P., Xu, C., Kynicky, J. and Coueslan, C.G., 2012, Trace-element composition and zoning in clinopyroxene- and amphibole-group minerals: Implications for element partitioning and evolution of carbonatites: Lithos, v. 128-131, p. 27-45.

Ruberti, E., Enrich, G.E.R., and Gomes, C.B., 2008, Hydrothermal REE fluorocarbonate mineralization at Barra Do Itapirapua, a multiple stockwork carbonatite, Southern Brazil: The Canadian Mineralogist, v. 46, p. 901-914.

Santos, R.V., Dardenne, M.A., and De Oliveira, C.G., 1996, Rare earth elements geochemistry of fluorite from the Mato Preto Carbonatite Complex, Southern Brazil: Revista Brasileira de Geociencias v. 26, p. 81-86.

Shock, E.L., and Helgeson, H.C., 1988, Calculation of the thermodynamic and transport properties of aqueous species at high pressures and temperatures: Correlation algorithms for ionic species and equation of state preditions to 5 kb and 1000°C: Geochimica et Cosmochimica Acta, v. 52, p. 2009-2036.

Shock, E.L., Sassani, D.C., Willis, M., and Sverjensky, D.A., 1997, Inorganic species in geologic fluids: Correlations among standard molal thermodynamic properties of aqueous ions and hydroxide complexes: Geochimica et Cosmochimica Acta, v. 61, p. 907-950.

Smith, M.P., and Henderson, P., 2000, Preliminary fluid inclusion constraints on fluid evolution in the Bayan Obo Fe-REE-Nb deposit, Inner Mongolia, China: Economic Geology, v. 95, p. 1371-1388.

Smith, M.P., Henderson, P., and Campbell, I.S., 2000, Fractionation of the REE during hydrothermal processes: Constraints from the Bayan Obo Fe-REE-Nb deposit, Inner Mongolia, China: Geochimica et Cosmochimica Acta, v. 64, p. 3141-3160.

Smith, M., Kynicky, J., Cheng, X., Song, W., Spratt, J., Jeffries, T., Brtnicky, M., Kopriva, A., and Cangelosi, D., 2018, The origin of secondary heavy rare earth element enrichment in carbonatites: Constraints from the evolution of the Huanglongpu district, China: Lithos, v. 308-309, p. 65-82.

Trofanenko, J., Williams-Jones, A.E., Simandl, G.J., Migdisov, A.A., 2016, The nature and origin of the REE mineralization in the Wicheeda carbonatite, British Columbia, Canada: Economic Geology, v. 111, p. 199-223.

Veksler, I.V. and Lentz, D.R., 2006, Parental magmas of plutonic carbonatites, carbonate-silicate immiscibility and decarbonation reactions: evidence from melt and fluid inclusions. In: Webster, J. (Ed) Melt inclusions in Plutonic Rocks. Mineralogical Association of Canada, Short Course volume 36, p. 123-150.

Wall, F. and Mariano, A., 1996, Rare earth minerals in carbonatites: a discussion centered on the Kangankunde Carbonatite, Malawi. In: Jones, A., Wall F., Williams, C.T. (Eds.), Rare Earth Minerals: Chemistry Origin and Ore Deposits. Chapman and Hall, London, p. 193-226.

Williams-Jones, A.E., and Palmer, D., 2002, The evolution of aqueous-carbonic fluids in the Amba Dongar carbonatite, India: implications for fenitisation: Chemical Geology, v. 185, p. 283-301.

Woolley, A.R., and Kjarsgaard, B.A., 2008, Paragenetic types of carbonatites as indicated by the diversty and relative abundances of associated silicate rocks: Evidence from a global database: Canadian Mineralogist, v. 46, p. 741-752.

Wyllie, P.J., and Tuttle, O.F., 1960, The system CaO-CO_2-H_2O and the origin of carbonatites: Journal of Petrology, v. 1, p. 1-46.

Xie, Y., Hou, Z., Yin, S., Dominy, S.C., Xu, J., Tian, S., and Xu, W., 2009, Continuous carbonatitic melt-fluid evolution of a REE mineralization system: evidence from inclusions in the Maoniuping REE deposit, western Sichuan, China: Ore Geology Reviews, v. 36, p. 90-105.

Xie, Y., Li, Y., Hou, Z., Cooke, D.R., Danyushevsky, L., Dominy, S.C., and Yin, S., 2015, A model for carbonatite hosted REE mineralisation – the Mianning-Dechang REE belt, Western Sichuan Province, China: Ore Geology Reviews, v. 70, p. 595-612.

Xu, C., Huang, Z.L., Liu, C.Q., Yuan, Z.F., Li, W.B., and Guan, T., 2004, Pb isotopic geochemistry of carbonatites in Maoniuping REE deposit, Sichuan Province, China: Acta Petrologica Sinica, v. 20, p. 495-500 (in Chinese with English abstract).

Xu, C., Campbell, I.H., Allen, C.M., Huang, Z., Qi, L., Zhang, H., and Zhang, G., 2007, Flat rare earth element patterns as an indicator of cumulate processes in the Lesser Qinling carbonatites, China: Lithos, v. 95, p. 267-278.

Xu, C., Campbell, I.H., Kynicky, J., Allen, C.M., Chen, Y.J., Huang, Z.L., Qi, L., 2008, Comparison of the Daluxiang and Maoniuping carbonatitic REE deposits with Bayan Obo REE deposit, China: Lithos v. 106, p. 12-24.

Xu, C., Taylor, R.N., Li, W., Kynicky, J., Chakhmouradian, A.R., Song, W., 2012, Comparison of fluorite geochemistry from REE deposits in the Panxi region and Bayan Obo, China: Journal of Asian Earth Sciences v. 57, p. 76-89.

Zhang, D., Liu, Y., Pan, J., Dai, T., and Bayless, R.C., 2019, Mineralogical and geochemical characteristics of the Miaoya REE prospect, Qinling orogenic Belt, China: Insights from Sr-Nd-C-O isotopes and LA-ICP-MS mineral chemistry: Ore Geology Reviews, v. 110, 102932.

Zhou, B., Li, Z., Chen, C., 2017, Global potential of rare earth resources and rare earth demand from clean technologies: Minerals, v. 7, p. 203-217.

Chapter 4 - The genesis of a potential scandium ore deposit at Crater Lake, Canada

Preface

Whereas Chapters 2 and 3 are devoted to a geological setting in which the lanthanides and Y were concentrated to potentially economic levels, this chapter focusses on the smallest of the REE, Sc, which in contrast to the incompatible behavior of the other REE in igneous systems, is a compatible element. In this chapter, we use mineral compositional data and mass balance calculations to identify the hosts of scandium in ferrosyenite at the Crater Lake deposit, hedenbergite and subordinate hastingsite, and evaluate the controls on Sc incorporation. Textural observations of these and the other minerals indicate a magmatic origin, and therefore, the concentration of scandium by magmatic processses. The observed mineral paragenesis, mineral compositional data collected for the study, and published Sc mineral-melt partition coefficients are used to model the processes responsible for the scandium enrichment. Chapter 4 characterizes the distribution of scandium in ferrosyenite at Crater Lake, the first known Sc deposit in Canada and the first known syenite-hosted Sc deposit anywhere.

Abstract

Because of a number of technological advances in the aerospace and automotive sectors and concerns about supply, scandium is now a critical metal for many countries and the target of significant exploration activity. The current study is based on the Crater Lake scandium deposit, which, to our knowledge, is the only syenite-hosted deposit with demonstrable production potential and in which scandium is the principal ore metal. Hedenbergite is the main scandium mineral at Crater Lake, but subordinate proportions of scandium are also hosted by hastingsite. These minerals are concentrated in cumulate layers of ferrosyenite. We have constructed a fractional crystallization model based on the observed mineral paragenesis and mineral compositional data collected for the study. The results of this modelling indicate that the ferrosyenite formed as a result of fractionation of fluorapatite, zircon, fayalite, hedenbergite, magnetite, and hastingsite, from a parental quartz monzonite liquid. The initial liquid was very strongly enriched in Fe (FeO/FeO+MgO = 0.95), which led to extremely high Sc clinopyroxene/melt partition coefficients and consequently, very Sc-rich clinopyroxene (up to 1400 ppm Sc). Subsequently, the hedenbergite (and the other mafic minerals) were physically segregated by gravitational settling and/or flow differentiation, into cumulate ferrosyenite, creating a potentially large scandium resource.

4.1 Introduction

Recent advances in materials science have resulted in a sharp increase in the demand for scandium for aluminum alloys, because of the low density, high tensile strength, corrosion resistance and weldability of scandium-aluminum alloys (e.g., Willey, 1971; Filatov Yu et al., 2000; Chhangani et al., 2020). These physical properties of Sc-Al alloys make them highly sought after in the aerospace, automotive, and shipbuilding industries. A second important application of scandium is as a stabilizing agent to replace yttrium in the electrolyte of solid oxide fuel cells, because of the resulting reduction in the operating temperature and consequent increase in cell life (Vasylyev et al., 2018). The increased demand for scandium has made discovery of new resources of this metal a priority for the critical metals sector of the mining industry.

As a result of the historically low demand for scandium, there are few mineral deposits from which it has been produced and, other than the study of Williams-Jones and Vasyukova

(2018), there has been little attempt to understand the behavior of scandium in nature and the reasons for its concentration in these deposits. Scandium is concentrated by a variety of processes involving magmas, hydrothermal fluids, and surface waters. Indeed, the three deposits in the world that currently produce scandium, Kovdor and Tomtor (Russia) and Bayan Obo (China) are either magmatic or formed from fluids released by magmas. At Kovdor, the principal ore mineral is Sc-rich magmatic baddeleyite hosted in carbonatite-related phoscorite (Liferovich et al., 1998; Kalashnikov et al., 2016) and the average ore grade is 800 ppm Sc (Kalashnikov et al., 2016). In contrast, at Bayan Obo, scandium is hosted dominantly in metasomatic aegirine (Chao et al., 1992; Fan et al., 2016), interpreted to have been deposited by carbonatite-derived hydrothermal fluids (Smith and Henderson, 2000). The average grade of the massive aegirine ore at Bayan Obo is 169 ppm Sc (Zhao, 1987). The ores in the last of these current producers, Tomtor, are the product of the weathering of carbonatite, which enriched the residue in Sc-bearing xenotime-(Y) to an average grade of 390 ppm Sc (Lapin et al., 2016). A major past producer was the Zhovti Vody deposit in the Ukraine, in which the scandium is concentrated in metasomatic aegirine and riebeckite in amphibolite (Tarkhanov et al., 1992). In addition, there has been minor production from magmatic thortveitite ($(Sc,Y)_2Si_2O_7$) in NYF granitic pegmatites in Madagascar (Murdock, 1963) and Norway (e.g., Müller et al., 2015). Thus, to date, the bulk of the scandium production has been from carbonatites, from a carbonatite-related metasomatic deposit and a metasomatic deposit for which the source of the fluid is unknown. A new scandium resource was recently discovered in ferrodiorite of the Kiviniemi mafic intrusion, Finland. The main carriers of scandium in these rocks are magmatic amphibole, clinopyroxene, and apatite, and though these minerals are strongly enriched in scandium, containing up to 1183 ppm, 1131 ppm, and 740 ppm, respectively, the average grade of the resource is only 163 ppm Sc due to dilution by Sc-poor minerals such as plagioclase (Halkoaho et al., 2020). Apart from this deposit, and those in NYF pegmatites, there are no examples of Sc deposits hosted by alkaline igneous rocks. Here we report the results of a study of a large, potentially high grade syenite-hosted scandium deposit, Crater Lake, in northern Québec, Canada.

Crater Lake is a recently discovered deposit that is currently the target of exploration and has been shown, through trenching and drilling, to contain large masses of ferrosyenite grading over 300 ppm Sc and locally in excess of 1000 ppm Sc (Daigle, 2017). It is the first Sc deposit to have been discovered in Canada, and the first known syenite-hosted Sc deposit anywhere. In this contribution, we use whole-rock geochemical and mineral chemical data to establish the distribution of the scandium in the ferrosyenite and model the processes responsible for its concentration to potentially economic levels.

4.2 The Geology of the Crater Lake Syenite Complex

The Crater Lake syenite complex was emplaced in the southern part of the Mistastin batholith (Fig. 1 of Petrella et al., 2014), one of a series of anorthosite-mangerite-charnockite-granite batholiths (Nain Plutonic Suite) that straddle the boundary between the Paleoproterozoic Churchill Province and the Archaean Nain Province (Emslie et al., 1994; Peck et al., 2010). The immediate host to the complex is an olivine-pyroxene-bearing rapakivi granite that has A-type affinity, manifested by an enrichment in K and a high Fe/Fe+Mg ratio, and is one of the two main lithological units in the Mistastin batholith (Emslie and Stirling, 1993); the other is anorthosite. This unit passes gradationally into an olivine-bearing quartz monzonite that is distinguished from the rapakivi granite only by a lower content of quartz (Petrella et al., 2014). Contacts between the quartz monzonite and the syenite are also gradational, marked by the loss of quartz and the disappearance of the plagioclase rim around alkali feldspar crystals in the syenite. The Mistastin rapakivi granite is reported to be 1420 Ma (J.C. Roddick, pers. comm. 1990, to Emslie and Stirling, 1993) and the syenite was dated at 1409.7 ± 1.2 Ma (David et al., 2012); both ages were determined using U-Pb radiometric methods applied to zircon.

Imperial Mining Group Ltd. is currently exploring the Crater Lake intrusion for scandium. The intrusion, which was discovered as the result of aeromagnetic survey that identified a prominent, 6 km wide ring-shaped anomaly (Dumont et al., 2010), was previously explored by Quest Rare Minerals Ltd. for rare earth element (REE) mineralization (under the name Misery Lake). Like the rapakivi granite of the Mistastin batholith, the Crater Lake intrusion also has A-type affinity, as evidenced by its low CaO content, high Fe/Fe+Mg ratio and a high content of large ion lithophile elements (LILE) (Petrella et al., 2014). Lithologically, it comprises three main units, namely ferrosyenite, felsic syenite, and pegmatite. Ferrosyenite was initially identified as amoeboid-shaped inclusions in felsic syenite, ranging in size from a few centimeters to several meters with long axes generally oriented parallel to local contacts (Petrella et al., 2014). More recent drilling, however, has revealed the occurrence of thick (up to 215 m, minimum) intervals of ferrosyenite. They are composed of early, sub- to euhedral fluorapatite, zircon, and ferromagnesian minerals (fayalite, hedenbergite, magnetite, and hastingsite) and small but variable proportions of interstitial perthite. This unit is interpreted to be a cumulate facies and is host to LREE mineralization in the form of LREE-enriched fluorapatite and metasomatic britholite (Petrella et al., 2014). Felsic syenites are the most important lithological unit volumetrically at Crater Lake and form the interior of the intrusion. They vary from coarse- to fine-grained and are composed dominantly of perthite with minor proportions of interstitial hedenbergite and amphibole. Some samples show evidence of local albitization of the alkali feldspar and may contain metasomatic arfvedsonite (Petrella et al., 2014). Pegmatites constitute the youngest lithological unit, crosscutting both the ferrosyenite and felsic syenites, and were largely emplaced in radial fractures oriented perpendicular to the local concentric strike of earlier units.

As first reported by Petrella et al., (2014) from a smaller data set, all the Crater Lake rocks define a very strong linear trend on a total alkalis versus silica diagram, and the Mistastin granites define a separate, almost perpendicular trend (Fig. 4.1A). This relationship is also true for scandium and silica (Fig. 4.1B). Petrella et al. (2014) interpreted the Crater Lake syenite to be a differentiation product of the Mistastin granite, on the basis of the gradational contact between the two bodies, their similar compatible trace element compositions, and the enrichment in incompatible elements (HFSE, REE) in the syenite relative to the granite. They also proposed that the initial Crater Lake melt composition is represented by the quartz monzonite, as samples of this unit lie at the intersection of the two magmatic trends on a total alkalis vs silica diagram (Fig 4.1). According to this hypothesis, the quartz monzonite magma fractionated ferromagnesian minerals that accumulated to form the ferrosyenites and produced a residual liquid enriched in alkalis and silica from which the felsic syenites crystallized (Petrella et al., 2014).

The Crater Lake intrusion was interpreted by Petrella et al. (2014) to be a ring dyke complex because of the concentric lithological zonation of quartz monzonite and felsic syenite, the steep dip of the bodies toward the center of the intrusion, the presence of numerous intrusion-scale discontinuous arcuate faults (interpreted from magnetic lineaments), and the occurrence

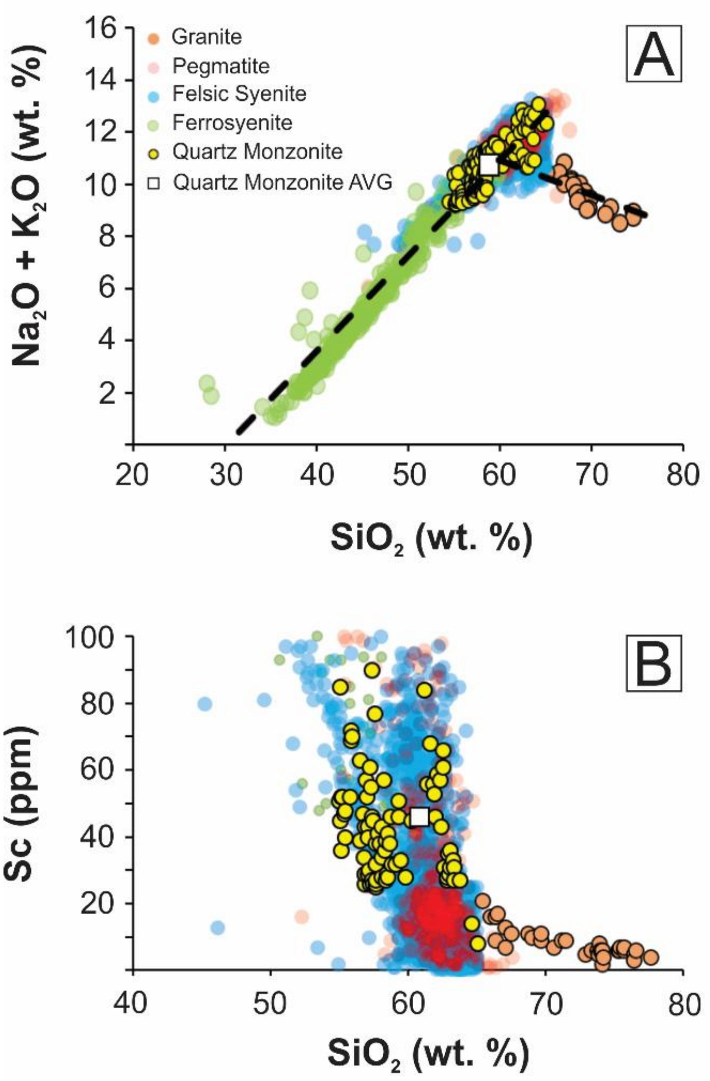

Figure 4.1: Total alkalis versus silica diagram for the Crater Lake intrusion

Bulk rock compositional data for the various lithological units of the Crater Lake intrusion and the Mistastin rapakivi granite, from drill core assays. A) a plot of total alkalis versus SiO_2 content and B) A plot of Sc content versus SiO_2 content. The data were supplied by Imperial Mining Group Ltd.

of several late radial faults (occupied by pegmatites), which are all characteristic features of ring complexes (e.g. Woolley, 2001; Coumans and Stix, 2016). Consistent with this interpretation, some of the Crater Lake felsic syenites feature a trachytic texture developed through the alignment of feldspar laths, indicative of flow before cooling. There is a strong correlation between the location of known ferrosyenite (the only lithological unit with an appreciable magnetite content) outcrops and magnetic susceptibility (Fig 4.2). Indeed, a magnetic susceptibility model (commissioned by Imperial Mining Group Ltd.) of the intrusion in three dimensions from an

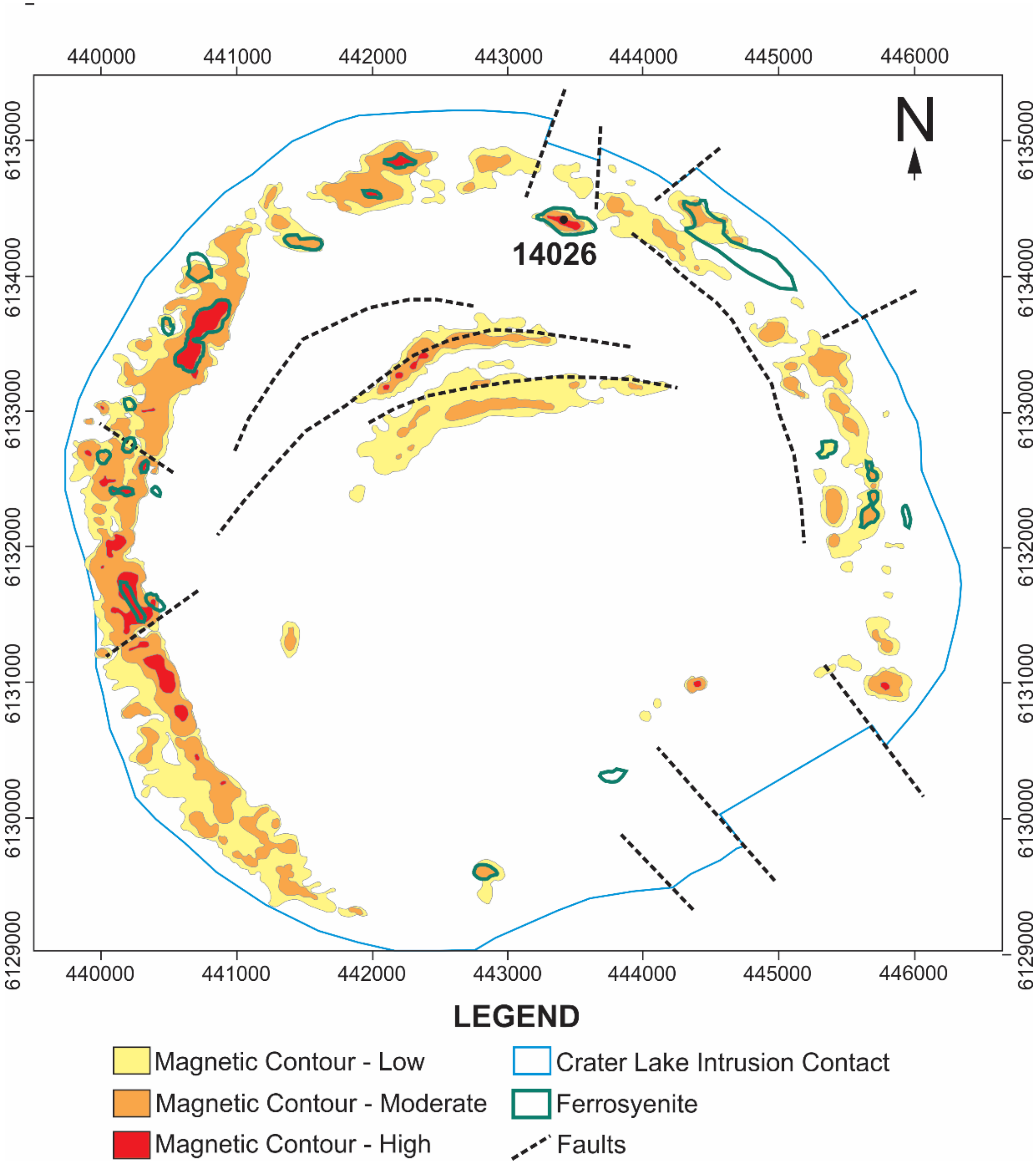

Figure 4.2: Magnetic susceptibility map of the Crater Lake intrusion

A magnetic susceptibility map of the Crater Lake intrusion, modeled from the results of a ground magnetometer survey showing the location of drill hole 14026, on which this study is mainly based, and known occurrences of ferrosyenite (green outlines). The map was supplied by Imperial Mining Group Ltd.

iteratively reweighted inversion of data from a recent GPS-integrated ground magnetic survey, suggests that the ferrosyenite is a subvertical ring dyke with some local sill-like lateral extensions. Although further drilling is required to confirm this model, it is supported by thick intersections of ferrosyenite in existing drill holes, and the steeply dipping layering in this unit. Hole 14026, on which the current study is based, hosts the longest intersection of ferrosyenite and the most continuous record of scandium mineralization encountered at Crater Lake to date. This mineralization is the focus of our study. Given the current understanding of the geometry of the ferrosyenite, it is important to specify that we use the term cumulate to indicate mineralogical layering produced by physical separation of minerals, whether by flow segregation or by gravity settling.

4.3 Ferrosyenite Textures and Bulk Rock Geochemistry

A schematic diagram illustrating the lithological log for the scandium mineralized zone in drill hole 14026 is provided in Figure 4.3, accompanied by photographs of thin sections of selected samples to highlight textural changes in the ferrosyenite with depth. In this hole, there are repeated layers displaying normal grading of mineral proportions. Each layer features a basal part with a high proportion of mafic minerals (fayalite and hedenbergite) and a low proportion of alkali feldspar (perthite), above which the proportions of mafic minerals and alkali feldspar progressively decrease and increase, respectively. The feldspar crystals are anhedral to subhedral at the base, occupying the interstitial space, whereas at the top of a layer, where the proportion of earlier mafic minerals is much lower, the feldspar crystals are larger and subhedral (Fig. 4.3). At the bottom of each layer, the fabric in the ferrosyenite is developed through layering of olivine and weak alignment of elongated clinopyroxene crystals, whereas at the top, the mafic minerals form more widely spaced layers, and later feldspar crystals are aligned (Fig. 4.3). These textures are indicative of crystal accumulation and increasing compaction (decreasing the volume of intercumulus liquid, represented by feldspar) with depth.

The above observations are broadly reflected in the bulk rock geochemistry. Bulk rock chemical data were obtained from the Quest Rare Minerals Ltd. database of Crater Lake drill core assays. The assays were performed by Activation Laboratories in Ancaster, Ontario, and included all bulk major elements and a large number of trace elements, including Sc. All the samples were ground to 95% -200 mesh and aliquots of each powder were fused with lithium metaborate

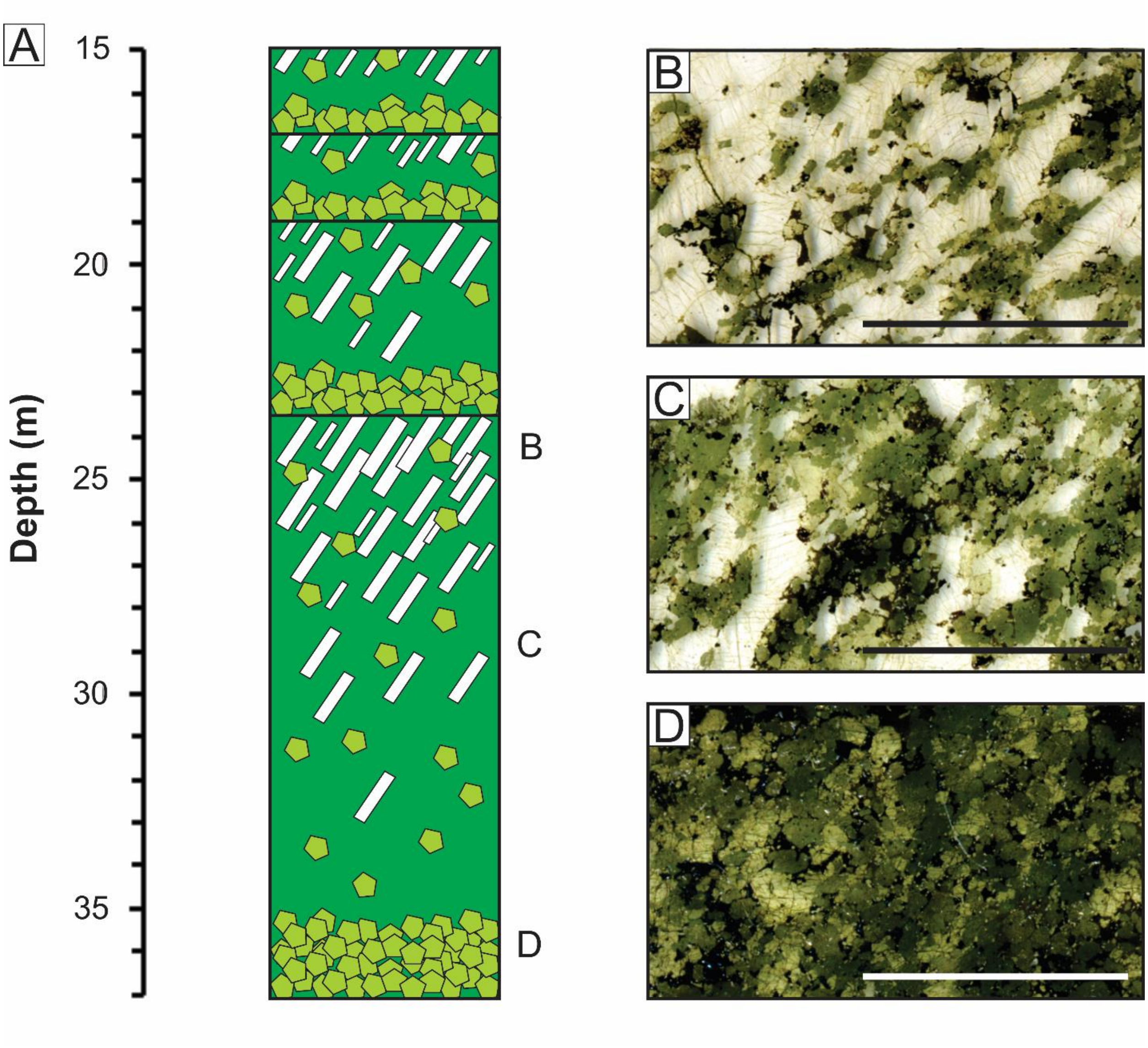

Figure 4.3: Ferrosyenite in drill hole 14026

A) A schematic lithological log of the ferrosyenite intersected at the top of drill hole 14026. The green pentagons represent olivine crystals, and the white rectangles represent feldspar crystals. Note the repetition of sequences of olivine-rich rocks at the base and feldspar-rich rocks at the top. B-D) Photographs of thin sections illustrating the mineralogical and textural changes with depth in a single sequence. B) Feldspar-rich ferrosyenite at the top of a sequence. C) Ferrosyenite with abundant feldspar, but composed dominantly of ferromagnesian minerals. D) Cumulate-textured ferrosyenite dominated by olivine (pale green) and clinopyroxene (darker green). All scale bars are 1 cm.

- tetraborate, followed by analysis using inductively coupled plasma optical emission spectrometry (ICP-OES) for the major elements and mass spectrometry (ICP-MS) for the trace elements. The loss on ignition (LOI) was determined after fusion. Samples (1 g) were heated in an oven at 1000°C for 1 h, cooled then weighed, with the % loss calculated from the difference in weight before and after heating. The fluorine content was measured on 0.2 g samples fused with lithium metaborate/tetraborate in a furnace to release F^- ions from the sample into a solution, which was analysed using an ion sensitive electrode.

The downhole major element oxide and Sc composition of the ferrosyenite is illustrated in Figure 4.4. Two opposing downhole trends are evident. The proportions of the mafic components CaO, FeO, MgO, MnO, and TiO_2 increase periodically and are matched by corresponding decreases in the proportions of the felsic components SiO_2, Al_2O_3, Na_2O and K_2O. The downhole distribution of Sc is the same as that of the mafic components, indicating that scandium is hosted by one of the cumulus phases. It should be noted that the geochemical signal of variable mineral proportions is dampened somewhat in the bulk rock geochemical data because of the assay sample lengths, which were all 2 m in the ferrosyenite, regardless of textural changes.

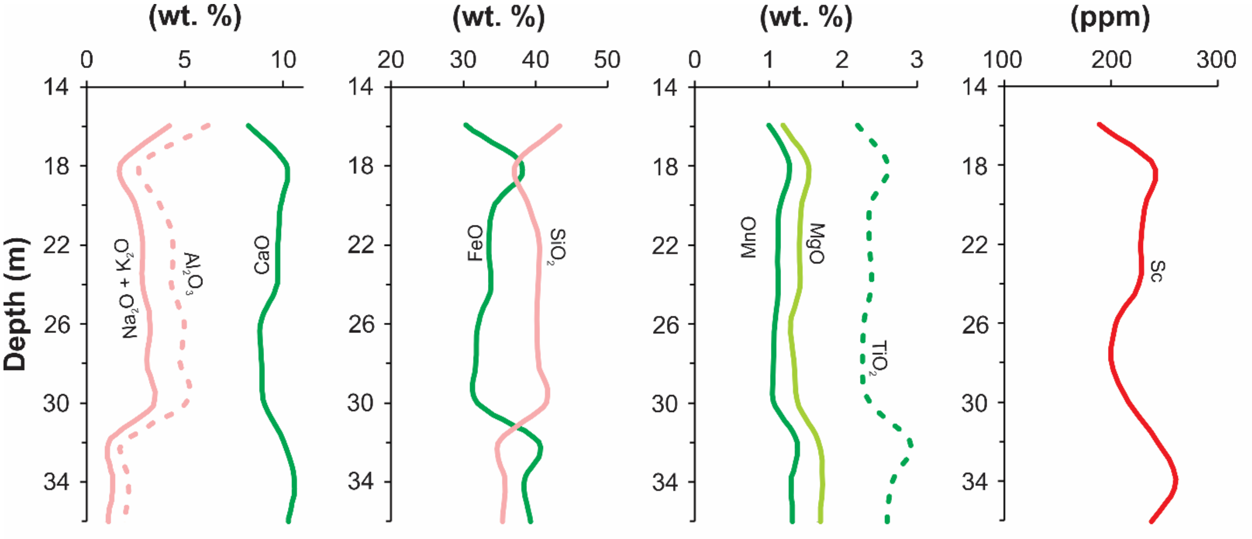

Figure 4.4: Major element and Sc strip logs for ferrosyenite in drill hole 14026

The Sc strip log is similar in shape to the strip logs for the mafic elements.

4.4 Mineral Chemistry and Paragenesis

Samples were examined petrographically using a combination of optical and scanning electron microscopy (SEM). A Hitachi SU5000 SEM, equipped with an Oxford Instruments X-Max^N 80 silicon drift detector was used for back-scattered electron (BSE) imaging and mineral identification. The modal mineralogy was estimated visually using an optical microscope.

Mineral compositions were measured in the Department of Earth and Planetary Sciences at McGill University using a Cameca SX100FE electron microprobe equipped with five wavelength-dispersive spectrometers and an Si(Li) energy-dispersive spectrometer. Spot analyses of clinopyroxene, amphibole, biotite, olivine, and magnetite were conducted at 20 kV with a 20 nA beam current. All analyses were performed with a 5 µm beam diameter. Data reduction was carried out using a ZAF correction procedure. Some samples were selected for WDS mapping and transects of point analyses at 10 µm intervals. The standards used, the counting times and the detection limits for each element in each mineral are reported in Appendix 4.1. The clinopyroxene was classified using the scheme of Morimoto (1988) and amphibole was classified based on crystal site assignments made using the program ACES (Locock, 2014).

All the samples are composed of variable proportions of the same minerals, namely fayalite, hedenbergite, hastingsite, magnetite, annite, perthite, zircon, fluorapatite and britholite (Table 4.1, Fig. 4.5). Fluorapatite and zircon occur as inclusions in all the other minerals, though most commonly in fayalite and hedenbergite. Britholite formed as a hydrothermal alteration product of fluorapatite (Petrella et al., 2014).

The fayalite occurs as discrete, subhedral crystals commonly containing fluorapatite inclusions (Fig. 4.6A-C), and has an extremely consistent composition that does not vary with depth. All the crystals analyzed have the composition, Fa93 (Appendix 4.2) and a Mg# of 0.02 - 0.03 (Fig. 4.7A). Scandium was not detected.

Hedenbergite occurs mainly as discrete, unzoned, subhedral crystals and as overgrowths on fayalite (Fig. 4.6A, B). In rare cases, the crystals contain cores rich in fluorapatite inclusions that have been partly altered to amphibole, and limpid unaltered rims that are interpreted to represent overgrowths (Fig. 4.6C-F). The cores of the zoned crystals have lower concentrations of

Table 4.1: Mineral proportions in ferrosyenite

		Modal (Volume) %							
Depth (m)	**Sample**	**Zrn**	**Ap**	**Fa**	**Hd**	**Mag**	**Hst**	**Bt**	**Afs**
15.00	142601	0.1	1	10	25	2	5	1	56
15.30	142602	0.1	2	20	30	5	10	3	30
16.85	142603	1	4	40	30	10	15	0	0
18.80	142604	1	2	30	40	5	10	3	9
19.05	142605	1	4	35	35	5	5	5	10
21.10	142607	0.1	5	15	34	5	15	1	25
23.25	142610	1	3	30	35	10	20	0.1	1
26.75	142611	1	3	15	30	3	7	5	36
31.60	142613	2	3	35	30	15	14	0.1	1
36.00	142614	1	5	40	35	10	5	3	1

		Mass %							
	density*	4.7	3.19	4.39	3.56	5.2	3.34	3.09	2.56
Depth (m)	**Sample**	**Zrn**	**Ap**	**Fa**	**Hd**	**Mag**	**Hst**	**Bt**	**Afs**
15.00	142601	0.2	1	14	29	3	5	1	46
15.30	142602	0.1	2	25	31	7	10	3	22
16.85	142603	1	3	44	27	13	12	0	0
18.80	142604	1	2	35	38	7	9	2	6
19.05	142605	1	3	40	33	7	4	4	7
21.10	142607	0.1	5	19	35	8	14	1	18
23.25	142610	1	2	34	32	13	17	0.1	1
26.75	142611	1	3	20	32	5	7	5	28
31.60	142613	2	2	38	26	19	11	0.1	1
36.00	142614	1	4	44	31	13	4	2	1
AVG all		1	3	31	31	10	9	2	13
AVG cumulus		1	3	37	37	11	11		

**densities taken from Deer et al., (1992)*

The term 'Zrn' refers to zircon, 'Ap' to fluorapatite, 'Fa' to fayalite, 'Hd' to hedenbergite,'Mag' to magnetite, 'Hst' to hastingsite, 'Bt' to biotite, and 'Afs' to alkali feldspar (perthite). Mineral abbreviations from Whitney and Evans (2010).

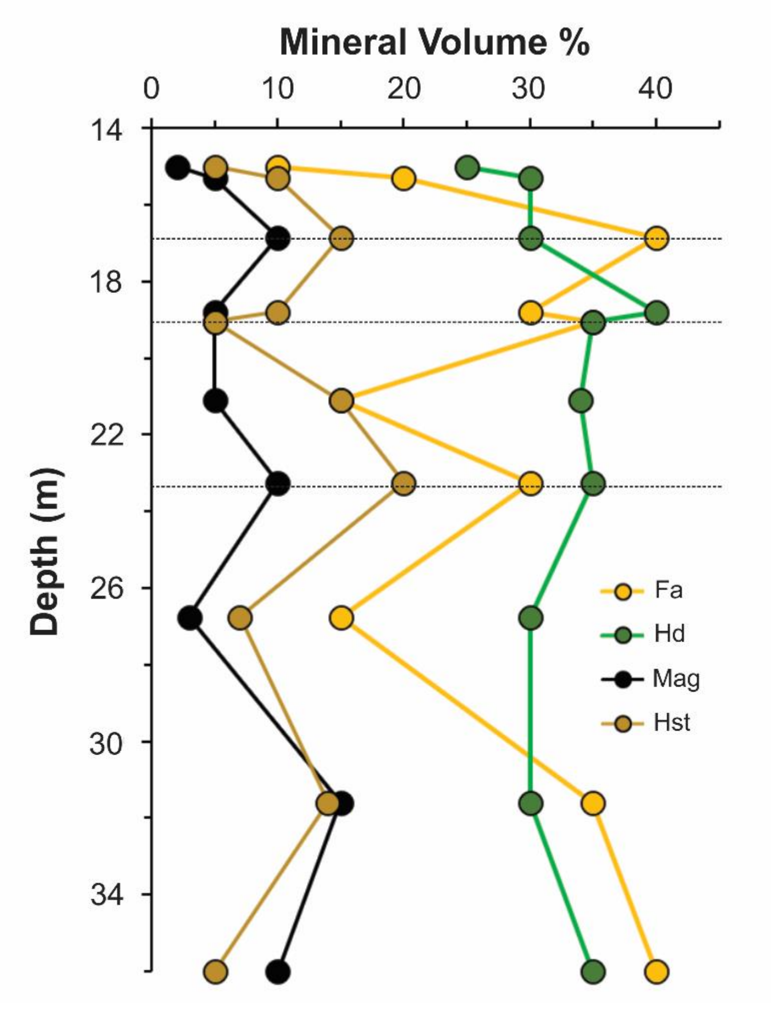

Figure 4.5: Mineral proportions with depth in drill hole 14026

Visual estimates of the proportions of the different ferromagnesian minerals, except for annite (trace to minor amounts), with depth in drill hole 14026. The dashed black lines correspond to peaks in fayalite proportion, interpreted to represent the base of cumulate layers (see text for further detail). The term "Fa" in the legend refers to fayalite, "Hd" to hedenbergite, "Mag" to magnetite, and "Hst" to hastingsite. Mineral abbreviations are from Whitney and Evans (2010).

Al, Ti, Mn, and Zn than the rims (Table 4.2) but a higher Mg# and Sc content than their rims (Fig. 4.7, Table 4.2). This Sc-rich character of the hedenbergite cores relative to their rims is apparent in WDS Sc maps (Fig. 4.6D, F). The average Mg# and Sc contents of the cores of zoned crystals from different samples ranges from 0.17 to 0.22 and from 812 to 1347 ppm, respectively, whereas the corresponding values for the overgrowths range from 0.14 to 0.17 and from 565 to 713 ppm, respectively (Table 4.2). The unzoned hedenbergite crystals are compositionally indistinguishable from the rims of the zoned crystals (Table 4.2). The Mg# of the cores of zoned hedenbergite

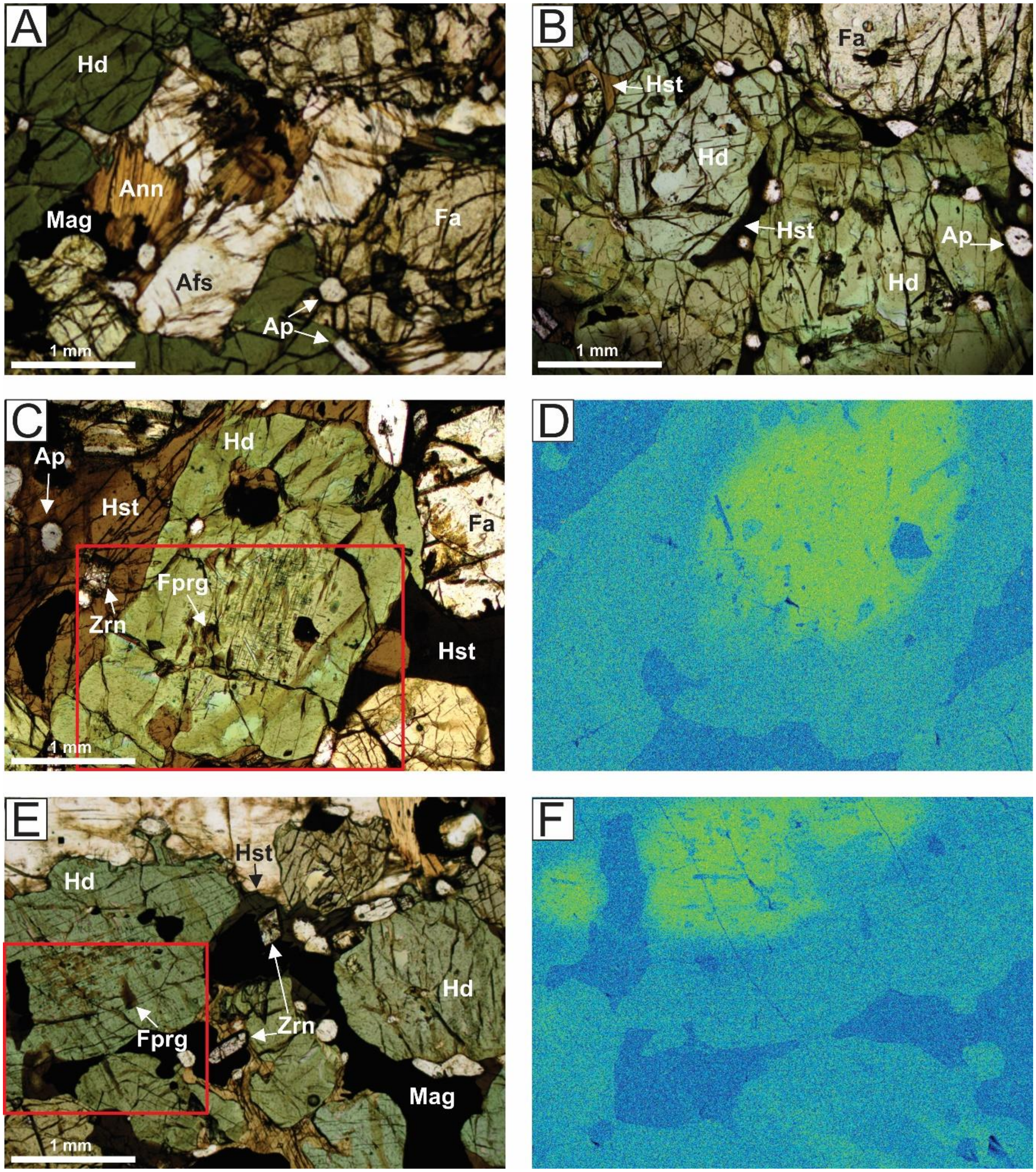

Figure 4.6: Photomicrographs of selected ferrosyenite samples.

A) Cumulus fayalite, hedenbergite, and fluorapatite accompanied by intercumulus magnetite, alkali-feldspar and annite. B) Cumulus fayalite, hedenbergite and fluorapatite with minor intercumulus hastingsite. C) Cumulus fayalite, hedenbergite and fluorapatite poikilitically enclosed by hastingsite. This image also displays a rare zoned hedenbergite crystal (red box) with an inclusion-rich core that has been partly altered to ferropargasite and a limpid rim. D) A Sc map (WDS) of the region outlined in red in C), showing that the core is enriched in Sc. E) Cumulus hedenbergite with intercumulus magnetite, hastingsite and alkali feldspar containing inclusions of zircon and fluorapatite. Annite is locally overgrown on hedenbergite. The clinopyroxene crystal within the upper part of the red box is zoned. F) A Sc map (WDS) of the region outlined in red in E), showing that the core is enriched in Sc .

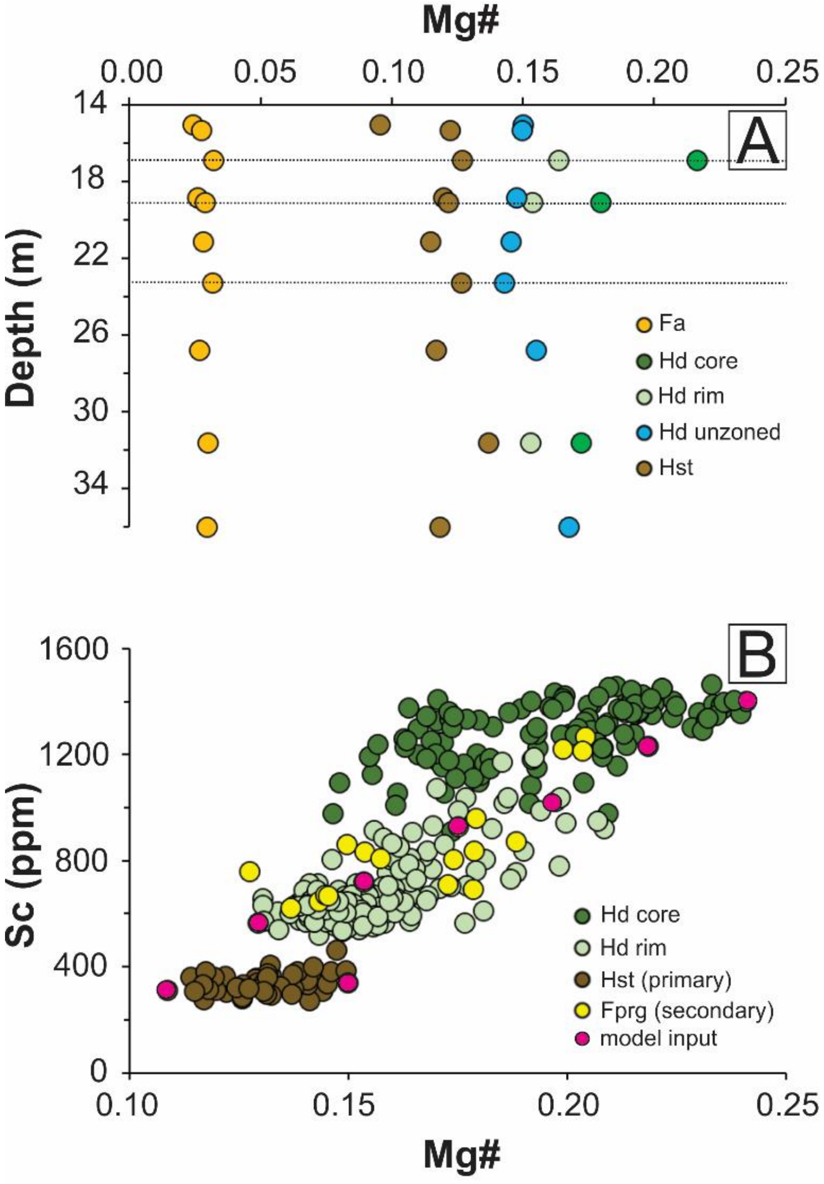

Figure 4.7: Mineral Mg# and Sc contents

A) The Mg# of selected minerals versus depth in drill hole 14026. The dashed lines correspond to the interpreted base of the fractionation sequences illustrated in Figure 3. B) Scandium content versus Mg# for the different types of hedenbergite, hastingsite and ferropargasite analyzed in samples from drill hole 14026. The hedenbergite Mg# and Sc content are positively correlated. The primary hastingsite has a relatively constant Sc content over a range of Mg# from 0.11 to 0.15, whereas the secondary ferropargasite composition lies within the field defined by the unzoned hedenbergite and the rims of zoned hedenbergite crystals. The pink points correspond to model input compositions (see text below for further explanation).

crystals do not vary systematically with depth, whereas the rims and the unzoned crystals show a weak overall increase in Mg# with depth within each of the sequences illustrated in Figure 4.3 (the base of which corresponds to a olivine-clinopyroxene cumulate) (Fig. 4.7A). Taken together, the crystals are all part of a continuum of Mg#s, that correlate positively with Sc content (Fig. 4.7B). The concentrations of the minor elements in unzoned clinopyroxene crystals and the rims of zoned crystals do not vary with depth (Table 4.2).

Magnetite occurs as discrete, subhedral crystals, but also commonly occupies the interstices between earlier cumulus fayalite and hedenbergite (Fig. 4.6C, E). The composition of the magnetite is variable, and is characterized by minor proportions of Si, Mn, Zn and Al, that do not vary systematically with depth (Appendix 4.3). Scandium was not detected in magnetite in any of the samples (80 ppm Sc detection limit).

There are two generations of amphibole, primary and secondary. Primary amphibole occurs mainly as overgrowths on fayalite, hedenbergite, and magnetite, or may poikilitically enclose them (Fig. 4.6B, C, E). Secondary amphibole preferentially altered clinopyroxene cores (Fig. 4.6C, E). All the primary amphibole has a hastingsite or Ti-rich hastingsite composition, whereas the secondary amphibole has a composition that varies between ferro-edenite and ferro-pargasite (Table 4.3, Appendix 4.4). For simplicity, primary and secondary amphibole will be referred to hereafter as hastingsite and ferro-pargasite, respectively. The Mg# of the primary hastingsite is less variable, from 0.10 to 0.15, than that of the hedenbergite and its scandium content is lower (251 – 465 ppm) and largely independent of Mg# (Fig. 4.7B, Table 4.3). The Mg# of primary hastingsite generally increases with increasing depth, within each sequence displayed in Figure 4.3. In contrast, the composition of the secondary amphibole reflects the composition of the precursor hedenbergite and is characterized by lower contents of the typical ferropargasite components (Al, Na, K, Ti, F, and Cl) and higher Ca and Mn contents than the primary hastingsite (Table 4.3). The secondary amphibole has a Mg# and Sc content ranging from 0.13 to 0.21 and from 624 to 961 ppm, respectively, and its composition lies on the trend in Mg# and Sc content defined by hedenbergite compositions (Fig. 4.7B, Table 4.3).

Annite was the last ferromagnesian mineral to crystallize and is strongly associated spatially with magnetite, especially where the latter is in contact with alkali feldspar (Fig. 4.6A).

Its composition does not vary with depth (Appendix 4.5). The Sc content of the annite is below the detection limit (80 ppm) (Appendix 4.5).

In all samples, alkali feldspar (perthite) was the latest phase to crystallize and is interstitial to the other minerals (Fig. 4.3, Fig. 4.6A). In summary, the observed paragenesis in the Crater Lake ferrosyenite corresponds to early crystallization of fluorapatite and zircon, followed by fayalite, and hedenbergite, all commonly as cumulus minerals, and then by intercumulus magnetite, and hastingsite, and finally annite and alkali feldspar. Hydrothermal alteration is evident through the occurrence of ferropargasite in the cores of zoned hedenbergite crystals.

Table 4.2: Mean major element oxide compositions and cation proportions of hedenbergite in ferrosyenite

Sample (Depth)	**142601 (15.00)**		**142602 (15.30)**		**142603 (16.85)**						**142604 (18.80)**	
type (n)	limpid (11)	1 σ	limpid (10)	1 σ	limpid (8)	1 σ	T-core (64)	1 σ	T-rim (61)	1 σ	limpid (7)	1 σ
Na_2O	0.70	0.11	0.81	0.44	0.71	0.08	0.73	0.08	0.78	0.08	0.72	0.12
MgO	2.46	0.20	2.45	0.21	2.57	0.17	3.56	0.20	2.68	0.25	2.44	0.10
SiO_2	47.74	0.24	47.85	0.25	47.82	0.17	49.15	0.28	48.76	0.29	47.71	0.40
Al_2O_3	0.92	0.29	0.90	0.27	1.03	0.19	0.78	0.18	0.89	0.13	0.82	0.27
K_2O	0.00	0.00	0.01	0.03	0.00	0.00	0.01	0.02	0.00	0.00	0.00	0.00
CaO	20.27	0.10	20.30	0.12	20.37	0.19	20.81	0.27	20.49	0.18	20.08	0.35
TiO_2	0.44	0.07	0.43	0.12	0.49	0.07	0.40	0.18	0.45	0.06	0.41	0.10
Cr_2O_3	bdl		bdl		bdl		bdl		bdl		bdl	
FeO	24.86	0.40	24.83	0.32	24.51	0.40	23.01	0.37	24.40	0.45	25.16	0.61
MnO	0.85	0.02	0.85	0.02	0.85	0.04	0.81	0.03	0.85	0.03	0.87	0.03
ZnO	0.09	0.01	0.08	0.01	0.08	0.02	0.07	0.01	0.07	0.02	0.07	0.02
Sc_2O_3	0.09	0.01	0.09	0.01	0.09	0.01	0.21	0.01	0.11	0.02	0.09	0.00
Total	98.49		98.69		98.56		99.61		99.56		98.53	
Sc ppm avg	565	58	608	40	591	62	1348	85	714	154	581	24
Sc min	502		552		521		978		564		534	
Sc max	692		654		690		1464		1191		605	
					O = 6							
Na	0.056		0.065		0.056		0.057		0.062		0.058	
Mg	0.151		0.150		0.157		0.214		0.162		0.151	
Si	1.969		1.971		1.967		1.982		1.981		1.973	
Al	0.045		0.044		0.050		0.037		0.043		0.040	
K	0.000		0.001		0.000		0.000		0.000		0.000	
Ca	0.896		0.896		0.898		0.899		0.892		0.890	
Ti	0.014		0.013		0.015		0.012		0.014		0.013	
Cr	0.000		0.000		0.000		0.000		0.000		0.000	
Fe	0.858		0.855		0.843		0.776		0.829		0.870	
Mn	0.030		0.030		0.029		0.028		0.029		0.031	
Zn	0.003		0.002		0.002		0.002		0.002		0.002	
Sc	0.003		0.003		0.003		0.007		0.004		0.003	
Total	4.023		4.030		4.022		4.024		4.027		4.030	
Mg#	0.150		0.149		0.157		0.216		0.164		0.147	

'T' in the type of hedenbergite refers to the mean composition from transects of point analyses across crystals

'bdl' – below the limit of detection

Table 4.2: Continued

Sample (Depth)	**142605 (19.05)**						**142607 (21.10)**		**142610 (23.25)**		**142611 (26.75)**	
type (n)	limpid (11)	1 σ	T-core (40)	1 σ	T-rim (59)	1 σ	limpid (9)	1 σ	limpid (10)	1 σ	limpid (16)	1 σ
Na_2O	0.74	0.08	0.85	0.21	0.79	0.08	0.69	0.06	0.71	0.13	0.70	0.09
MgO	2.59	0.16	2.97	0.28	2.53	0.28	2.41	0.16	2.37	0.14	2.55	0.21
SiO_2	47.92	0.19	49.06	0.30	48.95	0.23	47.33	0.30	47.45	0.75	47.46	0.55
Al_2O_3	0.97	0.21	0.80	0.23	0.78	0.21	1.03	0.28	0.86	0.22	1.33	0.19
K_2O	0.00	0.00	0.01	0.03	0.00	0.01	0.04	0.00	0.00	0.00	0.00	0.00
CaO	20.46	0.14	20.50	0.31	20.48	0.18	19.88	0.25	19.83	1.34	20.16	0.53
TiO_2	0.46	0.07	0.40	0.08	0.39	0.09	0.44	0.11	0.43	0.10	0.51	0.06
Cr_2O_3	bdl		bdl		bdl		bdl		bdl		bdl	
FeO	24.49	0.36	24.17	0.45	24.88	0.50	25.28	0.51	25.46	1.81	24.77	0.75
MnO	0.85	0.02	0.81	0.02	0.83	0.03	0.88	0.02	0.87	0.07	0.85	0.03
ZnO	0.07	0.02	0.07	0.02	0.07	0.01	0.07	0.02	0.08	0.01	0.07	0.01
Sc_2O_3	0.09	0.01	0.18	0.02	0.10	0.02	0.09	0.00	0.09	0.01	0.09	0.01
Total	98.71		99.92		99.89							
							98.24		98.21		98.55	
Sc ppm avg	591	44	1202	109	658	113	576	28	580	35	607	79
Sc min	538		978		534		558		526		469	
Sc max	688		1402		990		635		631		769	
O = 6												
Na	0.060		0.067		0.062		0.055		0.057		0.056	
Mg	0.160		0.179		0.153		0.149		0.146		0.156	
Si	1.969		1.983		1.985		1.963		1.968		1.954	
Al	0.046		0.038		0.037		0.050		0.042		0.065	
K	0.000		0.001		0.000		0.002		0.000		0.000	
Ca	0.901		0.888		0.890		0.883		0.881		0.889	
Ti	0.014		0.012		0.012		0.014		0.013		0.016	
Cr	0.000		0.000		0.000		0.000		0.000		0.000	
Fe	0.840		0.817		0.844		0.878		0.884		0.853	
Mn	0.030		0.028		0.028		0.031		0.031		0.030	
Zn	0.002		0.002		0.002		0.002		0.002		0.002	
Sc	0.003		0.006		0.004		0.003		0.003		0.003	
Total	4.025		4.032		4.028		4.031		4.028		4.024	
Mg#	0.158		0.179		0.154		0.145		0.143		0.155	

‘T’ in the type of hedenbergite refers to the mean composition from transects of point analyses across crystals

‘bdl’ – below the limit of detection

Table 4.2: Continued

Sample (Depth)	**142613 (31.60)**						**142614 (36.00)**	
type (n)	limpid (9)	1 σ	T-core (23)	1 σ	T-rim (73)	1 σ	limpid (11)	1 σ
Na_2O	0.68	0.08	0.81	0.06	0.76	0.08	0.72	0.09
MgO	2.52	0.09	2.84	0.10	2.51	0.16	2.74	0.20
SiO_2	47.46	0.58	49.14	0.17	48.89	0.33	47.88	0.78
Al_2O_3	0.97	0.15	0.75	0.11	0.83	0.18	1.12	0.39
K_2O	0.00	0.01	0.01	0.03	0.00	0.00	0.00	0.01
CaO	20.28	0.43	20.50	0.18	20.48	0.25	20.32	0.48
TiO_2	0.46	0.04	0.36	0.04	0.43	0.10	0.48	0.05
Cr_2O_3	bdl		bdl		bdl		bdl	
FeO	24.72	0.18	24.32	0.17	24.81	0.40	24.30	0.46
MnO	0.86	0.02	0.84	0.01	0.84	0.02	0.84	0.01
ZnO	0.07	0.02	0.07	0.01	0.07	0.02	0.06	0.01
Sc_2O_3	0.09	0.01	0.19	0.02	0.10	0.02	0.10	0.01
Total	98.17		99.93		99.80		98.67	
Sc ppm avg	609	56	1239	117	667	104	626	59
Sc min	559		913		522		578	
Sc max	715		1408		1073		769	
				O = 6				
Na	0.054		0.063		0.060		0.057	
Mg	0.155		0.171		0.152		0.168	
Si	1.964		1.987		1.984		1.966	
Al	0.047		0.036		0.040		0.054	
K	0.000		0.001		0.000		0.000	
Ca	0.899		0.888		0.891		0.894	
Ti	0.014		0.011		0.013		0.015	
Cr	0.000		0.000		0.000		0.000	
Fe	0.855		0.823		0.842		0.834	
Mn	0.030		0.029		0.029		0.029	
Zn	0.002		0.002		0.002		0.002	
Sc	0.003		0.007		0.004		0.003	
Total	4.025		4.029		4.025		4.023	
Mg#	0.154		0.172		0.153		0.167	

'T' in the type of hedenbergite refers to the mean composition from transects of point analyses across crystals
'bdl' – below the limit of detection

Table 4.3: Mean major element oxide compositions of amphibole in ferrosyenite

Sample (Depth)	**142601 (15.00)**		**142602 (15.30)**		**142603 (16.85)**				**142604 (18.80)**		**142605 (19.05)**			
Type (n)	1° (6)	1 σ	1° (7)	1 σ	1° (7)	1 σ	T-1° (20)	1 σ	1° (4)	1 σ	1° (10)	1 σ	T-1° (16)	1 σ
F	0.61	0.19	0.58	0.16	0.78	0.24	0.64	0.26	0.6	0.19	0.64	0.16	0.57	0.22
Na_2O	2.66	0.2	2.65	0.1	2.58	0.14	2.51	0.15	2.51	0.11	2.62	0.11	2.59	0.1
MgO	1.81	0.23	2.31	0.25	2.44	0.15	2.42	0.09	2.26	0.16	2.31	0.14	2.33	0.1
SiO_2	39.72	0.63	40.1	0.23	39.84	0.56	40.49	0.62	40.06	0.04	39.76	0.44	40.66	0.4
Al_2O_3	7.47	0.05	7.58	0.15	7.32	0.41	7.41	0.28	7.28	0.02	7.63	0.31	7.4	0.11
Cl	0.15	0.01	0.13	0.01	0.14	0.02	0.13	0.01	0.15	0.01	0.14	0.01	0.15	0.01
K_2O	1.46	0.06	1.5	0.03	1.46	0.05	1.48	0.04	1.47	0.01	1.49	0.04	1.46	0.07
CaO	9.57	0.54	9.83	0.17	9.76	0.2	9.86	0.32	9.79	0.11	9.77	0.39	9.84	0.43
TiO_2	2.46	0.33	2.52	0.32	2.69	0.14	2.7	0.09	2.66	0.15	2.69	0.2	2.54	0.08
Cr_2O_3	bdl		bdl		bdl		bdl		bdl		bdl		bdl	
FeO	30.58	0.87	29.59	0.51	29.69	0.56	29.74	0.51	29.67	0.14	29.45	0.48	30.03	0.76
MnO	0.58	0.06	0.55	0.04	0.58	0.04	0.62	0.04	0.58	0.02	0.6	0.07	0.56	0.02
ZnO	0.11	0.01	0.1	0.02	0.11	0.02	0.1	0.02	0.13	0.01	0.11	0.02	0.1	0.02
Sc_2O_3	0.04	0.01	0.04	0.01	0.05	0.01	0.06	0	0.05	0	0.05	0.01	0.05	0
Total	97.23		97.48		97.44		98.16		97.2		97.27		98.27	
Sc ppm avg	260	38	251	44	307	34	361	26	301	31	306	49	323	31
Sc min	191		156		269		326		263		223		278	
Sc max	293		287		362		416		339		368		382	

'1°' and '2°' refer to primary and secondary amphibole, respectively

'T' in the type of amphibole refers to the mean composition from transects of point analyses across crystals

'bdl' – below the limit of detection

Table 4.3: Continued

Sample (Depth)	**142607 (21.10)**		**142610 (23.25)**		**142611 (26.75)**		**142613 (31.60)**				**142614 (36.00)**		**16.85**	**19.05**
Type (n)	1° (7)	1 σ	1° (8)	1 σ	1° (15)	1 σ	1° (7)	1 σ	T-1° (26)	1 σ	1° (8)	1 σ	2° (Rep)	2° (Rep)
F	0.57	0.21	0.61	0.28	0.5	0.19	0.65	0.16	0.75	0.24	0.67	0.18	0.34	0.53
Na_2O	2.66	0.13	2.58	0.17	2.59	0.15	2.64	0.12	2.59	0.19	2.51	0.12	1.37	2.28
MgO	2.16	0.18	2.4	0.19	2.2	0.14	2.51	0.17	2.61	0.16	2.24	0.29	3.5	2.8
SiO_2	39.89	0.24	39.78	0.37	39.9	0.43	39.53	0.37	40.72	0.31	39.94	0.29	46.96	42.87
Al_2O_3	7.51	0.21	7.34	0.24	7.76	0.39	7.78	0.49	7.48	0.24	7.81	0.31	2.9	5.96
Cl	0.14	0.01	0.17	0.03	0.12	0.02	0.13	0.02	0.14	0.01	0.09	0.03	0.02	0.11
K_2O	1.49	0.02	1.47	0.04	1.47	0.05	1.49	0.1	1.5	0.1	1.46	0.06	0.31	0.96
CaO	9.81	0.12	9.84	0.28	9.88	0.18	9.92	0.34	10.02	0.24	9.95	0.3	17.6	12.46
TiO_2	2.72	0.13	2.65	0.15	2.57	0.32	2.61	0.27	2.69	0.18	2.34	0.33	1.05	2.14
Cr_2O_3	bdl		bdl		bdl		bdl		bdl		bdl		bdl	bdl
FeO	29.68	0.41	29.54	0.43	29.69	0.59	29.31	0.54	29.29	0.75	29.81	0.48	24.35	27.83
MnO	0.6	0.02	0.56	0.03	0.6	0.03	0.56	0.03	0.56	0.05	0.54	0.05	0.75	0.62
ZnO	0.1	0.02	0.11	0.01	0.11	0.02	0.1	0.01	0.1	0.02	0.1	0.01	0.08	0.11
Sc_2O_3	0.04	0	0.05	0	0.05	0.01	0.05	0.01	0.05	0.01	0.05	0.01	0.19	0.12
Total	97.37		97.11		97.47		97.3		98.49		97.53		99.44	98.8
Sc ppm avg	284	16	307	31	310	53	295	38	340	41	307	57		
Sc min	254		276		243		254		272		226			
Sc max	299		364		437		371		465		409			

"1°" and "2°" refer to primary and secondary amphibole, respectively
"Rep" – representative analysis
"T" in the type of hedenbergite refers to the mean composition from transects of point analyses across crystals
"bdl" – below the limits of detection

4.5 Discussion

4.5.1 Ferrosyenite Emplacement and Evolution

The concentration of fayalite and hedenbergite at ~16.85, ~19.05, ~23.25, and ~36 m in drill hole 14206 (Table 4.1, Fig. 4.5), coupled with the upward decrease in their proportions and increase in the proportion of alkali feldspar, shows that the ferrosyenite is layered. It also implies that the olivine and clinopyroxene concentrations are cumulates. One explanation for this rhythmic layering is that it developed *in situ* during fractional crystallization and sedimentation of crystals from of a single pulse of convecting liquid (e.g. Sparks et al., 1993). This explanation, however, is inconsistent with the observation that the Mg# of the fayalite do not change with depth over the interval in which ferrosyenite was intersected (Fig. 4.7A). We propose instead that the observed macro-layering represents multiple pulses of liquid, and that fayalite, and cores of zoned hedenbergite crystals (which are only observed in the cumulates), and zircon and fluorapatite (which occur as inclusions in the ferromagnesian minerals) crystallized in the magma chamber prior to emplacement. According to this hypothesis these crystals were suspended in each batch of liquid that was introduced to form the intrusion and accumulated by gravitational settling or flow differentiation. Unzoned hedenbergite crystals and the rims of zoned hedenbergite crystals represent an adcumulus phase that crystallized in situ and settled, producing the observed decrease in Mg# with decreasing depth (within each pulse, Fig. 4.7A). This trend is also recorded by the hastingsite, which is an intercumulus phase that crystallized later from a more fractionated residual liquid (Fig. 4.7A).

4.5.2 Scandium Distribution and Mass Balance

The mineral chemical data indicate that hedenbergite, and to a much lesser extent, the amphiboles, are the only significant hosts of Sc at Crater Lake. We have evaluated this observation using mass balance calculations. These calculations involved estimating the volume fractions (from petrography) of clinopyroxene and amphibole from their apparent proportions in thin section, multiplying these fractions by the corresponding mineral density and normalizing to convert to mass proportions (mass %, Table 4.1). The mass proportions of fayalite and hedenbergite so calculated were multiplied by the average measured Sc content of each of the minerals in a given sample to calculate a bulk rock Sc content (Table 4.4). For samples in which zoned hedenbergite crystals were identified, the cores were estimated to represent ~1%, on average, of the total hedenbergite population of the sample. The calculated bulk rock Sc contents are within 30 ppm of the measured contents, which is a much better than expected result, considering that the proportions of the minerals vary on a scale of centimeters, whereas the bulk rock compositions represent 2 m intervals of core. We note further that, if the estimated volume proportion is adjusted by < 5%, the calculated Sc content reproduces the measured Sc content to within 10 ppm (Table 4.4).

As mentioned earlier, clinopyroxene is also the scandium ore mineral at Bayan Obo, China, and was the principal host for Sc in the Zhovti Vody deposit, Ukraine. In those deposits, however, the clinopyroxene is aegirine. The Sc content of aegirine at Bayan Obo has been reported to reach 1.18 wt. % Sc (Shimazaki et al., 2008), although on average, it is only 210 ppm (Zhao et al., 1987). Aegirine from Zhovti Vody contains up to 1000 ppm Sc (Dudar et al., 2018). To our knowledge, the Sc contents for the Crater Lake hedenbergite reported here represent the highest Sc content in hedenbergite reported for any intrusion. For example, the Sc content of hedenbergite in the Kiviniemi intrusion, Finland, reaches 1131 ppm (Halkoaho et al., 2020), whereas the maximum measured Sc content of hedenbergite in ferrosyenite intersected in drill hole 14026 reaches 1465 ppm (Table 2). Elsewhere in the intrusion, the Sc content of hedenbergite commonly exceeds 2000 ppm and locally, is as high as 9000 ppm. The only other report of a comparably high Sc content in pyroxene is 820 ppm from a pyroxenite on Zabargad Island, Egypt (Vannucci et al., 1991). Clearly, the Sc-enrichment of the Crater Lake clinopyroxene is exceptional, as shown by the fact that the cores of the zoned hedenbergite crystals analyzed in this study, contain 1280 ppm Sc on average; the rims of these crystals and the unzoned hedenbergite contain 600 ppm Sc on average.

Table 4.4: Mass balance calculation results

Sample		**142601**	**142602**	**142603**	**142604**	**142605**	**142607**	**142610**	**142611**	**142613**	**142614**
Depth		15.00	15.30	16.85	18.80	19.05	21.10	23.25	26.75	31.60	36.00
Assay #		701676	701676	701677	701678	701678	701679	701680	701682	701684	701687
Bulk Rock Sc (ppm)		191	191	240	232	232	228	226	199	242	228
Mineral Mass Fraction	Hd	0.29	0.31	0.27	0.38	0.38	0.35	0.32	0.32	0.26	0.31
	Hst	0.05	0.10	0.12	0.09	0.04	0.14	0.17	0.07	0.11	0.04
Mean Mineral Sc Content (ppm)	Hd (C)			1347		1202				1239	
	Hd (R)	565	608	714	580	658	576	580	627	667	626
	Hst	260	251	361	200	323	186	208	367	340	208
Calc Bulk Rock Sc (ppm)		176	211	236	237	232	228	220	227	216	203
ΔSc (Calc-Meas, ppm)		-15	20	-4	5	0	0	-6	28	-26	-25
Mineral ΔVol. Fraction	Hd	0.01	-0.02						-0.02	0.03	0.02
	Hst								-0.02	0.01	0.02
Adjusted ΔSc (ppm)		-7	9	-4	5	0	0	-6	9	-6	-9
Hst Contribution to Bulk Rock Sc	ppm	14	24	45	18	14	27	35	26	39	9
	%	8	11	19	7	6	12	16	11	18	4

The suffixes ‘C’ and ‘R’ after hedenbergite refer to cores and rims/unzoned crystals, respectively

4.5.3 Scandium Substitution Mechanisms

The REE substitute into both the M1 and M2 site in clinopyroxene, although the preferred site depends on the ionic radii of the REE and the ideal radius of the M1 and M2 sites for the clinopyroxene in question. In the case of hedenbergite ($CaFeSi_2O_6$), the ideal radius of the eightfold coordinated M2 site is 1.12 Å (the ionic radius of Ca^{2+}) and the ideal radius of the sixfold coordinated M1 is 0.78 Å (the ionic radius of Fe^{2+}) (Shannon, 1976). As the ionic radius of sixfold coordinated Sc^{3+} is 0.75 Å (Shannon, 1976), which is close to that of the ideal radius of the M1 site and its eightfold coordinated radius (0.87 Å), is much smaller than the ideal radius of the M2 site, Sc has a strong preference for the M1 site (Fig. 6 in Williams-Jones and Vasyukova, 2018).

As the ideal charge of the M2 site is +2, a coupled substitution is required to balance the additional charge of Sc^{3+}. Possible coupled substitutions include:

$$Sc^{3+}\,[M1] + Al^{3+}\,[IV] = Me^{2+}\,[M1] + Si^{4+}\,[T] \qquad (1)$$

$$Sc^{3+}\,[M1] + Me^{+}\,[M2] = Me^{2+}\,[M1] + Me^{2+}\,[M2] \qquad (2)$$

where Me^{+} and Me^{2+} are metal cations with charges of 1 (e.g., Na^{+} and/or K^{+}) and 2 (Ca^{2+}), respectively. Incorporation of trivalent (and higher charge) trace metals in clinopyroxene through coupled substitution with tetrahedral Al^{3+} (Equation 1) has been well documented for many elements, including Sc (Bedard, 2014; Blundy et al., 1998; Forsythe et al., 1994; Hart and Dunn, 1993; Hill et al., 2000, 2011; Francis and Minarik, 2008; Lindstrom, 1976; Lundstrom et al., 1994, 1998; Mollo et al., 2013, 2016; Ray et al., 1983; Scarlato et al., 2014; Skulski et al., 1994; Sun and Liang, 2012, 2013; Ubide et al., 2019; Wood and Trigila, 2001; Yao et al., 2012). This substitution leads to an increase in the size of the site and the negative charge on it, resulting in a decrease in the size of the adjacent M1 site due to the decrease in bond length and increase in bond strength. Such a substitution should be evident in a positive correlation of the Sc concentration with the Al content of the tetrahedral site on an atoms per formula unit (a.p.f.u.) basis, which is not the case for the hedenbergite in our samples. On the contrary, the hedenbergite analyzed in this study displays a weak negative correlation (with the tetrahedral Al concentration (a.p.f.u., Fig. 4.8A) showing that Sc was not incorporated in this hedenbergite via the coupled substitution illustrated by Equation 1. In order to evaluate the second coupled substitution mechanism, in which the excess charge of Sc^{3+} is accommodated by the substitution of a +1 ion (Na^{+} and/or K^{+}), it was first necessary to balance the charge of the tetrahedral Al^{3+} by subtracting a corresponding proportion of Na^+ and K^+ from the molar mass of the mineral. We did this for analyses representing transects across single clinopyroxene crystals and plotted the Sc concentration against this excess (Na + K – Al(IV)). In these transects, one of which is illustrated in Figure 4.8B, the Sc concentration correlates positively with the excess alkali concentration, providing strong evidence that incorporation of Sc^{3+} in the M1 site was made possible by the incorporation of Na^+ and K^+ in the M2 site. The latter cations are larger than the Ca^{2+} ion (1.18 and 1.51, respectively, versus 1.12 Å, Shannon, 1976), and thus their substitution in M2 causes the site to swell, inducing shrinkage of the M1 site, favoring substitution of the smaller Sc^{3+} cation, while maintaining charge balance.

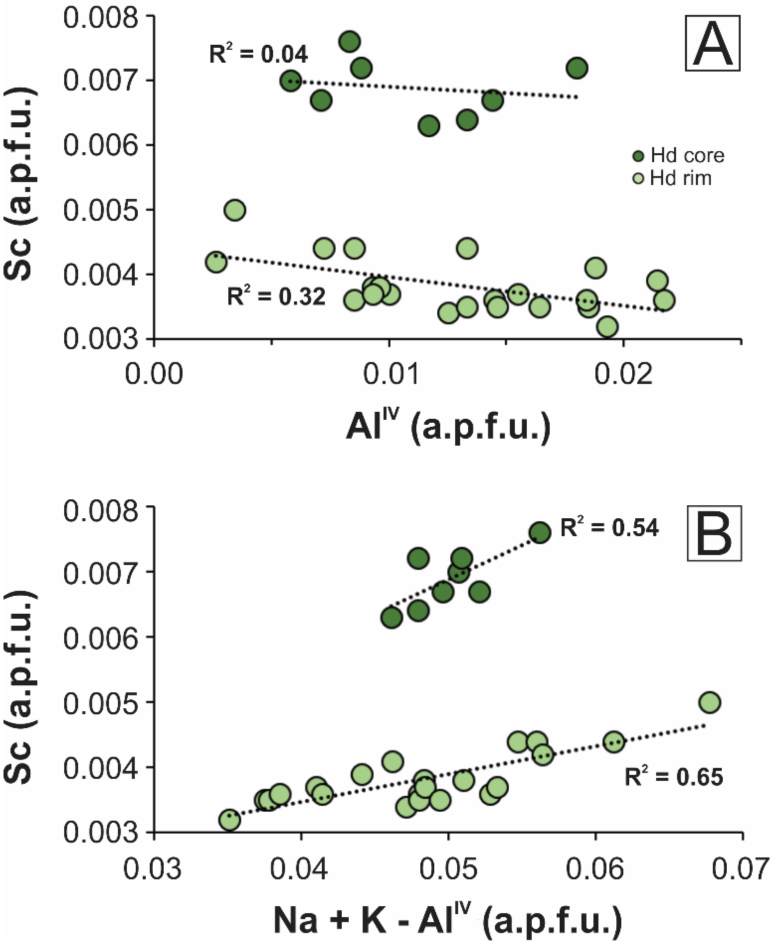

Figure 4.8: Selected hedenbergite cation proportions

A) The Sc content along a transect across a zoned hedenbergite crystal versus the corresponding tetrahedral aluminum content. B) The Sc content along a transect across a zoned hedenbergite crystal versus the corresponding excess Na + K (the transect in B was the same as that in A).

In amphibole, the sites corresponding to the M1 and the M2 sites in clinopyroxene are the M2 and M4 sites. Following the observations of Vasyukova and Williams-Jones (2019) for alkali amphiboles, we propose that Sc in the Crater Lake hastingsite substituted into the smaller M2 site. Although the charge needed to enable the incorporation of Sc in the M2 site was likely balanced by Na^+ and K^+, it was not possible to support this interpretation because these ions are major components of the amphibole (compare Tables 4.2 and 4.3), occupying an A site, which is not present in clinopyroxene.

4.5.4 Mineral-Melt Partitioning and the Magmatic Evolution of the Ferrosyenite

The mineral compositional data and mass balance calculations discussed above indicate that hedenbergite, and to a much lesser extent, hastingsite, are the only significant hosts of Sc in the Crater Lake ferrosyenite. Partition coefficients ($D^{mineral/melt}$) for Sc increase with decreasing melt MgO content for both clinopyroxene (Bedard, 2014) and amphibole (Williams-Jones and Vasyukova, 2018), and the same is true for the D values of olivine and silicate melt (Bedard, 2005). As the Mg# of the clinopyroxene reflects that of the magma from which it crystallized (Sisson and Grove, 1993; Bedard, 2010), it follows that Sc concentrations in the clinopyroxene should increase with decreasing Mg#. This is the opposite to that observed in our samples. Indeed, the cores of the zoned hedenbergite crystals show a weak trend of increasing Sc content with increasing Mg# and the rims of these crystals and the unzoned crystals show the same trend but more strongly so (Fig. 4.7B). Similarly, the Sc content of the primary hastingsite, instead of increasing with decreasing Mg#, remains relatively constant (Fig. 4.7B). We interpret this to indicate that the earlier, more Mg-rich hedenbergite crystallized from a Sc-rich liquid and that the Sc-depleting effect of this crystallization on the magma more than offset the progressive increase in the preference of Sc for the later, Mg-poor hedenbergite. The reason that the effect was more marked for the hedenbergite rims (and unzoned crystals), is that they crystallized *in situ* (see early part of discussion) and recorded a greater part of the crystallization history of the magma than was the case for the hedenbergite cores, which are interpreted to have crystallized in the magma chamber (see earlier discussion). According to this hypothesis, the rate of Sc-depletion of the magma at the time of primary hastingsite crystallization (late) was matched by the rate in the increase in $D_{Sc}^{amph/melt}$ and, consequently, the Sc content of the hastingsite was independent of the Mg#. The distribution of the Sc content of the secondary ferropargasite with Mg#, however, which is indistinguishable from that of unzoned hedenbergite and the rims of zoned hedenbergite crystals, as already noted, reflects the inheritance of the Sc content and Mg# of the hedenbergite that it replaced.

We have tested our interpretation of the behavior of Sc concentration with Mg# in the hedenbergite and hastingsite by constructing a simplified fractional crystallization model to trace the magma MgO and Sc contents, that reflects the changing mineral-melt partition coefficients, and evaluates magma evolution during the crystallization history of the ferrosyenite. The model assumes a closed system and involved crystallizing a magma with a predetermined initial composition in 1 wt. % aliquots, removing the minerals crystallized after each aliquot, calculating the composition of the residual magma and using it as the composition of the next aliquot. The initial magma composition was taken to be the average composition of the fayalite-bearing quartz monzonite estimated from drill core assays (see earlier discussion, Fig. 4.2, Table 4.5). The compositions of fayalite and magnetite used in the model were average compositions and as the Sc concentration was below detection for these minerals (<80 ppm), we assumed their Sc content to be half the detection limit (40 ppm, Table 4.5). The compositions of the hedenbergite and hastingsite fractionating in the model varied with each aliquot of liquid and were based on analyses selected for their Mg# (Fig. 4.7B, Table 4.5). The quality of fit of this model to the data was assessed by observing how well the slopes of the model residual liquids fit the slopes of the bulk rock data on binary oxide plots.

The best fit to the major oxide composition of rocks intersected in drill hole 14026 was obtained by fractionating out a starting assemblage comprising 91 % fayalite, 6.5 % fluorapatite, and 2.5 % zircon in 1 wt. % increments from the initial mass of melt. This assemblage satisfactorily reproduced the observed trend for the first 3 % of the melt crystallized. At this stage, with 97 % of the initial melt volume remaining, it was necessary to allow hedenbergite to begin to crystallize in order to ensure an optimum fit for the subsequent stages of crystallization. The required assemblage comprised 78 % fayalite, 13 % hedenbergite (core composition of zoned crystals), 6.5 % fluorapatite and 2.5 % zircon. The first aliquot of liquid crystallizing with this assemblage, and those preceding it are considered to represent fractionation within the magma chamber. Following emplacement, hedenbergite was the sole mineral to crystallize until 94 % of the initial mass of magma remained, at which point magnetite was introduced onto the liquidus in an assemblage consisting of 95 % hedenbergite and 5 % magnetite. Over the next 1 % of magma crystallization,

Table 4.5: Fractional crystallization model input compositions and results

	initial bulk melt	**Zrn***	**Ap***	**Fa**	**Hd (C)**	**Hd 2**	**Hd 3**	**Hd 4**	**Hd 5**	**Hd 6**	**Mag**	**Hst 1**	**Hst 2**
SiO_2	59.72	33.20		29.69	49.41	49.39	49.49	49.15	48.90	47.28	0.23	42.00	40.88
Al_2O_3	17.40				0.84	0.70	0.71	0.71	0.88	1.62		7.23	7.72
FeO	7.50			66.12	22.52	23.25	23.52	24.85	24.81	27.38	84.33	29.73	31.68
MnO	0.23			3.15	0.77	0.78	0.82	0.83	0.89	0.90	0.88	0.51	0.56
MgO	0.42			1.03	4.01	3.65	3.24	2.93	2.50	2.06		3.18	1.53
CaO	2.50		54.73		21.13	20.97	20.95	20.25	20.47	19.50		10.25	9.96
Na_2O	5.39				0.69	0.72	0.67	0.75	0.99	0.63		2.56	2.76
K_2O	5.59							0.03				1.47	1.52
TiO_2	0.55				0.41	0.34	0.43	0.36	0.45	0.56	14.55	2.42	2.53
P_2O_5	0.37		42.46										0.00
F	0.06		2.81									0.60	0.82
ZrO_2	0.28	66.80											0.00
Sc_2O_3	0.01			0.01	0.22	0.19	0.16	0.14	0.11	0.07	0.01	0.05	0.04
total	100	100	100	100	100	100	100	100	100	100	100	100	100
Sc (ppm)	47	0	0	40	1475	1235	1026	915	693	480	43	334	268
Total Mass Crystallized		1	3	35	38						12	12	
Avg Mass % (Petrography)		1	3	37	37						11	11	

The suffix '' denotes compositions from Petrella, 2012. All other compositions are from the current study* the proportion of magnetite was increased to 50 % of the assemblage. With 92 % of the initial melt volume remaining, hastingsite was brought on to the liquidus, and the proportions of magnetite and hedenbergite were decreased, until the final aliquot of liquid, when the assemblage was adjusted to 30 % magnetite and 70 % amphibole. The model was terminated at this stage as the residual liquid remaining after this last aliquot of crystallization (90 %) corresponded in composition to the most evolved felsic syenite in the bulk rock data set and the onset of pegmatite dominance (in terms of alkalis and silica, Figs. 4.2, 4.9A).

It is noteworthy that the relative proportions of the minerals crystallizing in the model are in good agreement with the volumetric proportions estimated petrographically (Table 4.5). The model reproduces bulk rock major element composition reasonably well, as shown by the fits of the model slopes to those of the bulk rock data set represented in binary oxide plots (Fig. 4.9).

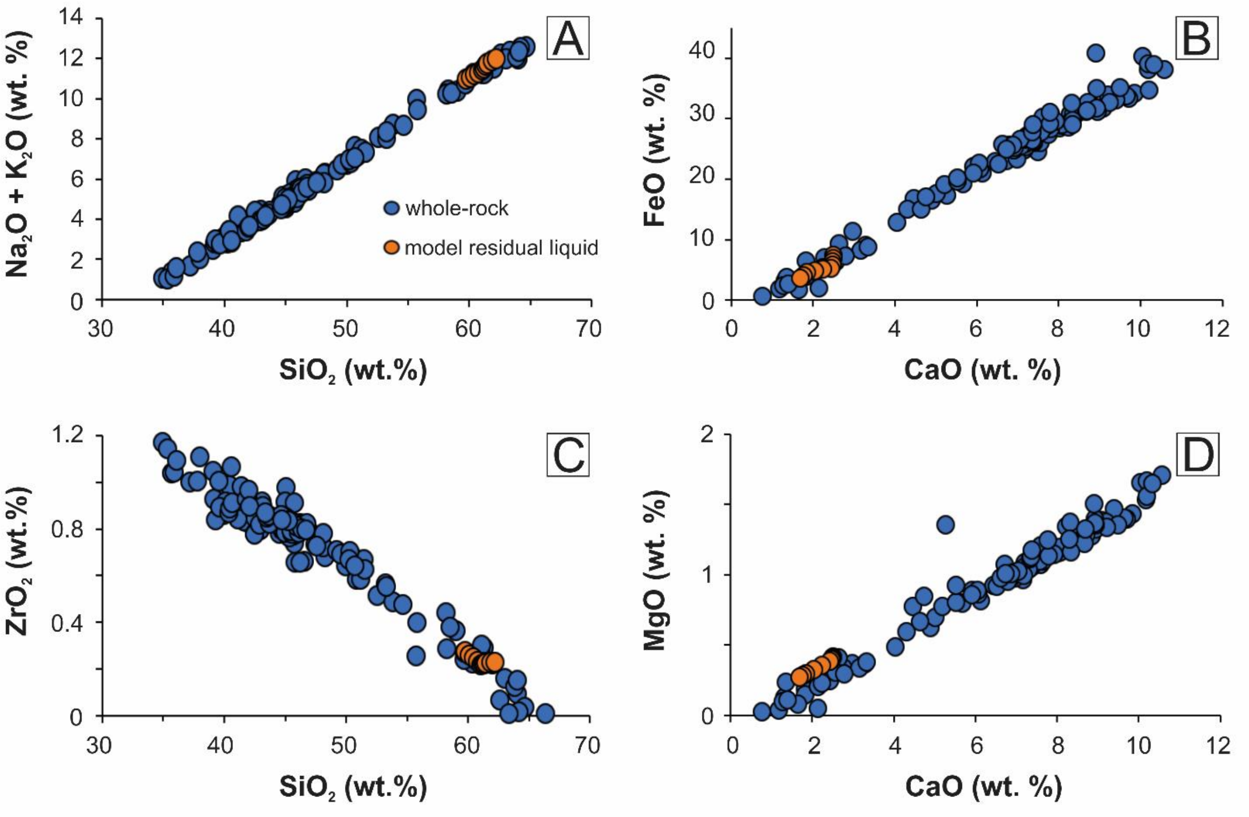

Figure 4.9: Binary major element oxide plots of ferrosyenite compositions

Binary major element oxide plots comparing the composition of the ferrosyenite in drill hole 14026 (blue) to that predicted by the fractional crystallization model employed in this study (orange).

These fits of the modeled to the measured major element composition and the good agreement between the modeled proportions of the fractionated minerals and their estimated proportions in thin section show that the model satisfactorily explains the crystallization of ferrosyenite from an initial bulk composition represented by the average quartz monzonite. Moreover, the model predicts that the ferrosyenite was produced by crystallization of 10% of the initial volume of quartz monzonite liquid, which is realistic given the relative volume proportions of the ferrosyenite to felsic syenites in outcrop and drill core.

Using the residual liquid MgO content calculated by the model following each 1% increment of crystallization, and equations of $D_{Sc}^{mineral/melt}$ as a function of melt MgO content, D values for each mineral were calculated for each stage of the evolution of the residual liquid. The equations for olivine and clinopyroxene were taken from Bedard (2005, 2014) and that for amphibole was taken from Williams-Jones and Vasyukova (2018) (Table 4.6). As a corresponding equation for of $D_{Sc}^{magnetite/melt}$ as a function of melt MgO content was not available to us, we produced one from a least-squares fit of partition data reported in the GERM database (https://earthref.org/KDD/e:21/) (Fig. 4.10, Table 4.6). In Figure 4.11A, we show the predicted evolution of scandium concentration in the residual liquid as a function of the MgO concentration of this liquid and, in Figure 4.11B, the corresponding evolution of the Sc content of the Sc-bearing minerals. Also shown are the changes in the D values of each of these minerals as a function of melt MgO content.

Table 4.6: Equations of scandium mineral-melt partition coefficients as a function of melt MgO content

Mineral	Equation	Source
olivine	LnD = -0.614241LnMgO-0.207763	Bedard, 2005
clinopyroxene	LnD = -0.896683LnMgO+2.57006	Bedard, 2014
amphibole	LnD = -1.0677LnMgO+2.7506	Williams-Jones and Vasyukova, 2018
magnetite	LnD = -0.322LnMgO+0.887562	this study

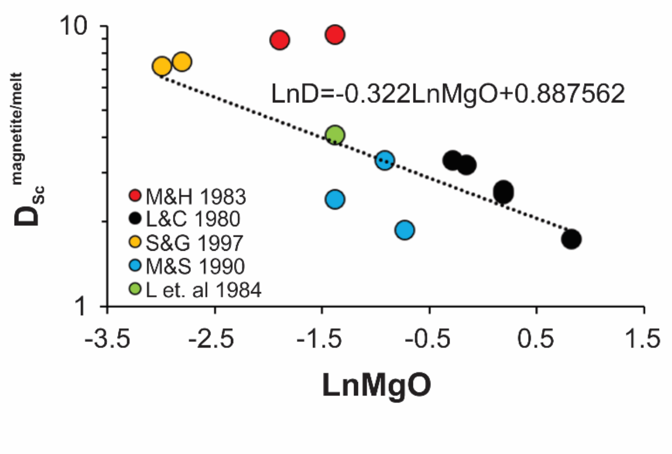

Figure 4.10: Magnetite-silicate melt Sc partition coefficients as a function of melt MgO content

A line of best fit through magnetite-silicate melt Sc partition coefficients versus melt LnMgO content. M&H = Mahood and Hildreth, 1983; L&C = Luhr and Carmichael, 1980; S&G = Streck and Grunder, 1997; M&S = Mahood and Stimac, 1990; L = Luhr et al., 1984

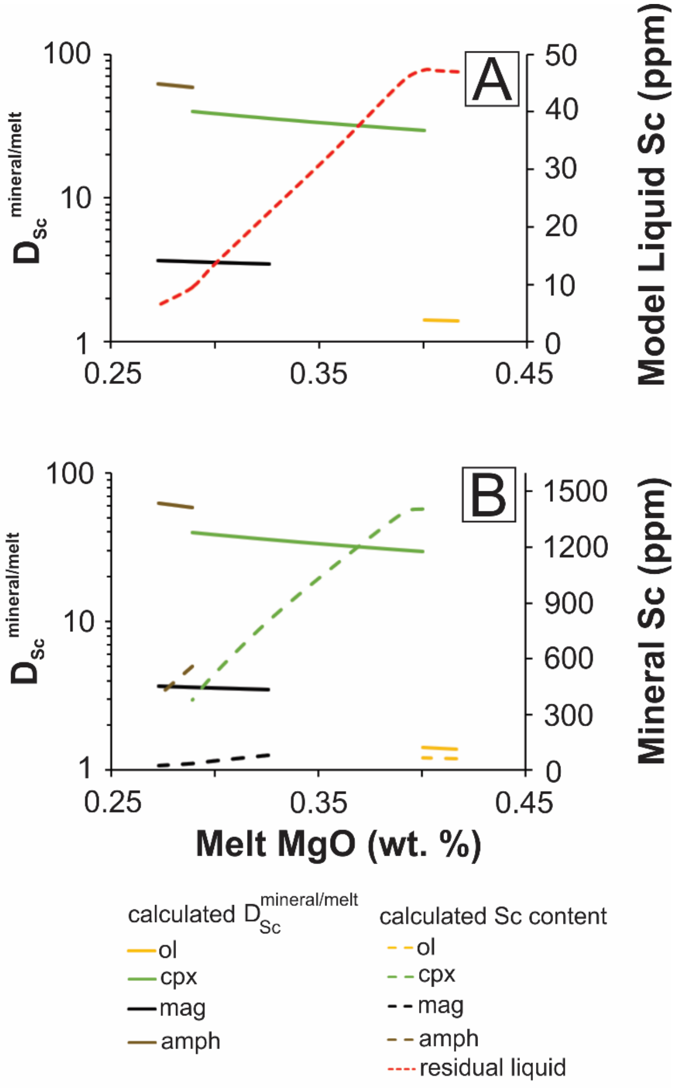

Figure 4.11: Model mineral and liquid Sc contents as a function of melt MgO content

A) The Sc content of the modeled residual liquid and the evolution of mineral-melt Sc partition coefficients as a function of the modeled MgO content of the liquid during the fractional crystallization of the ferrosyenite. B) The calculated Sc content of the minerals crystallizing from the evolving liquid and mineral-melt partition coefficients as a function of the modeled MgO content of the liquid.

From these two diagrams the overarching conclusion is that the decrease in Sc concentration in clinopyroxene, as proposed earlier, was due to fractionation of a large proportion of this mineral and the resulting depletion of Sc in the magma, despite increasing $D_{Sc}^{clinopyroxene/melt}$ values. Although the model described above is relatively simple and does not explicitly consider parameters like temperature and pressure, it reliably reproduces the variations in the measured Sc concentrations with magma MgO content for clinopyroxene. For example, the first clinopyroxene to crystallize (model) contains 1404 ppm, closely matching our richest clinopyroxene core (1465 ppm). Moreover, the range of calculated clinopyroxene Sc contents, from 1404 to 378 ppm, is very similar to the measured range (1465-502 ppm, Fig. 4.11B, Table 4.2). In contrast, the early model amphibole contains 560 ppm Sc, but evolves to 397 ppm Sc, which is significantly higher than the measured range of Sc contents (465-196 ppm, Fig. 4.11B, Table 4.3), and, though the Crater Lake amphibole display a range of Sc concentrations, they are independent of Mg# (Fig. 4.7B). This suggests that some parameter other than melt MgO content (e.g. temperature, pressure, fO_2) has an important effect on $D_{Sc}^{amphibole/melt}$, as is the case, for example, for $D_{LREE}^{amphibole/melt}$ which decreases strongly with increasing pressure (Adam and Green, 1994).

4.5.5 Relationship of the Crater Lake Intrusion to the Mistastin Granite

As mentioned above, the contacts between the Mistastin granite and quartz monzonite, and the quartz monzonite and the Crater Lake syenite, are both gradational, marked only by a steady decrease in quartz content towards the syenite. The absence of chill margins and/or brecciation at these contacts suggests a coeval relationship between the magmas. Also, both the Mistastin granite and Crater Lake syenite have A-type affinity, with the syenites being enriched in incompatible elements relative to the granites. This led Petrella et al. (2014) to conclude that the syenites were differentiates of the granite.

An explanation for the field relationships and trends in bulk rock geochemistry involving these different rock types is that the Crater Lake syenites represent the remnant of a ring dyke system formed by caldera collapse, with the quartz monzonite and Mistastin granite representing the primary magma chamber. According to this hypothesis, a parental magma is emplaced at depth, and after extensive fractionation, including flotation of feldspar, an evolved magma (represented by the quartz monzonite) is produced that is rich in incompatible elements. Caldera collapse causes faulting through the semi-rigid crystal mushes, and evolved melt is drawn upward. This interpretation is consistent with the spatial distribution of the syenites, the fault geometry within the Crater Lake intrusion (Fig. 4.2), and the similarity in the age of the intrusions. If correct, this ring dyke model would require a source chamber at a pressure of 3-5 kbar (Bonin, 2007), consistent with the estimated emplacement pressures of the Mistastin batholith (3.5 kbar, Emslie and Stirling, 1993). We note, also, that a similar model has been proposed for the Blatchford Lake Intrusive

Suite in the Northwest Territories, Canada, to relate the syenites and their host granite (Mumford, 2013).

The above model also effectively explains the observed trends in Sc distribution across rock types. The scandium content of the initial Crater Lake liquid, which we interpret to have had the composition of the average quartz monzonite, was 47 ppm. This reflects a considerable enrichment in Sc relative to typical A-type granites, which contain, on average, only 4 ppm (n= 148, Whalen et al., 1987). Indeed, the average Sc content of the Mistastin granite from drill core assays, is 8 ppm. Fractionation of large proportions of feldspar, in which Sc behaves incompatibly, drives its enrichment in the residual liquid, producing a Sc-rich quartz monzonite magma, consistent with the observation that the Sc content of the Mistastin granite decreases with increasing SiO_2 content (Fig. 4.1B).

4.6 Genetic Model

In summary, we propose the following model for the genesis of the scandium mineralization in the Crater Lake intrusion. Scandium was enriched in the residual liquid of the parental magma following extensive fractionation of feldspar, in which Sc is incompatible, in the Mistastin granite. This residual liquid became the Crater Lake quartz monzonite magma, which was enriched in scandium and iron. Fluorapatite, zircon, fayalite, and the cores of zoned hedenbergite crystals saturated in this magma chamber. Ring faults developed as a result of caldera collapse, and the magma and minerals were emplaced as a slurry into these faults. *In situ* fractionation of unzoned hedenbergite crystals and the rims of zoned hedenbergite crystals, magnetite, and hastingsite, and their physical segregation, with the previously crystallized minerals, formed the ferrosyenite. The extremely high FeO/FeO+MgO (0.95, Table 4.5) content of the quartz monzonite liquid resulted in high partition coefficients for Sc in the hedenbergite and hastingsite, allowing for incorporation of Sc in these minerals at exceptionally high concentrations under magmatic conditions. Physical segregation of hedenbergite and hastingsite in ferrosyenite cumulate rocks through gravitational settling and/or flow differentiation, concentrated the Sc-bearing minerals spatially within the intrusion, resulting in the first known potentially economic scandium deposit hosted by syenite.

Acknowledgements

The research presented in this manuscript was supported financially by a NSERC Collaborative Research development grant to AEW-J, in which Imperial Mining Group Ltd. was the financial partner. This company also provided access to the site, drill core and assay data. We are grateful to Lang Shi for extensive help with the microprobe analyses and to Olga Vasyukova, Pierre Guay and Peter Cashin for many helpful discussions.

References

Adam, J., and Green, T.H., 1994, The effects of pressure and temperature on the partitioning of Ti, Sr and REE between amphibole, clinopyroxene and basanitic melts: Chemical Geology, v. 117, p. 219-233.

Bedard, J.H., 2005, Partitioning coefficients between olivine and silicate melts: Lithos, v. 83, p. 394-419.

Bedard, J.H., 2010, Parameterization of the Fe=Mg exchange coefficient (Kd) between clinopyroxene and silicate melts; Chemical Geology, v. 274, p. 169-176

Bedard, J.H., 2014, Parameterizations of calcic clinopyroxene-melt trace element partition coefficients: Geochemistry Geophysics Geosystems, v. 15, p. 303-336.

Blundy, J.D., Robinson, J.A.C., and Wood, B.J., 1998, Heavy REE are compatible in clinopyroxene on the spinel lherzolite solidus: Earth and Planetary Science Letters, v. 160, p. 493-504.

Bonin, B., 2007, A-type granites and related rocks: Evolution of a concept, problems and prospects: Lithos, v. 97, p. 1-29.

Chao, E.C.T., Back, J.M., Minkin, J.A., and Ren, Y.C., 1992, Host-rock controlled epigenetic, hydrothermal metasomatic origin of the Bayan Obo REE-Fe-Nb ore deposit, Inner Mongolia, P.R.C.: Applied Geochemistry, v. 7, p. 443-458.

Chhangani, S., Kumar Masa, S., Mathew, R.T., Prasad, M.J.N.V., and Sujata, M., 2020, Microstructural evolution in Al-Mg-Sc alloy (AA5024): Effect of thermal treatment, compression deformation and friction stir welding: Materials Science & Engineering A, v. 772, 138790.

Coumans, J.P. and Stix, J., 2016, Caldera collapse at near-ridge seamounts: an experimental investigation: Bulletin of Volcanology, v. 78: 70

Daigle, P.J., 2017, Crater Lake Sc-Nb-REE Project, Quebec, Canada. NI 43-101 Technical Report, prepared by P. Daigle Consulting Services for Peak Mining Corporation, NQ Exploration Inc., and Imperial Mining Group Ltd., 68 p.

David, J., Simard, M., Bandyayera, A., Goutier, J., Hammouche, H., Pilote, P., Leclerc, F., and Dion, C., 2012, Datations U-Pb effectuees dans les provinces du Superieur et de Churchill en 2010-2011 : Geologie quebec, Ministère des Ressources Naturelles et de la Faune (MRNF), RP2012-01, 30 p.

Deer, W.A., Howie, R.A., and Zussman, J., 1992, An Introduction to the Rock-Forming Minerals, Pearson Education Ltd., 696 p.

Dudar, T., Lyschenko, G., and Buhera, M., 2018, Uranium resources of Ukraine: geology, mineralogy, and some mining aspects, (Ed.) Englebrecht, A., Kyiv, 2018

Dumont, R., Fortin, R., Hefford, S., and Dostaler, F., 2010, Serie des cartes geophysiques, parties des SNRC 13L, 13M, 23-I et 23P, leve geophysique Lac Ramusio, Region de Schefferville : Ministère des Ressources naturelles et de la Faune, DP2010-01, 6 p.

Emslie, R.F., and Stirling, J.A.R., 1993, Rapakivi and related granitoids of the Nain Plutonic Suite: Geochemistry, mineral assemblages and fluid equilibria: Canadian Mineralogist, v. 31, p. 821-847.

Emslie, R.F., Hamilton, M.A., and Theriault, R.J., 1994, Petrogenesis of a mid-Proterozoic anorthosite-mangerite-charnockite-granite (AMCG) complex: Isotopic and chemical evidence from the Nain Plutonic Suite: The Journal of Geology, v. 102, p. 539-558.

Fan, H.R., Yang, K.F., Hu, F.F., Liu, S., and Wang, K.Y., 2016, The giant Bayan Obo REE-Nb-Fe deposit, China: Controversy and ore genesis: Geoscience Frontiers, v. 7, p. 335-344.

Filatov Yu, A., Yelagin, V.J., and Zakharrov, V.V., 2000, New Al-Mg-Sc alloys: Materials Science & Engineering A, v. 280, p. 97-101.

Forsythe, L.M., Nielsen, R.L., and Fisk, M.R., 1994, High-field-strength element partitioning between pyroxene and basaltic to dacitic magmas: Chemical Geology, v. 117, p. 107-125.

Francis, D., and Minarik, W., 2008, Aluminum-dependent trace element partitioning in clinopyroxene: Contributions to Mineralogy and Petrology v. 156, p. 439-451.

Halkoaho, T., Ahven, M., Ramo, O.T., Hokka, J., and Huhma, H., 2020, Petrography, geochemistry, and geochronology of the Sc-enriched Kiviniemi ferrodiorite intrusion, eastern Finland: Mineralium Deposita, https://doi.org/10.007/s00126-020-00952-2

Hart, S.R., and Dunn, T., 1993, Experimental Cpx melt partitioning of 24 trace-elements: Contributions to Mineralogy and Petrology, v. 113, p. 1-8.

Hill, E., Wood, B.J., and Blundy, J.D., 2000, The effect of Ca-Tschermaks component on trace element partitioning between clinopyroxene and silicate melt: Lithos, v. 53, p. 203-215.

Hill, E., Blundy, J.D., and Wood, B.J., 2011, Clinopyroxene-melt trace element partitioning and the development of a predictive model for HFSE and Sc: Contributions to Mineralogy and Petrology v. 161, p. 423-438.

Kalashnikov, A.O, Yakovenchuk, V.N., Pakhomovsky, Y.A., Bazai, A.V., Sokharev, V.A., Konopleva, N.G., Mikhailova, J.A., Goryainov, P.M., and Ivanyuk, G.Y., 2016, Scandium of the Kovdor baddeleyite-apatite-magnetite deposit (Murmansk Region, Russia): Mineralogy, spatial distribution and potential resource: Ore Geology Reviews, v. 72, p. 532-537.

Lapin, A.V., Tolstov, A.V., and Kulikova, I.M., 2016, Distrbution of REE, Y, Sc, and Th in the unique complex rare-metal ores of the Tomtor deposit: Geochemistry International, v. 54, p. 1061-1078.

Liferovich, R.P., Subbotin, V.V., Pakhomovsky, Y.A. and Lyalina, M.F., 1998, A new type of scandium mineralization in phoscorites and carbonatites of the Kovdor massif, Russia: Canadian Mineralogist, v. 36, p. 971-980.

Lindstrom, D.J., 1976, Partitioning of ferric iron between diopside and silicate liquid: EOS Transactions of the American Geophysical Union, v. 57, p. 339-339.

Locock, A., 2014, An Excel spreadsheet to classify chemical analyses of amphiboles following the IMA 2012 recommendations: Computers and Geosciences, v. 62, p. 1-11.

Luhr, J.F., and Carmichael, I.S.E., 1980, The Colima Volcanic Complex, Mexico: I. Post-Caldera Andesitres from Volcan Colima: Contributions to Mineralogy and Petrology, v. 71, p. 343-372.

Luhr, J.F., Carmichael, I.S.E., and Varekamp, J.C., 1984, The 1982 eruptions of El Chichon volcano, Chiapas, Mexico: mineralogy and petrology of the anhydrite-bearing pumices: Journal of Volcanology and Geothermal Research v. 23: p. 69-108.

Lundstrom, C.C., Shaw, H.F., Ryerson, F.J., Phinney, D.L., Gill, J.B. and Williams, Q., 1994, Compositional controls on the partitioning of U, Th, Ba, Pb, Sr and Zr between clinopyroxene and haplobasaltic melts – implications for uranium series disequilibria in basalts: Earth and Planetary Science Letters, v. 128, p. 407-423.

Lundstrom, C.C., Shaw, H.F., Ryerson, F.J., Williams, Q., and Gill, J., 1998, Crystal chemical control of clinopyroxene-melt partitioning in the Di-Ab-An system: implications for elemental fractionations in the depleted mantle: Geochimica et Cosmochimica Acta, v. 62, p. 2849-2862.

Mahood, G.A., and Hildreth, E.W., 1983, Large partition coefficients for trace elements in high-silica rhyolites: Geochimica et Cosmochimica Acta, v. 47, p. 11-30.

Mahood, G.A., and Stimac, J.A., 1990, Trace-element partitioning in pantellerites and trachytes: Geochimica et Cosmochimica Acta, v. 54, p. 2257-2276.

Mollo, S., Blundy, J.D., Iezzi, G., Scarlato, P. and Langone, A., 2013, The partitioning of trace elements between clinopyroxene and trachybasaltic melt during rapid cooling and crystal growth: Contributions to Mineralogy and Petrology, v. 166, p. 1633-1654.

Mollo, S., Forni, F., Bachmann, O., Blundy, J.D., De Astis, G., and Scarlato, P., 2016, Trace element partitioning between clinopyroxene and trachy-phonolitic melts: A case study from the Campanian Ignimbrite (Campi Flegrei, Italy): Lithos, v. 252-253, p. 160-172.

Morimoto, N., 1988, Nomenclature of pyroxenes: Mineralogy and Petrology, v. 39, p. 55-76.

Müller, A., Ihlen, P.M., Snook, B., Larsen, R.B., Flem, B., Bingen, B., and Williamson, B., 2015, The chemistry of quartz in granitic pegmatites of southern Norway: Petrogenetic and economic implications: Economic Geology, v. 110, p. 1737-1757.

Mumford, T.R., 2013, Petrology of the Blatchford Lake Intrusive Suite, Northwest Territories, Canada: Unpublished Ph.D. thesis, Ottawa, Canada, Carleton University, 240 p.

Murdock, T.G., 1963, Mineral resources of the Malagasy Republic: United States Bureau of Mines, Information Circular 8196, p. 147.

Peck, W.H., Clechenko, C.C., Hamilton, M.A., and Valley, J.W., 2010, Oxygen isotopes in the Grenville and Nain AMCG suites: Regional aspects of the crustal component in massif anorthosites: Canadian Mineralogist, v. 48, p. 763-786.

Petrella, L., 2012, The nature and origin of REE mineralization in the Misery Syenitic intusion, Northern Quebec, Canada: Unpublished M.Sc. thesis, Montreal, Canada, McGill University, 152 p.

Petrella, L., Williams-Jones, A.E., Goutier, J., and Walsh, J., 2014, The nature and origin of the rare earth element mineralization in the Misery Syenitic Intrusion, Northern Quebec, Canada: Economic Geology, v. 109, p. 1643-1666.

Ray, G.L., Shimizu, N., and Hart, S.R., 1983, An ion microprobe study of the partitioning of trace-elements between clinopyroxene and liquid in the system diopside-albite-anorthite: Geochimica et Cosmochimica Acta, v. 47, p. 2131-2140.

Scarlato, P., Mollo, S., Blundy, J.D., Iezzi, G., and Tiepolo, M., 2014, The role of natural solidification paths on REE partitioning between clinopyroxene and melt: Bulletin of Volcanology, v. 76, 810.

Shannon, R.D., 1976, Revised effective ionic-radii and systematic studies of interatomic distances in halides and chalcogenides: Acta Crystallographica Section A, v. 32, p. 751-767.

Shimazaki, H., Yang, Z., Miyawaki, R., and Shigeoka, M., 2008, Scandium-bearing minerals in the Bayan Obo Nb-REE-Fe deposit, Inner Mongolia, China: Resource Geology, v. 58, p. 80-86.

Sisson, T.W., and Grove, T.L., 1993, Experimental investigations of the role of H2O in calc-alkaline differentiation and subduction zone magmatism: Contributions to Mineralogy and Petrology, v. 113, p. 143-166.

Skulski, T., Minarik, W., and Watson, E.B., 1994, High-pressure experimental trace-element partitioning between clinopyroxene and basaltic melts: Chemical Geology, v. 117, p. 127-147.

Smith, M.P., and Henderson, P., 2000, Preliminary fluid inclusion constraints on fluid evolution in the Bayan Obo Fe-REE-Nb deposit, Inner Mongolia, China: Economic Geology, v. 95, p. 1371-1388.

Sparks, R.S., Huppert, H.E., Koyaguchi, T., and Hallworth, M.A., 1993, Origin of modal and rhythmic igneous layering by sedimentation in a convecting magma chamber: Nature, v. 361, p. 246-249

Streck, M.J., and Grunder, A.L., 1997, Compositional gradients and gaps in high-silica rhyolites of the Rattlesnake Tuff, Oregon: Journal of Petrology, v. 38, p. 133-163.

Sun, C.G., and Liang, Y., 2012, Distribution of REE between clinopyroxene and basaltic melt along a mantle adiabat: effects of major element composition, water, and temperature: Contributions to Mineralogy and Petrology, v. 163, p. 807-823.

Sun, C.G., and Liang, Y., 2013, The importance of crystal chemistry on REE partitioning between mantle minerals (garnet, clinopyroxene, orthopyroxene, and olivine) and basaltic melts: Chemical Geology, v. 358, p. 23-36.

Tarkhanov, A.V., Kulayev, A.R., Petrin, A.V., and Kozyr'kov, V.D., 1992, The Zheltorechensk vanadium-scandium deposit: International Geology Review, v. 34, p. 496-502.

Ubide, T., Mollo, S., Zhao, J., Nazzari, M., and Scarlato, P., 2019, Sector-zoned clinopyroxene as a recorder of magma history, eruption triggers, and ascent rates: Geochimica et Cosmochimica Acta, v. 251, p. 265-283.

Vannucci, R., Shimizu, N., Bottazzi, P., Ottolini, L., Piccardo, G.B., and Rampone, E., 1991, Rare earth and trace element geochemistry of clinopyroxenes from the Zabargad peridotite-pyroxenite association: Journal of Petrology, Special Lherzolites Issue, p. 255-269.

Vasylyev, O.D., Brodnikovskyi, Y.M., V'yunov, O.I., Kovalenko, L.L., Yanchevskii, O.Z., and Belous, A.G., 2018, Zirconium oxide stabilized by scandium (III) and cerium (IV) complex oxides as the basis for preparation of thick films and multilayer structures for low temperature (600 degrees C) fuel cell: French-Ukrainian Journal of Chemistry, v. 6, p. 16-20.

Vasyukova, O.V. and Williams-Jones, A.E., 2019, Tracing the evolution of a fertile REE granite by modelling amphibole-melt partitioning, the Strange Lake story: Chemical Geology, v. 514, p. 79-89.

Whalen, J.B., Currie, K.L., and Chappell. B.W., 1987, A-type granites: geochemical characteristics, discrimination and petrogenesis: Contributions to Mineralogy and Petrology, v. 95, p. 407-419.

Whitney, D.L., and Evans, B.W., 2010, Abbreviations for names of rock-forming minerals: American Mineralogist, v. 95, p. 185-187.

Willey, L.A., 1971, Aluminum scandium alloy, U.S. Patent 3 (619), 181.

Williams-Jones, A.E., and Vasyukova, O.V., 2018, The economic geology of Scandium, the runt of the rare earth element litter: Economic Geology, v. 113, p. 973-998.

Wood, B.J., and Trigila, R., 2001, Experimental determination of aluminous clinopyroxene-melt partition coefficients for potassic liquids, with application to the evolution of the Roman province potassic magmas: Chemical Geology, v. 172, p. 213-223.

Woolley, A.R., 2001, Alkaline Rocks and Carbonatites of the World, Part 3: Africa. London: Geological Society Publishing House

Yao, L.J., Sun, C.G. and Liang, Y., 2012, A parameterized model for REE distribution between low-Ca pyroxene and basaltic melts with applications to REE partitioning in low-Ca pyroxene along a mantle adiabat and during pyroxenite derived melt and peridotite interaction: Contributions to Mineralogy and Petrology, v. 164, p. 261-280.

Zhao, C., 1987, Bayan Obo scandium: Baogangkeji, v. 04, p. 1-4.

Chapter 5 – Conclusions

5.1 General Conclusions

The mineral, bulk rock, and isotope study of the Eldor Carbonatite Complex and its Ashram REE deposit resulted in new discoveries that impact our understanding of the behaviour of the REE in carbonatites. These are summarized in the following paragraphs.

This study provides insights into the magmatic evolution and hydrothermal activity in the Eldor Carbonatite Complex that led to the concentration of the REE, and the unusual MHREE-enriched zone. Magmatic processes were important in determining the initial distribution of the REE. There were two stages of carbonatite emplacement, each geochemically distinct. The first stage produced the Rim and BD zones, and involved a magma with a low concentration of REE, and a high concentration of P. This was followed by the emplacement of a second carbonatite magma (likely an evolved batch of the earlier magma), represented by the B, A and MHREO zones, and characterized by high REE and F and low P contents. Both magmas crystallized their own distinct, primary apatite, though apatite was considerably more abundant in the Rim and BD zones (Stage 1 magma). Emplacement of the second carbonatite magma (Stage 2) was accompanied by brecciation. This magma exsolved an acidic, REE-F-bearing H_2O-CO_2 fluid that altered the B, A, and MHREO zones, as well as the BD zone (altered Rim dolomite carbonatite), using the breccia as a conduit to access the different REE-bearing units, with successive pulses armouring the pathway (i.e., reducing its pH buffering capacity), preventing neutralization and allowing for the transport of a large mass of the REE.

The REE mineralization at Ashram is hydrothermal in origin and was produced through a series of fluid-mediated replacement reactions. On interaction with its host (the Stage 2 carbonatites and late Stage 1 dolomite carbonatite), the exsolved REE-F-bearing H_2O-CO_2 fluid altered primary apatite to monazite and fluorite. In the apatite-poor B, A and MHREO zones, prolonged fluid-rock interaction resulted in nearly complete consumption of apatite, whereas in the apatite-rich BD zone, this was not the case. Evolution of the hydrothermal system led to the subsequent replacement of monazite by bastnäsite in the BD zone and deposition of fluorite in the B, A, and MHREO zones. The latter buffered the fluoride activity to very low levels, thereby largely precluding the replacement of monazite by bastnäsite in these zones. Xenotime was a late, trace mineral that saturated in the fluid after precipitation of most of the LREE as monazite. Finally, Nb was remobilized and deposited as trace aeschynite-(Nd) by late-stage fluids.

The deposit-scale zonation of the mineralogy and the REE distribution, including the zone of unusual MHREE enrichment, is attributed to the cooling and pH buffering of the hydrothermal fluid as it travelled upward and outward from the breccia. The fluid was at its highest temperature as it exited this conduit and its pH was buffered only weakly by siderite of the MHREO zone. This ensured that monazite proximal to the conduit was strongly depleted in La and enriched in Th (monazite-(Nd)). On leaving the breccia, the fluid cooled and was gradually buffered to higher pH as it passed through dolomitic rocks with progressively lower Fe content, allowing it to deposit monazite with correspondingly higher proportions of La and lower proportions of Th. In summary, the lightest REE were able to travel the furthest from the breccia and produce the deposit scale separation of the light from the heavy REE, which is a striking feature of the Ashram carbonatite. The evolving composition of the fluid and its interaction with host rocks of variable bulk composition and pH buffering capacity resulted in a REE-phosphate-rich deposit with large-scale, antipathic separation of monazite + fluorite and bastnäsite + apatite. Ashram had a long-lived history in which the combination of magmatic zone-refinement and hydrothermal mobilization contributed to the formation of a potentially economic carbonatite-hosted REE deposit.

The importance of hydrothermal alteration as a mineralizing process at Ashram was further demonstrated by a mass balance calculation that traced each REE individually across all minerals from primary magmatic to secondary hydrothermal stages in all zones of the Ashram deposit. The calculation showed quantitatively that at Ashram, all the REE were mobilized by hydrothermal fluids to be concentrated in REE minerals. The degree to which the individual elements were concentrated in REE minerals, however, decreased with increasing atomic number, and with decreasing fluid flow (fluid:rock ratio), such that, in all zones, La is more strongly concentrated than Lu, and across zones, La is most strongly concentrated in areas of greatest fluid flow. These trends are the result of the relative thermodynamic stability of the various REE-complexes and REE minerals in aqueous fluids. Overall, magmatic and non-REE phases host a low proportion of the whole-rock REE budget, especially the LREE.

The case study of Sc mineralization in the Crater Lake intrusion highlights the contrasting geochemical behaviour of this element with that of the other REE. In this contribution, whole-rock geochemical and mineral chemical data were used to establish the distribution of the scandium in the ferrosyenite and model the processes responsible for its concentration to potentially economic levels. This study is significant because Crater Lake is the first Sc deposit to have been discovered in Canada, and the first known syenite-hosted Sc deposit anywhere. At Crater Lake, Sc was enriched in the residual liquid of the parental magma following extensive fractionation of feldspar, in which Sc is incompatible, in the Mistastin granite. This residual liquid became the Crater Lake quartz monzonite magma, which was enriched in scandium and iron. Fluorapatite, zircon, fayalite, and the cores of zoned hedenbergite crystals saturated in this magma chamber. Ring faults developed as a result of caldera collapse, and the magma and minerals were emplaced as a slurry into these faults. *In situ* fractionation of unzoned hedenbergite crystals and the rims of zoned hedenbergite crystals, magnetite, and hastingsite, and their physical segregation, with the previously crystallized minerals, formed the ferrosyenite. The extremely high FeO/FeO+MgO (0.95) content of the quartz monzonite liquid resulted in high partition coefficients for Sc in the hedenbergite and hastingsite, allowing for incorporation of Sc in these minerals at exceptionally high concentrations under magmatic conditions. Physical segregation of hedenbergite and hastingsite in ferrosyenite cumulate rocks through gravitational settling and/or flow differentiation, concentrated the Sc-bearing minerals spatially within the intrusion, resulting in the first known potentially economic scandium deposit hosted by syenite.

5.2 Contributions to the scientific community

This study of the Ashram carbonatite-hosted lanthanide and Y and the Crater Lake syenite-hosted Sc deposits presents several new findings which contribute to the understanding of the contrasting geochemical behaviour of Sc and the other REE, and the different processes by which these metals may be concentrated. In Chapter 2, the processes that concentrated the REE, fractionated the HREE, and led to the formation of a REE-phosphate dominated deposit were identified. These were transport of the REE by carbonatite-derived hydrothermal fluid, alteration of primary phosphate minerals, interaction of the fluid with rocks of variable pH buffering capacity, and suppression of REE-fluorocarbonate deposition due to abundant precipitation of fluorite. The mass balance calculation quantitatively demonstrated that all the REE were mobilized by hydrothermal fluids to be concentrated in REE minerals, and that the degree to which the individual elements were concentrated in REE minerals increased with decreasing atomic number and with increasing fluid flow. This calculation has not been done previously for carbonatite-hosted REE deposits. Lastly, the Crater Lake study showed that scandium may be concentrated to potentially economic levels entirely by magmatic processes, namely, enrichment in the parental melt by protracted fractionation of feldspar, early crystallization of clinopyroxene in the quartz monzonite liquid, and physical segregation of clinopyroxene in cumulate rocks.

The overarching conclusion of this thesis, as exemplified by the Crater Lake and Ashram deposits is that, due to its compatible behaviour, Sc is concentrated by magmatic processes in early-forming minerals. This is in stark contrast to the lanthanides and Y, which are incompatible elements and as such, are concentrated by hydrothermal fluids in late-forming minerals.

Appendices

The appendices are organized by chapter and contain further details on the analytical methods and the individual measurements which were summarized in the tables of the article manuscripts.

Appendix 2.7: Analytical conditions and standards used during Electron Microprobe analyses

	Apatite			**Monazite**			**Bastnäsite**		
	Standard	Counting Time (s)	Detection Limit (ppm)	Standard	Counting Time (s)	Detection Limit (ppm)	Standard	Counting Time (s)	Detection Limit (ppm)
La	MAC-La	20	1646	MAC-La	20	4568	MAC-La	20	4251
Ce	MAC-Ce	20	1594	MAC-Ce	20	4873	MAC-Ce	20	4036
Pr	MAC-Pr	20	923	MAC-Pr	20	1663	MAC-Pr	20	1404
Nd	MAC-Nd	20	787	MAC-Nd	20	1172	MAC-Nd	20	1021
Sm	MAC-Sm	20	874	MAC-Sm	20	1527	MAC-Sm	20	1336
Eu	MAC-Eu	20	900	MAC-Eu	20	1551	MAC-Eu	20	1350
Gd	MAC-Gd	20	979	MAC-Gd	20	1615	MAC-Gd	20	1429
Tb									
Dy	MAC-Dy	20	1074	MAC-Dy	20	1786	MAC-Dy	20	1571
Y	MAC-Y	20	748	MAC-Y	20	1028	MAC-Y	20	929
Ho	MAC-Ho	20	1086	MAC-Ho	20	1791	MAC-Ho	20	1552
Er									
Tm									
Yb									
Lu									
Th	ThO2	20	471	ThO2	20	886	ThO2	20	827
U	UO2	20	795	UO2	20	782	UO2	20	706
Ca	Apatite	20	190	Apatite	20	259	Apatite	20	236
P	Apatite	20	345	Apatite	20	488	Apatite	20	443
F	Apatite	20	2926	Apatite	20	4532	Apatite	20	2001
Si	Diopside	20	260	Diopside	20	595	Diopside	20	526
Cl	Vanadinite	20	124	Vanadinite	20	201	Vanadinite	20	177
Pb	PbS	20	684	PbS	20	719	PbS	20	631
Fe	Fe2O3	20	665	Fe2O3	20	1463	Fe2O3	20	1348
Na	Albite	20	328	Albite	20	561	Albite	20	509
Sr	Sr_Feldspar	20	604	Sr_Feldspar	20	649	Sr_Feldspar	20	587
Ba	Ba_Feldspar	20	1800	Ba_Feldspar	20	4346	Ba_Feldspar	20	3688
Mg									
Mn									
Al									

Appendix 2.1A: Continued

	Xenotime			**Calcite, Dolomite, Siderite**		
	Standard	Counting Time (s)	Detection Limit (ppm)	Standard	Counting Time (s)	Detection Limit (ppm)
La						
Ce						
Pr						
Nd	MAC-Nd	20	2199			
Sm	MAC-Sm	20	2244			
Eu	MAC-Eu	20	2370			
Gd	MAC-Gd	20	2447			
Tb	MAC-Tb	20	1562			
Dy	MAC-Dy	20	1755			
Y	MAC-Y	20	960			
Ho	MAC-Ho	20	1654			
Er	MAC-Er	20	1731			
Tm	MAC-Tm	20	1810			
Yb	MAC-Yb	20	891			
Lu	MAC-Lu	20	924			
Th	ThO2	20	1285			
U	UO2	20	1248			
Ca	Apatite	20	233	Calcite	20	272
P	Apatite	20	368			
F	Apatite	20	2592			
Si	Diopside	20	413			
Cl						
Pb	PbS	20	1357			
Fe	Fe2O3	20	527	Siderite	20	423
Na						
Sr				Sr_Feldspar	40	359
Ba				Ba_Feldspar	40	1670
Mg				Dolomite	20	284
Mn				Siderite	20	356
Al				Garnet	20	259

Appendix 2.2: Major element oxide compositions and cation proportions for carbonate minerals in the Eldor Carbonatites

		Weight percent							**Apfu (O = 6)**						
Sample	**Unit**	**CaO**	**MgO**	**FeO**	**MnO**	**SrO**	**CO2**	**Total**	**Ca**	**Mg**	**Fe**	**Mn**	**Sr**	**C**	**Total**
CV15004-carb-234	A	27.63	13.08	11.63	1.72	0.60	45.34	100	0.963	0.634	0.316	0.047	0.011	2.014	3.986
CV15004-carb-237	A	28.46	15.37	8.21	1.35	0.12	46.48	100	0.971	0.730	0.219	0.036	0.002	2.021	3.979
CV15004-carb-239	A	28.66	19.35	2.02	0.16	0.44	49.37	100	0.938	0.881	0.052	0.004	0.008	2.059	3.941
CV15004-carb-240	A	28.34	17.76	2.65	0.17	0.64	50.44	100	0.923	0.805	0.067	0.004	0.011	2.094	3.906
CV15004-carb-241	A	27.61	13.95	9.35	1.58	0.23	47.27	100	0.940	0.661	0.249	0.043	0.004	2.051	3.949
CV15004-carb-242	A	27.87	14.22	9.14	1.60	0.23	46.94	100	0.951	0.675	0.243	0.043	0.004	2.041	3.959
CV15005-carb-235	A	28.09	14.11	10.48	1.55	0.29	45.49	100	0.973	0.680	0.283	0.042	0.005	2.008	3.992
CV15005-carb-236	A	29.24	18.76	3.79	0.26	0.20	47.76	100	0.973	0.869	0.098	0.007	0.004	2.025	3.975
CV15005-carb-266	A	27.88	14.04	10.40	1.80	0.22	45.66	100	0.964	0.676	0.281	0.049	0.004	2.013	3.987
CV15005-carb-267	A	27.92	13.63	11.20	1.76	0.22	45.26	100	0.971	0.660	0.304	0.048	0.004	2.006	3.994
CV15005-carb-269	A	27.13	14.65	7.56	1.35	0.14	49.17	100	0.905	0.680	0.197	0.036	0.003	2.090	3.910
CV15005-carb-270	A	28.33	19.01	3.47	0.33	0.68	48.17	100	0.940	0.877	0.090	0.009	0.012	2.036	3.964
CV15005-carb-272	A	29.51	20.68	1.69	0.15	0.42	47.55	100	0.978	0.953	0.044	0.004	0.008	2.007	3.993
CV15005-carb-273	A	28.83	20.38	1.70	0.14	0.20	48.76	100	0.945	0.930	0.043	0.004	0.003	2.037	3.963
CV15005-carb-274	A	28.79	20.01	2.47	0.18	0.44	48.11	100	0.951	0.920	0.064	0.005	0.008	2.026	3.974
CV15005-carb-275	A	28.01	15.30	8.29	1.54	0.29	46.57	100	0.956	0.726	0.221	0.041	0.005	2.025	3.975
CV15005-carb-276	A	28.06	15.56	7.91	1.51	0.30	46.66	100	0.956	0.737	0.210	0.041	0.006	2.025	3.975
CV15005-carb-277	A	28.04	14.98	8.89	1.56	0.33	46.20	100	0.961	0.715	0.238	0.042	0.006	2.019	3.981
CV15005-carb-278	A	27.93	15.02	8.61	1.96	0.17	46.32	100	0.956	0.716	0.230	0.053	0.003	2.021	3.979
CV15005-carb-279	A	28.38	16.26	7.05	1.32	0.16	46.83	100	0.962	0.767	0.187	0.035	0.003	2.023	3.977
CV15005-carb-280	A	28.33	15.92	7.65	1.40	0.29	46.42	100	0.966	0.755	0.204	0.038	0.005	2.016	3.984
CV15020-carb-379	A	28.54	16.96	6.44	1.19	0.25	46.62	100	0.967	0.800	0.170	0.032	0.005	2.013	3.987
CV15020-carb-380	A	28.60	16.80	6.69	1.37	0.17	46.37	100	0.972	0.794	0.177	0.037	0.003	2.008	3.992
CV15020-carb-381	A	28.67	16.70	6.67	1.34	0.16	46.47	100	0.974	0.789	0.177	0.036	0.003	2.011	3.989
CV15020-carb-382	A	28.57	17.35	6.00	1.10	0.21	46.77	100	0.965	0.816	0.158	0.029	0.004	2.014	3.986
CV15020-carb-383	A	28.54	17.17	5.89	1.20	0.20	47.01	100	0.963	0.806	0.155	0.032	0.004	2.021	3.979
CV15020-carb-384	A	28.36	16.92	6.52	1.32	0.17	46.71	100	0.961	0.797	0.172	0.035	0.003	2.016	3.984
CV15020-carb-385	A	28.67	16.75	6.45	1.22	0.19	46.72	100	0.971	0.789	0.171	0.033	0.003	2.016	3.984
CV15020-carb-386	A	28.66	16.37	7.03	1.05	0.31	46.58	100	0.974	0.774	0.186	0.028	0.006	2.016	3.984
CV15020-carb-387	A	28.67	16.71	7.14	1.04	0.29	46.16	100	0.977	0.792	0.190	0.028	0.005	2.004	3.996
CV15020-carb-389	A	28.38	17.50	5.95	1.34	0.15	46.67	100	0.960	0.823	0.157	0.036	0.003	2.011	3.989
CV15020-carb-390	A	28.73	18.75	4.61	0.25	0.50	47.15	100	0.963	0.874	0.121	0.007	0.009	2.013	3.987

CO_2 contents were calculated from the difference between the analytical total and 100 wt. %

Appendix 2.2: Continued

		Weight percent							**Apfu (O = 6)**						
Sample	**Unit**	**CaO**	**MgO**	**FeO**	**MnO**	**SrO**	**CO2**	**Total**	**Ca**	**Mg**	**Fe**	**Mn**	**Sr**	**C**	**Total**
CV15020-carb-391	A	28.79	16.97	6.83	1.10	0.27	46.05	100	0.981	0.804	0.182	0.030	0.005	1.999	4.001
CV15020-carb-392	A	29.10	16.30	7.94	0.55	0.14	45.97	100	0.994	0.775	0.212	0.015	0.003	2.001	3.999
CV15020-carb-393	A	28.45	14.26	10.50	1.57	0.00	45.23	100	0.987	0.688	0.284	0.043	0.000	1.999	4.001
CV15020-carb-394	A	29.03	17.97	5.38	0.52	0.02	47.09	100	0.975	0.840	0.141	0.014	0.000	2.015	3.985
CV15301-carb-375	A	27.75	14.56	10.20	1.55	0.26	45.68	100	0.958	0.700	0.275	0.042	0.005	2.010	3.990
CV15301-carb-376	A	27.99	13.84	10.97	1.59	0.24	45.38	100	0.972	0.669	0.297	0.043	0.005	2.007	3.993
CV15301-carb-377	A	28.21	15.43	8.86	1.39	0.27	45.84	100	0.969	0.738	0.237	0.038	0.005	2.006	3.994
CV15301-carb-378	A	28.27	15.74	8.17	1.31	0.21	46.31	100	0.965	0.748	0.218	0.035	0.004	2.015	3.985
CV15376-carb-246	A	28.45	14.99	8.69	2.07	0.17	45.62	100	0.980	0.719	0.234	0.056	0.003	2.004	3.996
CV15376-carb-247	A	28.81	15.92	8.38	0.54	0.16	46.18	100	0.984	0.756	0.223	0.015	0.003	2.009	3.991
CV15376-carb-248	A	28.09	14.00	10.84	1.42	0.31	45.34	100	0.975	0.676	0.294	0.039	0.006	2.005	3.995
CV15376-carb-249	A	28.29	14.87	8.60	2.20	0.22	45.82	100	0.974	0.712	0.231	0.060	0.004	2.010	3.990
CV15376-carb-250	A	28.13	13.59	11.65	1.45	0.26	44.93	100	0.982	0.660	0.317	0.040	0.005	1.998	4.002
CV15376-carb-251	A	28.29	13.74	11.36	1.38	0.26	44.96	100	0.986	0.666	0.309	0.038	0.005	1.997	4.003
CV15376-carb-252	A	28.19	11.61	13.79	1.26	0.42	44.73	100	0.993	0.569	0.379	0.035	0.008	2.008	3.992
CV15376-carb-252	A	28.19	11.61	13.79	1.26	0.42	44.73	100	0.993	0.569	0.379	0.035	0.008	2.008	3.992
CV15376-carb-253	A	28.43	11.54	14.12	1.30	0.35	44.28	100	1.006	0.568	0.390	0.036	0.007	1.997	4.003
CV15376-carb-253	A	28.43	11.54	14.12	1.30	0.35	44.28	100	1.006	0.568	0.390	0.036	0.007	1.997	4.003
CV15376-carb-254	A	28.32	12.25	13.56	1.38	0.28	44.22	100	1.000	0.602	0.374	0.039	0.005	1.990	4.010
CV15376-carb-254	A	28.32	12.25	13.56	1.38	0.28	44.22	100	1.000	0.602	0.374	0.039	0.005	1.990	4.010
CV15376-carb-255	A	27.77	11.83	14.51	1.45	0.31	44.14	100	0.984	0.583	0.401	0.040	0.006	1.993	4.007
CV15376-carb-255	A	27.77	11.83	14.51	1.45	0.31	44.14	100	0.984	0.583	0.401	0.040	0.006	1.993	4.007
CV15376-carb-256	A	28.27	14.73	9.60	1.43	0.26	45.71	100	0.975	0.707	0.258	0.039	0.005	2.008	3.992
CV15376-carb-257	A	27.67	16.06	8.00	1.03	0.31	46.93	100	0.939	0.758	0.212	0.028	0.006	2.029	3.971
CV15376-carb-258	A	27.45	11.88	13.87	1.56	0.29	44.95	100	0.965	0.581	0.380	0.043	0.005	2.013	3.987
CV15376-carb-258	A	27.45	11.88	13.87	1.56	0.29	44.95	100	0.965	0.581	0.380	0.043	0.005	2.013	3.987
CV15376-carb-259	A	26.93	11.34	14.82	1.58	0.28	45.05	100	0.948	0.555	0.407	0.044	0.005	2.020	3.980
CV15376-carb-259	A	26.93	11.34	14.82	1.58	0.28	45.05	100	0.948	0.555	0.407	0.044	0.005	2.020	3.980
CV15376-carb-260	A	27.39	12.15	12.84	1.51	0.26	45.85	100	0.953	0.588	0.349	0.042	0.005	2.032	3.968
CV15376-carb-260	A	27.39	12.15	12.84	1.51	0.26	45.85	100	0.953	0.588	0.349	0.042	0.005	2.032	3.968
CV15376-carb-261	A	27.15	11.89	13.91	1.51	0.28	45.25	100	0.952	0.580	0.381	0.042	0.005	2.020	3.980
CV15376-carb-261	A	27.15	11.89	13.91	1.51	0.28	45.25	100	0.952	0.580	0.381	0.042	0.005	2.020	3.980

CO_2 contents were calculated from the difference between the analytical total and 100 wt. %

Appendix 2.2: Continued

		Weight percent							Apfu (O = 6)						
Sample	**Unit**	**CaO**	**MgO**	**FeO**	**MnO**	**SrO**	**CO2**	**Total**	**Ca**	**Mg**	**Fe**	**Mn**	**Sr**	**C**	**Total**
CV15376-carb-262	A	27.45	10.73	15.09	1.57	0.27	44.89	100	0.969	0.527	0.416	0.044	0.005	2.019	3.981
CV16007-carb-288	A	28.65	15.29	8.24	1.12	0.45	46.25	100	0.980	0.728	0.220	0.030	0.008	2.016	3.984
CV16007-carb-289	A	28.61	18.72	3.97	0.87	0.55	47.28	100	0.958	0.872	0.104	0.023	0.010	2.017	3.983
CV16007-carb-290	A	28.64	18.76	3.85	0.31	0.71	47.74	100	0.954	0.870	0.100	0.008	0.013	2.027	3.973
CV16007-carb-291	A	23.10	14.60	4.33	0.85	0.33	56.78	100	0.721	0.634	0.105	0.021	0.006	2.257	3.743
CV16007-carb-292	A	28.63	15.91	8.07	1.05	0.43	45.91	100	0.981	0.758	0.216	0.028	0.008	2.004	3.996
CV16007-carb-293	A	28.66	15.86	7.93	0.98	0.45	46.12	100	0.980	0.755	0.212	0.027	0.008	2.009	3.991
CV16007-carb-294	A	28.44	15.45	8.44	1.01	0.46	46.21	100	0.973	0.736	0.225	0.027	0.008	2.015	3.985
CV16007-carb-295	A	28.23	13.81	10.36	1.30	0.83	45.48	100	0.979	0.667	0.280	0.036	0.016	2.011	3.989
CV15123-carb-213	B	28.85	18.62	3.79	0.36	0.49	47.89	100	0.960	0.862	0.098	0.010	0.009	2.031	3.969
CV15123-carb-214	B	28.76	19.82	2.28	0.28	0.34	48.52	100	0.947	0.908	0.059	0.007	0.006	2.036	3.964
CV15123-carb-215	B	28.91	20.22	1.95	0.26	0.43	48.23	100	0.953	0.928	0.050	0.007	0.008	2.027	3.973
CV15141-carb-183	B	28.77	19.94	1.95	0.32	0.60	48.42	100	0.948	0.915	0.050	0.008	0.011	2.034	3.966
CV15141-carb-184	B	28.60	20.34	2.18	0.57	0.69	47.62	100	0.949	0.939	0.056	0.015	0.012	2.014	3.986
CV15141-carb-185	B	28.63	17.10	5.57	1.76	0.20	46.74	100	0.968	0.805	0.147	0.047	0.004	2.015	3.985
CV15141-carb-186	B	28.66	17.65	4.91	1.12	0.48	47.19	100	0.964	0.826	0.129	0.030	0.009	2.022	3.978
CV15141-carb-187	B	28.69	18.96	3.61	0.68	0.77	47.29	100	0.960	0.882	0.094	0.018	0.014	2.016	3.984
CV15141-carb-188	B	28.50	17.26	4.91	1.53	0.42	47.38	100	0.958	0.807	0.129	0.041	0.008	2.029	3.971
CV15141-carb-189	B	28.62	17.32	4.92	1.44	0.46	47.24	100	0.963	0.811	0.129	0.038	0.008	2.025	3.975
CV15141-carb-190	B	28.60	19.83	2.43	0.41	0.60	48.13	100	0.946	0.913	0.063	0.011	0.011	2.029	3.971
CV15141-carb-191	B	28.42	16.87	5.28	1.97	0.13	47.33	100	0.957	0.790	0.139	0.052	0.002	2.030	3.970
CV15141-carb-194	B	27.94	19.19	3.14	0.51	0.86	48.35	100	0.925	0.884	0.081	0.013	0.015	2.040	3.960
CV15141-carb-197	B	28.56	19.71	2.80	0.50	0.76	47.67	100	0.950	0.912	0.073	0.013	0.014	2.019	3.981
CV15141-carb-198	B	28.64	19.91	1.95	0.41	0.54	48.54	100	0.943	0.912	0.050	0.011	0.010	2.037	3.963
CV15141-carb-199	B	28.46	17.19	5.27	1.85	0.15	47.08	100	0.959	0.806	0.139	0.049	0.003	2.022	3.978
CV15141-carb-201	B	28.36	17.41	4.90	1.86	0.16	47.32	100	0.953	0.814	0.128	0.049	0.003	2.026	3.974
CV15141-carb-204	B	28.69	17.80	4.68	1.51	0.41	46.91	100	0.967	0.834	0.123	0.040	0.008	2.014	3.986
CV15141-carb-205	B	28.53	20.38	1.64	0.48	0.25	48.74	100	0.936	0.930	0.042	0.012	0.004	2.038	3.962
CV15141-carb-206	B	28.81	20.23	1.88	0.55	0.28	48.25	100	0.950	0.928	0.048	0.014	0.005	2.027	3.973
CV15141-carb-207	B	28.75	20.56	1.63	0.40	0.22	48.44	100	0.945	0.941	0.042	0.010	0.004	2.029	3.971
CV15141-carb-208	B	28.75	18.93	3.35	0.71	0.46	47.81	100	0.957	0.876	0.087	0.019	0.008	2.027	3.973
CV15141-carb-209	B	28.60	18.03	4.28	1.43	0.65	47.02	100	0.962	0.844	0.112	0.038	0.012	2.016	3.984

CO_2 contents were calculated from the difference between the analytical total and 100 wt. %

Appendix 2.2: Continued

		Weight percent							**Apfu (O = 6)**						
Sample	**Unit**	**CaO**	**MgO**	**FeO**	**MnO**	**SrO**	**CO2**	**Total**	**Ca**	**Mg**	**Fe**	**Mn**	**Sr**	**C**	**Total**
CV15141-carb-210	B	28.11	17.39	4.95	1.75	0.38	47.43	100	0.944	0.813	0.130	0.046	0.007	2.030	3.970
CV15141-carb-211	B	28.41	16.71	5.79	1.98	0.23	46.88	100	0.961	0.786	0.153	0.053	0.004	2.021	3.979
CV15141-carb-212	B	28.15	17.46	4.77	1.55	0.50	47.58	100	0.944	0.815	0.125	0.041	0.009	2.033	3.967
CV16010-carb-157	B	28.53	19.84	2.45	0.85	0.26	48.07	100	0.944	0.913	0.063	0.022	0.005	2.026	3.974
CV16010-carb-158	B	28.83	19.68	2.49	0.80	0.30	47.90	100	0.956	0.908	0.064	0.021	0.005	2.023	3.977
CV16010-carb-161	B	28.71	19.01	2.82	0.96	0.17	48.32	100	0.950	0.875	0.073	0.025	0.003	2.037	3.963
CV16010-carb-163	B	28.97	20.23	1.67	0.76	0.20	48.17	100	0.956	0.929	0.043	0.020	0.004	2.025	3.975
CV16010-carb-166	B	29.00	20.75	1.31	0.69	0.20	48.06	100	0.956	0.952	0.034	0.018	0.004	2.019	3.981
CV16010-carb-167	B	28.87	19.19	3.05	0.90	0.20	47.80	100	0.959	0.887	0.079	0.024	0.004	2.024	3.976
CV16010-carb-168	B	28.94	19.77	2.17	0.87	0.15	48.10	100	0.957	0.909	0.056	0.023	0.003	2.026	3.974
CV16010-carb-171	B	28.96	20.14	1.66	0.87	0.16	48.21	100	0.955	0.924	0.043	0.023	0.003	2.026	3.974
CV16010-carb-173	B	28.85	20.57	1.47	0.80	0.20	48.11	100	0.951	0.944	0.038	0.021	0.004	2.021	3.979
CV16010-carb-174	B	28.65	18.91	3.81	0.89	0.21	47.53	100	0.956	0.877	0.099	0.024	0.004	2.020	3.980
CV16010-carb-175	B	28.38	19.80	2.70	0.81	0.23	48.09	100	0.939	0.911	0.070	0.021	0.004	2.027	3.973
CV15115-cc-79	BD	28.61	20.95	0.85	0.41	1.09	48.09	100	0.944	0.962	0.022	0.011	0.020	2.021	3.979
CV15115-cc-64	BD	28.72	20.59	0.96	0.50	1.06	48.18	100	0.947	0.945	0.025	0.013	0.019	2.025	3.975
CV15115-cc-69	BD	28.78	20.77	1.03	0.48	1.25	47.68	100	0.954	0.958	0.027	0.013	0.022	2.013	3.987
CV15115-cc-75	BD	28.78	20.92	1.35	0.47	0.95	47.53	100	0.954	0.965	0.035	0.012	0.017	2.008	3.992
CV15115-cc-74	BD	28.79	20.63	1.45	0.45	0.97	47.72	100	0.954	0.951	0.037	0.012	0.017	2.014	3.986
CV15115-cc-63	BD	28.88	20.66	1.47	0.46	0.97	47.57	100	0.958	0.953	0.038	0.012	0.017	2.011	3.989
CV15115-cc-73	BD	28.75	20.68	1.58	0.47	0.74	47.79	100	0.952	0.952	0.041	0.012	0.013	2.015	3.985
CV15115-cc-61	BD	28.62	20.42	1.68	0.52	0.85	47.91	100	0.947	0.940	0.043	0.014	0.015	2.020	3.980
CV15115-cc-78	BD	28.49	20.26	1.82	0.45	0.95	48.02	100	0.943	0.933	0.047	0.012	0.017	2.024	3.976
CV15115-cc-71	BD	28.80	19.65	2.30	0.59	0.93	47.73	100	0.957	0.908	0.060	0.015	0.017	2.021	3.979
CV15115-cc-77	BD	28.93	17.59	5.19	0.65	0.68	46.96	100	0.975	0.825	0.137	0.017	0.012	2.017	3.983
CV15115-cc-72	BD	29.21	17.47	5.40	0.73	0.53	46.66	100	0.987	0.822	0.143	0.020	0.010	2.010	3.990
CV15115-cc-76	BD	28.99	17.86	5.41	0.69	0.39	46.66	100	0.979	0.839	0.142	0.018	0.007	2.007	3.993
CV15115-cc-70	BD	28.86	17.34	5.45	0.75	0.62	46.98	100	0.973	0.814	0.144	0.020	0.011	2.019	3.981
CV15115-cc-62	BD	28.95	17.52	5.51	0.78	0.42	46.82	100	0.977	0.823	0.145	0.021	0.008	2.013	3.987
CV15115-cc-82	BD	30.03	17.67	5.86	0.99	0.23	45.23	100	1.028	0.841	0.156	0.027	0.004	1.972	4.028
CV15115-cc-66	BD	28.79	17.30	6.01	0.75	0.57	46.58	100	0.975	0.815	0.159	0.020	0.010	2.010	3.990
CV15115-cc-65	BD	28.80	16.91	6.44	0.79	0.34	46.73	100	0.975	0.796	0.170	0.021	0.006	2.016	3.984

CO_2 contents were calculated from the difference between the analytical total and 100 wt. %

Appendix 2.2: Continued

		Weight percent							**Apfu (O = 6)**						
Sample	**Unit**	**CaO**	**MgO**	**FeO**	**MnO**	**SrO**	**CO2**	**Total**	**Ca**	**Mg**	**Fe**	**Mn**	**Sr**	**C**	**Total**
CV15115-cc-80	BD	28.77	16.39	6.54	1.07	0.21	47.02	100	0.973	0.771	0.173	0.029	0.004	2.026	3.974
CV15115-cc-67	BD	28.96	16.16	7.59	0.94	0.20	46.15	100	0.988	0.767	0.202	0.025	0.004	2.007	3.993
CV15115-cc-81	BD	28.70	15.84	7.94	1.38	0.29	45.84	100	0.984	0.756	0.212	0.037	0.005	2.003	3.997
CV15115-cc-68	BD	28.78	14.53	9.65	1.35	0.08	45.62	100	0.993	0.697	0.260	0.037	0.001	2.006	3.994
CV15158-carb-96	BD	28.46	19.95	1.91	0.59	1.09	48.01	100	0.943	0.920	0.049	0.015	0.020	2.027	3.973
CV15158-carb-90	BD	28.22	19.82	2.18	0.55	0.85	48.37	100	0.932	0.911	0.056	0.014	0.015	2.036	3.964
CV15158-carb-86	BD	28.79	19.72	2.20	0.62	0.94	47.73	100	0.957	0.912	0.057	0.016	0.017	2.021	3.979
CV15158-carb-91	BD	28.33	19.57	2.59	0.65	0.89	47.98	100	0.940	0.903	0.067	0.017	0.016	2.028	3.972
CV15158-carb-89	BD	28.89	18.91	3.02	0.89	0.25	48.03	100	0.959	0.873	0.078	0.023	0.005	2.031	3.969
CV15158-carb-95	BD	28.85	19.49	3.14	0.76	0.43	47.34	100	0.962	0.905	0.082	0.020	0.008	2.012	3.988
CV15158-carb-102	BD	28.50	18.59	3.36	1.12	0.25	48.18	100	0.946	0.859	0.087	0.029	0.004	2.037	3.963
CV15158-carb-94	BD	29.35	18.43	3.80	0.87	0.41	47.15	100	0.984	0.859	0.099	0.023	0.007	2.014	3.986
CV15158-carb-93	BD	28.78	18.53	3.91	0.90	0.41	47.47	100	0.962	0.862	0.102	0.024	0.007	2.022	3.978
CV15158-carb-92	BD	28.81	18.60	4.30	0.65	0.37	47.28	100	0.964	0.866	0.112	0.017	0.007	2.017	3.983
CV15158-carb-103	BD	28.40	17.98	4.48	0.98	0.25	47.92	100	0.947	0.834	0.117	0.026	0.004	2.036	3.964
CV15158-carb-101	BD	28.81	17.78	4.86	1.03	0.16	47.36	100	0.966	0.830	0.127	0.027	0.003	2.023	3.977
CV15158-carb-87	BD	28.18	17.21	5.27	1.97	0.42	46.97	100	0.951	0.808	0.139	0.053	0.008	2.021	3.979
CV16028-carb-145	BD	29.25	20.70	1.21	0.49	0.58	47.78	100	0.967	0.952	0.031	0.013	0.010	2.013	3.987
CV16028-carb-146	BD	28.88	20.43	1.48	0.46	0.62	48.13	100	0.953	0.938	0.038	0.012	0.011	2.024	3.976
CV16028-carb-154	BD	28.80	19.67	2.54	0.74	0.53	47.72	100	0.957	0.909	0.066	0.020	0.009	2.020	3.980
CV16028-carb-147	BD	29.36	19.27	2.81	0.98	0.08	47.51	100	0.977	0.893	0.073	0.026	0.001	2.015	3.985
CV16028-carb-155	BD	29.22	18.87	2.95	0.86	0.18	47.92	100	0.970	0.872	0.077	0.022	0.003	2.028	3.972
CV16028-carb-153	BD	29.26	19.04	3.08	0.96	0.13	47.52	100	0.975	0.883	0.080	0.025	0.002	2.017	3.983
CV16028-carb-148	BD	29.07	17.64	4.85	0.75	0.29	47.41	100	0.974	0.823	0.127	0.020	0.005	2.025	3.975
CV16028-carb-149	BD	29.20	17.66	4.93	0.80	0.32	47.10	100	0.982	0.826	0.129	0.021	0.006	2.018	3.982
CV16028-carb-156	BD	28.98	17.53	5.43	0.75	0.16	47.16	100	0.974	0.820	0.142	0.020	0.003	2.020	3.980
CV16028-carb-151	BD	29.01	17.11	6.26	0.87	0.12	46.64	100	0.982	0.806	0.165	0.023	0.002	2.011	3.989
CV16028-carb-152	BD	29.20	16.36	6.76	0.92	0.05	46.72	100	0.990	0.771	0.179	0.025	0.001	2.017	3.983
CV16028-carb-150	BD	28.97	15.45	9.18	1.02	0.02	45.36	100	0.999	0.741	0.247	0.028	0.000	1.993	4.007
CV15337-carb-296	MHREO	0.30	5.18	51.53	3.87	0.03	39.09	100	0.012	0.288	1.604	0.122	0.001	1.987	4.013
CV15337-carb-297	MHREO	0.36	5.05	51.54	4.15	0.00	38.90	100	0.014	0.281	1.609	0.131	0.000	1.982	4.018
CV15337-carb-298	MHREO	0.58	5.13	51.23	3.77	0.00	39.30	100	0.023	0.284	1.591	0.118	0.000	1.992	4.008

CO_2 contents were calculated from the difference between the analytical total and 100 wt. %

Appendix 2.2: Continued

		Weight percent							Apfu (O = 6)						
Sample	**Unit**	**CaO**	**MgO**	**FeO**	**MnO**	**SrO**	**CO2**	**Total**	**Ca**	**Mg**	**Fe**	**Mn**	**Sr**	**C**	**Total**
CV15337-carb-299	MHREO	0.28	2.88	53.82	4.56	0.00	38.47	100	0.011	0.162	1.704	0.146	0.000	1.988	4.012
CV15337-carb-300	MHREO	0.46	2.93	53.43	4.61	0.01	38.56	100	0.019	0.165	1.689	0.148	0.000	1.990	4.010
CV15337-carb-301	MHREO	0.22	2.81	53.86	4.57	0.02	38.53	100	0.009	0.159	1.705	0.146	0.000	1.991	4.009
CV15337-carb-302	MHREO	0.40	7.80	48.13	3.83	0.00	39.84	100	0.016	0.424	1.470	0.118	0.000	1.986	4.014
CV15337-carb-303	MHREO	0.35	10.24	45.93	3.23	0.00	40.25	100	0.014	0.550	1.382	0.098	0.000	1.978	4.022
CV15337-carb-304	MHREO	0.34	6.81	49.65	3.76	0.00	39.44	100	0.013	0.374	1.529	0.117	0.000	1.983	4.017
CV15337-carb-305	MHREO	0.96	8.24	47.37	3.85	0.00	39.59	100	0.038	0.449	1.447	0.119	0.000	1.974	4.026
CV15337-carb-306	MHREO	0.87	8.29	47.40	3.78	0.00	39.66	100	0.034	0.451	1.446	0.117	0.000	1.976	4.024
CV15337-carb-311	MHREO	0.32	4.78	51.10	4.28	0.03	39.50	100	0.013	0.264	1.586	0.134	0.001	2.001	3.999
CV15337-carb-312	MHREO	0.25	4.38	51.13	4.13	0.02	40.09	100	0.010	0.241	1.578	0.129	0.000	2.021	3.979
CV15337-carb-313	MHREO	0.47	4.85	50.51	4.31	0.04	39.82	100	0.019	0.267	1.561	0.135	0.001	2.009	3.991
CV15337-carb-314	MHREO	0.38	4.82	50.89	4.21	0.01	39.69	100	0.015	0.266	1.575	0.132	0.000	2.006	3.994
CV15337-carb-315	MHREO	0.33	4.36	51.57	4.47	0.00	39.26	100	0.013	0.242	1.608	0.141	0.000	1.998	4.002
CV15337-carb-316	MHREO	0.80	7.87	47.16	3.92	0.02	40.23	100	0.031	0.426	1.432	0.121	0.000	1.995	4.005
CV15337-carb-317	MHREO	0.60	5.39	50.61	4.00	0.00	39.41	100	0.024	0.298	1.568	0.125	0.000	1.993	4.007
CV15337-carb-318	MHREO	0.55	6.31	49.53	3.79	0.01	39.82	100	0.022	0.345	1.521	0.118	0.000	1.997	4.003
CV15339-carb-321	MHREO	0.21	1.65	55.65	4.03	0.02	38.44	100	0.009	0.093	1.772	0.130	0.000	1.998	4.002
CV15339-carb-322	MHREO	0.35	1.85	55.68	4.05	0.00	38.07	100	0.014	0.105	1.779	0.131	0.000	1.985	4.015
CV15339-carb-323	MHREO	0.68	1.68	55.31	4.16	0.00	38.17	100	0.028	0.096	1.765	0.134	0.000	1.988	4.012
CV15339-carb-324	MHREO	0.24	1.88	55.08	4.43	0.00	38.36	100	0.010	0.107	1.753	0.143	0.000	1.994	4.006
CV15339-carb-325	MHREO	0.26	4.38	51.76	4.72	0.00	38.88	100	0.011	0.244	1.621	0.150	0.000	1.987	4.013
CV15339-carb-326	MHREO	0.31	4.57	51.82	4.26	0.00	39.05	100	0.012	0.254	1.618	0.135	0.000	1.990	4.010
CV15339-carb-327	MHREO	0.25	4.29	51.77	4.61	0.01	39.07	100	0.010	0.239	1.618	0.146	0.000	1.993	4.007
CV15339-carb-328	MHREO	0.82	7.30	47.66	4.68	0.01	39.54	100	0.032	0.399	1.462	0.146	0.000	1.980	4.020
CV15339-carb-329	MHREO	0.07	11.79	42.92	4.42	0.02	40.79	100	0.003	0.625	1.277	0.133	0.000	1.981	4.019
CV15339-carb-330	MHREO	0.06	7.84	48.24	4.19	0.00	39.67	100	0.002	0.428	1.476	0.130	0.000	1.982	4.018
CV15339-carb-331	MHREO	0.58	2.05	54.17	4.56	0.02	38.61	100	0.024	0.116	1.717	0.146	0.000	1.998	4.002
CV15339-carb-332	MHREO	0.43	2.75	53.61	4.17	0.00	39.03	100	0.017	0.154	1.687	0.133	0.000	2.004	3.996
CV15339-carb-333	MHREO	0.31	4.35	51.98	4.51	0.00	38.86	100	0.012	0.243	1.628	0.143	0.000	1.987	4.013
CV15339-carb-334	MHREO	0.49	4.70	50.01	4.59	0.02	40.19	100	0.019	0.258	1.540	0.143	0.000	2.020	3.980
CV15339-carb-335	MHREO	0.62	6.82	49.09	4.17	0.01	39.29	100	0.024	0.375	1.514	0.130	0.000	1.978	4.022
CV15339-carb-336	MHREO	0.37	1.97	54.91	4.27	0.02	38.46	100	0.015	0.112	1.745	0.137	0.000	1.995	4.005

CO_2 contents were calculated from the difference between the analytical total and 100 wt. %

Appendix 2.2: Continued

		Weight percent							Apfu (O = 6)						
Sample	**Unit**	**CaO**	**MgO**	**FeO**	**MnO**	**SrO**	**CO2**	**Total**	**Ca**	**Mg**	**Fe**	**Mn**	**Sr**	**C**	**Total**
CV15339-carb-337	MHREO	0.10	1.07	56.89	3.96	0.02	37.96	100	0.004	0.061	1.826	0.129	0.001	1.990	4.010
CV15339-carb-338	MHREO	0.35	2.06	55.25	4.37	0.01	37.95	100	0.014	0.117	1.766	0.141	0.000	1.980	4.020
CV15339-carb-339	MHREO	0.31	4.59	51.39	4.53	0.00	39.19	100	0.012	0.255	1.602	0.143	0.000	1.994	4.006
CV15339-carb-340	MHREO	0.23	4.42	48.61	4.06	0.01	42.68	100	0.009	0.236	1.456	0.123	0.000	2.088	3.912
CV15339-carb-341	MHREO	0.27	4.60	51.77	4.49	0.01	38.87	100	0.011	0.256	1.620	0.142	0.000	1.985	4.015
CV15339-carb-342	MHREO	0.74	9.05	46.48	3.84	0.01	39.89	100	0.029	0.489	1.411	0.118	0.000	1.976	4.024
CV15339-carb-343	MHREO	0.87	9.78	45.15	3.68	0.02	40.51	100	0.033	0.524	1.357	0.112	0.000	1.987	4.013
CV15301-carb-346	MHREO	0.20	2.10	55.16	4.23	0.00	38.32	100	0.008	0.119	1.755	0.136	0.000	1.991	4.009
CV15301-carb-347	MHREO	0.45	3.79	53.36	4.00	0.00	38.41	100	0.018	0.213	1.684	0.128	0.000	1.979	4.021
CV15301-carb-348	MHREO	0.22	2.11	55.60	3.91	0.00	38.16	100	0.009	0.120	1.773	0.126	0.000	1.986	4.014
CV15301-carb-349	MHREO	0.56	10.84	39.44	8.12	0.02	41.03	100	0.021	0.575	1.173	0.245	0.000	1.993	4.007
CV15301-carb-350	MHREO	0.60	10.05	42.31	6.53	0.01	40.50	100	0.023	0.538	1.270	0.198	0.000	1.985	4.015
CV15301-carb-351	MHREO	0.69	11.37	36.93	9.69	0.00	41.32	100	0.026	0.600	1.093	0.290	0.000	1.996	4.004
CV15301-carb-352	MHREO	0.49	14.55	39.65	4.18	0.00	41.13	100	0.018	0.760	1.162	0.124	0.000	1.968	4.032
CV15301-carb-353	MHREO	0.45	14.09	41.25	3.42	0.00	40.79	100	0.017	0.740	1.216	0.102	0.000	1.962	4.038
CV15301-carb-354	MHREO	0.29	2.28	54.21	4.41	0.03	38.79	100	0.012	0.128	1.714	0.141	0.001	2.002	3.998
CV15301-carb-356	MHREO	0.72	14.29	40.26	3.12	0.00	41.62	100	0.027	0.743	1.174	0.092	0.000	1.982	4.018
CV15301-carb-360	MHREO	0.58	13.59	41.23	3.32	0.01	41.27	100	0.022	0.712	1.211	0.099	0.000	1.978	4.022
CV15301-carb-363	MHREO	0.65	14.75	40.19	3.04	0.00	41.39	100	0.024	0.767	1.173	0.090	0.000	1.973	4.027
CV15301-carb-364	MHREO	0.16	3.51	53.80	4.03	0.00	38.52	100	0.006	0.197	1.698	0.129	0.000	1.985	4.015
CV15301-carb-365	MHREO	0.40	10.35	44.71	4.32	0.00	40.23	100	0.016	0.555	1.345	0.132	0.000	1.976	4.024
CV15301-carb-366	MHREO	0.40	13.91	40.96	3.86	0.00	40.87	100	0.015	0.731	1.207	0.115	0.000	1.966	4.034
CV15301-carb-367	MHREO	0.28	2.77	53.89	4.35	0.01	38.71	100	0.011	0.156	1.702	0.139	0.000	1.996	4.004
CV15301-carb-368	MHREO	0.24	5.00	50.95	4.59	0.00	39.22	100	0.009	0.277	1.585	0.145	0.000	1.992	4.008
CV15301-carb-369	MHREO	0.45	13.50	41.22	3.49	0.03	41.32	100	0.017	0.706	1.211	0.104	0.001	1.981	4.019
CV15301-carb-370	MHREO	0.54	14.87	39.06	4.15	0.02	41.36	100	0.020	0.774	1.140	0.123	0.000	1.971	4.029
CV15301-carb-371	MHREO	0.50	14.80	39.34	3.83	0.00	41.53	100	0.019	0.769	1.147	0.113	0.000	1.976	4.024
CV15301-carb-372	MHREO	0.54	10.57	43.69	4.79	0.02	40.39	100	0.021	0.566	1.311	0.146	0.000	1.978	4.022
15029-4-1	Rim 1	52.50	1.01	0.62	0.37	0.37	45.13	100	1.854	0.050	0.017	0.010	0.007	2.031	3.969
15029-4-2	Rim 1	52.41	1.02	0.51	0.38	0.34	45.33	100	1.847	0.050	0.014	0.011	0.007	2.036	3.964
15029-4-3	Rim 1	52.49	1.01	0.47	0.41	0.34	45.29	100	1.851	0.049	0.013	0.011	0.006	2.035	3.965
15029-4-4	Rim 1	52.98	0.60	0.12	0.40	0.31	45.59	100	1.863	0.029	0.003	0.011	0.006	2.043	3.957

CO_2 contents were calculated from the difference between the analytical total and 100 wt. %

Appendix 2.2: Continued

		Weight percent							**Apfu (O = 6)**						
Sample	**Unit**	**CaO**	**MgO**	**FeO**	**MnO**	**SrO**	**CO2**	**Total**	**Ca**	**Mg**	**Fe**	**Mn**	**Sr**	**C**	**Total**
15029-4-5	Rim 1	52.56	0.87	0.46	0.37	0.32	45.42	100	1.852	0.043	0.013	0.010	0.006	2.038	3.962
15029-2-2	Rim 1	53.23	0.54	0.24	0.42	0.48	45.09	100	1.882	0.027	0.007	0.012	0.009	2.032	3.968
15029-2-3	Rim 1	51.50	1.36	0.91	0.42	0.47	45.33	100	1.815	0.067	0.025	0.012	0.009	2.036	3.964
CV15029-cc-1	Rim1	54.50	0.10	0.56	0.64	0.29	43.92	100	1.950	0.005	0.016	0.018	0.006	2.003	3.997
CV15029-cc-11	Rim1	54.43	0.07	0.42	0.31	0.43	44.35	100	1.940	0.003	0.012	0.009	0.008	2.014	3.986
CV15029-cc-12	Rim1	55.27	0.09	0.47	0.28	0.54	43.34	100	1.989	0.005	0.013	0.008	0.010	1.987	4.013
CV15050-cc-33	Rim2	53.40	1.22	0.60	0.21	0.70	43.87	100	1.908	0.061	0.017	0.006	0.013	1.998	4.002
CV15050-cc-34	Rim2	52.44	1.03	0.51	0.20	0.76	45.06	100	1.855	0.051	0.014	0.006	0.015	2.030	3.970
CV15050-cc-35	Rim2	53.16	1.16	0.58	0.19	0.66	44.26	100	1.893	0.057	0.016	0.005	0.013	2.008	3.992
CV15050-cc-36	Rim2	52.68	1.26	0.64	0.22	0.68	44.53	100	1.871	0.062	0.018	0.006	0.013	2.015	3.985
CV15050-cc-37	Rim2	52.88	0.96	0.58	0.20	0.63	44.76	100	1.875	0.047	0.016	0.006	0.012	2.022	3.978
CV15050-cc-38	Rim2	55.76	0.37	0.53	0.26	0.48	42.61	100	2.019	0.018	0.015	0.007	0.009	1.966	4.034
CV15050-cc-41	Rim2	53.96	1.06	0.85	0.24	0.48	43.42	100	1.936	0.053	0.024	0.007	0.009	1.985	4.015
CV15050-cc-42	Rim2	53.31	1.22	0.94	0.26	0.50	43.77	100	1.907	0.061	0.026	0.007	0.010	1.995	4.005
CV15050-cc-45	Rim2	54.06	1.01	0.84	0.27	0.50	43.32	100	1.942	0.051	0.023	0.008	0.010	1.983	4.017
CV15050-cc-46	Rim2	52.59	1.42	0.99	0.31	0.50	44.19	100	1.873	0.070	0.027	0.009	0.010	2.005	3.995
CV15050-cc-50	Rim2	53.56	0.93	0.83	0.24	0.52	43.92	100	1.914	0.046	0.023	0.007	0.010	2.000	4.000
CV15050-cc-53	Rim2	52.55	1.42	1.08	0.24	0.50	44.21	100	1.871	0.070	0.030	0.007	0.010	2.006	3.994
CV15050-cc-58	Rim2	52.79	1.00	0.90	0.25	0.55	44.52	100	1.876	0.049	0.025	0.007	0.011	2.016	3.984
CV15050-cc-59	Rim2	57.24	0.17	0.18	0.41	0.01	41.99	100	2.082	0.008	0.005	0.012	0.000	1.946	4.054
CV15050-cc-60	Rim2	54.61	0.17	0.25	0.44	0.03	44.52	100	1.941	0.008	0.007	0.012	0.000	2.016	3.984
CV15086-carb-115	Rim3	29.50	20.80	0.77	0.61	0.30	48.01	100	0.972	0.954	0.020	0.016	0.005	2.016	3.984
CV15086-carb-114	Rim3	29.41	21.14	0.78	0.63	0.29	47.75	100	0.971	0.971	0.020	0.016	0.005	2.008	3.992
CV15086-carb-125	Rim3	29.75	20.52	0.78	0.57	0.34	48.04	100	0.981	0.941	0.020	0.015	0.006	2.018	3.982
CV15086-carb-123	Rim3	29.42	20.59	0.81	0.62	0.28	48.28	100	0.968	0.943	0.021	0.016	0.005	2.024	3.976
CV15086-carb-124	Rim3	29.53	20.46	0.85	0.61	0.32	48.23	100	0.972	0.937	0.022	0.016	0.006	2.023	3.977
CV15086-carb-116	Rim3	29.47	20.45	0.88	0.66	0.27	48.28	100	0.970	0.937	0.023	0.017	0.005	2.025	3.975
CV15109-carb-129	Rim3	29.19	20.40	1.05	0.79	0.44	48.13	100	0.963	0.936	0.027	0.021	0.008	2.023	3.977
CV15109-carb-132	Rim3	29.66	20.22	1.15	0.76	0.48	47.73	100	0.982	0.932	0.030	0.020	0.009	2.014	3.986
CV15109-carb-131	Rim3	29.38	20.12	1.15	0.76	0.40	48.19	100	0.969	0.924	0.030	0.020	0.007	2.025	3.975
CV15109-carb-137	Rim3	29.62	19.84	1.63	0.76	0.44	47.72	100	0.982	0.915	0.042	0.020	0.008	2.016	3.984
CV15109-carb-130	Rim3	29.11	19.98	1.66	0.77	0.36	48.12	100	0.962	0.918	0.043	0.020	0.007	2.025	3.975

CO_2 contents were calculated from the difference between the analytical total and 100 wt. %

Appendix 2.2: Continued

				Weight percent								Apfu (O = 6)			
Sample	**Unit**	**CaO**	**MgO**	**FeO**	**MnO**	**SrO**	**CO2**	**Total**	**Ca**	**Mg**	**Fe**	**Mn**	**Sr**	**C**	**Total**
CV15109-carb-139	Rim3	29.28	19.88	1.98	0.80	0.31	47.75	100	0.971	0.917	0.051	0.021	0.006	2.017	3.983
CV15109-carb-140	Rim3	29.16	19.28	2.50	0.68	0.38	48.01	100	0.966	0.889	0.065	0.018	0.007	2.028	3.972
CV15109-carb-138	Rim3	29.16	19.33	2.51	0.76	0.29	47.94	100	0.967	0.892	0.065	0.020	0.005	2.026	3.974
CV15086-carb-121	Rim3	29.39	19.26	3.40	0.39	0.10	47.46	100	0.979	0.893	0.088	0.010	0.002	2.014	3.986
CV15086-carb-122	Rim3	29.86	18.38	3.68	0.62	0.05	47.42	100	0.997	0.854	0.096	0.016	0.001	2.018	3.982
CV15086-carb-120	Rim3	29.40	18.85	3.94	0.41	0.11	47.30	100	0.982	0.876	0.103	0.011	0.002	2.013	3.987
CV15109-carb-134	Rim3	28.34	16.95	3.98	2.97	0.30	47.46	100	0.953	0.793	0.105	0.079	0.005	2.033	3.967
CV15109-carb-133	Rim3	28.98	16.79	5.29	1.62	0.19	47.13	100	0.977	0.787	0.139	0.043	0.004	2.025	3.975
CV15086-carb-119	Rim3	28.92	17.71	5.69	0.48	0.05	47.16	100	0.972	0.828	0.149	0.013	0.001	2.019	3.981
CV15086-carb-128	Rim3	28.93	17.71	5.77	0.42	0.05	47.12	100	0.972	0.828	0.151	0.011	0.001	2.018	3.982
CV15086-carb-117	Rim3	28.91	17.41	5.89	0.40	0.03	47.37	100	0.970	0.813	0.154	0.011	0.001	2.026	3.974
CV15086-carb-112	Rim3	29.30	17.00	5.95	0.48	0.03	47.25	100	0.985	0.795	0.156	0.013	0.000	2.025	3.975
CV15086-carb-118	Rim3	28.99	17.32	6.01	0.42	0.04	47.22	100	0.975	0.810	0.158	0.011	0.001	2.023	3.977
CV15086-carb-126	Rim3	29.04	17.30	6.18	0.41	0.05	47.03	100	0.978	0.811	0.162	0.011	0.001	2.018	3.982
CV15086-carb-127	Rim3	28.88	17.24	6.36	0.44	0.03	47.06	100	0.973	0.808	0.167	0.012	0.001	2.020	3.980
CV15109-carb-142	Rim3	29.20	17.12	6.37	0.45	0.11	46.75	100	0.987	0.805	0.168	0.012	0.002	2.013	3.987
CV15109-carb-143	Rim3	29.38	17.03	6.39	0.42	0.07	46.70	100	0.993	0.801	0.169	0.011	0.001	2.012	3.988
CV15109-carb-144	Rim3	29.23	17.01	6.41	0.44	0.09	46.83	100	0.987	0.800	0.169	0.012	0.002	2.016	3.984
CV15109-carb-141	Rim3	29.29	16.93	6.49	0.45	0.09	46.76	100	0.990	0.796	0.171	0.012	0.002	2.014	3.986
CV15109-carb-135	Rim3	29.36	16.64	6.62	0.49	0.09	46.81	100	0.993	0.783	0.175	0.013	0.002	2.017	3.983
CV15109-carb-136	Rim3	29.20	16.96	6.69	0.49	0.11	46.56	100	0.989	0.799	0.177	0.013	0.002	2.010	3.990
CV15004-carb-219	A vein	29.29	18.47	4.31	0.30	0.20	47.43	100	0.978	0.859	0.113	0.008	0.004	2.019	3.981
CV15004-carb-225	A vein	29.21	18.60	3.71	0.23	0.19	48.06	100	0.970	0.859	0.096	0.006	0.003	2.033	3.967
CV15004-carb-220	A vein	27.79	14.20	10.16	1.42	0.36	46.07	100	0.957	0.681	0.273	0.039	0.007	2.022	3.978
CV15004-carb-221	A vein	27.53	14.31	10.28	1.36	0.42	46.10	100	0.948	0.686	0.276	0.037	0.008	2.023	3.977
CV15004-carb-224	A vein	27.72	14.12	10.39	1.40	0.37	45.99	100	0.956	0.677	0.280	0.038	0.007	2.021	3.979
CV15004-carb-226	A vein	28.00	16.69	6.40	1.22	0.47	47.22	100	0.945	0.784	0.169	0.032	0.009	2.031	3.969
CV15004-carb-227	A vein	27.99	16.56	6.71	1.25	0.48	47.00	100	0.947	0.780	0.177	0.034	0.009	2.027	3.973
CV15004-carb-228	A vein	27.77	14.68	9.49	1.32	0.37	46.37	100	0.952	0.700	0.254	0.036	0.007	2.026	3.974
CV15004-carb-229	A vein	27.87	15.13	8.90	1.28	0.43	46.40	100	0.954	0.720	0.238	0.034	0.008	2.023	3.977
CV15004-carb-230	A vein	27.93	16.38	6.77	1.16	0.44	47.32	100	0.943	0.769	0.178	0.031	0.008	2.035	3.965
CV15004-carb-222	A vein	0.57	10.80	43.42	4.12	0.00	41.10	100	0.022	0.572	1.291	0.124	0.000	1.995	4.005

CO_2 contents were calculated from the difference between the analytical total and 100 wt. %

Appendix 2.2: Continued

		Weight percent							Apfu (O = 6)						
Sample	**Unit**	**CaO**	**MgO**	**FeO**	**MnO**	**SrO**	**CO2**	**Total**	**Ca**	**Mg**	**Fe**	**Mn**	**Sr**	**C**	**Total**
CV15004-carb-223	A vein	0.94	18.00	35.09	3.25	0.00	42.72	100	0.034	0.912	0.997	0.093	0.000	1.982	4.018
CV16007-carb-281	A vug	28.90	18.78	4.10	0.47	0.00	47.75	100	0.962	0.870	0.106	0.012	0.000	2.025	3.975
CV16007-carb-282	A vug	28.97	18.74	4.29	0.50	0.00	47.50	100	0.967	0.870	0.112	0.013	0.000	2.019	3.981
CV16007-carb-283	A vug	28.96	18.71	4.24	0.49	0.06	47.54	100	0.966	0.869	0.110	0.013	0.001	2.021	3.979
CV16007-carb-286	A vug	28.17	12.34	12.83	1.87	0.31	44.47	100	0.992	0.605	0.353	0.052	0.006	1.996	4.004
CV16007-carb-287	A vug	28.23	13.57	11.26	1.57	0.30	45.07	100	0.984	0.658	0.306	0.043	0.006	2.002	3.998
CV16007-carb-284	A vug	28.11	15.17	9.02	1.22	0.48	45.99	100	0.966	0.725	0.242	0.033	0.009	2.013	3.987
CV16007-carb-285	A vug	28.57	15.62	8.27	1.21	0.44	45.90	100	0.980	0.745	0.222	0.033	0.008	2.006	3.994
CV15004-carb-231	A vug	0.91	18.77	34.25	3.49	0.00	42.59	100	0.033	0.950	0.972	0.100	0.000	1.973	4.027
CV15004-carb-232	A vug	0.93	16.70	36.33	3.61	0.00	42.44	100	0.034	0.853	1.040	0.105	0.000	1.984	4.016
CV15004-carb-233	A vug	0.81	18.54	34.17	3.54	0.00	42.95	100	0.029	0.935	0.967	0.101	0.000	1.984	4.016
CV15004-carb-238	A vug	0.79	17.23	35.90	3.76	0.00	42.31	100	0.029	0.879	1.028	0.109	0.000	1.977	4.023
CV15004-carb-243	A vug	0.57	15.61	36.19	3.77	0.00	43.86	100	0.021	0.788	1.025	0.108	0.000	2.029	3.971
CV15004-carb-244	A vug	0.45	11.02	42.82	3.97	0.00	41.74	100	0.017	0.580	1.264	0.119	0.000	2.011	3.989
CV16010-carb-164	B vug	28.57	17.62	5.06	1.43	0.30	47.02	100	0.962	0.826	0.133	0.038	0.005	2.018	3.982
CV16010-carb-165	B vug	28.32	17.22	5.60	1.59	0.29	46.99	100	0.956	0.809	0.148	0.042	0.005	2.020	3.980
CV16010-carb-162	B vug	28.70	18.69	3.62	1.01	0.29	47.68	100	0.957	0.867	0.094	0.027	0.005	2.025	3.975
CV16010-carb-169	B vug	28.43	17.15	5.67	1.51	0.26	46.99	100	0.959	0.805	0.149	0.040	0.005	2.021	3.979
CV15158-carb-88	BD vug	28.40	18.28	4.25	1.32	0.30	47.46	100	0.951	0.851	0.111	0.035	0.005	2.024	3.976
CV15158-carb-84	BD vug	28.63	16.19	7.12	1.37	0.15	46.53	100	0.974	0.766	0.189	0.037	0.003	2.016	3.984
CV15158-carb-85	BD vug	28.59	16.73	6.20	1.32	0.14	47.02	100	0.966	0.786	0.163	0.035	0.002	2.023	3.977
CV15158-carb-83	BD vug	29.67	20.97	0.82	0.08	0.09	48.38	100	0.973	0.957	0.021	0.002	0.002	2.022	3.978
CV15392-carb-176	late vein	28.13	14.01	11.00	0.92	0.19	45.75	100	0.972	0.673	0.297	0.025	0.004	2.015	3.985
CV15392-carb-177	late vein	28.63	13.75	8.94	2.22	0.37	46.09	100	0.986	0.659	0.240	0.060	0.007	2.023	3.977
CV15392-carb-178	late vein	28.73	14.26	9.22	1.65	0.34	45.81	100	0.991	0.684	0.248	0.045	0.006	2.013	3.987
CV15392-carb-179	late vein	28.94	14.66	9.08	0.94	0.36	46.03	100	0.994	0.701	0.243	0.025	0.007	2.015	3.985
CV15392-carb-180	late vein	28.32	13.79	10.36	1.38	0.30	45.84	100	0.978	0.663	0.279	0.038	0.006	2.018	3.982
CV15392-carb-181	late vein	27.91	14.44	10.30	1.18	0.33	45.84	100	0.963	0.693	0.277	0.032	0.006	2.014	3.986
CV15392-carb-182	late vein	28.43	13.85	10.43	1.26	0.26	45.77	100	0.982	0.666	0.281	0.034	0.005	2.015	3.985
CV15337-carb-307	MHREO vug	29.21	17.18	6.37	0.80	0.00	46.45	100	0.990	0.810	0.168	0.021	0.000	2.005	3.995
CV15337-carb-308	MHREO vug	27.43	11.01	15.12	1.50	0.53	44.43	100	0.972	0.543	0.418	0.042	0.010	2.007	3.993
CV15337-carb-309	MHREO vug	27.86	10.69	15.47	1.49	0.50	43.99	100	0.993	0.530	0.430	0.042	0.010	1.998	4.002

CO_2 contents were calculated from the difference between the analytical total and 100 wt. %

Appendix 2.2: Continued

		Weight percent							Apfu (O = 6)						
Sample	**Unit**	**CaO**	**MgO**	**FeO**	**MnO**	**SrO**	**CO2**	**Total**	**Ca**	**Mg**	**Fe**	**Mn**	**Sr**	**C**	**Total**
CV15337-carb-310	MHREO vug	27.04	8.15	19.01	2.02	0.32	43.46	100	0.979	0.410	0.537	0.058	0.006	2.005	3.995
CV15337-carb-320	MHREO vug	28.30	14.05	11.59	0.77	0.17	45.13	100	0.984	0.679	0.315	0.021	0.003	1.999	4.001
CV15337-carb-319	MHREO vug	26.99	8.50	18.92	1.94	0.45	43.21	100	0.979	0.429	0.535	0.056	0.009	1.996	4.004
CV15339-carb-344	MHREO vug	28.15	13.44	12.69	1.01	0.26	44.45	100	0.988	0.656	0.348	0.028	0.005	1.988	4.012
CV15339-carb-345	MHREO vug	27.10	9.05	17.92	1.97	0.45	43.52	100	0.977	0.454	0.504	0.056	0.009	2.000	4.000
CV15050-cc-51	Rim 2 vug	28.80	17.74	5.39	0.37	0.21	47.49	100	0.965	0.827	0.141	0.010	0.004	2.027	3.973
CV15050-cc-52	Rim 2 vug	28.85	17.69	5.49	0.38	0.21	47.37	100	0.968	0.826	0.144	0.010	0.004	2.025	3.975
CV15050-cc-54	Rim 2 vug	28.79	16.80	7.11	0.39	0.20	46.71	100	0.975	0.792	0.188	0.011	0.004	2.016	3.984
CV15050-cc-56	Rim 2 vug	28.92	17.56	5.48	0.36	0.22	47.46	100	0.969	0.819	0.144	0.010	0.004	2.027	3.973
CV15050-cc-57	Rim 2 vug	29.04	17.90	5.26	0.36	0.17	47.27	100	0.974	0.835	0.138	0.009	0.003	2.020	3.980

CO_2 contents were calculated from the difference between the analytical total and 100 wt. %

Appendix 2.3: Trace element compositions of carbonate minerals in the different units of the Eldor Carbonatite Complex

			Concentration (ppm)																				
Unit	**Mineral**	**Sample**	**Sc**	**V**	**Zn**	**Sr**	**Ba**	**Pb**	**La**	**Ce**	**Pr**	**Nd**	**Sm**	**Eu**	**Gd**	**Tb**	**Dy**	**Y**	**Ho**	**Er**	**Tm**	**Yb**	**Lu**
Cal Carb 1	cc	15029	3.1	0.7	6.6	3411	886	11.6	16.5	68.7	13.4	52.9	15.3	5.9	20.9	3.4	22.0	135	5.4	14.3	2.2	12.0	1.7
	cc	15029	6.7	0.5	6.5	3780	865	16.0	18.4	66.0	11.6	45.9	14.4	5.9	22.5	3.9	27.7	184	7.4	22.6	3.6	20.9	3.1
	cc	15029	2.8	0.5	5.1	3207	954	15.0	20.2	89.4	17.1	70.8	17.6	6.4	23.2	3.1	19.5	104	4.2	10.4	1.6	8.4	1.2
	cc	15029	8.2	0.7	9.7	3949	991	17.8	21.5	83.3	14.8	58.0	17.5	6.7	26.4	4.4	32.1	207	8.3	24.0	3.9	21.8	3.1
	cc	15029	2.8	0.7	8.5	3101	1009	14.6	25.2	97.8	17.7	69.0	17.4	6.5	23.3	3.3	20.8	115	4.6	11.9	1.8	9.3	1.3
	cc	15029	2.6	0.8	8.9	3068	1018	14.7	25.9	99.0	18.5	70.2	18.0	6.5	23.4	3.1	19.6	108	4.2	11.1	1.7	8.5	1.2
	cc	15029	2.6	0.7	6.5	3043	1142	11.6	29.8	101.1	17.5	66.7	16.0	5.8	22.2	2.9	17.5	99	3.9	10.1	1.5	8.0	1.1
Cal Carb 2	cc	15059	12.4	0.1	5.3	8104	452	15.0	5.4	15.8	2.4	11.3	4.5	2.4	12.5	1.8	12.7	73	3.0	8.2	1.2	6.8	1.0
	cc	15059	5.2	0.1	6.3	7507	405	16.9	3.8	16.9	3.3	17.6	6.9	3.4	14.1	1.8	11.3	73	2.5	7.0	1.0	6.2	0.9
	cc	15059	6.5	0.0	4.4	7369	439	13.5	4.0	15.2	2.7	13.5	5.0	2.5	11.9	1.5	10.2	69	2.4	6.8	1.0	6.3	0.9
	cc	15059	13.4	0.0	4.5	7553	432	13.7	4.8	15.8	2.7	13.6	5.5	2.8	13.3	1.8	12.2	69	2.8	7.6	1.1	6.4	1.0
	cc	15059	19.5	0.1	6.7	7736	491	22.7	19.1	44.5	6.5	27.0	7.7	3.4	14.4	1.7	10.6	61	2.2	6.1	0.9	5.1	0.8
	cc	15059	12.9	0.1	9.9	6817	537	23.9	18.2	45.1	6.6	28.3	7.7	3.4	14.6	1.6	10.2	57	2.1	5.6	0.8	4.7	0.7
	cc	15059	14.5	0.1	7.5	7376	467	30.6	25.2	61.9	8.8	36.4	8.4	3.3	13.7	1.5	8.9	50	1.8	5.0	0.7	4.3	0.7
	cc	15059	7.2	0.1	8.7	6174	540	29.1	62.0	131.4	17.0	61.5	11.1	4.0	15.1	1.5	8.3	44	1.7	4.2	0.6	3.6	0.6
	cc	15059	3.7	0.1	5.4	5534	478	17.3	42.6	94.8	12.5	47.3	8.6	2.9	12.6	1.3	7.7	47	1.7	5.0	0.7	4.8	0.8
	cc	15059	2.9	0.2	5.9	4818	444	13.5	71.4	161.1	21.4	80.0	13.3	4.2	15.5	1.6	8.9	44	1.8	4.5	0.6	3.7	0.6
	cc	15059	4.3	0.1	8.7	5898	396	16.5	53.3	108.0	14.2	52.7	9.7	3.3	13.7	1.3	7.4	42	1.6	4.0	0.6	3.6	0.6
	cc	15059	2.4	0.6	4.9	3811	322	15.8	8.2	21.2	3.4	17.6	6.9	5.5	13.1	1.6	9.1	40	1.7	3.9	0.5	2.8	0.4
	cc	15059	8.2	0.3	3.8	5569	448	10.6	10.3	19.6	2.4	9.4	2.7	1.5	7.9	0.8	5.3	33	1.2	3.5	0.5	3.2	0.5
	cc	15059	9.0	0.1	9.2	6760	545	19.3	21.1	51.2	7.2	29.9	7.6	3.2	13.6	1.4	8.5	47	1.7	4.7	0.6	3.9	0.6
Dol Carb	dol 1	15109	4.5	7.3	26.0	4259	32	4.7	13.4	32.2	3.7	10.6	1.5	0.4	1.2	0.1	0.7	3	0.1	0.3	0.0	0.3	0.1
	dol 1	15109	6.4	5.5	36.1	4617	21	21.4	6.0	16.0	1.9	5.7	0.9	0.3	0.7	0.1	0.5	2	0.1	0.3	0.0	0.3	0.1
	dol 1	15109	4.0	3.8	26.9	3984	29	17.7	11.6	29.8	3.3	9.7	1.4	0.4	1.1	0.1	0.6	3	0.1	0.3	0.0	0.3	0.0
	dol 1	15109	3.7	3.6	25.9	4423	33	6.0	15.6	37.2	4.3	12.7	1.8	0.5	1.4	0.2	0.8	3	0.1	0.3	0.1	0.3	0.1
	dol 1	15109	3.4	4.3	23.8	3984	27	3.6	8.6	21.7	2.6	7.6	1.1	0.3	1.0	0.1	0.6	3	0.1	0.3	0.0	0.2	0.0
	dol 1	15109	5.4	5.8	31.0	4856	30	18.0	15.4	36.6	4.2	12.8	1.8	0.5	1.5	0.2	0.9	4	0.2	0.5	0.1	0.4	0.1
	dol 1	15109	5.4	4.6	23.7	4926	36	8.8	15.1	36.4	4.3	12.6	1.7	0.5	1.5	0.2	0.8	4	0.2	0.4	0.1	0.4	0.1
	dol comp	15109	10.0	4.5	22.6	3139	20	1.6	4.1	13.0	2.0	6.5	1.2	0.4	1.1	0.2	0.8	4	0.2	0.5	0.1	0.5	0.1
	dol comp	15109	13.9	4.9	20.3	3460	35	1.3	3.5	14.3	2.3	7.9	1.6	0.6	1.6	0.2	1.0	4	0.2	0.5	0.1	0.5	0.1
	dol comp	15109	13.2	4.0	20.6	3519	25	1.5	2.7	9.9	1.6	5.4	1.2	0.4	1.2	0.2	0.8	4	0.2	0.4	0.1	0.5	0.1
	dol comp	15109	14.1	5.2	18.9	3387	18	2.4	1.6	6.1	1.0	3.7	0.7	0.3	0.9	0.1	0.6	3	0.1	0.4	0.1	0.4	0.1
	dol comp	15109	15.4	4.8	21.2	3241	17	1.3	1.7	5.9	0.9	3.2	0.7	0.2	0.7	0.1	0.5	3	0.1	0.4	0.1	0.4	0.1
	dol comp	15109	16.0	4.4	19.0	3534	34	1.2	3.8	11.4	1.7	5.6	1.2	0.4	1.2	0.2	0.7	4	0.2	0.4	0.1	0.4	0.1
	dol comp	15109	11.3	4.5	19.2	3322	21	1.2	2.3	9.7	1.6	5.6	1.2	0.4	1.1	0.2	0.8	4	0.2	0.4	0.1	0.4	0.1

Appendix 2.3: Continued

			Concentration (ppm)																				
Unit	**Mineral**	**Sample**	**Sc**	**V**	**Zn**	**Sr**	**Ba**	**Pb**	**La**	**Ce**	**Pr**	**Nd**	**Sm**	**Eu**	**Gd**	**Tb**	**Dy**	**Y**	**Ho**	**Er**	**Tm**	**Yb**	**Lu**
BD zone	dol 1	15114	8.5	3.7	24.3	6408	43	2.5	5.1	13.9	1.9	6.4	1.4	0.5	1.5	0.2	1.1	7	0.2	0.7	0.1	0.8	0.1
	dol 1	15114	4.7	1.5	18.8	7513	51	5.8	24.0	61.7	7.4	22.4	3.1	0.8	2.6	0.3	1.1	5	0.2	0.5	0.1	0.4	0.1
	dol 1	15114	4.0	0.8	16.2	8714	45	4.5	21.4	54.9	7.4	20.8	2.7	0.7	2.2	0.2	1.0	4	0.2	0.4	0.1	0.3	0.1
	dol 1	15114	6.9	5.0	24.9	7571	58	6.3	28.3	79.5	10.7	34.0	6.6	1.6	4.3	0.4	1.8	9	0.3	0.8	0.1	0.6	0.1
	dol 1	15114	7.5	5.8	24.7	6269	53	2.5	15.0	39.7	4.8	14.6	2.6	0.8	2.5	0.3	1.9	10	0.4	1.0	0.2	0.9	0.2
	dol 1	15114	3.5	1.8	15.6	8115	43	2.8	20.6	53.1	6.4	19.0	2.7	0.7	2.1	0.2	1.0	4	0.2	0.5	0.1	0.4	0.1
	dol comp	16027	48.0	12.3	60.3	2446	55	2.5	2.0	10.1	2.2	10.5	4.3	1.8	5.5	1.2	6.5	27	1.2	3.0	0.4	2.4	0.4
	dol comp	16027	38.0	23.1	38.3	2861	33	2.4	2.2	7.7	1.2	4.5	1.3	0.6	1.5	0.2	1.3	5	0.3	0.7	0.1	0.7	0.1
	dol comp	16027	29.4	15.3	28.7	3651	37	2.3	4.1	13.2	1.8	6.6	1.5	0.7	1.6	0.2	1.2	4	0.2	0.6	0.1	0.6	0.1
	dol comp	16027	37.7	12.6	16.3	1656	36	1.1	1.0	5.3	1.3	7.7	3.7	1.6	5.0	1.0	5.5	26	1.1	2.7	0.4	2.1	0.3
	dol comp	16027	37.1	19.8	28.4	3151	44	2.9	1.3	5.9	1.1	4.6	1.3	0.7	1.6	0.2	1.2	5	0.2	0.6	0.1	0.6	0.1
	dol comp	16027	48.6	37.8	38.5	2453	48	2.4	2.1	6.9	1.1	4.1	1.3	0.6	1.7	0.3	1.5	7	0.3	0.9	0.1	0.9	0.2
B zone	dol comp	16019	17.1	19.2	26.6	1767	52	7.8	8.9	42.7	10.4	66.2	33.9	13.2	37.8	6.7	35.0	122	6.0	11.4	1.2	5.2	0.6
	dol comp	16019	21.7	22.5	19.0	1646	49	10.6	13.9	59.7	13.9	90.1	47.8	18.8	55.1	9.9	52.5	180	8.8	16.2	1.6	6.9	0.8
	dol comp	16019	26.3	20.8	59.6	1933	74	7.6	12.7	41.7	7.2	30.6	8.7	3.7	13.2	2.9	19.9	92	4.2	9.5	1.2	5.8	0.7
	dol comp	16019	28.1	16.8	42.2	1708	68	5.8	10.8	42.2	7.6	34.4	11.1	4.8	16.3	3.7	24.3	111	5.0	11.5	1.4	6.6	0.9
	dol comp	16019	25.9	23.2	61.1	2212	70	10.1	10.6	44.2	7.5	33.1	10.1	4.3	14.3	3.3	22.3	95	4.6	10.5	1.3	6.2	0.8
	dol comp	16019	31.5	23.2	20.9	1748	45	3.3	54.7	153.8	28.4	135.3	48.8	18.2	54.5	9.4	49.2	162	8.2	15.9	1.7	7.7	0.9
	dol comp	16019	30.0	28.4	29.9	1561	50	3.6	35.4	100.2	18.1	81.7	23.2	8.5	26.5	5.1	30.1	117	5.6	12.2	1.4	6.9	0.9
	dol comp	16019	25.5	24.8	63.0	1938	72	9.5	7.7	36.1	6.6	28.6	9.1	4.1	14.0	3.5	23.1	101	4.6	10.5	1.2	6.1	0.8
	dol comp	16019	26.1	24.0	63.7	1890	73	10.8	9.1	40.1	6.9	29.1	8.1	3.4	11.3	2.6	17.5	83	3.6	8.3	1.0	5.3	0.7
	dol comp	16019	19.3	18.4	50.8	2603	60	5.3	7.6	39.2	9.6	60.9	32.4	12.6	35.8	6.1	32.0	107	5.3	10.0	1.0	4.7	0.6
	dol comp	16019	23.0	24.6	26.0	2116	71	3.4	15.0	58.6	12.6	74.3	37.9	15.6	44.6	8.2	43.2	144	7.0	13.1	1.3	5.7	0.7
	dol comp	16019	9.1	13.3	115.2	3982	43	11.5	14.2	47.7	9.0	45.7	19.5	7.9	21.6	3.8	20.5	70	3.5	7.5	0.9	4.7	0.7
	dol comp	16019	21.2	30.8	11.5	1810	48	3.0	23.4	79.7	16.7	93.0	41.5	16.5	47.3	8.6	44.7	150	7.2	13.9	1.4	5.9	0.7
	dol comp	16019	5.4	7.7	197.6	5144	39	21.1	28.6	89.2	11.3	42.4	7.8	2.9	7.8	1.2	6.6	33	1.3	3.4	0.5	3.3	0.6
	dol comp	16019	1.1	0.8	163.9	5250	33	19.7	13.0	42.1	6.1	22.3	6.7	2.8	7.6	1.4	8.2	42	1.7	4.7	0.7	5.2	0.9
	dol comp	16019	6.0	2.6	147.0	6075	45	21.4	11.8	39.0	6.2	24.2	6.5	2.6	7.4	1.4	8.1	45	1.8	4.9	0.7	4.9	0.8
	dol comp	15127	31.7	24.9	63.1	2015	75	13.3	7.5	35.1	7.9	39.4	15.7	6.4	19.2	3.7	21.0	96	4.2	9.6	1.2	5.4	0.7
	dol comp	15127	32.3	26.8	78.6	2071	86	14.5	9.3	39.4	7.8	37.5	14.0	5.7	17.3	3.4	20.6	99	4.3	10.0	1.2	5.9	0.7
	dol comp	15127	32.4	24.6	80.9	2165	73	17.4	35.7	121.9	22.5	100.9	19.8	6.6	18.7	3.3	18.6	84	3.8	9.0	1.1	5.3	0.7
	dol comp	15127	32.5	26.0	64.6	2114	76	15.2	24.8	97.1	19.1	80.1	21.1	7.5	21.4	3.7	21.0	93	4.1	9.3	1.1	5.4	0.7
	dol comp	15127	29.4	20.0	40.5	1925	72	14.5	28.3	89.7	15.8	70.3	16.4	5.6	16.4	3.1	18.8	91	3.9	9.5	1.2	5.8	0.7
	dol comp	15127	29.0	19.6	35.6	1878	157	12.6	15.8	58.4	11.7	53.6	16.8	6.3	20.5	3.7	21.7	103	4.5	10.5	1.3	6.4	0.8
	dol comp	15127	28.8	20.5	53.5	2111	72	13.6	5.7	24.5	5.2	26.1	10.6	4.3	13.2	2.6	15.5	74	3.2	7.6	1.0	4.8	0.6

‘dol comp’ refers to composite samples (dolomite 2 + 3, see Chapter 2 for further detail)

Appendix 2.3: Continued

			Concentration (ppm)																				
Unit	**Mineral**	**Sample**	**Sc**	**V**	**Zn**	**Sr**	**Ba**	**Pb**	**La**	**Ce**	**Pr**	**Nd**	**Sm**	**Eu**	**Gd**	**Tb**	**Dy**	**Y**	**Ho**	**Er**	**Tm**	**Yb**	**Lu**
B zone	dol comp	15127	33.5	23.5	39.2	1969	95	13.1	12.9	48.6	9.2	45.4	17.5	7.1	23.7	4.5	27.1	125	5.5	12.9	1.6	7.6	0.9
	dol comp	15127	29.0	24.3	65.8	2140	118	14.4	6.2	27.0	5.7	29.1	11.5	4.9	16.1	2.9	16.8	81	3.5	8.3	1.0	4.9	0.6
A zone	dol comp	15020	44.7	30.4	164.1	2136	68	15.1	9.7	39.5	7.4	35.5	13.9	6.7	21.5	4.1	21.7	85	3.2	7.0	0.8	4.7	0.7
	dol comp	15020	41.3	29.1	158.6	2139	57	14.7	8.1	31.1	5.6	27.0	10.5	5.1	16.6	3.3	17.7	71	2.6	5.8	0.6	4.0	0.6
	dol comp	15020	40.0	38.3	150.3	1898	84	12.3	9.9	34.5	6.1	29.6	11.7	5.5	18.5	3.5	19.1	78	3.0	6.5	0.7	4.6	0.6
	dol comp	15020	39.0	36.3	274.2	1949	60	12.7	12.1	39.9	6.8	32.0	11.8	5.6	18.3	3.5	18.6	74	2.8	6.1	0.7	4.3	0.6
	dol comp	15020	38.4	33.1	108.0	1754	100	12.3	13.9	50.1	9.1	43.3	15.2	6.9	21.5	4.0	22.1	88	3.5	7.8	0.9	5.3	0.7
	dol comp	15020	40.7	39.2	108.5	1811	80	13.2	9.5	38.3	7.3	36.0	14.0	6.5	20.7	4.0	23.0	90	3.6	8.1	0.9	5.5	0.8
	dol comp	15020	36.6	36.5	105.2	1771	64	12.7	8.1	33.2	6.3	30.9	12.6	5.9	18.9	3.6	20.3	83	3.3	7.5	0.9	5.3	0.7
	dol comp	15020	34.4	32.7	100.4	1768	60	11.1	7.1	29.7	5.7	28.0	11.9	5.5	17.8	3.6	21.0	87	3.4	8.0	0.9	5.6	0.8
	dol comp	15020	36.0	40.8	73.8	1555	146	10.4	12.8	58.7	11.9	62.7	23.6	9.3	29.1	5.2	30.8	121	5.1	11.9	1.4	7.9	1.1
	dol comp	15020	33.4	35.6	148.8	2041	72	14.6	11.2	44.2	8.1	38.4	12.6	5.4	17.5	3.1	15.8	68	2.3	4.9	0.5	3.3	0.5
	dol comp	15020	35.3	36.3	88.6	1692	70	10.0	16.5	57.9	11.3	57.7	17.5	6.6	20.4	3.7	21.9	95	3.7	8.7	1.0	6.2	0.8
	dol comp	15020	36.7	51.9	94.2	1767	51	10.3	5.0	23.0	4.9	26.9	11.0	5.0	16.6	3.2	19.6	86	3.3	7.9	0.9	5.7	0.8
	dol comp	15020	40.5	47.7	94.8	1778	57	11.5	6.2	28.2	5.9	31.6	12.8	5.7	18.8	3.9	24.0	103	4.1	9.7	1.2	7.0	1.0
	dol comp	15020	39.9	43.9	85.0	1803	58	11.2	14.6	47.0	8.4	41.5	15.2	6.8	23.7	4.8	28.6	117	4.6	10.5	1.2	6.5	0.9
	dol comp	15020	36.3	33.5	81.2	1685	71	9.8	9.0	36.7	7.3	39.5	14.8	6.1	20.2	3.8	22.7	97	3.9	8.9	1.0	6.0	0.8
	dol comp	15020	38.9	25.4	120.1	1942	84	15.2	7.0	31.1	6.0	29.9	10.8	5.1	16.5	3.0	15.0	58	2.1	4.3	0.5	2.8	0.4
	dol comp	15020	40.0	28.4	94.8	1820	50	10.9	11.1	34.1	6.2	30.7	10.8	4.9	16.5	3.3	19.5	83	3.1	7.4	0.8	5.1	0.7
	dol comp	15020	37.7	38.1	91.7	1661	98	12.8	14.4	49.1	8.6	39.8	13.3	5.7	19.3	3.6	20.9	88	3.5	7.9	0.9	5.3	0.7
	dol comp	15020	39.8	25.9	81.9	1765	116	11.0	20.7	64.9	11.5	56.2	17.7	6.6	21.6	3.8	21.2	86	3.3	7.3	0.8	4.8	0.6
	dol comp	15020	30.5	51.6	74.6	1691	144	9.8	12.6	46.6	9.5	53.8	21.3	8.5	26.2	4.6	27.5	119	4.8	11.6	1.4	7.7	1.0
	dol comp	15020	35.3	29.5	100.0	1829	57	11.9	7.8	26.8	4.9	25.2	10.0	4.4	14.8	2.9	16.9	74	2.7	6.0	0.7	4.3	0.6
	dol comp	15020	33.2	34.4	84.6	1862	159	10.9	19.0	63.1	12.0	63.3	21.8	8.2	24.8	4.0	22.7	92	3.8	8.6	1.0	5.4	0.7
	dol comp	15026	69.2	30.7	170.5	2300	79	16.0	7.3	23.6	4.2	20.7	8.5	3.9	12.8	2.6	16.6	85	2.9	7.5	0.9	5.6	0.8
	dol comp	15026	72.2	32.0	169.1	2263	68	16.4	14.3	38.9	6.3	29.4	10.4	4.5	14.9	2.9	18.9	97	3.3	8.7	1.1	6.6	0.9
	dol comp	15026	62.7	24.5	158.2	2408	52	17.0	7.1	23.5	4.2	20.3	8.2	3.7	12.0	2.4	15.6	80	2.8	7.2	0.9	5.4	0.8
	dol comp	15026	64.9	33.9	153.6	2331	56	14.6	7.4	22.2	4.0	18.9	7.6	3.5	12.0	2.4	16.4	84	3.0	7.7	1.0	5.8	0.8
	dol comp	15026	71.6	52.6	162.1	2074	60	15.1	7.3	22.8	4.1	20.6	8.9	4.1	14.2	3.0	20.2	105	3.7	9.8	1.2	7.6	1.0
	dol comp	15026	69.2	36.3	164.8	2241	58	15.8	7.1	23.9	4.4	21.6	8.8	4.1	13.8	2.8	18.1	92	3.3	8.4	1.0	6.3	0.9
	dol comp	15026	63.3	17.5	162.0	2475	54	18.7	7.4	24.9	4.5	21.5	8.4	3.8	12.2	2.4	15.5	81	2.7	7.0	0.9	5.5	0.8
	dol comp	15026	50.8	27.6	152.2	2939	74	22.8	9.7	25.4	4.1	17.9	7.2	3.4	11.0	2.1	13.3	67	2.2	5.1	0.6	3.9	0.6
	dol comp	15026	59.6	43.8	126.1	2040	80	11.1	7.3	20.6	3.4	17.3	8.3	3.9	12.6	2.6	17.2	82	3.0	7.6	0.9	5.1	0.7
	dol comp	15026	60.2	46.5	122.1	2254	74	10.8	7.6	22.4	3.8	19.9	9.6	4.6	14.9	3.2	21.8	106	4.0	10.0	1.2	6.7	0.8
	dol comp	15026	62.8	39.5	120.1	2312	83	18.7	8.0	21.7	3.5	16.7	7.0	3.5	10.8	2.1	13.8	66	2.3	5.5	0.7	4.0	0.6

‘dol comp’ refers to composite samples (dolomite 2 + 3, see Chapter 2 for further detail)

Appendix 2.3: Continued

			Concentration (ppm)																				
Unit	**Mineral**	**Sample**	**Sc**	**V**	**Zn**	**Sr**	**Ba**	**Pb**	**La**	**Ce**	**Pr**	**Nd**	**Sm**	**Eu**	**Gd**	**Tb**	**Dy**	**Y**	**Ho**	**Er**	**Tm**	**Yb**	**Lu**
A zone	dol comp	15026	67.3	35.7	99.9	2028	119	15.5	7.1	20.6	3.4	17.2	7.7	3.7	12.3	2.4	16.2	79	2.7	6.9	0.8	4.8	0.7
	dol comp	15026	56.1	28.1	117.9	2253	88	16.4	6.5	19.2	3.1	14.8	6.4	3.2	10.8	2.0	13.2	63	2.3	5.4	0.6	3.6	0.5
	dol comp	15026	60.4	52.0	129.2	2266	82	27.3	14.9	34.2	5.2	25.6	10.4	4.8	15.5	3.2	21.7	98	3.8	9.2	1.1	6.3	0.8
	dol comp	15026	60.5	37.6	132.4	2460	70	13.4	6.4	19.3	3.2	16.3	7.6	3.8	12.5	2.7	18.3	87	3.1	7.9	0.9	5.4	0.7
	dol comp	15026	56.2	32.1	129.7	2234	73	14.0	12.4	30.4	5.0	27.0	11.8	5.6	16.2	3.1	20.0	82	3.6	7.7	0.9	5.0	0.7
	vug dol	15026	20.4	43.3	40.6	1262	23	3.4	0.3	1.0	0.2	1.0	0.5	0.3	1.2	0.3	2.4	15	0.6	1.9	0.3	1.9	0.3
	vug dol	15026	17.7	43.3	62.7	2535	43	4.1	0.8	2.0	0.3	1.6	0.6	0.4	1.5	0.4	3.5	24	1.0	3.5	0.5	3.0	0.4
	vug dol	15026	20.9	15.9	72.5	3947	182	12.5	2.5	6.1	1.0	4.6	1.7	0.9	4.1	0.5	3.3	18	0.6	1.6	0.2	1.2	0.2
	vug dol	15026	18.6	29.7	73.0	3092	83	7.6	1.8	4.4	0.7	3.3	1.2	0.6	2.4	0.4	3.4	18	0.7	2.2	0.3	1.7	0.2
	vug dol	15026	18.5	30.0	50.3	2855	72	6.6	1.1	2.9	0.5	2.2	0.9	0.5	2.1	0.3	2.6	14	0.6	1.5	0.2	1.3	0.2
	vug dol	15026	20.0	64.3	53.7	2032	8	1.1	0.3	0.7	0.1	0.6	0.3	0.2	0.8	0.3	3.2	21	0.9	3.2	0.4	2.6	0.4
	vug dol	15026	25.3	31.7	79.7	2641	39	5.6	1.9	4.3	0.7	3.0	1.2	0.8	2.3	0.5	3.8	20	0.7	2.1	0.3	1.4	0.2
	vug dol	15026	17.0	32.7	77.5	3161	74	6.0	1.7	3.8	0.6	2.7	1.1	0.7	2.2	0.4	3.0	17	0.6	1.7	0.2	1.2	0.2
	vug dol	15026	68.4	27.5	43.8	2732	57	2.5	1.9	4.0	0.6	2.8	1.1	0.6	2.0	0.4	2.6	13	0.5	1.3	0.2	1.0	0.2
	vug dol	15026	25.5	40.2	64.0	2411	38	3.7	1.0	2.4	0.4	1.8	0.8	0.5	1.7	0.4	3.4	20	0.9	2.7	0.4	2.2	0.3
MHREO zone	siderite	15014	7.0	15.2	240.7	1	6	3.5	0.1	0.4	0.1	0.6	0.2	0.1	0.4	0.1	0.4	3	0.1	0.3	0.0	0.3	0.1
	siderite	15014	7.4	20.7	266.2	5	8	7.7	0.1	0.6	0.1	1.0	0.4	0.1	0.6	0.1	0.7	5	0.2	0.5	0.1	0.7	0.1
	siderite	15014	9.7	17.5	234.2	7	8	0.4	0.1	0.6	0.1	0.9	0.4	0.2	0.7	0.1	0.9	6	0.2	0.6	0.1	0.6	0.1
	siderite	15014	9.0	12.2	221.6	3	8	4.1	0.1	0.7	0.2	1.2	0.5	0.2	0.7	0.1	0.8	6	0.2	0.6	0.1	0.7	0.1
	siderite	15014	10.6	31.3	353.2	4	13	3.4	0.2	1.0	0.2	1.7	0.8	0.4	1.1	0.2	1.3	7	0.3	0.8	0.1	0.7	0.1
	siderite	15014	12.5	86.5	317.2	6	12	2.4	0.2	0.8	0.2	1.4	0.6	0.2	1.0	0.2	1.3	9	0.3	0.9	0.1	0.8	0.1
	siderite	15014	14.9	21.1	311.3	7	11	1.8	0.1	0.8	0.2	1.7	0.9	0.3	1.4	0.2	2.0	13	0.4	1.5	0.2	1.4	0.2
	siderite	15014	18.2	103.1	200.2	10	16	2.3	0.2	1.0	0.2	1.7	0.9	0.4	1.5	0.3	2.6	18	0.6	2.0	0.3	1.7	0.2
	siderite	15014	20.0	90.0	341.1	11	18	7.0	0.3	1.6	0.4	2.7	1.3	0.4	1.6	0.3	2.5	19	0.6	2.0	0.3	1.8	0.3
	siderite	15014	14.6	71.4	561.6	9	21	3.5	0.2	1.0	0.2	1.8	1.1	0.4	1.6	0.4	3.0	22	0.7	2.5	0.3	2.2	0.3
	siderite	15014	29.3	33.5	204.4	8	13	2.5	0.1	0.7	0.2	1.7	1.2	0.5	2.0	0.4	3.4	25	0.8	2.8	0.4	2.7	0.4
	siderite	15014	23.5	34.4	137.6	15	11	6.2	0.1	0.7	0.2	1.6	1.2	0.5	2.1	0.4	3.6	25	0.8	2.7	0.4	2.5	0.4
	vug dol	15337	2.8	2.8	10.5	125	1	2.2	0.5	9.0	3.7	25.5	10.9	3.9	10.4	1.8	10.2	45	1.5	2.9	0.3	1.5	0.2
	vug dol	15337	48.7	12.5	89.0	2880	22	5.5	0.3	3.7	1.2	7.4	2.7	1.1	2.6	0.5	3.2	13	0.6	1.5	0.2	1.4	0.2
	vug dol	15337	34.2	19.8	138.3	2339	45	11.4	0.4	6.2	2.0	13.2	4.7	2.0	4.5	0.8	4.9	21	0.9	2.2	0.3	2.2	0.4
	vug dol	15337	49.9	24.1	115.6	2770	29	5.1	0.3	3.5	1.0	6.3	2.1	0.9	2.0	0.4	2.4	10	0.4	1.2	0.2	1.1	0.2
	vug dol	15337	21.9	11.1	37.3	1081	7	2.2	0.3	4.9	2.0	14.4	6.4	2.2	6.3	1.1	6.1	27	0.9	1.9	0.2	1.2	0.2
	vug dol	15337	34.1	14.9	69.8	1212	16	4.6	0.3	3.8	1.3	8.6	3.3	1.2	3.3	0.5	3.2	14	0.5	1.1	0.1	0.7	0.1
	vug dol	15337	40.3	34.1	119.1	1509	7	2.7	0.4	6.4	2.9	22.0	6.4	1.8	4.3	0.6	3.0	12	0.5	1.0	0.1	0.7	0.1

'dol comp' refers to composite samples (dolomite 2 + 3, see Chapter 2 for further detail)

Appendix 2.3: Continued

			Concentration (ppm)																				
Unit	**Mineral**	**Sample**	**Sc**	**V**	**Zn**	**Sr**	**Ba**	**Pb**	**La**	**Ce**	**Pr**	**Nd**	**Sm**	**Eu**	**Gd**	**Tb**	**Dy**	**Y**	**Ho**	**Er**	**Tm**	**Yb**	**Lu**
Breccia	dol	16038	11.6	13.0	83.9	700	10	5.3	3.1	8.5	1.4	5.9	1.8	1.0	2.7	0.6	4.7	53	1.1	3.4	0.4	3.0	0.4
	dol	16038	23.7	69.8	98.5	6598	14	12.1	2.2	6.6	1.0	4.6	1.5	0.7	2.2	0.4	3.2	31	0.7	2.1	0.3	1.9	0.3
	dol	16038	21.2	8.9	59.1	3263	32	5.7	0.9	5.2	1.1	5.6	1.8	0.7	1.7	0.2	1.2	5	0.2	0.5	0.1	0.5	0.1
	dol	16038	23.7	10.4	39.9	2847	35	1.5	0.9	4.7	1.0	5.0	1.6	0.7	1.8	0.2	1.3	6	0.2	0.5	0.1	0.5	0.1
	dol	16038	23.6	9.0	39.9	3172	37	2.6	0.9	5.3	1.1	5.5	1.8	0.7	1.8	0.2	1.2	6	0.2	0.6	0.1	0.5	0.1
	dol	16038	20.8	7.5	45.4	3066	33	2.7	1.2	6.4	1.3	6.5	2.1	0.8	1.9	0.3	1.4	6	0.2	0.6	0.1	0.5	0.1
	dol	16038	22.3	7.2	44.0	3518	33	4.7	1.0	6.0	1.2	6.1	2.0	0.8	1.9	0.2	1.4	6	0.2	0.7	0.1	0.5	0.1
	dol	16038	24.4	7.2	43.8	3048	36	4.8	1.2	6.1	1.2	5.8	1.8	0.8	1.9	0.3	1.4	7	0.3	0.7	0.1	0.6	0.1
	dol	16038	22.5	7.8	35.5	2928	28	2.1	0.9	5.1	1.0	5.3	1.7	0.7	1.8	0.2	1.3	6	0.2	0.6	0.1	0.5	0.1
	dol	16038	24.7	8.6	49.8	2739	32	3.3	1.3	6.4	1.3	6.3	2.1	0.9	2.3	0.3	1.9	9	0.3	0.9	0.1	0.7	0.1
	dol	16038	21.7	7.2	41.4	2530	35	9.6	1.2	5.6	1.1	5.3	1.7	0.7	1.8	0.3	1.4	7	0.2	0.6	0.1	0.5	0.1
	dol	16038	22.9	10.1	49.6	3053	30	4.0	1.5	9.3	1.6	7.6	2.4	1.0	2.5	0.3	2.0	9	0.3	0.9	0.1	0.7	0.1
	dol	16038	23.8	12.2	53.0	3030	56	4.7	1.1	6.5	1.2	5.9	2.0	0.9	2.2	0.3	1.6	7	0.3	0.7	0.1	0.6	0.1
	dol	16038	21.8	6.8	36.8	2994	31	2.1	0.8	4.7	0.9	4.8	1.6	0.7	1.6	0.2	1.2	6	0.2	0.5	0.1	0.5	0.1
	dol	16038	23.4	9.0	46.4	3046	33	4.4	1.2	6.7	1.4	7.1	2.1	0.9	2.1	0.3	1.6	8	0.3	0.8	0.1	0.7	0.1
	dol	16038	27.3	8.5	44.0	3587	36	4.7	1.4	8.4	1.8	9.4	3.0	1.2	2.8	0.4	1.9	8	0.3	0.9	0.1	0.7	0.1

Appendix 2.4: Major element oxide compositions and cation proportions of apatite in the different units of the Eldor Carbonatite Complex

Unit						A					
Sample	15193	15193	15193	15193	15193	15193	15193	15193	15193	15193	15194
La_2O_3 (*wt. %*)	0.23	0.00	0.00	0.00	0.00	0.00	0.00	0.00	0.00	0.00	0.00
Ce_2O_3	0.21	0.26	0.25	0.00	0.22	0.00	0.23	0.00	0.33	0.00	0.20
Pr_2O_3	0.00	0.00	0.00	0.00	0.00	0.00	0.00	0.00	0.00	0.00	0.00
Nd_2O_3	0.26	0.24	0.27	0.22	0.22	0.26	0.32	0.22	0.30	0.26	0.29
Sm_2O_3	0.00	0.14	0.00	0.00	0.00	0.11	0.00	0.12	0.00	0.00	0.14
Eu_2O_3	0.00	0.00	0.00	0.00	0.00	0.00	0.00	0.00	0.00	0.00	0.00
Gd_2O_3	0.17	0.00	0.00	0.00	0.17	0.20	0.11	0.00	0.00	0.00	0.29
Dy_2O_3	0.18	0.00	0.16	0.20	0.20	0.00	0.19	0.13	0.00	0.14	0.15
Y_2O_3	0.49	0.53	0.58	0.47	0.49	0.54	0.57	0.51	0.51	0.46	0.61
Ho_2O_3	0.00	0.00	0.00	0.00	0.00	0.00	0.00	0.00	0.00	0.00	0.00
ThO_2	0.00	0.07	0.00	0.00	0.00	0.00	0.00	0.00	0.17	0.00	0.00
UO_2	0.00	0.00	0.00	0.00	0.00	0.00	0.00	0.00	0.00	0.00	0.00
CaO	52.79	52.89	52.91	53.08	52.93	52.80	52.97	52.84	52.52	53.39	53.41
P_2O_5	41.42	41.49	42.06	41.63	41.61	41.71	42.05	41.70	41.09	41.53	41.59
F	3.86	4.06	3.95	3.61	4.08	3.70	3.63	3.93	3.46	3.68	3.90
Cl	0.00	0.00	0.00	0.00	0.00	0.00	0.00	0.00	0.00	0.00	0.00
SiO_2	0.00	0.00	0.00	0.00	0.00	0.00	0.00	0.00	0.00	0.00	0.00
PbO	0.08	0.00	0.00	0.00	0.00	0.00	0.00	0.00	0.00	0.00	0.00
FeO	0.00	0.00	0.00	0.00	0.00	0.00	0.00	0.00	0.09	0.00	0.00
Na_2O	0.30	0.28	0.28	0.26	0.27	0.35	0.31	0.34	0.33	0.31	0.33
SrO	1.41	1.48	1.43	1.36	1.36	1.43	1.41	1.32	1.38	1.40	0.93
BaO	0.00	0.00	0.00	0.00	0.00	0.00	0.00	0.00	0.00	0.00	0.00
-O-F	-1.62	-1.71	-1.66	-1.52	-1.72	-1.56	-1.53	-1.66	-1.46	-1.55	-1.64
Total	99.77	99.73	100.21	99.30	99.82	99.54	100.26	99.44	98.73	99.62	100.18
						O = 12.5					
La (*apfu*)	0.007	0.000	0.000	0.000	0.000	0.000	0.000	0.000	0.000	0.000	0.000
Ce	0.007	0.008	0.008	0.000	0.007	0.000	0.007	0.000	0.010	0.000	0.006
Pr	0.000	0.000	0.000	0.000	0.000	0.000	0.000	0.000	0.000	0.000	0.000
Nd	0.008	0.007	0.008	0.007	0.007	0.008	0.010	0.007	0.009	0.008	0.009
Sm	0.000	0.004	0.000	0.000	0.000	0.003	0.000	0.003	0.000	0.000	0.004
Eu	0.000	0.000	0.000	0.000	0.000	0.000	0.000	0.000	0.000	0.000	0.000
Gd	0.005	0.000	0.000	0.000	0.005	0.006	0.003	0.000	0.000	0.000	0.008
Dy	0.005	0.000	0.004	0.005	0.006	0.000	0.005	0.003	0.000	0.004	0.004
Y	0.022	0.024	0.026	0.021	0.022	0.024	0.026	0.023	0.023	0.021	0.028
Ho	0.000	0.000	0.000	0.000	0.000	0.000	0.000	0.000	0.000	0.000	0.000
Th	0.000	0.001	0.000	0.000	0.000	0.000	0.000	0.000	0.003	0.000	0.000
U	0.000	0.000	0.000	0.000	0.000	0.000	0.000	0.000	0.000	0.000	0.000
Ca	4.833	4.838	4.801	4.849	4.834	4.819	4.801	4.827	4.842	4.872	4.861
P	2.996	2.999	3.015	3.005	3.003	3.008	3.011	3.010	2.993	2.994	2.991
F	1.042	1.096	1.057	0.974	1.099	0.998	0.971	1.060	0.941	0.991	1.047
Cl	0.000	0.000	0.000	0.000	0.000	0.000	0.000	0.000	0.000	0.000	0.000
Si	0.000	0.000	0.000	0.000	0.000	0.000	0.000	0.000	0.000	0.000	0.000
Pb	0.002	0.000	0.000	0.000	0.000	0.000	0.000	0.000	0.000	0.000	0.000
Fe	0.000	0.000	0.000	0.000	0.000	0.000	0.000	0.000	0.007	0.000	0.000
Na	0.050	0.047	0.046	0.043	0.044	0.058	0.051	0.056	0.055	0.051	0.055
Sr	0.070	0.073	0.070	0.067	0.067	0.071	0.069	0.065	0.069	0.069	0.046
Ba	0.000	0.000	0.000	0.000	0.000	0.000	0.000	0.000	0.000	0.000	0.000
Total	8.004	8.002	7.978	7.998	7.995	7.997	7.983	7.995	8.012	8.018	8.012

Appendix 2.4: Continued

Unit						A					
Sample	15194	15194	15194	15194	15194	15194	15194	15194	15194	16007	16007
La_2O_3 (*wt. %*)	0.00	0.00	0.00	0.00	0.00	0.00	0.00	0.00	0.00	0.00	0.00
Ce_2O_3	0.00	0.00	0.00	0.00	0.31	0.00	0.26	0.00	0.19	0.26	0.31
Pr_2O_3	0.00	0.00	0.00	0.00	0.00	0.00	0.00	0.12	0.00	0.00	0.00
Nd_2O_3	0.25	0.25	0.24	0.26	0.23	0.34	0.31	0.34	0.28	0.26	0.32
Sm_2O_3	0.00	0.00	0.13	0.12	0.11	0.17	0.00	0.00	0.10	0.13	0.00
Eu_2O_3	0.00	0.00	0.00	0.00	0.00	0.00	0.00	0.00	0.00	0.00	0.00
Gd_2O_3	0.00	0.22	0.23	0.17	0.20	0.19	0.00	0.00	0.12	0.00	0.00
Dy_2O_3	0.17	0.00	0.00	0.16	0.00	0.16	0.00	0.00	0.00	0.00	0.13
Y_2O_3	0.53	0.61	0.55	0.56	0.44	0.40	0.45	0.41	0.38	0.57	0.58
Ho_2O_3	0.00	0.00	0.00	0.00	0.00	0.00	0.00	0.00	0.00	0.00	0.00
ThO_2	0.00	0.09	0.00	0.00	0.00	0.00	0.00	0.00	0.09	0.00	0.00
UO_2	0.00	0.00	0.00	0.00	0.00	0.00	0.00	0.00	0.00	0.00	0.00
CaO	53.46	53.34	53.47	53.27	53.17	53.39	53.11	53.22	53.21	53.29	53.29
P_2O_5	41.92	41.90	41.77	41.64	42.22	41.90	42.32	41.50	41.60	41.39	41.76
F	3.53	3.62	3.92	4.38	3.62	3.77	3.85	4.00	3.76	4.23	3.98
Cl	0.00	0.00	0.00	0.00	0.00	0.00	0.00	0.00	0.00	0.00	0.00
SiO_2	0.00	0.00	0.00	0.00	0.00	0.00	0.00	0.00	0.00	0.00	0.00
PbO	0.00	0.00	0.00	0.00	0.00	0.00	0.00	0.09	0.00	0.00	0.00
FeO	0.00	0.00	0.00	0.00	0.00	0.00	0.00	0.09	0.00	0.00	0.00
Na_2O	0.37	0.37	0.39	0.36	0.27	0.27	0.30	0.26	0.31	0.34	0.40
SrO	0.91	0.94	0.91	1.00	1.31	1.36	1.31	1.40	1.39	1.00	1.14
BaO	0.00	0.00	0.00	0.00	0.00	0.00	0.00	0.00	0.00	0.00	0.00
-O-F	-1.49	-1.52	-1.65	-1.84	-1.53	-1.59	-1.62	-1.68	-1.58	-1.78	-1.68
Total	99.66	99.82	99.96	100.07	100.35	100.37	100.28	99.75	99.84	99.70	100.23
						O = 12.5					
La (*apfu*)	0.000	0.000	0.000	0.000	0.000	0.000	0.000	0.000	0.000	0.000	0.000
Ce	0.000	0.000	0.000	0.000	0.010	0.000	0.008	0.000	0.006	0.008	0.010
Pr	0.000	0.000	0.000	0.000	0.000	0.000	0.000	0.004	0.000	0.000	0.000
Nd	0.008	0.008	0.007	0.008	0.007	0.010	0.009	0.010	0.008	0.008	0.010
Sm	0.000	0.000	0.004	0.004	0.003	0.005	0.000	0.000	0.003	0.004	0.000
Eu	0.000	0.000	0.000	0.000	0.000	0.000	0.000	0.000	0.000	0.000	0.000
Gd	0.000	0.006	0.006	0.005	0.006	0.005	0.000	0.000	0.003	0.000	0.000
Dy	0.005	0.000	0.000	0.004	0.000	0.004	0.000	0.000	0.000	0.000	0.003
Y	0.024	0.028	0.025	0.025	0.020	0.018	0.020	0.019	0.017	0.026	0.026
Ho	0.000	0.000	0.000	0.000	0.000	0.000	0.000	0.000	0.000	0.000	0.000
Th	0.000	0.002	0.000	0.000	0.000	0.000	0.000	0.000	0.002	0.000	0.000
U	0.000	0.000	0.000	0.000	0.000	0.000	0.000	0.000	0.000	0.000	0.000
Ca	4.854	4.843	4.860	4.856	4.806	4.842	4.800	4.863	4.852	4.875	4.842
P	3.007	3.006	3.000	2.999	3.016	3.002	3.022	2.996	2.997	2.992	2.998
F	0.946	0.970	1.053	1.177	0.967	1.010	1.026	1.078	1.012	1.143	1.068
Cl	0.000	0.000	0.000	0.000	0.000	0.000	0.000	0.000	0.000	0.000	0.000
Si	0.000	0.000	0.000	0.000	0.000	0.000	0.000	0.000	0.000	0.000	0.000
Pb	0.000	0.000	0.000	0.000	0.000	0.000	0.000	0.002	0.000	0.000	0.000
Fe	0.000	0.000	0.000	0.000	0.000	0.000	0.000	0.007	0.000	0.000	0.000
Na	0.061	0.060	0.064	0.060	0.044	0.044	0.050	0.042	0.051	0.056	0.066
Sr	0.045	0.046	0.045	0.049	0.064	0.067	0.064	0.069	0.068	0.050	0.056
Ba	0.000	0.000	0.000	0.000	0.000	0.000	0.000	0.000	0.000	0.000	0.000
Total	8.002	7.999	8.011	8.009	7.976	7.998	7.973	8.011	8.009	8.018	8.011

Appendix 2.4: Continued

Unit	A		B								
Sample	16007	16007	16010	16010	16010	16010	16010	16010	16010	16010	16010
La_2O_3 (*wt. %*)	0.00	0.00	0.00	0.00	0.00	0.00	0.00	0.00	0.00	0.00	0.00
Ce_2O_3	0.00	0.25	0.24	0.00	0.26	0.32	0.00	0.00	0.28	0.21	0.22
Pr_2O_3	0.00	0.00	0.00	0.00	0.00	0.00	0.00	0.00	0.00	0.00	0.00
Nd_2O_3	0.21	0.22	0.14	0.18	0.00	0.19	0.18	0.12	0.24	0.21	0.28
Sm_2O_3	0.13	0.00	0.00	0.00	0.00	0.00	0.00	0.00	0.00	0.00	0.00
Eu_2O_3	0.00	0.00	0.00	0.00	0.00	0.00	0.00	0.00	0.00	0.00	0.00
Gd_2O_3	0.00	0.15	0.00	0.00	0.00	0.00	0.00	0.00	0.00	0.00	0.00
Dy_2O_3	0.13	0.00	0.00	0.00	0.00	0.00	0.00	0.00	0.00	0.00	0.00
Y_2O_3	0.53	0.40	0.10	0.13	0.00	0.11	0.00	0.16	0.15	0.16	0.20
Ho_2O_3	0.00	0.00	0.00	0.00	0.00	0.00	0.00	0.00	0.00	0.00	0.00
ThO_2	0.00	0.00	0.00	0.00	0.00	0.00	0.00	0.00	0.00	0.00	0.00
UO_2	0.00	0.00	0.00	0.00	0.00	0.00	0.00	0.00	0.00	0.00	0.00
CaO	53.45	53.62	53.75	53.77	53.12	53.70	54.60	53.99	54.37	54.17	53.26
P_2O_5	41.55	41.85	42.26	41.90	41.50	41.62	41.60	41.30	41.73	41.31	41.48
F	4.03	3.94	4.01	4.10	3.69	3.59	4.27	3.82	3.60	3.56	3.83
Cl	0.00	0.00	0.00	0.00	0.00	0.00	0.00	0.00	0.00	0.00	0.00
SiO_2	0.00	0.00	0.00	0.00	0.07	0.00	0.00	0.00	0.00	0.00	0.15
PbO	0.00	0.00	0.00	0.00	0.00	0.00	0.11	0.00	0.00	0.00	0.00
FeO	0.00	0.00	0.00	0.00	0.00	0.00	0.00	0.00	0.00	0.00	0.00
Na_2O	0.29	0.28	0.12	0.16	0.11	0.18	0.14	0.14	0.16	0.17	0.24
SrO	1.03	1.02	2.09	1.90	2.31	1.78	1.44	1.74	1.42	1.51	1.87
BaO	0.00	0.00	0.00	0.00	0.00	0.00	0.00	0.00	0.00	0.00	0.00
-O-F	-1.70	-1.66	-1.69	-1.73	-1.55	-1.51	-1.80	-1.61	-1.51	-1.50	-1.61
Total	99.65	100.07	101.03	100.41	99.51	99.99	100.55	99.65	100.42	99.80	99.91
						O = 12.5					
La (*apfu*)	0.000	0.000	0.000	0.000	0.000	0.000	0.000	0.000	0.000	0.000	0.000
Ce	0.000	0.008	0.007	0.000	0.008	0.010	0.000	0.000	0.009	0.007	0.007
Pr	0.000	0.000	0.000	0.000	0.000	0.000	0.000	0.000	0.000	0.000	0.000
Nd	0.006	0.007	0.004	0.005	0.000	0.006	0.006	0.004	0.007	0.006	0.009
Sm	0.004	0.000	0.000	0.000	0.000	0.000	0.000	0.000	0.000	0.000	0.000
Eu	0.000	0.000	0.000	0.000	0.000	0.000	0.000	0.000	0.000	0.000	0.000
Gd	0.000	0.004	0.000	0.000	0.000	0.000	0.000	0.000	0.000	0.000	0.000
Dy	0.004	0.000	0.000	0.000	0.000	0.000	0.000	0.000	0.000	0.000	0.000
Y	0.024	0.018	0.005	0.006	0.000	0.005	0.000	0.007	0.007	0.007	0.009
Ho	0.000	0.000	0.000	0.000	0.000	0.000	0.000	0.000	0.000	0.000	0.000
Th	0.000	0.000	0.000	0.000	0.000	0.000	0.000	0.000	0.000	0.000	0.000
U	0.000	0.000	0.000	0.000	0.000	0.000	0.000	0.000	0.000	0.000	0.000
Ca	4.878	4.868	4.843	4.874	4.857	4.886	4.953	4.933	4.922	4.940	4.856
P	2.996	3.002	3.008	3.001	2.998	2.992	2.982	2.981	2.985	2.977	2.988
F	1.085	1.054	1.066	1.097	0.996	0.964	1.142	1.030	0.961	0.958	1.030
Cl	0.000	0.000	0.000	0.000	0.000	0.000	0.000	0.000	0.000	0.000	0.000
Si	0.000	0.000	0.000	0.000	0.006	0.000	0.000	0.000	0.000	0.000	0.013
Pb	0.000	0.000	0.000	0.000	0.000	0.000	0.002	0.000	0.000	0.000	0.000
Fe	0.000	0.000	0.000	0.000	0.000	0.000	0.000	0.000	0.000	0.000	0.000
Na	0.049	0.046	0.019	0.026	0.018	0.029	0.023	0.023	0.026	0.028	0.039
Sr	0.051	0.050	0.102	0.093	0.114	0.088	0.071	0.086	0.069	0.074	0.092
Ba	0.000	0.000	0.000	0.000	0.000	0.000	0.000	0.000	0.000	0.000	0.000
Total	8.011	8.002	7.989	8.006	8.001	8.016	8.036	8.034	8.024	8.039	8.012

Appendix 2.4: Continued

Unit	B							BD			
Sample	16010	16010	16010	16010	16010	16010	16010	15113	15113	15113	15113
La_2O_3 (*wt. %*)	0.00	0.00	0.00	0.00	0.00	0.00	0.00	0.00	0.00	0.00	0.00
Ce_2O_3	0.00	0.28	0.23	0.00	0.29	0.28	0.30	0.39	0.35	0.28	0.42
Pr_2O_3	0.11	0.00	0.00	0.00	0.00	0.00	0.00	0.11	0.00	0.00	0.00
Nd_2O_3	0.15	0.20	0.23	0.24	0.14	0.22	0.15	0.34	0.35	0.29	0.29
Sm_2O_3	0.00	0.00	0.00	0.00	0.00	0.00	0.00	0.12	0.00	0.00	0.00
Eu_2O_3	0.00	0.00	0.00	0.00	0.00	0.00	0.00	0.00	0.00	0.00	0.00
Gd_2O_3	0.00	0.13	0.17	0.00	0.17	0.00	0.00	0.00	0.00	0.00	0.00
Dy_2O_3	0.00	0.00	0.00	0.00	0.00	0.00	0.00	0.00	0.00	0.00	0.00
Y_2O_3	0.15	0.15	0.12	0.16	0.14	0.17	0.16	0.15	0.18	0.18	0.16
Ho_2O_3	0.00	0.00	0.00	0.00	0.00	0.00	0.00	0.00	0.00	0.00	0.00
ThO_2	0.00	0.00	0.00	0.00	0.00	0.00	0.00	0.00	0.00	0.00	0.00
UO_2	0.00	0.00	0.00	0.00	0.00	0.00	0.00	0.00	0.00	0.00	0.00
CaO	53.69	53.69	53.22	53.63	54.28	53.70	53.90	54.25	54.44	54.32	54.15
P_2O_5	41.73	41.76	41.24	41.84	41.98	41.85	41.92	42.03	42.20	41.84	41.63
F	3.90	3.76	3.60	4.12	3.82	3.95	3.83	3.98	3.46	3.85	4.03
Cl	0.00	0.00	0.00	0.00	0.00	0.00	0.00	0.00	0.00	0.00	0.00
SiO_2	0.00	0.00	0.00	0.00	0.00	0.00	0.00	0.00	0.00	0.00	0.00
PbO	0.00	0.08	0.00	0.00	0.00	0.00	0.00	0.00	0.00	0.00	0.00
FeO	0.00	0.00	0.00	0.00	0.00	0.00	0.00	0.00	0.00	0.00	0.00
Na_2O	0.15	0.18	0.20	0.17	0.15	0.19	0.12	0.26	0.23	0.20	0.21
SrO	2.01	2.11	1.85	1.68	1.39	1.81	1.81	0.59	0.53	0.67	0.60
BaO	0.00	0.00	0.00	0.00	0.00	0.00	0.00	0.00	0.00	0.00	0.37
-O-F	-1.64	-1.58	-1.52	-1.73	-1.61	-1.66	-1.61	-1.67	-1.46	-1.62	-1.70
Total	100.25	100.76	99.33	100.11	100.74	100.50	100.57	100.54	100.27	99.99	100.16
						O = 12.5					
La (*apfu*)	0.000	0.000	0.000	0.000	0.000	0.000	0.000	0.000	0.000	0.000	0.000
Ce	0.000	0.009	0.007	0.000	0.009	0.009	0.009	0.012	0.011	0.009	0.013
Pr	0.003	0.000	0.000	0.000	0.000	0.000	0.000	0.003	0.000	0.000	0.000
Nd	0.005	0.006	0.007	0.007	0.004	0.007	0.004	0.010	0.010	0.009	0.009
Sm	0.000	0.000	0.000	0.000	0.000	0.000	0.000	0.003	0.000	0.000	0.000
Eu	0.000	0.000	0.000	0.000	0.000	0.000	0.000	0.000	0.000	0.000	0.000
Gd	0.000	0.004	0.005	0.000	0.005	0.000	0.000	0.000	0.000	0.000	0.000
Dy	0.000	0.000	0.000	0.000	0.000	0.000	0.000	0.000	0.000	0.000	0.000
Y	0.007	0.007	0.005	0.007	0.006	0.008	0.007	0.007	0.008	0.008	0.007
Ho	0.000	0.000	0.000	0.000	0.000	0.000	0.000	0.000	0.000	0.000	0.000
Th	0.000	0.000	0.000	0.000	0.000	0.000	0.000	0.000	0.000	0.000	0.000
U	0.000	0.000	0.000	0.000	0.000	0.000	0.000	0.000	0.000	0.000	0.000
Ca	4.878	4.866	4.882	4.873	4.899	4.868	4.877	4.899	4.903	4.923	4.922
P	2.996	2.990	2.989	3.003	2.994	2.997	2.997	2.999	3.003	2.996	2.990
F	1.044	1.007	0.975	1.104	1.018	1.057	1.023	1.060	0.919	1.029	1.081
Cl	0.000	0.000	0.000	0.000	0.000	0.000	0.000	0.000	0.000	0.000	0.000
Si	0.000	0.000	0.000	0.000	0.000	0.000	0.000	0.000	0.000	0.000	0.000
Pb	0.000	0.002	0.000	0.000	0.000	0.000	0.000	0.000	0.000	0.000	0.000
Fe	0.000	0.000	0.000	0.000	0.000	0.000	0.000	0.000	0.000	0.000	0.000
Na	0.024	0.029	0.032	0.028	0.025	0.031	0.020	0.042	0.038	0.033	0.035
Sr	0.099	0.103	0.092	0.083	0.068	0.089	0.088	0.029	0.026	0.033	0.030
Ba	0.000	0.000	0.000	0.000	0.000	0.000	0.000	0.000	0.000	0.000	0.012
Total	8.011	8.016	8.020	8.002	8.010	8.008	8.004	8.004	7.999	8.009	8.018

Appendix 2.4: Continued

Unit	BD										
Sample	15113	15113	15113	15113	15113	15113	15113	15113	15113	16002	16002
La_2O_3 (*wt.* %)	0.00	0.00	0.00	0.00	0.00	0.00	0.00	0.00	0.00	0.00	0.00
Ce_2O_3	0.37	0.31	0.21	0.27	0.33	0.33	0.27	0.24	0.23	0.31	0.22
Pr_2O_3	0.00	0.20	0.11	0.00	0.00	0.00	0.00	0.00	0.00	0.00	0.00
Nd_2O_3	0.32	0.28	0.36	0.33	0.40	0.30	0.27	0.25	0.27	0.29	0.30
Sm_2O_3	0.00	0.00	0.00	0.12	0.00	0.11	0.00	0.00	0.00	0.00	0.14
Eu_2O_3	0.00	0.00	0.00	0.00	0.00	0.00	0.00	0.00	0.00	0.00	0.00
Gd_2O_3	0.16	0.00	0.00	0.12	0.00	0.00	0.00	0.00	0.17	0.00	0.00
Dy_2O_3	0.00	0.00	0.00	0.00	0.00	0.00	0.00	0.00	0.00	0.00	0.00
Y_2O_3	0.15	0.21	0.14	0.15	0.20	0.19	0.17	0.16	0.13	0.13	0.11
Ho_2O_3	0.00	0.00	0.00	0.00	0.00	0.00	0.00	0.00	0.00	0.00	0.00
ThO_2	0.00	0.00	0.00	0.00	0.00	0.00	0.08	0.00	0.00	0.00	0.00
UO_2	0.00	0.00	0.00	0.00	0.00	0.00	0.00	0.00	0.00	0.00	0.00
CaO	54.24	54.14	54.47	54.29	54.28	54.20	54.40	54.31	54.47	54.22	54.06
P_2O_5	41.84	41.93	41.91	41.66	41.67	41.71	41.68	41.55	41.82	41.95	41.88
F	4.57	3.75	3.89	4.04	3.59	3.76	4.22	3.72	4.45	4.34	4.22
Cl	0.00	0.00	0.00	0.00	0.00	0.00	0.00	0.00	0.00	0.00	0.00
SiO_2	0.00	0.00	0.00	0.00	0.00	0.00	0.00	0.00	0.00	0.00	0.00
PbO	0.00	0.00	0.00	0.00	0.00	0.00	0.00	0.00	0.00	0.00	0.00
FeO	0.00	0.00	0.00	0.00	0.00	0.00	0.00	0.00	0.00	0.00	0.00
Na_2O	0.23	0.19	0.20	0.20	0.25	0.21	0.17	0.20	0.19	0.20	0.18
SrO	0.55	0.59	0.58	0.56	0.58	0.55	0.58	0.67	0.58	1.05	1.07
BaO	0.00	0.00	0.00	0.00	0.00	0.00	0.00	0.00	0.00	0.00	0.00
-O-F	-1.92	-1.58	-1.64	-1.70	-1.51	-1.58	-1.78	-1.57	-1.87	-1.83	-1.78
Total	100.51	100.02	100.24	100.03	99.79	99.77	100.05	99.54	100.42	100.66	100.39
	O = 12.5										
La (*apfu*)	0.000	0.000	0.000	0.000	0.000	0.000	0.000	0.000	0.000	0.000	0.000
Ce	0.011	0.010	0.007	0.008	0.010	0.010	0.008	0.007	0.007	0.010	0.007
Pr	0.000	0.006	0.003	0.000	0.000	0.000	0.000	0.000	0.000	0.000	0.000
Nd	0.010	0.008	0.011	0.010	0.012	0.009	0.008	0.008	0.008	0.009	0.009
Sm	0.000	0.000	0.000	0.004	0.000	0.003	0.000	0.000	0.000	0.000	0.004
Eu	0.000	0.000	0.000	0.000	0.000	0.000	0.000	0.000	0.000	0.000	0.000
Gd	0.005	0.000	0.000	0.003	0.000	0.000	0.000	0.000	0.005	0.000	0.000
Dy	0.000	0.000	0.000	0.000	0.000	0.000	0.000	0.000	0.000	0.000	0.000
Y	0.007	0.009	0.006	0.007	0.009	0.009	0.008	0.007	0.006	0.006	0.005
Ho	0.000	0.000	0.000	0.000	0.000	0.000	0.000	0.000	0.000	0.000	0.000
Th	0.000	0.000	0.000	0.000	0.000	0.000	0.002	0.000	0.000	0.000	0.000
U	0.000	0.000	0.000	0.000	0.000	0.000	0.000	0.000	0.000	0.000	0.000
Ca	4.915	4.903	4.926	4.932	4.929	4.924	4.941	4.944	4.934	4.903	4.899
P	2.996	3.001	2.995	2.990	2.990	2.994	2.991	2.989	2.994	2.997	2.999
F	1.221	1.004	1.039	1.083	0.963	1.008	1.131	1.000	1.190	1.158	1.130
Cl	0.000	0.000	0.000	0.000	0.000	0.000	0.000	0.000	0.000	0.000	0.000
Si	0.000	0.000	0.000	0.000	0.000	0.000	0.000	0.000	0.000	0.000	0.000
Pb	0.000	0.000	0.000	0.000	0.000	0.000	0.000	0.000	0.000	0.000	0.000
Fe	0.000	0.000	0.000	0.000	0.000	0.000	0.000	0.000	0.000	0.000	0.000
Na	0.038	0.031	0.033	0.032	0.042	0.035	0.028	0.034	0.030	0.032	0.030
Sr	0.027	0.029	0.028	0.028	0.029	0.027	0.029	0.033	0.028	0.051	0.052
Ba	0.000	0.000	0.000	0.000	0.000	0.000	0.000	0.000	0.000	0.000	0.000
Total	8.009	7.998	8.010	8.014	8.020	8.011	8.014	8.022	8.012	8.008	8.005

Appendix 2.4: Continued

Unit	BD										
Sample	16002	16002	16002	16002	16002	16002	16002	16002	16002	16002	16002
La_2O_3 (*wt. %*)	0.00	0.00	0.00	0.00	0.00	0.00	0.00	0.00	0.00	0.00	0.00
Ce_2O_3	0.37	0.26	0.27	0.24	0.25	0.30	0.37	0.26	0.19	0.00	0.28
Pr_2O_3	0.00	0.00	0.00	0.00	0.00	0.00	0.00	0.00	0.00	0.00	0.00
Nd_2O_3	0.22	0.29	0.31	0.25	0.26	0.30	0.27	0.26	0.31	0.33	0.25
Sm_2O_3	0.00	0.00	0.00	0.13	0.00	0.00	0.00	0.11	0.11	0.00	0.11
Eu_2O_3	0.00	0.00	0.00	0.00	0.00	0.00	0.00	0.00	0.00	0.00	0.00
Gd_2O_3	0.13	0.00	0.00	0.16	0.00	0.00	0.00	0.00	0.00	0.00	0.00
Dy_2O_3	0.00	0.00	0.00	0.00	0.00	0.00	0.00	0.00	0.00	0.00	0.00
Y_2O_3	0.14	0.14	0.14	0.17	0.15	0.16	0.11	0.11	0.13	0.17	0.14
Ho_2O_3	0.00	0.00	0.00	0.00	0.00	0.00	0.00	0.00	0.00	0.00	0.00
ThO_2	0.00	0.00	0.00	0.00	0.00	0.00	0.00	0.00	0.00	0.00	0.00
UO_2	0.00	0.00	0.00	0.00	0.00	0.00	0.00	0.00	0.00	0.00	0.00
CaO	54.12	54.23	54.14	54.38	54.22	53.89	54.09	53.47	53.93	53.97	54.18
P_2O_5	41.63	41.73	41.62	41.98	41.84	41.68	41.82	41.17	41.64	42.11	41.50
F	4.30	3.84	4.20	3.68	3.53	3.76	3.95	4.25	4.15	4.01	3.57
Cl	0.00	0.00	0.00	0.00	0.00	0.00	0.00	0.00	0.00	0.00	0.00
SiO_2	0.00	0.00	0.00	0.00	0.00	0.00	0.00	0.55	0.00	0.00	0.00
PbO	0.00	0.08	0.00	0.00	0.00	0.00	0.00	0.00	0.00	0.00	0.00
FeO	0.00	0.00	0.00	0.00	0.00	0.00	0.00	0.00	0.19	0.00	0.00
Na_2O	0.20	0.20	0.21	0.22	0.22	0.19	0.23	0.57	0.26	0.22	0.19
SrO	1.04	1.02	0.94	0.92	0.96	0.92	0.98	1.00	0.95	0.94	1.06
BaO	0.00	0.00	0.00	0.00	0.00	0.00	0.00	0.00	0.00	0.00	0.00
-O-F	-1.81	-1.62	-1.77	-1.55	-1.49	-1.58	-1.66	-1.79	-1.75	-1.69	-1.50
Total	100.33	100.16	100.06	100.57	99.94	99.62	100.14	99.95	100.11	100.07	99.78
	O = 12.5										
La (*apfu*)	0.000	0.000	0.000	0.000	0.000	0.000	0.000	0.000	0.000	0.000	0.000
Ce	0.011	0.008	0.008	0.007	0.008	0.009	0.011	0.008	0.006	0.000	0.009
Pr	0.000	0.000	0.000	0.000	0.000	0.000	0.000	0.000	0.000	0.000	0.000
Nd	0.007	0.009	0.009	0.007	0.008	0.009	0.008	0.008	0.009	0.010	0.007
Sm	0.000	0.000	0.000	0.004	0.000	0.000	0.000	0.003	0.003	0.000	0.003
Eu	0.000	0.000	0.000	0.000	0.000	0.000	0.000	0.000	0.000	0.000	0.000
Gd	0.004	0.000	0.000	0.004	0.000	0.000	0.000	0.000	0.000	0.000	0.000
Dy	0.000	0.000	0.000	0.000	0.000	0.000	0.000	0.000	0.000	0.000	0.000
Y	0.006	0.006	0.006	0.008	0.007	0.007	0.005	0.005	0.006	0.008	0.006
Ho	0.000	0.000	0.000	0.000	0.000	0.000	0.000	0.000	0.000	0.000	0.000
Th	0.000	0.000	0.000	0.000	0.000	0.000	0.000	0.000	0.000	0.000	0.000
U	0.000	0.000	0.000	0.000	0.000	0.000	0.000	0.000	0.000	0.000	0.000
Ca	4.918	4.919	4.923	4.907	4.913	4.906	4.905	4.868	4.904	4.884	4.932
P	2.989	2.991	2.991	2.994	2.996	2.998	2.997	2.962	2.991	3.010	2.985
F	1.154	1.029	1.126	0.981	0.944	1.010	1.056	1.143	1.114	1.072	0.960
Cl	0.000	0.000	0.000	0.000	0.000	0.000	0.000	0.000	0.000	0.000	0.000
Si	0.000	0.000	0.000	0.000	0.000	0.000	0.000	0.047	0.000	0.000	0.000
Pb	0.000	0.002	0.000	0.000	0.000	0.000	0.000	0.000	0.000	0.000	0.000
Fe	0.000	0.000	0.000	0.000	0.000	0.000	0.000	0.000	0.014	0.000	0.000
Na	0.033	0.033	0.035	0.035	0.036	0.032	0.037	0.094	0.043	0.036	0.030
Sr	0.051	0.050	0.046	0.045	0.047	0.045	0.048	0.049	0.047	0.046	0.052
Ba	0.000	0.000	0.000	0.000	0.000	0.000	0.000	0.000	0.000	0.000	0.000
Total	8.019	8.018	8.019	8.012	8.014	8.006	8.011	8.045	8.022	7.993	8.025

Appendix 2.4: Continued

Unit	BD										
Sample	15114	15114	15114	15114	15114	15114	15114	15114	15114	15114	15114
La_2O_3 (*wt. %*)	0.00	0.00	0.00	0.00	0.00	0.00	0.22	0.00	0.00	0.00	0.00
Ce_2O_3	0.23	0.22	0.00	0.23	0.20	0.00	0.20	0.00	0.00	0.00	0.35
Pr_2O_3	0.00	0.00	0.00	0.00	0.00	0.00	0.00	0.00	0.00	0.00	0.00
Nd_2O_3	0.30	0.26	0.29	0.20	0.28	0.28	0.33	0.26	0.25	0.24	0.36
Sm_2O_3	0.00	0.00	0.00	0.00	0.00	0.00	0.00	0.00	0.00	0.00	0.00
Eu_2O_3	0.00	0.00	0.00	0.00	0.00	0.00	0.00	0.00	0.00	0.00	0.00
Gd_2O_3	0.00	0.00	0.16	0.00	0.19	0.12	0.00	0.00	0.00	0.00	0.00
Dy_2O_3	0.00	0.00	0.00	0.00	0.00	0.00	0.00	0.00	0.00	0.00	0.00
Y_2O_3	0.17	0.14	0.20	0.16	0.14	0.13	0.18	0.12	0.15	0.20	0.16
Ho_2O_3	0.00	0.00	0.00	0.00	0.00	0.00	0.00	0.00	0.00	0.00	0.00
ThO_2	0.00	0.00	0.00	0.00	0.00	0.00	0.00	0.00	0.00	0.00	0.00
UO_2	0.00	0.00	0.00	0.00	0.00	0.00	0.00	0.00	0.00	0.00	0.00
CaO	54.50	54.46	54.36	54.59	54.21	54.71	54.62	54.49	54.51	54.69	54.23
P_2O_5	41.51	41.71	40.54	41.75	41.92	41.89	41.75	41.57	41.62	41.83	41.39
F	4.33	4.20	4.26	4.00	4.19	3.96	4.07	4.27	4.32	3.73	3.87
Cl	0.00	0.00	0.00	0.00	0.00	0.00	0.00	0.00	0.00	0.00	0.00
SiO_2	0.00	0.00	0.00	0.00	0.00	0.00	0.00	0.00	0.00	0.00	0.00
PbO	0.00	0.00	0.00	0.00	0.00	0.00	0.00	0.00	0.00	0.00	0.00
FeO	0.00	0.00	0.00	0.00	0.00	0.00	0.00	0.00	0.00	0.00	0.00
Na_2O	0.20	0.21	0.20	0.21	0.20	0.18	0.23	0.18	0.23	0.20	0.25
SrO	0.63	0.63	0.60	0.61	0.71	0.59	0.62	0.65	0.66	0.71	0.69
BaO	0.00	0.00	0.00	0.00	0.00	0.00	0.00	0.00	0.00	0.00	0.00
-O-F	-1.82	-1.77	-1.79	-1.68	-1.76	-1.67	-1.72	-1.80	-1.82	-1.57	-1.63
Total	100.03	100.05	98.80	100.07	100.25	100.18	100.50	99.75	99.92	100.02	99.67
						O = 12.5					
La (*apfu*)	0.000	0.000	0.000	0.000	0.000	0.000	0.007	0.000	0.000	0.000	0.000
Ce	0.007	0.007	0.000	0.007	0.006	0.000	0.006	0.000	0.000	0.000	0.011
Pr	0.000	0.000	0.000	0.000	0.000	0.000	0.000	0.000	0.000	0.000	0.000
Nd	0.009	0.008	0.009	0.006	0.008	0.009	0.010	0.008	0.008	0.007	0.011
Sm	0.000	0.000	0.000	0.000	0.000	0.000	0.000	0.000	0.000	0.000	0.000
Eu	0.000	0.000	0.000	0.000	0.000	0.000	0.000	0.000	0.000	0.000	0.000
Gd	0.000	0.000	0.005	0.000	0.005	0.003	0.000	0.000	0.000	0.000	0.000
Dy	0.000	0.000	0.000	0.000	0.000	0.000	0.000	0.000	0.000	0.000	0.000
Y	0.008	0.006	0.009	0.007	0.006	0.006	0.008	0.005	0.007	0.009	0.007
Ho	0.000	0.000	0.000	0.000	0.000	0.000	0.000	0.000	0.000	0.000	0.000
Th	0.000	0.000	0.000	0.000	0.000	0.000	0.000	0.000	0.000	0.000	0.000
U	0.000	0.000	0.000	0.000	0.000	0.000	0.000	0.000	0.000	0.000	0.000
Ca	4.958	4.943	5.022	4.948	4.910	4.947	4.943	4.959	4.955	4.949	4.945
P	2.984	2.991	2.959	2.990	3.000	2.993	2.985	2.990	2.989	2.990	2.983
F	1.163	1.124	1.162	1.070	1.120	1.056	1.088	1.146	1.159	0.995	1.040
Cl	0.000	0.000	0.000	0.000	0.000	0.000	0.000	0.000	0.000	0.000	0.000
Si	0.000	0.000	0.000	0.000	0.000	0.000	0.000	0.000	0.000	0.000	0.000
Pb	0.000	0.000	0.000	0.000	0.000	0.000	0.000	0.000	0.000	0.000	0.000
Fe	0.000	0.000	0.000	0.000	0.000	0.000	0.000	0.000	0.000	0.000	0.000
Na	0.032	0.034	0.034	0.034	0.033	0.029	0.038	0.030	0.038	0.033	0.042
Sr	0.031	0.031	0.030	0.030	0.035	0.029	0.030	0.032	0.033	0.035	0.034
Ba	0.000	0.000	0.000	0.000	0.000	0.000	0.000	0.000	0.000	0.000	0.000
Total	8.029	8.020	8.067	8.022	8.004	8.016	8.026	8.024	8.029	8.023	8.032

Appendix 2.4: Continued

Unit	BD										
Sample	15114	15114	15114	15114	15158	15158	15158	15158	15158	15158	15158
La_2O_3 (*wt. %*)	0.00	0.00	0.00	0.00	0.00	0.00	0.00	0.00	0.00	0.00	0.00
Ce_2O_3	0.00	0.25	0.00	0.27	0.24	0.33	0.30	0.35	0.43	0.21	0.28
Pr_2O_3	0.00	0.00	0.00	0.00	0.00	0.00	0.00	0.00	0.00	0.00	0.00
Nd_2O_3	0.23	0.30	0.38	0.29	0.32	0.37	0.31	0.34	0.25	0.22	0.22
Sm_2O_3	0.00	0.00	0.10	0.00	0.00	0.00	0.00	0.12	0.11	0.11	0.00
Eu_2O_3	0.00	0.00	0.00	0.00	0.00	0.00	0.00	0.00	0.00	0.00	0.00
Gd_2O_3	0.00	0.00	0.00	0.00	0.00	0.12	0.00	0.15	0.15	0.00	0.00
Dy_2O_3	0.00	0.00	0.00	0.00	0.00	0.00	0.00	0.00	0.00	0.00	0.00
Y_2O_3	0.15	0.20	0.16	0.15	0.00	0.11	0.00	0.00	0.10	0.00	0.00
Ho_2O_3	0.00	0.00	0.00	0.00	0.00	0.00	0.00	0.00	0.00	0.00	0.00
ThO_2	0.00	0.00	0.00	0.00	0.00	0.05	0.00	0.00	0.00	0.00	0.00
UO_2	0.00	0.00	0.00	0.00	0.00	0.00	0.00	0.00	0.00	0.00	0.00
CaO	53.64	54.20	54.13	54.44	54.70	53.66	54.05	53.81	54.42	53.98	54.75
P_2O_5	41.29	41.78	41.72	41.96	41.60	41.55	41.64	41.81	41.94	41.01	42.17
F	3.90	4.11	4.31	4.06	3.84	3.62	3.94	3.98	4.08	3.91	3.62
Cl	0.00	0.00	0.00	0.00	0.00	0.00	0.00	0.00	0.00	0.00	0.00
SiO_2	0.00	0.00	0.00	0.00	0.00	0.00	0.00	0.16	0.00	0.00	0.00
PbO	0.00	0.00	0.00	0.00	0.00	0.00	0.00	0.00	0.00	0.00	0.00
FeO	0.00	0.00	0.00	0.00	0.00	0.00	0.00	0.00	0.00	0.11	0.00
Na_2O	0.19	0.20	0.21	0.21	0.19	0.20	0.20	0.19	0.16	0.11	0.13
SrO	0.60	0.65	0.61	0.65	0.65	0.75	0.78	0.81	0.82	0.68	0.81
BaO	0.00	0.00	0.00	0.00	0.00	0.00	0.00	0.00	0.00	0.00	0.00
-O-F	-1.64	-1.73	-1.82	-1.71	-1.62	-1.53	-1.66	-1.67	-1.72	-1.65	-1.52
Total	98.36	99.97	99.80	100.32	99.92	99.25	99.57	100.03	100.74	98.70	100.44
	O = 12.5										
La (*apfu*)	0.000	0.000	0.000	0.000	0.000	0.000	0.000	0.000	0.000	0.000	0.000
Ce	0.000	0.008	0.000	0.008	0.008	0.010	0.009	0.011	0.013	0.007	0.009
Pr	0.000	0.000	0.000	0.000	0.000	0.000	0.000	0.000	0.000	0.000	0.000
Nd	0.007	0.009	0.012	0.009	0.010	0.011	0.010	0.010	0.007	0.007	0.007
Sm	0.000	0.000	0.003	0.000	0.000	0.000	0.000	0.004	0.003	0.003	0.000
Eu	0.000	0.000	0.000	0.000	0.000	0.000	0.000	0.000	0.000	0.000	0.000
Gd	0.000	0.000	0.000	0.000	0.000	0.003	0.000	0.004	0.004	0.000	0.000
Dy	0.000	0.000	0.000	0.000	0.000	0.000	0.000	0.000	0.000	0.000	0.000
Y	0.007	0.009	0.007	0.007	0.000	0.005	0.000	0.000	0.004	0.000	0.000
Ho	0.000	0.000	0.000	0.000	0.000	0.000	0.000	0.000	0.000	0.000	0.000
Th	0.000	0.000	0.000	0.000	0.000	0.001	0.000	0.000	0.000	0.000	0.000
U	0.000	0.000	0.000	0.000	0.000	0.000	0.000	0.000	0.000	0.000	0.000
Ca	4.933	4.920	4.924	4.922	4.966	4.902	4.924	4.882	4.915	4.968	4.929
P	3.000	2.997	2.998	2.997	2.984	2.999	2.997	2.997	2.993	2.982	2.999
F	1.060	1.102	1.158	1.083	1.028	0.977	1.060	1.065	1.089	1.062	0.961
Cl	0.000	0.000	0.000	0.000	0.000	0.000	0.000	0.000	0.000	0.000	0.000
Si	0.000	0.000	0.000	0.000	0.000	0.000	0.000	0.013	0.000	0.000	0.000
Pb	0.000	0.000	0.000	0.000	0.000	0.000	0.000	0.000	0.000	0.000	0.000
Fe	0.000	0.000	0.000	0.000	0.000	0.000	0.000	0.000	0.000	0.008	0.000
Na	0.032	0.033	0.034	0.035	0.032	0.034	0.033	0.031	0.026	0.019	0.021
Sr	0.030	0.032	0.030	0.032	0.032	0.037	0.039	0.040	0.040	0.034	0.039
Ba	0.000	0.000	0.000	0.000	0.000	0.000	0.000	0.000	0.000	0.000	0.000
Total	8.009	8.008	8.008	8.009	8.031	8.002	8.012	7.992	8.007	8.028	8.004

Appendix 2.4: Continued

Unit	BD			Cal Carb 1							
Sample	15158	15158	15158	15029	15029	15029	15029	15029	15029	15029	15029
La_2O_3 (*wt. %*)	0.00	0.00	0.00	0.00	0.00	0.00	0.00	0.00	0.00	0.00	0.20
Ce_2O_3	0.21	0.22	0.00	0.00	0.29	0.23	0.00	0.23	0.26	0.22	0.37
Pr_2O_3	0.00	0.00	0.00	0.00	0.00	0.00	0.00	0.00	0.00	0.00	0.00
Nd_2O_3	0.23	0.27	0.18	0.00	0.18	0.22	0.00	0.14	0.14	0.12	0.23
Sm_2O_3	0.18	0.00	0.00	0.00	0.00	0.00	0.00	0.00	0.00	0.00	0.00
Eu_2O_3	0.00	0.00	0.00	0.00	0.00	0.00	0.00	0.00	0.00	0.00	0.00
Gd_2O_3	0.00	0.00	0.00	0.00	0.00	0.00	0.00	0.00	0.00	0.00	0.00
Dy_2O_3	0.00	0.00	0.00	0.00	0.00	0.00	0.00	0.00	0.00	0.00	0.00
Y_2O_3	0.00	0.11	0.00	0.00	0.00	0.00	0.00	0.00	0.00	0.00	0.13
Ho_2O_3	0.00	0.00	0.00	0.00	0.00	0.00	0.00	0.00	0.00	0.00	0.00
ThO_2	0.00	0.00	0.00	0.00	0.00	0.00	0.00	0.00	0.00	0.00	0.00
UO_2	0.00	0.00	0.00	0.00	0.00	0.00	0.00	0.00	0.00	0.00	0.00
CaO	54.54	54.32	54.48	55.22	54.81	54.59	55.03	55.28	54.78	54.76	54.33
P_2O_5	41.81	41.76	41.67	42.03	42.34	41.83	41.64	41.93	42.00	41.89	41.66
F	3.98	4.00	4.11	3.77	3.96	3.88	3.80	3.76	3.96	3.67	3.79
Cl	0.00	0.00	0.00	0.00	0.00	0.00	0.00	0.00	0.00	0.00	0.00
SiO_2	0.00	0.00	0.00	0.06	0.00	0.14	0.23	0.14	0.07	0.00	0.00
PbO	0.00	0.00	0.00	0.00	0.00	0.00	0.00	0.00	0.00	0.00	0.00
FeO	0.00	0.00	0.00	0.00	0.00	0.00	0.00	0.00	0.00	0.00	0.00
Na_2O	0.16	0.17	0.09	0.14	0.20	0.12	0.17	0.13	0.17	0.22	0.24
SrO	0.74	0.74	0.84	0.40	0.57	0.42	0.34	0.40	0.48	0.60	0.65
BaO	0.00	0.00	0.00	0.00	0.20	0.00	0.00	0.00	0.00	0.00	0.00
-O-F	-1.67	-1.69	-1.73	-1.59	-1.67	-1.63	-1.60	-1.58	-1.67	-1.54	-1.60
Total	100.17	99.91	99.64	100.03	100.89	99.80	99.61	100.42	100.19	99.93	100.01
						O = 12.5					
La (*apfu*)	0.000	0.000	0.000	0.000	0.000	0.000	0.000	0.000	0.000	0.000	0.006
Ce	0.007	0.007	0.000	0.000	0.009	0.007	0.000	0.007	0.008	0.007	0.012
Pr	0.000	0.000	0.000	0.000	0.000	0.000	0.000	0.000	0.000	0.000	0.000
Nd	0.007	0.008	0.006	0.000	0.005	0.007	0.000	0.004	0.004	0.004	0.007
Sm	0.005	0.000	0.000	0.000	0.000	0.000	0.000	0.000	0.000	0.000	0.000
Eu	0.000	0.000	0.000	0.000	0.000	0.000	0.000	0.000	0.000	0.000	0.000
Gd	0.000	0.000	0.000	0.000	0.000	0.000	0.000	0.000	0.000	0.000	0.000
Dy	0.000	0.000	0.000	0.000	0.000	0.000	0.000	0.000	0.000	0.000	0.000
Y	0.000	0.005	0.000	0.000	0.000	0.000	0.000	0.000	0.000	0.000	0.006
Ho	0.000	0.000	0.000	0.000	0.000	0.000	0.000	0.000	0.000	0.000	0.000
Th	0.000	0.000	0.000	0.000	0.000	0.000	0.000	0.000	0.000	0.000	0.000
U	0.000	0.000	0.000	0.000	0.000	0.000	0.000	0.000	0.000	0.000	0.000
Ca	4.941	4.931	4.956	4.976	4.920	4.943	4.983	4.975	4.945	4.952	4.932
P	2.993	2.995	2.995	2.993	3.003	2.993	2.979	2.982	2.995	2.994	2.988
F	1.063	1.073	1.103	1.002	1.049	1.038	1.016	0.999	1.056	0.980	1.016
Cl	0.000	0.000	0.000	0.000	0.000	0.000	0.000	0.000	0.000	0.000	0.000
Si	0.000	0.000	0.000	0.005	0.000	0.012	0.020	0.012	0.006	0.000	0.000
Pb	0.000	0.000	0.000	0.000	0.000	0.000	0.000	0.000	0.000	0.000	0.000
Fe	0.000	0.000	0.000	0.000	0.000	0.000	0.000	0.000	0.000	0.000	0.000
Na	0.025	0.028	0.014	0.023	0.032	0.020	0.027	0.021	0.028	0.036	0.039
Sr	0.036	0.036	0.042	0.020	0.028	0.021	0.017	0.019	0.023	0.029	0.032
Ba	0.000	0.000	0.000	0.000	0.007	0.000	0.000	0.000	0.000	0.000	0.000
Total	8.014	8.011	8.012	8.017	8.004	8.002	8.025	8.020	8.010	8.022	8.022

Appendix 2.4: Continued

Unit	Cal Carb 1									Cal Carb 2	
Sample	15029	15029	15029	15029	15029	15029	15029	15029	15029	15049	15049
La_2O_3 (*wt. %*)	0.00	0.00	0.00	0.00	0.00	0.00	0.00	0.00	0.00	0.19	0.00
Ce_2O_3	0.00	0.22	0.26	0.36	0.00	0.34	0.19	0.00	0.00	0.43	0.00
Pr_2O_3	0.00	0.00	0.13	0.00	0.00	0.00	0.00	0.00	0.00	0.00	0.00
Nd_2O_3	0.16	0.09	0.22	0.15	0.15	0.22	0.16	0.13	0.13	0.21	0.22
Sm_2O_3	0.00	0.00	0.00	0.00	0.00	0.00	0.00	0.00	0.00	0.00	0.00
Eu_2O_3	0.00	0.00	0.00	0.00	0.00	0.00	0.00	0.00	0.00	0.00	0.00
Gd_2O_3	0.00	0.00	0.14	0.00	0.00	0.25	0.00	0.00	0.00	0.00	0.00
Dy_2O_3	0.00	0.00	0.00	0.00	0.00	0.00	0.00	0.00	0.00	0.00	0.00
Y_2O_3	0.00	0.00	0.21	0.00	0.25	0.22	0.00	0.00	0.00	0.00	0.00
Ho_2O_3	0.00	0.00	0.00	0.00	0.00	0.00	0.00	0.00	0.00	0.00	0.00
ThO_2	0.00	0.00	0.00	0.00	0.00	0.00	0.00	0.00	0.00	0.00	0.00
UO_2	0.00	0.00	0.00	0.00	0.00	0.00	0.00	0.00	0.00	0.00	0.00
CaO	55.04	54.94	54.40	54.84	54.36	54.65	54.92	55.10	54.83	54.77	54.98
P_2O_5	41.90	41.85	42.15	41.98	41.55	41.01	41.50	41.71	41.59	40.55	41.34
F	3.83	3.66	3.65	3.79	3.68	3.31	3.79	3.94	3.86	3.00	3.25
Cl	0.00	0.00	0.00	0.00	0.00	0.00	0.00	0.00	0.00	0.00	0.00
SiO_2	0.09	0.11	0.00	0.00	0.00	0.00	0.00	0.07	0.00	0.32	0.25
PbO	0.00	0.00	0.00	0.00	0.00	0.00	0.00	0.00	0.00	0.00	0.00
FeO	0.00	0.00	0.00	0.00	0.00	0.00	0.00	0.00	0.00	0.00	0.00
Na_2O	0.14	0.14	0.23	0.17	0.22	0.17	0.21	0.15	0.19	0.12	0.09
SrO	0.45	0.42	0.65	0.50	0.55	0.69	0.49	0.45	0.50	0.43	0.46
BaO	0.00	0.00	0.00	0.00	0.00	0.00	0.00	0.00	0.00	0.00	0.00
-O-F	-1.61	-1.54	-1.54	-1.60	-1.55	-1.39	-1.60	-1.66	-1.62	-1.26	-1.37
Total	99.99	99.90	100.49	100.18	99.21	99.46	99.66	99.90	99.48	98.74	99.22
						O = 12.5					
La (*apfu*)	0.000	0.000	0.000	0.000	0.000	0.000	0.000	0.000	0.000	0.006	0.000
Ce	0.000	0.007	0.008	0.011	0.000	0.011	0.006	0.000	0.000	0.013	0.000
Pr	0.000	0.000	0.004	0.000	0.000	0.000	0.000	0.000	0.000	0.000	0.000
Nd	0.005	0.003	0.007	0.005	0.004	0.007	0.005	0.004	0.004	0.006	0.007
Sm	0.000	0.000	0.000	0.000	0.000	0.000	0.000	0.000	0.000	0.000	0.000
Eu	0.000	0.000	0.000	0.000	0.000	0.000	0.000	0.000	0.000	0.000	0.000
Gd	0.000	0.000	0.004	0.000	0.000	0.007	0.000	0.000	0.000	0.000	0.000
Dy	0.000	0.000	0.000	0.000	0.000	0.000	0.000	0.000	0.000	0.000	0.000
Y	0.000	0.000	0.009	0.000	0.011	0.010	0.000	0.000	0.000	0.000	0.000
Ho	0.000	0.000	0.000	0.000	0.000	0.000	0.000	0.000	0.000	0.000	0.000
Th	0.000	0.000	0.000	0.000	0.000	0.000	0.000	0.000	0.000	0.000	0.000
U	0.000	0.000	0.000	0.000	0.000	0.000	0.000	0.000	0.000	0.000	0.000
Ca	4.970	4.965	4.901	4.952	4.953	4.996	4.991	4.988	4.985	5.026	4.997
P	2.990	2.988	3.001	2.995	2.991	2.962	2.980	2.983	2.988	2.940	2.969
F	1.020	0.976	0.971	1.011	0.989	0.894	1.017	1.053	1.035	0.814	0.870
Cl	0.000	0.000	0.000	0.000	0.000	0.000	0.000	0.000	0.000	0.000	0.000
Si	0.008	0.010	0.000	0.000	0.000	0.000	0.000	0.006	0.000	0.027	0.021
Pb	0.000	0.000	0.000	0.000	0.000	0.000	0.000	0.000	0.000	0.000	0.000
Fe	0.000	0.000	0.000	0.000	0.000	0.000	0.000	0.000	0.000	0.000	0.000
Na	0.022	0.023	0.037	0.027	0.036	0.028	0.035	0.025	0.032	0.019	0.015
Sr	0.022	0.021	0.032	0.024	0.027	0.034	0.024	0.022	0.025	0.021	0.023
Ba	0.000	0.000	0.000	0.000	0.000	0.000	0.000	0.000	0.000	0.000	0.000
Total	8.017	8.016	8.002	8.013	8.023	8.054	8.042	8.029	8.033	8.059	8.031

Appendix 2.4: Continued

Unit	Cal Carb 2										
Sample	15049	15049	15049	15049	15049	15049	15049	15049	15049	15049	15049
La_2O_3 (*wt. %*)	0.00	0.00	0.21	0.00	0.00	0.00	0.19	0.00	0.22	0.20	0.00
Ce_2O_3	0.27	0.26	0.31	0.26	0.00	0.47	0.25	0.37	0.41	0.49	0.25
Pr_2O_3	0.00	0.00	0.00	0.00	0.00	0.00	0.00	0.00	0.00	0.00	0.00
Nd_2O_3	0.13	0.15	0.19	0.20	0.00	0.16	0.22	0.12	0.27	0.24	0.25
Sm_2O_3	0.00	0.00	0.00	0.00	0.00	0.00	0.00	0.00	0.00	0.00	0.00
Eu_2O_3	0.00	0.00	0.00	0.00	0.00	0.00	0.00	0.00	0.00	0.00	0.00
Gd_2O_3	0.00	0.00	0.00	0.00	0.00	0.00	0.00	0.00	0.00	0.00	0.00
Dy_2O_3	0.00	0.00	0.00	0.00	0.00	0.00	0.00	0.00	0.00	0.00	0.00
Y_2O_3	0.00	0.00	0.00	0.00	0.00	0.00	0.00	0.00	0.00	0.00	0.00
Ho_2O_3	0.00	0.00	0.00	0.00	0.00	0.00	0.00	0.00	0.00	0.00	0.00
ThO_2	0.00	0.00	0.00	0.00	0.00	0.00	0.00	0.00	0.00	0.00	0.00
UO_2	0.00	0.00	0.00	0.00	0.00	0.00	0.00	0.00	0.00	0.00	0.00
CaO	54.86	54.87	54.75	54.91	55.06	54.82	55.09	54.35	54.81	54.61	54.71
P_2O_5	41.16	40.99	41.14	41.31	41.70	41.35	41.56	40.49	41.17	40.96	41.08
F	3.35	3.56	2.96	3.16	2.90	3.06	3.18	3.16	3.19	3.27	3.43
Cl	0.00	0.00	0.00	0.00	0.00	0.00	0.00	0.00	0.00	0.00	0.00
SiO_2	0.30	0.22	0.44	0.26	0.07	0.24	0.18	0.41	0.47	0.36	0.44
PbO	0.00	0.00	0.00	0.00	0.00	0.00	0.00	0.00	0.00	0.00	0.00
FeO	0.00	0.00	0.00	0.00	0.00	0.00	0.33	0.10	0.23	0.16	0.15
Na_2O	0.11	0.00	0.06	0.10	0.00	0.09	0.05	0.07	0.11	0.09	0.15
SrO	0.55	0.64	0.46	0.43	0.86	0.52	0.56	0.50	0.43	0.51	0.44
BaO	0.00	0.00	0.00	0.00	0.00	0.00	0.00	0.00	0.00	0.00	0.00
-O-F	-1.41	-1.50	-1.24	-1.33	-1.22	-1.29	-1.34	-1.33	-1.34	-1.38	-1.44
Total	99.31	99.19	99.28	99.29	99.37	99.41	100.26	98.23	99.96	99.51	99.45
						O = 12.5					
La (*apfu*)	0.000	0.000	0.007	0.000	0.000	0.000	0.006	0.000	0.007	0.006	0.000
Ce	0.008	0.008	0.010	0.008	0.000	0.014	0.008	0.012	0.013	0.015	0.008
Pr	0.000	0.000	0.000	0.000	0.000	0.000	0.000	0.000	0.000	0.000	0.000
Nd	0.004	0.004	0.006	0.006	0.000	0.005	0.007	0.004	0.008	0.007	0.007
Sm	0.000	0.000	0.000	0.000	0.000	0.000	0.000	0.000	0.000	0.000	0.000
Eu	0.000	0.000	0.000	0.000	0.000	0.000	0.000	0.000	0.000	0.000	0.000
Gd	0.000	0.000	0.000	0.000	0.000	0.000	0.000	0.000	0.000	0.000	0.000
Dy	0.000	0.000	0.000	0.000	0.000	0.000	0.000	0.000	0.000	0.000	0.000
Y	0.000	0.000	0.000	0.000	0.000	0.000	0.000	0.000	0.000	0.000	0.000
Ho	0.000	0.000	0.000	0.000	0.000	0.000	0.000	0.000	0.000	0.000	0.000
Th	0.000	0.000	0.000	0.000	0.000	0.000	0.000	0.000	0.000	0.000	0.000
U	0.000	0.000	0.000	0.000	0.000	0.000	0.000	0.000	0.000	0.000	0.000
Ca	4.994	5.013	4.977	4.990	4.986	4.979	4.974	5.005	4.965	4.977	4.976
P	2.960	2.959	2.955	2.966	2.984	2.968	2.965	2.946	2.947	2.950	2.953
F	0.900	0.960	0.793	0.847	0.776	0.819	0.847	0.859	0.853	0.879	0.921
Cl	0.000	0.000	0.000	0.000	0.000	0.000	0.000	0.000	0.000	0.000	0.000
Si	0.026	0.019	0.037	0.022	0.006	0.020	0.015	0.035	0.040	0.031	0.037
Pb	0.000	0.000	0.000	0.000	0.000	0.000	0.000	0.000	0.000	0.000	0.000
Fe	0.000	0.000	0.000	0.000	0.000	0.000	0.023	0.007	0.016	0.012	0.011
Na	0.018	0.000	0.010	0.017	0.000	0.014	0.007	0.012	0.019	0.015	0.024
Sr	0.027	0.032	0.022	0.021	0.042	0.026	0.027	0.025	0.021	0.025	0.022
Ba	0.000	0.000	0.000	0.000	0.000	0.000	0.000	0.000	0.000	0.000	0.000
Total	8.037	8.036	8.025	8.030	8.018	8.026	8.031	8.044	8.035	8.038	8.038

Appendix 2.4: Continued

Unit						Cal Carb 2					
Sample	15049	15050	15050	15050	15050	15050	15050	15050	15050	15050	15050
La_2O_3 (*wt. %*)	0.00	0.20	0.25	0.00	0.00	0.00	0.21	0.00	0.00	0.00	0.00
Ce_2O_3	0.29	0.38	0.33	0.40	0.49	0.36	0.33	0.22	0.41	0.40	0.29
Pr_2O_3	0.00	0.00	0.00	0.00	0.00	0.00	0.00	0.14	0.00	0.00	0.00
Nd_2O_3	0.16	0.26	0.22	0.21	0.21	0.21	0.22	0.21	0.15	0.18	0.20
Sm_2O_3	0.00	0.00	0.00	0.00	0.00	0.00	0.00	0.00	0.00	0.00	0.00
Eu_2O_3	0.00	0.00	0.00	0.00	0.00	0.00	0.00	0.00	0.00	0.00	0.00
Gd_2O_3	0.00	0.00	0.00	0.00	0.00	0.00	0.00	0.00	0.00	0.00	0.00
Dy_2O_3	0.00	0.00	0.00	0.00	0.00	0.00	0.00	0.00	0.00	0.00	0.00
Y_2O_3	0.00	0.00	0.00	0.00	0.00	0.00	0.00	0.00	0.00	0.00	0.00
Ho_2O_3	0.00	0.00	0.00	0.00	0.00	0.00	0.00	0.00	0.00	0.00	0.00
ThO_2	0.00	0.00	0.00	0.00	0.00	0.00	0.00	0.00	0.00	0.00	0.00
UO_2	0.00	0.00	0.00	0.00	0.00	0.00	0.00	0.00	0.00	0.00	0.00
CaO	55.01	54.61	54.93	54.59	54.42	54.33	54.24	54.30	54.13	54.62	54.58
P_2O_5	41.65	42.13	41.99	41.73	41.34	41.09	42.09	41.98	41.77	42.32	42.04
F	3.27	3.60	3.14	3.26	3.24	3.24	2.97	3.22	3.10	3.29	3.38
Cl	0.00	0.00	0.00	0.00	0.00	0.00	0.00	0.00	0.00	0.00	0.00
SiO_2	0.19	0.00	0.00	0.00	0.00	0.00	0.00	0.00	0.00	0.00	0.00
PbO	0.00	0.00	0.00	0.00	0.00	0.00	0.00	0.00	0.00	0.00	0.00
FeO	0.15	0.00	0.00	0.00	0.00	0.00	0.00	0.00	0.00	0.00	0.00
Na_2O	0.07	0.21	0.15	0.14	0.31	0.37	0.12	0.17	0.18	0.15	0.20
SrO	0.64	0.69	0.38	0.53	0.65	0.66	0.64	0.56	0.62	0.55	0.62
BaO	0.00	0.00	0.00	0.00	0.00	0.00	0.00	0.00	0.00	0.00	0.00
-O-F	-1.38	-1.51	-1.32	-1.37	-1.36	-1.36	-1.25	-1.35	-1.31	-1.38	-1.42
Total	100.03	100.55	100.07	99.48	99.29	98.89	99.56	99.45	99.05	100.13	99.88
						O = 12.5					
La (*apfu*)	0.000	0.006	0.008	0.000	0.000	0.000	0.006	0.000	0.000	0.000	0.000
Ce	0.009	0.012	0.010	0.012	0.015	0.011	0.010	0.007	0.013	0.012	0.009
Pr	0.000	0.000	0.000	0.000	0.000	0.000	0.000	0.004	0.000	0.000	0.000
Nd	0.005	0.008	0.007	0.006	0.006	0.007	0.007	0.006	0.005	0.005	0.006
Sm	0.000	0.000	0.000	0.000	0.000	0.000	0.000	0.000	0.000	0.000	0.000
Eu	0.000	0.000	0.000	0.000	0.000	0.000	0.000	0.000	0.000	0.000	0.000
Gd	0.000	0.000	0.000	0.000	0.000	0.000	0.000	0.000	0.000	0.000	0.000
Dy	0.000	0.000	0.000	0.000	0.000	0.000	0.000	0.000	0.000	0.000	0.000
Y	0.000	0.000	0.000	0.000	0.000	0.000	0.000	0.000	0.000	0.000	0.000
Ho	0.000	0.000	0.000	0.000	0.000	0.000	0.000	0.000	0.000	0.000	0.000
Th	0.000	0.000	0.000	0.000	0.000	0.000	0.000	0.000	0.000	0.000	0.000
U	0.000	0.000	0.000	0.000	0.000	0.000	0.000	0.000	0.000	0.000	0.000
Ca	4.969	4.917	4.953	4.954	4.963	4.976	4.905	4.919	4.923	4.913	4.930
P	2.973	2.997	2.992	2.992	2.979	2.974	3.008	3.005	3.002	3.008	3.000
F	0.872	0.956	0.835	0.874	0.872	0.876	0.792	0.860	0.833	0.873	0.900
Cl	0.000	0.000	0.000	0.000	0.000	0.000	0.000	0.000	0.000	0.000	0.000
Si	0.016	0.000	0.000	0.000	0.000	0.000	0.000	0.000	0.000	0.000	0.000
Pb	0.000	0.000	0.000	0.000	0.000	0.000	0.000	0.000	0.000	0.000	0.000
Fe	0.011	0.000	0.000	0.000	0.000	0.000	0.000	0.000	0.000	0.000	0.000
Na	0.011	0.034	0.024	0.023	0.050	0.061	0.020	0.028	0.029	0.024	0.033
Sr	0.031	0.033	0.018	0.026	0.032	0.033	0.031	0.028	0.030	0.027	0.030
Ba	0.000	0.000	0.000	0.000	0.000	0.000	0.000	0.000	0.000	0.000	0.000
Total	8.023	8.008	8.012	8.013	8.046	8.061	7.987	7.998	8.002	7.990	8.008

Appendix 2.4: Continued

Unit						Rim Dol Carb					
Sample	15109	15109	15109	15109	15109	15109	15096	15096	15096	15096	15096
La_2O_3 (*wt. %*)	0.00	0.00	0.00	0.00	0.00	0.20	0.00	0.00	0.00	0.00	0.00
Ce_2O_3	0.33	0.35	0.28	0.38	0.35	0.46	0.40	0.40	0.27	0.36	0.36
Pr_2O_3	0.00	0.00	0.00	0.00	0.00	0.00	0.00	0.13	0.00	0.00	0.00
Nd_2O_3	0.12	0.00	0.14	0.22	0.18	0.18	0.16	0.14	0.17	0.16	0.11
Sm_2O_3	0.00	0.00	0.00	0.00	0.00	0.00	0.00	0.00	0.00	0.00	0.00
Eu_2O_3	0.00	0.00	0.00	0.00	0.00	0.00	0.00	0.00	0.00	0.00	0.00
Gd_2O_3	0.00	0.18	0.00	0.00	0.00	0.00	0.00	0.00	0.00	0.00	0.00
Dy_2O_3	0.00	0.00	0.00	0.00	0.00	0.00	0.00	0.00	0.00	0.00	0.00
Y_2O_3	0.00	0.00	0.00	0.00	0.00	0.00	0.00	0.00	0.00	0.00	0.00
Ho_2O_3	0.00	0.00	0.00	0.00	0.00	0.00	0.00	0.00	0.00	0.00	0.00
ThO_2	0.00	0.00	0.00	0.00	0.00	0.00	0.00	0.00	0.00	0.00	0.00
UO_2	0.00	0.00	0.00	0.00	0.00	0.00	0.00	0.00	0.00	0.00	0.00
CaO	54.98	55.05	55.03	54.88	54.90	54.80	54.75	54.91	54.72	54.28	54.90
P_2O_5	41.87	41.71	41.76	41.82	41.64	41.36	41.49	41.66	41.80	41.51	41.69
F	3.42	3.62	3.50	3.56	3.88	3.34	4.01	3.97	3.98	4.15	4.16
Cl	0.00	0.00	0.00	0.00	0.00	0.00	0.00	0.00	0.00	0.00	0.00
SiO_2	0.13	0.15	0.18	0.08	0.15	0.24	0.07	0.07	0.07	0.24	0.08
PbO	0.00	0.00	0.00	0.00	0.00	0.00	0.00	0.00	0.00	0.00	0.00
FeO	0.00	0.00	0.00	0.00	0.00	0.00	0.00	0.00	0.00	0.00	0.00
Na_2O	0.12	0.10	0.12	0.16	0.12	0.13	0.10	0.11	0.10	0.10	0.12
SrO	0.49	0.46	0.44	0.34	0.53	0.48	0.49	0.54	0.54	0.52	0.52
BaO	0.00	0.00	0.00	0.00	0.00	0.00	0.00	0.00	0.00	0.00	0.00
-O-F	-1.44	-1.52	-1.48	-1.50	-1.63	-1.41	-1.69	-1.67	-1.68	-1.75	-1.75
Total	100.01	100.07	99.98	99.93	100.12	99.77	99.77	100.27	99.98	99.58	100.18
						O = 12.5					
La (*apfu*)	0.000	0.000	0.000	0.000	0.000	0.006	0.000	0.000	0.000	0.000	0.000
Ce	0.010	0.011	0.009	0.012	0.011	0.014	0.012	0.012	0.008	0.011	0.011
Pr	0.000	0.000	0.000	0.000	0.000	0.000	0.000	0.004	0.000	0.000	0.000
Nd	0.003	0.000	0.004	0.007	0.006	0.005	0.005	0.004	0.005	0.005	0.003
Sm	0.000	0.000	0.000	0.000	0.000	0.000	0.000	0.000	0.000	0.000	0.000
Eu	0.000	0.000	0.000	0.000	0.000	0.000	0.000	0.000	0.000	0.000	0.000
Gd	0.000	0.005	0.000	0.000	0.000	0.000	0.000	0.000	0.000	0.000	0.000
Dy	0.000	0.000	0.000	0.000	0.000	0.000	0.000	0.000	0.000	0.000	0.000
Y	0.000	0.000	0.000	0.000	0.000	0.000	0.000	0.000	0.000	0.000	0.000
Ho	0.000	0.000	0.000	0.000	0.000	0.000	0.000	0.000	0.000	0.000	0.000
Th	0.000	0.000	0.000	0.000	0.000	0.000	0.000	0.000	0.000	0.000	0.000
U	0.000	0.000	0.000	0.000	0.000	0.000	0.000	0.000	0.000	0.000	0.000
Ca	4.961	4.975	4.970	4.961	4.970	4.973	4.979	4.971	4.955	4.939	4.971
P	2.985	2.979	2.980	2.987	2.978	2.965	2.981	2.980	2.991	2.985	2.983
F	0.911	0.964	0.934	0.951	1.036	0.894	1.076	1.061	1.064	1.115	1.111
Cl	0.000	0.000	0.000	0.000	0.000	0.000	0.000	0.000	0.000	0.000	0.000
Si	0.011	0.012	0.015	0.007	0.012	0.021	0.006	0.006	0.006	0.020	0.007
Pb	0.000	0.000	0.000	0.000	0.000	0.000	0.000	0.000	0.000	0.000	0.000
Fe	0.000	0.000	0.000	0.000	0.000	0.000	0.000	0.000	0.000	0.000	0.000
Na	0.019	0.016	0.019	0.025	0.020	0.021	0.016	0.018	0.016	0.017	0.019
Sr	0.024	0.022	0.022	0.017	0.026	0.023	0.024	0.027	0.026	0.026	0.025
Ba	0.000	0.000	0.000	0.000	0.000	0.000	0.000	0.000	0.000	0.000	0.000
Total	8.013	8.020	8.018	8.016	8.022	8.029	8.023	8.022	8.008	8.003	8.020

Appendix 2.4: Continued

Unit	Rim Dol Carb				
Sample	15096	15096	15096	15096	15096
La_2O_3 (*wt. %*)	0.00	0.00	0.00	0.00	0.00
Ce_2O_3	0.42	0.25	0.00	0.29	0.36
Pr_2O_3	0.00	0.00	0.00	0.00	0.00
Nd_2O_3	0.17	0.00	0.20	0.23	0.19
Sm_2O_3	0.00	0.00	0.00	0.00	0.00
Eu_2O_3	0.00	0.00	0.00	0.00	0.00
Gd_2O_3	0.00	0.00	0.00	0.00	0.00
Dy_2O_3	0.00	0.00	0.00	0.00	0.00
Y_2O_3	0.00	0.00	0.00	0.00	0.00
Ho_2O_3	0.00	0.00	0.00	0.00	0.00
ThO_2	0.00	0.00	0.00	0.00	0.00
UO_2	0.00	0.00	0.00	0.00	0.00
CaO	54.62	54.85	54.85	54.46	54.87
P_2O_5	41.85	41.59	41.83	41.93	42.38
F	3.76	4.03	4.00	3.66	4.00
Cl	0.00	0.00	0.00	0.00	0.00
SiO_2	0.00	0.11	0.06	0.00	0.06
PbO	0.00	0.00	0.00	0.00	0.00
FeO	0.00	0.00	0.00	0.00	0.00
Na_2O	0.11	0.07	0.11	0.10	0.14
SrO	0.61	0.54	0.60	0.63	0.65
BaO	0.00	0.00	0.00	0.00	0.00
-O-F	-1.58	-1.69	-1.69	-1.54	-1.69
Total	99.96	99.74	99.96	99.77	100.97
			O = 12.5		
La (*apfu*)	0.000	0.000	0.000	0.000	0.000
Ce	0.013	0.008	0.000	0.009	0.011
Pr	0.000	0.000	0.000	0.000	0.000
Nd	0.005	0.000	0.006	0.007	0.006
Sm	0.000	0.000	0.000	0.000	0.000
Eu	0.000	0.000	0.000	0.000	0.000
Gd	0.000	0.000	0.000	0.000	0.000
Dy	0.000	0.000	0.000	0.000	0.000
Y	0.000	0.000	0.000	0.000	0.000
Ho	0.000	0.000	0.000	0.000	0.000
Th	0.000	0.000	0.000	0.000	0.000
U	0.000	0.000	0.000	0.000	0.000
Ca	4.947	4.979	4.965	4.934	4.918
P	2.995	2.984	2.991	3.001	3.002
F	1.004	1.079	1.070	0.979	1.059
Cl	0.000	0.000	0.000	0.000	0.000
Si	0.000	0.009	0.005	0.000	0.005
Pb	0.000	0.000	0.000	0.000	0.000
Fe	0.000	0.000	0.000	0.000	0.000
Na	0.019	0.012	0.018	0.016	0.023
Sr	0.030	0.026	0.030	0.031	0.032
Ba	0.000	0.000	0.000	0.000	0.000
Total	8.008	8.018	8.014	7.998	7.995

Appendix 2.5: Trace element compositions of apatite in the different units of the Eldor Carbonatite Complex

			Concentration (ppm)																		
Unit	**Sample**	**Type**	**Na**	**Mn**	**Sr**	**Ba**	**La**	**Ce**	**Pr**	**Nd**	**Sm**	**Eu**	**Gd**	**Tb**	**Dy**	**Y**	**Ho**	**Er**	**Tm**	**Yb**	**Lu**
Cal Carb 1	15029	Rim1-p	1244	246	4763	19	992	2626	320	1187	196	55	151	18	94	371	16	36	4	17	1.78
	15029	Rim1-p	1101	133	5432	26	1583	3704	453	1634	248	67	189	21	105	394	17	38	4	16	1.67
	15029	Rim1-p	1021	204	5649	16	971	3281	336	1165	174	47	124	13	63	219	10	20	2	10	1.11
	15029	Rim1-p	791	284	3328	16	621	2061	230	822	125	35	96	11	50	186	8	19	2	9	0.97
	15029	Rim1-p	946	316	3752	16	633	1884	218	767	118	31	84	9	40	141	6	13	1	7	0.77
	15029	Rim1-p	815	240	4517	15	811	2497	284	984	150	42	111	12	59	209	9	21	2	10	1.11
	15029	Rim1-p	1042	323	4471	15	654	2140	230	827	124	34	94	10	50	193	8	20	2	10	1.06
	15029	Rim1-p	733	277	3646	14	610	2265	233	801	118	33	85	9	39	122	6	12	1	6	0.73
	15029	Rim1-p	1019	286	5140	18	795	2609	264	877	125	36	88	9	39	136	6	12	1	5	0.65
	15029	Rim1-p	823	222	4187	17	792	2751	280	987	139	38	101	11	46	163	7	15	2	7	0.78
	15029	Rim1-p	791	277	3276	15	597	2081	224	781	118	32	87	8	34	120	5	11	1	6	0.66
	15029	Rim1-p	1011	190	5345	16	1055	3500	342	1118	159	43	109	10	41	126	6	11	1	5	0.48
	15029	Rim1-s	1535	133	5423	45	936	3023	422	1766	424	145	419	65	406	1821	75	190	21	95	10.30
	15029	Rim1-s	1804	75	7056	27	612	2274	364	1617	396	132	392	60	362	1765	64	156	16	74	7.83
	15029	Rim1-s	1360	82	6100	39	812	2708	392	1647	381	134	385	58	361	1636	67	167	18	87	9.21
	15029	Rim1-s	1336	85	6073	38	703	2433	346	1449	352	114	335	53	335	1508	63	156	17	83	9.06
Cal Carb 2	15049	Rim2	526	230	4775	16	1111	3828	408	1492	222	57	164	15	68	232	10	22	2	11	1.24
	15049	Rim2	428	1481	4841	23	907	3218	340	1263	173	47	134	13	59	202	9	20	2	10	1.15
	15049	Rim2	501	220	4619	14	1100	3752	420	1515	228	57	167	16	70	237	11	22	2	11	1.29
	15049	Rim2	412	367	5074	33	1012	3467	349	1322	193	51	142	14	62	226	9	21	2	11	1.28
	15049	Rim2	509	230	4633	16	992	3448	365	1352	193	51	139	13	61	207	9	19	2	10	1.16
	15049	Rim2	477	399	4684	27	983	3422	362	1282	186	50	139	14	58	202	9	20	2	9	1.14
	15049	Rim2	479	230	4728	31	924	3318	353	1285	185	50	137	13	56	195	8	18	2	10	1.07
	15049	Rim2	305	205	5788	14	887	3040	296	1062	156	41	115	11	50	196	8	18	2	10	1.20
	15049	Rim2	621	226	3953	16	1037	3863	413	1466	211	56	149	15	67	216	10	22	2	11	1.20
	15049	Rim2	603	232	4261	20	960	3621	384	1407	197	54	151	14	64	205	9	20	2	10	1.14
Dol Carb	15109	Rim3	711	195	4316	17	883	2781	345	1243	179	49	126	12	53	170	8	16	2	8	0.90
	15109	Rim3	760	185	4469	17	812	2589	316	1137	172	47	124	12	55	184	8	18	2	9	1.02
	15109	Rim3	965	177	4432	15	877	2875	360	1303	207	58	148	16	72	238	11	22	2	11	1.29
	15109	Rim3	1126	199	4379	20	868	2704	340	1219	182	50	131	13	61	195	9	19	2	9	1.07
	15096	Rim3	625	183	5836	21	859	3053	326	1159	169	46	120	11	50	169	7	17	2	9	1.15
	15096	Rim3	566	184	5786	22	769	2818	286	1009	142	39	100	10	45	149	7	15	2	8	0.90
	15096	Rim3	643	149	5543	19	903	3277	319	1082	150	42	100	10	43	141	6	14	1	7	0.74
	15096	Rim3	581	212	5466	19	724	2447	268	921	126	34	89	9	37	118	5	12	1	5	0.59
	15096	Rim3	648	139	4833	21	833	3393	331	1182	169	46	117	12	55	188	8	18	2	11	1.33

Appendix 2.5: Continued

			Concentration (ppm)																		
Unit	**Sample**	**Type**	**Na**	**Mn**	**Sr**	**Ba**	**La**	**Ce**	**Pr**	**Nd**	**Sm**	**Eu**	**Gd**	**Tb**	**Dy**	**Y**	**Ho**	**Er**	**Tm**	**Yb**	**Lu**
BD zone	15114	BD-p	511	228	4730	16	1127	3878	404	1515	229	55	162	16	68	233	10	22	2	11	1.34
	15114	BD-p	443	695	5335	17	909	3010	309	1145	173	43	124	12	55	194	8	17	2	9	1.09
	15114	BD-p	510	223	4646	14	1112	3778	414	1549	232	57	168	16	70	240	11	23	2	11	1.38
	15114	BD-p	522	214	4653	18	992	3428	358	1366	197	50	139	14	60	206	9	19	2	10	1.15
	15114	BD-p	498	366	4688	24	981	3468	365	1341	194	50	143	14	60	207	9	20	2	10	1.19
	15114	BD-p	661	231	3910	16	1067	3832	409	1484	213	57	152	15	67	220	10	22	2	11	1.24
	15114	BD-p	624	233	4137	19	988	3705	395	1422	203	56	149	14	64	211	10	21	2	11	1.17
	15114	BD-s	1170	110	5939	53	353	2255	415	2208	641	211	518	61	271	1151	40	86	9	43	5.38
	15114	BD-s	1266	64	6098	51	384	2150	421	2259	664	216	552	67	301	1286	45	95	10	49	5.87
	15114	BD-s	1160	1090	5640	58	343	2199	413	2164	619	194	514	55	249	1098	35	78	8	41	4.94
	15114	BD-s	1134	62	5597	42	352	2063	404	2151	629	196	514	58	260	1127	38	81	8	41	5.14
	15114	BD-s	1118	73	6019	78	315	2537	371	2115	547	184	442	49	218	891	33	69	7	36	4.81
	15113	BD-s	1318	74	5932	24	419	3268	491	2380	578	183	447	54	265	1198	41	99	12	69	8.34
	15113	BD-s	1249	82	5598	49	407	2980	464	2202	528	170	431	50	253	1152	39	98	12	67	8.44
	15113	BD-s	1308	68	5726	37	422	3172	469	2302	562	179	441	54	264	1180	42	100	12	70	8.46
	15113	BD-s	1339	68	5317	30	417	3007	473	2318	562	178	435	54	261	1169	42	97	12	70	8.67
	15113	BD-s	1225	69	5260	57	393	2803	453	2264	556	173	430	52	248	1061	39	91	10	56	6.83
	15113	BD-s	1308	73	5297	53	399	2805	464	2337	586	185	457	56	269	1134	41	94	11	59	6.90
	15113	BD-s	1277	71	5652	44	395	2666	456	2211	568	177	445	54	255	1121	40	93	11	58	7.05
	15113	BD-s	1280	73	5253	57	406	2662	463	2297	586	182	457	57	264	1137	41	96	11	60	7.01
	15113	BD-s	1366	78	5633	41	452	2875	488	2401	598	189	459	57	272	1175	43	99	11	61	7.13
	15113	BD-s	1398	79	5497	58	458	3014	496	2460	607	193	470	58	279	1178	43	99	11	61	7.41
	15113	BD-s	1330	69	5719	77	427	2916	475	2364	595	189	457	55	266	1167	41	96	11	60	7.41
	15113	BD-s	1246	65	5496	66	419	2849	465	2290	573	180	444	53	257	1102	39	93	11	60	6.70
	15113	BD-s	1172	71	5352	45	377	3052	506	2227	556	180	444	53	248	1059	39	91	10	57	7.05
B zone	16010	B	930	684	19439	51	456	1652	214	872	163	52	139	19	117	584	21	53	6	29	3.52
	16010	B	1752	657	15718	63	695	2490	346	1368	249	82	220	29	172	778	30	77	9	41	5.34
	16010	B	915	596	16212	49	388	1321	175	668	138	47	123	17	101	498	18	45	5	29	3.48
	16010	B	3512	566	15336	41	595	2291	292	1178	241	75	181	24	147	900	26	65	7	37	4.33
	16010	B	4437	451	16128	46	571	2354	289	1262	270	88	228	31	185	1015	33	77	9	42	5.25
	16010	B	3050	1263	13832	49	629	2456	308	1399	303	99	253	34	200	1107	35	84	9	46	4.93
	16010	B	5420	1061	14750	29	608	2064	296	1227	271	90	220	30	185	979	33	80	9	46	5.19
	16010	B	1545	448	15218	40	482	2005	296	1276	306	101	258	34	195	999	34	81	9	43	5.33
	16010	B	2095	378	15284	51	590	2417	328	1416	292	100	248	32	190	1020	34	83	9	46	5.66
	16010	B	1378	376	16044	51	500	2230	405	1792	415	126	321	39	214	1132	37	91	9	46	5.18
	16010	B	2504	551	15871	35	586	2184	300	1244	267	87	225	30	175	1009	31	76	9	43	5.08
	16010	B	1561	441	16062	43	578	2246	344	1477	311	100	253	34	201	1248	37	93	10	53	6.28

Appendix 2.5: Continued

			Concentration (ppm)																		
Unit	**Sample**	**Type**	**Na**	**Mn**	**Sr**	**Ba**	**La**	**Ce**	**Pr**	**Nd**	**Sm**	**Eu**	**Gd**	**Tb**	**Dy**	**Y**	**Ho**	**Er**	**Tm**	**Yb**	**Lu**
B zone	16010	B	1163	513	17459	66	525	2064	317	1355	300	103	257	36	215	1262	38	102	13	68	8.94
	16010	B	1520	576	16655	64	547	2145	310	1347	288	95	249	33	196	1197	35	92	10	52	6.68
	16010	B	1248	494	17268	60	593	2396	343	1476	323	102	278	37	217	1232	40	101	12	59	7.00
A zone	15194	A-p	1847	300	6291	36	694	2476	391	1750	485	172	504	87	527	2051	80	157	14	66	7.01
	15194	A-p	1550	619	5780	36	651	2104	327	1454	390	132	395	64	369	1465	56	111	10	49	5.31
	15194	A-p	1940	305	6342	33	619	2072	338	1612	491	175	523	83	464	1782	70	138	13	58	6.31
	15194	A-p	1761	309	6236	33	626	2100	335	1549	440	158	468	77	456	1803	71	141	13	60	6.60
	15194	A-p	1968	477	6148	36	732	2309	342	1489	350	118	340	53	311	1309	49	99	9	43	4.95
	15194	A-p	1529	336	5125	35	764	2427	364	1527	339	110	318	46	268	1126	42	86	8	40	4.49
	15194	A-p	2020	303	6361	39	619	2010	325	1566	492	177	540	90	537	2005	81	157	14	65	7.13
	15194	A-p	1971	327	7179	29	692	2271	358	1614	429	149	444	73	436	1754	68	134	12	57	6.12
	15194	A-p	1710	341	7029	34	661	2158	337	1480	370	126	372	60	366	1518	57	116	11	52	5.81
	15194	A-p	2303	310	6803	50	669	2250	377	1848	605	223	677	112	664	2482	102	198	18	80	8.56
	15194	A-p	2234	321	6854	48	698	2337	390	1910	632	231	719	118	690	2479	103	198	18	78	8.54
	15194	A-p	2229	2085	7408	53	701	2366	386	1892	627	229	728	116	673	2317	100	187	16	68	7.39
	15194	A-p	1679	786	5595	38	638	2030	324	1473	391	135	413	69	404	1584	61	118	11	50	5.51
	15194	A-p	2035	241	5693	46	721	2368	390	1841	551	196	603	98	578	2231	89	176	16	74	8.05
	15194	A-p	1952	851	5815	32	581	1949	327	1574	509	180	556	91	543	2051	83	162	15	66	7.09
	15194	A-p	1157	246	4293	27	814	2471	359	1476	284	87	252	34	185	815	29	60	6	29	3.46
	15194	A-p	1774	231	5479	46	641	2158	348	1639	491	174	530	85	504	1983	78	153	14	65	7.11
	15193	A-s	3313	453	9559	52	517	2742	414	2110	769	324	971	166	964	4273	158	354	38	161	16.00
	15193	A-s	2736	194	9427	107	367	2000	320	1625	605	257	805	133	731	3027	118	252	25	111	10.82
	15193	A-s	1898	272	13170	92	390	2426	373	1958	758	278	800	158	958	4823	146	272	25	106	12.30
	15193	A-s	1802	314	12096	62	372	2260	361	1817	691	257	697	139	844	4399	128	246	22	98	11.43
	15193	A-s	2043	256	12198	76	384	2398	386	1907	759	276	744	149	872	4573	136	260	23	99	11.22
	15193	A-s	1670	265	11936	75	375	2271	387	1828	701	265	729	148	875	4343	134	260	22	99	12.01
	15193	A-s	1752	258	12860	56	424	2541	368	1786	702	254	695	132	794	3938	124	248	23	103	12.10
	15193	A-s	1630	279	12186	72	390	2215	325	1709	653	243	675	129	755	3358	122	238	23	101	12.30
	15193	A-s	1644	258	12399	78	393	2283	321	1671	624	232	621	115	696	3130	112	215	22	98	12.69
	15193	A-s	1475	297	13425	73	367	2099	313	1547	620	230	658	124	719	3305	115	230	22	108	12.63
	15193	A-s	1555	297	12226	91	349	2056	372	1593	621	242	684	124	754	3350	119	232	22	104	11.72
	15193	A-s	2043	306	12483	87	416	1664	329	1740	681	242	719	140	832	3215	117	257	22	113	12.48
	15194	A-s	2023	176	8664	84	359	2328	328	1802	851	355	1206	252	1779	7481	263	489	45	198	22.90
	15194	A-s	2254	190	9018	76	377	2212	336	1907	856	333	1097	199	1215	4012	165	286	23	94	9.93
	15194	A-s	2173	170	8540	47	358	2085	331	1716	785	319	1041	194	1106	3965	159	272	23	93	9.57
	15194	A-s	2484	153	8331	55	339	2033	301	1743	802	325	1093	189	1089	3775	162	289	23	98	9.44
	15194	A-s	2551	201	9557	141	348	2246	341	1797	834	343	1169	210	1230	4493	178	320	27	118	11.96

Appendix 2.5: Continued

			Concentration (ppm)																			
Unit	**Sample**	**Type**	**Na**	**Mn**	**Sr**	**Ba**	**La**	**Ce**	**Pr**	**Nd**	**Sm**	**Eu**	**Gd**	**Tb**	**Dy**	**Y**	**Ho**	**Er**	**Tm**	**Yb**	**Lu**
A zone	15194	A-s	1528	296	12616	90	335	2098	356	1759	627	245	657	107	617	2569	89	171	15	73	8.40
	15194	A-s	1366	282	11677	87	338	2114	330	1740	645	229	656	110	626	2488	90	178	16	77	8.62
	15194	A-s	2277	322	10855	86	337	2076	335	1735	645	224	690	108	583	2608	90	171	16	72	8.16
	15194	A-s	1636	301	11069	86	332	2016	337	1769	647	224	654	108	605	2777	93	175	15	72	7.99
	15194	A-s	1525	314	12816	92	389	2316	361	1875	635	224	650	110	612	2875	94	189	17	84	9.85

Appendix 2.6: Trace element compositions of fluorite in the different units of the Eldor Carbonatite Complex

		Concentration (ppm)																
Unit	**Sample**	**Sr**	**Ba**	**La**	**Ce**	**Pr**	**Nd**	**Sm**	**Eu**	**Gd**	**Tb**	**Dy**	**Y**	**Ho**	**Er**	**Tm**	**Yb**	**Lu**
BD zone	15116	442	4.8	3.1	6.7	1.2	7.4	3.2	1.4	4.9	0.7	5.2	140	1.1	3.8	0.5	4.0	0.6
	15116	603	7.2	3.2	7.3	1.5	10.4	4.8	2.1	7.8	1.0	7.0	203	1.4	4.7	0.7	5.4	0.8
	15116	702	6.6	2.8	6.9	1.6	10.6	4.7	2.0	7.1	0.8	5.5	150	1.1	3.9	0.6	4.9	0.7
	15116	549	7.4	3.2	8.1	1.6	12.4	5.9	2.3	8.4	1.0	6.1	163	1.1	3.1	0.5	4.3	0.6
	15116	632	12.5	3.3	8.6	1.9	12.7	5.1	2.0	8.0	0.9	5.7	161	1.2	4.3	0.6	5.2	0.8
	15116	415	7.4	4.6	10.8	1.6	8.6	3.3	1.3	5.0	0.7	4.9	128	1.1	3.2	0.5	3.7	0.6
	15116	621	7.1	2.0	5.5	1.5	10.7	4.6	1.8	6.8	0.8	5.1	137	1.0	3.5	0.5	4.5	0.7
breccia	16038	1088	3.5	0.9	1.6	0.3	1.8	0.9	0.5	2.2	0.3	1.9	131	0.4	1.1	0.1	0.7	0.1
	16038	1124	5.3	1.0	1.8	0.3	2.0	0.8	0.4	2.3	0.2	1.3	117	0.3	0.7	0.1	0.6	0.1
	16038	1252	4.2	1.1	1.8	0.4	1.9	0.8	0.4	2.5	0.3	1.8	128	0.4	1.1	0.1	0.7	0.1
	16038	1237	4.4	1.4	2.7	0.5	2.7	1.2	0.6	2.6	0.3	1.8	132	0.3	1.0	0.1	0.7	0.1
	16038	1104	4.0	1.2	2.6	0.5	3.0	1.4	0.7	3.1	0.3	2.0	106	0.4	1.0	0.1	0.7	0.1
	16038	1063	5.6	1.4	2.8	0.6	3.6	1.7	0.7	3.2	0.3	2.0	111	0.4	1.0	0.1	0.7	0.1
	16038	1211	10.1	1.6	3.0	0.7	4.1	2.0	0.9	3.9	0.5	2.9	141	0.5	1.4	0.1	0.9	0.1
	16038	1097	4.4	1.4	3.0	0.6	4.0	2.2	1.0	4.0	0.5	3.0	104	0.6	1.3	0.1	0.9	0.1
	16038	1150	10.6	1.8	3.7	0.7	4.4	2.1	0.9	4.3	0.5	2.7	125	0.6	1.4	0.2	0.9	0.1
	16038	1201	10.3	1.6	3.5	0.6	3.5	2.1	0.9	4.5	0.5	3.0	140	0.6	1.6	0.2	1.1	0.2
	16038	1068	7.0	1.3	3.1	0.6	4.4	2.5	1.1	4.6	0.6	3.2	109	0.6	1.5	0.2	1.0	0.1
	16038	1191	14.9	1.9	3.8	0.7	4.4	1.8	0.9	5.0	0.5	3.0	150	0.6	1.6	0.2	0.9	0.1
	16038	1093	7.6	1.7	3.6	0.7	4.8	2.7	1.2	5.1	0.6	3.4	109	0.6	1.5	0.2	1.1	0.1
late veins	15222	336	2.6	0.4	1.2	0.4	4.1	3.0	1.4	6.6	0.9	5.9	190	1.1	2.9	0.3	2.0	0.3
	15222	352	3.8	0.5	1.3	0.3	3.2	2.4	1.3	5.8	0.8	5.0	183	1.0	2.7	0.3	2.0	0.3
	15222	343	2.2	0.3	1.0	0.4	3.8	2.8	1.4	6.5	0.9	5.7	198	1.1	2.9	0.3	2.1	0.3
	15222	335	2.6	0.5	1.5	0.4	4.6	3.1	1.4	6.9	1.0	6.1	205	1.2	3.0	0.3	2.1	0.3
	15222	484	3.6	0.9	1.7	0.4	3.6	2.3	1.3	6.2	0.8	5.1	183	1.0	2.9	0.3	2.2	0.3
	15222	385	6.8	0.8	1.7	0.4	3.8	2.6	1.4	7.0	0.9	5.5	190	1.0	2.9	0.3	2.1	0.3
	15222	2726	0.4	0.4	1.3	0.4	3.4	2.6	1.5	4.6	0.9	6.4	209	1.4	4.7	0.7	5.5	0.9
	15222	1331	0.3	0.5	1.5	0.4	3.2	2.4	1.2	4.1	0.8	5.0	166	1.1	3.3	0.4	3.3	0.5
	15222	1241	0.2	0.3	1.0	0.3	3.0	2.1	1.3	4.0	0.8	5.1	166	1.1	3.3	0.4	3.2	0.5
	15222	2238	0.3	0.3	1.0	0.4	3.2	2.6	1.4	4.9	0.9	6.5	208	1.4	4.7	0.7	5.7	0.9
	15222	1956	0.4	0.2	1.0	0.3	3.2	2.4	1.3	4.4	0.8	5.7	178	1.2	4.0	0.6	4.6	0.8
	15222	1261	0.1	0.1	0.7	0.3	2.8	2.2	1.3	4.0	0.8	5.2	176	1.1	3.4	0.4	3.2	0.5
	15222	1637	0.3	0.2	0.7	0.2	2.4	1.8	1.0	3.0	0.6	3.8	115	0.8	2.5	0.4	2.8	0.4
	15222	3398	0.5	0.4	1.3	0.4	3.9	3.1	1.7	5.7	1.1	7.7	243	1.8	5.5	0.9	6.8	1.1
	15222	1971	0.6	0.6	1.6	0.4	3.4	2.7	1.4	5.2	0.9	5.4	172	1.0	2.6	0.3	1.7	0.3
	15222	2094	1.4	0.3	1.1	0.3	3.0	2.5	1.3	4.7	0.8	4.6	156	0.9	2.3	0.2	1.7	0.3

Appendix 2.6: Continued

		Concentration (ppm)																
Unit	**Sample**	**Sr**	**Ba**	**La**	**Ce**	**Pr**	**Nd**	**Sm**	**Eu**	**Gd**	**Tb**	**Dy**	**Y**	**Ho**	**Er**	**Tm**	**Yb**	**Lu**
late veins	15222	2279	0.7	0.2	0.9	0.3	2.8	2.5	1.4	4.7	0.9	6.4	218	1.5	4.5	0.6	3.6	0.5
	15396	1735	0.3	0.2	0.6	0.2	1.8	1.8	1.1	5.1	0.9	5.6	183	1.0	2.5	0.2	1.5	0.2
	15396	1755	0.3	0.2	0.5	0.2	1.8	1.7	1.1	4.9	0.9	5.4	180	1.0	2.4	0.2	1.5	0.2
	15396	1700	0.3	0.2	0.6	0.2	1.8	1.8	1.1	4.8	0.9	5.7	186	1.1	2.5	0.3	1.5	0.2
	15396	1745	0.3	0.2	0.6	0.2	1.8	1.7	1.0	4.4	0.8	5.3	175	1.0	2.4	0.3	1.5	0.2
	15396	1786	0.2	0.1	0.5	0.2	1.9	1.8	1.2	5.1	0.9	5.7	195	1.0	2.6	0.3	1.6	0.2
	15396	1684	0.2	0.1	0.5	0.2	1.8	1.9	1.1	5.0	0.9	5.7	183	1.0	2.4	0.3	1.5	0.2
	15396	1663	0.3	0.2	0.5	0.2	1.8	1.8	1.2	5.2	0.9	5.7	181	1.0	2.5	0.2	1.5	0.2
	15396	1648	0.2	0.2	0.5	0.2	1.6	1.8	1.1	5.0	0.9	5.5	176	1.0	2.3	0.2	1.5	0.2
	15396	1730	0.3	0.2	0.6	0.2	1.9	1.8	1.1	5.1	0.9	5.6	181	1.0	2.5	0.3	1.5	0.2
	15396	1749	0.1	0.2	0.5	0.2	1.7	1.7	1.1	4.5	0.8	5.4	181	1.1	2.5	0.3	1.5	0.2
	15396	1812	0.3	0.2	0.6	0.2	1.9	1.7	1.2	5.1	0.9	5.8	191	1.1	2.6	0.3	1.6	0.2
	15396	1694	0.4	0.2	0.5	0.2	1.6	1.6	1.0	4.7	0.9	5.8	186	1.0	2.5	0.3	1.5	0.2
	15396	1720	0.3	0.2	0.5	0.2	1.8	1.8	1.1	5.1	0.9	5.7	193	1.1	2.6	0.3	1.6	0.2
	15396	1730	0.5	0.2	0.6	0.2	1.8	1.7	1.1	5.0	0.9	5.7	185	1.1	2.6	0.3	1.6	0.2
	15396	1709	0.4	0.2	0.6	0.2	1.8	1.8	1.1	5.0	0.9	5.2	175	1.0	2.4	0.2	1.4	0.2
MHREO	15348	2438	2.7	0.3	1.9	0.9	11.3	9.0	4.0	19.0	3.3	23.5	717	4.2	9.9	0.9	4.7	0.5
	15348	2397	3.4	0.4	2.0	0.9	10.9	8.3	4.0	18.9	3.3	22.3	705	4.0	9.2	0.9	4.5	0.5
	15348	2515	1.3	0.3	1.6	0.9	11.0	8.8	4.3	18.5	3.4	23.4	700	4.3	10.1	0.9	4.9	0.5
	15348	2392	1.9	0.3	1.6	0.9	10.3	8.6	4.1	17.5	3.1	21.9	672	3.9	9.1	0.9	4.8	0.5
	15348	2192	2.6	0.6	2.3	1.0	10.3	7.7	3.8	16.7	2.9	19.4	602	3.5	8.2	0.8	4.1	0.5
	15348	2459	1.7	0.2	1.6	1.0	11.7	9.4	4.6	19.8	3.5	23.4	724	4.3	10.3	0.9	5.4	0.6
	15348	2176	1.5	0.2	1.3	0.8	10.7	8.5	4.2	19.5	3.5	22.7	765	4.1	9.9	0.9	4.8	0.5
	15348	2253	0.4	0.1	0.9	0.6	8.5	7.3	3.4	16.2	2.8	19.4	634	3.5	8.2	0.8	3.9	0.4
	15348	2063	0.7	0.2	0.7	0.4	5.1	5.1	2.9	13.8	3.0	22.1	506	3.9	9.0	0.8	3.9	0.4
	15348	2330	0.8	0.1	1.2	0.8	9.9	8.1	3.9	17.9	3.1	21.3	685	3.8	9.0	0.8	4.4	0.5
	15348	2002	0.8	0.1	0.9	0.6	7.8	6.7	3.1	15.1	2.6	17.7	607	3.3	7.7	0.7	3.9	0.4
	15348	2217	0.8	0.1	1.1	0.7	9.8	8.5	4.0	19.4	3.3	22.2	742	4.1	9.7	0.9	4.8	0.5
	15348	2089	2.3	0.5	1.9	0.9	8.5	6.0	3.3	14.0	2.4	16.0	518	2.9	7.0	0.6	3.5	0.4
	15348	2294	1.3	0.2	1.3	0.8	8.2	7.1	3.5	15.7	2.8	19.4	583	3.4	8.1	0.7	3.9	0.4
	15013	1714	1.9	0.4	1.0	0.4	4.7	3.5	1.5	7.2	1.1	8.0	338	1.6	4.2	0.5	2.7	0.3
	15013	1607	9.2	0.6	1.6	0.5	5.6	4.2	2.0	9.6	1.3	9.2	345	1.8	4.8	0.5	3.1	0.4
	15013	1689	1.3	0.5	1.3	0.5	5.6	4.0	1.8	8.2	1.3	9.3	403	1.9	4.9	0.5	3.3	0.4
	15013	1725	1.3	0.4	1.1	0.5	5.4	4.0	1.8	8.1	1.3	9.1	398	1.8	4.9	0.5	3.3	0.4
	15013	1689	1.6	0.4	1.1	0.5	5.4	3.9	1.8	7.9	1.2	9.0	390	1.8	4.8	0.5	3.2	0.4
	15013	1627	1.8	0.2	0.7	0.3	2.9	2.6	1.3	6.2	1.0	7.5	312	1.5	4.0	0.4	2.6	0.3

Appendix 2.6: Continued

		Concentration (ppm)																
Unit	**Sample**	**Sr**	**Ba**	**La**	**Ce**	**Pr**	**Nd**	**Sm**	**Eu**	**Gd**	**Tb**	**Dy**	**Y**	**Ho**	**Er**	**Tm**	**Yb**	**Lu**
MHREO	15013	1659	2.5	0.5	1.4	0.5	5.6	3.8	1.7	7.7	1.2	8.4	356	1.7	4.5	0.5	2.8	0.3
	15013	1571	2.8	0.3	0.8	0.3	3.8	3.4	1.6	7.7	1.2	9.0	393	1.8	4.8	0.5	3.2	0.4
	15013	1553	1.3	0.3	0.7	0.3	4.0	3.7	1.8	8.6	1.4	10.4	454	2.1	5.6	0.6	3.7	0.4
	15013	1658	1.5	0.2	0.5	0.2	2.9	3.2	1.6	7.8	1.3	9.3	403	1.8	4.8	0.5	3.0	0.4
	15013	1605	1.6	0.3	0.6	0.2	3.4	3.3	1.6	7.4	1.2	9.0	393	1.8	4.6	0.5	3.1	0.3
	15013	1550	1.8	0.2	0.5	0.2	2.5	2.3	1.1	5.0	0.8	6.1	291	1.1	3.3	0.3	2.0	0.2
	15013	1569	1.8	0.1	0.3	0.1	1.6	2.1	1.0	4.5	0.7	5.3	256	1.1	2.9	0.3	1.8	0.2
	15013	1489	1.9	0.2	0.6	0.2	2.5	2.7	1.3	6.0	0.9	7.7	333	1.7	4.6	0.5	3.0	0.3
	15013	1463	2.2	0.2	0.5	0.2	2.8	2.9	1.4	6.2	1.0	8.2	340	1.7	4.9	0.5	3.0	0.3
	15013	1442	2.3	0.4	0.9	0.3	3.6	2.6	1.1	4.9	0.7	5.5	253	1.1	3.0	0.3	1.8	0.2
	15013	1607	3.1	0.4	0.9	0.3	3.5	2.9	1.4	6.5	1.0	7.4	323	1.5	3.8	0.4	2.3	0.3
Dol Carb	15109	842	10.6	3.5	12.2	2.8	17.7	6.9	2.6	10.3	1.5	11.0	127	2.7	8.9	1.4	9.6	1.3
	15109	764	7.9	3.2	10.9	2.4	14.2	5.9	2.3	8.8	1.4	10.5	131	2.6	8.7	1.3	9.1	1.2
	15109	896	7.4	2.9	8.9	1.8	11.5	4.9	2.0	7.5	1.1	8.6	114	2.0	6.9	0.9	6.5	0.8
	15109	841	6.3	3.2	9.2	1.7	9.3	3.1	1.2	5.5	0.8	6.0	101	1.5	4.6	0.6	4.0	0.5
	15109	601	12.1	3.7	17.4	5.3	40.2	16.1	5.5	18.8	2.4	17.1	154	3.9	13.6	2.2	15.3	2.2
	15109	637	6.2	3.4	15.5	4.6	34.2	13.7	4.8	15.5	2.2	15.7	152	3.7	12.9	2.1	14.4	2.0
	15109	681	9.4	3.2	15.2	4.4	33.0	12.9	4.4	14.7	2.0	13.6	117	3.1	10.5	1.7	12.2	1.7
	15109	523	10.3	4.4	20.9	5.6	40.2	14.5	4.9	16.7	2.2	15.8	147	3.7	13.1	2.0	14.9	2.1
	15109	525	8.0	3.0	9.0	1.9	11.2	4.1	1.6	6.2	0.9	6.3	121	1.4	4.7	0.7	4.5	0.6
	15109	865	9.2	3.5	16.5	4.3	28.2	8.4	2.8	9.7	1.3	9.4	110	2.1	7.1	1.0	7.4	1.0
	15109	743	9.5	3.1	15.9	4.7	33.4	12.6	4.3	14.2	1.9	13.8	124	3.1	10.6	1.6	11.7	1.6
	15109	456	6.6	3.0	10.4	2.4	15.7	6.0	2.0	7.7	1.1	8.1	122	1.9	6.4	0.9	6.8	0.9
	15109	540	8.4	3.5	17.1	5.1	38.1	13.1	4.5	14.0	1.9	12.7	134	2.8	9.6	1.5	10.8	1.5
	15109	521	4.9	2.9	14.7	4.3	32.1	11.5	3.9	11.8	1.6	11.3	127	2.5	8.5	1.3	9.5	1.3
	15109	788	6.4	3.3	15.7	4.4	30.6	10.0	3.3	11.0	1.5	10.8	115	2.5	8.2	1.3	9.0	1.2

Appendix 2.7: Major element oxide compositions and cation proportions of monazite-(Ce) and monazite-(Nd) in the different units of the Ashram deposit

Unit	**A**										
Sample	15004	15004	15004	15004	15004	15004	15004	15004	15004	15004	15004
La_2O_3 (*wt. %*)	16.68	16.93	16.85	17.20	17.06	16.32	16.83	16.45	16.62	16.79	16.81
Ce_2O_3	33.13	32.54	32.30	32.17	33.90	34.70	35.17	33.34	34.24	32.27	35.69
Pr_2O_3	3.58	3.56	3.69	3.59	3.51	3.55	3.55	3.59	3.71	3.46	3.53
Nd_2O_3	9.88	9.89	9.90	9.72	9.81	10.69	10.02	11.07	10.73	11.18	10.39
Sm_2O_3	1.39	1.51	1.48	1.41	1.31	1.06	0.96	1.54	1.07	1.51	1.19
Eu_2O_3	0.00	0.22	0.22	0.00	0.00	0.00	0.00	0.22	0.00	0.00	0.00
Gd_2O_3	0.57	0.68	0.75	0.75	0.56	0.45	0.41	0.73	0.58	0.75	0.64
Dy_2O_3	0.00	0.00	0.00	0.00	0.00	0.00	0.00	0.00	0.00	0.00	0.00
Y_2O_3	0.35	0.34	0.35	0.30	0.35	0.28	0.22	0.42	0.30	0.29	0.28
Ho_2O_3	0.00	0.00	0.00	0.00	0.00						
ThO_2	2.43	2.25	2.29	2.54	1.75	1.27	1.15	2.06	1.20	2.18	1.02
UO_2	0.00	0.00	0.00	0.00	0.00	0.00	0.00	0.00	0.00	0.00	0.00
CaO	0.65	0.38	0.36	0.80	0.79	0.68	0.39	0.82	0.18	0.30	0.67
P_2O_5	28.76	29.68	28.90	29.02	28.90	29.45	29.30	29.02	29.60	29.09	29.66
F	0.57	0.64	0.62	0.62	0.62	0.71	0.59	0.52	0.60	0.69	0.56
Cl	0.00	0.00	0.00	0.00	0.00	0.00	0.00	0.00	0.00	0.03	0.00
SiO_2	0.71	0.43	0.44	0.49	0.34	0.30	0.30	0.42	0.30	0.31	0.28
PbO	0.16	0.14	0.24	0.24	0.20	0.13	0.00	0.18	0.00	0.14	0.10
FeO	0.26	0.34	0.00	0.00	0.00	0.00	0.20	0.44	0.00	0.00	0.00
SrO	0.00	0.18	0.00	0.13	0.08						
O=F	-0.24	-0.27	-0.26	-0.26	-0.26	-0.30	-0.25	-0.22	-0.25	-0.29	-0.24
Total	98.87	99.41	98.12	98.73	98.91	99.27	98.84	100.59	98.87	98.70	100.59
	O = 4										
La (*apfu*)	0.243	0.243	0.247	0.250	0.249	0.235	0.244	0.237	0.240	0.245	0.241
Ce	0.479	0.464	0.470	0.465	0.491	0.497	0.507	0.477	0.492	0.467	0.507
Pr	0.051	0.050	0.053	0.052	0.050	0.051	0.051	0.051	0.053	0.050	0.050
Nd	0.139	0.138	0.141	0.137	0.139	0.149	0.141	0.154	0.150	0.158	0.144
Sm	0.019	0.020	0.020	0.019	0.018	0.014	0.013	0.021	0.014	0.021	0.016
Eu	0.000	0.003	0.003	0.000	0.000	0.000	0.000	0.003	0.000	0.000	0.000
Gd	0.007	0.009	0.010	0.010	0.007	0.006	0.005	0.009	0.008	0.010	0.008
Dy	0.000	0.000	0.000	0.000	0.000	0.000	0.000	0.000	0.000	0.000	0.000
Y	0.007	0.007	0.007	0.006	0.007	0.006	0.005	0.009	0.006	0.006	0.006
Ho	0.000	0.000	0.000	0.000	0.000	0.000	0.000	0.000	0.000	0.000	0.000
Th	0.022	0.020	0.021	0.023	0.016	0.011	0.010	0.018	0.011	0.020	0.009
U	0.000	0.000	0.000	0.000	0.000	0.000	0.000	0.000	0.000	0.000	0.000
Ca	0.028	0.016	0.015	0.034	0.033	0.028	0.016	0.034	0.008	0.013	0.028
P	0.961	0.979	0.973	0.969	0.967	0.975	0.977	0.960	0.983	0.974	0.974
F	0.071	0.079	0.078	0.077	0.078	0.088	0.073	0.065	0.075	0.086	0.069
Cl	0.000	0.000	0.000	0.000	0.000	0.000	0.000	0.000	0.000	0.002	0.000
Si	0.028	0.017	0.017	0.019	0.013	0.012	0.012	0.016	0.012	0.012	0.011
Pb	0.002	0.001	0.003	0.002	0.002	0.001	0.000	0.002	0.000	0.002	0.001
Fe	0.008	0.011	0.000	0.000	0.000	0.000	0.007	0.014	0.000	0.000	0.000
Sr	0.000	0.000	0.000	0.000	0.000	0.000	0.000	0.000	0.000	0.000	0.000
Total	1.995	1.978	1.981	1.987	1.993	1.985	1.988	2.007	1.977	1.977	1.994

Appendix 2.7: Continued

Unit						**A**					
Sample	15004	15005	15005	15005	15005	15005	15005	15005	15005	15005	15005
La_2O_3 (*wt. %*)	16.92	15.49	16.54	15.96	16.45	15.86	15.71	16.11	15.26	15.67	15.58
Ce_2O_3	35.76	35.80	34.51	33.95	35.50	35.08	35.14	35.01	35.34	35.50	34.21
Pr_2O_3	3.76	3.69	3.66	3.62	3.65	3.76	3.75	3.65	3.67	3.73	3.72
Nd_2O_3	10.89	10.38	10.14	10.35	10.16	10.27	10.46	10.33	10.52	10.49	10.77
Sm_2O_3	1.21	0.92	0.90	0.96	0.87	0.96	0.98	0.90	0.95	0.92	0.96
Eu_2O_3	0.00	0.00	0.00	0.00	0.00	0.00	0.00	0.00	0.00	0.00	0.00
Gd_2O_3	0.55	0.56	0.56	0.42	0.41	0.51	0.45	0.44	0.50	0.39	0.50
Dy_2O_3	0.00	0.00	0.00	0.00	0.00	0.24	0.00	0.00	0.00	0.00	0.00
Y_2O_3	0.32	0.28	0.33	0.25	0.26	0.22	0.29	0.25	0.26	0.20	0.24
Ho_2O_3											
ThO_2	1.19	1.53	1.58	1.73	1.60	1.84	1.69	1.46	1.84	1.74	1.88
UO_2	0.00	0.00	0.00	0.00	0.00	0.00	0.00	0.00	0.00	0.00	0.00
CaO	0.17	0.29	0.89	0.81	0.58	0.42	0.65	0.30	0.91	0.45	0.39
P_2O_5	29.63	29.26	29.48	29.31	29.14	29.31	29.35	29.54	29.44	29.39	29.34
F	0.53	0.64	0.56	0.59	0.59	0.66	0.63	0.62	0.58	0.58	0.61
Cl	0.00	0.00	0.00	0.00	0.00	0.00	0.00	0.00	0.00	0.00	0.00
SiO_2	0.28	0.41	0.36	0.35	0.35	0.38	0.36	0.32	0.44	0.36	0.36
PbO	0.00	0.16	0.12	0.00	0.11	0.20	0.14	0.10	0.14	0.18	0.21
FeO	0.00	0.00	0.00	0.00	0.00	0.00	0.00	0.00	0.00	0.00	0.00
SrO											
O=F	-0.22	-0.27	-0.23	-0.25	-0.25	-0.28	-0.27	-0.26	-0.24	-0.24	-0.26
Total	100.97	99.12	99.38	98.06	99.41	99.42	99.32	98.77	99.59	99.34	98.52
						O = 4					
La (*apfu*)	0.242	0.225	0.238	0.232	0.239	0.229	0.227	0.233	0.220	0.227	0.227
Ce	0.509	0.515	0.494	0.490	0.511	0.504	0.504	0.503	0.505	0.510	0.494
Pr	0.053	0.053	0.052	0.052	0.052	0.054	0.053	0.052	0.052	0.053	0.053
Nd	0.151	0.146	0.141	0.146	0.143	0.144	0.146	0.145	0.147	0.147	0.152
Sm	0.016	0.012	0.012	0.013	0.012	0.013	0.013	0.012	0.013	0.012	0.013
Eu	0.000	0.000	0.000	0.000	0.000	0.000	0.000	0.000	0.000	0.000	0.000
Gd	0.007	0.007	0.007	0.006	0.005	0.007	0.006	0.006	0.007	0.005	0.007
Dy	0.000	0.000	0.000	0.000	0.000	0.003	0.000	0.000	0.000	0.000	0.000
Y	0.007	0.006	0.007	0.005	0.005	0.005	0.006	0.005	0.005	0.004	0.005
Ho	0.000	0.000	0.000	0.000	0.000	0.000	0.000	0.000	0.000	0.000	0.000
Th	0.011	0.014	0.014	0.016	0.014	0.016	0.015	0.013	0.016	0.016	0.017
U	0.000	0.000	0.000	0.000	0.000	0.000	0.000	0.000	0.000	0.000	0.000
Ca	0.007	0.012	0.037	0.034	0.024	0.018	0.027	0.013	0.038	0.019	0.016
P	0.974	0.974	0.975	0.979	0.970	0.973	0.974	0.982	0.972	0.976	0.980
F	0.064	0.080	0.069	0.074	0.073	0.082	0.078	0.076	0.071	0.072	0.076
Cl	0.000	0.000	0.000	0.000	0.000	0.000	0.000	0.000	0.000	0.000	0.000
Si	0.011	0.016	0.014	0.014	0.014	0.015	0.014	0.013	0.017	0.014	0.014
Pb	0.000	0.002	0.001	0.000	0.001	0.002	0.001	0.001	0.001	0.002	0.002
Fe	0.000	0.000	0.000	0.000	0.000	0.000	0.000	0.000	0.000	0.000	0.000
Sr	0.000	0.000	0.000	0.000	0.000	0.000	0.000	0.000	0.000	0.000	0.000
Total	1.988	1.981	1.993	1.987	1.991	1.982	1.987	1.978	1.993	1.985	1.980

Appendix 2.7: Continued

Unit	**A**										
Sample	15005	15005	15005	15005	15005	15005	15005	15005	15005	15005	15005
La_2O_3 (*wt. %*)	16.11	15.81	15.43	15.54	16.34	15.55	15.10	15.29	16.12	15.81	15.47
Ce_2O_3	36.09	35.19	35.53	34.28	35.50	35.23	34.37	34.85	35.72	35.16	36.13
Pr_2O_3	3.54	3.73	3.80	3.83	3.76	3.73	3.86	3.86	3.85	3.67	3.62
Nd_2O_3	10.43	10.47	10.61	10.61	10.66	10.74	10.98	10.81	10.66	10.75	10.63
Sm_2O_3	0.83	0.96	0.97	0.99	0.90	1.01	1.07	1.08	0.98	1.06	0.99
Eu_2O_3	0.00	0.00	0.00	0.00	0.23	0.00	0.00	0.00	0.00	0.00	0.00
Gd_2O_3	0.48	0.38	0.49	0.55	0.56	0.59	0.47	0.47	0.50	0.63	0.43
Dy_2O_3	0.00	0.00	0.00	0.00	0.00	0.00	0.00	0.00	0.00	0.00	0.00
Y_2O_3	0.22	0.27	0.21	0.17	0.27	0.23	0.17	0.26	0.16	0.23	0.21
Ho_2O_3											
ThO_2	1.73	1.67	1.65	1.87	1.72	1.68	1.66	1.84	1.85	1.79	1.87
UO_2	0.00	0.00	0.00	0.00	0.00	0.00	0.00	0.00	0.00	0.00	0.00
CaO	0.52	0.44	0.24	0.56	0.24	0.23	0.34	0.25	0.20	0.33	0.19
P_2O_5	29.57	29.38	29.78	29.40	29.71	29.55	29.36	29.24	29.41	29.33	29.20
F	0.70	0.55	0.67	0.69	0.57	0.54	0.63	0.57	0.60	0.60	0.55
Cl	0.00	0.00	0.00	0.00	0.00	0.00	0.00	0.00	0.00	0.00	0.00
SiO_2	0.36	0.36	0.37	0.39	0.47	0.34	0.37	0.37	0.37	0.42	0.43
PbO	0.10	0.11	0.08	0.17	0.20	0.12	0.14	0.18	0.18	0.20	0.13
FeO	0.00	0.00	0.00	0.00	0.00	0.00	0.00	0.00	0.00	0.00	0.00
SrO											
O=F	-0.29	-0.23	-0.28	-0.29	-0.24	-0.23	-0.27	-0.24	-0.25	-0.25	-0.23
Total	100.39	99.09	99.53	98.73	100.87	99.30	98.25	98.83	100.34	99.73	99.62
	O = 4										
La (*apfu*)	0.231	0.229	0.222	0.225	0.233	0.225	0.220	0.223	0.232	0.228	0.224
Ce	0.513	0.506	0.506	0.493	0.503	0.506	0.497	0.504	0.511	0.504	0.520
Pr	0.050	0.053	0.054	0.055	0.053	0.053	0.056	0.055	0.055	0.052	0.052
Nd	0.145	0.147	0.148	0.149	0.147	0.150	0.155	0.152	0.149	0.150	0.149
Sm	0.011	0.013	0.013	0.013	0.012	0.014	0.015	0.015	0.013	0.014	0.013
Eu	0.000	0.000	0.000	0.000	0.003	0.000	0.000	0.000	0.000	0.000	0.000
Gd	0.006	0.005	0.006	0.007	0.007	0.008	0.006	0.006	0.006	0.008	0.006
Dy	0.000	0.000	0.000	0.000	0.000	0.000	0.000	0.000	0.000	0.000	0.000
Y	0.004	0.006	0.004	0.004	0.005	0.005	0.004	0.006	0.003	0.005	0.004
Ho	0.000	0.000	0.000	0.000	0.000	0.000	0.000	0.000	0.000	0.000	0.000
Th	0.015	0.015	0.015	0.017	0.015	0.015	0.015	0.017	0.016	0.016	0.017
U	0.000	0.000	0.000	0.000	0.000	0.000	0.000	0.000	0.000	0.000	0.000
Ca	0.021	0.019	0.010	0.023	0.010	0.010	0.014	0.011	0.008	0.014	0.008
P	0.972	0.977	0.982	0.977	0.974	0.981	0.981	0.977	0.972	0.973	0.972
F	0.086	0.068	0.082	0.086	0.070	0.066	0.079	0.071	0.074	0.075	0.068
Cl	0.000	0.000	0.000	0.000	0.000	0.000	0.000	0.000	0.000	0.000	0.000
Si	0.014	0.014	0.014	0.015	0.018	0.013	0.015	0.014	0.014	0.017	0.017
Pb	0.001	0.001	0.001	0.002	0.002	0.001	0.001	0.002	0.002	0.002	0.001
Fe	0.000	0.000	0.000	0.000	0.000	0.000	0.000	0.000	0.000	0.000	0.000
Sr	0.000	0.000	0.000	0.000	0.000	0.000	0.000	0.000	0.000	0.000	0.000
Total	1.983	1.986	1.975	1.980	1.983	1.981	1.978	1.981	1.983	1.984	1.984

Appendix 2.7: Continued

Unit						**A**					
Sample	15005	15020	15020	15020	15020	15020	15020	15020	15020	15020	15020
La_2O_3 (*wt. %*)	16.14	22.89	22.24	22.62	21.97	22.74	22.71	22.53	22.15	22.25	22.15
Ce_2O_3	35.01	32.16	32.48	31.90	32.41	32.12	32.43	32.20	32.74	33.31	33.21
Pr_2O_3	3.86	3.06	3.16	3.24	3.08	3.04	2.99	3.06	3.09	3.07	3.22
Nd_2O_3	10.46	8.26	8.36	8.17	8.35	8.26	8.11	8.07	7.99	8.25	8.48
Sm_2O_3	1.04	0.83	0.94	0.75	0.73	0.84	0.76	0.72	0.75	0.75	0.81
Eu_2O_3	0.00	0.00	0.00	0.00	0.00	0.00	0.00	0.00	0.00	0.00	0.00
Gd_2O_3	0.58	0.83	0.81	0.65	0.67	0.68	0.76	0.50	0.75	0.59	0.62
Dy_2O_3	0.24	0.27	0.00	0.25	0.27	0.00	0.00	0.23	0.30	0.00	0.00
Y_2O_3	0.24	0.46	0.48	0.54	0.54	0.40	0.46	0.41	0.48	0.42	0.21
Ho_2O_3		0.00	0.00	0.00	0.00	0.00	0.00	0.00	0.00	0.00	0.00
ThO_2	1.95	0.33	0.32	0.33	0.32	0.27	0.36	0.34	0.36	0.42	0.61
UO_2	0.00	0.00	0.00	0.00	0.00	0.00	0.00	0.00	0.00	0.00	0.00
CaO	0.51	0.41	0.31	0.42	0.64	0.38	0.33	0.52	0.49	0.18	0.07
P_2O_5	28.97	29.96	30.28	29.86	29.58	29.45	29.89	29.78	29.74	29.64	29.66
F	0.67	0.49	0.60	0.47	0.51	0.57	0.61	0.48	0.55	0.49	0.00
Cl	0.00	0.00	0.00	0.00	0.00	0.00	0.00	0.00	0.00	0.00	0.00
SiO_2	0.41	0.00	0.00	0.00	0.00	0.00	0.14	0.00	0.17	0.00	0.17
PbO	0.14	0.00	0.00	0.15	0.00	0.00	0.00	0.09	0.00	0.00	0.09
FeO	0.00	0.00	0.00	0.00	0.00	0.19	0.00	0.00	0.00	0.00	0.00
SrO		0.09	0.00	0.00	0.00	0.00	0.00	0.00	0.00	0.00	0.00
O=F	-0.28	-0.20	-0.25	-0.20	-0.22	-0.24	-0.26	-0.20	-0.23	-0.21	0.00
Total	99.94	99.82	99.72	99.15	98.84	98.70	99.28	98.73	99.33	99.15	99.28
						O = 4					
La (*apfu*)	0.234	0.329	0.318	0.327	0.319	0.331	0.326	0.326	0.319	0.323	0.323
Ce	0.503	0.459	0.460	0.457	0.466	0.464	0.463	0.463	0.468	0.480	0.481
Pr	0.055	0.043	0.045	0.046	0.044	0.044	0.042	0.044	0.044	0.044	0.046
Nd	0.147	0.115	0.116	0.114	0.117	0.116	0.113	0.113	0.111	0.116	0.120
Sm	0.014	0.011	0.013	0.010	0.010	0.011	0.010	0.010	0.010	0.010	0.011
Eu	0.000	0.000	0.000	0.000	0.000	0.000	0.000	0.000	0.000	0.000	0.000
Gd	0.008	0.011	0.010	0.008	0.009	0.009	0.010	0.007	0.010	0.008	0.008
Dy	0.003	0.003	0.000	0.003	0.003	0.000	0.000	0.003	0.004	0.000	0.000
Y	0.005	0.009	0.010	0.011	0.011	0.008	0.009	0.009	0.010	0.009	0.004
Ho	0.000	0.000	0.000	0.000	0.000	0.000	0.000	0.000	0.000	0.000	0.000
Th	0.017	0.003	0.003	0.003	0.003	0.002	0.003	0.003	0.003	0.004	0.005
U	0.000	0.000	0.000	0.000	0.000	0.000	0.000	0.000	0.000	0.000	0.000
Ca	0.022	0.017	0.013	0.017	0.027	0.016	0.014	0.022	0.020	0.008	0.003
P	0.963	0.988	0.993	0.990	0.985	0.983	0.986	0.990	0.983	0.987	0.993
F	0.083	0.060	0.074	0.058	0.064	0.071	0.075	0.060	0.068	0.061	0.000
Cl	0.000	0.000	0.000	0.000	0.000	0.000	0.000	0.000	0.000	0.000	0.000
Si	0.016	0.000	0.000	0.000	0.000	0.000	0.005	0.000	0.007	0.000	0.007
Pb	0.002	0.000	0.000	0.002	0.000	0.000	0.000	0.001	0.000	0.000	0.001
Fe	0.000	0.000	0.000	0.000	0.000	0.006	0.000	0.000	0.000	0.000	0.000
Sr	0.000	0.000	0.000	0.000	0.000	0.000	0.000	0.000	0.000	0.000	0.000
Total	1.989	1.988	1.980	1.990	1.994	1.991	1.982	1.990	1.989	1.987	2.002

Appendix 2.7: Continued

Unit	**A**										
Sample	15020	15020	15020	15020	15020	15020	15020	15020	15020	15020	15020
La_2O_3 (*wt. %*)	22.23	22.24	21.47	22.43	22.25	22.23	22.45	22.89	15.48	13.40	12.87
Ce_2O_3	32.50	32.73	31.44	32.98	32.09	32.15	32.26	32.79	32.54	34.05	31.07
Pr_2O_3	3.05	3.16	3.08	3.06	3.08	3.05	3.11	3.11	4.13	4.33	4.37
Nd_2O_3	8.36	8.39	8.58	8.18	8.24	8.11	8.10	8.14	12.50	15.25	14.86
Sm_2O_3	0.85	0.86	1.03	0.78	0.82	0.76	0.75	0.81	1.44	1.63	1.68
Eu_2O_3	0.00	0.00	0.22	0.00	0.00	0.00	0.00	0.00	0.19	0.23	0.37
Gd_2O_3	0.75	0.61	0.98	0.80	0.86	0.76	1.00	0.91	0.73	0.96	1.17
Dy_2O_3	0.00	0.00	0.00	0.00	0.27	0.23	0.00	0.00	0.00	0.00	0.00
Y_2O_3	0.23	0.24	0.20	0.39	0.50	0.28	0.36	0.28	0.38	0.24	0.44
Ho_2O_3	0.00	0.00	0.00	0.00	0.00	0.00	0.00	0.00	0.00		
ThO_2	0.47	0.52	0.72	0.46	0.51	0.48	0.42	0.42	0.57	0.64	0.65
UO_2	0.00	0.00	0.00	0.00	0.00	0.00	0.00	0.00	0.00	0.00	0.00
CaO	0.10	0.17	0.21	0.43	0.42	0.31	0.37	0.21	0.55	0.33	0.81
P_2O_5	29.70	29.77	29.66	29.87	29.77	29.44	29.83	29.87	29.20	29.58	29.62
F	0.61	0.53	0.62	0.48	0.46	0.61	0.00	0.68	0.00	0.61	0.62
Cl	0.00	0.00	0.00	0.00	0.00	0.00	0.00	0.00	0.00	0.00	0.00
SiO_2	0.17	0.19	0.15	0.00	0.00	0.00	0.00	0.00	0.18	0.25	0.22
PbO	0.10	0.00	0.09	0.00	0.08	0.11	0.00	0.00	0.00	0.00	0.08
FeO	0.00	0.00	0.00	0.00	0.00	0.00	0.00	0.00	0.31	0.00	0.26
SrO	0.00	0.10	0.26	0.00	0.09	0.00	0.00	0.00	0.00		
O=F	-0.26	-0.22	-0.26	-0.20	-0.19	-0.26	0.00	-0.28	0.00	-0.26	-0.26
Total	98.86	99.30	98.44	99.66	99.25	98.26	98.65	99.80	98.20	101.25	98.81
	O = 4										
La (*apfu*)	0.322	0.321	0.312	0.323	0.322	0.325	0.328	0.329	0.228	0.192	0.186
Ce	0.467	0.469	0.453	0.471	0.461	0.466	0.467	0.468	0.476	0.483	0.445
Pr	0.044	0.045	0.044	0.044	0.044	0.044	0.045	0.044	0.060	0.061	0.062
Nd	0.117	0.117	0.121	0.114	0.115	0.115	0.114	0.113	0.178	0.211	0.208
Sm	0.011	0.012	0.014	0.011	0.011	0.010	0.010	0.011	0.020	0.022	0.023
Eu	0.000	0.000	0.003	0.000	0.000	0.000	0.000	0.000	0.003	0.003	0.005
Gd	0.010	0.008	0.013	0.010	0.011	0.010	0.013	0.012	0.010	0.012	0.015
Dy	0.000	0.000	0.000	0.000	0.003	0.003	0.000	0.000	0.000	0.000	0.000
Y	0.005	0.005	0.004	0.008	0.010	0.006	0.007	0.006	0.008	0.005	0.009
Ho	0.000	0.000	0.000	0.000	0.000	0.000	0.000	0.000	0.000	0.000	0.000
Th	0.004	0.005	0.006	0.004	0.005	0.004	0.004	0.004	0.005	0.006	0.006
U	0.000	0.000	0.000	0.000	0.000	0.000	0.000	0.000	0.000	0.000	0.000
Ca	0.004	0.007	0.009	0.018	0.018	0.013	0.016	0.009	0.024	0.014	0.034
P	0.986	0.986	0.988	0.987	0.988	0.986	1.000	0.985	0.987	0.971	0.982
F	0.076	0.066	0.077	0.060	0.057	0.076	0.000	0.083	0.000	0.075	0.076
Cl	0.000	0.000	0.000	0.000	0.000	0.000	0.000	0.000	0.000	0.000	0.000
Si	0.007	0.008	0.006	0.000	0.000	0.000	0.000	0.000	0.007	0.010	0.009
Pb	0.001	0.000	0.001	0.000	0.001	0.001	0.000	0.000	0.000	0.000	0.001
Fe	0.000	0.000	0.000	0.000	0.000	0.000	0.000	0.000	0.010	0.000	0.008
Sr	0.000	0.000	0.000	0.000	0.000	0.000	0.000	0.000	0.000	0.000	0.000
Total	1.978	1.981	1.974	1.990	1.989	1.983	2.004	1.980	2.016	1.990	1.992

Appendix 2.7: Continued

Unit						**A**					
Sample	15020	15020	15020	15020	15020	15020	15020	15020	15020	15020	15020
La_2O_3 (*wt. %*)	14.67	15.03	15.83	15.99	14.72	20.99	21.21	21.45	22.67	21.14	21.08
Ce_2O_3	31.46	31.80	31.33	31.03	31.60	32.16	31.09	31.95	31.50	31.03	32.65
Pr_2O_3	4.08	4.08	4.04	3.99	4.01	3.25	3.18	3.37	2.85	3.22	3.18
Nd_2O_3	14.39	14.10	13.75	13.69	13.85	9.92	10.02	9.89	8.88	9.73	9.85
Sm_2O_3	1.57	1.51	1.44	1.60	1.57	0.92	1.06	0.90	0.61	0.85	0.96
Eu_2O_3	0.00	0.33	0.28	0.32	0.26	0.00	0.00	0.00	0.00	0.00	0.00
Gd_2O_3	0.92	0.91	0.94	1.04	0.97	0.71	0.74	0.62	0.73	0.70	0.65
Dy_2O_3	0.00	0.00	0.00	0.00	0.00	0.00	0.25	0.25	0.00	0.00	0.00
Y_2O_3	0.30	0.25	0.27	0.27	0.27	0.41	0.40	0.50	0.41	0.55	0.48
Ho_2O_3											
ThO_2	0.64	0.59	1.02	1.04	0.99	0.35	0.33	0.36	0.27	0.33	0.33
UO_2	0.00	0.00	0.00	0.00	0.00	0.00	0.00	0.00	0.00	0.00	0.00
CaO	0.64	0.28	0.53	0.60	0.18	0.23	0.42	0.46	0.65	0.85	0.48
P_2O_5	29.47	29.52	29.66	29.80	29.06	29.61	29.95	29.70	29.69	29.95	29.64
F	0.56	0.00	0.50	0.49	0.55	0.49	0.52	0.56	0.56	0.53	0.60
Cl	0.00	0.00	0.00	0.00	0.00	0.00	0.00	0.00	0.00	0.05	0.00
SiO_2	0.23	0.17	0.23	0.22	0.20	0.00	0.00	0.00	0.00	0.00	0.00
PbO	0.00	0.10	0.00	0.10	0.11	0.00	0.00	0.11	0.00	0.00	0.10
FeO	0.00	0.00	0.00	0.00	0.00	0.00	0.00	0.00	0.00	0.00	0.00
SrO											
O=F	-0.24	0.00	-0.21	-0.20	-0.23	-0.21	-0.22	-0.24	-0.24	-0.22	-0.25
Total	98.69	98.66	99.61	99.98	98.08	98.83	98.94	99.86	98.59	98.70	99.74
						O = 4					
La (*apfu*)	0.213	0.220	0.228	0.230	0.216	0.305	0.306	0.309	0.328	0.304	0.304
Ce	0.453	0.463	0.448	0.443	0.461	0.464	0.445	0.457	0.453	0.444	0.467
Pr	0.058	0.059	0.058	0.057	0.058	0.047	0.045	0.048	0.041	0.046	0.045
Nd	0.202	0.200	0.192	0.190	0.197	0.140	0.140	0.138	0.125	0.136	0.138
Sm	0.021	0.021	0.019	0.022	0.022	0.013	0.014	0.012	0.008	0.011	0.013
Eu	0.000	0.004	0.004	0.004	0.004	0.000	0.000	0.000	0.000	0.000	0.000
Gd	0.012	0.012	0.012	0.013	0.013	0.009	0.010	0.008	0.009	0.009	0.008
Dy	0.000	0.000	0.000	0.000	0.000	0.000	0.003	0.003	0.000	0.000	0.000
Y	0.006	0.005	0.006	0.006	0.006	0.009	0.008	0.010	0.009	0.011	0.010
Ho	0.000	0.000	0.000	0.000	0.000	0.000	0.000	0.000	0.000	0.000	0.000
Th	0.006	0.005	0.009	0.009	0.009	0.003	0.003	0.003	0.002	0.003	0.003
U	0.000	0.000	0.000	0.000	0.000	0.000	0.000	0.000	0.000	0.000	0.000
Ca	0.027	0.012	0.022	0.025	0.008	0.010	0.018	0.019	0.027	0.036	0.020
P	0.982	0.994	0.982	0.983	0.981	0.988	0.992	0.982	0.987	0.990	0.981
F	0.070	0.000	0.061	0.060	0.069	0.061	0.064	0.069	0.070	0.065	0.075
Cl	0.000	0.000	0.000	0.000	0.000	0.000	0.000	0.000	0.000	0.003	0.000
Si	0.009	0.007	0.009	0.009	0.008	0.000	0.000	0.000	0.000	0.000	0.000
Pb	0.000	0.001	0.000	0.001	0.001	0.000	0.000	0.001	0.000	0.000	0.001
Fe	0.000	0.000	0.000	0.000	0.000	0.000	0.000	0.000	0.000	0.000	0.000
Sr	0.000	0.000	0.000	0.000	0.000	0.000	0.000	0.000	0.000	0.000	0.000
Total	1.989	2.004	1.990	1.991	1.983	1.987	1.985	1.991	1.990	1.990	1.990

Appendix 2.7: Continued

Unit						**A**					
Sample	15020	15020	15020	15020	15024	15024	15024	15024	15024	15024	15024
La_2O_3 (*wt.* %)	21.37	21.42	21.66	21.96	16.74	16.66	16.08	15.34	14.63	18.31	16.64
Ce_2O_3	31.42	32.06	32.46	32.94	33.56	33.82	33.11	33.98	34.60	33.32	33.09
Pr_2O_3	3.06	3.27	3.23	3.24	3.83	3.89	3.83	3.84	3.81	3.65	3.81
Nd_2O_3	9.16	9.64	9.25	9.29	13.09	13.04	12.57	12.91	12.95	12.10	12.82
Sm_2O_3	0.76	0.82	0.75	0.81	1.29	1.34	1.39	1.45	1.50	1.26	1.42
Eu_2O_3	0.00	0.00	0.00	0.00	0.28	0.18	0.23	0.29	0.22	0.00	0.19
Gd_2O_3	0.61	0.61	0.60	0.64	0.80	0.77	0.86	0.71	1.10	0.73	0.80
Dy_2O_3	0.00	0.00	0.23	0.21	0.00	0.00	0.00	0.00	0.26	0.00	0.00
Y_2O_3	0.40	0.35	0.39	0.38	0.31	0.42	0.50	0.49	0.43	0.40	0.50
Ho_2O_3					0.00	0.00	0.00	0.00	0.00	0.00	0.00
ThO_2	0.39	0.39	0.37	0.40	0.97	1.00	1.30	1.15	1.04	0.88	1.27
UO_2	0.00	0.00	0.00	0.00	0.00	0.00	0.00	0.00	0.00	0.00	0.00
CaO	0.74	0.34	0.19	0.20	0.18	0.09	0.14	0.22	0.24	0.12	0.15
P_2O_5	29.79	29.74	29.59	29.74	28.76	29.07	29.29	29.03	28.84	28.54	28.71
F	0.63	0.61	0.60	0.50	0.63	0.55	0.66	0.65	0.52	0.54	0.61
Cl	0.00	0.00	0.00	0.00	0.00	0.00	0.03	0.00	0.00	0.00	0.00
SiO_2	0.00	0.00	0.00	0.00	0.27	0.31	0.46	0.30	0.41	0.23	0.35
PbO	0.00	0.00	0.09	0.10	0.14	0.13	0.00	0.12	0.11	0.16	0.00
FeO	0.00	0.00	0.00	0.00	0.00	0.00	0.00	0.00	0.00	0.00	0.00
SrO					0.09	0.00	0.12	0.21	0.15	0.10	0.16
O=F	-0.26	-0.26	-0.25	-0.21	-0.27	-0.23	-0.28	-0.27	-0.22	-0.23	-0.26
Total	98.05	99.01	99.14	100.20	100.67	101.03	100.28	100.41	100.58	100.10	100.24
						O = 4					
La (*apfu*)	0.310	0.310	0.314	0.316	0.243	0.241	0.231	0.222	0.212	0.268	0.242
Ce	0.452	0.460	0.467	0.471	0.484	0.485	0.473	0.488	0.498	0.485	0.478
Pr	0.044	0.047	0.046	0.046	0.055	0.055	0.054	0.055	0.055	0.053	0.055
Nd	0.128	0.135	0.130	0.130	0.184	0.182	0.175	0.181	0.182	0.172	0.181
Sm	0.010	0.011	0.010	0.011	0.017	0.018	0.019	0.020	0.020	0.017	0.019
Eu	0.000	0.000	0.000	0.000	0.004	0.002	0.003	0.004	0.003	0.000	0.002
Gd	0.008	0.008	0.008	0.008	0.010	0.010	0.011	0.009	0.014	0.010	0.010
Dy	0.000	0.000	0.003	0.003	0.000	0.000	0.000	0.000	0.003	0.000	0.000
Y	0.008	0.007	0.008	0.008	0.006	0.009	0.010	0.010	0.009	0.008	0.011
Ho	0.000	0.000	0.000	0.000	0.000	0.000	0.000	0.000	0.000	0.000	0.000
Th	0.003	0.003	0.003	0.004	0.009	0.009	0.012	0.010	0.009	0.008	0.011
U	0.000	0.000	0.000	0.000	0.000	0.000	0.000	0.000	0.000	0.000	0.000
Ca	0.031	0.014	0.008	0.008	0.008	0.004	0.006	0.009	0.010	0.005	0.006
P	0.991	0.987	0.985	0.983	0.959	0.964	0.967	0.964	0.961	0.960	0.959
F	0.078	0.076	0.075	0.062	0.079	0.068	0.081	0.081	0.064	0.068	0.077
Cl	0.000	0.000	0.000	0.000	0.000	0.000	0.002	0.000	0.000	0.000	0.000
Si	0.000	0.000	0.000	0.000	0.011	0.012	0.018	0.012	0.016	0.009	0.014
Pb	0.000	0.000	0.001	0.001	0.002	0.001	0.000	0.001	0.001	0.002	0.000
Fe	0.000	0.000	0.000	0.000	0.000	0.000	0.000	0.000	0.000	0.000	0.000
Sr	0.000	0.000	0.000	0.000	0.000	0.000	0.000	0.000	0.000	0.000	0.000
Total	1.985	1.983	1.983	1.989	1.992	1.993	1.980	1.986	1.995	1.996	1.989

Appendix 2.7: Continued

Unit	**A**										
Sample	15024	15024	15024	15024	15024	15024	15024	15024	15024	15024	15024
La_2O_3 (*wt. %*)	17.04	17.04	16.47	16.96	15.71	17.04	16.89	16.48	13.98	16.10	17.07
Ce_2O_3	33.55	33.70	32.81	33.91	34.01	33.48	33.41	33.25	32.66	31.45	32.14
Pr_2O_3	3.73	3.82	3.84	3.86	3.86	3.69	3.78	3.77	4.17	4.00	3.82
Nd_2O_3	12.88	12.65	12.95	12.91	13.27	12.78	12.99	12.90	14.39	13.47	13.03
Sm_2O_3	1.42	1.31	1.34	1.36	1.46	1.26	1.38	1.30	1.34	1.41	1.21
Eu_2O_3	0.00	0.18	0.22	0.00	0.21	0.00	0.27	0.20	0.27	0.19	0.25
Gd_2O_3	0.82	0.68	0.81	0.77	0.70	0.58	0.97	0.87	0.77	0.63	0.73
Dy_2O_3	0.00	0.21	0.00	0.00	0.00	0.00	0.00	0.00	0.00	0.00	0.00
Y_2O_3	0.26	0.49	0.36	0.41	0.46	0.36	0.42	0.36	0.35	0.42	0.31
Ho_2O_3	0.00	0.00	0.00	0.00	0.00	0.00	0.00	0.00			
ThO_2	1.00	1.07	1.08	1.02	1.06	1.00	1.13	0.98	1.14	1.04	1.03
UO_2	0.00	0.00	0.00	0.00	0.00	0.00	0.00	0.00	0.00	0.00	0.00
CaO	0.17	0.12	0.12	0.23	0.19	0.18	0.11	0.09	0.67	0.49	0.30
P_2O_5	28.56	28.56	29.49	28.79	28.68	28.77	28.61	29.51	29.45	29.68	29.51
F	0.59	0.61	0.69	0.55	0.63	0.61	0.64	0.54	0.53	0.55	0.60
Cl	0.00	0.00	0.00	0.00	0.00	0.00	0.02	0.00	0.00	0.00	0.00
SiO_2	0.33	0.33	0.30	0.25	0.26	0.23	0.30	0.46	0.20	0.20	0.26
PbO	0.11	0.00	0.13	0.12	0.00	0.12	0.11	0.10	0.16	0.00	0.09
FeO	0.00	0.25	0.00	0.00	0.00	0.00	0.00	0.00	0.00	0.00	0.00
SrO	0.00	0.08	0.00	0.00	0.11	0.13	0.00	0.08			
O=F	-0.25	-0.26	-0.29	-0.23	-0.26	-0.26	-0.27	-0.23	-0.22	-0.23	-0.25
Total	100.21	100.85	100.31	100.90	100.33	99.95	100.74	100.66	99.85	99.39	100.08
						O = 4					
La (*apfu*)	0.249	0.248	0.237	0.246	0.229	0.249	0.246	0.236	0.202	0.232	0.246
Ce	0.486	0.486	0.468	0.489	0.492	0.485	0.483	0.473	0.468	0.450	0.460
Pr	0.054	0.055	0.055	0.055	0.056	0.053	0.054	0.053	0.059	0.057	0.054
Nd	0.182	0.178	0.180	0.182	0.187	0.181	0.183	0.179	0.201	0.188	0.182
Sm	0.019	0.018	0.018	0.018	0.020	0.017	0.019	0.017	0.018	0.019	0.016
Eu	0.000	0.002	0.003	0.000	0.003	0.000	0.004	0.003	0.004	0.002	0.003
Gd	0.011	0.009	0.010	0.010	0.009	0.008	0.013	0.011	0.010	0.008	0.010
Dy	0.000	0.003	0.000	0.000	0.000	0.000	0.000	0.000	0.000	0.000	0.000
Y	0.005	0.010	0.007	0.009	0.010	0.008	0.009	0.008	0.007	0.009	0.006
Ho	0.000	0.000	0.000	0.000	0.000	0.000	0.000	0.000	0.000	0.000	0.000
Th	0.009	0.010	0.010	0.009	0.010	0.009	0.010	0.009	0.010	0.009	0.009
U	0.000	0.000	0.000	0.000	0.000	0.000	0.000	0.000	0.000	0.000	0.000
Ca	0.007	0.005	0.005	0.010	0.008	0.008	0.004	0.004	0.028	0.021	0.013
P	0.958	0.953	0.973	0.959	0.959	0.964	0.955	0.972	0.977	0.983	0.976
F	0.074	0.076	0.084	0.068	0.078	0.076	0.080	0.066	0.066	0.068	0.074
Cl	0.000	0.000	0.000	0.000	0.000	0.000	0.001	0.000	0.000	0.000	0.000
Si	0.013	0.013	0.012	0.010	0.010	0.009	0.012	0.018	0.008	0.008	0.010
Pb	0.001	0.000	0.001	0.001	0.000	0.001	0.001	0.001	0.002	0.000	0.001
Fe	0.000	0.008	0.000	0.000	0.000	0.000	0.000	0.000	0.000	0.000	0.000
Sr	0.000	0.000	0.000	0.000	0.000	0.000	0.000	0.000	0.000	0.000	0.000
Total	1.995	1.998	1.980	1.998	1.992	1.990	1.992	1.985	1.994	1.987	1.986

Appendix 2.7: Continued

Unit						**A**					
Sample	15024	15024	15024	15024	15024	15024	15024	15024	15024	15024	15024
La_2O_3 (*wt. %*)	16.54	16.87	16.02	13.23	13.34	14.18	17.61	16.54	16.18	16.35	16.55
Ce_2O_3	31.97	33.04	31.46	32.41	32.89	31.69	32.04	32.20	31.84	31.59	32.32
Pr_2O_3	3.93	4.03	3.96	4.23	4.13	3.92	3.78	3.83	3.84	3.65	3.90
Nd_2O_3	12.99	13.49	13.18	14.93	14.41	13.51	13.13	13.54	13.34	12.99	12.96
Sm_2O_3	1.27	1.29	1.49	1.37	1.41	1.36	1.30	1.37	1.34	1.32	1.27
Eu_2O_3	0.22	0.20	0.00	0.28	0.23	0.27	0.19	0.23	0.24	0.27	0.00
Gd_2O_3	0.73	0.65	0.75	0.82	0.72	0.72	0.64	0.71	0.83	0.76	0.71
Dy_2O_3	0.00	0.00	0.00	0.00	0.00	0.00	0.00	0.00	0.00	0.00	0.00
Y_2O_3	0.32	0.26	0.32	0.50	0.45	0.40	0.38	0.24	0.40	0.41	0.29
Ho_2O_3											
ThO_2	1.02	0.75	1.15	1.27	1.43	1.25	0.96	1.08	1.04	1.09	0.97
UO_2	0.00	0.00	0.00	0.00	0.00	0.00	0.00	0.00	0.00	0.00	0.00
CaO	0.54	0.34	0.31	0.53	0.70	1.29	0.11	0.13	0.35	0.22	0.15
P_2O_5	29.50	29.51	28.91	29.70	29.59	29.45	29.53	29.42	29.68	29.14	29.83
F	0.50	0.64	0.62	0.56	0.65	0.55	0.00	0.56	0.56	0.62	0.64
Cl	0.00	0.00	0.00	0.00	0.00	0.00	0.00	0.02	0.00	0.00	0.00
SiO_2	0.27	0.18	0.31	0.14	0.20	0.21	0.23	0.24	0.24	0.22	0.22
PbO	0.12	0.15	0.09	0.08	0.15	0.13	0.00	0.09	0.00	0.11	0.00
FeO	0.26	0.00	0.20	0.00	0.27	0.40	0.00	0.00	0.00	0.00	0.00
SrO											
O=F	-0.21	-0.27	-0.26	-0.24	-0.27	-0.23	0.00	-0.23	-0.24	-0.26	-0.27
Total	99.97	101.12	98.48	99.81	100.30	99.09	99.91	99.95	99.64	98.47	99.55
						O = 4					
La (*apfu*)	0.238	0.242	0.235	0.191	0.191	0.205	0.256	0.239	0.233	0.239	0.238
Ce	0.457	0.470	0.457	0.463	0.468	0.454	0.463	0.462	0.455	0.458	0.461
Pr	0.056	0.057	0.057	0.060	0.058	0.056	0.054	0.055	0.055	0.053	0.055
Nd	0.181	0.187	0.187	0.208	0.200	0.189	0.185	0.190	0.186	0.184	0.181
Sm	0.017	0.017	0.020	0.018	0.019	0.018	0.018	0.018	0.018	0.018	0.017
Eu	0.003	0.003	0.000	0.004	0.003	0.004	0.003	0.003	0.003	0.004	0.000
Gd	0.009	0.008	0.010	0.011	0.009	0.009	0.008	0.009	0.011	0.010	0.009
Dy	0.000	0.000	0.000	0.000	0.000	0.000	0.000	0.000	0.000	0.000	0.000
Y	0.007	0.005	0.007	0.010	0.009	0.008	0.008	0.005	0.008	0.009	0.006
Ho	0.000	0.000	0.000	0.000	0.000	0.000	0.000	0.000	0.000	0.000	0.000
Th	0.009	0.007	0.010	0.011	0.013	0.011	0.009	0.010	0.009	0.010	0.009
U	0.000	0.000	0.000	0.000	0.000	0.000	0.000	0.000	0.000	0.000	0.000
Ca	0.023	0.014	0.013	0.022	0.029	0.054	0.005	0.005	0.015	0.010	0.006
P	0.976	0.971	0.972	0.982	0.974	0.976	0.987	0.977	0.982	0.978	0.985
F	0.062	0.079	0.078	0.069	0.080	0.067	0.000	0.069	0.070	0.077	0.079
Cl	0.000	0.000	0.000	0.000	0.000	0.000	0.000	0.001	0.000	0.000	0.000
Si	0.010	0.007	0.012	0.006	0.008	0.008	0.009	0.009	0.009	0.009	0.009
Pb	0.001	0.002	0.001	0.001	0.002	0.001	0.000	0.001	0.000	0.001	0.000
Fe	0.008	0.000	0.007	0.000	0.009	0.013	0.000	0.000	0.000	0.000	0.000
Sr	0.000	0.000	0.000	0.000	0.000	0.000	0.000	0.000	0.000	0.000	0.000
Total	1.996	1.990	1.988	1.987	1.993	2.006	2.005	1.984	1.984	1.982	1.976

Appendix 2.7: Continued

Unit						**A**					
Sample	15024	15024	15024	15024	15024	15024	15024	15024	15024	15024	15024
La_2O_3 (*wt. %*)	16.20	17.24	16.30	15.88	15.78	15.72	17.07	16.08	15.66	15.56	16.26
Ce_2O_3	32.17	33.52	32.26	32.57	32.71	32.40	32.64	31.32	32.26	32.21	32.60
Pr_2O_3	3.98	3.72	3.88	3.85	4.01	3.84	3.83	4.04	3.91	3.94	3.81
Nd_2O_3	13.18	12.71	12.86	13.27	13.41	13.04	13.09	13.11	13.06	13.35	13.32
Sm_2O_3	1.27	1.13	1.38	1.27	1.23	1.33	1.35	1.32	1.22	1.42	1.30
Eu_2O_3	0.23	0.00	0.21	0.00	0.28	0.00	0.00	0.00	0.22	0.19	0.00
Gd_2O_3	0.69	0.67	0.75	0.81	0.70	0.75	0.77	0.76	0.70	0.85	0.67
Dy_2O_3	0.00	0.00	0.00	0.00	0.00	0.00	0.00	0.00	0.00	0.00	0.00
Y_2O_3	0.43	0.31	0.35	0.38	0.33	0.37	0.46	0.38	0.38	0.41	0.22
Ho_2O_3											
ThO_2	1.08	0.93	1.04	0.95	0.97	0.95	0.97	1.05	0.87	1.12	0.81
UO_2	0.00	0.00	0.00	0.00	0.00	0.00	0.00	0.00	0.00	0.00	0.00
CaO	0.17	0.09	0.11	0.37	0.17	0.10	0.37	0.25	0.20	0.14	0.18
P_2O_5	29.53	29.85	29.43	29.39	29.29	29.64	29.23	29.19	29.47	29.76	29.30
F	0.57	0.58	0.61	0.63	0.00	0.47	0.51	0.53	0.58	0.53	0.49
Cl	0.00	0.00	0.00	0.00	0.00	0.00	0.00	0.00	0.00	0.00	0.00
SiO_2	0.23	0.22	0.24	0.24	0.27	0.21	0.23	0.25	0.26	0.31	0.21
PbO	0.08	0.00	0.10	0.00	0.09	0.10	0.08	0.00	0.11	0.12	0.00
FeO	0.00	0.00	0.27	0.00	0.00	0.00	0.00	0.00	0.23	0.00	0.27
SrO											
O=F	-0.24	-0.25	-0.26	-0.27	0.00	-0.20	-0.22	-0.22	-0.24	-0.22	-0.21
Total	99.58	100.72	99.55	99.33	99.22	98.72	100.38	98.06	98.87	99.68	99.23
						O = 4					
La (*apfu*)	0.234	0.247	0.236	0.230	0.231	0.228	0.247	0.236	0.227	0.224	0.237
Ce	0.462	0.476	0.463	0.468	0.476	0.467	0.468	0.455	0.465	0.460	0.471
Pr	0.057	0.053	0.056	0.055	0.058	0.055	0.055	0.058	0.056	0.056	0.055
Nd	0.185	0.176	0.180	0.186	0.190	0.184	0.183	0.186	0.183	0.186	0.188
Sm	0.017	0.015	0.019	0.017	0.017	0.018	0.018	0.018	0.017	0.019	0.018
Eu	0.003	0.000	0.003	0.000	0.004	0.000	0.000	0.000	0.003	0.003	0.000
Gd	0.009	0.009	0.010	0.011	0.009	0.010	0.010	0.010	0.009	0.011	0.009
Dy	0.000	0.000	0.000	0.000	0.000	0.000	0.000	0.000	0.000	0.000	0.000
Y	0.009	0.006	0.007	0.008	0.007	0.008	0.010	0.008	0.008	0.009	0.005
Ho	0.000	0.000	0.000	0.000	0.000	0.000	0.000	0.000	0.000	0.000	0.000
Th	0.010	0.008	0.009	0.009	0.009	0.009	0.009	0.009	0.008	0.010	0.007
U	0.000	0.000	0.000	0.000	0.000	0.000	0.000	0.000	0.000	0.000	0.000
Ca	0.007	0.004	0.005	0.016	0.007	0.004	0.016	0.011	0.008	0.006	0.008
P	0.980	0.980	0.978	0.977	0.986	0.989	0.970	0.982	0.981	0.984	0.978
F	0.071	0.071	0.075	0.078	0.000	0.059	0.063	0.067	0.072	0.065	0.061
Cl	0.000	0.000	0.000	0.000	0.000	0.000	0.000	0.000	0.000	0.000	0.000
Si	0.009	0.008	0.009	0.009	0.011	0.008	0.009	0.010	0.010	0.012	0.008
Pb	0.001	0.000	0.001	0.000	0.001	0.001	0.001	0.000	0.001	0.001	0.000
Fe	0.000	0.000	0.009	0.000	0.000	0.000	0.000	0.000	0.008	0.000	0.009
Sr	0.000	0.000	0.000	0.000	0.000	0.000	0.000	0.000	0.000	0.000	0.000
Total	1.982	1.982	1.985	1.985	2.006	1.981	1.995	1.984	1.984	1.981	1.991

Appendix 2.7: Continued

Unit	**A**										
Sample	15024	15026	15026	15026	15026	15026	15026	15026	15026	15026	15026
La_2O_3 (*wt. %*)	16.38	20.59	21.13	19.84	19.51	19.82	17.98	17.81	18.80	18.79	18.66
Ce_2O_3	32.28	31.71	30.22	31.56	31.15	31.01	30.40	30.68	31.54	31.30	31.50
Pr_2O_3	3.96	3.18	3.04	3.22	3.14	3.14	3.45	3.50	3.25	3.25	3.40
Nd_2O_3	13.36	9.16	8.88	9.10	8.98	9.11	10.60	10.44	9.37	9.26	11.01
Sm_2O_3	1.44	1.18	1.06	1.17	1.13	1.19	1.48	1.49	1.31	1.32	1.30
Eu_2O_3	0.28	0.00	0.00	0.00	0.23	0.00	0.22	0.20	0.26	0.00	0.00
Gd_2O_3	0.79	0.78	0.80	0.66	0.86	0.72	0.78	0.81	0.91	0.69	0.75
Dy_2O_3	0.00	0.00	0.00	0.00	0.00	0.00	0.22	0.00	0.00	0.22	0.00
Y_2O_3	0.34	0.41	0.68	0.40	0.46	0.41	0.49	0.36	0.62	0.50	0.40
Ho_2O_3		0.00	0.00	0.00	0.00	0.00	0.00	0.00	0.00	0.00	0.00
ThO_2	1.09	1.07	1.41	1.70	1.72	1.59	2.38	2.08	2.16	2.11	1.96
UO_2	0.00	0.00	0.00	0.00	0.00	0.00	0.00	0.00	0.00	0.00	0.00
CaO	0.33	0.32	0.28	0.59	0.57	0.87	0.50	0.70	0.73	0.36	0.68
P_2O_5	29.41	29.27	29.20	29.44	29.28	29.14	29.24	28.97	29.23	29.23	28.53
F	0.53	0.58	0.54	0.58	0.63	0.46	0.58	0.67	0.65	0.64	0.49
Cl	0.00	0.00	0.00	0.00	0.00	0.00	0.00	0.00	0.00	0.00	0.00
SiO_2	0.19	0.34	0.18	0.22	0.25	1.02	0.39	0.40	0.31	0.27	0.66
PbO	0.00	0.10	0.16	0.22	0.12	0.15	0.21	0.21	0.17	0.18	0.16
FeO	0.00	0.29	0.00	0.00	0.22	0.24	0.00	0.22	0.25	0.00	0.78
SrO		0.00	0.53	0.15	0.14	0.11	0.15	0.13	0.16	0.17	0.14
O=F	-0.22	-0.24	-0.23	-0.25	-0.26	-0.19	-0.24	-0.28	-0.27	-0.27	-0.21
Total	100.16	98.74	97.87	98.62	98.11	98.77	98.83	98.36	99.44	98.02	100.21
	O = 4										
La (*apfu*)	0.237	0.299	0.310	0.288	0.284	0.286	0.261	0.260	0.272	0.275	0.271
Ce	0.463	0.457	0.440	0.455	0.451	0.444	0.439	0.444	0.453	0.454	0.453
Pr	0.056	0.046	0.044	0.046	0.045	0.045	0.050	0.050	0.046	0.047	0.049
Nd	0.187	0.129	0.126	0.128	0.127	0.127	0.149	0.148	0.131	0.131	0.155
Sm	0.019	0.016	0.015	0.016	0.015	0.016	0.020	0.020	0.018	0.018	0.018
Eu	0.004	0.000	0.000	0.000	0.003	0.000	0.003	0.003	0.003	0.000	0.000
Gd	0.010	0.010	0.010	0.009	0.011	0.009	0.010	0.011	0.012	0.009	0.010
Dy	0.000	0.000	0.000	0.000	0.000	0.000	0.003	0.000	0.000	0.003	0.000
Y	0.007	0.009	0.014	0.008	0.010	0.008	0.010	0.008	0.013	0.011	0.008
Ho	0.000	0.000	0.000	0.000	0.000	0.000	0.000	0.000	0.000	0.000	0.000
Th	0.010	0.010	0.013	0.015	0.015	0.014	0.021	0.019	0.019	0.019	0.018
U	0.000	0.000	0.000	0.000	0.000	0.000	0.000	0.000	0.000	0.000	0.000
Ca	0.014	0.013	0.012	0.025	0.024	0.036	0.021	0.029	0.031	0.015	0.029
P	0.975	0.976	0.983	0.982	0.980	0.964	0.976	0.970	0.970	0.981	0.950
F	0.066	0.072	0.068	0.072	0.078	0.056	0.072	0.084	0.080	0.080	0.061
Cl	0.000	0.000	0.000	0.000	0.000	0.000	0.000	0.000	0.000	0.000	0.000
Si	0.008	0.013	0.007	0.009	0.010	0.040	0.015	0.016	0.012	0.011	0.026
Pb	0.000	0.001	0.002	0.002	0.001	0.002	0.002	0.002	0.002	0.002	0.002
Fe	0.000	0.010	0.000	0.000	0.007	0.008	0.000	0.007	0.008	0.000	0.026
Sr	0.000	0.000	0.000	0.000	0.000	0.000	0.000	0.000	0.000	0.000	0.000
Total	1.990	1.989	1.975	1.983	1.984	1.998	1.981	1.987	1.990	1.975	2.012

Appendix 2.7: Continued

Unit						**A**					
Sample	15026	15026	15026	15026	15026	15026	15026	15026	15026	15026	15026
La_2O_3 (*wt. %*)	18.07	16.80	15.45	15.73	15.97	16.40	17.03	16.08	16.03	19.29	19.37
Ce_2O_3	31.86	31.37	31.08	32.14	31.73	31.45	32.02	31.07	31.30	31.44	31.61
Pr_2O_3	3.35	3.51	3.71	3.66	3.65	3.73	3.64	3.78	3.87	3.51	3.33
Nd_2O_3	11.74	11.92	12.50	12.36	12.36	12.20	12.47	12.93	12.60	10.71	10.60
Sm_2O_3	1.42	1.34	1.47	1.41	1.31	1.48	1.43	1.42	1.48	1.14	1.17
Eu_2O_3	0.00	0.00	0.23	0.21	0.00	0.00	0.00	0.25	0.23	0.25	0.20
Gd_2O_3	0.97	0.86	0.95	0.84	0.80	0.81	0.78	1.04	0.85	0.79	0.72
Dy_2O_3	0.00	0.00	0.00	0.00	0.00	0.00	0.00	0.00	0.00	0.00	0.00
Y_2O_3	0.32	0.37	0.49	0.41	0.43	0.43	0.43	0.47	0.51	0.37	0.35
Ho_2O_3	0.00										
ThO_2	2.15	1.98	1.79	1.65	1.65	1.67	1.64	1.63	1.67	1.63	1.64
UO_2	0.00	0.00	0.00	0.00	0.00	0.00	0.00	0.00	0.00	0.00	0.00
CaO	0.46	0.74	0.83	0.26	0.81	0.43	0.40	0.57	0.67	0.52	0.36
P_2O_5	28.89	29.25	29.42	29.44	29.08	29.28	29.15	29.63	29.57	29.66	29.45
F	0.60	0.56	0.51	0.52	0.61	0.52	0.62	0.62	0.53	0.53	0.60
Cl	0.00	0.00	0.00	0.00	0.00	0.00	0.00	0.00	0.00	0.00	0.00
SiO_2	0.45	0.24	0.20	0.23	0.20	0.22	0.25	0.22	0.19	0.13	0.20
PbO	0.23	0.17	0.17	0.09	0.21	0.22	0.20	0.14	0.10	0.19	0.18
FeO	0.00	0.00	0.21	0.00	0.00	0.00	0.00	0.00	0.00	0.00	0.00
SrO	0.16										
O=F	-0.25	-0.23	-0.21	-0.22	-0.26	-0.22	-0.26	-0.26	-0.22	-0.22	-0.25
Total	100.41	98.87	98.79	98.73	98.55	98.63	99.79	99.60	99.37	99.94	99.53
						O = 4					
La (*apfu*)	0.262	0.244	0.224	0.229	0.233	0.239	0.247	0.232	0.232	0.278	0.280
Ce	0.458	0.453	0.448	0.464	0.460	0.456	0.461	0.444	0.449	0.450	0.454
Pr	0.048	0.050	0.053	0.053	0.053	0.054	0.052	0.054	0.055	0.050	0.048
Nd	0.165	0.168	0.176	0.174	0.175	0.172	0.175	0.180	0.176	0.150	0.149
Sm	0.019	0.018	0.020	0.019	0.018	0.020	0.019	0.019	0.020	0.015	0.016
Eu	0.000	0.000	0.003	0.003	0.000	0.000	0.000	0.003	0.003	0.003	0.003
Gd	0.013	0.011	0.012	0.011	0.010	0.011	0.010	0.013	0.011	0.010	0.009
Dy	0.000	0.000	0.000	0.000	0.000	0.000	0.000	0.000	0.000	0.000	0.000
Y	0.007	0.008	0.010	0.009	0.009	0.009	0.009	0.010	0.011	0.008	0.007
Ho	0.000	0.000	0.000	0.000	0.000	0.000	0.000	0.000	0.000	0.000	0.000
Th	0.019	0.018	0.016	0.015	0.015	0.015	0.015	0.015	0.015	0.014	0.015
U	0.000	0.000	0.000	0.000	0.000	0.000	0.000	0.000	0.000	0.000	0.000
Ca	0.019	0.031	0.035	0.011	0.034	0.018	0.017	0.024	0.028	0.022	0.015
P	0.961	0.977	0.981	0.984	0.975	0.981	0.971	0.980	0.981	0.981	0.978
F	0.075	0.069	0.063	0.065	0.077	0.065	0.077	0.076	0.066	0.066	0.075
Cl	0.000	0.000	0.000	0.000	0.000	0.000	0.000	0.000	0.000	0.000	0.000
Si	0.018	0.010	0.008	0.009	0.008	0.009	0.010	0.009	0.007	0.005	0.008
Pb	0.002	0.002	0.002	0.001	0.002	0.002	0.002	0.001	0.001	0.002	0.002
Fe	0.000	0.000	0.007	0.000	0.000	0.000	0.000	0.000	0.000	0.000	0.000
Sr	0.000	0.000	0.000	0.000	0.000	0.000	0.000	0.000	0.000	0.000	0.000
Total	1.990	1.991	1.995	1.982	1.992	1.986	1.988	1.985	1.990	1.988	1.984

Appendix 2.7: Continued

Unit	A									B	
Sample	15026	15026	15026	15026	15026	16007	16007	16007	16007	15123	15123
La_2O_3 (*wt.* %)	20.19	19.65	19.08	17.87	17.41	13.67	13.57	13.91	12.77	25.92	25.50
Ce_2O_3	31.69	31.94	32.26	32.61	31.42	31.87	31.68	32.18	32.27	33.26	32.83
Pr_2O_3	3.26	3.34	3.48	3.72	3.52	3.89	3.81	4.01	4.08	2.75	2.92
Nd_2O_3	10.72	10.73	10.88	11.83	11.46	13.91	13.86	13.62	13.59	7.61	7.32
Sm_2O_3	1.18	1.24	1.22	1.30	1.37	1.81	1.76	1.81	1.81	0.33	0.47
Eu_2O_3	0.23	0.19	0.00	0.26	0.22	0.33	0.40	0.29	0.29	0.00	0.00
Gd_2O_3	0.82	0.82	0.87	0.81	0.79	0.99	1.13	0.82	0.84	0.24	0.29
Dy_2O_3	0.00	0.00	0.00	0.00	0.00	0.36	0.00	0.00	0.31	0.00	0.00
Y_2O_3	0.37	0.47	0.45	0.34	0.24	0.60	0.75	0.34	0.51	0.34	0.32
Ho_2O_3						0.00	0.00	0.00	0.00		
ThO_2	1.72	1.71	1.52	1.68	1.83	3.40	3.21	3.38	3.54	0.27	0.20
UO_2	0.00	0.00	0.00	0.00	0.00	0.00	0.00	0.00	0.00	0.00	0.00
CaO	0.33	0.84	0.37	0.36	1.00	0.62	0.63	0.31	0.32	0.19	0.34
P_2O_5	29.21	29.29	29.42	29.32	29.15	28.45	28.02	27.95	28.60	29.65	30.54
F	0.58	0.59	0.61	0.59	0.60	0.58	0.59	0.61	0.70	0.50	0.50
Cl	0.00	0.00	0.00	0.00	0.00	0.02	0.00	0.00	0.00	0.00	0.00
SiO_2	0.26	0.24	0.00	0.31	0.15	0.81	0.64	0.43	0.66	0.00	0.00
PbO	0.09	0.14	0.10	0.13	0.11	0.32	0.26	0.24	0.29	0.00	0.00
FeO	0.00	0.00	0.00	0.00	0.30	0.00	0.00	0.00	0.20	0.00	0.00
SrO						0.21	0.27	0.55	0.20		
O=F	-0.24	-0.25	-0.26	-0.25	-0.25	-0.25	-0.25	-0.26	-0.30	-0.21	-0.21
Total	100.41	100.94	100.00	100.87	99.31	101.62	100.32	100.19	100.70	100.84	101.02
						O = 4					
La (*apfu*)	0.292	0.282	0.276	0.257	0.253	0.197	0.199	0.205	0.185	0.372	0.361
Ce	0.455	0.455	0.463	0.466	0.453	0.456	0.461	0.471	0.464	0.474	0.461
Pr	0.046	0.047	0.050	0.053	0.050	0.055	0.055	0.058	0.058	0.039	0.041
Nd	0.150	0.149	0.153	0.165	0.161	0.194	0.197	0.195	0.191	0.106	0.100
Sm	0.016	0.017	0.016	0.017	0.019	0.024	0.024	0.025	0.025	0.004	0.006
Eu	0.003	0.003	0.000	0.003	0.003	0.004	0.005	0.004	0.004	0.000	0.000
Gd	0.011	0.011	0.011	0.010	0.010	0.013	0.015	0.011	0.011	0.003	0.004
Dy	0.000	0.000	0.000	0.000	0.000	0.005	0.000	0.000	0.004	0.000	0.000
Y	0.008	0.010	0.009	0.007	0.005	0.012	0.016	0.007	0.011	0.007	0.007
Ho	0.000	0.000	0.000	0.000	0.000	0.000	0.000	0.000	0.000	0.000	0.000
Th	0.015	0.015	0.014	0.015	0.016	0.030	0.029	0.031	0.032	0.002	0.002
U	0.000	0.000	0.000	0.000	0.000	0.000	0.000	0.000	0.000	0.000	0.000
Ca	0.014	0.035	0.015	0.015	0.042	0.026	0.027	0.013	0.014	0.008	0.014
P	0.969	0.965	0.978	0.968	0.971	0.942	0.942	0.946	0.951	0.977	0.992
F	0.072	0.072	0.076	0.073	0.075	0.072	0.074	0.077	0.087	0.061	0.060
Cl	0.000	0.000	0.000	0.000	0.000	0.002	0.000	0.000	0.000	0.000	0.000
Si	0.010	0.009	0.000	0.012	0.006	0.032	0.025	0.017	0.026	0.000	0.000
Pb	0.001	0.001	0.001	0.001	0.001	0.003	0.003	0.003	0.003	0.000	0.000
Fe	0.000	0.000	0.000	0.000	0.010	0.000	0.000	0.000	0.007	0.000	0.000
Sr	0.000	0.000	0.000	0.000	0.000	0.000	0.000	0.000	0.000	0.000	0.000
Total	1.989	1.999	1.987	1.990	2.001	1.996	1.998	1.987	1.985	1.993	1.986

Appendix 2.7: Continued

Unit						**B**					
Sample	15123	15123	15123	15123	15123	15123	15123	15123	15123	15123	15123
La_2O_3 (*wt. %*)	25.96	25.75	25.30	25.15	25.12	23.59	23.56	25.01	25.36	24.64	24.02
Ce_2O_3	33.36	32.78	33.70	32.90	33.77	32.46	34.02	33.40	33.60	33.89	34.21
Pr_2O_3	2.95	2.88	2.86	2.89	2.84	2.76	2.84	2.80	2.70	2.73	2.95
Nd_2O_3	7.41	7.19	7.18	7.34	7.12	7.53	7.75	7.33	7.27	7.31	7.60
Sm_2O_3	0.37	0.37	0.33	0.45	0.36	0.43	0.51	0.41	0.33	0.34	0.42
Eu_2O_3	0.00	0.00	0.00	0.00	0.00	0.00	0.00	0.00	0.00	0.00	0.00
Gd_2O_3	0.31	0.26	0.40	0.25	0.22	0.32	0.29	0.25	0.31	0.37	0.45
Dy_2O_3	0.00	0.00	0.00	0.00	0.00	0.00	0.00	0.00	0.00	0.00	0.00
Y_2O_3	0.28	0.36	0.30	0.24	0.19	0.32	0.41	0.25	0.23	0.26	0.36
Ho_2O_3											
ThO_2	0.21	0.32	0.27	0.31	0.28	0.31	0.39	0.21	0.25	0.30	0.19
UO_2	0.00	0.00	0.00	0.00	0.00	0.00	0.00	0.00	0.00	0.00	0.00
CaO	0.62	0.34	0.57	0.76	0.43	1.17	0.21	0.11	0.95	0.77	0.88
P_2O_5	29.53	29.55	29.51	29.52	29.80	28.83	30.06	29.78	29.78	29.60	29.94
F	0.46	0.56	0.00	0.49	0.64	0.57	0.53	0.53	0.48	0.59	0.00
Cl	0.00	0.00	0.00	0.00	0.00	0.00	0.00	0.00	0.00	0.00	0.00
SiO_2	0.00	0.00	0.00	0.00	0.00	0.00	0.00	0.00	0.00	0.00	0.00
PbO	0.09	0.00	0.00	0.00	0.00	0.00	0.00	0.00	0.00	0.00	0.00
FeO	0.00	0.00	0.00	0.00	0.00	0.00	0.00	0.00	0.00	0.00	0.00
SrO											
O=F	-0.19	-0.23	0.00	-0.21	-0.27	-0.24	-0.22	-0.22	-0.20	-0.25	0.00
Total	101.35	100.10	100.42	100.10	100.49	98.04	100.36	99.86	101.05	100.54	101.01
						O = 4					
La (*apfu*)	0.372	0.371	0.367	0.362	0.360	0.346	0.337	0.360	0.362	0.353	0.344
Ce	0.474	0.469	0.485	0.471	0.480	0.473	0.483	0.478	0.476	0.482	0.487
Pr	0.042	0.041	0.041	0.041	0.040	0.040	0.040	0.040	0.038	0.039	0.042
Nd	0.103	0.100	0.101	0.102	0.099	0.107	0.107	0.102	0.100	0.101	0.106
Sm	0.005	0.005	0.004	0.006	0.005	0.006	0.007	0.005	0.004	0.005	0.006
Eu	0.000	0.000	0.000	0.000	0.000	0.000	0.000	0.000	0.000	0.000	0.000
Gd	0.004	0.003	0.005	0.003	0.003	0.004	0.004	0.003	0.004	0.005	0.006
Dy	0.000	0.000	0.000	0.000	0.000	0.000	0.000	0.000	0.000	0.000	0.000
Y	0.006	0.007	0.006	0.005	0.004	0.007	0.009	0.005	0.005	0.005	0.007
Ho	0.000	0.000	0.000	0.000	0.000	0.000	0.000	0.000	0.000	0.000	0.000
Th	0.002	0.003	0.002	0.003	0.002	0.003	0.003	0.002	0.002	0.003	0.002
U	0.000	0.000	0.000	0.000	0.000	0.000	0.000	0.000	0.000	0.000	0.000
Ca	0.026	0.014	0.024	0.032	0.018	0.050	0.009	0.005	0.039	0.032	0.037
P	0.971	0.978	0.983	0.976	0.979	0.971	0.987	0.985	0.975	0.974	0.986
F	0.056	0.069	0.000	0.061	0.078	0.072	0.065	0.065	0.058	0.073	0.000
Cl	0.000	0.000	0.000	0.000	0.000	0.000	0.000	0.000	0.000	0.000	0.000
Si	0.000	0.000	0.000	0.000	0.000	0.000	0.000	0.000	0.000	0.000	0.000
Pb	0.001	0.000	0.000	0.000	0.000	0.000	0.000	0.000	0.000	0.000	0.000
Fe	0.000	0.000	0.000	0.000	0.000	0.000	0.000	0.000	0.000	0.000	0.000
Sr	0.000	0.000	0.000	0.000	0.000	0.000	0.000	0.000	0.000	0.000	0.000
Total	2.006	1.992	2.019	2.002	1.989	2.007	1.986	1.986	2.006	1.999	2.021

Appendix 2.7: Continued

Unit						**B**					
Sample	15123	15123	15123	15123	15123	15123	15123	15123	15123	15123	15123
La_2O_3 (*wt. %*)	23.90	25.88	24.75	24.29	25.52	24.74	24.15	24.92	24.32	23.72	23.98
Ce_2O_3	32.64	32.64	33.57	34.14	33.85	33.14	33.84	34.48	32.76	33.42	33.62
Pr_2O_3	2.86	2.61	2.82	2.83	2.75	2.89	2.87	2.80	2.92	2.92	2.81
Nd_2O_3	7.38	6.96	7.47	7.31	7.52	7.39	7.88	7.66	7.74	7.81	7.80
Sm_2O_3	0.48	0.36	0.45	0.35	0.36	0.31	0.43	0.32	0.34	0.37	0.44
Eu_2O_3	0.00	0.00	0.00	0.00	0.00	0.00	0.00	0.00	0.00	0.00	0.00
Gd_2O_3	0.38	0.31	0.37	0.37	0.19	0.32	0.25	0.27	0.25	0.33	0.20
Dy_2O_3	0.00	0.00	0.00	0.00	0.00	0.00	0.00	0.00	0.00	0.00	0.00
Y_2O_3	0.28	0.30	0.33	0.31	0.17	0.26	0.30	0.19	0.20	0.23	0.35
Ho_2O_3											
ThO_2	0.34	0.22	0.32	0.36	0.20	0.25	0.26	0.25	0.26	0.28	0.32
UO_2	0.00	0.00	0.00	0.00	0.00	0.00	0.00	0.00	0.00	0.00	0.00
CaO	0.72	0.64	0.43	0.50	0.42	0.42	0.23	0.54	0.74	0.29	0.54
P_2O_5	30.01	29.73	29.53	29.50	29.72	29.54	29.83	29.74	30.04	29.74	29.51
F	0.52	0.52	0.58	0.57	0.54	0.46	0.49	0.00	0.52	0.61	0.52
Cl	0.00	0.00	0.00	0.00	0.00	0.00	0.00	0.00	0.00	0.00	0.03
SiO_2	0.00	0.00	0.00	0.00	0.00	0.00	0.00	0.00	0.00	0.00	0.00
PbO	0.00	0.00	0.00	0.00	0.09	0.00	0.09	0.17	0.00	0.00	0.00
FeO	0.00	0.00	0.00	0.00	0.00	0.00	0.00	0.00	0.24	0.00	0.00
SrO											
O=F	-0.22	-0.22	-0.24	-0.24	-0.23	-0.19	-0.21	0.00	-0.22	-0.26	-0.22
Total	99.27	99.97	100.36	100.28	101.10	99.51	100.40	101.34	100.10	99.45	99.88
						O = 4					
La (*apfu*)	0.343	0.372	0.356	0.350	0.365	0.358	0.347	0.359	0.347	0.342	0.346
Ce	0.465	0.466	0.480	0.488	0.481	0.476	0.482	0.493	0.465	0.478	0.482
Pr	0.041	0.037	0.040	0.040	0.039	0.041	0.041	0.040	0.041	0.042	0.040
Nd	0.103	0.097	0.104	0.102	0.104	0.104	0.110	0.107	0.107	0.109	0.109
Sm	0.006	0.005	0.006	0.005	0.005	0.004	0.006	0.004	0.005	0.005	0.006
Eu	0.000	0.000	0.000	0.000	0.000	0.000	0.000	0.000	0.000	0.000	0.000
Gd	0.005	0.004	0.005	0.005	0.002	0.004	0.003	0.004	0.003	0.004	0.003
Dy	0.000	0.000	0.000	0.000	0.000	0.000	0.000	0.000	0.000	0.000	0.000
Y	0.006	0.006	0.007	0.006	0.003	0.005	0.006	0.004	0.004	0.005	0.007
Ho	0.000	0.000	0.000	0.000	0.000	0.000	0.000	0.000	0.000	0.000	0.000
Th	0.003	0.002	0.003	0.003	0.002	0.002	0.002	0.002	0.002	0.002	0.003
U	0.000	0.000	0.000	0.000	0.000	0.000	0.000	0.000	0.000	0.000	0.000
Ca	0.030	0.027	0.018	0.021	0.017	0.018	0.009	0.022	0.031	0.012	0.023
P	0.989	0.981	0.976	0.975	0.976	0.982	0.983	0.983	0.985	0.985	0.978
F	0.064	0.064	0.071	0.071	0.066	0.058	0.060	0.000	0.063	0.075	0.064
Cl	0.000	0.000	0.000	0.000	0.000	0.000	0.000	0.000	0.000	0.000	0.002
Si	0.000	0.000	0.000	0.000	0.000	0.000	0.000	0.000	0.000	0.000	0.000
Pb	0.000	0.000	0.000	0.000	0.001	0.000	0.001	0.002	0.000	0.000	0.000
Fe	0.000	0.000	0.000	0.000	0.000	0.000	0.000	0.000	0.008	0.000	0.000
Sr	0.000	0.000	0.000	0.000	0.000	0.000	0.000	0.000	0.000	0.000	0.000
Total	1.991	1.996	1.994	1.995	1.996	1.995	1.990	2.019	1.998	1.985	1.996

Appendix 2.7: Continued

Unit	**B**										
Sample	15125	15125	15125	15125	15125	15125	15125	15125	15125	15125	15125
La_2O_3 (*wt.* %)	11.12	11.56	12.46	24.71	25.61	24.36	25.06	25.72	24.26	24.99	25.07
Ce_2O_3	34.34	34.82	35.12	34.60	32.51	35.38	34.70	34.59	34.65	34.88	34.01
Pr_2O_3	4.71	4.80	4.46	2.75	2.85	2.84	2.83	2.76	2.83	2.91	2.70
Nd_2O_3	14.80	14.49	13.12	6.46	6.46	6.34	6.40	6.43	6.41	6.38	6.26
Sm_2O_3	1.54	1.41	1.28	0.33	0.54	0.55	0.38	0.38	0.53	0.46	0.41
Eu_2O_3	0.24	0.19	0.00	0.00	0.00	0.00	0.00	0.00	0.00	0.00	0.00
Gd_2O_3	0.64	0.54	0.87	0.46	0.29	0.36	0.27	0.43	0.34	0.32	0.35
Dy_2O_3	0.00	0.00	0.00	0.00	0.00	0.00	0.00	0.00	0.00	0.00	0.00
Y_2O_3	0.43	0.41	0.46	0.26	0.24	0.33	0.24	0.27	0.28	0.30	0.30
Ho_2O_3	0.00	0.00	0.00	0.00	0.00	0.00	0.00	0.00	0.00	0.00	0.00
ThO_2	0.71	0.64	0.52	0.25	0.21	0.22	0.31	0.27	0.19	0.30	0.25
UO_2	0.00	0.00	0.00	0.00	0.00	0.00	0.00	0.00	0.00	0.00	0.00
CaO	0.26	0.37	0.99	0.11	0.22	0.37	0.20	0.22	0.60	0.29	0.18
P_2O_5	29.46	29.82	28.91	29.95	29.77	29.93	29.74	30.00	30.02	29.78	29.80
F	0.47	0.62	0.60	0.55	0.57	0.50	0.57	0.55	0.51	0.68	0.56
Cl	0.00	0.00	0.00	0.00	0.00	0.00	0.00	0.00	0.00	0.00	0.00
SiO_2	0.41	0.38	0.33	0.21	0.21	0.26	0.25	0.25	0.26	0.18	0.41
PbO	0.15	0.00	0.00	0.08	0.00	0.00	0.09	0.00	0.00	0.00	0.00
FeO	0.00	0.00	0.27	0.00	0.00	0.21	0.34	0.00	0.00	0.00	0.00
SrO	0.12	0.08	0.17	0.00	0.00	0.00	0.00	0.00	0.00	0.00	0.00
O=F	-0.20	-0.26	-0.25	-0.23	-0.24	-0.21	-0.24	-0.23	-0.22	-0.29	-0.23
Total	99.21	99.88	99.29	100.48	99.24	101.43	101.13	101.62	100.67	101.18	100.07
	O = 4										
La (*apfu*)	0.161	0.165	0.181	0.353	0.369	0.345	0.357	0.364	0.345	0.356	0.358
Ce	0.494	0.495	0.506	0.490	0.465	0.498	0.491	0.486	0.489	0.492	0.482
Pr	0.067	0.068	0.064	0.039	0.041	0.040	0.040	0.039	0.040	0.041	0.038
Nd	0.208	0.201	0.184	0.089	0.090	0.087	0.088	0.088	0.088	0.088	0.087
Sm	0.021	0.019	0.017	0.004	0.007	0.007	0.005	0.005	0.007	0.006	0.005
Eu	0.003	0.003	0.000	0.000	0.000	0.000	0.000	0.000	0.000	0.000	0.000
Gd	0.008	0.007	0.011	0.006	0.004	0.005	0.004	0.005	0.004	0.004	0.004
Dy	0.000	0.000	0.000	0.000	0.000	0.000	0.000	0.000	0.000	0.000	0.000
Y	0.009	0.008	0.010	0.005	0.005	0.007	0.005	0.006	0.006	0.006	0.006
Ho	0.000	0.000	0.000	0.000	0.000	0.000	0.000	0.000	0.000	0.000	0.000
Th	0.006	0.006	0.005	0.002	0.002	0.002	0.003	0.002	0.002	0.003	0.002
U	0.000	0.000	0.000	0.000	0.000	0.000	0.000	0.000	0.000	0.000	0.000
Ca	0.011	0.016	0.042	0.004	0.009	0.015	0.008	0.009	0.025	0.012	0.008
P	0.980	0.980	0.963	0.982	0.984	0.974	0.973	0.975	0.979	0.972	0.978
F	0.059	0.076	0.075	0.067	0.071	0.061	0.070	0.066	0.062	0.083	0.068
Cl	0.000	0.000	0.000	0.000	0.000	0.000	0.000	0.000	0.000	0.000	0.000
Si	0.016	0.015	0.013	0.008	0.008	0.010	0.010	0.009	0.010	0.007	0.016
Pb	0.002	0.000	0.000	0.001	0.000	0.000	0.001	0.000	0.000	0.000	0.000
Fe	0.000	0.000	0.009	0.000	0.000	0.007	0.011	0.000	0.000	0.000	0.000
Sr	0.000	0.000	0.000	0.000	0.000	0.000	0.000	0.000	0.000	0.000	0.000
Total	1.986	1.981	2.004	1.985	1.983	1.997	1.994	1.990	1.994	1.987	1.985

Appendix 2.7: Continued

Unit	**B**										
Sample	15125	15125	15125	15125	15125	15125	15125	15125	15125	15125	15125
La_2O_3 (*wt. %*)	23.88	24.76	24.97	23.09	23.94	23.41	22.91	22.49	24.42	25.41	24.40
Ce_2O_3	33.36	34.38	34.22	33.32	33.92	32.54	32.83	33.94	32.99	33.45	33.07
Pr_2O_3	2.67	2.88	2.83	2.90	2.92	2.77	2.83	2.80	2.92	2.85	3.01
Nd_2O_3	6.43	6.48	6.39	6.76	7.01	7.37	7.11	6.84	6.82	6.74	6.28
Sm_2O_3	0.44	0.32	0.51	0.79	0.60	0.66	0.60	0.53	0.59	0.52	0.53
Eu_2O_3	0.00	0.00	0.00	0.00	0.00	0.00	0.00	0.00	0.00	0.00	0.00
Gd_2O_3	0.38	0.64	0.37	0.39	0.24	0.37	0.61	0.53	0.42	0.38	0.25
Dy_2O_3	0.00	0.00	0.00	0.00	0.00	0.00	0.00	0.00	0.00	0.00	0.00
Y_2O_3	0.30	0.29	0.28	0.19	0.30	0.24	0.30	0.24	0.18	0.30	0.34
Ho_2O_3	0.00	0.00	0.00	0.00	0.00	0.00	0.00	0.00	0.00	0.00	0.00
ThO_2	0.30	0.27	0.26	0.37	0.31	0.37	0.37	0.31	0.43	0.34	0.22
UO_2	0.00	0.00	0.00	0.00	0.00	0.00	0.00	0.00	0.00	0.00	0.00
CaO	0.13	0.19	0.15	0.28	0.18	0.23	0.75	1.03	0.12	0.31	0.67
P_2O_5	29.91	29.90	29.74	29.46	29.44	29.34	29.72	29.28	29.69	29.93	29.45
F	0.61	0.56	0.52	0.00	0.50	0.59	0.51	0.63	0.48	0.50	0.63
Cl	0.00	0.00	0.00	0.00	0.00	0.00	0.00	0.00	0.00	0.00	0.00
SiO_2	0.30	0.19	0.19	0.20	0.18	0.21	0.24	0.24	0.20	0.18	0.20
PbO	0.09	0.00	0.00	0.00	0.00	0.13	0.00	0.00	0.00	0.00	0.00
FeO	0.00	0.00	0.00	0.00	0.00	0.00	0.00	0.23	0.40	0.00	0.35
SrO	0.00	0.00	0.00	0.00	0.00	0.00	0.09	0.00	0.00	0.00	0.00
O=F	-0.26	-0.24	-0.22	0.00	-0.21	-0.25	-0.21	-0.27	-0.20	-0.21	-0.27
Total	98.54	100.62	100.21	97.75	99.33	97.98	98.66	98.83	99.47	100.70	99.14
	O = 4										
La (*apfu*)	0.344	0.354	0.358	0.340	0.347	0.342	0.331	0.325	0.352	0.363	0.352
Ce	0.477	0.487	0.488	0.487	0.488	0.472	0.470	0.487	0.472	0.474	0.473
Pr	0.038	0.041	0.040	0.042	0.042	0.040	0.040	0.040	0.042	0.040	0.043
Nd	0.090	0.090	0.089	0.096	0.098	0.104	0.099	0.096	0.095	0.093	0.088
Sm	0.006	0.004	0.007	0.011	0.008	0.009	0.008	0.007	0.008	0.007	0.007
Eu	0.000	0.000	0.000	0.000	0.000	0.000	0.000	0.000	0.000	0.000	0.000
Gd	0.005	0.008	0.005	0.005	0.003	0.005	0.008	0.007	0.005	0.005	0.003
Dy	0.000	0.000	0.000	0.000	0.000	0.000	0.000	0.000	0.000	0.000	0.000
Y	0.006	0.006	0.006	0.004	0.006	0.005	0.006	0.005	0.004	0.006	0.007
Ho	0.000	0.000	0.000	0.000	0.000	0.000	0.000	0.000	0.000	0.000	0.000
Th	0.003	0.002	0.002	0.003	0.003	0.003	0.003	0.003	0.004	0.003	0.002
U	0.000	0.000	0.000	0.000	0.000	0.000	0.000	0.000	0.000	0.000	0.000
Ca	0.005	0.008	0.006	0.012	0.007	0.010	0.031	0.043	0.005	0.013	0.028
P	0.989	0.980	0.980	0.995	0.979	0.983	0.984	0.972	0.983	0.980	0.974
F	0.075	0.069	0.064	0.000	0.062	0.073	0.062	0.079	0.060	0.061	0.078
Cl	0.000	0.000	0.000	0.000	0.000	0.000	0.000	0.000	0.000	0.000	0.000
Si	0.012	0.007	0.007	0.008	0.007	0.008	0.009	0.009	0.008	0.007	0.008
Pb	0.001	0.000	0.000	0.000	0.000	0.001	0.000	0.000	0.000	0.000	0.000
Fe	0.000	0.000	0.000	0.000	0.000	0.000	0.000	0.008	0.013	0.000	0.012
Sr	0.000	0.000	0.000	0.000	0.000	0.000	0.000	0.000	0.000	0.000	0.000
Total	1.976	1.986	1.988	2.003	1.989	1.983	1.991	2.001	1.991	1.990	1.997

Appendix 2.7: Continued

Unit						**B**					
Sample	15125	15125	15125	15125	15125	15125	15125	15125	15125	15125	15125
La_2O_3 (*wt.* %)	24.94	23.03	22.77	21.65	22.89	22.30	22.54	22.32	22.77	22.83	25.44
Ce_2O_3	33.86	33.92	34.03	34.63	33.27	33.23	34.56	34.40	34.19	34.90	33.16
Pr_2O_3	2.94	2.95	3.00	3.03	2.86	2.92	3.12	3.02	2.95	3.08	2.71
Nd_2O_3	6.64	7.43	7.61	7.97	7.93	7.98	7.95	8.01	7.78	8.03	6.55
Sm_2O_3	0.62	0.60	0.65	0.73	0.74	0.73	0.73	0.76	0.72	0.76	0.59
Eu_2O_3	0.00	0.00	0.00	0.00	0.00	0.00	0.00	0.00	0.00	0.00	0.00
Gd_2O_3	0.42	0.40	0.28	0.49	0.39	0.64	0.51	0.48	0.51	0.61	0.49
Dy_2O_3	0.00	0.00	0.00	0.00	0.00	0.00	0.00	0.00	0.00	0.00	0.00
Y_2O_3	0.30	0.29	0.33	0.31	0.16	0.25	0.25	0.24	0.24	0.23	0.29
Ho_2O_3	0.00	0.00	0.00	0.00	0.00	0.00	0.00	0.00	0.00	0.00	0.00
ThO_2	0.32	0.50	0.44	0.33	0.40	0.42	0.40	0.31	0.30	0.31	0.25
UO_2	0.00	0.00	0.00	0.00	0.00	0.00	0.00	0.00	0.00	0.00	0.00
CaO	0.41	0.69	0.59	0.20	0.32	0.12	0.20	0.17	0.28	0.22	0.11
P_2O_5	29.64	29.74	29.47	29.74	29.74	29.68	29.75	29.89	30.06	29.96	29.98
F	0.56	0.51	0.53	0.52	0.46	0.50	0.52	0.65	0.59	0.58	0.75
Cl	0.00	0.00	0.00	0.00	0.00	0.00	0.00	0.00	0.00	0.00	0.00
SiO_2	0.21	0.23	0.20	0.25	0.19	0.25	0.30	0.17	0.27	0.24	0.20
PbO	0.09	0.00	0.00	0.00	0.00	0.00	0.08	0.00	0.00	0.00	0.00
FeO	0.00	0.00	0.00	0.00	0.00	0.00	0.00	0.00	0.00	0.00	0.00
SrO	0.08	0.09	0.00	0.08	0.00	0.15	0.00	0.00	0.00	0.09	0.00
O=F	-0.23	-0.21	-0.22	-0.22	-0.20	-0.21	-0.22	-0.27	-0.25	-0.24	-0.32
Total	100.80	100.16	99.66	99.70	99.15	98.95	100.69	100.14	100.41	101.59	100.20
						O = 4					
La (*apfu*)	0.357	0.330	0.328	0.311	0.331	0.323	0.322	0.319	0.324	0.324	0.363
Ce	0.481	0.482	0.487	0.494	0.477	0.477	0.491	0.489	0.483	0.491	0.469
Pr	0.041	0.042	0.043	0.043	0.041	0.042	0.044	0.043	0.042	0.043	0.038
Nd	0.092	0.103	0.106	0.111	0.111	0.112	0.110	0.111	0.107	0.110	0.090
Sm	0.008	0.008	0.009	0.010	0.010	0.010	0.010	0.010	0.010	0.010	0.008
Eu	0.000	0.000	0.000	0.000	0.000	0.000	0.000	0.000	0.000	0.000	0.000
Gd	0.005	0.005	0.004	0.006	0.005	0.008	0.006	0.006	0.006	0.008	0.006
Dy	0.000	0.000	0.000	0.000	0.000	0.000	0.000	0.000	0.000	0.000	0.000
Y	0.006	0.006	0.007	0.006	0.003	0.005	0.005	0.005	0.005	0.005	0.006
Ho	0.000	0.000	0.000	0.000	0.000	0.000	0.000	0.000	0.000	0.000	0.000
Th	0.003	0.004	0.004	0.003	0.004	0.004	0.004	0.003	0.003	0.003	0.002
U	0.000	0.000	0.000	0.000	0.000	0.000	0.000	0.000	0.000	0.000	0.000
Ca	0.017	0.029	0.025	0.008	0.013	0.005	0.008	0.007	0.011	0.009	0.005
P	0.973	0.977	0.976	0.982	0.986	0.986	0.976	0.982	0.982	0.975	0.981
F	0.068	0.063	0.065	0.064	0.057	0.062	0.064	0.080	0.072	0.070	0.092
Cl	0.000	0.000	0.000	0.000	0.000	0.000	0.000	0.000	0.000	0.000	0.000
Si	0.008	0.009	0.008	0.010	0.007	0.010	0.012	0.006	0.011	0.009	0.008
Pb	0.001	0.000	0.000	0.000	0.000	0.000	0.001	0.000	0.000	0.000	0.000
Fe	0.000	0.000	0.000	0.000	0.000	0.000	0.000	0.000	0.000	0.000	0.000
Sr	0.000	0.000	0.000	0.000	0.000	0.000	0.000	0.000	0.000	0.000	0.000
Total	1.993	1.995	1.995	1.985	1.988	1.981	1.989	1.981	1.984	1.987	1.976

Appendix 2.7: Continued

Unit	**B**										
Sample	15125	15125	15125	15125	15125	15127	15127	15127	15127	15127	15127
La_2O_3 (*wt. %*)	23.32	25.02	25.30	24.16	25.43	14.04	14.55	14.56	14.68	15.00	15.49
Ce_2O_3	33.81	34.61	34.80	34.76	34.06	34.15	33.62	33.32	33.61	34.09	34.14
Pr_2O_3	3.12	2.79	2.69	2.91	2.75	4.38	4.25	4.01	3.98	4.14	4.10
Nd_2O_3	8.01	6.42	6.25	6.42	6.48	15.06	13.89	12.26	13.34	12.32	12.20
Sm_2O_3	0.59	0.46	0.42	0.44	0.39	1.52	1.11	1.31	1.04	1.17	1.16
Eu_2O_3	0.00	0.00	0.00	0.00	0.00	0.19	0.20	0.24	0.00	0.00	0.00
Gd_2O_3	0.47	0.26	0.40	0.47	0.33	0.77	0.54	0.75	0.55	0.48	0.43
Dy_2O_3	0.00	0.00	0.00	0.22	0.00	0.23	0.00	0.00	0.00	0.00	0.00
Y_2O_3	0.21	0.24	0.29	0.28	0.24	0.44	0.35	0.58	0.33	0.36	0.42
Ho_2O_3	0.00	0.00	0.00	0.00	0.00	0.00		0.00		0.00	0.00
ThO_2	0.41	0.21	0.29	0.20	0.23	0.43	0.49	0.47	0.32	0.51	0.39
UO_2	0.00	0.00	0.00	0.00	0.00	0.00	0.00	0.00	0.00	0.00	0.00
CaO	0.21	0.65	0.50	0.83	0.28	0.60	0.86	0.68	0.84	0.50	0.49
P_2O_5	30.11	29.34	29.21	29.48	30.09	28.74	29.35	29.47	29.18	29.92	29.53
F	0.56	0.55	0.51	0.00	0.56	0.46	0.53	0.57	0.59	0.61	0.50
Cl	0.00	0.00	0.00	0.00	0.00	0.00	0.00	0.00	0.00	0.00	0.00
SiO_2	0.23	0.19	0.26	0.24	0.24	0.20	0.13	0.15	0.00	0.00	0.00
PbO	0.00	0.00	0.00	0.00	0.00	0.11	0.08	0.00	0.09	0.13	0.00
FeO	0.00	0.00	0.21	0.27	0.00	0.19	0.22	0.32	0.21	0.00	0.00
SrO	0.00	0.10	0.00	0.00	0.00	0.17		0.12		0.11	0.00
O=F	-0.24	-0.23	-0.22	0.00	-0.23	-0.19	-0.22	-0.24	-0.25	-0.26	-0.21
Total	100.81	100.61	100.89	100.68	100.81	101.49	99.95	98.58	98.52	99.07	98.63
	O = 4										
La (*apfu*)	0.331	0.359	0.364	0.348	0.361	0.203	0.210	0.211	0.214	0.216	0.225
Ce	0.477	0.493	0.496	0.497	0.480	0.491	0.482	0.479	0.487	0.488	0.493
Pr	0.044	0.040	0.038	0.041	0.039	0.063	0.061	0.057	0.057	0.059	0.059
Nd	0.110	0.089	0.087	0.090	0.089	0.211	0.194	0.172	0.189	0.172	0.172
Sm	0.008	0.006	0.006	0.006	0.005	0.021	0.015	0.018	0.014	0.016	0.016
Eu	0.000	0.000	0.000	0.000	0.000	0.003	0.003	0.003	0.000	0.000	0.000
Gd	0.006	0.003	0.005	0.006	0.004	0.010	0.007	0.010	0.007	0.006	0.006
Dy	0.000	0.000	0.000	0.003	0.000	0.003	0.000	0.000	0.000	0.000	0.000
Y	0.004	0.005	0.006	0.006	0.005	0.009	0.007	0.012	0.007	0.007	0.009
Ho	0.000	0.000	0.000	0.000	0.000	0.000	0.000	0.000	0.000	0.000	0.000
Th	0.004	0.002	0.003	0.002	0.002	0.004	0.004	0.004	0.003	0.005	0.004
U	0.000	0.000	0.000	0.000	0.000	0.000	0.000	0.000	0.000	0.000	0.000
Ca	0.009	0.027	0.021	0.035	0.011	0.025	0.036	0.029	0.036	0.021	0.021
P	0.982	0.967	0.963	0.975	0.981	0.955	0.973	0.981	0.978	0.990	0.987
F	0.068	0.068	0.063	0.000	0.068	0.057	0.065	0.071	0.073	0.075	0.062
Cl	0.000	0.000	0.000	0.000	0.000	0.000	0.000	0.000	0.000	0.000	0.000
Si	0.009	0.007	0.010	0.009	0.009	0.008	0.005	0.006	0.000	0.000	0.000
Pb	0.000	0.000	0.000	0.000	0.000	0.001	0.001	0.000	0.001	0.001	0.000
Fe	0.000	0.000	0.007	0.009	0.000	0.006	0.007	0.010	0.007	0.000	0.000
Sr	0.000	0.000	0.000	0.000	0.000	0.000	0.000	0.000	0.000	0.000	0.000
Total	1.984	2.000	2.005	2.027	1.987	2.012	2.005	1.993	2.000	1.982	1.991

Appendix 2.7: Continued

Unit						**B**					
Sample	15127	15127	15127	15127	15127	15127	15127	15127	15127	15127	15127
La_2O_3 (*wt. %*)	15.62	15.67	15.93	15.94	15.95	15.99	16.01	16.02	16.07	16.09	16.17
Ce_2O_3	33.61	33.57	33.21	33.63	34.47	34.25	33.56	32.39	33.87	32.59	34.27
Pr_2O_3	3.99	3.97	4.04	4.12	4.12	3.99	4.09	3.79	3.97	3.99	4.06
Nd_2O_3	13.67	12.22	13.85	13.50	13.68	13.40	12.21	13.32	11.69	13.38	11.75
Sm_2O_3	1.05	1.10	1.25	1.07	1.03	1.07	1.14	1.09	1.14	1.10	1.03
Eu_2O_3	0.00	0.00	0.23	0.00	0.00	0.00	0.19	0.00	0.00	0.00	0.00
Gd_2O_3	0.65	0.51	0.57	0.37	0.47	0.56	0.54	0.54	0.51	0.53	0.54
Dy_2O_3	0.00	0.00	0.00	0.00	0.00	0.00	0.00	0.00	0.00	0.00	0.00
Y_2O_3	0.45	0.37	0.48	0.24	0.24	0.41	0.31	0.38	0.38	0.50	0.44
Ho_2O_3		0.00					0.00		0.00		0.00
ThO_2	0.31	0.42	0.38	0.21	0.37	0.41	0.50	0.39	0.41	0.36	0.38
UO_2	0.00	0.00	0.00	0.00	0.00	0.00	0.00	0.00	0.00	0.00	0.00
CaO	0.19	0.76	0.80	0.25	0.48	0.13	0.56	0.41	0.37	0.34	0.36
P_2O_5	29.34	29.77	29.56	29.36	29.53	29.93	29.61	29.50	29.60	29.70	29.62
F	0.62	0.00	0.53	0.51	0.49	0.48	0.49	0.56	0.52	0.00	0.51
Cl	0.00	0.00	0.00	0.00	0.00	0.00	0.00	0.05	0.00	0.02	0.00
SiO_2	0.15	0.18	0.00	0.00	0.00	0.14	0.00	0.18	0.14	0.00	0.00
PbO	0.00	0.10	0.00	0.00	0.00	0.00	0.14	0.00	0.00	0.00	0.00
FeO	0.00	0.00	0.00	0.00	0.19	0.00	0.33	0.00	0.00	0.00	0.00
SrO		0.00					0.00		0.00		0.00
O=F	-0.26	0.00	-0.22	-0.21	-0.21	-0.20	-0.21	-0.23	-0.22	0.00	-0.21
Total	99.37	98.64	100.60	99.00	100.82	100.54	99.46	98.37	98.44	98.59	98.90
						O = 4					
La (*apfu*)	0.227	0.228	0.229	0.233	0.229	0.229	0.232	0.233	0.233	0.236	0.235
Ce	0.484	0.485	0.474	0.487	0.492	0.487	0.482	0.467	0.489	0.473	0.494
Pr	0.057	0.057	0.057	0.059	0.059	0.056	0.058	0.054	0.057	0.058	0.058
Nd	0.192	0.172	0.193	0.191	0.191	0.186	0.171	0.187	0.164	0.190	0.165
Sm	0.014	0.015	0.017	0.015	0.014	0.014	0.015	0.015	0.015	0.015	0.014
Eu	0.000	0.000	0.003	0.000	0.000	0.000	0.003	0.000	0.000	0.000	0.000
Gd	0.008	0.007	0.007	0.005	0.006	0.007	0.007	0.007	0.007	0.007	0.007
Dy	0.000	0.000	0.000	0.000	0.000	0.000	0.000	0.000	0.000	0.000	0.000
Y	0.009	0.008	0.010	0.005	0.005	0.009	0.006	0.008	0.008	0.010	0.009
Ho	0.000	0.000	0.000	0.000	0.000	0.000	0.000	0.000	0.000	0.000	0.000
Th	0.003	0.004	0.003	0.002	0.003	0.004	0.004	0.003	0.004	0.003	0.003
U	0.000	0.000	0.000	0.000	0.000	0.000	0.000	0.000	0.000	0.000	0.000
Ca	0.008	0.032	0.033	0.011	0.020	0.005	0.023	0.017	0.016	0.014	0.015
P	0.977	0.995	0.975	0.983	0.975	0.984	0.984	0.984	0.987	0.998	0.987
F	0.078	0.000	0.065	0.063	0.061	0.059	0.061	0.069	0.065	0.000	0.064
Cl	0.000	0.000	0.000	0.000	0.000	0.000	0.000	0.003	0.000	0.002	0.000
Si	0.006	0.007	0.000	0.000	0.000	0.005	0.000	0.007	0.005	0.000	0.000
Pb	0.000	0.001	0.000	0.000	0.000	0.000	0.002	0.000	0.000	0.000	0.000
Fe	0.000	0.000	0.000	0.000	0.006	0.000	0.011	0.000	0.000	0.000	0.000
Sr	0.000	0.000	0.000	0.000	0.000	0.000	0.000	0.000	0.000	0.000	0.000
Total	1.985	2.011	2.002	1.990	2.001	1.987	1.998	1.984	1.985	2.004	1.988

Appendix 2.7: Continued

Unit						**B**					
Sample	15127	15127	15127	15127	15127	15127	15127	15127	15127	15127	15127
La_2O_3 (*wt. %*)	16.17	16.28	16.28	16.66	19.81	19.90	23.09	22.92	22.67	22.71	23.25
Ce_2O_3	34.01	34.36	34.40	33.24	33.49	34.71	33.50	33.69	33.01	32.84	33.19
Pr_2O_3	3.99	4.05	4.07	4.11	3.51	3.49	3.07	3.12	3.06	3.06	3.01
Nd_2O_3	11.86	11.67	11.78	13.41	10.63	10.83	8.12	8.25	8.27	8.09	8.00
Sm_2O_3	1.07	1.10	0.98	0.96	0.93	1.02	0.62	0.68	0.67	0.72	0.65
Eu_2O_3	0.00	0.00	0.00	0.00	0.00	0.00	0.00	0.00	0.00	0.00	0.00
Gd_2O_3	0.51	0.52	0.40	0.51	0.56	0.56	0.50	0.36	0.35	0.32	0.42
Dy_2O_3	0.00	0.00	0.00	0.00	0.00	0.00	0.00	0.00	0.00	0.00	0.00
Y_2O_3	0.27	0.25	0.22	0.25	0.35	0.39	0.19	0.21	0.22	0.22	0.28
Ho_2O_3	0.00	0.00	0.00		0.00	0.00	0.00	0.00	0.00	0.00	0.00
ThO_2	0.28	0.50	0.21	0.22	0.33	0.36	0.22	0.20	0.22	0.23	0.24
UO_2	0.00	0.00	0.00	0.00	0.00	0.00	0.00	0.00	0.00	0.00	0.00
CaO	0.39	0.21	0.20	0.17	0.24	0.34	0.20	0.27	0.07	0.21	0.42
P_2O_5	29.86	29.73	29.82	29.64	29.71	28.88	29.94	29.88	30.05	29.38	29.96
F	0.67	0.56	0.57	0.53	0.60	0.48	0.48	0.57	0.00	0.61	0.48
Cl	0.00	0.00	0.00	0.00	0.00	0.00	0.00	0.00	0.00	0.00	0.00
SiO_2	0.14	0.15	0.13	0.00	0.00	0.00	0.00	0.00	0.00	0.00	0.00
PbO	0.10	0.11	0.13	0.00	0.09	0.00	0.00	0.00	0.00	0.00	0.11
FeO	0.00	0.00	0.00	0.00	0.00	0.00	0.00	0.00	0.00	0.00	0.00
SrO	0.00	0.00	0.00		0.00	0.10	0.00	0.00	0.00	0.00	0.00
O=F	-0.28	-0.23	-0.24	-0.22	-0.25	-0.20	-0.20	-0.24	0.00	-0.25	-0.20
Total	99.04	99.23	98.95	99.49	99.98	100.85	99.74	99.90	98.58	98.13	99.80
						O = 4					
La (*apfu*)	0.233	0.235	0.235	0.241	0.285	0.289	0.332	0.329	0.330	0.332	0.334
Ce	0.486	0.493	0.494	0.478	0.479	0.501	0.479	0.481	0.477	0.477	0.473
Pr	0.057	0.058	0.058	0.059	0.050	0.050	0.044	0.044	0.044	0.044	0.043
Nd	0.165	0.163	0.165	0.188	0.148	0.152	0.113	0.115	0.117	0.115	0.111
Sm	0.014	0.015	0.013	0.013	0.012	0.014	0.008	0.009	0.009	0.010	0.009
Eu	0.000	0.000	0.000	0.000	0.000	0.000	0.000	0.000	0.000	0.000	0.000
Gd	0.007	0.007	0.005	0.007	0.007	0.007	0.007	0.005	0.005	0.004	0.005
Dy	0.000	0.000	0.000	0.000	0.000	0.000	0.000	0.000	0.000	0.000	0.000
Y	0.006	0.005	0.005	0.005	0.007	0.008	0.004	0.004	0.005	0.005	0.006
Ho	0.000	0.000	0.000	0.000	0.000	0.000	0.000	0.000	0.000	0.000	0.000
Th	0.003	0.004	0.002	0.002	0.003	0.003	0.002	0.002	0.002	0.002	0.002
U	0.000	0.000	0.000	0.000	0.000	0.000	0.000	0.000	0.000	0.000	0.000
Ca	0.016	0.009	0.008	0.007	0.010	0.014	0.008	0.011	0.003	0.009	0.018
P	0.987	0.986	0.989	0.986	0.982	0.964	0.989	0.986	1.005	0.986	0.988
F	0.083	0.069	0.070	0.066	0.074	0.060	0.059	0.070	0.000	0.076	0.059
Cl	0.000	0.000	0.000	0.000	0.000	0.000	0.000	0.000	0.000	0.000	0.000
Si	0.006	0.006	0.005	0.000	0.000	0.000	0.000	0.000	0.000	0.000	0.000
Pb	0.001	0.001	0.001	0.000	0.001	0.000	0.000	0.000	0.000	0.000	0.001
Fe	0.000	0.000	0.000	0.000	0.000	0.000	0.000	0.000	0.000	0.000	0.000
Sr	0.000	0.000	0.000	0.000	0.000	0.000	0.000	0.000	0.000	0.000	0.000
Total	1.980	1.982	1.981	1.986	1.986	2.003	1.987	1.986	1.997	1.983	1.991

Appendix 2.7: Continued

Unit						**B**					
Sample	15127	15127	15127	15127	15127	15127	15127	15127	15127	15127	15127
La_2O_3 (*wt.* %)	23.62	23.70	24.08	23.67	20.58	20.40	20.46	23.09	23.09	20.95	22.93
Ce_2O_3	32.89	33.99	33.39	33.39	34.35	33.92	34.43	32.08	33.04	32.69	34.06
Pr_2O_3	2.91	2.99	2.91	2.95	3.55	3.32	3.48	3.05	3.08	3.14	3.14
Nd_2O_3	9.04	8.86	8.78	9.06	10.29	10.20	10.55	9.33	9.40	9.75	9.34
Sm_2O_3	0.70	0.66	0.82	0.71	0.78	0.84	0.82	0.64	0.66	0.80	0.61
Eu_2O_3	0.00	0.00	0.00	0.00	0.00	0.00	0.00	0.00	0.00	0.00	0.00
Gd_2O_3	0.35	0.29	0.22	0.32	0.45	0.39	0.35	0.37	0.32	0.30	0.37
Dy_2O_3	0.00	0.00	0.00	0.00	0.00	0.00	0.00	0.00	0.00	0.00	0.00
Y_2O_3	0.21	0.19	0.26	0.27	0.25	0.36	0.31	0.22	0.25	0.19	0.22
Ho_2O_3	0.00	0.00	0.00	0.00	0.00	0.00	0.00				
ThO_2	0.30	0.34	0.25	0.32	0.26	0.32	0.35	0.24	0.25	0.34	0.21
UO_2	0.00	0.00	0.00	0.00	0.00	0.00	0.00	0.00	0.00	0.00	0.00
CaO	0.21	0.23	0.14	0.24	0.30	0.32	0.57	0.07	0.07	0.42	0.30
P_2O_5	29.72	29.04	29.29	28.71	28.98	29.03	28.90	29.70	29.25	29.27	29.35
F	0.58	0.70	0.52	0.64	0.49	0.47	0.62	0.53	0.62	0.48	0.48
Cl	0.00	0.03	0.00	0.02	0.00	0.02	0.00	0.02	0.00	0.00	0.00
SiO_2	0.00	0.15	0.00	0.32	0.13	0.00	0.00	0.00	0.00	0.00	0.00
PbO	0.00	0.11	0.00	0.10	0.09	0.00	0.00	0.00	0.00	0.00	0.00
FeO	0.00	0.00	0.00	0.00	0.00	0.19	0.00	0.00	0.00	0.00	0.00
SrO	0.00	0.00	0.00	0.00	0.00	0.00	0.00				
O=F	-0.24	-0.29	-0.22	-0.27	-0.20	-0.20	-0.26	-0.22	-0.26	-0.20	-0.20
Total	100.28	100.97	100.43	100.47	100.30	99.59	100.58	99.13	99.77	98.14	100.81
						O = 4					
La (*apfu*)	0.340	0.342	0.349	0.343	0.299	0.298	0.297	0.335	0.335	0.307	0.331
Ce	0.469	0.487	0.480	0.481	0.496	0.491	0.496	0.461	0.476	0.476	0.488
Pr	0.041	0.043	0.042	0.042	0.051	0.048	0.050	0.044	0.044	0.046	0.045
Nd	0.126	0.124	0.123	0.127	0.145	0.144	0.148	0.131	0.132	0.138	0.131
Sm	0.009	0.009	0.011	0.010	0.011	0.011	0.011	0.009	0.009	0.011	0.008
Eu	0.000	0.000	0.000	0.000	0.000	0.000	0.000	0.000	0.000	0.000	0.000
Gd	0.005	0.004	0.003	0.004	0.006	0.005	0.005	0.005	0.004	0.004	0.005
Dy	0.000	0.000	0.000	0.000	0.000	0.000	0.000	0.000	0.000	0.000	0.000
Y	0.004	0.004	0.005	0.006	0.005	0.008	0.006	0.005	0.005	0.004	0.005
Ho	0.000	0.000	0.000	0.000	0.000	0.000	0.000	0.000	0.000	0.000	0.000
Th	0.003	0.003	0.002	0.003	0.002	0.003	0.003	0.002	0.002	0.003	0.002
U	0.000	0.000	0.000	0.000	0.000	0.000	0.000	0.000	0.000	0.000	0.000
Ca	0.009	0.009	0.006	0.010	0.013	0.013	0.024	0.003	0.003	0.018	0.012
P	0.981	0.961	0.973	0.956	0.967	0.972	0.962	0.988	0.975	0.985	0.973
F	0.071	0.087	0.065	0.080	0.060	0.059	0.077	0.066	0.077	0.061	0.059
Cl	0.000	0.002	0.000	0.002	0.000	0.001	0.000	0.001	0.000	0.000	0.000
Si	0.000	0.006	0.000	0.013	0.005	0.000	0.000	0.000	0.000	0.000	0.000
Pb	0.000	0.001	0.000	0.001	0.001	0.000	0.000	0.000	0.000	0.000	0.000
Fe	0.000	0.000	0.000	0.000	0.000	0.006	0.000	0.000	0.000	0.000	0.000
Sr	0.000	0.000	0.000	0.000	0.000	0.000	0.000	0.000	0.000	0.000	0.000
Total	1.987	1.992	1.994	1.996	2.001	2.000	2.002	1.982	1.987	1.992	1.999

Appendix 2.7: Continued

Unit						**B**					
Sample	15127	15127	15127	15127	15127	15127	15127	15127	15127	15127	15127
La_2O_3 (*wt. %*)	22.67	21.16	23.63	22.59	24.00	23.89	22.61	23.35	22.92	23.54	23.81
Ce_2O_3	32.34	32.69	31.99	32.76	32.43	31.98	33.47	32.73	33.24	31.86	33.17
Pr_2O_3	3.09	3.27	3.08	3.11	3.08	3.12	3.13	3.04	3.00	3.08	3.09
Nd_2O_3	9.12	9.96	9.11	9.09	8.87	9.06	9.10	9.04	9.25	8.96	8.99
Sm_2O_3	0.75	0.81	0.65	0.69	0.72	0.63	0.74	0.64	0.75	0.72	0.53
Eu_2O_3	0.00	0.00	0.00	0.00	0.00	0.00	0.00	0.00	0.00	0.00	0.00
Gd_2O_3	0.33	0.40	0.28	0.42	0.38	0.36	0.43	0.35	0.43	0.45	0.32
Dy_2O_3	0.00	0.00	0.00	0.00	0.00	0.00	0.00	0.00	0.00	0.00	0.00
Y_2O_3	0.22	0.23	0.24	0.36	0.27	0.23	0.32	0.28	0.27	0.29	0.24
Ho_2O_3											
ThO_2	0.24	0.31	0.29	0.24	0.24	0.22	0.25	0.28	0.26	0.24	0.17
UO_2	0.00	0.00	0.00	0.00	0.00	0.00	0.00	0.00	0.00	0.00	0.00
CaO	0.22	0.43	0.33	0.13	0.31	0.31	0.13	0.10	0.20	0.22	0.30
P_2O_5	29.94	29.43	29.64	29.11	29.30	29.45	29.67	29.09	29.64	29.55	29.32
F	0.54	0.61	0.55	0.63	0.52	0.00	0.00	0.48	0.55	0.55	0.52
Cl	0.00	0.00	0.00	0.00	0.04	0.00	0.00	0.00	0.00	0.00	0.00
SiO_2	0.00	0.00	0.00	0.00	0.00	0.00	0.00	0.00	0.00	0.00	0.00
PbO	0.00	0.00	0.00	0.00	0.00	0.00	0.00	0.00	0.00	0.00	0.09
FeO	0.00	0.00	0.00	0.00	0.00	0.00	0.00	0.00	0.00	0.00	0.00
SrO											
O=F	-0.23	-0.26	-0.23	-0.26	-0.22	0.00	0.00	-0.20	-0.23	-0.23	-0.22
Total	99.22	99.03	99.53	98.86	99.93	99.23	99.85	99.18	100.26	99.23	100.31
						O = 4					
La (*apfu*)	0.327	0.307	0.341	0.330	0.348	0.350	0.329	0.342	0.330	0.341	0.345
Ce	0.463	0.471	0.459	0.475	0.467	0.465	0.483	0.475	0.475	0.459	0.477
Pr	0.044	0.047	0.044	0.045	0.044	0.045	0.045	0.044	0.043	0.044	0.044
Nd	0.127	0.140	0.127	0.129	0.124	0.128	0.128	0.128	0.129	0.126	0.126
Sm	0.010	0.011	0.009	0.009	0.010	0.009	0.010	0.009	0.010	0.010	0.007
Eu	0.000	0.000	0.000	0.000	0.000	0.000	0.000	0.000	0.000	0.000	0.000
Gd	0.004	0.005	0.004	0.005	0.005	0.005	0.006	0.005	0.006	0.006	0.004
Dy	0.000	0.000	0.000	0.000	0.000	0.000	0.000	0.000	0.000	0.000	0.000
Y	0.004	0.005	0.005	0.008	0.006	0.005	0.007	0.006	0.006	0.006	0.005
Ho	0.000	0.000	0.000	0.000	0.000	0.000	0.000	0.000	0.000	0.000	0.000
Th	0.002	0.003	0.003	0.002	0.002	0.002	0.002	0.003	0.002	0.002	0.002
U	0.000	0.000	0.000	0.000	0.000	0.000	0.000	0.000	0.000	0.000	0.000
Ca	0.009	0.018	0.014	0.005	0.013	0.013	0.005	0.004	0.008	0.009	0.012
P	0.991	0.981	0.983	0.977	0.975	0.990	0.991	0.977	0.980	0.984	0.974
F	0.066	0.076	0.068	0.078	0.065	0.000	0.000	0.060	0.068	0.068	0.064
Cl	0.000	0.000	0.000	0.000	0.003	0.000	0.000	0.000	0.000	0.000	0.000
Si	0.000	0.000	0.000	0.000	0.000	0.000	0.000	0.000	0.000	0.000	0.000
Pb	0.000	0.000	0.000	0.000	0.000	0.000	0.000	0.000	0.000	0.000	0.001
Fe	0.000	0.000	0.000	0.000	0.000	0.000	0.000	0.000	0.000	0.000	0.000
Sr	0.000	0.000	0.000	0.000	0.000	0.000	0.000	0.000	0.000	0.000	0.000
Total	1.983	1.989	1.989	1.986	1.994	2.011	2.007	1.993	1.989	1.987	1.997

Appendix 2.7: Continued

Unit	**B**										
Sample	15127	15127	15141	15141	15141	15141	15141	15141	15141	15141	15141
La_2O_3 (*wt. %*)	23.13	23.10	18.75	19.20	19.24	19.30	19.55	19.66	19.74	19.77	20.59
Ce_2O_3	32.30	32.70	36.88	34.27	36.51	38.14	35.00	34.62	35.37	37.01	35.79
Pr_2O_3	3.09	3.15	3.46	3.39	3.58	3.34	3.50	3.48	3.32	3.53	3.45
Nd_2O_3	9.20	9.29	9.10	9.03	8.91	8.73	9.19	9.04	8.78	8.55	8.93
Sm_2O_3	0.71	0.65	0.87	0.82	0.80	0.76	0.94	0.90	0.86	0.78	0.83
Eu_2O_3	0.00	0.00	0.00	0.00	0.00	0.00	0.00	0.00	0.00	0.00	0.00
Gd_2O_3	0.39	0.48	0.32	0.40	0.00	0.26	0.32	0.55	0.32	0.37	0.35
Dy_2O_3	0.00	0.00	0.00	0.00	0.00	0.00	0.00	0.00	0.00	0.00	0.00
Y_2O_3	0.21	0.25	0.23	0.23	0.25	0.15	0.29	0.23	0.14	0.23	0.26
Ho_2O_3			0.00	0.00	0.00	0.00	0.00	0.00	0.00	0.00	0.00
ThO_2	0.25	0.20	0.46	0.47	0.31	0.30	0.31	0.46	0.27	0.28	0.38
UO_2	0.00	0.00	0.00	0.00	0.00	0.00	0.00	0.00	0.00	0.00	0.00
CaO	0.08	0.23	0.15	0.46	0.08	0.08	0.16	0.29	0.12	0.18	0.33
P_2O_5	29.25	29.38	30.25	29.67	29.58	29.55	29.56	29.37	29.93	29.83	29.57
F	0.63	0.50	0.53	0.61	0.69	0.55	0.53	0.52	0.55	0.59	0.49
Cl	0.00	0.00	0.00	0.00	0.00	0.00	0.00	0.00	0.00	0.00	0.00
SiO_2	0.17	0.00	0.30	0.33	1.28	0.34	0.23	0.28	0.32	0.28	0.35
PbO	0.00	0.00	0.00	0.08	0.00	0.00	0.00	0.00	0.00	0.00	0.00
FeO	0.00	0.00	0.00	0.00	0.00	0.00	0.00	0.00	0.00	0.00	0.00
SrO			0.00	0.00	0.11	0.00	0.00	0.00	0.00	0.00	0.00
O=F	-0.27	-0.21	-0.22	-0.26	-0.29	-0.23	-0.22	-0.22	-0.23	-0.25	-0.20
Total	99.13	99.71	101.08	98.68	101.05	101.29	99.35	99.17	99.48	101.14	101.09
	O = 4										
La (*apfu*)	0.336	0.335	0.266	0.277	0.271	0.276	0.283	0.285	0.283	0.281	0.294
Ce	0.466	0.471	0.519	0.491	0.510	0.541	0.502	0.498	0.504	0.523	0.508
Pr	0.044	0.045	0.048	0.048	0.050	0.047	0.050	0.050	0.047	0.050	0.049
Nd	0.130	0.131	0.125	0.126	0.122	0.121	0.129	0.127	0.122	0.118	0.124
Sm	0.010	0.009	0.012	0.011	0.011	0.010	0.013	0.012	0.012	0.010	0.011
Eu	0.000	0.000	0.000	0.000	0.000	0.000	0.000	0.000	0.000	0.000	0.000
Gd	0.005	0.006	0.004	0.005	0.000	0.003	0.004	0.007	0.004	0.005	0.004
Dy	0.000	0.000	0.000	0.000	0.000	0.000	0.000	0.000	0.000	0.000	0.000
Y	0.004	0.005	0.005	0.005	0.005	0.003	0.006	0.005	0.003	0.005	0.005
Ho	0.000	0.000	0.000	0.000	0.000	0.000	0.000	0.000	0.000	0.000	0.000
Th	0.002	0.002	0.004	0.004	0.003	0.003	0.003	0.004	0.002	0.002	0.003
U	0.000	0.000	0.000	0.000	0.000	0.000	0.000	0.000	0.000	0.000	0.000
Ca	0.003	0.010	0.006	0.019	0.003	0.003	0.007	0.012	0.005	0.007	0.014
P	0.976	0.979	0.984	0.983	0.956	0.969	0.981	0.978	0.986	0.975	0.970
F	0.079	0.062	0.065	0.076	0.083	0.067	0.066	0.065	0.068	0.072	0.060
Cl	0.000	0.000	0.000	0.000	0.000	0.000	0.000	0.000	0.000	0.000	0.000
Si	0.007	0.000	0.011	0.013	0.049	0.013	0.009	0.011	0.013	0.011	0.013
Pb	0.000	0.000	0.000	0.001	0.000	0.000	0.000	0.000	0.000	0.000	0.000
Fe	0.000	0.000	0.000	0.000	0.000	0.000	0.000	0.000	0.000	0.000	0.000
Sr	0.000	0.000	0.000	0.000	0.000	0.000	0.000	0.000	0.000	0.000	0.000
Total	1.984	1.993	1.983	1.983	1.979	1.990	1.986	1.989	1.980	1.987	1.996

Appendix 2.7: Continued

Unit	**B**										
Sample	15141	15141	15141	15141	15141	15141	15141	16018	16018	16018	16018
La_2O_3 (*wt. %*)	21.09	22.49	21.58	21.99	21.44	20.33	20.23	21.63	21.12	23.62	24.23
Ce_2O_3	35.93	34.12	34.20	33.39	35.37	35.65	36.08	34.91	33.07	34.76	33.86
Pr_2O_3	3.38	3.26	3.19	3.25	3.36	3.38	3.46	3.26	3.09	2.90	2.79
Nd_2O_3	8.67	8.52	8.72	8.27	8.80	9.11	8.78	8.38	8.07	7.73	7.58
Sm_2O_3	0.78	0.74	0.88	0.75	0.87	0.87	0.66	0.59	0.55	0.46	0.34
Eu_2O_3	0.00	0.00	0.00	0.00	0.00	0.00	0.00	0.00	0.00	0.00	0.00
Gd_2O_3	0.00	0.38	0.36	0.26	0.43	0.37	0.41	0.32	0.28	0.00	0.32
Dy_2O_3	0.00	0.00	0.00	0.00	0.00	0.00	0.00	0.00	0.00	0.00	0.00
Y_2O_3	0.24	0.27	0.25	0.47	0.31	0.18	0.21	0.17	0.19	0.29	0.18
Ho_2O_3	0.00	0.00	0.00	0.00	0.00	0.00	0.00	0.00	0.00	0.00	0.00
ThO_2	0.32	0.26	0.13	0.33	0.35	0.24	0.28	0.81	0.74	0.51	0.61
UO_2	0.00	0.00	0.00	0.00	0.00	0.00	0.00	0.00	0.00	0.00	0.00
CaO	0.22	0.10	0.06	0.16	0.11	0.12	0.04	0.36	0.44	0.19	0.13
P_2O_5	29.84	30.07	29.98	29.85	30.07	30.14	29.72	29.36	28.78	28.84	29.56
F	0.55	0.67	0.67	0.62	0.46	0.58	0.49	0.63	0.70	0.54	0.52
Cl	0.00	0.00	0.00	0.00	0.00	0.00	0.00	0.00	0.03	0.00	0.00
SiO_2	0.26	0.31	0.26	0.24	0.28	0.30	0.25	0.24	2.00	0.00	0.13
PbO	0.00	0.00	0.00	0.00	0.00	0.00	0.00	0.00	0.00	0.00	0.00
FeO	0.00	0.00	0.00	0.00	0.00	0.00	0.00	0.00	0.00	0.00	0.00
SrO	0.00	0.00	0.00	0.08	0.11	0.00	0.00	0.00	0.16	0.08	0.00
O=F	-0.23	-0.28	-0.28	-0.26	-0.20	-0.24	-0.21	-0.26	-0.30	-0.23	-0.22
Total	101.04	100.90	100.00	99.38	101.77	101.01	100.41	100.37	98.92	99.70	100.03
	O = 4										
La (*apfu*)	0.300	0.319	0.308	0.316	0.304	0.288	0.290	0.311	0.301	0.346	0.350
Ce	0.508	0.480	0.485	0.476	0.497	0.502	0.514	0.499	0.468	0.505	0.485
Pr	0.048	0.046	0.045	0.046	0.047	0.047	0.049	0.046	0.044	0.042	0.040
Nd	0.120	0.117	0.121	0.115	0.121	0.125	0.122	0.117	0.111	0.110	0.106
Sm	0.010	0.010	0.012	0.010	0.011	0.012	0.009	0.008	0.007	0.006	0.005
Eu	0.000	0.000	0.000	0.000	0.000	0.000	0.000	0.000	0.000	0.000	0.000
Gd	0.000	0.005	0.005	0.003	0.006	0.005	0.005	0.004	0.004	0.000	0.004
Dy	0.000	0.000	0.000	0.000	0.000	0.000	0.000	0.000	0.000	0.000	0.000
Y	0.005	0.006	0.005	0.010	0.006	0.004	0.004	0.003	0.004	0.006	0.004
Ho	0.000	0.000	0.000	0.000	0.000	0.000	0.000	0.000	0.000	0.000	0.000
Th	0.003	0.002	0.001	0.003	0.003	0.002	0.002	0.007	0.007	0.005	0.005
U	0.000	0.000	0.000	0.000	0.000	0.000	0.000	0.000	0.000	0.000	0.000
Ca	0.009	0.004	0.003	0.007	0.005	0.005	0.002	0.015	0.018	0.008	0.006
P	0.976	0.979	0.983	0.984	0.978	0.981	0.979	0.970	0.941	0.968	0.979
F	0.067	0.081	0.083	0.076	0.056	0.070	0.060	0.078	0.086	0.067	0.064
Cl	0.000	0.000	0.000	0.000	0.000	0.000	0.000	0.000	0.002	0.000	0.000
Si	0.010	0.012	0.010	0.009	0.011	0.011	0.010	0.009	0.077	0.000	0.005
Pb	0.000	0.000	0.000	0.000	0.000	0.000	0.000	0.000	0.000	0.000	0.000
Fe	0.000	0.000	0.000	0.000	0.000	0.000	0.000	0.000	0.000	0.000	0.000
Sr	0.000	0.000	0.000	0.000	0.000	0.000	0.000	0.000	0.000	0.000	0.000
Total	1.989	1.979	1.977	1.979	1.988	1.982	1.987	1.990	1.981	1.995	1.988

Appendix 2.7: Continued

Unit	B							BD			
Sample	16018	16018	16019	16019	16019	16019	16019	15158	15158	15158	15158
La_2O_3 (*wt. %*)	24.07	24.19	27.13	26.17	25.55	27.15	26.30	10.59	10.81	11.03	11.90
Ce_2O_3	33.63	33.62	32.16	33.56	33.38	32.81	33.34	34.13	33.04	32.82	33.70
Pr_2O_3	2.81	2.90	2.49	2.65	2.62	2.53	2.56	4.63	4.53	4.39	4.49
Nd_2O_3	7.36	7.56	6.56	6.95	7.17	6.56	7.09	16.86	16.23	16.61	16.21
Sm_2O_3	0.46	0.48	0.31	0.41	0.41	0.39	0.51	2.10	1.97	1.99	1.94
Eu_2O_3	0.00	0.00	0.00	0.00	0.00	0.00	0.00	0.31	0.25	0.45	0.33
Gd_2O_3	0.00	0.40	0.00	0.00	0.30	0.24	0.23	0.65	0.59	0.69	0.67
Dy_2O_3	0.00	0.00	0.00	0.00	0.00	0.00	0.00	0.00	0.00	0.00	0.00
Y_2O_3	0.16	0.00	0.00	0.00	0.16	0.18	0.00	0.17	0.14	0.24	0.17
Ho_2O_3	0.00	0.00	0.00	0.00	0.00	0.00	0.00	0.00	0.00	0.00	0.00
ThO_2	0.57	0.59	0.00	0.15	0.22	0.11	0.23	1.14	0.98	0.79	0.87
UO_2	0.00	0.00	0.00	0.00	0.00	0.00	0.00	0.00	0.00	0.00	0.00
CaO	0.30	0.29	0.04	0.13	0.00	0.08	0.20	0.28	0.57	0.84	0.40
P_2O_5	28.92	29.83	29.36	29.85	29.65	29.70	29.16	28.73	29.07	29.32	29.14
F	0.67	0.60	0.57	0.55	0.61	0.59	0.66	0.58	0.50	0.52	0.68
Cl	0.00	0.00	0.02	0.02	0.00	0.00	0.00	0.00	0.00	0.00	0.00
SiO_2	0.28	0.00	0.00	0.00	0.00	0.13	0.18	0.36	0.22	0.22	0.17
PbO	0.00	0.00	0.00	0.00	0.00	0.00	0.00	0.13	0.00	0.00	0.18
FeO	0.00	0.00	0.00	0.00	0.00	0.00	0.00	0.00	0.00	0.00	0.00
SrO	0.11	0.00	0.00	0.00	0.00	0.00	0.08	0.00	0.11	0.25	0.23
O=F	-0.28	-0.25	-0.24	-0.23	-0.26	-0.25	-0.28	-0.25	-0.21	-0.22	-0.29
Total	99.06	100.19	98.40	100.21	99.81	100.22	100.25	100.40	98.79	99.94	100.80
						O = 4					
La (*apfu*)	0.351	0.347	0.396	0.376	0.369	0.390	0.380	0.154	0.158	0.159	0.172
Ce	0.486	0.479	0.466	0.478	0.478	0.468	0.478	0.493	0.480	0.471	0.483
Pr	0.040	0.041	0.036	0.038	0.037	0.036	0.037	0.067	0.065	0.063	0.064
Nd	0.104	0.105	0.093	0.097	0.100	0.091	0.099	0.238	0.230	0.232	0.227
Sm	0.006	0.006	0.004	0.006	0.006	0.005	0.007	0.029	0.027	0.027	0.026
Eu	0.000	0.000	0.000	0.000	0.000	0.000	0.000	0.004	0.003	0.006	0.004
Gd	0.000	0.005	0.000	0.000	0.004	0.003	0.003	0.008	0.008	0.009	0.009
Dy	0.000	0.000	0.000	0.000	0.000	0.000	0.000	0.000	0.000	0.000	0.000
Y	0.003	0.000	0.000	0.000	0.003	0.004	0.000	0.004	0.003	0.005	0.003
Ho	0.000	0.000	0.000	0.000	0.000	0.000	0.000	0.000	0.000	0.000	0.000
Th	0.005	0.005	0.000	0.001	0.002	0.001	0.002	0.010	0.009	0.007	0.008
U	0.000	0.000	0.000	0.000	0.000	0.000	0.000	0.000	0.000	0.000	0.000
Ca	0.013	0.012	0.002	0.005	0.000	0.003	0.008	0.012	0.024	0.035	0.017
P	0.967	0.983	0.985	0.984	0.983	0.979	0.967	0.960	0.976	0.973	0.966
F	0.083	0.074	0.072	0.068	0.076	0.072	0.082	0.073	0.063	0.064	0.084
Cl	0.000	0.000	0.001	0.001	0.000	0.000	0.000	0.000	0.000	0.000	0.000
Si	0.011	0.000	0.000	0.000	0.000	0.005	0.007	0.014	0.009	0.009	0.007
Pb	0.000	0.000	0.000	0.000	0.000	0.000	0.000	0.001	0.000	0.000	0.002
Fe	0.000	0.000	0.000	0.000	0.000	0.000	0.000	0.000	0.000	0.000	0.000
Sr	0.000	0.000	0.000	0.000	0.000	0.000	0.000	0.000	0.000	0.000	0.000
Total	1.987	1.985	1.982	1.985	1.982	1.985	1.989	1.995	1.992	1.996	1.988

Appendix 2.7: Continued

Unit	**BD**	**MHREO**									
Sample	15158	15002	15002	15002	15002	15014	15337	15337	15337	15337	15337
La_2O_3 (*wt. %*)	12.11	11.88	12.70	12.17	12.81	4.05	2.85	2.43	2.82	2.95	2.90
Ce_2O_3	34.18	31.04	30.58	31.29	31.68	23.53	23.08	23.66	24.88	23.70	24.25
Pr_2O_3	4.42	3.92	3.92	3.99	3.98	5.28	5.75	5.59	5.72	5.81	6.08
Nd_2O_3	15.98	10.91	12.92	12.97	13.31	24.64	25.36	26.74	26.78	27.26	27.03
Sm_2O_3	1.79	1.54	1.75	1.75	1.74	3.72	3.40	3.52	3.48	3.56	3.75
Eu_2O_3	0.34	0.28	0.54	0.36	0.31	0.78	0.63	0.65	0.58	0.68	0.62
Gd_2O_3	0.83	1.02	0.80	0.95	0.90	1.33	0.90	1.35	1.35	1.28	1.24
Dy_2O_3	0.00	0.23	0.00	0.00	0.00	0.00	0.25	0.24	0.00	0.00	0.00
Y_2O_3	0.20	0.32	0.41	0.48	0.42	0.50	0.42	0.46	0.43	0.40	0.48
Ho_2O_3	0.00	0.00				0.00	0.00	0.00	0.00	0.00	0.00
ThO_2	0.80	4.25	2.28	3.29	3.04	4.64	4.95	4.72	4.52	3.79	3.11
UO_2	0.00	0.00	0.00	0.00	0.00	0.00	0.00	0.00	0.00	0.00	0.00
CaO	0.17	3.08	0.86	0.99	1.58	1.18	0.43	0.26	0.31	0.31	0.30
P_2O_5	28.58	28.52	28.37	28.90	28.62	27.72	26.38	26.88	27.09	27.82	28.39
F	0.57	0.69	0.69	0.60	0.56	0.61	0.47	0.00	0.52	0.53	0.62
Cl	0.00	0.00	0.02	0.00	0.00	0.03	0.06	0.03	0.04	0.04	0.03
SiO_2	0.16	0.51	0.47	0.24	0.34	0.87	1.09	1.18	1.23	1.03	0.71
PbO	0.16	0.30	0.21	0.29	0.26	0.31	0.31	0.44	0.43	0.20	0.25
FeO	0.00	0.00	3.12	0.27	0.38	1.32	3.69	2.85	0.44	1.01	0.80
SrO	0.26	0.52				0.69	0.61	0.28	0.19	0.19	0.37
O=F	-0.24	-0.29	-0.29	-0.25	-0.24	-0.26	-0.20	0.00	-0.22	-0.22	-0.26
Total	100.32	98.72	99.35	98.28	99.68	100.93	100.44	101.26	100.60	100.33	100.69
						O = 4					
La (*apfu*)	0.177	0.172	0.184	0.178	0.186	0.059	0.042	0.036	0.042	0.043	0.042
Ce	0.497	0.447	0.440	0.455	0.458	0.341	0.341	0.349	0.366	0.345	0.350
Pr	0.064	0.056	0.056	0.058	0.057	0.076	0.085	0.082	0.084	0.084	0.087
Nd	0.227	0.153	0.181	0.184	0.188	0.348	0.365	0.384	0.384	0.387	0.381
Sm	0.024	0.021	0.024	0.024	0.024	0.051	0.047	0.049	0.048	0.049	0.051
Eu	0.005	0.004	0.007	0.005	0.004	0.011	0.009	0.009	0.008	0.009	0.008
Gd	0.011	0.013	0.010	0.013	0.012	0.017	0.012	0.018	0.018	0.017	0.016
Dy	0.000	0.003	0.000	0.000	0.000	0.000	0.003	0.003	0.000	0.000	0.000
Y	0.004	0.007	0.009	0.010	0.009	0.010	0.009	0.010	0.009	0.008	0.010
Ho	0.000	0.000	0.000	0.000	0.000	0.000	0.000	0.000	0.000	0.000	0.000
Th	0.007	0.038	0.020	0.030	0.027	0.042	0.045	0.043	0.041	0.034	0.028
U	0.000	0.000	0.000	0.000	0.000	0.000	0.000	0.000	0.000	0.000	0.000
Ca	0.007	0.130	0.036	0.042	0.067	0.050	0.019	0.011	0.013	0.013	0.012
P	0.961	0.950	0.945	0.973	0.956	0.928	0.901	0.916	0.921	0.936	0.948
F	0.072	0.086	0.085	0.076	0.070	0.076	0.060	0.000	0.066	0.067	0.078
Cl	0.000	0.000	0.002	0.000	0.000	0.002	0.004	0.002	0.002	0.003	0.002
Si	0.006	0.020	0.018	0.010	0.013	0.035	0.044	0.047	0.050	0.041	0.028
Pb	0.002	0.003	0.002	0.003	0.003	0.003	0.003	0.005	0.005	0.002	0.003
Fe	0.000	0.000	0.103	0.009	0.013	0.044	0.124	0.096	0.015	0.033	0.026
Sr	0.000	0.000	0.000	0.000	0.000	0.000	0.000	0.000	0.000	0.000	0.000
Total	1.993	2.017	2.037	1.994	2.016	2.014	2.050	2.058	2.003	2.003	1.992

Appendix 2.7: Continued

Unit	**MHREO**									
Sample	15337	15337	15337	15337	15337	15337	15337	15337	15337	15337
La_2O_3 (*wt. %*)	2.70	2.68	2.98	2.75	2.60	3.05	2.87	2.59	2.37	2.59
Ce_2O_3	24.35	24.14	24.33	24.22	23.98	24.43	24.42	24.35	24.12	23.39
Pr_2O_3	5.78	5.80	5.91	5.76	5.70	5.79	5.92	5.79	5.85	5.78
Nd_2O_3	26.11	25.67	26.84	26.21	26.24	27.22	26.71	27.43	27.38	28.02
Sm_2O_3	3.83	3.48	3.75	3.53	3.59	3.81	3.77	3.75	3.70	3.91
Eu_2O_3	0.72	0.73	0.73	0.68	0.66	0.74	0.66	0.56	0.71	0.61
Gd_2O_3	1.24	1.21	1.02	1.20	1.10	1.03	1.16	1.25	1.31	1.33
Dy_2O_3	0.00	0.00	0.00	0.00	0.23	0.00	0.00	0.27	0.00	0.00
Y_2O_3	0.46	0.42	0.51	0.42	0.48	0.26	0.37	0.34	0.56	0.53
Ho_2O_3	0.00	0.00	0.00	0.00	0.00	0.00	0.00	0.00	0.00	0.00
ThO_2	3.40	3.26	3.90	4.72	4.30	3.29	3.72	3.47	4.48	3.24
UO_2	0.00	0.00	0.00	0.00	0.00	0.00	0.00	0.00	0.00	0.00
CaO	0.76	1.39	0.52	0.99	1.02	0.39	0.32	0.28	0.19	0.19
P_2O_5	28.38	27.82	27.66	27.43	27.39	28.02	28.27	27.55	27.37	27.79
F	0.59	0.60	0.54	0.58	0.75	0.00	0.56	0.62	0.54	0.66
Cl	0.04	0.03	0.00	0.03	0.04	0.04	0.04	0.04	0.03	0.03
SiO_2	0.69	0.60	0.77	0.91	0.94	0.65	0.64	1.01	1.19	0.94
PbO	0.29	0.24	0.39	0.36	0.32	0.26	0.38	0.25	0.35	0.23
FeO	0.91	1.38	0.52	0.57	0.89	1.10	1.28	0.68	0.44	1.51
SrO	0.51	0.52	0.44	0.44	0.40	0.58	0.56	0.21	0.00	0.14
O=F	-0.25	-0.25	-0.23	-0.24	-0.31	0.00	-0.24	-0.26	-0.23	-0.28
Total	100.52	99.72	100.55	100.54	100.31	100.65	101.38	100.18	100.35	100.63
	O = 4									
La (*apfu*)	0.039	0.039	0.044	0.040	0.038	0.045	0.042	0.038	0.035	0.038
Ce	0.352	0.352	0.356	0.354	0.350	0.358	0.353	0.356	0.354	0.339
Pr	0.083	0.084	0.086	0.084	0.083	0.085	0.085	0.084	0.085	0.084
Nd	0.368	0.365	0.383	0.374	0.373	0.390	0.376	0.392	0.392	0.397
Sm	0.052	0.048	0.052	0.049	0.049	0.053	0.051	0.052	0.051	0.053
Eu	0.010	0.010	0.010	0.009	0.009	0.010	0.009	0.008	0.010	0.008
Gd	0.016	0.016	0.013	0.016	0.015	0.014	0.015	0.017	0.017	0.018
Dy	0.000	0.000	0.000	0.000	0.003	0.000	0.000	0.004	0.000	0.000
Y	0.010	0.009	0.011	0.009	0.010	0.005	0.008	0.007	0.012	0.011
Ho	0.000	0.000	0.000	0.000	0.000	0.000	0.000	0.000	0.000	0.000
Th	0.030	0.030	0.035	0.043	0.039	0.030	0.033	0.032	0.041	0.029
U	0.000	0.000	0.000	0.000	0.000	0.000	0.000	0.000	0.000	0.000
Ca	0.032	0.059	0.022	0.042	0.043	0.017	0.013	0.012	0.008	0.008
P	0.947	0.937	0.936	0.928	0.924	0.950	0.944	0.932	0.928	0.933
F	0.073	0.076	0.069	0.073	0.094	0.000	0.070	0.078	0.068	0.083
Cl	0.003	0.002	0.000	0.002	0.003	0.003	0.002	0.003	0.002	0.002
Si	0.027	0.024	0.031	0.036	0.037	0.026	0.025	0.040	0.048	0.037
Pb	0.003	0.003	0.004	0.004	0.003	0.003	0.004	0.003	0.004	0.002
Fe	0.030	0.046	0.017	0.019	0.030	0.037	0.042	0.023	0.015	0.050
Sr	0.000	0.000	0.000	0.000	0.000	0.000	0.000	0.000	0.000	0.000
Total	2.000	2.021	2.002	2.007	2.007	2.022	2.001	1.999	2.000	2.007

Appendix 2.8: Major element oxide compositions and cation proportions of bastnäsite-(Ce) in the different units of the Ashram deposit

Unit						**B**					
Sample	15141	15141	15141	15141	15141	15141	15141	15141	15141	15141	15141
La_2O_3 (*wt* %)	26.67	26.48	27.86	25.92	26.59	24.57	24.73	27.04	26.49	24.62	23.17
Ce_2O_3	38.13	36.03	35.33	36.41	36.68	36.54	36.71	36.70	36.36	38.52	37.36
Pr_2O_3	3.31	3.12	2.85	3.03	3.07	3.33	3.33	3.10	3.10	3.29	3.57
Nd_2O_3	7.98	7.83	7.40	8.26	8.17	9.27	9.57	8.14	8.15	8.59	8.89
Sm_2O_3	0.53	0.55	0.46	0.41	0.45	0.57	0.60	0.55	0.66	0.75	0.70
Eu_2O_3	0.14	0.14	0.14	0.14	0.14	0.14	0.14	0.14	0.14	0.14	0.14
Gd_2O_3	0.33	0.45	0.22	0.22	0.40	0.37	0.18	0.41	0.31	0.25	0.18
Dy_2O_3	0.00	0.00	0.00	0.00	0.00	0.00	0.00	0.00	0.00	0.00	0.00
Y_2O_3	0.13	0.19	0.26	0.26	0.27	0.25	0.40	0.23	0.27	0.23	0.22
Ho_2O_3	0.00	0.00	0.00	0.00	0.00	0.00	0.00	0.00	0.00	0.00	0.00
ThO_2	0.08	0.19	0.10	0.11	0.15	0.23	0.13	0.30	0.22	0.27	0.29
CaO	0.05	0.11	0.14	0.00	0.06	0.10	0.10	0.15	0.17	0.21	0.14
F	7.79	8.52	8.21	8.26	8.14	8.19	7.99	7.97	8.17	7.99	8.16
Cl	0.00	0.00	0.00	0.00	0.00	0.00	0.00	0.00	0.00	0.00	0.00
SiO_2	0.35	0.30	0.26	0.26	0.23	0.28	0.25	0.31	0.22	0.25	0.25
PbO	0.00	0.09	0.00	0.00	0.00	0.07	0.07	0.00	0.07	0.00	0.00
FeO	0.00	0.00	0.00	0.00	0.00	0.00	0.00	0.00	0.00	0.00	0.00
SrO	0.00	0.00	0.00	0.00	0.00	0.00	0.00	0.00	0.00	0.00	0.09
O=F	-3.28	-3.59	-3.46	-3.48	-3.43	-3.45	-3.36	-3.36	-3.44	-3.36	-3.44
CO_2	17.80	19.59	20.22	20.21	19.08	19.55	19.19	18.31	19.11	18.27	20.27
Total	100.00	100.00	100.00	100.00	100.00	100.00	100.00	100.00	100.00	100.00	100.00
						O = 4					
La	0.371	0.352	0.367	0.342	0.359	0.328	0.334	0.371	0.357	0.339	0.306
Ce	0.527	0.475	0.462	0.477	0.492	0.485	0.492	0.500	0.487	0.526	0.489
Pr	0.045	0.041	0.037	0.040	0.041	0.044	0.044	0.042	0.041	0.045	0.046
Nd	0.108	0.101	0.094	0.105	0.107	0.120	0.125	0.108	0.107	0.114	0.114
Sm	0.007	0.007	0.006	0.005	0.006	0.007	0.008	0.007	0.008	0.010	0.009
Eu	0.002	0.002	0.002	0.002	0.002	0.002	0.002	0.002	0.002	0.002	0.002
Gd	0.004	0.005	0.003	0.003	0.005	0.004	0.002	0.005	0.004	0.003	0.002
Dy	0.000	0.000	0.000	0.000	0.000	0.000	0.000	0.000	0.000	0.000	0.000
Y	0.003	0.004	0.005	0.005	0.005	0.005	0.008	0.005	0.005	0.004	0.004
Ho	0.000	0.000	0.000	0.000	0.000	0.000	0.000	0.000	0.000	0.000	0.000
Th	0.001	0.002	0.001	0.001	0.001	0.002	0.001	0.003	0.002	0.002	0.002
Ca	0.002	0.004	0.005	0.000	0.002	0.004	0.004	0.006	0.007	0.008	0.005
F	0.929	0.971	0.928	0.934	0.943	0.939	0.925	0.939	0.945	0.942	0.923
Cl	0.000	0.000	0.000	0.000	0.000	0.000	0.000	0.000	0.000	0.000	0.000
Si	0.013	0.011	0.009	0.009	0.008	0.010	0.009	0.011	0.008	0.009	0.009
Pb	0.000	0.001	0.000	0.000	0.000	0.001	0.001	0.000	0.001	0.000	0.000
Fe	0.000	0.000	0.000	0.000	0.000	0.000	0.000	0.000	0.000	0.000	0.000
Sr	0.000	0.000	0.000	0.000	0.000	0.000	0.000	0.000	0.000	0.000	0.002
C	0.917	0.964	0.987	0.986	0.954	0.967	0.959	0.931	0.955	0.930	0.989
Total	1.999	1.968	1.978	1.974	1.982	1.979	1.988	1.991	1.983	1.992	1.979

CO_2 calculated from the difference between the analytical total and 100 wt. %

Appendix 2.8: Continued

Unit						**B**					
Sample	15141	15141	15141	15141	15141	15141	15141	15141	15141	15141	15141
La_2O_3 (*wt %*)	26.03	26.66	25.01	25.91	24.80	25.81	26.89	26.80	26.93	26.33	26.15
Ce_2O_3	35.76	35.72	36.15	36.48	35.45	37.37	36.81	36.81	36.41	36.96	37.16
Pr_2O_3	3.09	3.15	3.38	3.26	3.29	3.16	3.19	3.06	3.10	3.15	3.14
Nd_2O_3	8.42	8.40	8.32	8.26	8.51	8.06	7.80	7.96	7.73	7.95	8.00
Sm_2O_3	0.62	0.73	0.58	0.48	0.52	0.55	0.55	0.51	0.56	0.61	0.57
Eu_2O_3	0.14	0.14	0.14	0.14	0.14	0.14	0.14	0.14	0.14	0.14	0.14
Gd_2O_3	0.44	0.38	0.27	0.35	0.23	0.40	0.29	0.29	0.18	0.31	0.34
Dy_2O_3	0.00	0.00	0.00	0.00	0.00	0.00	0.00	0.00	0.00	0.00	0.00
Y_2O_3	0.19	0.16	0.21	0.20	0.22	0.18	0.26	0.19	0.31	0.25	0.16
Ho_2O_3	0.00	0.00	0.00	0.00	0.00	0.00	0.00	0.00	0.00	0.00	0.00
ThO_2	0.35	0.35	0.16	0.08	0.13	0.12	0.00	0.10	0.18	0.11	0.15
CaO	0.14	0.37	0.06	0.04	0.00	0.05	0.42	0.45	0.14	0.44	0.07
F	8.19	8.08	8.50	8.21	8.17	8.13	8.19	8.06	8.07	8.08	8.21
Cl	0.00	0.00	0.00	0.00	0.00	0.00	0.00	0.00	0.00	0.00	0.00
SiO_2	0.22	0.28	0.20	0.23	0.31	0.27	0.26	0.16	0.26	0.23	0.31
PbO	0.00	0.00	0.00	0.00	0.00	0.00	0.00	0.00	0.00	0.00	0.00
FeO	0.00	0.00	0.00	0.00	0.00	0.00	0.00	0.00	0.00	0.00	0.00
SrO	0.08	0.14	0.07	0.09	0.11	0.00	0.00	0.00	0.00	0.00	0.00
O=F	-3.45	-3.40	-3.58	-3.45	-3.44	-3.42	-3.45	-3.39	-3.40	-3.40	-3.46
CO_2	19.79	18.85	20.53	19.72	21.56	19.20	18.66	18.87	19.40	18.84	19.05
Total	100.00	100.00	100.00	100.00	100.00	100.00	100.00	100.00	100.00	100.00	100.00
						O = 4					
La (*apfu)*	0.347	0.361	0.327	0.345	0.319	0.348	0.365	0.364	0.361	0.357	0.353
Ce	0.473	0.481	0.469	0.483	0.452	0.500	0.496	0.496	0.485	0.497	0.498
Pr	0.041	0.042	0.044	0.043	0.042	0.042	0.043	0.041	0.041	0.042	0.042
Nd	0.109	0.110	0.105	0.107	0.106	0.105	0.103	0.105	0.100	0.104	0.105
Sm	0.008	0.009	0.007	0.006	0.006	0.007	0.007	0.006	0.007	0.008	0.007
Eu	0.002	0.002	0.002	0.002	0.002	0.002	0.002	0.002	0.002	0.002	0.002
Gd	0.005	0.005	0.003	0.004	0.003	0.005	0.003	0.003	0.002	0.004	0.004
Dy	0.000	0.000	0.000	0.000	0.000	0.000	0.000	0.000	0.000	0.000	0.000
Y	0.004	0.003	0.004	0.004	0.004	0.003	0.005	0.004	0.006	0.005	0.003
Ho	0.000	0.000	0.000	0.000	0.000	0.000	0.000	0.000	0.000	0.000	0.000
Th	0.003	0.003	0.001	0.001	0.001	0.001	0.000	0.001	0.001	0.001	0.001
Ca	0.005	0.015	0.002	0.002	0.000	0.002	0.017	0.018	0.005	0.017	0.003
F	0.935	0.939	0.953	0.938	0.901	0.940	0.954	0.938	0.929	0.940	0.950
Cl	0.000	0.000	0.000	0.000	0.000	0.000	0.000	0.000	0.000	0.000	0.000
Si	0.008	0.010	0.007	0.008	0.011	0.010	0.010	0.006	0.009	0.008	0.011
Pb	0.000	0.000	0.000	0.000	0.000	0.000	0.000	0.000	0.000	0.000	0.000
Fe	0.000	0.000	0.000	0.000	0.000	0.000	0.000	0.000	0.000	0.000	0.000
Sr	0.002	0.003	0.002	0.002	0.002	0.000	0.000	0.000	0.000	0.000	0.000
C	0.975	0.946	0.993	0.973	1.026	0.957	0.938	0.948	0.964	0.946	0.951
Total	1.979	1.990	1.966	1.979	1.974	1.982	1.988	1.992	1.985	1.991	1.980

CO_2 calculated from the difference between the analytical total and 100 wt. %

Appendix 2.8: Continued

Unit	**B**	**BD**									
Sample	15141	15113	15113	15114	15114	15114	15114	15114	15114	15114	15114
La_2O_3 (*wt %*)	27.25	15.69	16.96	15.68	15.61	15.84	15.92	17.34	15.22	14.96	17.09
Ce_2O_3	37.75	37.70	37.05	37.71	35.85	37.93	36.46	37.00	37.90	38.79	37.93
Pr_2O_3	3.06	4.38	4.47	4.49	4.52	4.47	4.34	4.09	4.42	4.70	4.30
Nd_2O_3	7.80	12.93	12.67	13.03	14.17	13.53	12.99	12.42	13.83	14.28	12.31
Sm_2O_3	0.52	0.85	0.82	1.09	1.25	1.12	0.99	0.95	1.19	1.19	0.79
Eu_2O_3	0.14	0.14	0.14	0.14	0.14	0.14	0.14	0.14	0.14	0.14	0.14
Gd_2O_3	0.19	0.30	0.50	0.34	0.50	0.40	0.00	0.33	0.49	0.51	0.39
Dy_2O_3	0.00	0.00	0.00	0.00	0.00	0.00	0.00	0.00	0.00	0.00	0.00
Y_2O_3	0.18	0.13	0.00	0.18	0.22	0.25	0.26	0.13	0.20	0.28	0.15
Ho_2O_3	0.00	0.00	0.00	0.00	0.00	0.00	0.00	0.00	0.00	0.00	0.00
ThO_2	0.15	1.25	1.25	0.49	0.74	0.65	0.44	0.47	0.68	0.71	0.35
CaO	0.10	0.61	0.25	0.87	0.69	0.13	0.60	0.48	0.29	0.25	0.83
F	8.16	8.08	8.16	7.91	8.01	8.04	8.22	8.12	7.35	7.84	8.15
Cl	0.00	0.00	0.00	0.02	0.00	0.00	0.00	0.00	0.00	0.00	0.00
SiO_2	0.22	0.38	0.28	0.30	0.35	0.34	0.35	0.43	0.55	0.35	0.33
PbO	0.08	0.10	0.12	0.00	0.00	0.08	0.00	0.00	0.09	0.00	0.00
FeO	0.00	0.00	0.00	0.72	0.34	0.00	0.00	0.25	0.00	0.00	0.44
SrO	0.00	0.17	0.12	0.08	0.07	0.12	0.08	0.13	0.00	0.00	0.00
O=F	-3.44	-3.40	-3.44	-3.33	-3.37	-3.38	-3.46	-3.42	-3.10	-3.30	-3.43
CO_2	17.86	20.69	20.64	20.28	20.91	20.35	22.68	21.15	20.74	19.31	20.22
Total	100.00	100.00	100.00	100.00	100.00	100.00	100.00	100.00	100.00	100.00	100.00
						O = 4					
La (*apfu)*	0.377	0.205	0.222	0.206	0.203	0.209	0.200	0.224	0.200	0.202	0.225
Ce	0.519	0.489	0.482	0.493	0.463	0.497	0.454	0.475	0.496	0.520	0.495
Pr	0.042	0.057	0.058	0.058	0.058	0.058	0.054	0.052	0.058	0.063	0.056
Nd	0.105	0.164	0.161	0.166	0.178	0.173	0.158	0.155	0.176	0.187	0.157
Sm	0.007	0.010	0.010	0.013	0.015	0.014	0.012	0.011	0.015	0.015	0.010
Eu	0.002	0.002	0.002	0.002	0.002	0.002	0.002	0.002	0.002	0.002	0.002
Gd	0.002	0.004	0.006	0.004	0.006	0.005	0.000	0.004	0.006	0.006	0.005
Dy	0.000	0.000	0.000	0.000	0.000	0.000	0.000	0.000	0.000	0.000	0.000
Y	0.004	0.002	0.000	0.003	0.004	0.005	0.005	0.002	0.004	0.006	0.003
Ho	0.000	0.000	0.000	0.000	0.000	0.000	0.000	0.000	0.000	0.000	0.000
Th	0.001	0.010	0.010	0.004	0.006	0.005	0.003	0.004	0.006	0.006	0.003
Ca	0.004	0.023	0.009	0.033	0.026	0.005	0.022	0.018	0.011	0.010	0.032
F	0.969	0.906	0.918	0.894	0.894	0.909	0.885	0.900	0.830	0.908	0.919
Cl	0.000	0.000	0.000	0.000	0.000	0.000	0.000	0.000	0.000	0.000	0.000
Si	0.008	0.013	0.010	0.011	0.012	0.012	0.012	0.015	0.020	0.013	0.012
Pb	0.001	0.001	0.001	0.000	0.000	0.001	0.000	0.000	0.001	0.000	0.000
Fe	0.000	0.000	0.000	0.021	0.010	0.000	0.000	0.007	0.000	0.000	0.013
Sr	0.000	0.003	0.002	0.002	0.001	0.002	0.002	0.003	0.000	0.000	0.000
C	0.915	1.001	1.002	0.988	1.007	0.994	1.054	1.012	1.011	0.965	0.984
Total	1.986	1.985	1.976	2.006	1.992	1.981	1.977	1.985	2.005	1.992	1.994

CO_2 calculated from the difference between the analytical total and 100 wt. %

Appendix 2.8: Continued

Unit	**BD**										
Sample	15114	15114	15114	15115	15115	15115	15115	15115	15115	15115	15115
La_2O_3 (*wt %*)	16.21	15.63	14.76	15.06	14.15	14.25	13.96	14.53	14.12	13.49	13.30
Ce_2O_3	36.65	37.65	36.77	37.51	35.81	36.42	36.97	36.27	35.09	35.97	35.11
Pr_2O_3	4.38	4.65	4.55	4.74	4.96	4.76	4.87	4.68	4.71	4.78	5.02
Nd_2O_3	13.16	14.12	13.99	14.17	14.77	14.24	14.67	14.26	14.57	15.43	15.54
Sm_2O_3	1.11	1.14	1.36	0.99	1.09	1.00	1.17	1.01	1.25	1.31	1.48
Eu_2O_3	0.14	0.14	0.14	0.14	0.14	0.14	0.14	0.14	0.14	0.14	0.14
Gd_2O_3	0.77	0.46	0.65	0.50	0.46	0.37	0.40	0.37	0.41	0.31	0.48
Dy_2O_3	0.00	0.00	0.00	0.00	0.00	0.00	0.00	0.00	0.00	0.00	0.00
Y_2O_3	0.14	0.22	0.27	0.16	0.27	0.34	0.22	0.22	0.24	0.21	0.29
Ho_2O_3	0.00	0.00	0.00	0.00	0.00	0.00	0.00	0.00	0.00	0.00	0.00
ThO_2	0.71	0.81	1.05	0.23	0.46	0.25	0.54	0.25	0.48	0.62	0.86
CaO	0.29	0.58	0.59	0.31	0.44	0.77	0.41	0.67	1.17	0.37	0.34
F	7.99	7.56	8.00	8.25	8.22	8.51	8.03	8.27	8.53	8.17	8.39
Cl	0.00	0.00	0.00	0.00	0.00	0.00	0.00	0.00	0.00	0.00	0.00
SiO_2	0.36	0.32	0.39	0.33	0.30	0.31	0.26	0.24	0.29	0.29	0.32
PbO	0.10	0.07	0.12	0.00	0.00	0.00	0.00	0.08	0.00	0.08	0.11
FeO	0.00	0.00	0.38	0.00	0.25	0.19	0.00	0.33	0.25	0.00	0.00
SrO	0.00	0.00	0.12	0.00	0.00	0.00	0.00	0.00	0.00	0.00	0.00
O=F	-3.36	-3.18	-3.37	-3.47	-3.46	-3.58	-3.38	-3.48	-3.59	-3.44	-3.53
CO_2	21.36	19.84	20.24	21.09	22.17	22.05	21.73	22.17	22.35	22.27	22.15
Total	100.00	100.00	100.00	100.00	100.00	100.00	100.00	100.00	100.00	100.00	100.00
	O = 4										
La (*apfu*)	0.210	0.209	0.195	0.195	0.180	0.180	0.179	0.184	0.177	0.171	0.169
Ce	0.471	0.501	0.481	0.482	0.451	0.457	0.471	0.456	0.437	0.453	0.442
Pr	0.056	0.061	0.059	0.061	0.062	0.059	0.062	0.059	0.058	0.060	0.063
Nd	0.165	0.183	0.179	0.178	0.181	0.174	0.183	0.175	0.177	0.190	0.191
Sm	0.013	0.014	0.017	0.012	0.013	0.012	0.014	0.012	0.015	0.016	0.018
Eu	0.002	0.002	0.002	0.002	0.002	0.002	0.002	0.002	0.002	0.002	0.002
Gd	0.009	0.006	0.008	0.006	0.005	0.004	0.005	0.004	0.005	0.004	0.006
Dy	0.000	0.000	0.000	0.000	0.000	0.000	0.000	0.000	0.000	0.000	0.000
Y	0.003	0.004	0.005	0.003	0.005	0.006	0.004	0.004	0.004	0.004	0.005
Ho	0.000	0.000	0.000	0.000	0.000	0.000	0.000	0.000	0.000	0.000	0.000
Th	0.006	0.007	0.009	0.002	0.004	0.002	0.004	0.002	0.004	0.005	0.007
Ca	0.011	0.022	0.023	0.012	0.016	0.028	0.015	0.025	0.043	0.014	0.012
F	0.887	0.868	0.905	0.916	0.894	0.923	0.884	0.899	0.918	0.889	0.913
Cl	0.000	0.000	0.000	0.000	0.000	0.000	0.000	0.000	0.000	0.000	0.000
Si	0.013	0.012	0.014	0.012	0.010	0.011	0.009	0.008	0.010	0.010	0.011
Pb	0.001	0.001	0.001	0.000	0.000	0.000	0.000	0.001	0.000	0.001	0.001
Fe	0.000	0.000	0.011	0.000	0.007	0.005	0.000	0.009	0.007	0.000	0.000
Sr	0.000	0.000	0.003	0.000	0.000	0.000	0.000	0.000	0.000	0.000	0.000
C	1.023	0.984	0.988	1.012	1.041	1.032	1.033	1.040	1.039	1.047	1.040
Total	1.981	2.006	1.993	1.975	1.978	1.973	1.982	1.981	1.978	1.975	1.966

CO_2 calculated from the difference between the analytical total and 100 wt. %

Appendix 2.8: Continued

Unit						**BD**					
Sample	15115	15115	15115	15115	15115	15115	15115	15115	15115	15115	15115
La_2O_3 (*wt %*)	14.07	14.06	14.04	14.48	15.26	13.77	13.98	13.79	13.62	14.16	13.82
Ce_2O_3	35.28	36.00	36.03	35.22	35.59	35.20	35.13	35.87	35.92	35.08	35.79
Pr_2O_3	4.79	4.69	4.55	4.66	4.57	4.35	4.70	4.83	4.65	4.66	4.79
Nd_2O_3	14.49	14.81	14.38	14.07	13.58	13.70	14.17	14.72	14.61	14.25	14.65
Sm_2O_3	1.40	1.64	1.38	1.41	1.35	1.21	1.31	1.38	1.24	1.41	1.52
Eu_2O_3	0.18	0.22	0.25	0.14	0.14	0.14	0.14	0.14	0.20	0.14	0.19
Gd_2O_3	0.66	0.64	0.54	0.47	0.50	0.53	0.66	0.43	0.43	0.69	0.91
Dy_2O_3	0.00	0.00	0.00	0.00	0.00	0.20	0.00	0.00	0.00	0.00	0.00
Y_2O_3	0.24	0.24	0.31	0.21	0.33	0.44	0.34	0.21	0.20	0.39	0.37
Ho_2O_3	0.00	0.00	0.00	0.00	0.00	0.00	0.00	0.00	0.00	0.00	0.00
ThO_2	0.92	0.95	0.90	0.85	0.98	0.88	1.03	1.00	0.84	0.85	0.85
CaO	0.51	0.64	0.62	0.93	0.54	0.83	0.72	0.60	0.93	0.63	0.38
F	8.07	8.00	7.84	8.42	7.94	7.99	8.31	7.93	8.29	8.02	7.94
Cl	0.00	0.00	0.00	0.00	0.00	0.02	0.00	0.02	0.00	0.00	0.00
SiO_2	0.30	0.24	0.28	0.30	0.25	0.29	0.29	0.34	0.28	0.34	0.30
PbO	0.13	0.07	0.00	0.16	0.00	0.00	0.09	0.07	0.00	0.07	0.08
FeO	0.19	0.00	0.00	0.37	0.00	1.16	0.18	0.26	0.41	0.00	0.00
SrO	0.10	0.08	0.14	0.00	0.00	0.10	0.00	0.07	0.07	0.08	0.09
O=F	-3.40	-3.37	-3.30	-3.54	-3.34	-3.36	-3.50	-3.34	-3.49	-3.38	-3.34
CO_2	22.09	21.08	22.05	21.84	22.31	22.56	22.45	21.68	21.82	22.61	21.65
Total	100.00	100.00	100.00	100.00	100.00	100.00	100.00	100.00	100.00	100.00	100.00
						O = 4					
La (*apfu)*	0.179	0.183	0.179	0.184	0.194	0.173	0.176	0.177	0.173	0.179	0.178
Ce	0.446	0.465	0.457	0.445	0.449	0.440	0.440	0.458	0.454	0.439	0.458
Pr	0.060	0.060	0.058	0.059	0.057	0.054	0.059	0.061	0.058	0.058	0.061
Nd	0.179	0.187	0.178	0.173	0.167	0.167	0.173	0.183	0.180	0.174	0.183
Sm	0.017	0.020	0.016	0.017	0.016	0.014	0.015	0.017	0.015	0.017	0.018
Eu	0.002	0.003	0.003	0.002	0.002	0.002	0.002	0.002	0.002	0.002	0.002
Gd	0.008	0.008	0.006	0.005	0.006	0.006	0.008	0.005	0.005	0.008	0.011
Dy	0.000	0.000	0.000	0.000	0.000	0.002	0.000	0.000	0.000	0.000	0.000
Y	0.004	0.005	0.006	0.004	0.006	0.008	0.006	0.004	0.004	0.007	0.007
Ho	0.000	0.000	0.000	0.000	0.000	0.000	0.000	0.000	0.000	0.000	0.000
Th	0.007	0.008	0.007	0.007	0.008	0.007	0.008	0.008	0.007	0.007	0.007
Ca	0.019	0.024	0.023	0.034	0.020	0.030	0.026	0.022	0.034	0.023	0.014
F	0.882	0.893	0.860	0.918	0.865	0.862	0.899	0.874	0.905	0.867	0.877
Cl	0.000	0.000	0.000	0.000	0.000	0.000	0.000	0.000	0.000	0.000	0.000
Si	0.010	0.009	0.010	0.010	0.009	0.010	0.010	0.012	0.010	0.012	0.011
Pb	0.001	0.001	0.000	0.002	0.000	0.000	0.001	0.001	0.000	0.001	0.001
Fe	0.005	0.000	0.000	0.011	0.000	0.033	0.005	0.008	0.012	0.000	0.000
Sr	0.002	0.002	0.003	0.000	0.000	0.002	0.000	0.001	0.001	0.002	0.002
C	1.042	1.015	1.044	1.028	1.050	1.051	1.047	1.032	1.029	1.056	1.032
Total	1.982	1.987	1.990	1.980	1.984	2.000	1.976	1.990	1.985	1.982	1.984

CO_2 calculated from the difference between the analytical total and 100 wt. %

Appendix 2.8: Continued

Unit	**BD**				**A**						
Sample	15116	15116	15116	15116	15004	15004	15004	15004	15020	16007	16007
La_2O_3 (*wt %*)	16.41	15.90	15.42	16.03	23.36	23.67	22.97	23.77	28.80	20.98	19.83
Ce_2O_3	39.42	39.81	38.07	39.34	34.77	34.85	33.94	34.90	32.69	35.42	35.82
Pr_2O_3	4.43	4.37	4.39	4.58	3.29	3.40	3.24	3.30	2.75	3.53	3.66
Nd_2O_3	12.94	12.57	13.28	13.24	9.26	9.36	8.92	9.04	7.52	12.35	12.32
Sm_2O_3	0.87	0.85	0.95	0.91	0.89	1.04	0.94	0.96	0.61	0.93	0.89
Eu_2O_3	0.14	0.14	0.14	0.14	0.14	0.14	0.14	0.14	0.14	0.14	0.14
Gd_2O_3	0.39	0.51	0.35	0.35	0.40	0.64	0.56	0.46	0.57	0.51	0.56
Dy_2O_3	0.00	0.00	0.00	0.00	0.00	0.00	0.00	0.00	0.00	0.00	0.23
Y_2O_3	0.28	0.23	0.34	0.27	0.28	0.40	0.31	0.37	0.46	0.50	0.60
Ho_2O_3	0.00	0.00	0.00	0.00	0.00	0.00	0.00	0.00	0.00	0.00	0.00
ThO_2	0.32	0.51	0.65	0.72	0.64	0.53	0.70	0.68	0.34	0.96	0.95
CaO	0.11	0.33	0.89	0.38	1.20	0.79	2.86	0.89	0.28	0.20	0.21
F	7.79	8.35	8.15	7.72	8.95	8.43	8.82	8.86	8.33	8.01	7.94
Cl	0.00	0.00	0.00	0.00	0.00	0.00	0.00	0.00	0.00	0.02	0.00
SiO_2	0.35	0.38	0.34	0.33	0.00	0.12	0.00	0.00	0.00	0.12	0.12
PbO	0.08	0.00	0.00	0.00	0.07	0.00	0.10	0.00	0.10	0.08	0.00
FeO	0.00	0.00	0.32	0.00	0.00	0.00	0.00	0.00	0.00	0.00	0.00
SrO	0.00	0.00	0.00	0.00	0.08	0.00	0.16	0.16	0.00	0.15	0.17
O=F	-3.28	-3.52	-3.43	-3.25	-3.77	-3.55	-3.71	-3.73	-3.51	-3.37	-3.34
CO_2	19.77	19.57	20.15	19.25	20.44	20.18	20.05	20.21	20.92	19.50	19.91
Total	100.00	100.00	100.00	100.00	100.00	100.00	100.00	100.00	100.00	100.00	100.00
						O = 4					
La (*apfu)*	0.220	0.212	0.203	0.217	0.304	0.311	0.299	0.311	0.375	0.282	0.265
Ce	0.524	0.526	0.497	0.528	0.448	0.455	0.438	0.453	0.422	0.473	0.475
Pr	0.059	0.057	0.057	0.061	0.042	0.044	0.042	0.043	0.035	0.047	0.048
Nd	0.168	0.162	0.169	0.173	0.116	0.119	0.112	0.114	0.095	0.161	0.159
Sm	0.011	0.011	0.012	0.011	0.011	0.013	0.011	0.012	0.007	0.012	0.011
Eu	0.002	0.002	0.002	0.002	0.002	0.002	0.002	0.002	0.002	0.002	0.002
Gd	0.005	0.006	0.004	0.004	0.005	0.008	0.007	0.005	0.007	0.006	0.007
Dy	0.000	0.000	0.000	0.000	0.000	0.000	0.000	0.000	0.000	0.000	0.003
Y	0.005	0.004	0.006	0.005	0.005	0.008	0.006	0.007	0.009	0.010	0.011
Ho	0.000	0.000	0.000	0.000	0.000	0.000	0.000	0.000	0.000	0.000	0.000
Th	0.003	0.004	0.005	0.006	0.005	0.004	0.006	0.005	0.003	0.008	0.008
Ca	0.004	0.013	0.034	0.015	0.045	0.030	0.108	0.034	0.010	0.008	0.008
F	0.894	0.954	0.919	0.895	0.996	0.950	0.984	0.994	0.930	0.924	0.909
Cl	0.000	0.000	0.000	0.000	0.000	0.000	0.000	0.000	0.000	0.000	0.000
Si	0.013	0.014	0.012	0.012	0.000	0.004	0.000	0.000	0.000	0.005	0.004
Pb	0.001	0.000	0.000	0.000	0.001	0.000	0.001	0.000	0.001	0.001	0.000
Fe	0.000	0.000	0.010	0.000	0.000	0.000	0.000	0.000	0.000	0.000	0.000
Sr	0.000	0.000	0.000	0.000	0.002	0.000	0.003	0.003	0.000	0.003	0.003
C	0.980	0.965	0.982	0.964	0.983	0.982	0.966	0.978	1.008	0.971	0.984
Total	1.992	1.975	1.993	1.999	1.969	1.980	2.001	1.967	1.974	1.986	1.988

CO_2 calculated from the difference between the analytical total and 100 wt. %

Appendix 2.8: Continued

Unit	**A**		**MHREO**								
Sample	16007	16007	15002	15002	15002	15002	15002	15002	15002	15002	15002
La_2O_3 (*wt %*)	20.69	20.47	18.05	17.83	17.85	18.23	18.96	18.10	18.75	18.96	19.01
Ce_2O_3	35.99	34.85	34.80	33.93	33.78	34.39	34.81	34.55	34.47	34.82	35.15
Pr_2O_3	3.83	3.67	3.93	3.76	3.99	3.89	3.81	3.91	3.78	3.94	3.90
Nd_2O_3	12.22	12.32	11.55	11.53	11.35	11.48	11.19	11.20	11.06	11.26	11.36
Sm_2O_3	1.03	1.02	1.19	1.30	1.33	1.29	1.17	1.17	1.18	1.27	1.23
Eu_2O_3	0.14	0.14	0.14	0.19	0.14	0.19	0.14	0.14	0.14	0.14	0.14
Gd_2O_3	0.70	0.48	0.68	0.71	0.80	0.74	0.62	0.69	0.80	0.65	0.69
Dy_2O_3	0.00	0.00	0.00	0.00	0.00	0.00	0.00	0.00	0.21	0.00	0.00
Y_2O_3	0.37	0.60	0.49	0.45	0.44	0.49	0.42	0.50	0.27	0.45	0.41
Ho_2O_3	0.00	0.00	0.00	0.00	0.00	0.00	0.00	0.00	0.00	0.00	0.00
ThO_2	0.97	0.81	2.03	1.34	1.28	1.86	2.21	2.34	2.23	1.34	1.49
CaO	0.20	0.69	1.13	2.73	1.92	0.88	0.47	1.38	0.52	0.38	0.44
F	7.61	7.88	7.97	7.76	7.87	7.83	7.99	8.38	8.19	8.09	8.53
Cl	0.00	0.00	0.02	0.06	0.00	0.00	0.00	0.00	0.00	0.03	0.00
SiO_2	0.14	0.00	0.00	0.00	0.00	0.00	0.00	0.00	0.14	0.12	0.11
PbO	0.12	0.13	0.20	0.00	0.08	0.16	0.27	0.10	0.28	0.10	0.10
FeO	0.00	0.30	0.29	0.95	0.83	0.89	0.00	0.32	0.00	0.00	0.24
SrO	0.13	0.12	0.23	0.22	0.18	0.19	0.32	0.34	0.36	0.27	0.27
O=F	-3.20	-3.32	-3.36	-3.27	-3.31	-3.30	-3.36	-3.53	-3.45	-3.41	-3.59
CO_2	19.07	19.83	20.67	20.51	21.49	20.78	20.98	20.42	21.08	21.61	20.53
Total	100.00	100.00	100.00	100.00	100.00	100.00	100.00	100.00	100.00	100.00	100.00
						O = 4					
La (*apfu)*	0.282	0.273	0.237	0.233	0.230	0.239	0.248	0.237	0.244	0.244	0.249
Ce	0.487	0.462	0.453	0.440	0.431	0.447	0.452	0.449	0.445	0.446	0.456
Pr	0.052	0.048	0.051	0.049	0.051	0.050	0.049	0.051	0.049	0.050	0.050
Nd	0.161	0.159	0.147	0.146	0.141	0.146	0.142	0.142	0.139	0.141	0.144
Sm	0.013	0.013	0.015	0.016	0.016	0.016	0.014	0.014	0.014	0.015	0.015
Eu	0.002	0.002	0.002	0.002	0.002	0.002	0.002	0.002	0.002	0.002	0.002
Gd	0.009	0.006	0.008	0.008	0.009	0.009	0.007	0.008	0.009	0.008	0.008
Dy	0.000	0.000	0.000	0.000	0.000	0.000	0.000	0.000	0.002	0.000	0.000
Y	0.007	0.011	0.009	0.008	0.008	0.009	0.008	0.009	0.005	0.008	0.008
Ho	0.000	0.000	0.000	0.000	0.000	0.000	0.000	0.000	0.000	0.000	0.000
Th	0.008	0.007	0.016	0.011	0.010	0.015	0.018	0.019	0.018	0.011	0.012
Ca	0.008	0.027	0.043	0.103	0.072	0.033	0.018	0.053	0.020	0.014	0.017
F	0.890	0.903	0.897	0.869	0.868	0.880	0.897	0.941	0.914	0.894	0.956
Cl	0.000	0.000	0.000	0.000	0.000	0.000	0.000	0.000	0.000	0.000	0.000
Si	0.005	0.000	0.000	0.000	0.000	0.000	0.000	0.000	0.005	0.004	0.004
Pb	0.001	0.001	0.002	0.000	0.001	0.002	0.003	0.001	0.003	0.001	0.001
Fe	0.000	0.009	0.009	0.028	0.024	0.027	0.000	0.009	0.000	0.000	0.007
Sr	0.003	0.003	0.005	0.005	0.004	0.004	0.007	0.007	0.007	0.005	0.006
C	0.963	0.981	1.004	0.992	1.023	1.008	1.017	0.990	1.015	1.031	0.994
Total	2.002	2.002	2.000	2.042	2.021	2.008	1.985	1.991	1.978	1.980	1.971

CO_2 calculated from the difference between the analytical total and 100 wt. %

Appendix 2.9: Major element oxide compositions and cation proportions of xenotime-(Y) in the different units of the Ashram deposit

Unit	**MHREO**										
Sample	15013	15013	15013	15013	15013	15013	15013	15013	15013	15013	15014
Nd_2O_3 (*wt. %*)	0.00	1.48	0.00	0.00	0.26	0.65	0.00	0.37	0.29	0.31	0.26
Sm_2O_3	1.41	1.43	1.52	1.05	1.52	1.28	1.34	1.32	1.64	0.84	1.21
Eu_2O_3	1.15	0.88	1.04	0.68	1.02	0.84	0.82	0.97	1.03	0.65	1.06
Gd_2O_3	6.45	5.17	6.21	5.67	6.65	5.86	6.27	5.97	5.98	4.72	5.68
Tb_2O_3	1.69	1.20	1.56	1.55	1.63	1.46	1.42	1.17	1.49	1.12	1.41
Dy_2O_3	11.74	7.58	10.38	11.18	10.70	9.82	10.86	7.66	9.17	7.73	9.63
Y_2O_3	32.51	35.62	34.40	35.00	34.99	35.46	33.86	40.11	35.95	39.28	35.88
Ho_2O_3	1.79	1.37	1.72	1.93	1.77	1.66	1.82	1.12	1.45	1.45	1.63
Er_2O_3	4.03	2.95	3.56	3.98	3.51	3.62	3.96	2.51	3.21	3.14	3.49
Tm_2O_3	0.51	0.43	0.41	0.50	0.44	0.51	0.53	0.33	0.41	0.42	0.41
Yb_2O_3	2.42	1.78	2.07	2.51	2.32	2.29	2.49	1.46	2.15	2.16	2.15
Lu_2O_3	0.25	0.19	0.21	0.26	0.21	0.28	0.24	0.17	0.28	0.18	0.22
ThO_2	0.30	1.36	0.78	0.00	0.00	1.01	0.56	0.53	1.28	0.00	0.26
UO_2	0.00	0.00	0.00	0.00	0.00	0.00	0.00	0.00	0.00	0.00	0.00
CaO	0.19	0.27	0.03	0.00	0.00	0.15	0.00	0.07	0.20	0.36	0.16
P_2O_5	35.56	34.25	34.58	35.54	34.28	35.22	35.12	35.00	34.96	37.08	36.52
F	0.41	0.38	0.30	0.47	0.42	0.41	0.29	0.45	0.35	0.49	0.44
SiO_2	0.00	0.37	0.12	0.00	0.00	0.23	0.00	0.92	0.24	0.00	0.00
PbO	0.00	0.00	0.00	0.00	0.00	0.00	0.00	0.00	0.00	0.00	0.00
FeO	0.37	1.29	1.63	0.20	0.00	0.18	0.00	0.11	0.36	0.42	0.23
-O=F	-0.17	-0.16	-0.12	-0.20	-0.18	-0.17	-0.12	-0.19	-0.15	-0.21	-0.18
Total	100.61	97.81	100.39	100.30	99.54	100.77	99.47	100.06	100.28	100.13	100.44
	O = 4										
Nd (*apfu*)	0.000	0.018	0.000	0.000	0.003	0.008	0.000	0.004	0.004	0.004	0.003
Sm	0.016	0.017	0.018	0.012	0.018	0.015	0.016	0.015	0.019	0.009	0.014
Eu	0.013	0.010	0.012	0.008	0.012	0.010	0.010	0.011	0.012	0.007	0.012
Gd	0.073	0.059	0.070	0.064	0.076	0.066	0.071	0.066	0.067	0.051	0.063
Tb	0.019	0.014	0.017	0.017	0.019	0.016	0.016	0.013	0.017	0.012	0.015
Dy	0.128	0.084	0.114	0.122	0.119	0.107	0.120	0.082	0.100	0.081	0.103
Y	0.587	0.652	0.625	0.630	0.643	0.637	0.618	0.709	0.648	0.683	0.634
Ho	0.019	0.015	0.019	0.021	0.019	0.018	0.020	0.012	0.016	0.015	0.017
Er	0.043	0.032	0.038	0.042	0.038	0.038	0.043	0.026	0.034	0.032	0.036
Tm	0.005	0.005	0.004	0.005	0.005	0.005	0.006	0.003	0.004	0.004	0.004
Yb	0.025	0.019	0.022	0.026	0.024	0.024	0.026	0.015	0.022	0.021	0.022
Lu	0.003	0.002	0.002	0.003	0.002	0.003	0.002	0.002	0.003	0.002	0.002
Th	0.002	0.011	0.006	0.000	0.000	0.008	0.004	0.004	0.010	0.000	0.002
U	0.000	0.000	0.000	0.000	0.000	0.000	0.000	0.000	0.000	0.000	0.000
Ca	0.007	0.010	0.001	0.000	0.000	0.005	0.000	0.003	0.007	0.013	0.006
P	1.022	0.997	1.000	1.017	1.002	1.006	1.020	0.984	1.003	1.025	1.027
F	0.044	0.041	0.032	0.050	0.045	0.044	0.031	0.047	0.038	0.050	0.046
Si	0.000	0.013	0.004	0.000	0.000	0.008	0.000	0.031	0.008	0.000	0.000
Pb	0.000	0.000	0.000	0.000	0.000	0.000	0.000	0.000	0.000	0.000	0.000
Fe	0.011	0.037	0.046	0.006	0.000	0.005	0.000	0.003	0.010	0.011	0.006
Total	1.974	1.994	2.000	1.971	1.981	1.977	1.973	1.983	1.984	1.972	1.968

Appendix 2.9: Continued

Unit	**MHREO**					**A**					
Sample	15014	15014	15301	15013	15013	15020	15020	15020	15020	15020	15020
Nd_2O_3 (*wt. %*)	0.31	0.36	0.40	0.26	0.29	0.40	0.28	0.32	0.27	0.42	0.00
Sm_2O_3	1.34	0.61	0.76	0.88	1.23	1.34	0.50	0.36	0.53	0.90	1.05
Eu_2O_3	0.95	0.51	0.69	0.00	0.00	0.00	1.10	0.00	1.12	0.00	0.00
Gd_2O_3	6.21	2.93	5.47	4.07	4.71	5.14	4.02	4.01	3.70	5.88	5.39
Tb_2O_3	1.18	0.75	1.44	1.27	1.17	1.32	1.35	1.29	1.27	1.70	1.56
Dy_2O_3	7.62	5.46	10.57	9.86	7.10	10.02	10.12	9.42	11.54	11.67	10.70
Y_2O_3	39.10	43.84	34.90	38.01	38.85	37.42	37.61	38.98	35.64	35.18	36.76
Ho_2O_3	1.17	1.11	1.95	1.74	1.31	1.52	1.87	1.66	2.00	1.85	1.62
Er_2O_3	2.11	2.39	4.19	4.04	2.78	3.23	4.51	3.97	3.93	3.55	3.52
Tm_2O_3	0.22	0.34	0.48	0.52	0.37	0.37	0.46	0.44	0.45	0.40	0.39
Yb_2O_3	1.00	1.73	2.42	2.61	1.74	1.88	2.41	2.26	2.64	1.89	1.92
Lu_2O_3	0.11	0.24	0.23	0.28	0.22	0.22	0.24	0.29	0.29	0.20	0.20
ThO_2	0.26	1.25	0.36	0.18	0.58	0.50	0.00	0.00	0.00	0.53	0.61
UO_2	0.00	0.00	0.00	0.00	0.00	0.00	0.00	0.00	0.00	0.00	0.00
CaO	0.41	0.91	0.28	0.16	0.22	0.39	0.17	0.25	0.41	0.21	0.56
P_2O_5	37.98	36.42	34.86	35.46	34.74	35.43	35.55	36.07	35.76	34.45	34.74
F	0.36	0.60	0.36	0.63	0.53	0.69	0.75	0.59	0.00	0.00	0.00
SiO_2	0.28	1.22	0.16	0.00	0.00	0.00	0.00	0.00	0.00	0.00	0.00
PbO	0.00	0.00	0.00	0.00	0.00	0.00	0.00	0.00	0.00	0.00	0.00
FeO	0.45	0.35	0.07	0.21	1.55	0.18	0.16	0.23	0.17	0.25	0.45
-O=F	-0.15	-0.25	-0.15	-0.26	-0.22	-0.29	-0.32	-0.25	0.00	0.00	0.00
Total	100.88	100.75	99.43	99.89	97.16	99.74	100.78	99.90	99.71	99.08	99.45
						O = 4					
Nd (*apfu*)	0.004	0.004	0.005	0.003	0.004	0.005	0.003	0.004	0.003	0.005	0.000
Sm	0.015	0.007	0.009	0.010	0.014	0.015	0.006	0.004	0.006	0.011	0.012
Eu	0.010	0.006	0.008	0.000	0.000	0.000	0.013	0.000	0.013	0.000	0.000
Gd	0.066	0.031	0.062	0.045	0.053	0.057	0.044	0.044	0.041	0.068	0.061
Tb	0.012	0.008	0.016	0.014	0.013	0.015	0.015	0.014	0.014	0.019	0.018
Dy	0.079	0.056	0.116	0.107	0.078	0.108	0.109	0.101	0.126	0.130	0.118
Y	0.668	0.744	0.635	0.678	0.704	0.668	0.668	0.688	0.642	0.649	0.670
Ho	0.012	0.011	0.021	0.019	0.014	0.016	0.020	0.018	0.022	0.020	0.018
Er	0.021	0.024	0.045	0.043	0.030	0.034	0.047	0.041	0.042	0.039	0.038
Tm	0.002	0.003	0.005	0.005	0.004	0.004	0.005	0.005	0.005	0.004	0.004
Yb	0.010	0.017	0.025	0.027	0.018	0.019	0.025	0.023	0.027	0.020	0.020
Lu	0.001	0.002	0.002	0.003	0.002	0.002	0.002	0.003	0.003	0.002	0.002
Th	0.002	0.009	0.003	0.001	0.004	0.004	0.000	0.000	0.000	0.004	0.005
U	0.000	0.000	0.000	0.000	0.000	0.000	0.000	0.000	0.000	0.000	0.000
Ca	0.014	0.031	0.010	0.006	0.008	0.014	0.006	0.009	0.015	0.008	0.020
P	1.032	0.984	1.009	1.007	1.002	1.006	1.004	1.013	1.025	1.010	1.007
F	0.036	0.060	0.039	0.067	0.057	0.073	0.079	0.062	0.000	0.000	0.000
Si	0.009	0.039	0.005	0.000	0.000	0.000	0.000	0.000	0.000	0.000	0.000
Pb	0.000	0.000	0.000	0.000	0.000	0.000	0.000	0.000	0.000	0.000	0.000
Fe	0.012	0.009	0.002	0.006	0.044	0.005	0.004	0.006	0.005	0.007	0.013
Total	1.970	1.985	1.980	1.973	1.993	1.973	1.970	1.973	1.990	1.997	2.005

Appendix 2.9: Continued

Unit					**A**					
Sample	15024	15024	15024	15024	15024	15024	15024	15024	15024	15024
Nd_2O_3 (*wt. %*)	0.28	0.50	0.34	0.29	0.00	0.46	0.66	0.41	0.32	0.31
Sm_2O_3	0.40	1.14	1.05	0.69	0.79	1.37	1.13	0.83	0.83	1.06
Eu_2O_3	0.00	0.00	0.00	0.78	0.00	0.00	0.00	0.79	0.00	0.95
Gd_2O_3	3.41	4.03	4.86	4.35	4.20	4.05	3.95	4.03	4.56	4.82
Tb_2O_3	0.92	1.12	1.48	1.42	1.35	1.41	1.11	1.00	0.97	1.23
Dy_2O_3	6.89	7.51	9.28	8.23	8.01	6.66	7.53	7.78	8.77	9.55
Y_2O_3	46.37	38.35	38.17	39.18	39.33	40.60	39.27	39.13	37.00	37.06
Ho_2O_3	1.06	1.28	1.52	1.40	1.36	1.31	1.37	1.38	1.52	1.67
Er_2O_3	2.09	3.37	3.67	3.32	3.35	3.09	3.49	3.50	3.90	3.84
Tm_2O_3	0.00	0.39	0.50	0.37	0.37	0.38	0.49	0.47	0.50	0.54
Yb_2O_3	0.90	2.42	2.47	2.25	2.39	2.37	2.58	2.42	2.50	2.50
Lu_2O_3	0.27	0.35	0.41	0.48	0.48	0.33	0.41	0.32	0.35	0.23
ThO_2	0.00	1.11	0.23	0.28	0.45	1.52	1.57	0.28	0.32	0.00
UO_2	0.00	0.00	0.00	0.00	0.00	0.00	0.00	0.00	0.00	0.00
CaO	0.23	0.29	0.06	0.16	0.13	0.10	0.07	0.20	0.10	0.17
P_2O_5	37.00	34.45	35.21	36.16	36.24	35.97	35.94	34.87	36.61	34.39
F	0.74	0.79	0.57	0.69	0.56	0.52	0.82	0.52	0.69	0.58
SiO_2	0.00	0.00	0.00	0.00	0.00	0.00	0.00	0.00	0.00	0.00
PbO	0.00	0.00	0.00	0.00	0.00	0.00	0.00	0.00	0.00	0.00
FeO	0.00	0.47	0.42	0.42	0.28	0.34	0.19	0.17	0.82	1.04
-O=F	-0.31	-0.33	-0.24	-0.29	-0.23	-0.22	-0.34	-0.22	-0.29	-0.24
Total	100.23	97.22	100.00	100.17	99.06	100.25	100.22	97.87	99.45	99.67
					O = 4					
Nd (*apfu*)	0.003	0.006	0.004	0.003	0.000	0.005	0.008	0.005	0.004	0.004
Sm	0.004	0.013	0.012	0.008	0.009	0.016	0.013	0.010	0.009	0.012
Eu	0.000	0.000	0.000	0.009	0.000	0.000	0.000	0.009	0.000	0.011
Gd	0.036	0.046	0.054	0.048	0.046	0.044	0.043	0.045	0.050	0.054
Tb	0.010	0.013	0.016	0.015	0.015	0.015	0.012	0.011	0.011	0.014
Dy	0.071	0.083	0.101	0.088	0.086	0.071	0.080	0.085	0.093	0.105
Y	0.791	0.699	0.683	0.689	0.695	0.715	0.692	0.709	0.652	0.672
Ho	0.011	0.014	0.016	0.015	0.014	0.014	0.014	0.015	0.016	0.018
Er	0.021	0.036	0.039	0.034	0.035	0.032	0.036	0.037	0.041	0.041
Tm	0.000	0.004	0.005	0.004	0.004	0.004	0.005	0.005	0.005	0.006
Yb	0.009	0.025	0.025	0.023	0.024	0.024	0.026	0.025	0.025	0.026
Lu	0.003	0.004	0.004	0.005	0.005	0.003	0.004	0.003	0.003	0.002
Th	0.000	0.009	0.002	0.002	0.003	0.011	0.012	0.002	0.002	0.000
U	0.000	0.000	0.000	0.000	0.000	0.000	0.000	0.000	0.000	0.000
Ca	0.008	0.011	0.002	0.006	0.005	0.003	0.002	0.007	0.004	0.006
P	1.004	0.998	1.003	1.011	1.019	1.007	1.007	1.004	1.026	0.992
F	0.075	0.086	0.061	0.072	0.059	0.055	0.086	0.056	0.072	0.062
Si	0.000	0.000	0.000	0.000	0.000	0.000	0.000	0.000	0.000	0.000
Pb	0.000	0.000	0.000	0.000	0.000	0.000	0.000	0.000	0.000	0.000
Fe	0.000	0.014	0.012	0.012	0.008	0.010	0.005	0.005	0.023	0.030
Total	1.971	1.973	1.979	1.970	1.968	1.975	1.961	1.979	1.963	1.993

Appendix 2.9: Continued

Unit	**A**									
Sample	15024	15024	15024	15024	15026	15026	15026	16007	16007	16007
Nd_2O_3 (*wt. %*)	0.49	0.00	0.47	0.35	0.31	0.00	0.00	0.35	0.43	0.46
Sm_2O_3	1.39	1.10	1.44	1.13	0.61	0.73	0.69	1.67	1.92	1.54
Eu_2O_3	1.46	0.85	0.00	0.00	0.00	1.43	0.00	0.84	1.20	1.11
Gd_2O_3	5.12	4.95	4.41	5.19	5.19	4.63	6.48	5.71	5.66	5.15
Tb_2O_3	1.29	1.11	1.12	1.28	1.38	1.15	1.60	1.41	1.36	1.29
Dy_2O_3	9.83	9.01	8.59	9.33	11.49	9.27	11.30	9.27	8.52	8.15
Y_2O_3	36.49	36.37	37.33	38.50	36.99	36.31	37.12	34.49	34.55	35.55
Ho_2O_3	1.67	1.47	1.65	1.45	1.73	1.48	1.48	1.52	1.41	1.38
Er_2O_3	3.85	3.68	3.81	3.69	3.90	3.12	3.33	3.71	3.52	3.41
Tm_2O_3	0.46	0.46	0.48	0.48	0.42	0.39	0.41	0.47	0.49	0.50
Yb_2O_3	2.53	2.39	2.66	2.49	2.33	2.02	2.10	2.74	2.65	2.76
Lu_2O_3	0.31	0.23	0.31	0.21	0.18	0.18	0.18	0.23	0.25	0.29
ThO_2	0.57	0.18	1.29	0.51	0.51	1.20	0.51	1.70	2.77	1.72
UO_2	0.00	0.00	0.00	0.00	0.00	0.00	0.00	0.00	0.00	0.00
CaO	0.20	0.14	0.17	0.17	0.32	1.95	0.19	0.25	0.86	0.15
P_2O_5	34.06	35.36	35.23	35.37	33.63	34.35	33.73	34.16	34.02	35.08
F	0.00	0.60	0.66	0.60	0.58	0.63	0.68	0.43	0.37	0.39
SiO_2	0.00	0.00	0.00	0.00	0.00	0.00	0.00	0.29	0.48	0.32
PbO	0.00	0.00	0.00	0.00	0.00	0.00	0.00	0.27	0.00	0.00
FeO	0.49	0.78	0.44	0.00	0.43	0.74	0.44	0.57	0.14	0.07
-O=F	0.00	-0.25	-0.28	-0.25	-0.25	-0.27	-0.29	-0.18	-0.15	-0.16
Total	100.18	98.42	99.76	100.49	99.76	99.32	99.93	99.87	100.45	99.15
	O = 4									
Nd (*apfu*)	0.006	0.000	0.006	0.004	0.004	0.000	0.000	0.004	0.005	0.006
Sm	0.016	0.013	0.017	0.013	0.007	0.009	0.008	0.020	0.023	0.018
Eu	0.017	0.010	0.000	0.000	0.000	0.017	0.000	0.010	0.014	0.013
Gd	0.059	0.056	0.049	0.058	0.059	0.052	0.074	0.065	0.064	0.058
Tb	0.015	0.012	0.012	0.014	0.016	0.013	0.018	0.016	0.015	0.014
Dy	0.109	0.098	0.093	0.101	0.128	0.101	0.125	0.103	0.094	0.089
Y	0.670	0.656	0.669	0.686	0.679	0.656	0.679	0.631	0.629	0.643
Ho	0.018	0.016	0.018	0.015	0.019	0.016	0.016	0.017	0.015	0.015
Er	0.042	0.039	0.040	0.039	0.042	0.033	0.036	0.040	0.038	0.036
Tm	0.005	0.005	0.005	0.005	0.004	0.004	0.004	0.005	0.005	0.005
Yb	0.027	0.025	0.027	0.025	0.025	0.021	0.022	0.029	0.028	0.029
Lu	0.003	0.002	0.003	0.002	0.002	0.002	0.002	0.002	0.003	0.003
Th	0.004	0.001	0.010	0.004	0.004	0.009	0.004	0.013	0.022	0.013
U	0.000	0.000	0.000	0.000	0.000	0.000	0.000	0.000	0.000	0.000
Ca	0.007	0.005	0.006	0.006	0.012	0.071	0.007	0.009	0.031	0.005
P	0.995	1.014	1.005	1.002	0.982	0.986	0.981	0.994	0.986	1.010
F	0.000	0.064	0.071	0.063	0.064	0.068	0.074	0.047	0.040	0.042
Si	0.000	0.000	0.000	0.000	0.000	0.000	0.000	0.010	0.017	0.011
Pb	0.000	0.000	0.000	0.000	0.000	0.000	0.000	0.002	0.000	0.000
Fe	0.014	0.022	0.012	0.000	0.012	0.021	0.013	0.016	0.004	0.002
Total	2.009	1.974	1.973	1.975	1.994	2.010	1.989	1.987	1.993	1.972

Appendix 2.9: Continued

Unit					**A**					
Sample	16007	16007	16007	16007	16007	16007	16007	16007	16007	16007
Nd_2O_3 (*wt. %*)	0.00	0.40	0.00	0.00	0.00	0.50	0.39	0.00	0.29	0.00
Sm_2O_3	0.75	1.72	0.53	1.59	1.08	1.87	1.03	0.79	1.00	0.56
Eu_2O_3	0.46	1.30	0.00	1.06	0.96	0.94	0.44	0.57	0.84	0.38
Gd_2O_3	3.15	5.60	3.18	5.55	4.88	4.88	3.99	4.63	4.23	2.82
Tb_2O_3	1.15	1.35	1.00	1.33	1.37	1.07	0.97	1.13	1.33	1.07
Dy_2O_3	8.72	8.61	8.85	8.79	9.14	8.13	7.73	9.28	9.00	8.76
Y_2O_3	35.56	35.77	36.78	36.91	36.91	37.03	37.27	37.57	38.26	38.36
Ho_2O_3	1.96	1.47	1.81	1.39	1.70	1.31	1.44	1.55	1.70	1.70
Er_2O_3	4.82	3.47	4.97	3.61	3.99	3.74	3.49	3.99	3.84	4.34
Tm_2O_3	0.71	0.91	0.59	0.50	0.51	0.52	0.49	0.54	0.45	0.53
Yb_2O_3	4.08	2.69	3.85	2.85	2.86	2.82	2.66	3.05	2.79	3.42
Lu_2O_3	0.46	0.25	0.48	0.26	0.28	0.38	0.26	0.41	0.23	0.45
ThO_2	0.53	1.56	0.57	0.89	1.26	0.49	1.19	0.61	0.66	1.56
UO_2	0.00	0.00	0.00	0.00	0.00	0.00	0.00	0.00	0.00	0.00
CaO	0.16	0.17	0.56	0.07	0.26	0.23	2.21	0.14	0.12	0.41
P_2O_5	35.60	33.51	34.98	33.71	33.74	34.90	35.47	35.25	33.46	34.04
F	0.44	0.49	0.51	0.29	0.62	0.35	0.44	0.40	0.42	0.53
SiO_2	0.00	0.20	0.14	0.10	0.35	0.10	0.23	0.00	0.11	0.47
PbO	0.00	0.00	0.00	0.00	0.00	0.00	0.00	0.00	0.00	0.00
FeO	1.00	0.00	0.52	0.09	0.50	0.17	0.12	0.31	0.84	0.59
-O=F	-0.19	-0.21	-0.21	-0.12	-0.26	-0.15	-0.19	-0.17	-0.17	-0.22
Total	99.36	99.25	99.10	98.87	100.16	99.28	99.61	100.03	99.37	99.78
					O = 4					
Nd (*apfu*)	0.000	0.005	0.000	0.000	0.000	0.006	0.005	0.000	0.004	0.000
Sm	0.009	0.021	0.006	0.019	0.013	0.022	0.012	0.009	0.012	0.007
Eu	0.005	0.015	0.000	0.013	0.011	0.011	0.005	0.007	0.010	0.004
Gd	0.035	0.064	0.036	0.064	0.055	0.055	0.044	0.052	0.048	0.032
Tb	0.013	0.015	0.011	0.015	0.015	0.012	0.011	0.013	0.015	0.012
Dy	0.095	0.096	0.097	0.098	0.101	0.089	0.083	0.101	0.100	0.096
Y	0.639	0.661	0.664	0.682	0.672	0.671	0.660	0.675	0.703	0.693
Ho	0.021	0.016	0.020	0.015	0.018	0.014	0.015	0.017	0.019	0.018
Er	0.051	0.038	0.053	0.039	0.043	0.040	0.036	0.042	0.042	0.046
Tm	0.007	0.010	0.006	0.005	0.005	0.005	0.005	0.006	0.005	0.006
Yb	0.042	0.028	0.040	0.030	0.030	0.029	0.027	0.031	0.029	0.035
Lu	0.005	0.003	0.005	0.003	0.003	0.004	0.003	0.004	0.002	0.005
Th	0.004	0.012	0.004	0.007	0.010	0.004	0.009	0.005	0.005	0.012
U	0.000	0.000	0.000	0.000	0.000	0.000	0.000	0.000	0.000	0.000
Ca	0.006	0.006	0.020	0.002	0.009	0.008	0.079	0.005	0.005	0.015
P	1.018	0.985	1.004	0.992	0.977	1.005	1.000	1.007	0.978	0.979
F	0.047	0.054	0.055	0.032	0.068	0.037	0.046	0.043	0.045	0.057
Si	0.000	0.007	0.005	0.003	0.012	0.003	0.008	0.000	0.004	0.016
Pb	0.000	0.000	0.000	0.000	0.000	0.000	0.000	0.000	0.000	0.000
Fe	0.028	0.000	0.015	0.003	0.014	0.005	0.003	0.009	0.024	0.017
Total	1.979	1.985	1.985	1.992	1.990	1.984	2.004	1.982	2.004	1.993

Appendix 2.9: Continued

Unit	**A**			**B**						
Sample	16007	16007	16007	15018	15018	15018	15018	15018	15018	15018
Nd_2O_3 (*wt. %*)	0.00	0.00	0.30	0.00	0.00	0.00	0.36	0.30	0.00	0.00
Sm_2O_3	0.89	0.57	0.88	0.69	0.40	0.42	0.67	0.60	0.00	0.31
Eu_2O_3	0.92	0.47	0.65	0.00	0.00	0.00	0.86	0.00	0.00	0.00
Gd_2O_3	4.76	4.08	4.18	3.94	3.70	3.58	3.10	2.95	1.88	2.65
Tb_2O_3	0.99	1.23	1.15	1.11	1.38	1.13	1.02	0.90	0.69	0.88
Dy_2O_3	8.04	8.60	8.13	9.03	11.10	9.10	8.27	7.31	5.74	7.44
Y_2O_3	39.11	39.57	39.69	36.08	37.27	40.73	36.72	42.34	45.27	43.38
Ho_2O_3	1.51	1.61	1.55	1.53	1.97	1.58	1.56	1.41	1.25	1.52
Er_2O_3	3.83	3.64	3.65	3.80	4.98	3.55	3.32	3.30	3.95	4.18
Tm_2O_3	0.52	0.50	0.50	0.53	0.66	0.44	0.42	0.43	0.44	0.41
Yb_2O_3	2.97	2.84	2.68	2.72	3.37	2.42	2.28	2.39	2.31	2.22
Lu_2O_3	0.30	0.37	0.28	0.24	0.42	0.22	0.18	0.24	0.30	0.27
ThO_2	0.27	0.00	0.45	0.32	0.00	0.00	0.00	0.00	0.00	0.00
UO_2	0.00	0.00	0.00	0.00	0.00	0.00	0.00	0.00	0.00	0.00
CaO	0.04	0.07	0.25	1.33	0.34	0.41	0.33	0.19	0.72	0.14
P_2O_5	34.71	35.50	35.20	34.49	35.09	35.65	33.31	35.88	36.64	35.64
F	0.42	0.42	0.49	0.63	0.58	0.67	0.60	0.70	0.69	0.65
SiO_2	0.00	0.00	0.00	0.00	0.00	0.00	0.00	0.00	0.00	0.00
PbO	0.00	0.00	0.00	0.00	0.00	0.00	0.00	0.00	0.00	0.00
FeO	0.95	0.53	0.07	1.14	0.28	0.39	1.91	0.32	0.26	0.00
-O=F	-0.17	-0.18	-0.21	-0.26	-0.24	-0.28	-0.25	-0.29	-0.29	-0.27
Total	100.04	99.79	99.89	97.31	101.30	100.02	94.66	98.97	99.84	99.41
						O = 4				
Nd (*apfu*)	0.000	0.000	0.004	0.000	0.000	0.000	0.005	0.004	0.000	0.000
Sm	0.010	0.007	0.010	0.008	0.005	0.005	0.008	0.007	0.000	0.004
Eu	0.011	0.005	0.007	0.000	0.000	0.000	0.010	0.000	0.000	0.000
Gd	0.053	0.045	0.047	0.045	0.041	0.039	0.036	0.032	0.020	0.029
Tb	0.011	0.014	0.013	0.013	0.015	0.012	0.012	0.010	0.007	0.010
Dy	0.088	0.093	0.088	0.100	0.120	0.097	0.094	0.078	0.060	0.079
Y	0.704	0.705	0.709	0.658	0.666	0.718	0.689	0.745	0.778	0.764
Ho	0.016	0.017	0.017	0.017	0.021	0.017	0.018	0.015	0.013	0.016
Er	0.041	0.038	0.038	0.041	0.053	0.037	0.037	0.034	0.040	0.043
Tm	0.005	0.005	0.005	0.006	0.007	0.005	0.005	0.004	0.004	0.004
Yb	0.031	0.029	0.027	0.028	0.035	0.024	0.024	0.024	0.023	0.022
Lu	0.003	0.004	0.003	0.002	0.004	0.002	0.002	0.002	0.003	0.003
Th	0.002	0.000	0.003	0.002	0.000	0.000	0.000	0.000	0.000	0.000
U	0.000	0.000	0.000	0.000	0.000	0.000	0.000	0.000	0.000	0.000
Ca	0.001	0.002	0.009	0.049	0.012	0.014	0.013	0.007	0.025	0.005
P	0.993	1.006	1.000	1.000	0.998	1.000	0.994	1.004	1.002	0.998
F	0.044	0.044	0.052	0.068	0.062	0.070	0.067	0.073	0.070	0.067
Si	0.000	0.000	0.000	0.000	0.000	0.000	0.000	0.000	0.000	0.000
Pb	0.000	0.000	0.000	0.000	0.000	0.000	0.000	0.000	0.000	0.000
Fe	0.027	0.015	0.002	0.033	0.008	0.011	0.056	0.009	0.007	0.000
Total	1.996	1.985	1.982	2.000	1.984	1.982	2.001	1.974	1.982	1.977

Appendix 2.9: Continued

Unit			**B**		
Sample	15018	15018	15018	15018	15018
Nd_2O_3 (*wt. %*)	0.00	0.32	0.00	0.00	0.00
Sm_2O_3	0.29	1.02	0.00	0.00	0.37
Eu_2O_3	0.00	0.00	0.00	0.79	0.00
Gd_2O_3	2.45	4.98	2.57	3.22	2.39
Tb_2O_3	0.73	1.37	0.99	1.08	0.74
Dy_2O_3	7.73	8.99	8.36	9.15	6.89
Y_2O_3	42.42	37.77	43.55	42.11	38.90
Ho_2O_3	1.51	1.38	1.54	1.58	1.49
Er_2O_3	3.46	3.40	3.70	3.76	5.16
Tm_2O_3	0.40	0.51	0.49	0.47	0.70
Yb_2O_3	2.13	2.44	2.66	2.68	4.18
Lu_2O_3	0.19	0.27	0.30	0.36	0.52
ThO_2	0.00	0.55	0.00	0.00	0.20
UO_2	0.00	0.00	0.00	0.00	0.00
CaO	1.27	0.79	0.23	0.31	0.73
P_2O_5	35.78	35.42	36.26	35.98	35.59
F	0.66	0.57	0.62	0.60	0.81
SiO_2	0.00	0.00	0.00	0.00	0.00
PbO	0.00	0.00	0.00	0.00	0.00
FeO	0.48	0.57	0.31	0.37	1.12
-O=F	-0.28	-0.24	-0.26	-0.25	-0.34
Total	99.22	100.07	101.30	102.19	99.46
			O = 4		
Nd (*apfu*)	0.000	0.004	0.000	0.000	0.000
Sm	0.003	0.012	0.000	0.000	0.004
Eu	0.000	0.000	0.000	0.009	0.000
Gd	0.027	0.055	0.028	0.035	0.026
Tb	0.008	0.015	0.011	0.012	0.008
Dy	0.082	0.097	0.088	0.096	0.074
Y	0.743	0.672	0.754	0.731	0.688
Ho	0.016	0.015	0.016	0.016	0.016
Er	0.036	0.036	0.038	0.039	0.054
Tm	0.004	0.005	0.005	0.005	0.007
Yb	0.021	0.025	0.026	0.027	0.042
Lu	0.002	0.003	0.003	0.004	0.005
Th	0.000	0.004	0.000	0.000	0.001
U	0.000	0.000	0.000	0.000	0.000
Ca	0.045	0.028	0.008	0.011	0.026
P	0.996	1.003	0.998	0.994	1.001
F	0.068	0.060	0.063	0.062	0.085
Si	0.000	0.000	0.000	0.000	0.000
Pb	0.000	0.000	0.000	0.000	0.000
Fe	0.013	0.016	0.008	0.010	0.031
Total	1.995	1.988	1.982	1.987	1.985

Appendix 2.10: Carbon and oxygen isotope compositions ($\delta^{13}C$ and $\delta^{18}O$) of carbonate minerals in the different units of the Eldor Carbonatite Complex

Unit	**Mineral**	**$\delta^{13}C$ V-PDB**	**$\delta^{18}O$ V-SMOW**
Cal Carb 1	calcite	-5.44	7.94
	calcite	-4.49	8.90
	calcite	-5.22	8.89
	calcite	-5.06	9.53
	calcite	-5.33	7.73
Cal Carb 2	calcite	-5.35	8.47
	calcite	-5.46	8.85
	calcite	-5.42	9.03
	calcite	-5.19	8.11
	calcite	-5.38	7.49
	calcite	-5.26	9.45
	calcite	-5.07	9.76
	calcite	-5.36	8.18
Dol Carb	dol composite	-2.09	15.22
	dol composite	-0.49	15.89
	dol composite	-0.87	15.84
	dol composite	-1.96	15.68
	dol composite	-1.46	12.99
	dol composite	-1.19	15.17
	dol composite	-0.78	15.45
	dol composite	-0.60	16.41
	dol composite	-1.29	14.42
	dol composite	-1.17	16.05
BD zone	dol 1	-4.42	10.17
	dol 1	-4.62	9.57
	dol 1	-4.44	10.52
	dol 1	-4.39	9.92
	dol 1	-4.21	10.86
	dol 1	-4.29	9.14
	dol 1	-3.74	10.87
	dol 1	-3.82	10.21
	dol 1	-3.96	10.74
	dol 1	-3.77	10.36
	dol 1	-4.02	9.95
	dol 1	-3.53	10.62
	dol 1	-4.56	9.25
	dol 1	-4.51	9.62

Appendix 2.10: Continued

Unit	Mineral	$\delta^{13}C$ V-PDB	$\delta^{18}O$ V-SMOW
BD zone	dol 1	-4.48	9.20
	dol 1	-4.32	10.30
	dol 1	-4.62	9.14
	dol composite	-3.28	11.47
	dol composite	-2.88	12.81
	dol composite	-3.04	13.95
	dol composite	-2.10	15.44
	dol composite	-2.20	15.42
	dol composite	-2.04	14.70
	dol composite	-2.65	14.53
	dol composite	-2.01	15.28
	dol composite	-2.89	11.16
	dol composite	-2.51	11.98
	dol composite	-2.72	11.15
B zone	dol composite	-2.62	14.48
	dol composite	-0.94	17.72
	dol composite	-2.94	10.34
	dol composite	-2.53	14.83
	dol composite	-3.01	10.00
	dol composite	-2.00	16.34
	dol composite	-2.63	14.89
	dol composite	0.26	17.00
	dol composite	-2.83	12.10
	dol composite	-2.86	14.41
	dol composite	-1.57	17.47
	dol composite	-1.49	15.15
	dol composite	-3.17	13.56
	dol composite	-2.72	12.63
	dol composite	-2.41	13.18
	dol composite	-1.97	15.79
	dol composite	-2.76	14.40
	dol composite	-1.81	16.95
	dol composite	-2.24	13.84
	dol composite	-2.78	11.93
	dol composite	-2.80	12.37
	dol composite	-2.60	12.16

Appendix 2.10: Continued

Unit	**Mineral**	**$\delta^{13}C$ V-PDB**	**$\delta^{18}O$ V-SMOW**
A zone	dol composite	-2.68	15.41
	dol composite	-1.60	17.54
	dol composite	-2.37	15.57
	dol composite	-2.84	14.98
	dol composite	-2.44	16.28
	dol composite	-2.36	16.25
	dol composite	-2.32	15.47
	dol composite	-2.17	16.90
	dol composite	-1.91	15.39
	dol composite	-2.63	15.82
	dol composite	-2.37	15.00
	dol composite	-2.86	13.42
MHREO zone	siderite	-2.49	17.09
	siderite	-2.86	17.03
	siderite	-3.73	15.75
	siderite	-2.74	17.02
	siderite	-3.21	15.74
	siderite	-3.33	14.88
	siderite	-3.30	16.54
	siderite	-3.10	16.15
	siderite	-3.22	15.97

Appendix 3.1: Calculated mineral contributions (percent) to the individual REE for the MHREO zone

Mineral*	Ap	Fl	Carb	Mnz	REEflc	Xtm	Total
La	0.3	0.0	0.3	23	76	0.0	100
Ce	1	0.0	0.4	43	56	0.0	100
Pr	1	0.0	0.5	57	42	0.0	100
Nd	1	0.0	1	65	34	0.1	100
Sm	2	0.1	2	65	30	2	100
Eu	3	0.1	3	53	34	7	100
Gd	4	0.3	4	43	31	17	100
Tb	7	0.5	8	25	23	37	100
Dy	10	1	10	14	7	58	100
Y	11	6	12	8	14	50	100
Ho	12	1	14	3	3	67	100
Er	11	1	17	0.0	0.0	70	100
Tm	9	1	17	0.0	0.0	73	100
Yb	8	1	20	0.0	0.0	71	100
Lu	7	1	23	0.0	0.0	69	100

**Mineral species or group have been abbreviated as: Ap = fluorapatite, Fl = fluorite, Carb = calcite + dolomite + siderite, Mnz = monazite, REEflc = bastnäsite + synchysite, Xtm = xenotime*

Where the calculated value was < 1 %, one decimal place was used.

Appendix 3.2: Calculated mineral contributions (percent) to the individual REE for the A zone

Mineral*	Ap	Fl	Carb	Mnz	REEflc	Xtm	Total
La	0.0	0.0	0.2	69	30	0.0	100
Ce	0.0	0.0	0.3	72	27	0.0	100
Pr	0.0	0.0	0.6	74	25	0.0	100
Nd	0.0	0.0	1	75	24	0.0	100
Sm	0.0	0.4	3	74	20	3	100
Eu	0.0	0.9	5	67	18	9	100
Gd	0.0	1	6	60	15	18	100
Tb	0.1	3	8	41	11	36	100
Dy	0.1	6	12	10	8	65	100
Y	0.1	29	12	13	5	41	100
Ho	0.1	12	14	5	2	66	100
Er	0.1	16	15	0.0	0.0	69	100
Tm	0.1	15	14	0.0	0.0	71	100
Yb	0.1	2	19	0.0	0.0	79	100
Lu	0.0	19	19	0.0	0.0	62	100

**Mineral species or group have been abbreviated as: Ap = fluorapatite, Fl = fluorite, Carb = calcite + dolomite + siderite, Mnz = monazite, REEflc = bastnäsite + synchysite, Xtm = xenotime*

Where the calculated value was < 1 %, one decimal place was used.

Appendix 3.3: Calculated mineral contributions (percent) to the individual REE for the B zone

Mineral*	Ap	Fl	Carb	Mnz	REEflc	Xtm	Total
La	0.2	0.0	0.3	67	32	0.0	100
Ce	0.4	0.0	0.6	74	25	0.0	100
Pr	0.5	0.0	1	79	20	0.0	100
Nd	0.8	0.1	2	80	17	0.0	100
Sm	2	0.3	5	80	12	1	100
Eu	2	0.4	8	75	12	2	100
Gd	3	0.8	11	67	12	6	100
Tb	4	1	22	47	12	14	100
Dy	5	2	30	27	7	29	100
Y	7	10	32	23	5	24	100
Ho	7	2	45	12	2	32	100
Er	8	4	50	0.0	0.0	39	100
Tm	7	4	48	0.0	0.0	41	100
Yb	6	6	43	0.0	0.0	44	100
Lu	6	7	42	0.0	0.0	45	100

**Mineral species or group have been abbreviated as: Ap = fluorapatite, Fl = fluorite, Carb = calcite + dolomite + siderite, Mnz = monazite, REEflc = bastnäsite + synchysite, Xtm = xenotime*

Where the calculated value was < 1 %, one decimal place was used.

Appendix 3.4: Calculated mineral contributions (percent) to the individual REE for the BD zone

Mineral*	Ap	Fl	Carb	Mnz	REEflc	Xtm	Total
La	5	0.0	1	10	83	0.0	100
Ce	13	0.0	1	11	74	0.0	100
Pr	17	0.0	1	11	71	0.0	100
Nd	24	0.0	1	13	62	0.0	100
Sm	48	0.0	1	11	38	1	100
Eu	57	0.0	2	9	29	4	100
Gd	59	0.0	2	6	24	9	100
Tb	59	0.0	2	3	18	17	100
Dy	54	0.0	2	1	10	32	100
Y	58	0.3	3	1	5	33	100
Ho	58	0.1	3	0.3	4	35	100
Er	57	0.1	4	0.0	0.0	39	100
Tm	52	0.1	4	0.0	0.0	43	100
Yb	51	0.2	5	0.0	0.0	44	100
Lu	49	0.2	6	0.0	0.0	45	100

**Mineral species or group have been abbreviated as: Ap = fluorapatite, Fl = fluorite, Carb = calcite + dolomite + siderite, Mnz = monazite, REEflc = bastnäsite + synchysite, Xtm = xenotime*

Where the calculated value was < 1 %, one decimal place was used.

Appendix 4.1: Analytical conditions and standards used during Electron Microprobe analyses

	Clinopyroxene, Amphibole, Biotite		**Olivine**		**Magnetite**	
	Standards	Counting Time (s)	Standards	Counting Time (s)	Standards	Counting Time (s)
F	CaF2 (Muskrat Lake)	20		20		20
Na	Albite (Taylor)	20		20		20
Mg	Diopside (Taylor)	20	Olivine (Taylor)	20	Chromite (Taylor)	20
Si	Diopside (Taylor)	20	Olivine (Taylor)	20	Olivine (Taylor)	20
Al	Sanidine (Astimex)	20		20	Chromite (Taylor)	20
Cl	Tugtupite (Astimex)	20		20		20
K	Sanidine (Astimex)	20		20		20
Ca	Diopside (Taylor)	20		20		20
Ti	Rutile (Taylor)	20		20	Ilmenite (Smithsonian)	20
Cr	Chromite (Taylor)	20		20	Chromite (Taylor)	20
Fe	Hematite (Taylor)	20	Olivine (Taylor)	20	Hematite (Taylor)	20
Mn	Spessartine (Taylor)	20	Spessartine (Taylor)	20	Spessartine (Taylor)	20
Zn	Willemite (Taylor)	20	Willemite (Taylor)	20	Willemite (Taylor)	20
Sc	ScPO4 (Smithsonian)	40	ScPO4 (Smithsonian)	40	ScPO4 (Smithsonian)	40
Ni			NiO (Cameca)	40	NiO (Cameca)	40
Nb					Ilmenite (Smithsonian)	20
V					Vanadinite (Cameca)	20

Appendix 4.2: Mean major element oxide compositions and cation proportions of fayalite throughout the ferrosyenite intersected in drill hole 14026

Depth (m)	15	15.3	16.85	18.8	19.05	21.1	23.25	26.75	31.6	36
Sample	142601	142602	142603	142604	142605	142607	142610	142611	142613	142614
n	5	6	4	5	11	6	7	9	5	10
SiO_2 (*wt. %*)	29.68	29.42	29.82	29.98	28.94	30.11	30.16	29.09	30.18	29.62
MgO	0.92	1.04	1.23	0.99	1.10	1.08	1.21	1.01	1.15	1.12
FeO	66.10	65.98	66.12	66.45	66.11	66.42	66.13	66.10	66.31	65.85
MnO	3.00	2.91	2.98	2.92	2.95	2.97	2.93	3.00	2.91	2.95
NiO	bdl	bdl	bdl	bdl	bdl	bdl	bdl	bdl	bdl	bdl
ZnO	0.17	0.14	0.16	0.15	0.15	0.16	0.16	0.17	0.14	0.15
Sc_2O_3	bdl	bdl	bdl	bdl	bdl	bdl	bdl	bdl	bdl	bdl
Total	99.87	99.48	100.31	100.49	99.25	100.74	100.60	99.37	100.69	99.69
O = 4										
Si	1.00	1.00	1.00	1.00	0.99	1.00	1.01	0.99	1.01	1.00
Mg	0.05	0.05	0.06	0.05	0.06	0.05	0.06	0.05	0.06	0.06
Fe	1.86	1.87	1.85	1.86	1.88	1.85	1.84	1.88	1.85	1.86
Mn	0.09	0.08	0.08	0.08	0.09	0.08	0.08	0.09	0.08	0.08
Ni	bdl	bdl	bdl	bdl	bdl	bdl	bdl	bdl	bdl	bdl
Zn	0.00	0.00	0.00	0.00	0.00	0.00	0.00	0.00	0.00	0.00
Sc	bdl	bdl	bdl	bdl	bdl	bdl	bdl	bdl	bdl	bdl
Total	3.00	3.00	3.00	3.00	3.01	3.00	2.99	3.01	2.99	3.00
Mg#	0.024	0.027	0.032	0.026	0.029	0.028	0.032	0.027	0.030	0.029
Fa	93	93	93	93	93	93	93	93	93	93

Appendix 4.3: Mean major element oxide compositions of magnetite throughout the ferrosyenite intersected in drill hole 14026

Sample	n	SiO_2 (*wt. %*)	MgO	FeO	MnO	ZnO	Sc_2O_3	Al_2O_3	TiO_2	Total
142601	6	0.69	bdl	79.60	0.68	0.52	bdl	0.26	11.46	93.23
142602	7	0.24	bdl	80.58	0.64	0.12	bdl	0.45	11.18	93.26
142603	6	0.42	bdl	77.67	0.93	0.22	bdl	0.44	14.31	94.07
142604	6	0.10	bdl	79.31	1.05	0.12	bdl	0.25	13.35	94.24
142605	9	0.14	bdl	74.77	0.98	0.16	bdl	0.53	17.24	93.87
142607	6	0.10	bdl	81.00	0.67	0.14	bdl	0.31	11.74	94.01
142610	9	0.07	bdl	77.27	0.84	0.26	bdl	0.34	15.81	94.66
142611	8	0.25	bdl	76.46	0.92	0.08	bdl	0.44	15.22	93.42
142613	6	0.07	bdl	75.90	0.92	0.34	bdl	0.41	17.02	94.68
142614	9	0.06	bdl	79.66	0.72	0.23	bdl	0.42	12.58	93.73

Appendix 4.4: Formulae of mean primary amphibole and representative secondary amphibole throughout the ferrosyenite intersected in drill hole 14026

	Sample (Depth)	**142601 (15.00)**	**142602 (15.30)**	**142603 (16.85)**		**142604 (18.80)**	**142605 (19.05)**		**142607 (21.10)**	**142610 (23.25)**	**142611 (26.75)**	**142613 (31.60)**		**142614 (36.00)**	**16.85**	**19.05**
	Type (n)	1° (6)	1° (7)	1° (7)	T-1° (20)	1° (4)	1° (10)	T-1° (16)	1° (7)	1° (8)	1° (15)	1° (7)	T-1° (26)	1° (8)	2° (Rep)	2° (Rep)
T = 8	Si	6.549	6.568	6.543	6.587	6.591	6.531	6.606	6.552	6.549	6.535	6.485	6.602	6.543	7.360	6.660
	Al	1.451	1.432	1.417	1.413	1.409	1.469	1.394	1.448	1.425	1.465	1.505	1.398	1.457	0.535	1.340
	Ti			0.040						0.026		0.010			0.105	
C = 5	Ti	0.305	0.310	0.292	0.331	0.329	0.333	0.310	0.336	0.302	0.316	0.312	0.328	0.289	0.019	0.293
	Al		0.030		0.009	0.002	0.008	0.022	0.005		0.034		0.031	0.050		0.083
	Sc	0.006	0.005	0.007	0.008	0.007	0.007	0.007	0.006	0.007	0.007	0.006	0.007	0.007	0.026	0.014
	Fe^{3+}	0.779	0.691	0.797	0.703	0.700	0.756	0.678	0.731	0.756	0.714	0.794	0.640	0.678		0.419
	Zn	0.013	0.012	0.013	0.012	0.016	0.014	0.012	0.012	0.013	0.014	0.012	0.012	0.012	0.010	0.011
	Mn^{2+}	0.016	0.025	0.014	0.007	0.009	0.027	0.005	0.035	0.022	0.027	0.034	0.020	0.010	0.099	0.074
	Fe^{2+}	3.437	3.361	3.280	3.343	3.382	3.290	3.402	3.345	3.311	3.352	3.228	3.332	3.406	3.192	3.454
	Mg	0.444	0.564	0.597	0.587	0.555	0.566	0.564	0.529	0.589	0.537	0.614	0.630	0.548	0.818	0.651
B = 2	Mn^{2+}	0.065	0.050	0.067	0.078	0.071	0.057	0.072	0.047	0.056	0.057	0.043	0.057	0.065		0.013
	Ca	1.690	1.726	1.717	1.719	1.725	1.720	1.713	1.726	1.736	1.733	1.744	1.741	1.746	2.000	1.836
	Na	0.245	0.224	0.216	0.203	0.203	0.223	0.215	0.227	0.208	0.210	0.213	0.201	0.189		0.151
A ≤ 1	Ca														0.956	
	Na	0.605	0.617	0.604	0.590	0.596	0.609	0.601	0.622	0.615	0.614	0.626	0.612	0.607	0.418	0.692
	K	0.307	0.312	0.305	0.307	0.308	0.312	0.302	0.311	0.308	0.307	0.313	0.310	0.306	0.062	0.283
W = 2	OH	1.029	1.042	0.890	0.972	0.989	0.962	1.044	0.992	0.977	1.073	0.980	0.922	1.049	1.576	1.137
	F	0.320	0.300	0.406	0.331	0.310	0.331	0.294	0.296	0.318	0.260	0.340	0.382	0.347	0.169	0.241
	Cl	0.041	0.037	0.039	0.035	0.042	0.040	0.040	0.040	0.048	0.035	0.036	0.040	0.025	0.006	0.036
	O	0.610	0.621	0.665	0.662	0.659	0.667	0.621	0.672	0.657	0.633	0.644	0.657	0.578	0.249	0.587
	Total	15.912	15.927	15.909	15.897	15.903	15.922	15.903	15.932	15.923	15.922	15.939	15.921	15.913	15.6	15.974
	Species*	Ti-Hst	Ti-Hst	Hst	Hst	Ti-Hst	Ti-Hst	Ti-Hst	Ti-Hst	Ti-Hst	Ti-Hst	Ti-Hst	Ti-Hst	Hst	Ed	Prg

**Amphibole group mineral species are abbreviated as: Ti-Hst = Ti-rich hastingsite, Hst = hastingsite, Ed = ferro-edenite, Prg = ferro-pargasite*

Appendix 4.5: Mean major element oxide compositions and cation proportions of biotite throughout the ferrosyenite intersected in drill hole 14026

Sample (Depth)	**142601 (15.00)**	**142602 (15.30)**	**142604 (18.80)**	**142605 (19.05)**	**142607 (21.10)**	**142610 (23.25)**	**142611 (26.75)**	**142613 (31.6)**	**142614 (36.00)**
n	1	5	5	14	1	2	6	6	3
F	0.51	0.86	0.93	0.72	0.64	0.97	0.67	0.83	0.65
Na_2O	0.18	0.15	0.18	0.25	0.07	0.12	0.40	0.19	0.11
MgO	2.75	3.12	3.19	3.09	2.23	3.22	2.95	3.78	2.77
SiO_2	34.39	34.73	34.46	34.40	34.31	34.31	34.28	34.44	34.38
Al_2O_3	11.78	11.82	11.52	11.70	11.24	11.50	11.30	11.85	11.60
Cl	0.08	0.11	0.11	0.13	0.08	0.15	0.15	0.09	0.04
K_2O	8.87	8.56	8.49	8.57	8.84	8.66	7.94	8.01	8.56
CaO	0.03	0.06	0.07	0.05	0.02	0.06	0.13	0.18	0.02
TiO_2	4.41	4.68	4.70	4.92	6.14	4.29	4.11	4.54	4.27
FeO	32.50	32.21	32.11	31.86	32.79	32.51	33.16	31.16	33.06
MnO	0.24	0.25	0.23	0.24	0.17	0.26	0.28	0.24	0.25
ZnO	0.15	0.10	0.09	0.10	0.00	0.10	0.09	0.12	0.10
Sc_2O_3	bdl	bdl	bdl	bdl	bdl	bdl	bdl	bdl	bdl
Total	95.90	96.67	96.10	96.05	96.59	96.18	95.50	95.47	95.84
					O = 12				
F	0.13	0.22	0.24	0.19	0.17	0.26	0.18	0.22	0.17
Na	0.03	0.02	0.03	0.04	0.01	0.02	0.06	0.03	0.02
Mg	0.34	0.38	0.39	0.38	0.27	0.40	0.37	0.47	0.34
Si	2.85	2.86	2.86	2.85	2.83	2.86	2.87	2.85	2.86
Al	1.15	1.15	1.13	1.14	1.09	1.13	1.11	1.16	1.14
Cl	0.01	0.02	0.02	0.02	0.01	0.02	0.02	0.01	0.01
K	0.94	0.90	0.90	0.91	0.93	0.92	0.85	0.85	0.91
Ca	0.00	0.01	0.01	0.00	0.00	0.00	0.01	0.02	0.00
Ti	0.28	0.29	0.29	0.31	0.38	0.27	0.26	0.28	0.27
Fe	2.25	2.22	2.23	2.20	2.26	2.27	2.32	2.16	2.30
Mn	0.02	0.02	0.02	0.02	0.01	0.02	0.02	0.02	0.02
Zn	0.01	0.01	0.01	0.01	0.00	0.01	0.01	0.01	0.01
Sc	bdl	bdl	bdl	bdl	bdl	bdl	bdl	bdl	bdl
Total	7.857	7.855	7.870	7.852	7.801	7.907	7.870	7.836	7.855